Linear and nonlinear parametric hydrodynamic models for wave energy converters identified from recorded data

Simone Giorgi

A thesis submitted for the degree of
Doctor of Philosophy

Faculty of Science and Engineering
Electronic Engineering Department
Maynooth University

Supervisor: **Prof. John V. Ringwood**
Head of the Department: Dr. Ronan Farrell

July 2017

Table of Contents

Abstract

Ocean waves represent an important resource of renewable energy, which can provide a significant support to the development of more sustainable energy solutions and to the reduction of CO_2 emissions. The amount of extracted energy from the ocean waves can be increased by optimizing the geometry and the control strategy of the wave energy converter (WEC), which both require mathematical hydrodynamic models, able to correctly describe the WEC-fluid interaction. In general, the construction of a model is based on physical laws describing the system under investigation. The hydrodynamic laws are the foundation for a complete description of the WEC-fluid interaction, but their solution represents a very complex and challenging problem. Different approaches to hydrodynamic WEC-fluid interaction modelling, such as computational fluid dynamics (CFD) and linear potential theory (LPT), lead to different mathematical models, each one characterised by different accuracy and computational speed. Fully nonlinear CFD models are able to describe the full range of hydrodynamic effects, but are very computationally expensive. On the other hand, LPT is based on the strong assumptions of inviscid fluid, irrotational flow, small waves and small body motion, which completely remove the hydrodynamic nonlinearity of the WEC-fluid interaction. Linear models have good computational speed, but are not able to properly describe nonlinear hydrodynamic effects, which are relevant in some WEC power production conditions, since WECs are designed to operate over a wide range of wave amplitudes, experience large motions, and generate viscous drag and vortex shedding. The main objective of this thesis is to propose and investigate an alternative pragmatic framework, for hydrodynamic model construction, based on system identification methodologies. The goal is to obtain models which are between the CFD and LPT extremes, a good compromise able to describe the most important nonlinearities of the physical system, without requiring excessively computational time. The identified models remain sufficiently fast and simple to run in real-time. System identification techniques can 'inject' into the model only the information contained in the identification data; therefore, the models obtained from LPT data are not able to describe nonlinear hydrodynamic effects. In this thesis, instead of traditional LPT data, experimental wave tank data (both numerical wave tank (NWT), implemented with a CFD software package, and real wave tank (RWT)) are proposed for hydrodynamic model identification, since CFD-NWT and RWT data can contain the full range of nonlinear hydrodynamic effects. In this thesis, different typologies of wave tank experiments and excitation signals are investigated in order to generate informative data and reduce the experiment duration. Indeed, the reduction of the experiment duration represents an important advantage since, in the case of a CFD-NWT, the amount of computation time can become unsustainable whereas, in the case of a RWT, a set of long tank experiments corresponds to an increase of the facility renting costs.

Declaration of authorship

I, Simone Giorgi, declare that this thesis titled 'Linear and nonlinear parametric hydrodynamic models for wave energy converters identified from recorded data' and the work presented in it are my own. I confirm that:

- This work was done wholly or mainly while in candidature for a research degree at this University.
- Where any part of this thesis has previously been submitted for a degree or any other qualification at this University or any other institution, this has been clearly stated.
- Where I have consulted the published work of others, this is always clearly attributed.
- Where I have quoted from the work of others, the source is always given. With the exception of such quotations, this thesis is entirely my own work.
- I have acknowledged all main sources of help.
- Where the thesis is based on work done by myself jointly with others, I have made clear exactly what was done by others and what I have contributed myself.

Date: _____

Signature: _____

Acknowledgement

First of all, I would like to thank my supervisor Professor John Ringwood for the advices he gave me on any matter relating not only my research work, but also my technical English writing and presentation skills.

I would like to thank Josh Davidson for the closed collaboration we had over the course of this research, and for providing me the CFD-NWT data utilised in this thesis.

Thanks to Morten Jakobsen and the Aalborg University for providing me access to their data, recorded at the Coastal Ocean And Sediment Transport Laboratory of Plymouth University, and utilised in this thesis.

I would like to thank the present and past members of COER, who have provided stimulating conversations and enjoyable collaborations, over the course of this research: Francesco Paparella, Markel Penalba Retes, Giuseppe Giorgi, Thomas Kelly, Alexis Mérigaud, Giorgio Bacelli, Trong Tue Vu, Romain Genest, Jochem Weber, Davide Padeletti, Marco Guerrini, Andrej Rössling, Paula Garcia-Rosa, and Ronan Costello.

Thanks to Luca Puggini for our discussions regarding statistics and machine-learning.

I would like to thank Ann and Joanne, from the administration office, and John Maloco and Denis, from the technical staff, for their assistance during my stay at COER.

Acronyms

2D	Two dimensional.
3D	Three dimensional.
ANN	Artificial neural network.
ARX	Autoregressive with exogenous input.
BEM	Boundary element method.
BIEM	Boundary integral equation method.
BONL	Block-oriented nonlinear.
BVP	Boundary value problem.
CFD	Computational fluid dynamics.
COAST	Coastal ocean and sediment transport.
CT	Continuous time.
DoF	Degrees of Freedom.
DT	Discrete time.
EMEC	European marine energy centre.
FBO	Feedback block-oriented.
FDM	Finite difference method.
FEM	Finite element method.
FNPT	Fully nonlinear potential theory.
FSE	Free surface elevation.
FVM	Finite volume method.
GA	Genetic algorithm.
KGP	Kolmogorov-Gabor Polynomial.
LF	Loss function.
LPT	Linear potential theory.
LS	Least squares.
MAPE	Mean absolute percentage error.
MFSE	Mean free surface elevation.
MLP	Multi-layer perceptron.
MSE	Mean squared error.
MSS	Marine systems simulator.
NARX	Nonlinear autoregressive with exogenous input.
NLS	Nonlinear static.
NRMSE	Normalised root mean-squared error.
NVTD	Normalised validation training degradation.
NWT	Numerical wave tank.
ODE	Ordinary differential equation.
OWC	Oscillating water column.
PDE	Partial differential equation.
PDF	Probability density function.

PMF	Probability mass function.
PRBS	Pseudorandom binary signal
PTO	Power Take Off.
RARP	Random amplitude random period.
RBS	Random binary signal
RG	Regressor generator.
RMS	Root mean square.
ROC	Region of convergence.
RP	Regressor processing.
RWT	Real wave tank.
SI	System identification.
SUMT	Sequential unconstrained minimization technique.
VOF	Volume of fluid.
WEC	Wave energy converter.
WT	Wave tank.

List of symbols

A general convention adopted in this thesis is the use of the bold font style is used for multidimensional variables, such as matrices (e.g. $\mathbf{M}$ and $\mathbf{\Phi}$) and vectors (e.g $\mathbf{x}$ and $\boldsymbol{\theta}$).

Greek Symbols

α	Volume fraction.
$\gamma[.]$	DT model structure.
$\mathbf{\Gamma}^{(tot)}$	Generalised total force vector.
$\mathbf{\Gamma}_{fl}$	Generalised fluid-body force vector.
$\mathbf{\Gamma}_{g}$	Generalised gravitational force vector.
$\mathbf{\Gamma}_{pto}$	Generalised PTO force vector.
$\mathbf{\Gamma}_{m}$	Generalised mooring force vector.
Δ_{cyl}	Hydraulic cylinder displacement.
δ_k	Step size, at the k-th step, in a line search algorithm.
ΔV_b	Submerged body volume variation.
ε	Prediction error.
$\boldsymbol{\varepsilon}$	Prediction error vector.
ζ	Base function.
η	Free surface elevation.
$\eta \rightarrow f_e$	Family of all models having the FSE as input and the excitation force as output.
$\eta \rightarrow y$	Family of all models having the FSE as input and the body displacement as output.
$\overline{\eta}(\omega)$	Fourier transform of $\eta(t)$.
θ	Parameter.
$\boldsymbol{\theta}$	Parameter vector.
$\hat{\boldsymbol{\theta}}$	Estimated parameter vector.
$\boldsymbol{\theta}_{ann}$	Parameter vector of an ANN model.
$\boldsymbol{\theta}_{arx}$	Parameter vector of an ARX model.
$\boldsymbol{\theta}_{F_{arx}}$	Parameter vector of the ARX block of a FBO model.
$\boldsymbol{\theta}_{F_c}$	Parameter vector of the static block of a FBO model.
$\boldsymbol{\theta}_{H_{arx}}$	Parameter vector of the ARX block of a Hammerstein model.
$\boldsymbol{\theta}_{H_c}$	Parameter vector of the static block of a Hammerstein model.
$\boldsymbol{\theta}_{kgp}$	Parameter vector of a KGP model.
λ	Wavelength.
$\boldsymbol{\lambda}$	Lagrangian multiplier vector.
λ_{bv}	Bulk viscosity.
λ_j	Lagrangian multiplier.
μ	Shear viscosity.
$\boldsymbol{\nu}_k^{\nabla}$	Direction vector, at the k-th step, in a line search algorithm.
$\boldsymbol{\xi}$	Generalised position vector.
$\mathbf{\Xi}$	Viscous stress tensor.

ξ_n	Additive noise.
ρ	Water density.
ρ_α	Mixture water-air density.
ρ_a	Air density.
ρ_b	Body density.
$\mathbf{\Sigma}$	Total stress tensor.
τ	Number of data values utilised as initial conditions for DT models.
ϕ	Total velocity potential.
$\mathbf{\Phi}$	Regressor matrix.
ϕ_d	Diffraction velocity potential.
ϕ_i	Incident velocity potential.
ϕ_{ra}	Radiation velocity potential.
φ	Regressor.
$\boldsymbol{\varphi}$	Regressor vector.
$\boldsymbol{\varphi}_{arx}$	Regressor vector of the ARX model.
$\boldsymbol{\varphi}_{H_c}$	Regressor vector of the static block of the Hammerstein model.
$\boldsymbol{\varphi}_{kgp}$	Regressor vector of the KGP model.
Ψ	ANN activation function.
ω	Wave frequency.
ω_m	Resonant frequency.
ω_m^{BEM}	Resonant frequency calculated from BEM data.
ω_m^{WT}	Resonant frequency calculated from WT experiments.
ω_o	Undamped natural frequency.
ω_o^{BEM}	Undamped natural frequency calculated from BEM data.
ω_{od}	Damped natural frequency.
ω_{od}^{BEM}	Damped natural frequency calculated from BEM data.
ω_{od}^{NWT}	Damped natural frequency calculated from WT experiments.
ω_{od}^{WT}	Damped natural frequency calculated from WT experiments.
Ω	Body volume.
∇J	Gradient of the loss function.

Latin Symbols

A_c	Body characteristic area.
A_{cr}	Horizontal cross-sectional body area.
A_r	Rectangular pulse amplitude.
$A_r^{(max)}$	Maximum rectangular pulse amplitude.
$A_r^{(min)}$	Minimum rectangular pulse amplitude.
$Arg()$	Argument of a complex number.
A_w	Wave amplitude.
C	Unsteady Bernoulli constant.
C_j^{in}	Optimization inequality constraint.
$\mathbf{C}^{in}$	Optimization inequality constraint vector.
$\mathbb{C}$	Complex number set.
C_d	Drag viscous coefficient.
C_r	Crest factor.
c_v	Specific heat at constant volume.
dS	Infinitesimal surface element.
$d\Omega$	Infinitesimal body volume.
D_{cyl}	Hydraulic cylinder damping coefficient.
e	Energy.

$\tilde{\mathbf{f}}_{su}$	Surface force vector.
$\tilde{\mathbf{f}}_{\Omega}$	Per unit mass force vector.
f_{A_r}	PDF of A_r.
f_b	Buoyancy force.
f_{cyl}	Hydraulic cylinder force.
f_d	Diffraction force.
f_e	Excitation force.
f_{fk}	Froude-Krylov force.
f_{fl}	Total fluid-body force.
f_{fl}^{D}	Dynamic fluid-body force.
f_{fl}^{S}	Static fluid-body force.
f_g	Gravitational force.
f_{in}	Summation of f_e, f_m and f_{pto}
$f_{in} \rightarrow y$	Family of all models having f_{in} as input and the body displacement as output.
f_m	Mooring force.
f_{pto}	PTO force.
f_{ra}	Radiation force.
f_{re}	Restoring force.
f_{T_r}	PDF of T_r.
$\mathscr{F}[.]$	Fourier transform.
$\mathscr{F}^{-1}[.]$	Inverse Fourier transform.
g	Gravitational acceleration.
g_{ra}	Approximation of the reduced radiation impulse response function.
$G_{ra}(\omega)$	Approximation of the reduced radiation transfer function.
h	Water depth.
h_e	Excitation impulse response function.
$H_e(\omega)$	Excitation force.
$H_e^{(ul)}(\omega)$	Excitation force per unit length.
$H_{f_{in}\rightarrow y}(\omega)$	Transfer function of a $f_{in} \rightarrow y$ model.
$H_{f_{in}\rightarrow y}^{BEM}(\omega)$	Transfer function of a $f_{in} \rightarrow y$ model calculated from BEM data.
$H_{f_{in}\rightarrow y}^{WT}(\omega)$	Transfer function of a $f_{in} \rightarrow y$ model calculated from WT experiments.
$H_{\eta\rightarrow y}(\omega)$	Transfer function of a $\eta \rightarrow y$ model.
$H_{\eta\rightarrow y}^{BEM}(\omega)$	Transfer function of a $\eta \rightarrow y$ model calculated from BEM data.
h_{ra}	Reduced radiation impulse response function.
$H_{ra}(\omega)$	Reduced radiation transfer function.
H_s	Significant wave height.
i	Imaginary unit.
I	Moment of inertia.
$\mathbb{I}$	Imaginary number set.
$\mathbf{I}_3$	3×3 identity matrix.
$Im[.]$	Imaginary part of a complex number.
J	Loss function.
J_{ALF}	Augmented Lagrangian function.
k	Wave number.
K	Restoring coefficient.
K_{cyl}	Hydraulic cylinder restoring coefficient.
K_{dc}	DC gain.
k_T	Thermal conductivity.
$\mathscr{L}[.]$	Laplace transform.
$\mathscr{L}^{-1}[.]$	Inverse Laplace transform.
m_∞	Added mass at infinite frequency.
$m_a(\omega)$	Added mass.

$m_a^{(ul)}(\omega)$	Added mass per unit length.
M	Body mass.
$\mathbf{M}$	Body mass matrix.
$\mathbf{n}$	Unit normal vector.
N	Number of samples.
$N(\omega)$	Radiation resistance.
$N^{(ul)}(\omega)$	Radiation resistance per unit length.
$\mathbb{N}$	Natural number set.
$\widetilde{N}$	Last possible predicted DT model output.
n_1	Number of neurons in the ANN hidden layer 1.
n_2	Number of neurons in the ANN hidden layer 2.
n_a	AR model order.
n_b	Exogenous model order.
n_c	Static curve polynomial order.
N_c	Number of constraints.
n_d	Input delay time.
n_p	KGP polynomial order.
N_{par}	Number of parameters.
N_s	Number of sinusoids.
N_{sw}	Number of samples in a sweep period.
$Oxyz$	Global frame.
$O'x'y'z'$	Body-fixed local frame.
p	Total fluid pressure.
p_d	Dynamic fluid pressure.
p_s	Static fluid pressure.
p_i	Total fluid pressure of the incident wave.
q_j	Optimization shift.
$\mathbf{q}$	Optimization shift vector.
$\dot{q}$	Rate of volumetric heat addition per unit mass.
$\mathbf{r}$	Position vector.
R	Specific gas constant.
$\mathbf{r}_{co}$	Center of mass vector.
$\Re$	Real number set.
$Re[.]$	Real part of a complex number.
s	Laplace complex frequency.
S	Wetted body surface.
t	Time.
T_{fl}	Fluid temperature.
T_{od}^{WT}	Damped natural period calculated from WT experiments.
T_p	Peak period.
T_r	Rectangular pulse width.
$T_r^{(max)}$	Maximum rectangular pulse width.
$T_r^{(min)}$	Minimum rectangular pulse width.
T_s	Sampling period.
T_{sw}	Sweep period of a chirp signal.
u	Generic model input.
u_{peak}	Signal peak value.
u_{rms}	RMS value.
u_{rmse}	Effective RMS value.
$\mathbf{v}$	Fluid velocity vector.
v_b	Body velocity.
V_b	Submerged body volume.

V_b^0	Submerged body volume at equilibrium.
$w_i^{(out)}$	ANN weight of the i-th perceptron neuron of the linear output layer.
$w_{ij}^{(1)}$	ANN weight of the i-th perceptron neuron of the hidden layer 1.
$w_{ij}^{(2)}$	ANN weight of the i-th perceptron neuron of the hidden layer 2.
$\mathbf{x}$	State vector.
x_i	i-th state variable.
$\mathbf{x_s}$	State vector of the radiation sub-system.
y	Body displacement.
y_{RH}	Relative float heave displacement.
y_{zi}	Output zero-input component.
y_{zs}	Output zero-state component.
$Z_{ra}(\omega)$	Radiation impedance.

Chapter 1

Introduction

In the last two hundred years, the energy demand of the industrialised world has constantly grown, in order to cater for numerous human activities. The majority of the current energy consumption level is based on fossil fuels, which creates environmental problems (related to CO_2 emissions, climate change and pollution) and imposes the dependency of nations on fuel supply from other countries, in order to guarantee their political and economical stability [1] [2]. Renewable energy sources, such as wind, hydro, solar, ocean energy and biomass, represents a growing alternative to fossil fuels, since these resources will be available as long as the sun is shining. The Roadmap 2050 of the European Union states that EU nations should cut greenhouse gas emissions to 80% below 1990 levels, by 2050 [3].

The energy transported by ocean waves represents an important contribution to potentially provide a sustainable and endless renewable energy mix. Winds, blowing over the surface of the sea, create waves with an amplitude depending upon the wind speed, the distance of water over which it blows (the fetch) and the seafloor bathymetry. Therefore, wave energy resources are not uniformly spread around the globe, and are mainly concentrated between 40° and 60° latitude, in both hemispheres (i.e. Western coasts of Europe, North-America and Australia) [4]. Wave energy converters (WECs) are a new and rapidly growing technology, able to harness the energy from ocean waves and to convert it into electricity. Over the last 25 years, more than one thousand WEC prototypes have been developed but, despite this, WEC technology is not commercially viable yet, since development costs are particularly high, and is not technically reliable and economically attractive yet [4] [5]. However, research to improve and optimise WEC structures and control strategies, together with economics of scale, are expected to reduce the wave energy cost per kw, bringing it to a level which is comparable with other more mature renewable energy technologies, such as offshore wind. In the near future, the development of reliable WEC technology is expected to make countries more energetically self-sufficient and to contribute to the creation of innovation and employment.

The large number of WECs developed can be grouped depending on different properties and characteristics. A first criterion of classification is based on the size and direction of the device, with respect to the incoming wave [1] [4] [6].

• *Attenuator*. This type of WEC is a long structure, with the dominant horizontal dimension comparable with the wavelength of the incident wave field. The structure is located parallel to the wave direction and the wave, moving along the WEC, is attenuated.

• *Point-absorber*. The dimension of this type of WEC is significantly smaller than the incident wavelength; therefore, the scattered wave field can be neglected and the hydrodynamic force, on the body, is well approximated by the incident wave field only. A useful characteristic of point-absorbers is that they are able to harness energy, regardless of wave direction.

• *Terminator*. This type of WEC is a long structure, with a horizontal dimension comparable with the wavelength (similar to attenuators), with the predominant dimension oriented perpendicular to wave propagation direction.

A second criterion of classification is based on the distance of the WEC location from the coast [1] [4].
• *Onshore devices*. These WECs are located on shore and are integrated in breakwaters, dams or cliffs, providing easy installation and convenient maintenance access. Furthermore, these WECs do not need mooring systems nor long electric cables, with a consequent capital investment reduction. These WECs, by their nature, are terminators.
• *Nearshore devices*. These WECs are deployed in moderate water depths (10-25 m), in the proximity of the coast. They are often bottom mounted, but floating structures are not uncommon.
• *Offshore devices*. These WECs are floating or submerged devices (moored to the seafloor), deployed far from the shore in deep waters (more than 40 m depth). The significant distance from the coast increases maintenance and electric cable costs. Furthermore, the large wave amplitudes in the open sea create a problem for the survivability of the structure, which has to be able to sustain very high loads.
A third classification of WECs is based on their working principle.
• *Floating structures*. The fundamental component of this WEC is a floating body, moved by the waves. Usually, the float oscillates in heave, in pitch or in a combination of them.
• *Oscillating wave surge converters (or impact devices)*. These converters are articulated structures, located perpendicular to the wave direction (i.e. terminators), oscillating back and forth in surge, due to the wave impact.
• *Overtopping devices*. The basic idea of these kind of WECs is the conversion of the wave kinetic energy into potential energy. The water, running up over a ramp, is captured in a storage reservoir (located above the sea level) and then released to pass through a turbine, connected to a generator, to return into the sea.
• *Oscillating water column (OWC)*. These WECs are partially submerged hollow structures, where a large volume of water oscillates vertically in response to incident waves, working as a piston in a cylinder. The air, contained in the chamber, is compressed and decompressed by the water column and flows through a turbine, which is used to generate electricity.

1.1 Motivation

The use of mathematical models is crucial in many areas of science and engineering. Virtually, every system can be described by a mathematical model, which quantifies the relationship between input and output variables. Mathematical models are the foundation for the analysis, simulation, and design of systems. Once an accurate model of the system under investigation is developed, a computer can be programmed in order to emulate the system, by solving the mathematical model equations. Mathematical modelling of WECs has many uses, including simulation of device motion, power production assessment and as a basis for model based control design. In all these cases, it is important to describe how the body moves in the water, interacting with the waves propagating on the fluid surface. In general, the construction of a model is based on physical laws, which describe the system under investigation. The hydrodynamic laws are the foundation for a complete description of the WEC-fluid interaction, but their solution represents a very complex and challenging problem. Different approaches to WEC-fluid interaction modelling, such as computational fluid dynamics (CFD) and linear potential theory (LPT), lead to different mathematical models, each one characterised by different accuracy and computational speed. Fully nonlinear CFD models are able to describe the full range of hydrodynamic effects, but are very computationally expensive. On the other hand, LPT is based on the strong assumptions of inviscid fluid, irrotational flow, small waves and small body motion, which completely remove the hydrodynamic nonlinearity of the WEC-fluid interaction. Linear models have good computational speed, but are not able to properly describe nonlinear hydrodynamic effects, which are relevant in some WEC power production conditions, since WECs are designed to operate over a wide range of wave amplitudes, experience large motions, and generate viscous drag and vortex shedding. It is strongly desirable to develop hydrodynamic models with characteristics between the CFD and

LPT extremes; ideally, a good compromise able to describe the most important nonlinearities of the real system, without requiring excessive computational time.

1.2 Main objectives and contributions

The main objectives and novel contributions of this thesis are summarised as follows:

1. **Objective.** It is important to provide a review of the complexity of the hydrodynamic WEC-fluid interaction and of the different mathematical approaches already available to resolve it. The understanding of advantages and disadvantages of each methodology (such as accuracy and computational speed) is crucial in order to define the characteristics of a new and alternative strategy to resolve the problem. The review represents the first foundations layer of this thesis.
   Contribution. Chapter 2 presents a detailed review of the hydrodynamic WEC-fluid interaction problem and of the state-of-the-art methodologies to solve it. The main characteristics of models, based on Cummins' equation (and its extensions), CFD, LPT and fully nonlinear potential theory (FNPT), are reviewed.

2. **Objective.** The main objective of this thesis is to propose and test an alternative pragmatic framework for hydrodynamic model construction, based on system identification (SI) techniques, where models are determined from wave tank (WT) recorded data. The goal is to obtain models which are between CFD and LPT extremes, a good compromise able to describe the most important nonlinearities of the physical system, without requiring excessive computational time.
   Contribution. Chapters 3 and 4 propose a framework for hydrodynamic model identification, characterised by an iterative sequence of four steps (i.e. experiment design and data gathering, model order and structure selection, fitting criterion and identification algorithm selection, and model validation). At the end of the SI procedure, a hydrodynamic parametric model is provided. Work published in [7] [8] [9] [10].

3. **Objective.** In the context of wave energy modelling, SI is generally utilised for finding suitable low-order approximations to nonparametric impulse response or frequency response data, generated by LPT boundary element method (BEM) solvers. SI techniques can 'inject' into the model only the information contained in the identification data; therefore, since LPT is based on strong assumptions of inviscid fluid, irrotational flow, small waves and small body motion, the models obtained from LPT-BEM data are not able to describe nonlinear hydrodynamic effects. An important objective, for model identification, is the use of data containing information regarding the nonlinear hydrodynamic effects.
   Contribution. This thesis proposes the use of identification data, generated in a CFD numerical wave tank (NWT), or measured in a real wave tank (RWT), since NWT and RWT data can contain the full range of nonlinear hydrodynamic effects, described by the Navier-Stokes equations. In this thesis, the utilised CFD-NWT data are provided by Josh Davidson from COER, Maynooth University, and the utilised RWT data are provided by Morten Jakobsen from Aalborg University. Work published in [7] [8] [9] [10] [11] [12] [13] [14].

4. **Objective.** The identification of an accurate model requires the use of informative data, which are strongly dependent on the excitation signals utilised to influence the process during the experiment. Furthermore, by extending the duration of an experiment, usually, the amount of information contained in the data increases. On the other hand, the reduction of the experiment duration represents an important aspect since, in the case of a CFD-NWT, the amount of computation time can become unsustainable whereas, in the case of a RWT, a set of long tank experiments corresponds to an increase of the facility renting costs. An important objective is the development of WT experiment design criteria, in order to provide

informative identification data in a reduced experiment duration.
Contribution. Chapter 4 proposes different WT experiment typologies (i.e. preliminary, identification, free decay, input wave, input force and prescribed motion experiments) and describes the signal characteristics (i.e. the spectral content, amplitude range and amplitude distribution), in order to evaluate and improve the quality of an excitation signal. In particular, Chapter 4 proposes WT experiments, characterised by the use of an input power take off (PTO) force (applied directly to the WEC by an actuator), which provides a large freedom over the choice of the input signal and, at the same time, a shorter experiment duration. Chapter 4 proposes a variety of 'time-shrunk' input signals (characterised by a high concentration of information) which contain the wide range of frequencies and amplitudes, necessary to excite the system over the whole range of operation, in a more compacted time frame (i.e. random amplitude random period (RARP), multisine and chirp signals). Work published in [7] [8] [9] [10] [13].

5. **Objective.** Continuous time (CT) hydrodynamic model structures provide a good insight into system understanding since, usually, CT models are derived from physical laws and the identified model parameters are strongly related to the physical system properties. An important aspect of any identification problem is the use of prior available information regarding the system under study, which is, in this thesis, a body floating on water, characterised by the properties of stability and passivity. Therefore, an objective is that the identified model inherits these properties, in order to ensure compatibility with the real system. In the wave energy literature, passivity and stability are not enforced as constraints during the model identification with LPT data, and only post identification methodologies are proposed, thus obtaining suboptimal solutions.
Contribution. In Chapter 5, new a-priori constraints on the parameters are introduced in the optimisation, in order to guarantee the stability and passivity of the identified CT linear models. Work published in [9] [11].

6. **Objective.** One of the main drawbacks of the use of CT model structures is the consequent requirement of nonconvex optimization strategies, which are necessary in order to identify the model parameter vector, since the loss function, associated with the CT model structure, is characterised by the presence of multiple local minima and, therefore, a strong sensitivity to the initial optimization seed. An important objective of this thesis is the presentation of hydrodynamic model structures, which are linear in the parameters, with the consequent employment of convex optimization strategies, in order to identify the parameter vector.
Contribution. Chapter 3 proposes the use of discrete time (DT) model structures, which have the advantage of providing greater flexibility (compared to CT models) in the construction of nonlinear input/output model structures, which are linear in the parameters (i.e. the Hammerstein, feedback block-oriented (FBO) and Kolmogorov-Gorov polynomial (KGP) model structures). Work published in [8] [9] [10] [12] [13].

7. **Objective.** The comparison between data generated by a WT (in the case of small wave and body displacements) and a LPT-BEM software package can be useful in order to verify the presence of nonlinearity in the WT experiments. In the case of a two-dimensional (2D) NWT, the comparison with three-dimensional (3D) BEM data is not straightforward; indeed, in a 2D NWT, the body geometry is an infinitely long horizontal bar, having a constant vertical cross-sectional area. An objective of this thesis is to propose a methodology to compare 2D NWT data with 3D BEM data.
Contribution. Chapter 4 proposes a methodology based on the transformation of the original 3D body geometry into a new 3D horizontal bar geometry (having an appropriate length), in order to compare 2D NWT data with 3D BEM.

8. **Objective.** An important aspect of nonlinear systems is that they have dynamics that are amplitude dependent, which means that, by changing the excitation signal, the system can show different characteristics and properties. Therefore, the WEC can show different attributes, depending on the sea state environment. In the case where experimental data sets are available from different sea states, an objective is to understand how to utilise the identification data. In order to obtain an accurate identified model on a particular sea state, it is useful to analyse if it is better to train the models only on the same sea state (to specialise the models only for the specific sea condition), or if it is always better to train the models by using all the information available, even if the extra information are from different sea states.
   Contribution. In Chapter 7, two different strategies are compared in the case of RWT data (collected by Morten Jakobsen, from Aalborg University, at the Coastal Ocean And Sediment Transport Laboratory of Plymouth University), in order to obtain accurate models, able to generalize on fresh validation data. With single training, for each model structure, a different parameter vector is identified for each available sea state; with mixed training, for each model structure, a unique parameter vector is identified and utilised to describe the behaviour of the WEC in any sea condition.

1.2.1 List of publications

• S. Giorgi, J. Davidson, J. V. Ringwood, 'Identification of wave energy device models from numerical wave tank data - Part 2: Data-based model determination', IEEE Transactions on Sustainable Energy, 2016 [8].

• J. Davidson, S. Giorgi, and J. V. Ringwood, 'Identification of wave energy device models from numerical wave tank data - Part 1: Numerical wave tank identification tests', IEEE Transactions on Sustainable Energy, 2016 [7].

• J. V. Ringwood, J. Davidson, S. Giorgi, 'System identification', Book chapter of 'Numerical Modelling of Wave Energy Converters: State-of-the-Art Techniques for Single Devices and Arrays', Elsevier Science & Technology Books, 2016 [9].

• J. Davidson, S. Giorgi, and J. V. Ringwood, 'Linear parametric hydrodynamic models for ocean wave energy converters identified from numerical wave tank experiments', Ocean Engineering, 2015 [11].

• S. Giorgi, J. Davidson, and J. V. Ringwood, 'Identification of nonlinear excitation force kernels using numerical wave tank experiments', in Proceedings of the 9th European Wave and Tidal Energy Conference, 2015 [12].

• J. V. Ringwood, J. Davidson, and S. Giorgi, 'Optimising numerical wave tank tests for the parametric identification of wave energy device models', in Proceedings of the 34th International Conference on Ocean, Offshore and Arctic Engineering, 2015 [10].

• J. Davidson, S. Giorgi, and J. V. Ringwood, 'Numerical wave tank identification of nonlinear discrete time hydrodynamic models', in Proceedings of the 1st International Conference on Renewable Energies Offshore, 2014 [13].

• J. Davidson, S. Giorgi, and J. Ringwood, 'Linear parametric hydrodynamic models based on numerical wave tank experiments', in Proceedings of the 10th European Wave and Tidal Energy Conference, 2013 [14].

1.3 Organisation of the thesis

The thesis is composed of 8 chapters, the subjects of which are outlined in the following part of this section. Each chapter is provided with a dedicated literature review, as the nature of the subjects of the chapters is substantially different.

• Chapter 2 summarises the background theory regarding the WEC-fluid hydrodynamic interaction problem, showing the main methodologies to solve it (such as CFD, LPT-BEM, FNPT and nonlinear Cummins' equation extensions), and their main advantages and limitations.

• In Chapter 3, the fundamental aspects of SI are introduced, and utilised to create a framework for WEC hydrodynamic model identification. The chapter proposes different CT and DT WEC hydrodynamic models, together with convex and nonconvex optimization techniques, utilised for the estimation of model parameter vectors.

• In Chapter 4, a framework for WT experiment design (in order to obtain informative data for hydrodynamic model SI) is proposed. A set of different WT experiments is shown, together with different typologies of input excitation signals.

• In Chapter 5, a new methodology for CT linear hydrodynamic parametric model identification is presented, which is based on the use of free decay 3D CFD-NWT data, instead of traditional LPT-BEM data. The methodology is applied to model the dynamics of a floating vertical cylinder.

• In Chapter 6, the developed SI framework is applied in four different case studies, in order to identify DT hydrodynamic models. The utilised data are generated in 2D and 3D CFD-NWTs. Details of the experimental data, model structures and model validation are shown.

• In Chapter 7, the SI framework, already applied to NWT data, is broadened to the context of data generated in a RWT, analysing the performance of identified linear and nonlinear models. The data utilised are generated in hydrodynamic tests, carried out on a scaled WEC point-absorber, at the COAST Laboratory of Plymouth University.

• The thesis is concluded in Chapter 8 with a summary and a discussion on the contributions and results, as well as a discussion on future work.

Chapter 2

Current hydrodynamic WEC models (background)

2.1 Introduction

The WECs deployed in water, interacting with the incoming waves, are subject to hydrodynamic forces, which induce alternating motion of the WEC structures. The energy, transported by the waves, is transferred to the WEC in the form of kinetic and potential energy, which are partially extracted, by electrical or hydraulic power take off (PTO) systems. The amount of extracted energy can be increased by optimizing the WEC shape and the WEC control strategy, both strongly related to the complex interaction between the water and the WEC. Therefore, it is crucial to construct mathematical hydrodynamic models, able to correctly describe the WEC as a rigid-body, interacting with the forces applied by the water, gravity, the mooring and PTO systems. Consider a rigid-body of mass, M, bounded by a surface, S, which encloses a volume Ω. The kinematic body description needs two different coordinate system frames: a global (also called inertial or absolute) frame, $Oxyz$, and a body-fixed local (also called relative) frame, $O'x'y'z'$. The body position is described as the position of the local frame with respect to the global frame, using the generalised position vector $\boldsymbol{\xi} = (x, y, z, \varphi, \theta, \psi)^T \in \Re^{6\times 1}$, where the first three coordinates represent the body translations and the last three the body rotations (see Fig. 2.1). The minimal number of independent coordinates, necessary to uniquely specify the position and orientation of the body, is called the number of degrees of freedom (DoF) of the system (if the body is unconstrained, the

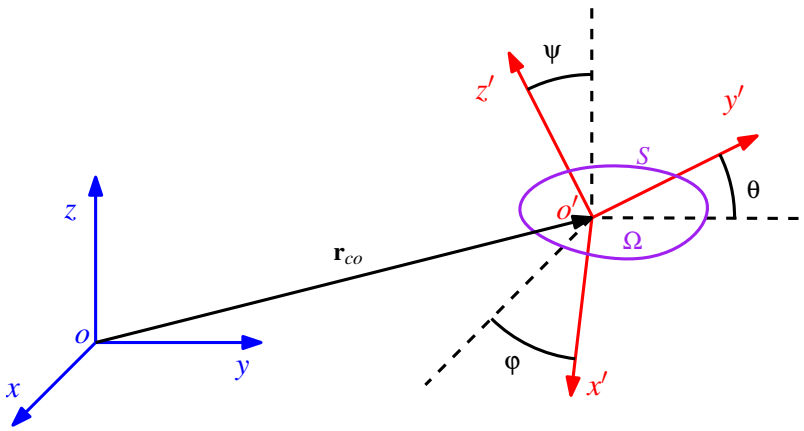

Figure 2.1: The global frame, $Oxyz$, and the body-fixed local frame, $O'x'y'z'$, are used to describe the kinematic of a rigid-body, bounded by a surface, S, which encloses a volume Ω.

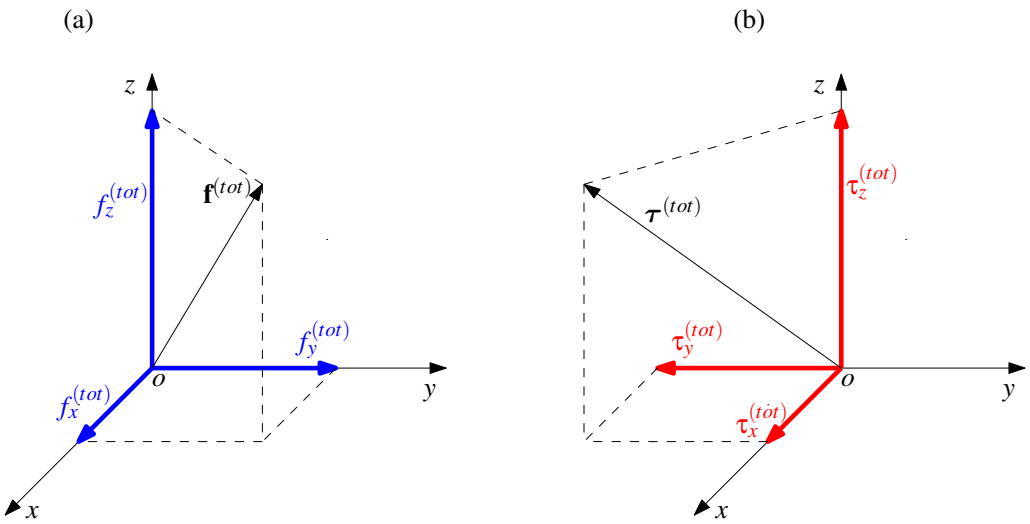

Figure 2.2: Graphical representation of (a) The total external force $\mathbf{f}^{(tot)} = (f_x^{(tot)}, f_y^{(tot)}, f_z^{(tot)})$ applied on the body (b) The total external force moment (torque) $\boldsymbol{\tau}^{(tot)} = (\tau_x^{(tot)}, \tau_y^{(tot)}, \tau_z^{(tot)})$ applied on the body.

number of DoF is six) [15]. The center of mass of the body with respect to the global frame is defined as:

$$\mathbf{r}_{co} = \frac{1}{M} \int_{\Omega} \rho_b(\mathbf{r}) \mathbf{r} d\Omega \tag{2.1}$$

where $\mathbf{r}$ is the position vector of the infinitesimal body volume $d\Omega$ and ρ_b is the body density (in general ρ_b is a function of the position $\mathbf{r}$). In the case where the origin of the local frame is located at the center of mass of the body, the body dynamics are described by Newton-Euler equations, which in matrix form are [15][16] [17] [18]:

$$\mathbf{M}\ddot{\boldsymbol{\xi}}(t) = \boldsymbol{\Gamma}^{(tot)}(t) \tag{2.2}$$

where:

$$\mathbf{M} = \begin{bmatrix} M & 0 & 0 & 0 & 0 & 0 \\ 0 & M & 0 & 0 & 0 & 0 \\ 0 & 0 & M & 0 & 0 & 0 \\ 0 & 0 & 0 & I_{xx} & -I_{xy} & -I_{xz} \\ 0 & 0 & 0 & -I_{yx} & I_{yy} & -I_{yz} \\ 0 & 0 & 0 & -I_{zx} & -I_{zy} & I_{zz} \end{bmatrix} \tag{2.3}$$

is the body mass matrix, I_{ij} are the moments of inertia about the x ,y and z axes (with $i = j$), I_{ij} are the products of inertia of the rigid-body, with respect to the center of mass (with $i \neq j$), $\boldsymbol{\Gamma}^{(tot)} = (f_x^{(tot)}, f_y^{(tot)}, f_z^{(tot)}, \tau_x^{(tot)}, \tau_y^{(tot)}, \tau_z^{(tot)})^T$ is a 6×1 generalised total force vector, where $f_x^{(tot)}$, $f_y^{(tot)}$ and $f_z^{(tot)}$ are the components of the total external force, $\mathbf{f}^{(tot)}$, applied on the body and $\tau_x^{(tot)}$, $\tau_y^{(tot)}$ and $\tau_z^{(tot)}$ are the components of the total external force moment (torque), $\boldsymbol{\tau}^{(tot)}$, acting on the body, with respect to the origin of the global frame (see Fig. 2.2). The WEC can be seen as a rigid-body, mainly subject to the following generalised forces: a fluid force applied from the water to the body, $\boldsymbol{\Gamma}_{fl}$, a gravitational force, $\boldsymbol{\Gamma}_g$, a PTO force, $\boldsymbol{\Gamma}_{pto}$ and a mooring force, $\boldsymbol{\Gamma}_m$. Therefore, equation (2.2) becomes:

$$\mathbf{M}\ddot{\boldsymbol{\xi}}(t) = \boldsymbol{\Gamma}_{fl}(t) + \boldsymbol{\Gamma}_g(t) + \boldsymbol{\Gamma}_{pto}(t) + \boldsymbol{\Gamma}_m(t). \tag{2.4}$$

Equation (2.4) represents the starting point of the modelling problem to be resolved. The generalised force, $\boldsymbol{\Gamma}_{fl}$, applied from the water to the body, depends on the body motion and on the flow

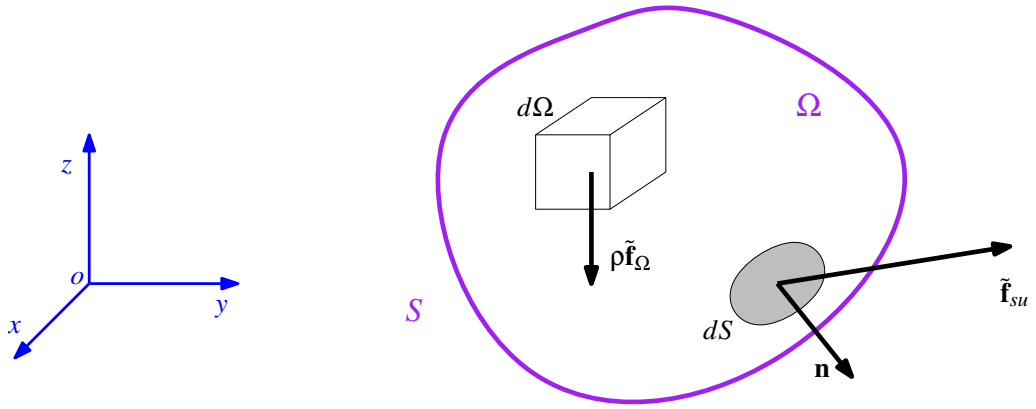

Figure 2.3: Given a portion of fluid bounded by the surface, S, containing the control volume Ω, the surrounding environment interacts with the portion of fluid, applying two different kinds of forces: the volume force, $\rho\tilde{\mathbf{f}}_\Omega$ and the surface force $\tilde{\mathbf{f}}_{su}$.

of the fluid around the body; therefore, the calculation of $\mathbf{\Gamma}_{fl}$ is particularly tedious and challenging. In this chapter, a hydrodynamic background is provided, together with the main modelling tools to solve the problem (2.4).

The outline of the chapter is as follows: in Section 2.2, the fundamental hydrodynamic laws are introduced, in order to formulate the general problem to be solved. In Section 2.3, the fully nonlinear CFD model is introduced and its main advantages and limitations underlined. In Section 2.4, LPT and its resolution utilising boundary element methods (BEMs) is presented, analysing the hypotheses that LPT is based on. The main advantages and limitations, in using LPT, are also provided. Section 2.5 presents a brief introduction to fully nonlinear potential theory (FNPT) and the use of BEMs to find a numerical solution. Furthermore, the hypotheses, the main advantages, and limitations of FNPT are presented. In Section 2.6.1, the linear Cummins' equation is provided, introducing the main techniques to obtain the associated parametric forms. In Section 2.6.2, different strategies, to extend Cummins' equation to more complex nonlinear models, are presented. Finally, conclusions are drawn in Section 2.7.

2.2 Hydrodynamics background

In the simulation and prediction of the WEC motion, it is fundamental to calculate the force applied from the water to the body (as seen is Section 2.1 with equation (2.4)). The description of the behaviour of a fluid requires the knowledge, in space and time, of the fluid pressure $p(x,y,z,t)$ and fluid velocity components $v_x(x,y,z,t)$, $v_y(x,y,z,t)$ and $v_z(x,y,z,t)$. The characterization of the fluid behaviour demands also the knowledge of fluid characteristics, like density, $\rho(x,y,z,t)$ and shear viscosity, $\mu(x,y,z,t)$. In the dynamic study of solid bodies, the momentum and energy conservation laws can be obtained given a quantity of matter (control mass approach). On the other hand, in the study of a fluid, it is not convenient to select a fraction of matter and describing the motion and the interaction with the surrounding environment. Instead, it is preferable to describe the fluid flow within a certain spatial region (control volume approach) [19] . The fundamental governing equations of fluid dynamics are the conservation laws for mass, momentum and energy, which are described, respectively, in Sections 2.2.2, 2.2.3 and 2.2.4.

2.2.1 External forces and moments applied on a region of fluid

Consider a global coordinate system frame, *Oxyz*, with the z-axis vertical and positive upwards (see Fig. 2.3). Given a portion of fluid bounded by the surface, S, containing the control volume Ω, the surrounding environment interacts with the portion of fluid, applying two different kinds of

forces [20] [21] [22] [23]:
• A volume force, $\rho\tilde{\mathbf{f}}_\Omega = \rho(\tilde{f}_{\Omega x}, \tilde{f}_{\Omega y}, \tilde{f}_{\Omega z})$, which acts without a physical contact, directly on each infinitesimal fluid volume $d\Omega$, contained in the volume Ω (e.g. gravitational, electric and magnetic forces). $\tilde{\mathbf{f}}_\Omega$ is a force per unit mass (or equivalently an acceleration) and $\rho\tilde{\mathbf{f}}_\Omega$ is a force per unit volume. If the only volume force present is the gravitational force, it follows that:

$$\tilde{\mathbf{f}}_\Omega = (0, 0, -g) \tag{2.5}$$

where g is the gravitational acceleration.
• A surface force, $\tilde{\mathbf{f}}_{su}$, which acts on each infinitesimal surface element dS belonging to S. The unit normal vector to the surface pointing outward is represented by $\mathbf{n}$ (see Fig. 2.3). $\tilde{\mathbf{f}}_{su}$ is generated by the normal pressure stresses and by the viscous stresses and it is a force per unit area. $\tilde{\mathbf{f}}_{su}$ can be expressed [24] as:

$$\tilde{\mathbf{f}}_{su} = \boldsymbol{\Sigma}\,\mathbf{n} \tag{2.6}$$

with

$$\boldsymbol{\Sigma} = \begin{bmatrix} \sigma_{11} & \sigma_{12} & \sigma_{13} \\ \sigma_{21} & \sigma_{22} & \sigma_{23} \\ \sigma_{31} & \sigma_{32} & \sigma_{33} \end{bmatrix} = -p\mathbf{I}_3 + \boldsymbol{\Xi} \tag{2.7}$$

where $\boldsymbol{\Sigma}$ is the total stress tensor, p is the total fluid pressure, $\mathbf{I}_3$ is a 3×3 identity matrix and $\boldsymbol{\Xi}$ is the viscous stress tensor. The diagonal elements of $\boldsymbol{\Sigma}$ represent the normal stress components (orthogonal to the surface) and both pressure and viscosity provide a contribution. The off-diagonal elements represent the shear stress components (tangential to the surface) and only the viscosity provides a contribution. A Newtonian fluid, by definition, has a linear relationship between viscous forces and the partial derivatives of the fluid velocity (the shear viscosity μ is constant) [23]. For an incompressible and Newtonian fluid (like water) [22] [23] [25]:

$$\boldsymbol{\Xi} = \begin{bmatrix} \delta_{11} & \delta_{12} & \delta_{13} \\ \delta_{21} & \delta_{22} & \delta_{23} \\ \delta_{31} & \delta_{32} & \delta_{33} \end{bmatrix} = 2\mu \begin{bmatrix} \frac{\partial v_x}{\partial x} & \frac{1}{2}\left(\frac{\partial v_x}{\partial y} + \frac{\partial v_y}{\partial x}\right) & \frac{1}{2}\left(\frac{\partial v_x}{\partial z} + \frac{\partial v_z}{\partial x}\right) \\ \frac{1}{2}\left(\frac{\partial v_y}{\partial x} + \frac{\partial v_x}{\partial y}\right) & \frac{\partial v_y}{\partial y} & \frac{1}{2}\left(\frac{\partial v_y}{\partial z} + \frac{\partial v_z}{\partial y}\right) \\ \frac{1}{2}\left(\frac{\partial v_z}{\partial x} + \frac{\partial v_x}{\partial z}\right) & \frac{1}{2}\left(\frac{\partial v_z}{\partial y} + \frac{\partial v_y}{\partial z}\right) & \frac{\partial v_z}{\partial z} \end{bmatrix} \tag{2.8}$$

It is possible to see in (2.8) that both shear (the off-diagonal elements) and normal (the diagonal elements) viscous stresses depend on velocity gradients in the flow. The total surface force and moment, applied from the surrounding environment on the fluid bounded by the surface S, are obtained by integrating the contribution from each infinitesimal surface element dS [20] :

$$\mathbf{f}_{su} = \int_S \tilde{\mathbf{f}}_{su}\, dS = \int_S \boldsymbol{\Sigma}\,\mathbf{n}\, dS \tag{2.9}$$

$$\boldsymbol{\tau}_{su} = \int_S \mathbf{r} \times \tilde{\mathbf{f}}_{su}\, dS = \int_S \mathbf{r} \times (\boldsymbol{\Sigma}\,\mathbf{n})\, dS \tag{2.10}$$

In the case of a motionless fluid (all the velocity components and their partial derivatives are zero) or for an inviscid fluid ($\mu = 0$), the viscous stress tensor is zero and the only contribution to the surface force is provided by the pressure, therefore, equations (2.9) and (2.10) become [26] [27] :

$$\mathbf{f}_{su}(t) = -\int_S p(x, y, z, t)\,\mathbf{n}\, dS \tag{2.11}$$

$$\boldsymbol{\tau}_{su}(t) = -\int_S p(x, y, z, t)\,(\mathbf{r} \times \mathbf{n})\, dS \tag{2.12}$$

It is important to underline that equations (2.9) and (2.10) can be also used to calculate the force and moment applied from the fluid to a rigid-body, bounded by the surface S [24]. Therefore, in equation (2.4), it is possible to introduce:

$$\boldsymbol{\Gamma}_{fl}(t) = (\mathbf{f}_{su}(t), \boldsymbol{\tau}_{su}(t)) \tag{2.13}$$

2.2.2 Conservation of mass

The first conservation law introduced is the conservation of mass (also called the continuity equation): the net mass flow out of the control volume, through the surface, is equal to the time rate of decrease of mass inside the control volume. Mathematically, the law of conservation of mass can be expressed [24] as:

$$\frac{\partial \rho}{\partial t} + \nabla \cdot (\rho \mathbf{v}) = 0 \tag{2.14}$$

where $\mathbf{v} = (v_x, v_y, v_z)$ is the water velocity vector.

2.2.3 Conservation of momentum (Navier-Stoke equations)

The Navier-Stoke equations are a consequence of Newton's 2nd law (force is equal to mass times acceleration) [23] :

$$\frac{\partial (\rho v_x)}{\partial t} + \nabla \cdot (\rho v_x \mathbf{v}) = -\frac{\partial p}{\partial x} + \frac{\partial \delta_{11}}{\partial x} + \frac{\partial \delta_{21}}{\partial y} + \frac{\partial \delta_{31}}{\partial z} + \rho \tilde{f}_{\Omega x} \tag{2.15}$$

$$\frac{\partial (\rho v_y)}{\partial t} + \nabla \cdot (\rho v_y \mathbf{v}) = -\frac{\partial p}{\partial y} + \frac{\partial \delta_{12}}{\partial x} + \frac{\partial \delta_{22}}{\partial y} + \frac{\partial \delta_{32}}{\partial z} + \rho \tilde{f}_{\Omega y} \tag{2.16}$$

$$\frac{\partial (\rho v_z)}{\partial t} + \nabla \cdot (\rho v_z \mathbf{v}) = -\frac{\partial p}{\partial z} + \frac{\partial \delta_{13}}{\partial x} + \frac{\partial \delta_{23}}{\partial y} + \frac{\partial \delta_{33}}{\partial z} + \rho \tilde{f}_{\Omega z} \tag{2.17}$$

where δ_{ij} are given by (2.8). If the only volume force acting is the gravitational force, $\tilde{\mathbf{f}}_\Omega = (\tilde{f}_{\Omega x}, \tilde{f}_{\Omega y}, \tilde{f}_{\Omega z})$ is given by (2.5).

2.2.4 Conservation of energy

The law of conservation of energy, $e(x,y,z,t)$, states: the rate of change of energy, inside the fluid element, is equal to the net flux of heat into the element, plus the rate of work done on the element due to volume and surface forces. In mathematical form, the law of conservation of energy can be expressed [23] as:

$$\begin{aligned}
&\frac{\partial (\rho e)}{\partial t} + \nabla \cdot (\rho e \mathbf{v}) = \rho \dot{q} + \frac{\partial}{\partial z}\Big(k_T \frac{\partial T_{fl}}{\partial z}\Big) + \frac{\partial}{\partial y}\Big(k_T \frac{\partial T_{fl}}{\partial y}\Big) + \frac{\partial}{\partial z}\Big(k_T \frac{\partial T_{fl}}{\partial z}\Big) - \\
&p\Big(\frac{\partial v_x}{\partial x} + \frac{\partial v_y}{\partial y} + \frac{\partial v_z}{\partial z}\Big) + \lambda_{bv}\Big(\frac{\partial v_x}{\partial x} + \frac{\partial v_y}{\partial y} + \frac{\partial v_z}{\partial z}\Big)^2 + \\
&\mu\Big[2\Big(\frac{\partial v_x}{\partial x}\Big)^2 + 2\Big(\frac{\partial v_y}{\partial y}\Big)^2 + 2\Big(\frac{\partial v_z}{\partial z}\Big)^2 + \Big(\frac{\partial v_x}{\partial y} + \frac{\partial v_y}{\partial x}\Big)^2 + \Big(\frac{\partial v_x}{\partial z} + \frac{\partial v_z}{\partial x}\Big)^2 + \Big(\frac{\partial v_y}{\partial z} + \frac{\partial v_z}{\partial y}\Big)^2\Big]
\end{aligned} \tag{2.18}$$

where $\dot{q}$ is the rate of volumetric heat addition per unit mass, $\dot{q}_x$, $\dot{q}_y$ and $\dot{q}_z$ are the heat flows transferred in the x, y and z directions, respectively, per unit time per unit area by thermal conduction, k_T is the thermal conductivity, λ_{bv} is the bulk viscosity coefficient and T_{fl} is the fluid temperature.

2.2.5 The hydrodynamic problem to be solved

The continuity equation (2.14), the Navier-Stoke equations (2.15), (2.16) and (2.17) and the energy equation (2.18) together represent a system of five partial differential equations in terms of seven unknown flow-field variables, ρ, p, v_x, v_y, v_x, T_{fl} and e. Therefore, the system requires two more equations to be solved, the thermal and caloric equations of state [20] [23] :

$$p = p(\rho, T_{fl}) \tag{2.19}$$

$$e = e(\rho, T_{fl}) \tag{2.20}$$

The most frequently used thermal and caloric equations are [23]:

$$p = \rho R T_{fl} \tag{2.21}$$

$$e = c_v T_{fl} \tag{2.22}$$

where R is the specific gas constant and c_v is the specific heat at constant volume. Now the system contains seven equations and seven unknown flow-field variables ρ, p, v_x, v_y, v_x, e and T_{fl}. The parameters λ_{bv}, μ and k_T are assumed known from experimental data [20]. It is important to underline that, under the hypothesis of an incompressible fluid, the energy equation is mathematically uncoupled from the continuity and Navier-Stoke equations [20]; therefore, the system of equations can be reduced to the continuity equation (2.14) and the Navier-Stoke equations (2.15), (2.16) and (2.17), obtaining a system of four differential equations and four unknown flow-field variables p, v_x, v_y and v_z [20]. No general closed-form solution exists, therefore, the use of numerical methods is required.

2.2.6 Bernoulli's equation

In the case where a fluid has an irrotational motion (the fluid elements do not rotate relative to their own center of gravity), it is possible to write $\nabla \times \mathbf{v} = 0$, which leads to the possibility of defining a velocity potential $\phi(x,y,z,t)$, which can be used to derive the fluid velocity everywhere [26] [28]:

$$\mathbf{v} = (v_x, v_y, v_z) = \nabla\phi \tag{2.23}$$

Adding the hypotheses of an inviscid ($\mu = 0$) and incompressible fluid (ρ is constant and not a function of time or space), from the Navier-Stoke equations (2.15), (2.16) and (2.17), it is possible to obtain the Bernoulli's equation for an unstationary flow, in which the velocity can be written in terms of the velocity potential [26] [21]:

$$\frac{\partial\phi}{\partial t} + \frac{1}{2}(\nabla\phi)^2 + \frac{p}{\rho} + gz = C(t) \tag{2.24}$$

where $C(t)$ is the unsteady Bernoulli constant and $(\nabla\phi)^2 = [\left(\frac{\partial\phi}{\partial x}\right)^2 + \left(\frac{\partial\phi}{\partial y}\right)^2 + \left(\frac{\partial\phi}{\partial z}\right)^2]$. $C(t)$ is a function of time but not of space and its value is associated with a related constant in ϕ, which does not affect the velocity vector (the gradient operator is insensitive to constant values). Therefore, $C(t)$ can be set to zero, and (2.24) becomes [22] [28] :

$$\frac{\partial\phi}{\partial t} + \frac{1}{2}(\nabla\phi)^2 + \frac{p}{\rho} + gz = 0 \tag{2.25}$$

Equation (2.25) can be rearranged as:

$$p = -\rho\left(\frac{\partial\phi}{\partial t} + \frac{1}{2}(\nabla\phi)^2 + gz\right) \tag{2.26}$$

From (2.26), it is possible to define the dynamic pressure, p_d, depending on the water velocity:

$$p_d = -\rho\left(\frac{\partial\phi}{\partial t} + \frac{1}{2}(\nabla\phi)^2\right) \tag{2.27}$$

and the static pressure, p_s:

$$p_s = -\rho g z \tag{2.28}$$

Linearizing Bernoulli's equation (2.26) leads to:

$$p = -\rho\frac{\partial\phi}{\partial t} - \rho g z \tag{2.29}$$

2.2.7 Buoyancy and restoring forces

Given a motionless floating body in still water, the hydrostatic force (also called the buoyancy force), f_b, applied from the water to the body, is provided by the integration of the static pressure, p_s, over the wetted body surface, S (see (2.11)). If z represents the vertical body displacement from its equilibrium position, considering the motionless body in different vertical displacement, the amount of submerged body volume is a function of the displacement [29]:

$$V_b(z) = V_b^0 + \Delta V_b(z) \tag{2.30}$$

where V_b^0 is the submerged body volume at equilibrium ($z = 0$), and $\Delta V_b(z)$ is the submerged body volume variation, obtained by moving the body from its equilibrium. Therefore,

$$f_b(z) = -\int_{S(z)} p_s \, \mathbf{n} \, dS = \rho g V_b(z) = \rho g\Big(V_b^0 + \Delta V_b(z)\Big) \tag{2.31}$$

At equilibrium, the buoyancy force and the gravitational force have the same intensity (but opposite directions):

$$\rho g V_b^0 = Mg \tag{2.32}$$

If the body has a constant horizontal cross-sectional area, A_{cr}, it follows, under the hypothesis that the body does not leave the water or that it is not completely submerged:

$$\Delta V_b(z) = -A_{cr} z \tag{2.33}$$

The negative sign takes into consideration the fact that, for positive (upward) body displacement, the amount of submerged body decreases. From (2.31), (2.32) and (2.33), it follows that:

$$f_b(z) = Mg - \rho g A_{cr} z \tag{2.34}$$

For a body with a variable horizontal cross-sectional area, in the case of a small body displacement (compared to the vertical size of the body), equation (2.31) can be approximated with the linear equation (2.34), where, in this case, A_{cr} is the horizontal cross-sectional area at the equilibrium position.

The restoring force, f_{re}, arises from the mismatch between the gravitational force, Mg, and f_b:

$$f_{re}(z) = f_b(z) - Mg = \rho g\Big(V_b^0 + \Delta V_b(z)\Big) - Mg = \rho g \Delta V_b(z) \tag{2.35}$$

If the body has a constant horizontal cross-sectional area, A_{cr}, from (2.33) and (2.35), it follows that:

$$f_{re}(z) = \rho g \Delta V_b(z) = -\rho g A_{cr} z = -Kz \tag{2.36}$$

where

$$K = \rho g A_{cr} \tag{2.37}$$

is the restoring coefficient, with $K > 0$. For a body with a variable horizontal cross-sectional area, if the body displacement is small compared to the vertical size of the body, the nonlinear restoring force (2.35) can be approximated with the linear (2.36), where A_{cr}, in this case, is the horizontal cross-sectional area at the equilibrium position.

2.3 CFD: fully nonlinear computationl fluid dynamics

CFD is a branch of hydrodynamics that produces the simulation of fluid dynamic phenomena on the basis of the conservation laws for mass (2.14), momentum (2.15), (2.16), (2.17), and energy (2.18). In general, these equations have no known analytical solution; however, they may be solved numerically, by discretizing the domains of space and time, in order to form a system of algebraic

equations, which are computer implementable. The result concerns the value of variables such as pressure, velocity, and temperature, at specific time instants and locations. In particular, CFD can be utilised to simulate (at great computational expense) the hydrodynamic force acting on an object floating in water, allowing fully nonlinear hydrodynamic calculations, including effects neglected by traditional linear velocity potential methods, such as viscosity, large wave amplitude, large body motion, green water and vortex shedding.

The main spatial discretization methods for CFD are mesh techniques such as the finite difference method (FDM), finite volume method (FVM) and finite element method (FEM) [30] [31]. The FDM is one of the first techniques developed to solve partial differential equations (PDEs). In each node of the grid, the differential equation is approximated replacing the partial derivatives with a truncated Taylor series expansion or a fitting polynomial. Therefore, each node of the grid is associated with an algebraic equation, in which, the unknown variable value at a node is expressed as a function of neighbouring nodes [19][31] [32]. The FDM is applied utilising a structured (or regular) grid; furthermore, the FDM is usually restricted to simple body geometries [30]. The advantages of FDM are simplicity and its easy implementation, on the other hand, the main disadvantage is that the conservation of the quantities, like mass and momentum, is not enforced. In the case of the FVM, the solution domain is subdivided into a finite number of contiguous control volumes. The conservation laws are applied at the centre of each control volume, obtaining an algebraic equation for each control volume, in which the unknown variable value is expressed as a function of neighbouring control volumes. The possibility of using any irregular mesh makes the FVM suitable for complex geometries [33]. The FEM, originally introduced by Turner [34], is similar to FVM, indeed, the domain is broken into a set of unstructured finite elements. In the FEM, in contrast to the FVM, the equations are multiplied by a weight function before they are integrated over the entire domain [19] [35] [36].

The study of floating objects involves the necessity of tracking, with good accuracy, the separating surface between water and air, $\eta(x,y,t)$, called the free surface elevation (FSE). The simulation of a moving fluid interface is very challenging in CFD, because the position of the free surface is not known in advance, but has to be calculated as part of the solution [19] [30]. In recent years, numerical techniques have been developed in order to describe the motion of a fluid with a moving free surface, like the volume of fluid (VOF) method, originally proposed by Hirt and Nichols [37]. The VOF method is based on the fact that two different fluids cannot occupy the same volume at the same time; therefore, each cell of the mesh contains a fraction α of water and a fraction $1-\alpha$ of air, where $\alpha \leq 1$. The non-dimensional fraction α is an additional unknown, introduced in the system of equations to solve. If the cell is filled with water, $\alpha = 1$, if the cell is filled with air, $\alpha = 0$ and if in the cell both fluids are present, $0 < \alpha < 1$ [30] [38]. The VOF method, in addition to the conservation laws for mass and momentum, has to resolve an equation for the volume fraction α of each cell [19] [39]. The density of the fluid in the cells with $0 < \alpha < 1$ (there is a mixture of water and air) is calculated as:

$$\rho_\alpha = \alpha\rho + (1-\alpha)\rho_a \tag{2.38}$$

where ρ_α is the density of the mixture of water and air, ρ is the water density and ρ_a is the air density [38]. The interface between air and water is represented by the cells with $0 < \alpha < 1$; therefore, it is important to have a mesh with a fine vertical resolution in the region where the free surface interface is likely to appear, to accurately locate the free surface. The VOF method has been shown to be an efficient and performing technique, and it has been implemented in OpenFOAM [30] and Ansys Fluent [40] CFD codes.

The CFD simulations are never completely exact (any model is an approximation of the real world); indeed, different sources of error are involved in the simulations. The most common sources of error in CFD are:

• The discretization methods, utilised to resolve the system of PDEs, replace a governing equation with an approximated time and space discretized version. Increasing the number of points of the grid, the discretization error reduces [24] [41].

• Errors are introduced when the chosen governing equations are not sufficiently representative of the studied system. The equations utilised to describe turbulence effects are a prime example [41].
• Another relevant source of error is the iteration (or convergence) error, which is the deviation of the calculated but not fully converged solution from the fully converged solution (both calculated on the same finite number of points on the grid). If the iterative calculation could continue indefinitely, the convergence error would be zero but, for obvious time constraints, the calculation is stopped once a preset level of tolerance is reached. The balance between the time constraint and the required accuracy has to be the result of a pragmatic compromise [41] [42].

The use of CFD, in the simulation of wave energy converters, has been validated against experimental data and shown to produce accurate results by many researchers. In [43] and [44], OpenFOAM models, describing OWCs, have been validated against wave tank (WT) experiments, exhibiting good agreement for air pressure and FSE measurements, in the case of monochromatic waves. In [45], the Blow Jet WEC is implemented in OpenFOAM and good agreement is shown for the pressure exerted on the WEC surface, between a model and experimental data. In [30], a fixed truncated cylinder, a moored buoy, the Wavestar WEC prototype device, and the Seabased WEC prototype device are studied in OpenFOAM. The simulations are validated against WT experimental data. In [46], a solver for wave generation and absorption is implemented. The simulations are verified against published experimental data or numerical results. In [47], an oscillating wave surge converter is implemented with the CFD package ANSYS FLUENT and simulations are validated against experimental measurements, showing good agreement. In [48], an oscillating wave surge converter is implemented in OpenFOAM and the simulations are compared with experimental data, showing good agreement, in both regular and irregular waves. In [49], a model for numerical prediction of the hydrodynamic forces on a point-absorber WEC (a point-absorber WEC has geometrical dimensions much smaller than the wavelength) is implemented in OpenFOAM. The radiation force, calculated in CFD, is validated against experimental results for different heave oscillation test conditions.

2.3.1 OpenFOAM

The variety of CFD software packages capable of implementing a numerical wave tank (NWT) are numerous, the choice of OpenFOAM [50], for the generation of data utilised for this thesis, is due to its flexibility, its open-source licensing, and its increasing popularity in the wave energy research community [51]. Furthermore, OpenFOAM is developed to run on open-source Unix/Linux systems, in this way entirely eliminating any software costs from the NWT implementation. OpenFOAM is basically a collection of C++ code managed by text-based commands, that offers full control over the software, giving the user freedom to modify it to suit their needs. For example: Jacobsen et al. [52] modified a fluid solver in order to generate and absorb waves, and Palm et al. [53] modified a rigid-body solver in order to couple it to an external solver for mooring loads. OpenFOAM is constantly improving and evolving, implementing libraries and toolboxes for different applications. The open-source nature of OpenFOAM often leads to the free sharing of useful toolboxes and libraries in the public domain.

OpenFOAM has been used in a wide range of science and engineering applications, such as heat transfer and chemical reactions. In recent years, examples of use of OpenFOAM for the implementation of NWTs for wave energy experiments are numerous; for example, Morgan et al. [54] used OpenFOAM to reproduce experimental results for the propagation of monochromatic waves over a submerged bar; Chenari et al. [55] modelled the propagation and breaking of regular waves; Li and Lin [56], using a two-dimensional NWT, finding good agreement with experimental and numerical results of other researchers, simulating the interaction between a body and monochromatic waves, in water of finite depth, with flat and sloping bottoms. A similar investigation, with irregular waves and varying water depth, was performed by Li and Lin [57]. Chen et al. [58] studied the performance of OpenFOAM, investigating nonlinear wave interactions with offshore structures, for a range of wave conditions. Furthermore, the performance of

a range of WECs, with different working principles, has been analysed with OpenFOAM: OWCs have been simulated by Iturrioz et al. [59] and Souza et al. [60]. Schmitt et al. [61] and Henry et al. [62] modelled, in OpenFOAM, the Oyster, the Aquamarine Power Ltd. oscillating wave surge converter. Akimoto et al. [63] simulated a rotational WEC, based on a drag-type vertical axis water turbine. A two-phase flow phenomena in horizontal pipelines was simulated by Thaker and Banerjee [64], in order to investigate WECs, such as the Vigor. Two-dimensional (2D) simulations of the Bombora, the membrane based WEC, has been performed by King [65]. The overtopping behaviour of the Wave Dragon device was simulated by Eskilsson et al. [66]. In [67], a latching control strategy is applied to a 0.125 m heave sphere in a three-dimensional (3D) OpenFOAM NWT.

2.3.2 Advantages and limitations of CFD-NWT

The main advantages of CFD-NWT models in comparison to RWT are:
• The WECs can be studied at full scale, eliminating scaling effects of real tank tests.
• A wide variety of excitation signals, including incident waves and forces directly applied to the device, can be implemented (as well as free response tests).
• The device can be constrained to different modes of motion without requiring mechanical restraints, which can add friction, alter the device dynamics and increase the costs.
• Signals can be passively measured without requiring physical sensor devices, which can alter the device or fluid dynamics and are subject to measurement error. Furthermore, no additive costs are necessary to acquire sensors and interface cards.
• Specialist equipment, including a prototype WEC device, is not required.
• In a NWT, the wave reflections can be effectively controlled by numerical absorption techniques.
• CFD produces detailed calculation of all relevant variables, such as pressure and fluid velocity, throughout the domain of interest.
However, NWTs are not without their drawbacks [9]:
• The chief disadvantage, over a conventional wave tank, is the excessively long time to perform the numerical computation of the response. Typical computation time can be up to 1000 times the simulation time (i.e. 1 s of simulation time takes 1000 s to compute). Therefore, a NWT experiment having a simulation time of 15 minutes, would require 10 days of computation time. Parallel computation can be used to reduce the computation time, indeed, the fluid domain is divided in regions and every region can be solved, almost independently, on separate computers [68].
• NWTs can take considerable experience to use well, in particular setting up a spatial mesh, which offers a reasonable compromise between computation time and accuracy.
• The pressure peaks, due to the impact between waves and the WEC, occur over short time scales; therefore, it is necessary to utilise small time steps, in order to accurately describe the pressure peaks, which increases the simulation time.

2.4 Linear potential theory and BEMs

The system of nonlinear PDEs, composed of the continuity equation (2.14) and the Navier-Stoke equations (2.15), (2.16), and (2.17), is difficult and time-consuming to solve numerically; therefore, some simplifying assumptions are introduced in order to obtain LPT. The present state of the art, in order to model the wave-WEC interaction, uses LPT in conjunction with BEMs, obtaining a solution with a satisfactory accuracy and a relatively low computation effort. In this section, LPT is briefly explained, underlining the hypotheses which it is based on.

Consider a body with a generic shape, floating in water and a global three-dimensional system of coordinates with the z-axis perpendicular to the free-surface, vertically upward and with its origin on the mean FSE (see Fig. 2.4). The waves are propagating in the x-axis positive direction. The FSE, $\eta(x,y,t)$, represents the elevation of the water free surface from its equilibrium position, being positive when the surface is above the x-y plane.

LPT is based upon the following assumptions regarding the fluid:

- The fluid is inviscid ($\mu = 0$); (2.39)

therefore, there are no viscous stresses applied on fluid elements, only normal pressure stresses are observed (see Section 2.2.1).

- The fluid motion is irrotational ($\nabla \times \mathbf{v} = 0$), (2.40)

which leads to $\mathbf{v} = (v_x, v_y, v_z) = \nabla\phi$ (see Section 2.2.6). It is useful to underline that, if an inviscid flow is initially irrotational, then it stays irrotational at all subsequent times [69].

- The fluid is incompressible (ρ is constant). (2.41)

Furthermore, LPT is based upon the following assumptions [24] [70]:

- The ratio of the wave amplitude, A_w, to the wavelength, λ, is small; therefore,

$$\frac{A_w}{\lambda} << 1 \tag{2.42}$$

- The amplitude of the body motion is much smaller than the dimension of the body (2.43)

Under hypotheses (2.40) and (2.41), the continuity equation (2.14) becomes the Laplace equation, in which the fluid velocity is described with the velocity potential [69] [71] :

$$\nabla^2\phi = 0 \tag{2.44}$$

Together with the Laplace equation (2.44), the flow has to satisfy some boundary conditions, defined at the water's free surface, at the sea bottom and at the body surface. At the water's free surface $z = \eta(x,y)$, the water pressure has to be equal to the atmospheric pressure; mathematically, the velocity potential has to satisfy [9] [71]:

$$\frac{\partial\phi}{\partial t} + \frac{1}{2}(\nabla\phi)^2 + g\eta = 0 \qquad (\text{at } z = \eta(x,y)) \tag{2.45}$$

The nonlinear equation (2.45) is called the nonlinear dynamic boundary condition. The second physical condition, imposed at the FSE, is that the water particles can not escape from the sea and, therefore, the component of the fluid velocity normal to the surface must equal the surface velocity. Mathematically, at $z = \eta(x,y)$, the velocity potential has to satisfy [9] [71]:

$$\frac{\partial\phi}{\partial z} = \frac{\partial\eta}{\partial t} + \frac{\partial\phi}{\partial x}\frac{\partial\eta}{\partial x} + \frac{\partial\phi}{\partial y}\frac{\partial\eta}{\partial y} \qquad (\text{at } z = \eta(x,y)) \tag{2.46}$$

The nonlinear equation (2.46) is called the kinematic boundary condition. The physical boundary condition for the wetted body surface imposes the impermeability of the body. Therefore, the component of the fluid velocity normal to the body surface, $\frac{\partial\phi}{\partial n}$, has to be equal to the body velocity normal to the body surface, u_n [9] [72] :

$$\frac{\partial\phi}{\partial n} = u_n \qquad (\text{on the wetted body surface } S) \tag{2.47}$$

The impermeable and flat seafloor conditions, at a depth equal to h, impose a vertical component of the fluid velocity, $\frac{\partial\phi}{\partial z}$, equal to zero, at $z = -h$ [9] [71] :

$$\frac{\partial\phi}{\partial z} = 0 \qquad (\text{at } z = -h) \tag{2.48}$$

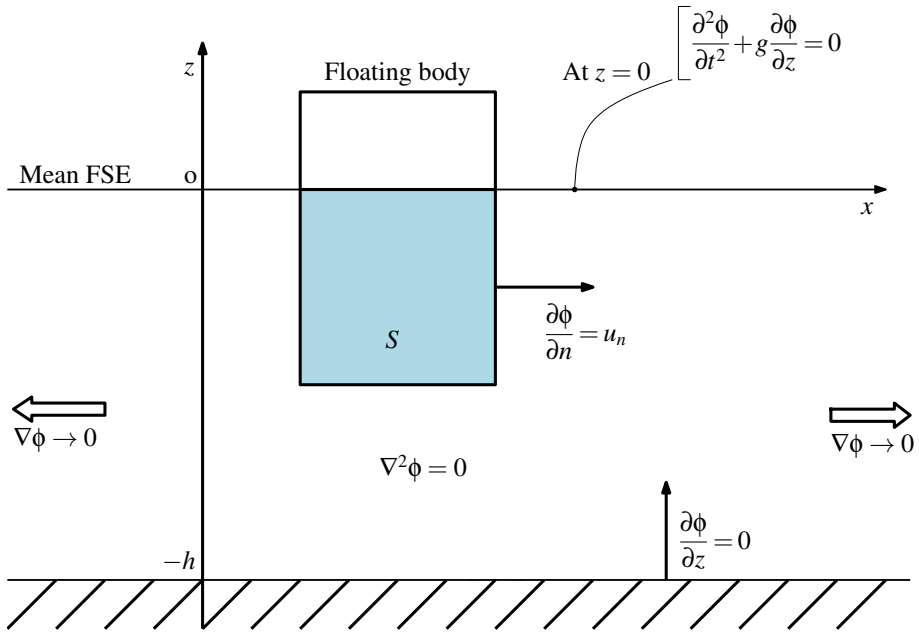

Figure 2.4: Graphical representation of the LPT-BVP in the time domain, described by the system of equations (2.44), (2.47), (2.48), (2.49) and (2.52).

The last physical condition imposes a decaying amplitude of the wave field, as the distance from the body increases [9] [71]:

$$\nabla\phi\to 0 \qquad (\text{at } \sqrt{x^2+y^2}\to\infty) \tag{2.49}$$

The system of equations (2.44), (2.45), (2.46), (2.47), (2.48) and (2.49) represents the FNPT boundary value problem (BVP) in the time domain.

In LPT, the nonlinear equations (2.45) and (2.46) are linearised under hypotheses (2.42) and (2.43) [24] [70]. Furthermore, in LPT, on the water's free surface, the boundary conditions are considered on the undisturbed FSE ($\eta(x,y,t)=0$ everywhere), instead of on the instantaneous FSE. Consequently, equations (2.45) and (2.46), at $z=0$, become [9]:

$$\frac{\partial\phi}{\partial t}+g\eta=0 \qquad (\text{at } z=0) \tag{2.50}$$

$$\frac{\partial\eta}{\partial t}=\frac{\partial\phi}{\partial z} \qquad (\text{at } z=0) \tag{2.51}$$

Equations (2.50) and (2.51) can be combined obtaining [72] [73]:

$$\frac{\partial^2\phi}{\partial t^2}+g\frac{\partial\phi}{\partial z}=0 \qquad (\text{at } z=0) \tag{2.52}$$

The system of equations (2.44), (2.47), (2.48), (2.49) and (2.52) represents the LPT-BVP in the time domain [28] and it is represented in Fig. 2.4. Once ϕ is known, the FSE can be obtained by rearranging equation (2.50) [73]:

$$\eta=-\frac{1}{g}\frac{\partial\phi}{\partial t} \tag{2.53}$$

2.4.1 Hydrodynamic problem decomposition

Under the hypotheses of LPT, the wave field surrounding a floating body can be described as a superposition of an incident, a diffracted and a radiated wave field [26] [74]. The incident wave field, ϕ_i, is defined as the wave propagating in the absence of the floating body. The diffracted wave field, ϕ_d, is a consequence of the interaction between the incident wave and the floating body, when the body is kept fixed at its equilibrium position. For the generation of the radiation wave field, ϕ_{ra}, the floating body is forced to oscillate due to an external force, in the absence of an incident wave field. Therefore, the total velocity potential, ϕ, can be obtained as:

$$\phi(x,y,z,t) = \phi_i(x,y,z,t) + \phi_d(x,y,z,t) + \phi_{ra}(x,y,z,t) \tag{2.54}$$

As explained in Section 2.2.1, in absence of viscous stress components, the force and moment applied from the fluid to the body are given by the integration of the total pressure over the wetted body surface, as described in (2.11) and (2.12). In LPT, the surface S corresponds to the motionless wetted body surface in calm water. Introducing equations (2.29) and (2.54) into (2.11), it follows [26] that:

$$\mathbf{f}_{fl}(t) = \rho \int_S \Big(\frac{\partial \phi_i(x,y,z,t)}{\partial t} + \frac{\partial \phi_d(x,y,z,t)}{\partial t} + \frac{\partial \phi_{ra}(x,y,z,t)}{\partial t} + gz \Big) \mathbf{n} \cdot dS \tag{2.55}$$

$$= \mathbf{f}_{fk}(t) + \mathbf{f}_d(t) + \mathbf{f}_{ra}(t) + \mathbf{f}_b(t) \tag{2.56}$$

where

$$\mathbf{f}_{fk}(t) = \rho \int_S \frac{\partial \phi_i(x,y,z,t)}{\partial t} \mathbf{n} \, dS \tag{2.57}$$

is the Froude-Krylov force,

$$\mathbf{f}_d(t) = \rho \int_S \frac{\partial \phi_d(x,y,z,t)}{\partial t} \mathbf{n} \, dS \tag{2.58}$$

is the diffraction force,

$$\mathbf{f}_{ra}(t) = \rho \int_S \frac{\partial \phi_{ra}(x,y,z,t)}{\partial t} \mathbf{n} \, dS \tag{2.59}$$

is the radiation force and $\mathbf{f}_b$ is the linearised buoyancy force given by (2.34). It is important to underline that, in (2.57), (2.58) and (2.59), S is the wetted surface of the fixed body, considered below the undisturbed mean FSE, as shown in Fig. 2.4 [9]. Similarly, introducing equations (2.29) and (2.54) into (2.12), it follows [26] that:

$$\boldsymbol{\tau}_{fl}(t) = \rho \int_S \Big(\frac{\partial \phi_i(x,y,z,t)}{\partial t} + \frac{\partial \phi_d(x,y,z,t)}{\partial t} + \frac{\partial \phi_{ra}(x,y,z,t)}{\partial t} + gz \Big) \, (\mathbf{r} \times \mathbf{n}) \, dS \tag{2.60}$$

$$= \boldsymbol{\tau}_{fk}(t) + \boldsymbol{\tau}_d(t) + \tau_{ra}(t) + \tau_b(t) \tag{2.61}$$

where

$$\boldsymbol{\tau}_{fk}(t) = \rho \int_S \frac{\partial \phi_i(x,y,z,t)}{\partial t} \, (\mathbf{r} \times \mathbf{n}) \, dS \tag{2.62}$$

is the Froude-Krylov moment,

$$\boldsymbol{\tau}_d(t) = \rho \int_S \frac{\partial \phi_d(x,y,z,t)}{\partial t} \, (\mathbf{r} \times \mathbf{n}) \, dS \tag{2.63}$$

is the diffraction moment,

$$\boldsymbol{\tau}_{ra}(t) = \rho \int_S \frac{\partial \phi_{ra}(x,y,z,t)}{\partial t} \, (\mathbf{r} \times \mathbf{n}) \, dS \tag{2.64}$$

is the radiation moment.

The summation of Froude-Krylov and diffraction forces is called the excitation force:

$$\mathbf{f}_e(t) = \mathbf{f}_{fk}(t) + \mathbf{f}_d(t); \tag{2.65}$$

therefore, the total force applied from the fluid to the body is given by:

$$\mathbf{f}_{fl}(t) = \mathbf{f}_e(t) + \mathbf{f}_{ra}(t) + \mathbf{f}_b(t). \tag{2.66}$$

Similarly, the summation of Froude-Krylov and diffraction moments is called the excitation moment:

$$\boldsymbol{\tau}_e(t) = \boldsymbol{\tau}_{fk}(t) + \boldsymbol{\tau}_d(t) \tag{2.67}$$

and the total moment applied from the fluid to the body is given by:

$$\boldsymbol{\tau}_{fl}(t) = \boldsymbol{\tau}_e(t) + \boldsymbol{\tau}_{ra}(t) + \boldsymbol{\tau}_b(t) \tag{2.68}$$

In the following Sections 2.4.1.1 and 2.4.1.2, more details regarding the excitation, radiation and buoyancy forces are provided where, for simplicity, the general 6 DoF problem has been reduced to a heave single DoF.

2.4.1.1 Excitation force

The excitation force is the force acting on the body, when it is held fixed in the presence of waves [75] [69]. In the context of LPT, the excitation force is the superposition of the Froude-Krylov force (2.57) and of the diffraction force (2.58) [9], where the Froude-Krylov force is obtained by integrating the pressure, due to the undisturbed incident wave field, over the mean wetted surface of the fixed body, as explained in Section 2.4.1. Therefore, the Froude-Krylov force can be considered as the force interaction between the waves and a 'ghost' body, which feels and reacts to the incident wave field, but does not alter it [9]. In the case of a body, having dimensions significantly smaller than the wavelength, the diffraction force is not significant compared to the Froude-Krylov force [9], indicating that the Froude-Krylov force is a reasonable approximation of the excitation force, with the computational advantage of avoiding the resolution of the diffraction problem. In the literature, the definition of the Froude-Krylov force is not unique, it can be calculated considering only the dynamic pressure, due to the incident field [69] [76] or it can be calculated utilising the total pressure (static plus dynamic pressure) [77] [78] [79]. In the present work, the excitation force counts only the dynamic part of the pressure; in this way, the excitation force is zero if there are no incident waves (otherwise, the excitation force would be equal to the buoyancy force, in the absence of incident waves). This definition will be useful in Section 6.2, where the excitation force represents the output of the system under investigation. In the case of a single DoF body, moving in heave, the excitation force is given by [74]:

$$f_e(t) = \int_{-\infty}^{\infty} h_e(t-\zeta)\eta(\zeta)d\zeta \tag{2.69}$$

where $h_e(t)$ is the excitation impulse response function. It is important to note that, in (2.69), the upper limit of the convolution integral is $+\infty$, indicating that it is necessary to know the future values of η, in order to calculate f_e at the present instant t. The fact that the relationship between η and f_e is noncausal can be intuitively understood in the case where η is defined with respect to a point placed in the centre of the body; indeed, the body will experience a force before the wave crest has arrived to the body centre [80] [81]. Moreover, the causality is not guaranteed even if η is considered in a location on the upstream side and outside the body [82]. The noncausal relationship between η and f_e becomes particularly important for real-time WEC control strategies, where wave forecasting is required [83] [84]. Taking the Fourier transform of (2.69), it follows that:

$$F_e(\omega) = H_e(\omega)\overline{\eta}(\omega) \tag{2.70}$$

where $H_e(\omega)$ is the Fourier transform of $h_e(t)$ and $\overline{\eta}(\omega)$ is the Fourier transform of $\eta(t)$ [74].

2.4.1.2 Radiation force

In the case of a body oscillating in the absence of incident waves, the hydrodynamic force, applied from the fluid to the body, is called the radiation force. It is important to underline that, in LTP, the calculation of the radiation force has an inconsistency, since the body is supposed to be moving to generate radiated waves but, at the same time, the wetted body surface is supposed to be unaltered in (2.59). In LPT, the body motion generates a time-changing fluid pressure, which is integrated on a constant surface, S, creating a time-changing radiation force. In the case of a single DoF body moving in heave, the radiation force is given by [85]:

$$f_{ra}(t) = -m_{\infty}\ddot{z}(t) - \int_{-\infty}^{t} h_{ra}(t-\zeta)\dot{z}(\zeta)d\zeta \tag{2.71}$$

where $z(t)$ is the position of the body, m_{∞} the high-frequency asymptote of the added-mass and $h_{ra}(t)$ the reduced radiation impulse response function. The shape of the wetted body surface determines the hydrodynamic radiation force felt by the body, when it moves in the fluid. The convolution integral, in (2.71), describes the water memory effect and it is evaluated from minus infinity to the present time instant t, indicating that the relationship between the body velocity, $\dot{z}$, and the radiation force, f_{ra}, is causal. In the frequency domain, the relationship between the body's velocity and the radiation force is given by the radiation impedance, $Z_{ra}(\omega)$ [69]:

$$F_{ra}(\omega) = -Z_{ra}(\omega)i\omega Z(\omega) \tag{2.72}$$

where $F_{ra}(\omega)$ and $i\omega Z(\omega)$ are the Fourier transform of $f_{ra}(t)$ and $\dot{z}(t)$ respectively and

$$Z_{ra}(\omega) = N(\omega) + i\omega m_a(\omega) \tag{2.73}$$

The real part of the radiation impedance, $N(\omega)$, is the radiation resistance, also called the hydrodynamic damping coefficient, which describes the dissipative effect of the energy, transmitted from the oscillating body to the waves (the waves propagate away from the body). The imaginary part of the radiation impedance is the radiation reactance, given by the product of the frequency, ω, and the added mass, $m_a(\omega)$. The radiation reactance refers to the alternate exchange of kinetic energy, associated with the velocity of the water, and the gravitational potential energy related to the lifted water [9]. The added mass represents the additional inertial effect due to the acceleration of the water, which moves together with the body. At infinite frequency, the added mass tends to the finite constant, m_{∞}, which is utilised to form the reduced radiation impedance, H_{ra}:

$$H_{ra}(\omega) = Z_{ra}(\omega) - i\omega m_{\infty} = N(\omega) + i\omega\big[m_a(\omega) - m_{\infty}\big]. \tag{2.74}$$

The inverse Fourier transform of $H_{ra}(\omega)$ is the reduced radiation impulse response function, $h_{ra}(t)$. $H_{ra}(\omega)$ and $h_{ra}(t)$ satisfy the following properties [86]:

$$\lim_{\omega\to 0} H_{ra}(\omega) = 0 \tag{2.75}$$

$$\lim_{\omega\to\infty} H_{ra}(\omega) = 0 \tag{2.76}$$

$$h_{ra}(t) = \frac{2}{\pi}\int_0^{\infty} N(\omega)\cos(\omega t)d\omega \tag{2.77}$$

$$N(\omega) \geq 0 \quad \forall\ \omega \tag{2.78}$$

$$\lim_{t\to 0^+} h_{ra}(t) \neq 0 \tag{2.79}$$

$$\lim_{t\to\infty} h_{ra}(t) = 0 \tag{2.80}$$

Equation (2.77) derives from the causality of $h_{ra}(t)$ [69] [74]. Equation (2.78) is a consequence of the system passivity (passivity describes an intrinsic characteristic of systems that can store and

dissipate energy, but not create it). For linear time-invariant systems, a necessary and sufficient condition for passivity is that the real part of the system transfer function is positive for all frequencies [86] [87]. Equation (2.79) is a consequence of equations (2.77) and (2.78) [88]. In the frequency domain, equation (2.71) becomes:

$$F_{ra}(\omega) = m_{\infty}\omega^2 Z(\omega) - H_{ra}(\omega) i\omega Z(\omega). \tag{2.81}$$

2.4.2 Solving the LPT-BVP utilising BEMs

The separation of the total potential flow, ϕ, into the incident potential ϕ_i, diffraction potential ϕ_d and radiation potential ϕ_{ra}, introduced in Section 2.4.1, allows breaking the LPT-BVP, represented by the system of equations (2.44), (2.47), (2.48), (2.49) and (2.52), into three simpler sub-problems: the incident, radiation and diffraction problems. The velocity potential of the original entire problem is then obtained by superimposing the individual velocity potentials of the sub-problems (see Fig. 2.5) [27].

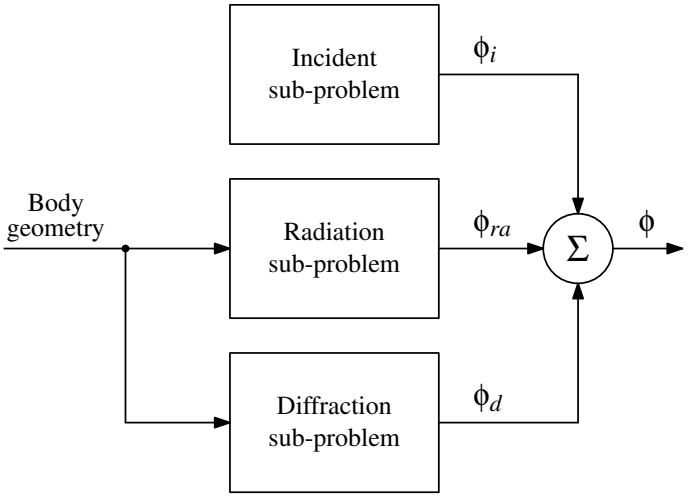

Figure 2.5: The LPT-BVP is divided into the incident, radiation and diffraction sub-problems. The velocity potential of the original entire problem is then obtained by superimposing the velocity potentials of the sub-problems.

• *The incident sub-problem.* The velocity potential, ϕ_i, has to satisfy the Laplace equation (2.44), the boundary condition at the seabed (2.48) and the linearised boundary condition at the free surface elevation (2.52). In the incident sub-problem, the body is not present; therefore, the boundary condition equation (2.47) is not taken into account. The solution is found under the hypothesis of time-harmonic motion with a specified frequency, ω, and, given the linearity of the problem, a more general case, such as the response to a random sea, can be obtained as superposition of harmonics utilising Fourier analysis [72][73]. The analytical solution of the incident potential problem, for a finite water depth, h, is given by [26] [27] [73]:

$$\phi_i = \frac{A_w g}{\omega} \frac{\cosh[k(h+z)]}{\cosh(kh)} \sin(kx - \omega t) \tag{2.82}$$

where A_w is the wave amplitude ($2A_w$ is the wave height), $k = 2\pi/\lambda$ is the wave number, λ is the wavelength and ω is the wave frequency. The connection between ω and k is provided by the dispersion relationship:

$$\frac{\omega^2}{g} = k \tanh(kh) \tag{2.83}$$

Using (2.53) and (2.82), and imposing $z = 0$, it is possible to obtain the FSE expression:

$$\eta = A_w \cos(kx - \omega t) \tag{2.84}$$

Equation (2.84) represents a harmonic plane wave moving in the x direction. Introducing (2.82) into the linearised Bernoulli's equation (2.29), it follows [26] that:

$$p_i = -\rho g z + \rho g A_w \frac{\cosh[k(h+z)]}{\cosh(kh)} \cos(kx - \omega t) \tag{2.85}$$

• *The radiation sub-problem*. The velocity potential, ϕ_{ra}, has to satisfy the LPT-BVP, represented by the system of equations (2.44), (2.47), (2.48), (2.49) and (2.52), The radiation problem is analytically resolvable only for very simple geometries and, therefore, the application of numerical methods is necessary.
• *The diffraction sub-problem*. The velocity potential, ϕ_d, has to satisfy the LPT-BVP, represented by the system of equations (2.44), (2.47), (2.48), (2.49) and (2.52), with the particularity that, in (2.47) the body velocity is zero [27]. Like the radiation problem, the diffraction problem needs the application of numerical methods.

Different possibilities are available for the numerical resolution of a system of PDEs, such as BEMs (also called boundary integral equation methods (BIEMs)), FEMs and FDMs [27] [89] [90] [91]. As explained in Section 2.3, in both FEM and FDM, the whole spatial domain is divided utilising a mesh, in contrast to BEMs, in which the spatial discretization is performed only at the bounding surface. Therefore, BEMs, compared to FEM and FDM, lead to a more efficient computation and less required computer memory, thanks to a reduction of the linear system dimension [89]. Furthermore, in numerical modelling, the mesh preparation is one of the most demanding processes [68]; since BEMs require the mesh of the only bounding surface, the mesh preparation is more cost effective [89] [90]. Furthermore, the adjustment of the mesh is more efficient with BEMs, in the case of problems involving moving boundaries [89].

The generic solution of a linear system can be written as a superposition of harmonic solutions at different frequencies ω, leading to the LPT-BVP in the frequency domain, whose unknowns are the frequency domain hydrodynamic coefficients $Fe(\omega)$, introduced in (2.70), $N(\omega)$ and $m_a(\omega)$, presented in (2.73) [28]. BEMs are based on a form of Green's theorem, which describes velocity potential as a distributions of singularities (sources or dipoles) over the wetted body (discretized) surface. For more details see [72] [92] [93] [94]. Numerically solving the resulting system of linear equations, the potential flow field is obtained, which can be used to calculate the fluid pressure, by using Bernoulli's equation (2.29) [9].

In recent years, many BEM codes have been developed to resolve the LPT-BVP in the time or frequency domain. The most common codes working in the frequency domain are WAMIT [95], ANSYS Aqwa [35] [96] [97], Aquaplus and Nemoh [98]. A code, working in the time domain, is Achil3D [99] [100]. LPT and BEMs have been utilised in order to model a wide range of WECs since the 1980s: in [101], the submerged pitching WEC Duck is modelled to predict the power absorption efficiency. In [102], the pitching Salter's Duck is numerically modelled. In [103] and [104], tha Pelamis WEC is modelled. In [105], the effect of water depth on the performance of a small surging WEC is studied. In [106], the dynamic behaviour of OWCs is studied, utilising an adaptation of the BEM code AQUADYN [107]. In [108] and [109], the SEAREV, the floating oscillating WEC containing an internal moving mass, is investigated. In [110], a bottom-hinged flap WEC is modelled. In [111], the Anaconda WEC (a submerged flooded rubber tube) is investigated. Different studies show good agreement between linear theory and experiments, in small and moderate sea states [112] [113] [114] [115].

2.4.3 Advantages and limitations of LPT

The main advantages of LPT are:
• Since the model is linear, superposition can be used to decompose the fluid-body hydrodynamic

force into Froude-Krylov, diffraction and radiation forces, in order to simplify the problem (see Sections 2.4.1 and 2.4.2).
• Since the model is linear, all time-varying variables (such as pressure, fluid velocity and body displacement) can be represented as a superposition of harmonics, in this way leading to a frequency domain description of the system.
The main limitations of LPT are:
• LPT has an applicability restricted to waves which have small amplitudes with respect to their wavelengths.
• LPT has an applicability restricted to body oscillations which are small with respect to the body dimensions.
• The model accuracy reduces particularly around resonance, where body oscillations typically increase considerably.
• The hypothesis of inviscid fluid removes any viscous effects from the models, reducing the accuracy where flow separation and vortex shedding are present.
• LPT does not account for wave breaking (the wave steepness is assumed to be well below the point of wave collapse).

2.5 Fully nonlinear potential theory and BEMs

In Section 2.4, the FNPT-BVP in the time domain has been introduced, which is represented by the system of equations (2.44), (2.45), (2.46), (2.47), (2.48) and (2.49). FNPT is based on some of the hypotheses utilised for LPT: an inviscid (2.39) and incompressible (2.41) fluid and an irrotational flow (2.40). Therefore, also in FNPT, it is possible to define a velocity potential ϕ (2.23). In contrast to LPT, hypotheses (2.42) and (2.43) are not utilised in FNPT. Furthermore, in contrast to LPT, the boundary conditions are not linearised and the boundary conditions are applied at the instantaneous water FSE, $\eta(t)$, and at the instantaneous wetted body surface, $S(t)$, as shown in Fig. 2.6. The fact that the boundaries themselves vary in time makes the analytical solution of the problem very difficult and rare, necessitating the use of numerical methods.

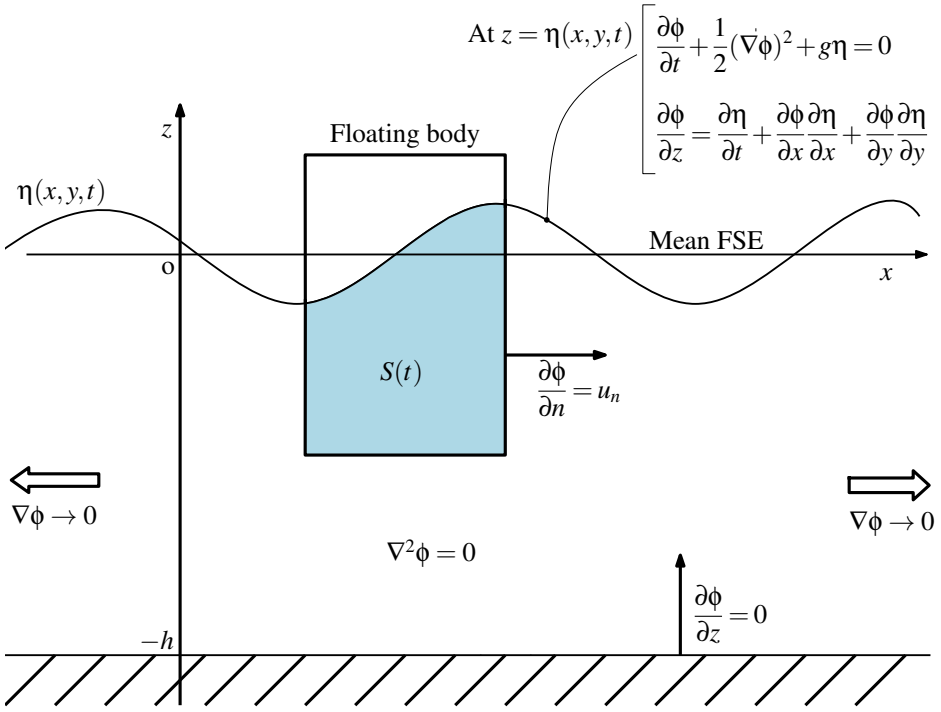

Figure 2.6: Graphical representation of the LPT-BVP in the time domain, described by the system of equations: (2.44), (2.45), (2.46), (2.47), (2.48) and (2.49).

It is important to underline that the nonlinear nature of the problem does not allow the separation of the total potential flow into an incident, a diffraction and a radiation potential, in contrast to equation (2.54), for LPT. Consequently, in FNPT, the superposition of hydrodynamic forces is lost [9]. Therefore, the FNPT-BVP can not be separated in sub-problems, like in LPT, but has to be solved by directly finding the total potential velocity ϕ [116] [117]. However, there is still the possibility of defining an excitation problem (when the body is fixed and subject to incident waves) or a radiation problem (when the body oscillates without the presence of incident waves), but the superposition of the two separated excitation and radiation problems does not provide the correct solution for the problem with both incident waves and body oscillations [9]. The change in time of the boundary (the FSE and the body position) leads to the formulation of a new BVP at each time step, increasing considerably the problem complexity [9]. For more details regarding FNPT, see [9] [71] [118].

In recent years, a considerable number of FNPT solvers have been implemented in order to simulate the interaction between waves and floating structures, the generation of radiating waves by large oscillating bodies, and the propagation of nonlinear waves. The study of the propagation of nonlinear free surface waves was presented in [119] for a two dimensional case, and generalised to three dimensions by [120] [121] [122]. Guerber et al. [117] [123] modelled, in two dimensions, the interaction between an inviscid fluid and a submerged cylinder undergoing large motions. The wave generation, propagation, and breaking have been studied in a two-dimensional NWT, implemented utilising FNPT in [124] [125]. The investigation of large amplitude oscillations of a submerged body is reported in [126]. In [127], a vertical cylinder is forced to oscillate in a NWT, in order to generate nonlinear waves. The nonlinear hydrodynamic responses of an OWC are investigated in two dimensions in [128]. In [118], a study is reported of propagation, breaking and runup on slopes of waves; furthermore, the wave interaction with submerged and emerged structures is investigated. In [129], the nonlinear time domain simulation of a land-based OWC is presented. The numerical analysis of the Backward Bent Duct Buoy (BBDB) WEC is reported in [130] and [131]. In [116], the nonlinear interactions between large waves and freely floating bodies are simulated in a two-dimensional NWT. In [127], [132] and [133], the interaction of a single floating structure with the surrounding fluid is investigated in 6 DoF. Siddorn, in [134], reduces the size of the simulation domain, developing numerical methods, capable of effectively damping an outgoing wave and generating steep incident waves in short distances. A two-dimensional wave-induced motion (sway, heave and roll) of a floating body is computed and compared with corresponding real experiments in [135].

2.5.1 Advantages and limitations of FNPF

The main advantages of FNPT are:
• There are no limitations in the wave amplitude and steepness (as long as wave breaking does not occur), in contrast to LPT.
• Large finite body displacements are permitted, in contrast to LPT.
• FNPT models can simulate wave propagation with significant less numerical dissipation and higher accuracy than CFD models [9].
• FNPT models are less computationally intensive than CFD models [9].
The main limitations of FNPT are:
• FNPT is not able to model turbulence and viscous effects.
• The superposition of Froude-Krylov, diffraction and radiation forces is not applicable.
• It is not possible to model situations involving wave breaking, slamming, green water and air entrainment. Therefore, FNPT is not adequate for a WEC survivability study [28].

2.6 Models based on Cummins' equation and associated nonlinear extensions

2.6.1 Cummins' equation and associated parametric forms

A large number of models, employed in the simulation and analysis of WECs, are based on the time domain integro-differential Cummins' equation [136], initially developed for the offshore and ship industry. Cummins' equation is based on Newton's second law, describing the motion of a body of mass, M, floating in water, with zero forward speed, subject to fluid, gravity and other external forces (such as a mooring force, f_m, and a PTO force, f_{pto}). The fluid force is derived under the simplifying hypotheses of LPT. For simplicity, consider a single DoF body moving in heave, and a global y-axis vertical and positive upwards, having its origin at the mean FSE. From equations (2.4), (2.36) and (2.71), it follows that:

$$(M+m_\infty)\ddot{y}(t)+\int_{-\infty}^{t} h_{ra}(t-\zeta)\dot{y}(\zeta)d\zeta+Ky(t)=f_{in}(t) \tag{2.86}$$

where y is the body displacement from its equilibrium position, K is the restoring coefficient given by (2.37), and

$$f_{in}(t)=f_e(t)+f_{pto}(t)+f_m(t) \tag{2.87}$$

with $f_e(t)$ provided by (2.69):

$$f_e(t)=\int_{-\infty}^{\infty} h_e(t-\zeta)\eta(\zeta)d\zeta \tag{2.88}$$

The fluid-body interaction in (2.86) is modelled linearly, but the external forces, represented by f_{in}, could be nonlinear [9] [28]. Taking the Fourier transform of (2.86), it follows [88] [137] that:

$$\{-\omega^2[M+m_a(\omega)]+i\omega N(\omega)+K\}Y(\omega)=F_{in}(\omega) \tag{2.89}$$

where $N(\omega)$ and $m_a(\omega)$ were introduced in (2.73) and

$$F_{in}(\omega)=F_e(\omega)+F_{pto}(\omega)+F_m(\omega) \tag{2.90}$$

with $F_e(\omega)$ expressed by (2.70):

$$F_e(\omega)=H_e(\omega)\overline{\eta}(\omega) \tag{2.91}$$

The hydrodynamic coefficients $h_{ra}(t)$, $h_e(t)$, m_∞, $m_a(\omega)$, $N(\omega)$ and $H_e(\omega)$, provided by BEM software packages, can be introduced into equations (2.86) and (2.89), in order to obtain nonparametric models. The use of the nonparametric Cummins' equation, in particular for the presence of the radiation convolution, is time consuming in simulations and may require significant amounts of computer memory [85] [88]. Therefore, the integro-differential Cummins' equation (2.86) is often approximated with a finite-order constant-coefficient differential equation, in order to obtain a parametric model.

A generic linear time-invariant (LTI) system, having $u(t)$ and $v(t)$ as input and output, respectively, has the following four equivalent parametric mathematical descriptions (as shown in Fig.2.7) [138] [139] [140] [141] [142]:

• *Constant-coefficient differential equation*. Consider a LTI system defined by the following ordinary differential equation (ODE):

$$\sum_{i=0}^{n} a_i v^{(i)}(t)=\sum_{i=0}^{m} b_i u^{(i)}(t) \tag{2.92}$$

where $a_n=1$ and $v^{(i)}$ indicates the i-th derivative of $v(t)$. In this representation, $a_0,...,a_{n-1},b_0,...,b_m$ are the parameters.

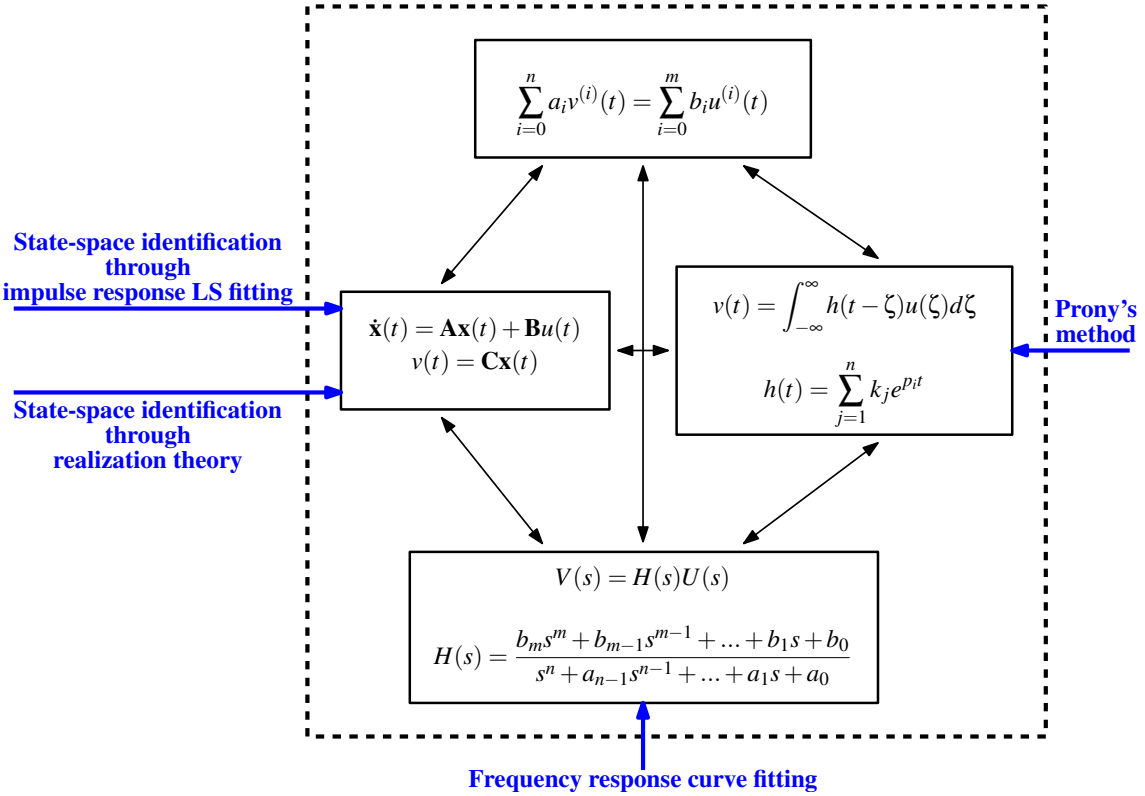

Figure 2.7: The four equivalent mathematical descriptions of a generic LTI system are represented inside the dashed line. The most common methods, used to approximate the original integro-differential Cummins equation with one of the parametric representations, are also shown.

• *Transfer function*. Applying the Laplace transform to (2.92), under the assumption that all initial conditions are zero [139], it follows that:

$$V(s) = H(s)U(s) \tag{2.93}$$

where $H(s)$ is a complex rational function given by:

$$H(s) = \frac{b_m s^m + b_{m-1}s^{m-1} + \ldots + b_1 s + b_0}{s^n + a_{n-1}s^{n-1} + \ldots + a_1 s + a_0} \tag{2.94}$$

In this representation, $a_0, \ldots, a_{n-1}, b_0, \ldots, b_m$ are the real parameters. Applying the partial fraction expansion (see Appendix Section A.4) to (2.94), it follows [139] that:

$$H(s) = \sum_{j=1}^{n} \frac{k_j}{s - p_j} \tag{2.95}$$

where k_j is the residue at the pole $p_j = \alpha_j + i\,\beta_j$. In this representation, $k_1, \ldots, k_n, \alpha_1, \ldots, \alpha_n, \beta_1, \ldots, \beta_n$ are the parameters. It is important to underline that, rational functions represent just a possible subset of all possible transfer functions. A common example of a transfer function, which is not a rational function, is one representing a pure delay block with delay time, t_d; its transfer function is $H(s) = e^{-t_d s}$.

• *Convolution integral*. Applying the inverse Laplace transform to (2.93), it follows that:

$$v(t) = \int_{-\infty}^{\infty} h(t-\zeta)u(\zeta)d\zeta, \tag{2.96}$$

where, utilising (2.95), $h(t)$ can be represented [143] as:

$$h(t) = \sum_{j=1}^{n} k_j e^{p_j t} \tag{2.97}$$

Equation (2.97) means that the impulse response is exactly given by the summation of complex exponentials. In this representation, $k_1,...,k_n$,$\alpha_1,...,\alpha_n$,$\beta_1,...,\beta_n$ are the parameters.
• *State-space*. The n-th-order ODE (2.92) can be transformed into a system of n first-order ODEs (also called state-space) [144] as:

$$\begin{aligned} \dot{\mathbf{x}}(t) &= \mathbf{A}\mathbf{x}(t) + \mathbf{B}u(t) \\ v(t) &= \mathbf{C}\mathbf{x}(t) \end{aligned} \tag{2.98}$$

where $\mathbf{x}(t)$ is the state vector. In (2.98), the parameters are the elements of the matrices **A**, **B** and **C**. It is important to underline that, given a system of ODEs, there are many equivalent state-space descriptions, and among them, there are different equivalent canonical forms [144]. Given the matrices **A**, **B** and **C**, it is possible to obtain the impulse response function [138]:

$$h(t) = \mathbf{C}e^{\mathbf{A}t}\mathbf{B} \tag{2.99}$$

and the transfer function:

$$H(s) = \mathbf{C}(s\mathbf{I} - \mathbf{A})^{-1}\mathbf{B} \tag{2.100}$$

The output of the state-space system of (2.98) is the superposition of the zero-input component and the zero initial state component, evaluated as [138] [145]:

$$y(t) = \mathbf{C}e^{\mathbf{A}(t-t_0)}\mathbf{x}(t_0) + \int_{t_0}^{t} \mathbf{C}e^{\mathbf{A}(t-\tau)}\mathbf{B}u(\tau)d\tau \tag{2.101}$$

There is a variety of methods to approximate the original integro-differential Cummins' equation (2.86), with one of the parametric representations (2.92) (2.94) (2.97) (2.98). The parameters can be identified either in the time or in the frequency domain; usually, the employed approximation method and the utilised BEM data share the same domain. For example, a frequency domain BEM data often is used in conjunction with a frequency domain approximation method [146]. The most common methods are:

◇ *Prony's method*. A way to obtain the parametric representation (2.97) is Prony's method, which was developed in 1795 by Baron de Prony, during his studies regarding the expansion of different gases. Prony's method is utilised to approximate an impulse response function, as a summation of damped complex exponentials [147] [148]. An example of application of Prony's method in ocean energy, can be found in [149], where the dynamics of a WEC point-absorber are simulated in heave, roll and pitch and compared with experimental tests, performed in a small wave flume. The radiation impulse response $h_{ra}(t)$, obtained by a BEM package, is approximated by a sum of exponential functions with Prony's method. Successively, the approximated integro-differential Cummins' equation is transformed into a system of ODEs and solved with a fifth-order Runge-Kutta scheme. In [150] and [151], a time domain numerical model of the SEAREV WEC is provided. The hydrodynamic forces are derived by LPT, with Prony's method utilised to replace the radiation convolution term and obtain the equation of motion in ODE form.

◇ *Frequency response curve fitting*. From nonparametric data in the frequency domain $H_e(\omega)$, $N(\omega)$ and $m_a(\omega)$, provided by a BEM package, it is possible to use frequency domain regression to obtain a least squares (LS) fitting of the parametric transfer function (2.94) [86] [88]. In [152], the added mass and damping coefficient curves are approximated in the frequency domain. In [153], the curves in the frequency domain, associated with radiation and excitation forces, are fitted with rational approximations. The method is presented using a floating cylinder, a sphere, and a Salter's Duck WEC, for both 2-dimensional and 3-dimensional cases. In [154], a method, which utilises only $N(\omega)$ in order to identify $H_{ra}(\omega)$, is presented. Perez and Fossen, in [155], develop a MATLAB toolbox for the radiation force identification, in the frequency domain, of marine structures. The toolbox estimates the fluid-memory transfer function and the infinite-frequency added

mass. The toolbox is an independent component of the Marine Systems Simulator (MSS) and is freely available [156]. In [85], the nonparametric curves of the added mass and damping are fitted in the frequency domain, with polynomials having different orders. The body is an ellipsoidal hull moving in pitch. An overview, regarding the frequency domain identification of marine structures, can be found in [85] [86] [155] [157].

◇ *State-space model identification through impulse response LS fitting*. Given a nonparametric impulse response of a system, it is possible to identify the parameters of the continuous-time state-space model in (2.98), carrying out the time domain LS fitting, of the impulse response (2.99). The problem is nonlinear in the parameters and can be solved by employing nonlinear optimization techniques [86] [88].

◇ *State-space model identification through realization theory*. Realization theory identifies a state-space model in the time domain, utilising the known nonparametric impulse response of the system. Usually, the identification is carried out for a discrete-time state-space model, because the realization problem is easier to pose in discrete-time. Once the discrete-time model is identified, it is possible to convert it to a continuous-time model, if required, utilising different techniques [88].

The use of realization theory, in order to identify the radiation force model of marine structures, was proposed in Kristiansen and Egeland [158] and Kristiansen et al. [159]. [86] and [88] provide a good introduction to realization theory, for the identification of radiation force models of marine structures.

The use of state-space models in hydrodynamics was proposed independently by Schmiechen [160] and Booth [161]. Since then, it has been common to replace the computationally costly nonparametric radiation convolution integral with a state-space model, the latter being more convenient for the analysis and design of control systems and very much in use in control engineering [28] [162]. For more details, regarding the replacement of the radiation convolution integral of Cummins' equation with a state-space model, see [74] [155] [163]. In [164], a state-space model is utilised in order to model a two-body WEC moving in heave. In [165], the piston-like movement, of an OWC moving in heave, is described using state-space models. In [74], a floating cylinder is studied and the convolution integrals of the excitation force and radiation force are replaced with state-space models. In [166], an OWC is modelled with a state-space model, by including in the model the hydrodynamic and hydrostatic forces, viscous loss in water, pressure drop in the valves, air chamber compressibility with mass and volume change, and valve opening and closing. In [167] and [162], a five-body WEC with 10 DoF is studied. The radiation force model is described with a state-space model.

2.6.2 Nonlinear extensions of Cummins' equation

As explained in Section 2.6.1, Cummins' equation (2.86) is a consequence of LPT, which divides the fluid-body force into an incident, a diffraction and a radiation force. When the wave amplitude and body displacement increase significantly, nonlinear hydrodynamic effects arise, the fluid-body force separation loses fidelity and LPT models reduce in accuracy. CFD and FNPT models, introduced in Sections 2.3 and 2.5, respectively, are consistent nonlinear models, in the sense that they do not separate the fluid-body force into an incident, a diffraction and a radiation force. Between linear models, on one side, and consistent nonlinear models, on the other side, a no-man's land exists , where the fluid-body force is separated into nonlinear incident, diffraction and radiation forces. The resulting nonlinear models are clearly inconsistent, because the separation of the fluid-body force would be possible only if the models were linear (which they are not!). However, nonlinear models, constructed in this way, may have a better accuracy compared to linear models. In short, the linear Cummins' equation can be used as a good basis structure for more complex nonlinear hydrodynamic models. In the following Sections 2.6.2.1, 2.6.2.2, 2.6.2.3 and 2.6.2.4, the restoring, Froude-Krylov, radiation and viscous drag terms are used in order to

include some nonlinearities in the models. Depending on the shape of the WEC, the sea condition and the control strategy utilised, not all the aforementioned nonlinear terms may be significant and necessary in the model. Therefore, it is convenient to use caution in introducing nonlinearities, since a significant increase of computational costs may be added to the control calculations and/or simulation time [168]. In [169], the relevant nonlinear terms are reported for various types of devices. Once a particular nonlinear Cummins' equation extension is decided, the information, necessary to complete the different parts of the model, can be provided by different sources (such as LPT, FNPT, CFD and real tank experiments) and are represented in the modelling structure, as shown in Fig. 2.8.

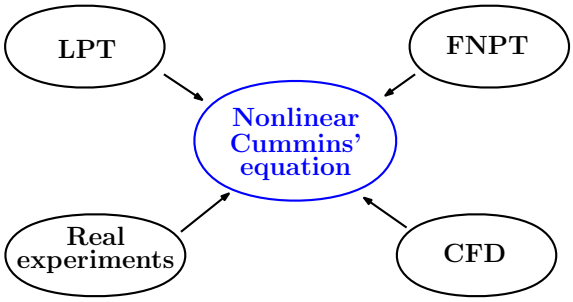

Figure 2.8: The information, provided by LPT, FNPT, CFD and real tank experiments, can coexist in a particular nonlinear Cummins' equation extension.

2.6.2.1 Nonlinear restoring force

In Section 2.2.7, it was explained that the restoring force, f_{re}, is the superposition of the gravitational and buoyancy forces. In Cummins' equation (2.86), the restoring force is represented by the linearised (around the equilibrium position) term:

$$f_{re} = -Ky \tag{2.102}$$

where y is the body displacement from the equilibrium position, $K = \rho g A_{cr}$ is the restoring coefficient and A_{cr} is the horizontal cross-sectional area at equilibrium. By increasing the amplitude of the body oscillations, the linearity of the restoring term could be lost. If the device has a constant horizontal cross-sectional area, the restoring force is always linear with respect to the vertical body displacement but, if the horizontal cross-sectional area changes with the body displacement, the relation between f_{re} and y is nonlinear:

$$f_{re} = -g(y) \tag{2.103}$$

where $g(.)$ is a general nonlinear static function, which depends only on the geometric shape of the device. Different researchers studied the problem of the introduction of the nonlinear restoring force into hydrodynamic models. In [170], a method for the calculation of the nonlinear restoring force, valid for any heaving axisymmetric point-absorber, is presented. In [76], a method is presented in order to calculate the nonlinear restoring force on a conical float, in the case of regular and irregular waves. The nonlinear buoyancy force is calculated numerically, by integrating the hydrostatic pressure, over the instantaneous wetted body surface. In [171], a 2 DoF heave-pitch model is implemented for a conical shaped float, in order to simulate free decay experiments, with different initial displacements; the nonlinear restoring force and momentum are calculated analytically. In [172], the nonlinear hydrostatic restoring force and moment, applied to vessels with three different hull shapes, are calculated by integrating the hydrostatic pressure over the instantaneous wetted body surface. Successively, the 6 DoF equation of motion is solved with the nonlinear hydrostatic load. In [173], the nonlinear buoyancy force is calculated for a heave ellipsoid-shaped

float by integrating the hydrostatic pressure over the instantaneous wetted body surface. In [75], a nonlinear hydrostatic restoring moment is introduced into the numerical model by fitting a cubic polynomial function to laboratory test results.

2.6.2.2 Nonlinear Froude-Krylov force

In LPT, the Froude-Krylov force is computed by integrating the incident pressure (2.85), (the incident pressure is obtained by the incident potential velocity and the linearised Bernoulli's equation (2.29)), over the constant wetted body surface (see Section 2.4.1.1). The accuracy of the Froude-Krylov force may be improved by taking into consideration some nonlinearities:
• The incident pressure is obtained from the nonlinear Bernoulli's equation (2.26),
• The incident pressure is integrated over the instantaneous wetted body surface, which leads to a significant additional computational cost; indeed, the change of the surface of integration leads to the use of either an automatic remeshing routine of the surface [174] or a very fine mesh [78].

In [76], a method is presented in order to calculate the nonlinear Froude-Krylov force on a conical float, in the case of regular and irregular waves. The nonlinear Froude-Krylov force is calculated numerically, by integrating the hydrodynamic incident pressure over the instantaneous wetted body surface. In [78], the nonlinear Froude-Krylov force is calculated over the instantaneous wetted body surface of a SEAREV WEC, in order to predict the parametric roll phenomenon. In [175], a nonlinear hydrodynamic model structure is developed for a single body device moving in heave and utilised to simulate the motion under latching control. The same model structure is studied for two different geometries (a sphere and a cylinder). The model structure is obtained by introducing the Froude-Krylov force as an individual nonlinearity. In [77], a numerical model for a two body WEC was developed in order to determine the large relative amplitude motion of the two bodies, which are subject to incoming regular waves. The linear diffraction and linear radiation forces are computed utilising ACHIL3D code, whereas the nonlinear Froude-Krylov force is calculated by integrating the incident wave pressure over the instantaneous wetted body surface. In [170], a method is presented for the computationally efficient calculation of the nonlinear Froude-Krylov force, valid for any heaving axisymmetric point-absorber. In [173], the nonlinear Froude-Krylov force is computed by integrating the hydrodynamic pressure over the instantaneous wetted body surface, in the case of a heaving ellipsoid-shaped float. In [79], the nonlinear Froude-Krylov force is calculated for a sphere, having a single DoF (moving in heave).

It is important to underline that the inclusion of the nonlinear FroudeKrylov force in the hydrodynamic model is particularly relevant when the wetted body surface changes significantly. The presence of large incident waves and large body oscillations is not sufficient to cause a relevant change in the wetted body surface, in the case where the device behaves like a wave follower. Furthermore, the change of the wetted body surface depends significantly on the energy maximising control strategy, which exaggerates the amplitude of motion and prevents the device from behaving as a wave follower [170] [176] [177]. The use of the nonlinear FroudeKrylov force is particularly useful when the excitation force is dominated by the FroudeKrylov force; this is the case for the heave force applied on point-absorber WECs, but it is less true for large bodies or surge/pitch forces [169] [9].

2.6.2.3 Nonlinear radiation force

Linear radiation force models are usually reasonably adequate in the case of point-absorber WECs [9] [169]. The use of a nonlinear radiation force has been studied in different works, showing the limited improvement of the model performance, progressing from a linear to a nonlinear radiation force [169]. In [178], Clement and Ferrant show that, in the case of floating bodies, the radiation nonlinearities are negligible. In [79], linear and nonlinear radiation forces are implemented for a heaving point-absorber, showing that progressing from a linear to a nonlinear radiation force model has minor effects on body dynamic simulations.

2.6.2.4 Nonlinear viscous drag force

The viscous force, generated by shear stress (see Section 2.2.1), is not present in Cummins' equation 2.86 (the fluid is assumed to be inviscid). Neglecting the viscous effect may lead to an unrealistically large prediction of the device response and of the extracted power, especially near the resonance and in particular for a point-absorber [69] [94] [179]. Usually, the additional viscous damping term introduced into the hydrodynamic model is based on Morison's equation [180], which describes the force applied on a submerged body by an oscillatory flow. The viscous drag damping force is given by [94]:

$$f_v = \frac{1}{2}\rho C_d A_c (v - v_b)|v - v_b| \tag{2.104}$$

where ρ is the fluid density, C_d is the drag (viscous) coefficient, A_c is the body characteristic area, v is the flow velocity, and v_b is the body velocity; therefore, $(v - v_b)$ is the relative fluid velocity. The experimental measure of the drag coefficient C_d is carried out mainly utilising two methods [73]:

- Free body oscillations in an otherwise calm fluid.
- The body is held fixed inside a large U-tube structure, where the fluid is made to oscillate at a certain fixed frequency.

Details, regarding the value of the empirical coefficient for different body shapes, can be found in [181]. Different researchers investigated the introduction of the viscous effect into linear hydrodynamic models. For example, in [75] and [182], a nonlinear viscous drag moment is introduced into the numerical model of a hemispherical WEC; the value of the drag coefficient is obtained by real wave tank (RWT) experiments. In [183], the dynamics of small seabed-mounted bottom-hinged WECs (which have the same physical principle of EB Frond, WaveRoller, Oyster and BioWave WECs) are studied, by introducing a nonlinear viscous term into the linear Cummins' equation. In [179], hydrodynamic models of WECs with different working principles have been implemented, in order to estimate mean annual power absorption. A nonlinear viscous term is introduced into the models. In [184], the linear model for a three-body WEC is extended with the introduction of a nonlinear viscous term. In [185], a nonlinear state-space model, obtained by introducing a viscous term into Cummins' equation, is developed in order to simulate free decay experiments for a point-absorber WEC. In [186], viscous effects and flow vorticity are studied at solid body boundaries, in a NWT implemented with OpenFOAM. The device under investigation is a vertically fixed submerged flap. Bhinder, in [187] [188] [189], introduces a viscous term into Cummins' equation, in order to describe the dynamics of floating and surging WECs; the drag coefficient is identified by utilising CFD experiments. In [190], the drag coefficient of a floating plate, moving in heave, is estimated by utilising CFD experiments. In [177], different identification techniques, for drag coefficient estimation (in the case of a floating heaving point absorber), are implemented, evaluated and compared, underlining the inconsistency in the literature, about both the drag coefficient values themselves, and the identification methods utilised.

2.7 Summary and discussion

This chapter has introduced the complexity of the hydrodynamic problem which has to be resolved to obtain an accurate description of the dynamics of a WEC interacting with waves. Sections 2.3, 2.4, 2.5 and 2.6 have shown that different problem approaches lead to different mathematical models, each one characterised by different accuracy and computational velocity. It is crucial to underline that a mathematical model is always an approximation of the natural world, but a model that better describes the reality is not necessarily the best model; the assessment of a model depends on its purpose and application [191] [192]. Indeed, the high accuracy performance of CFD models, introduced in Section 2.3, is not sufficient to justify their use in all WEC model applications, such as simulation of device motion, power production assessment or WEC control. For example,

the use of CFD models, in order to perform seasonal WEC power production calculations, would require decades of computation. Furthermore, a WEC mathematical model, utilised for control, has to be able to produce an output simulation in real-time, certainly beyond the CFD possibility. On the other hand, linear models have a good computational speed, but are not able to properly describe nonlinear hydrodynamic effects, which are relevant in some WEC power production conditions. Therefore, the main objective of this thesis is to obtain models which are between these two extremes, a good compromise able to describe the most important nonlinearities of the real system, without requiring excessive computational speed.

The available margin in reducing the model complexity, without losing significantly in accuracy, is based on the fact that the continuity and Navier-Stoke equations intrinsically contain the knowledge to predict velocity and pressure of the fluid, at any point of the spacial domain and in any possible condition and situation. Many of these possible solutions are not relevant in the wave energy production context, but may be relevant for WEC survival assessment. Furthermore, the final objective of a WEC mathematical model is simulating the total force applied by the fluid to the body and predicting the consequent body position, whereas the knowledge of the fluid velocity and pressure, in the whole domain around the WEC, is not relevant for the final objective. Therefore, a way to reduce the model complexity is to move from a mathematical description (represented by (2.14), (2.15), (2.16) and (2.15)), which utilises 'spatially distributed' information in the fluid domain, to a description that concentrates all the necessary information only on the body dynamics. From a mathematical point of view, this model reduction process transforms the continuous infinite-dimensional space and time PDEs into finite-order ODEs. This kind of approximation is already utilised in a variety of engineering disciplines, such as electrical systems (including electronics), magnetic circuits, heat transfer and acoustics, where a 'spatially distributed' model is transformed into a lumped parameter model, representing the connection of discrete entities. For example, under certain assumptions, the electromagnetic Maxwell's equations are simplified into Kirchhoff's circuit laws. In this way, the 'spatially distributed' electric and magnetic fields are converted into voltage and current variables and the system is transformed into a circuit composed of resistances, capacitors, inductances and generators. Part of the original and unnecessary complexity can be removed, in order to obtain simpler but sufficiently accurate models (under the assumed working hypotheses). Similarly, in the WEC model, the velocity and pressure of the fluid can be replaced with the body position (or velocity) and the total applied force.

The synthesis process of WEC models, shown in Sections 2.4 and 2.5 for LPT and FNPT respectively, is based on the physical laws describing the fluid-body interaction and on some simplifying hypotheses, these latter utilised to reduce the model complexity. An alternative modelling approach, utilised in this thesis, is that of system identification, where models are determined from recorded experimental data. The experimental data, utilised in this thesis for the identification of hydrodynamic models, are generated either in a CFD-NWT (see the case studies in Chapters 5 and 6) or in a RWT (see the case study in Chapter 7). The problem of the excessive CFD computation time, which impedes the use of highly accurate CFD codes for real-time applications, is bypassed by utilising CFD-NWTs only for the generation of experimental data in an off-line modality (in this way, the price of the highly demanding CFD-NWT computation time is paid only once). Successively, with the use of system identification tools, the essential nonlinearities of the real system are extracted from the recorded data and 'injected' into the nonlinear parametric models, which remain sufficiently fast and simple to run in real-time, in on-line modality (see Fig. 2.9).

The use of CFD experimental data and of system identification, in order to obtain the reduction of model complexity, has already been utilised in different engineering sectors [193]. For example, in [194], a linear state-space model is identified from CFD experiments, in order to describe the behaviour of supersonic and hypersonic vehicles. In [195], [196] and [197] a linear model is identified from CFD experiments, in order to control the temperature of a ventilation chamber. In [198], an on-line parametric model is developed in order to control a rotary kiln incinerator; the model parameters are updated by utilising a CFD experiment database (the experiments have been simulated in an off-line modality). In [199], CFD experiments are utilised in order to identify

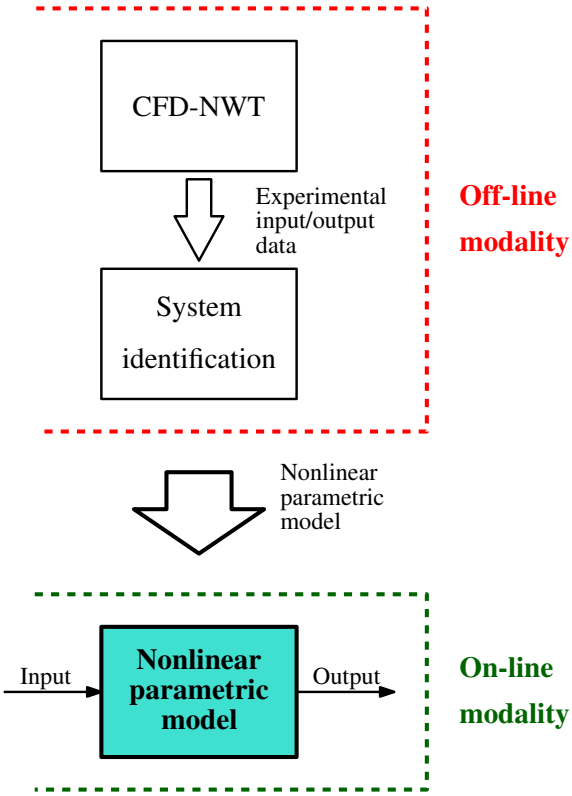

Figure 2.9: The nonlinear parametric models are able to capture the essential nonlinearities, simultaneously retaining a sufficient simplicity that allows the models to be run in real-time (on-line modality). The price of the demanding CFD-NWT computation time is paid only once during the simulation of the identification experiments (in an off-line modality).

models for controlling melt temperature in plastic injection molding. In [200], CFD simulations are used to identify a model which describes the flow of an incompressible viscous fluid through a two-dimensional channel. In [201], a grey-box parametric model is identified from CFD simulations, in order to control the spatial temperature in a climate chamber. In [202], CFD simulations are utilised to identify parametric models, in order to predict ship maneuverings in calm water. In [203], a linear model is identified by CFD simulations, in order to predict instabilities in the aeroelastic behaviour of aerospace structures.

Chapter 3

System identification as a tool for hydrodynamic modelling

3.1 System identification introduction

The use of mathematical models is crucial in science and engineering, as explained in Chapter 1. A way to construct a mathematical model of a system under investigation (also called process [204] [205]) involves breaking the system into subsystems and, by applying the physical laws to them, building up a mathematical description between the significant variables. In the case of complex systems, the procedure may take an unacceptable amount of time and would provide a very complicated model, which could be difficult to utilise. A different approach is employed in system identification (SI), where models are determined from data measured from the process [204]. SI, which can be considered to be the dynamical equivalent of static function approximation, has its origins in the methods developed by Legendre, Laplace, and Gauss in the 19th century, which were used to fit functional forms to (typically) astronomical data [206]. However, since the 1960s, the field of dynamical SI has been consolidated and many successful applications have been reported using a wide variety of methods across a broad range of application areas [207]. SI finds particular application in areas where:

• First principles models are too difficult to formulate,

• The dynamics of a system change with time and an on-line model updating is required (e.g. in adaptive control).

Identification experiments collect data by exciting the process with an input signal (or imposing some system initial conditions), in order to generate an output signal, which contains information regarding the system dynamics. SI techniques, by analysing the collected input and output data, provide the mathematical description of the process. Fig. 3.1 shows the basic principle of SI. In many cases, SI is seen as a pragmatic and time-efficient method of obtaining dynamical models, particularly in situations where system variables (inputs, outputs) are relatively straightforward to measure. In the context of wave energy modelling, SI is generally utilised for finding suitable low-order approximations to nonparametric impulse response or frequency response data, generated by LPT-BEM solvers. As introduced in Section 2.6.1, LPT is based on strong hypotheses, which completely deny the nonlinear characteristics of the process, and so, generating data already compromised; an important part of the information regarding the nonlinearity of the process is already lost. The work developed in this thesis has a different approach. The models are identified from experimental data, measured in CFD-NWT or RWT, with the intent of utilising data rich information, not available in the data generated by LPT-BEM solvers. In the sector of wave energy, examples of the combined use of SI methods and experimental data (from NWT or RWT) can be found in the literature. For example, Bhinder, in [187] [188] [189], identifies a non-

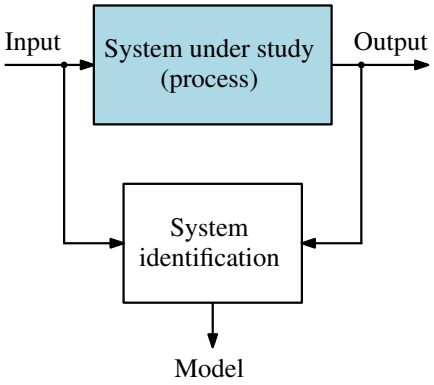

Figure 3.1: System identification basic principle.

linear viscous term to add to a linear hydrodynamic model, which is based on Cummins' equation and BEM (see Section 2.6.2.4), by utilising data generated in a CFD-NWT. In [208], numerical simulations of an OWC are employed to identify a nonlinear thermodynamic model of the OWC. In [75], a nonlinear hydrostatic restoring moment is introduced into a numerical model founded on Cummins' equation, by fitting a cubic polynomial function to laboratory test results. In [75] and [182], measurements of a hemispherical WEC, carried out in a RWT, are utilised to identify a nonlinear viscous term, which is introduced in a linear model based on Cummins' equation and BEM. In [209], measurements of a scaled OWC, installed in a 20 m length wave flume, are utilised to identify an artificial neural network model. In [210] and [211], measurements carried out at the Pico WEC plant (located on the Azores archipelago), consisting of time evolution of the FSE inside the chamber and around 60 m in front of the OWC chamber, are utilised for the identification of linear and nonlinear models, able to forecast the FSE inside the chamber. In [212] and [213], by developing, in a RWT, the concept utilised in [8] and [11] in CFD-NWTs, linear parametric and nonparamtric models for a WEC moving in heave are identified, by utilising experimental data collected at the maneuvering and sea-keeping (MASK) basin in Bethesda, US.

3.1.1 System identification requirements

The identification procedure is based on a sequence of four main steps [204] [214] [215] [216]:
1) *Experiment design and data gathering*. A suitable input signal is applied to excite the system, and the response measured.
2) *Model order and structure selection*. A parametric structure of the model is chosen (linear or nonlinear).
3) *Fitting criterion and identification algorithm selection*. Given the recorded input/output signals, an identification algorithm is used to determine the optimal model parameters, which minimize some error metric (also denoted fitting criterion) between the measured output and the output predicted by the identified parametric model.
4) *Model validation*. Once the model is identified, it is necessary to check whether this model is 'good enough' according to a chosen criterion.

It is very important to underline that SI is based on an iterative sequence of the previously mentioned four steps, which form a closed-loop block diagram (see Fig. 3.2); indeed, if the estimated model does not pass the model validation test, it is necessary to go back and review the previous steps [216]. The (rejected) identified model may be deficient for different reasons [204]:
• The data set was not informative enough in order to provide sufficient knowledge regarding the system characteristics.
• The selected model structure was not appropriate; therefore, the dynamical properties of the model are not sufficiently good to describe the dynamics of the data.
• The identification algorithm failed to find the best model parameters, according to the chosen criterion.

The main ingredients of SI (excitation signals, models, identification algorithms, and validation) are introduced in Sections 3.1.1.1, 3.1.1.2, 3.1.1.3 and 3.1.1.4, respectively.

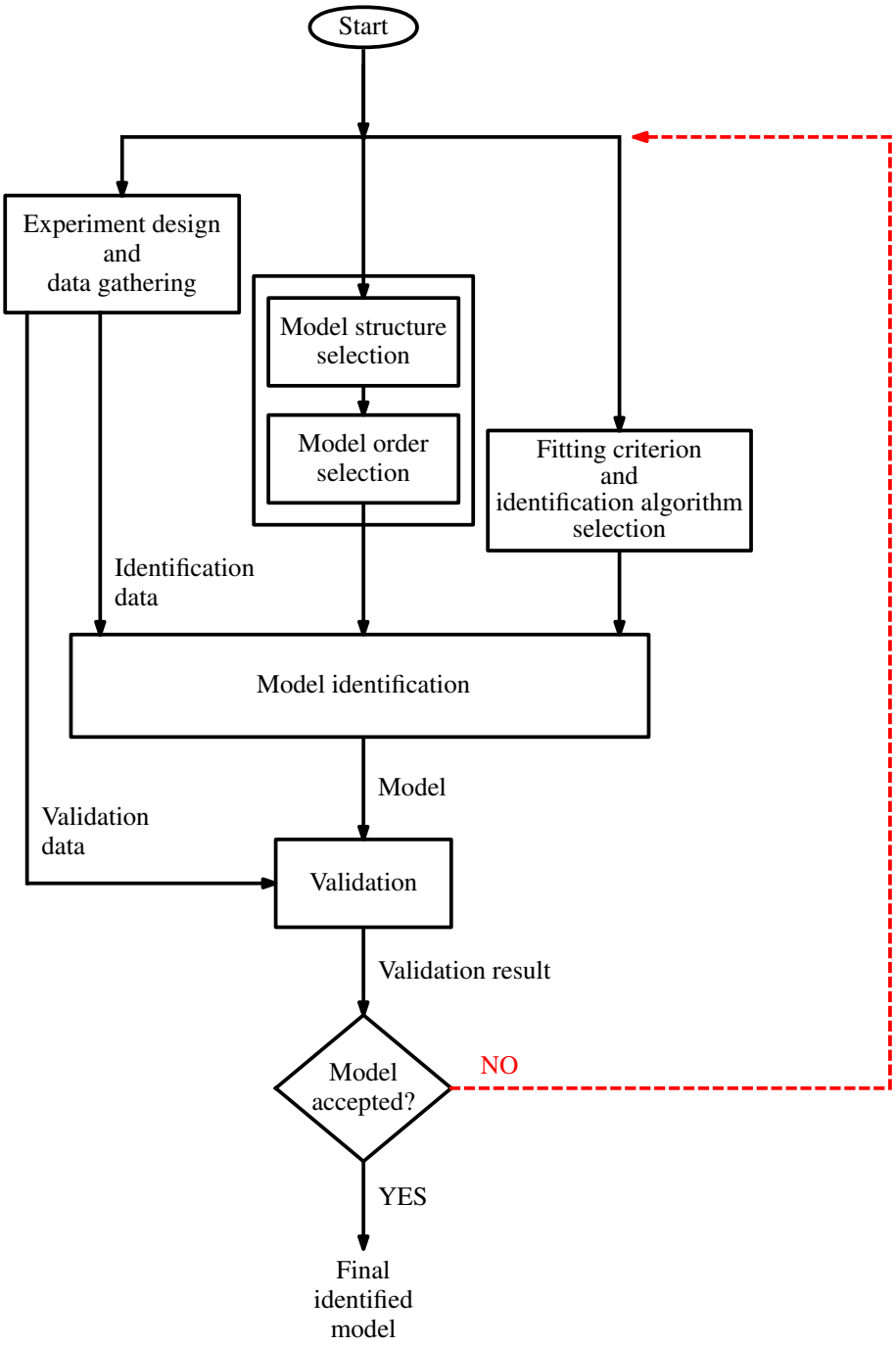

Figure 3.2: Closed-loop block diagram to identify models from recorded data.

3.1.1.1 Experiment design and data gathering

One of the most important steps in SI is the design of the appropriate experiments and excitation signals, utilised to generate identification data. The excitation signal is utilised to influence the process and to obtain some information about the characteristics and behaviour of the process. In most real-world applications, significant limitations and restrictions exist on the characteristics of the employed excitation signals; for example, the measurement time is always limited and

the input signal must be bounded between a minimum and a maximum value. Besides these constraints, there is still freedom for the user in the design of a variety of excitation signals. Nonlinear dynamic systems are significantly more complex than linear ones; therefore, the data, utilised for the identification of nonlinear systems, must contain considerably more information than the data utilised for linear systems. Consequently, in the case of nonlinear SI, the choice of an excitation signal becomes even more crucial. SI is the methodology which extracts the information contained in the data, to construct an accurate mathematical model of the process. Therefore, if the gathered data are not informative enough, the constructed model will not be sufficiently accurate; aside from the selected model structure, the chosen excitation signal determines an upper bound on the identified model performance.

In general, a good test signal should satisfy the following properties [204] [205] [217]:
• Good coverage of the full input and output amplitude signal ranges (if the system is nonlinear), because model extrapolation is more inaccurate than model interpolation.
• Good coverage of the frequencies where the system has a significant non-zero frequency response. For example, a purely sinusoidal input signal will only give information of the system's behaviour at a single frequency.
• The signal should excite the system over its whole range of operation, providing information of the system's behaviour for all the conditions which the identified model will be required to replicate.
• The amplitude distribution of the input signal should be equally distributed, in order to excite the system uniformly.
• Economic use of the test time, the experiment should show and record process behaviour in the shortest possible time.

Details regarding an experiment design and the choice of an excitation signal in a wave tank, in order to obtain data for WEC model system identification, are presented in Chapter 4.

3.1.1.2 Model structure and order selection

The choice of a model structure, in order to obtain a correct description of the relationship between input and output, is an important and difficult step; engineering intuition and 'a priori' knowledge of the studied system have to be combined, in order to help in choosing a candidate model structure [204]. Adopting a SI approach offers considerable flexibility, in both linear and nonlinear model parametrisation, regarding the relationship to physical quantities and the desired complexity/fidelity trade-off. As shown in Fig. 3.2, the selection of a model is based on two main steps: a model structure selection and a model order selection.

MODEL STRUCTURE SELECTION
In the literature, a large variety of model structures are available, each one characterised by different properties. The main properties to classify the model structures are:
Parametric or nonparametric model
• Parametric models provide the input/output relationship, through equations explicitly containing a finite number of parameters [141] [192] [218]. An example of parametric model is the transfer function of a filter described by a finite number of zeros and poles.
• Nonparametric models describe the input/output relationship utilising tables or sampled curves. In principle, an infinite number of measurements are requested to represent the system; in practice, the system is described with a finite number of measurements. An example of nonparametric model is a sampled impulse response.
Linear or nonlinear input/output relationship
• Given a mathematical model F, with input $u(t)$ and output $y(t)$, the model is said to be linear if it satisfies [219]:

$$y(t) = F\Big(k_1 u_1(t) + k_2 u_2(t)\Big) = k_1 F\Big(u_1(t)\Big) + k_2 F\Big(u_2(t)\Big) \tag{3.1}$$

where k_1, k_1 are two general constants and $u_1(t)$, $u_2(t)$ are two general time evolutions of the input.
• If (3.1) is not satisfied for any k_1, k_2, $u_1(t)$ and $u_2(t)$, the system is said to be nonlinear.

Linear or nonlinear in the parameters

• A model is linear in the parameters when the relationship between the model output and the parameters is linear [215] [218] [220] [221]. It is important not to confuse a model which is linear in the parameters with a model having a linear input/output relationship. Indeed, a model can have a nonlinear input/output relationship but be linear in the parameters. A model which is linear in the parameters can drastically reduce the complexity of the parameter identification problem, leading to LS estimation.
• If the relationship between the model output and the parameters is nonlinear, the model is said to be nonlinear in the parameters. A model nonlinear in the parameters results in a nonconvex optimization problem to determine the parameters and care must be taken in the choice of a search algorithm, which has to be able to deal with the presence of multiple local minima.

Shades of grey

So called white and grey-box models present the significant benefit of a structure well related to physical aspects of the system and the model variables usually represent physical quantities. As the shade of grey gets darker, the connection with the physical world diminishes, until the only connection of black-box models with the physical world is the representation of the overall model input and output [207].

Continuous/discrete time

• In a continuous time (CT) model, the time variable assumes values over the entire real number line, between any two time points, there are an infinite number of other points [214]. CT models are described by utilising differential equations.
• In a discrete time (DT) model, the relation between inputs and outputs, is described at discrete time points. Usually, it is assumed that the time points are equidistant. DT models are described by using difference equations.

Causal or noncausal

• A model is causal if the output at any instant t^* depends only on the input for $t \leq t^*$; in other words, the output of the system is influenced by the present and the past, but not by the future [69] [222].
• A system is noncausal if the output at any instant t^* depends on the input for some $t > t^*$ (i.e. the present output depends on the future input).

Static or dynamic

• The output of a static model, at a specific time instant t^*, depends only on the input at the same time instant t^* and not on input values at previous ($t < t^*$) or later ($t > t^*$) time instants (i.e. there is no memory effect) [142] [223] [224].
• The output of a dynamic model at a specific time instant depends also on input values at previous or future time instants (i.e. there is memory effect).

Section 3.2 details WEC hydrodynamic models that are utilised together with SI techniques. Different parametric model structures are presented, beginning with grey-box models, with structures derived from first principles, and moving onto discrete-time black-box model structures.

MODEL ORDER SELECTION

The model order of a parametric model is represented by the number of parameters utilised. By increasing the order, the model becomes more flexible and able to show more complex dynamical behaviours but, at the same time, unnecessarily high orders can make the model less able to generalise on new data (i.e. overfitting) [225]. Indeed, a model is identified by maximizing its performance on a training data set but, if the model begins to 'memorize' the training data rather than 'learning' to generalize, the model loses any utility. In general, it is necessary to determine a *parsimonious* model order [214][225] [226], which will work well with the training data and, at the same time, generalises well to other new data. A compatible requirement is that it is not desirable to add complexity to the model for little gain. This idea is in line with the common sense: 'Do not

use extra parameters if you do not need them'. Soderstrom states the parsimony principle in [214]: 'Given two or more possible models, which all explain the data well, the model with the smallest order should be selected'. In the case of nonlinear dynamic systems, the problem of the model order determination is still not satisfactorily solved. A widely applied approach is to identify different models having increasing orders and to select the best compromise between complexity and accuracy [205], An indication that a correct model order has been selected is provided by the fact that the model performance does not increase significantly by increasing the model order beyond a certain order [141]. More details, regarding the model order selection, are reported in Section 3.2.4.

3.1.1.3 Fitting criterion and identification algorithm selection

Given the experimental data and a parametric model structure, characterised by the parameter vector $\boldsymbol{\theta}$, it is necessary to identify some parameter values $\hat{\boldsymbol{\theta}}$, in order to obtain the 'best' model able to describe the data. A way to quantify the model performance is provided by the use of a loss function (LF), $J(\boldsymbol{\theta})$, (also denoted fitting criterion or error metric), between the experimental data and the model prediction. Therefore, given the experimental data, a model structure, and a LF, each parameter vector value produces a singular scalar number, which represents the model performance. Mathematically, it is possible to write that:

$$J : \boldsymbol{\theta} \in \Re^q \rightarrow \Re \tag{3.2}$$

where q is the number of parameters. One of the most common and utilised LFs is the mean squared error (MSE), as explained in Section 3.3.1. By changing all possible parameter values, J describes a multi-dimensional surface (in general multimodal), having a global minimum and multiple local minima. The objective of the identification algorithm is to find the parameter values $\hat{\boldsymbol{\theta}}$ which minimize J, in order to identify the best model able to fit the experimental data. Numerous identification algorithms, available in the literature, are characterised by different performance in residual fitting error, convergence speed and computational cost. The identification algorithms can be classified, depending on the properties considered:

Linear/nonlinear optimization

• If the model output is a linear function of $\boldsymbol{\theta}$ and the MSE is used as a fitting criteria, then $J(\boldsymbol{\theta})$ is a quadratic function with an unique minimum and an analytical solution exists (linear optimization) [205].

• If the model output is nonlinear in $\boldsymbol{\theta}$ then, in general, $J(\boldsymbol{\theta})$ is a multimodal function, no analytical solution exists and a numerical analysis is required (nonlinear optimization).

Off-line/on-line

• In the case of off-line identification, the experimental data, obtained by process measurements, are first stored and, only when the experiment is completed, are utilised for the identification. This approach has the advantage that an identification experiment can be carefully designed, in order to extract a large amount of information from the process [227].

• In many applications, especially if the process characteristics are time varying, it is important to track the process in real-time and to adapt the model parameters as the process develops [220]. In the case of on-line identification, the model identification is performed concurrently with the experiment [141] [228].

Non-recursive/recursive

• In the case when the analytical solution of the identification problem is available (e.g. linear optimization), the algorithm provides the solution with the use of an equation, without the necessity for recursive search (i.e. a non-recursive algorithm is employed).

• In the case of nonlinear optimization, the presence of multiple local minima of the LF imposes the use of recursive algorithms, which require stopping criteria, based on minimum accuracy achieved or on maximum computation time utilised.

See Section 3.3 for details regarding hydrodynamic WEC parameter estimation.

3.1.1.4 Model validation

The last important step in SI is that of model validation, where the model is tested in order to verify its accuracy, in describing the system under investigation. The comparison of model predictions with the training data can always be improved by increasing the model complexity, but an unnecessarily model complexity can reduce the ability of the model in generalising on new data (i.e. overfitting), making the model worthless. Therefore, it is very important to verify the performance of the identified model on fresh data (validation data) and, in cases where the validation test is not passed, it is necessary to return to the previous SI steps, as shown in Fig. 3.2. In Section 3.4, details regarding hydrodynamic WEC model validation are provided.

3.2 Hydrodynamic WEC model structures

3.2.1 Introduction

Mathematical modelling of WECs has many uses, including the simulation of device motion, power production assessment and as a basis for model-based control design. In all these cases, it is important to describe how the body moves in the water, interacting with waves propagating on the fluid surface. From a modelling point of view, this corresponds to the description of a mathematical relationship between the FSE, η, (the model input) and the body displacement from an equilibrium position, y, (the model output). In the present work, the family of all models (linear/nonlinear and CT/DT), having η as input and y as output, is denoted $\eta \rightarrow y$. In Section 2.6.1, Newton's 2nd law, under the hypotheses of LPT, was used to derive Cummins' equation (2.86), where $f_{in}(t) = f_e(t) + f_{pto}(t) + f_m(t)$ represents the model input (where only f_{pto} is directly manipulable in the experiments) and y the model output. In this work, the family of all models (linear/nonlinear and CT/DT), having f_{in} as input and y as output, is denoted $f_{in} \rightarrow y$.

3.2.2 Continuous-time model structures

The fundamental physical laws, such as Newton's laws of dynamics or the Navier-Stokes equations, are expressed as differential equations in CT; therefore, models, derived from physical principles, are inherently constructed in CT. An advantage of CT models is that they provide a good insight into system understanding, because the model parameters are strongly related to the physical system properties. In contrast, the physical meaning of the parameters is usually lost in the process of time discretization [229] [230] [231]. On the other hand, DT models have some important advantages over CT models, as explained in Section 3.2.3. In the case where the final objective is the construction of a DT model, the strong link of CT models with the physical world can be used as starting point to suggest DT model structures. A fundamental CT equation describing WEC dynamics is Cummins' equation (2.86), whose block diagram is represented in Fig. 3.3, where the dashed line bands together the dynamics of the WEC (the $f_{in} \rightarrow y$ model). The block diagram of Fig. 3.3 can be transformed into the block diagram of Fig. 3.4, where the excitation force is completely separate from the other hydrodynamic forces. It is worthwhile underlining that the blocks of Fig. 3.3 are all linear, whereas the blocks $\eta \rightarrow f_e$ and $f_{in} \rightarrow y$, in Fig. 3.4, can be linear or nonlinear. Note that, in both Figs. 3.3 and 3.4, the block $f_{in} \rightarrow y$ takes as input the summation of f_e, f_{pto} and f_m; therefore, the block is not able to differentiate between these three forces. This equivalence will be utilised in Section 4.3.2.3 for the identification of $f_{in} \rightarrow y$ models, by applying a dynamically rich PTO force.

In Fig. 3.4, the $\eta \rightarrow f_e$ block describes the relationship between the undisturbed free surface elevation η, measured in a position that corresponds to the centre of mass of the body, and the excitation force, f_e, that is the force experienced by the body when it is held fixed in the presence of waves (see Section 2.4.1.1). If η is assumed to change very slowly, the relationship between

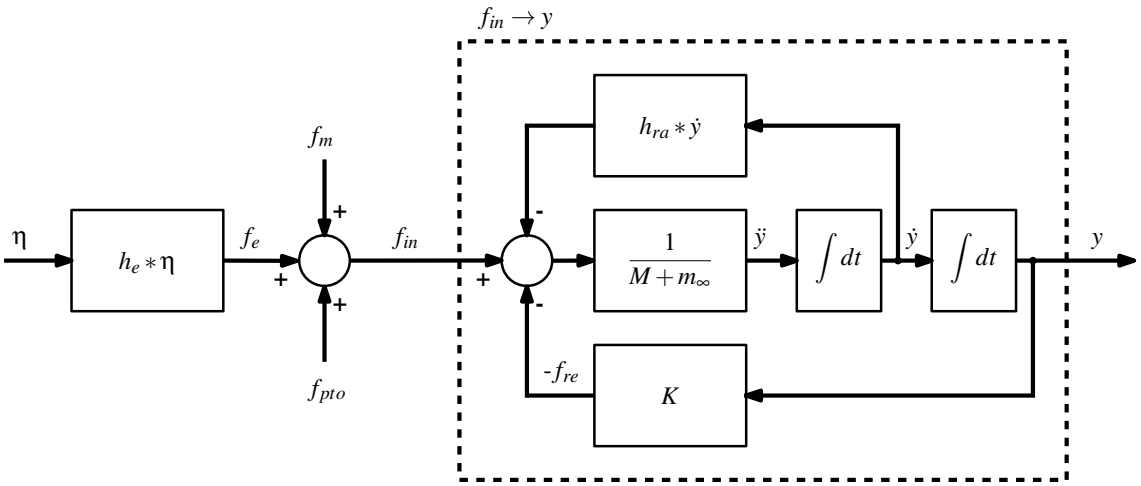

Figure 3.3: Cummins' equation block diagram; the dashed line bands together the dynamics of the WEC (the $f_{in} \to y$ model).

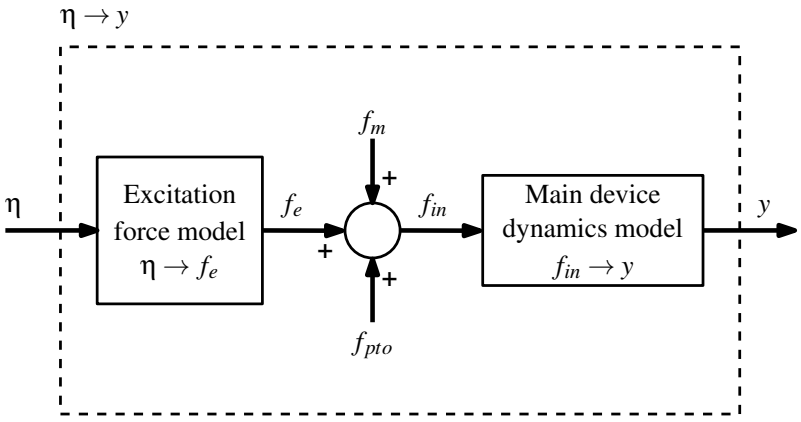

Figure 3.4: General block diagram of a WEC model, inspired by the CT Cummins' equation. The blocks $\eta \to f_e$ and $f_{in} \to y$ can be linear or nonlinear. The dashed line bands together the $\eta \to y$ model.

η and f_e is just a static curve, r , representing the restoring force acting on the body (see Section 2.2.7). The dynamic part of the relationship between η and f_e can be introduced in the model with a linear dynamic block, connected with a cascade configuration and following the static block (see Fig. 3.5). The model structure, represented in Fig. 3.5, is denoted a Hammerstein model, and is described in Section 3.2.3.3.

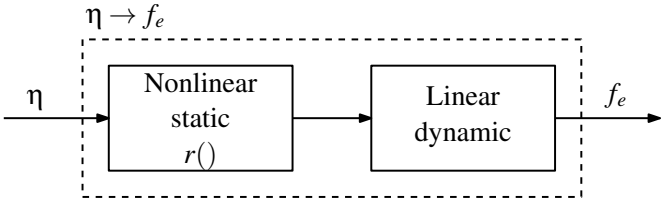

Figure 3.5: Block diagram of the Hammerstein model, describing the η and f_e relationship. The static block, *r*, models the restoring force acting on the body.

In Fig. 3.3, the linear $f_{in} \rightarrow y$ model, bounded together by the dashed line, can be used as a basis for a nonlinear WEC model structure. Indeed, it is possible to introduce a nonlinear restoring term in the model, by replacing equation (2.102) with equation (2.103). The result is the substitution of the linear restoring block K with a general nonlinear static restoring block g and the gathering of all the other model blocks into a single linear block, as shown by the dash dotted line in Fig. 3.6(a). Therefore, the overall result is a negative feedback scheme, as represented in Fig. 3.6(b).

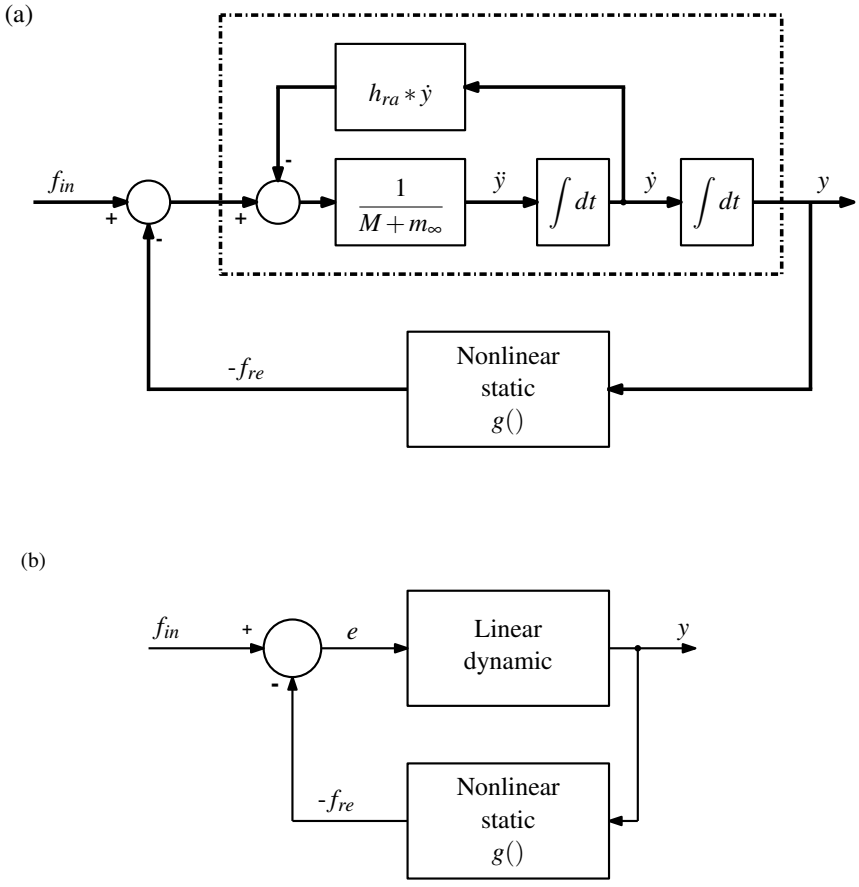

Figure 3.6: (a) Nonlinear $f_{in} \rightarrow y$ model, obtained by the CT Cummins' equation, by replacing the linear restoring K block with a general nonlinear static restoring g block. The dash dotted line gathers all the other linear blocks. (b) Compacted block diagram representation.

3.2.3 Discrete-time model structures

The physical world is naturally described by utilising CT differential equations but, despite this, SI is usually utilised to generate DT models for the following reasons:
• Typically, experimental data are available only at DT instants [221] [232] [233].
• The nature of DT data is particularly compatible with digital computer calculations.
• The majority of SI techniques are based on discrete time models [204]; however, identification of continuous time models can also be performed [229] [230] [231].
• From the point of view of control applications, DT model descriptions are more suitable, since model-based control algorithms (like model predictive control) are usually formulated in DT; furthermore, signal measurement and control actions are usually taken at DT instances [232] [233] [234], and implemented using digital computers.
• The estimation of nonlinear CT models can be computationally involved and it is not a trivial task; indeed, it may imply the computing of integrals or time-derivatives of nonlinear functions of the measured signals [229] [234].
• In the case where the estimation of physical system parameters is not needed, the use of DT models may be an alternative [234].
• In DT, model structures which are linear in the parameters are easily constructed, providing the possibility to use linear optimization methods for parameter estimation.

In the context of offshore engineering and wave energy, the majority of the implemented models are CT models, as shown in Chapter 2, but there are some DT examples, such as in [235], where DT ARMA models, utilised for the simulation of random FSE at a spatial point, are identified utilising FSE historical data. In [210] and [236], DT AR models are identified and utilised for FSE forecasting. In [237], a linear DT state space model, for a single DoF heave point absorber, is developed, utilising hydrodynamic coefficients from WAMIT.

In contrast to CT models, DT modelling uses signals only specified at the discrete time instants $t = kT_s$, where T_s is the sampling period and k is an integer. For example, the values of η, f_{in} and y at the time instant kT_s are represented by $\eta(k)$, $f_{in}(k)$ and $y(k)$, respectively. In general, the relationship between η and y is noncausal [82]; therefore, the chosen model structure has to provide the possibility of such noncausality in the identified model. In this work, nonlinear autoregressive with exogenous input (NARX) models [205] are utilized. In Fig. 3.7(a), a general linear or nonlinear DT block is represented, with input $u(k)$ and output $y(k)$; $u(k)$ and $y(k)$ can represent any physical quantity, such as excitation force, wave elevation, body displacement, etc., as shown in Chapter 6. If a NARX model is utilised to describe the relationship between $u(k)$ and $y(k)$, the present value of the output $y(k)$ depends on the past values of the output $y(k-1),...,y(k-n_a)$ and the input values $u(k-n_d),u(k-n_d-1),...,u(k-n_d-n_b)$. The NARX model may be summarized [221] with:

$$y(k) = \gamma\Big[y(k-1) \;\; ... \;\; y(k-n_a) \;\; u(k-n_d) \;\; u(k-n_d-1) \;\; ... \;\; u(k-n_d-n_b)\Big], \tag{3.3}$$

where $\gamma[.]$ is a linear or nonlinear function (see Fig. 3.7(b)). Equation (3.3) suggests that $y(k)$ is a function of n_a previous output and n_b+1 input values, taken at different time instants (in total n_a+n_b+1 variables). Once n_a, n_b and n_d are selected, it is possible to obtain different model structures by changing the function $\gamma[.]$.

As introduced in Section 3.1.1.2, the linearity of the model in the parameters is an important property, which can be mathematically expressed (regardless of whether the input/output relationship is linear or nonlinear) as:

$$y(k) = \sum_{i=1}^{q} \varphi_i(k)\theta_i = \boldsymbol{\varphi}(k)^T\boldsymbol{\theta}, \tag{3.4}$$

where

$$\boldsymbol{\varphi}(k) = [\varphi_1(k) \;\; ... \;\; \varphi_q(k)]^T \tag{3.5}$$

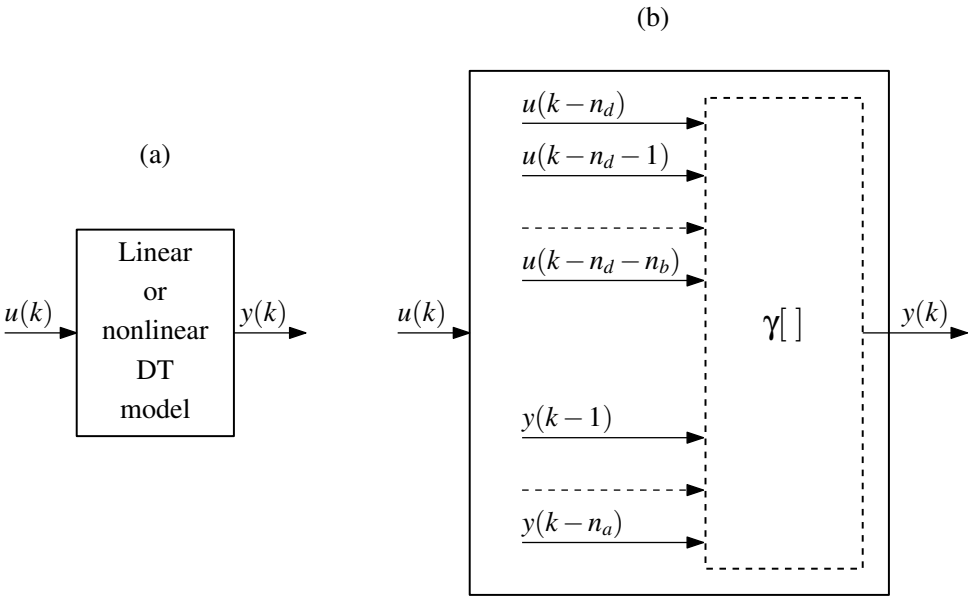

Figure 3.7: (a) General linear or nonlinear DT block, where $u(k)$ and $y(k)$ can represent any physical quantity, such as excitation force, wave elevation, body displacement, etc. (b) Block diagram for a general NARX discrete-time model.

is a regressor vector and

$$\boldsymbol{\theta} = [\theta_1 \ \ldots \ \theta_q]^T \tag{3.6}$$

is the unknown parameter vector. The regressors $\varphi_i(k)$ are a linear or nonlinear transformation of the vector $[y(k-1) \ \ldots \ y(k-n_a) \ \ u(k-n_d) \ \ u(k-n_d-1) \ \ \ldots \ \ u(k-n_d-n_b)]$. Fig. 3.8 shows the block diagram of a model which is always linear in the parameters, regardless of whether the input/output relationship is linear or nonlinear, where the regressors $\varphi_i(k)$ are constructed by the regressor generator (RG) block. Therefore, the nonlinearity, if present, between the output and the input is contained in the regressors φ_i and is not reflected in the parameter vector $\boldsymbol{\theta}$ [204] [205] [238].

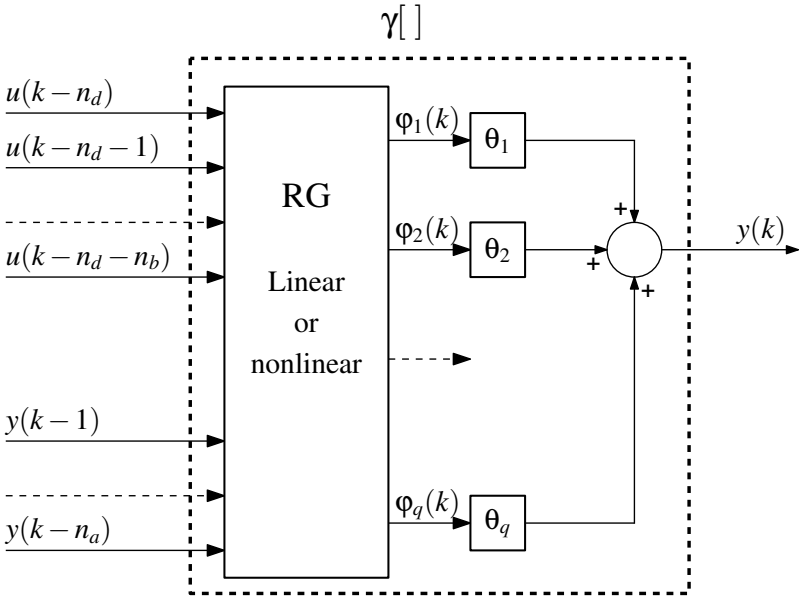

Figure 3.8: Block diagram of a general NARX DT model, which is linear in the parameters, where $y(k) = \sum_{i=1}^{q} \varphi_i(k)\theta_i$. The regressors φ_i are constructed by the RG block.

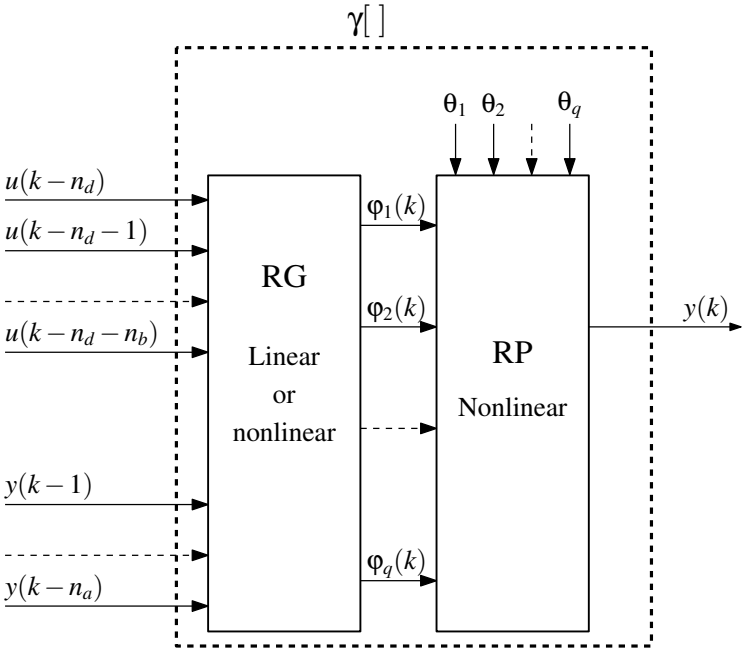

Figure 3.9: Block diagram for a general NARX discrete-time model, nonlinear in the parameters.

On the other hand, if the relationship between model output and parameters is not described by equation (3.4), the model is nonlinear in the parameters. Fig. 3.9 shows the block diagram of a model which is nonlinear in the parameters, where the regressors $\varphi_i(k)$ are processed in a nonlinear way by the regressor processing (RP) block.

The integer quantities n_a and n_b represent the dynamical order of the model and, by increasing n_a and n_b, the model becomes more flexible but, at the same time, excessively high orders may lead to overfitting, as seen in Section 3.1.1.2. The integer quantity n_d is the input delay time and represents (for $n_d \geq 0$) the number of samples before the output reacts to the input, as shown in Figs. 3.10 and 3.11; if $n_d \geq 0$ the system is causal and the output does not depend on future values of the input. If $n_d < 0$, as shown in Fig. 3.12, the system is noncausal and n_d represents the number of future input values, which influence the present value of the output.

A number of different types of NARX models are described in this chapter, which can be obtained by changing the function $\gamma[.]$ in equation (3.3), namely: the autoregressive with exogenous input (ARX) model, the Kolmogorov-Gorov polynomial (KGP) model, the artificial neural network (ANN) model, the nonlinear static (NLS) model and the block-oriented nonlinear (BONL) model. An overview of the different models' properties is shown in Table 3.1. For more details regarding these models see [205] [239].

PROPERTY	ARX	KGP	ANN	NLS	BONL
Input/output relationship	L	NL	NL	NL	NL
Parameters/output relationship (Optimization)	L	L	NL	L	L
Shade of grey	B	B	B	G	G
Memory	D	D	D	S	D

Table 3.1: Properties overview of the ARX, KGP, ANN, NLS and BONL models (L=linear, NL=nonlinear, B=black-box, G=grey-box, D=dynamic and S=static).

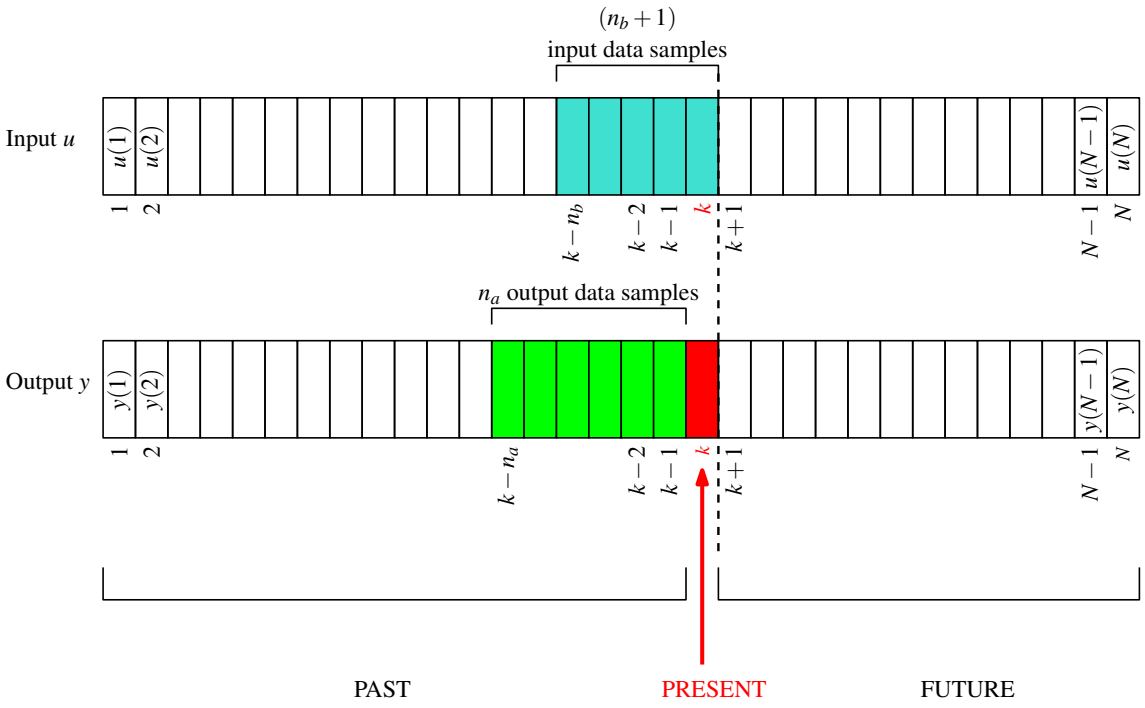

Figure 3.10: Causal system with no delay ($n_d = 0$).

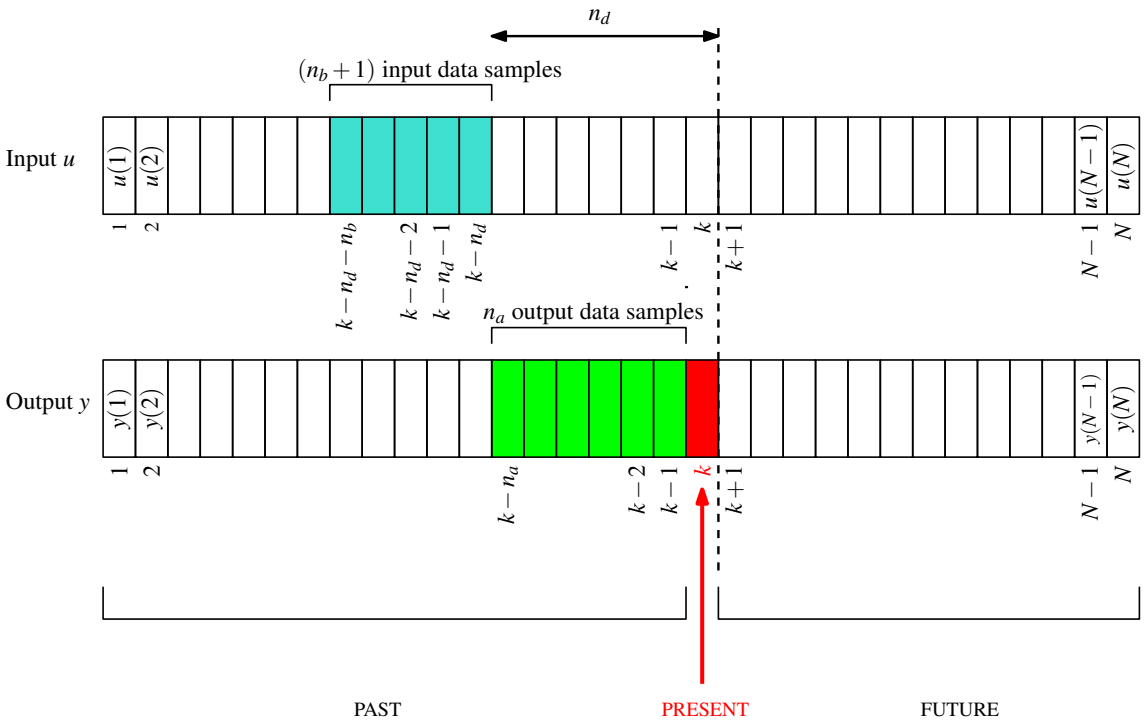

Figure 3.11: Causal system with delay ($n_d > 0$).

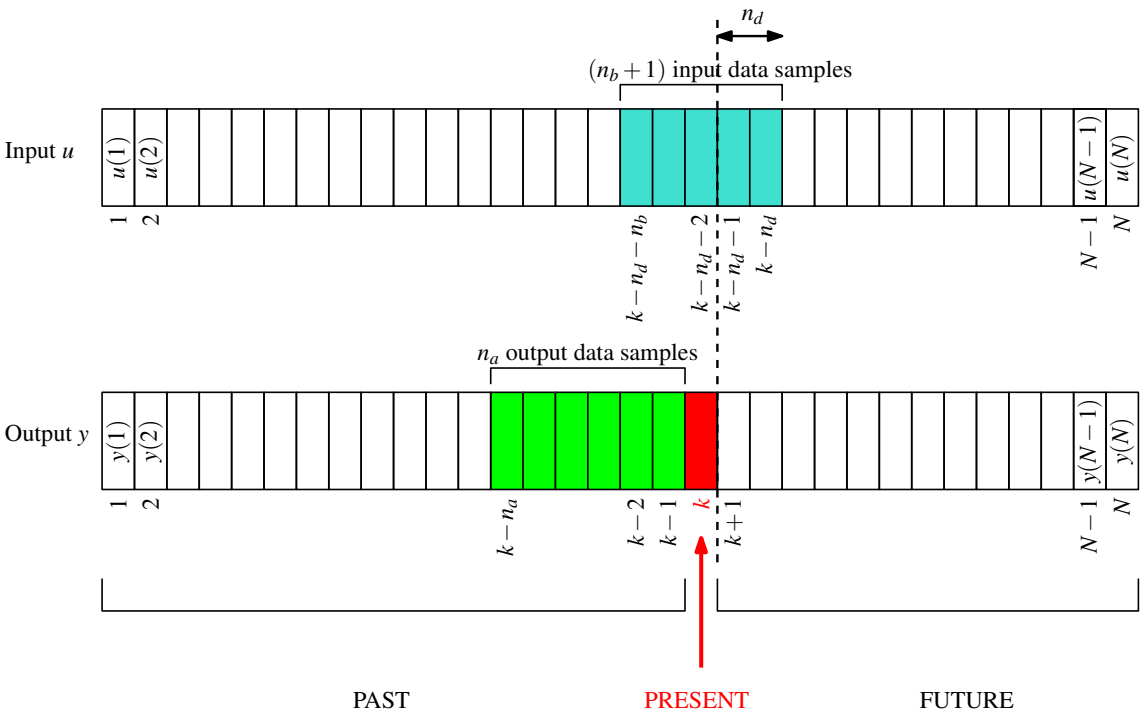

Figure 3.12: Noncausal system ($n_d < 0$).

3.2.3.1 Autoregressive with exogenous input model

The ARX model is a well-known black-box model which is linear in the parameters a_i and b_i, characterised by a linear input/output relationship [204]. For an ARX model, equation (3.3) becomes:

$$y(k) = \sum_{i=1}^{n_a} a_i y(k-i) + \sum_{i=0}^{n_b} b_i u(k-n_d-i) \tag{3.7}$$

and the parameter vector is given by:

$$\boldsymbol{\theta}_{arx} = \begin{bmatrix} a_1 & a_2 & \dots & a_{n_a} & b_0 & b_1 & \dots & b_{n_b} \end{bmatrix}^T. \tag{3.8}$$

Therefore, the number of parameters to be estimated is given by:

$$N_{par} = n_a + n_b + 1. \tag{3.9}$$

Examples of ARX models are shown in the case studies of Sections 6.3.1, 6.3.2, 6.2, 6.4 and 7.4.

3.2.3.2 Nonlinear static model

A simple way to model a nonlinear relationship between the input, $u(k)$, and the output, $y(k)$, of a model is to utilise a nonlinear static block r, obtaining:

$$y(k) = r\Big(u(k)\Big). \tag{3.10}$$

Equation (3.10) shows that, in the model, there is no memory effect, the output at the instant k depends only on the input at the same instant k. The static function, r, can be approximated with a linear combination of basis functions $\{\zeta_1, \zeta_2, ..., \zeta_{n_c}\}$; therefore equation 3.10 becomes:

$$y(k) = \sum_{i=1}^{n_c} c_i \zeta_i\Big(u(k)\Big). \tag{3.11}$$

Examples of NLS models are shown in the case studies in Sections 6.3.1 and 6.2.

3.2.3.3 Hammerstein model

Connecting linear dynamic ARX and NLS blocks, in various configurations, it is possible to obtain a variety of BONL model structures [221] [239] [240]. A well known example of a BONL model is the Hammerstein model (introduced in Section 3.2.2), which consists of a cascade connection of a NLS block, followed by an ARX block, as shown in Fig. 3.13. In the case of an Hammerstein model, equation (3.3) becomes [240]:

$$y(k) = \sum_{i=1}^{n_a} a_i y(k-i) + \sum_{i=0}^{n_b} b_i r\Big(u(k-n_d-i)\Big) \tag{3.12}$$

where r is a nonlinear static function. The Hammerstein model is characterized by a nonlinear input/output relationship (if r is not linear), but is linear in the parameters a_i and b_i.

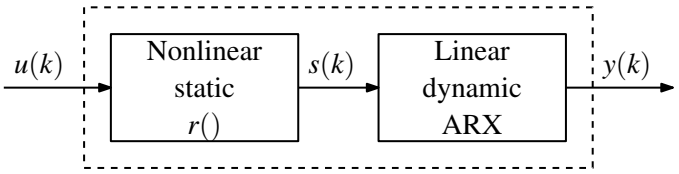

Figure 3.13: Block diagram of a Hammerstein model.

In the Hammerstein model, the static relationship between input and output is given by the product of the static function, r, and the DC gain of the ARX model, K_{dc}. Therefore, the characterization of the DC gain of the two blocks is not unique, any pair $(K_{dc}/\alpha\ ,\ \alpha r)$, where α is an arbitrary constant, will produce the same input and output [241]. In order to remove this ambiguity, the K_{dc} of the ARX block is generally set to unity, which allows the DC gain for the entire Hammerstein model to be solely represented by the nonlinear static function r. The Z-transfer function of the ARX model (3.7), given by:

$$H(z) = \frac{Y(z)}{U(z)} = \frac{z^{-n_d}\left(b_0 + b_1 z^{-1} + b_2 z^{-2} + ... + b_{n_b} z^{-n_b}\right)}{1 - a_1 z^{-1} - a_2 z^{-2} - ... - a_{n_a} z^{-n_a}}, \tag{3.13}$$

can be utilised in order to obtain the DC gain of the ARX model; indeed, the DC gain corresponds to the $H(z)$, given by (3.13), calculated for $z = 1$ (in the case there are no poles at $z = 1$) [242]:

$$K_{dc} = H(z)\Big|_{z=1} = 1 \tag{3.14}$$

Therefore, from equations (3.13) and (3.14), it follows [240] that:

$$\frac{\sum_{i=0}^{n_b} b_i}{1 - \sum_{i=1}^{n_a} a_i} = 1 \tag{3.15}$$

and, by manipulating (3.15), it follows that:

$$\sum_{i=1}^{n_a} a_i + \sum_{i=0}^{n_b} b_i = 1 \tag{3.16}$$

The parameter vector of the ARX block of the Hammerstein model is given (see Section 3.2.3.1) by:

$$\boldsymbol{\theta}_{H_{arx}} = \Big[a_1\ \ a_2\ \ ...\ \ a_{n_a}\ \ b_0\ \ b_1\ \ ...\ \ b_{n_b}\Big]^T; \tag{3.17}$$

therefore, equation (3.16) can be written in a matrix form [240] as:

$$\mathbf{A}\boldsymbol{\theta}_{H_{arx}} = d, \tag{3.18}$$

where $\mathbf{A} = [1\ \ 1\ \ ...\ \ 1] \in \Re^{1\times(n_a+n_b+1)}$ is composed of only unitary coefficients and $d = 1$. Examples of Hammerstein models are shown in the case studies of Sections 6.3.1 and 6.2. It is important to underline that a limitation of the Hammerstein model is that is able to model only static nonlinearities.

3.2.3.4 Feedback block-oriented model

Another well known DT BONL model is the feedback block-oriented (FBO) model, characterised by the negative feedback structure, shown in Fig. 3.14. It is useful to underline that the FBO model, presented in this section, is the DT version of the CT model structure represented in Fig. 3.6(b); for this reason, the signal at the output of the NLS block, corresponding to the static function $g()$, is denoted $-f_{re}$ in both Figs. 3.6(b) and 3.14. From Fig. 3.14, it is possible to

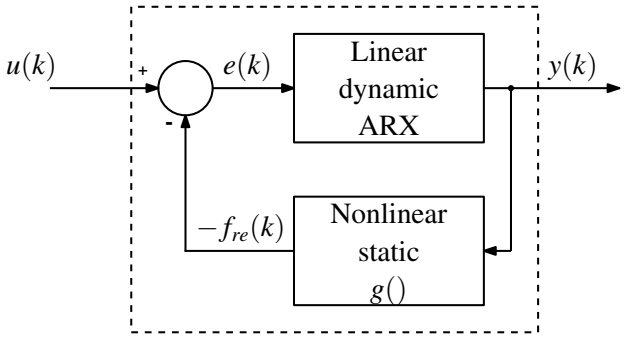

Figure 3.14: Block diagram of the FBO model.

observe that the three governing equations of the FBO model are:

$$y(k) = \sum_{i=1}^{n_a} a_i y(k-i) + \sum_{i=0}^{n_b} b_i e(k-n_d-i), \tag{3.19}$$

$$e(k) = u(k) - \Big(-f_{re}(k) \Big), \tag{3.20}$$

and

$$-f_{re}(k) = g\Big(y(k)\Big). \tag{3.21}$$

From equations (3.19) and (3.20), it follows that:

$$y(k) = \sum_{i=1}^{n_a} a_i y(k-i) + \sum_{i=0}^{n_b} b_i \Big[u(k-n_d-i) - \Big(-f_{re}(k-n_d-i) \Big) \Big] \tag{3.22}$$

By utilising (3.21) in (3.22), it follows that:

$$y(k) = \sum_{i=1}^{n_a} a_i y(k-i) + \sum_{i=0}^{n_b} b_i \Big[u(k-n_d-i) - g\Big(y(k-n_d-i)\Big) \Big] \tag{3.23}$$

Therefore, in the case of a BOF model, equation (3.3) becomes [240]:

$$y(k) = \sum_{i=1}^{n_a} a_i y(k-i) - \sum_{i=0}^{n_b} b_i \, g\Big(y(k-n_d-i)\Big) + \sum_{i=0}^{n_b} b_i u(k-n_d-i) \tag{3.24}$$

An example of FBO a model is shown in the case study of Section 6.3.1.

3.2.3.5 Nonlinear Kolmogorov-Gabor polynomial model

The KGP model utilises a polynomial nonlinearity to describe the system dynamics [205] [243] and equation (3.3) becomes:

$$\begin{aligned} y(k) &= \sum_{i=1}^{n_a} a_{i1} y(k-i) + \sum_{i=0}^{n_b} b_{i1} u(k-n_d-i) \\ &+ \quad \ldots \\ &+ \quad \sum_{i=1}^{n_a} a_{ip} y^{n_p}(k-i) + \sum_{i=0}^{n_b} b_{ip} u^{n_p}(k-n_d-i) \\ &+ \quad \sum_{i=1}^{n_a} \sum_{j=0}^{n_b} c_{ij} y(k-i) u(k-n_d-j) \\ &+ \quad \ldots \end{aligned} \tag{3.25}$$

where n_p is the maximum polynomial order for the terms involving u and y alone, as well as the cross-product terms. The KGP model is a black-box model having a nonlinear input/output relationship, but is linear in the parameters a_{ij}, b_{ij} and c_{ij}. However, the presence of the cross-product terms (between u and y) in the KGP model structure can lead to potential, and unpredictable, stability problems. In essence, cross-product terms introduce input-dependent terms into the (notionally linearised) model Jacobian, which make the stability properties dependent on the input used. In fact, some experiences with cross-product terms showed the model response on validation data to be clearly unstable, even though the model response on training data was stable, in spite of the fact that the spectral and distribution characteristics of training and validation data were similar. For this reason, the cross-product terms in the model of equation (3.25) can be removed, obtaining the simpler model [9][12]:

$$y(k) = \sum_{j=1}^{n_p} \Big[\sum_{i=1}^{n_a} a_{ij} y^j(k-i) + \sum_{i=0}^{n_b} b_{ij} u^j(k-n_d-i) \Big]$$

In the absence of cross-product terms, the number of parameters to be estimated for the KGP model is given by:

$$N_{par} = n_p(n_a + n_b + 1). \tag{3.26}$$

Examples of KGP models are shown in the case studies in Sections 6.3.2, 6.2, 6.4 and 7.4. An advantage of the KGP model, compared to the Hammerstein model, is its reasonably general nonlinear dynamical input/output relationship.

3.2.3.6 Artificial neural network model

A multi-layer perceptron (MLP) artificial neural network is a black-box model having a nonlinear input/output relationship and is nonlinear in the parameters. In order to simplify the notation, define the vector:

$$\mathbf{V}(k) = \Big[v_1(k) \ldots v_{n_v}(k) \Big] = \Big[y(k-1) \ldots y(k-n_a)\ u(k-n_d)\ u(k-n_d-1) \ldots u(k-n_d-n_b) \Big] \tag{3.27}$$

where $n_v = n_a + n_b + 1$. Therefore, the output of a NARX model, described by equation (3.3), becomes:

$$y(k) = \gamma\Big[\mathbf{V}(k) \Big] \tag{3.28}$$

In the case where a single perceptron neuron is utilised in a ANN, the block diagram, in Fig. 3.7, becomes the block diagram in Fig. 3.15(a).

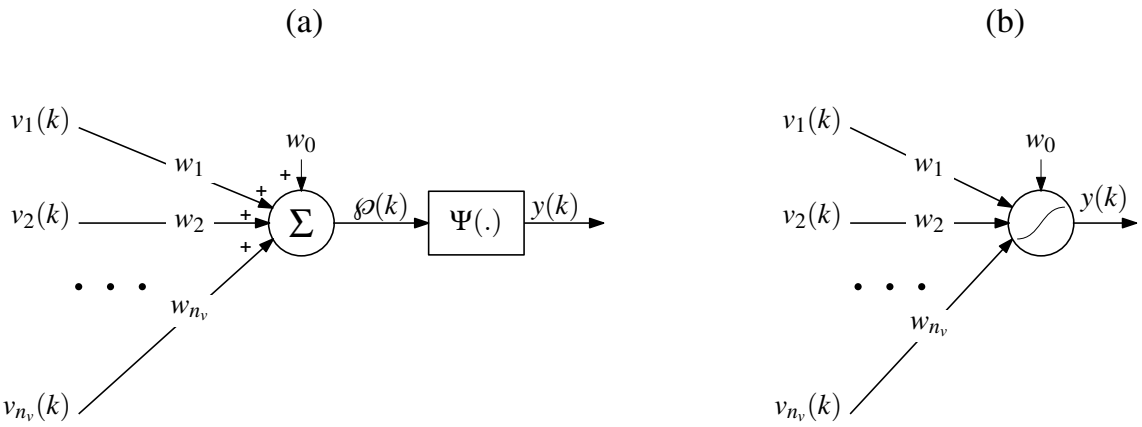

Figure 3.15: (a) Perceptron neuron block diagram. (b) Perceptron neuron symbol.

The signals $v_i(k)$ are multiplied by weights w_1,...,w_{n_v} and then added together with a constant scalar bias w_0, in order to form the signal $\wp(k)$. The signal $\wp(k)$ is subsequently passed through the activation function Ψ (which can be linear or nonlinear), producing the scalar output $y(k)$, which can be expressed as [205]:

$$y(k) = \Psi\Big(\wp(k)\Big) = \Psi\Big(w_0 + \sum_{l=1}^{n_v} w_l v_l(k)\Big) = \Psi\Big(\sum_{l=0}^{n_v} w_l v_l(k)\Big) \tag{3.29}$$

where, by definition, $v_0(k) = 1\ \forall k$. In the case of a linear activation function (see Fig. 3.16(a)):

$$\Psi(\wp) = \wp \tag{3.30}$$

Instead, in the case of a nonlinear activation function, a common choice is the tan-sigmoid function [244] (see Fig. 3.16(b)), defined as:

$$\Psi(\wp) = \frac{2}{1+e^{-2\wp}} - 1 \tag{3.31}$$

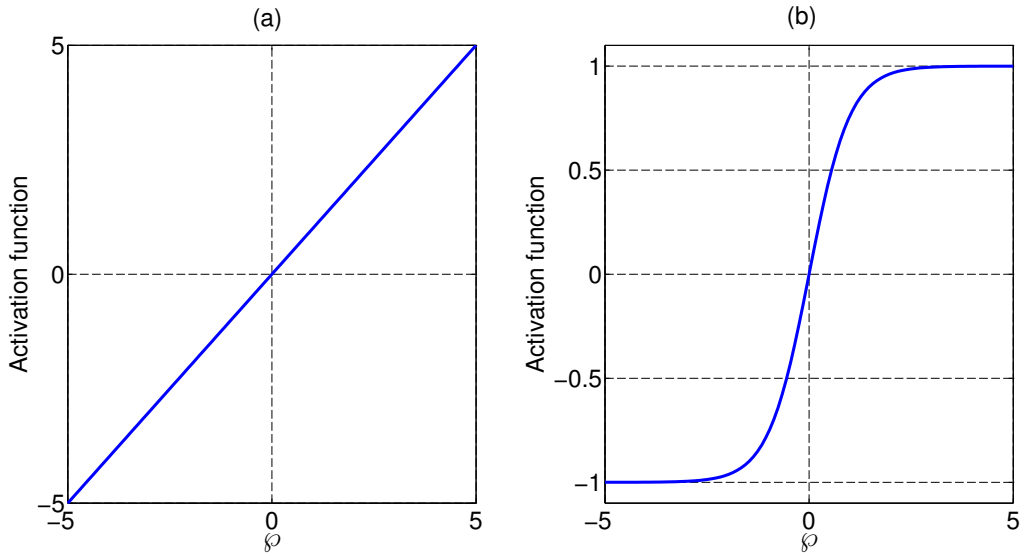

Figure 3.16: Activation function of a perceptron neuron. (a) Linear activation function $\Psi(\wp) = \wp$. (b) Tan-sigmoid activation function $\Psi(\wp) = 2/(1+e^{-2\wp}) - 1$.

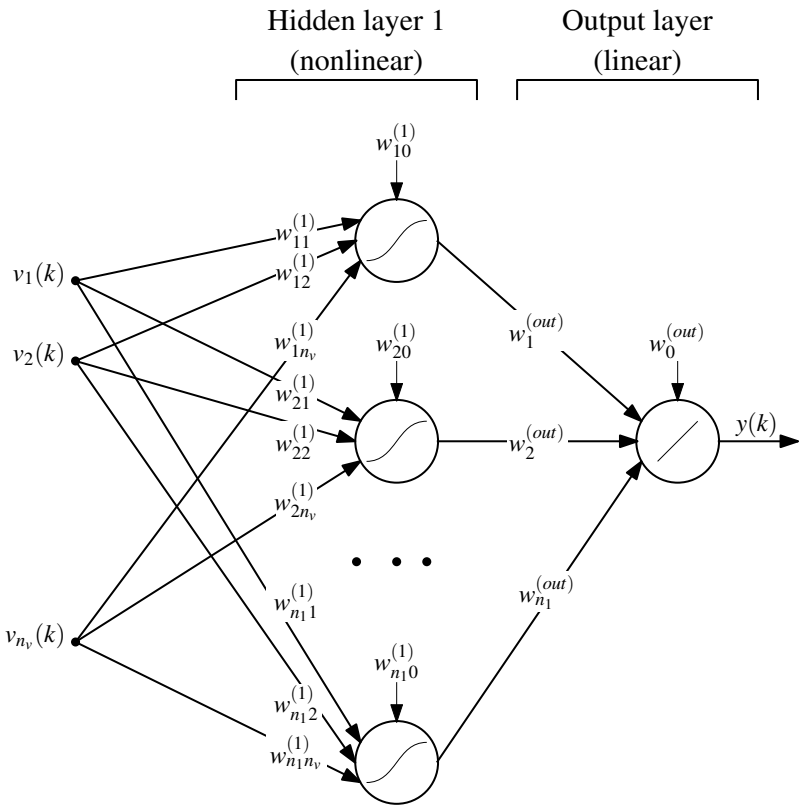

Figure 3.17: MLP-ANN with one nonlinear hidden layer and one linear output layer.

When n_1 perceptron neurons are used in parallel and are connected to an linear output neuron, the MLP-ANN with one hidden layer is obtained (see Fig. 3.17) and equation (3.3) can be written [205] as:

$$y(k) = \sum_{i=0}^{n_1} w_i^{(out)} \Psi_i \Big(\sum_{l=0}^{n_v} w_{il}^{(1)} v_l(k) \Big) \tag{3.32}$$

where $w_{il}^{(1)}$ are the unknown weights (and biases) of the i-th perceptron neuron of the hidden layer, $w_i^{(out)}$ are the unknown weights (and biases) of the linear output perceptron neuron and $v_l(k)$ are defined in equation (3.27).

While a two layer networks, with sigmoid activation functions in the hidden layer and linear activation functions in the output layer, can give an arbitrary approximation capability [245] [246], two hidden layers usually require a lower total neuron count, for a given level of approximation accuracy. Equation (3.3), in the case of a MLP-ANN, with two nonlinear hidden layers and one linear output layer, can be written [205] as:

$$y(k) = \sum_{i=0}^{n_2} w_i^{(out)} \Psi_i \Big(\sum_{j=0}^{n_1} w_{ij}^{(2)} \Psi_j \big(\sum_{l=0}^{n_v} w_{jl}^{(1)} v_l(k) \big) \Big) \tag{3.33}$$

where n_1 and n_2 are the number of neurons in the hidden layers 1 and 2, respectively and $w_{ij}^{(2)}$ are the unknown weights (and biases) of the i-th perceptron neuron of the hidden layer 2. Equation (3.33) shows that the model output y is not linear in the parameters (in the weights and biases). In Fig. 3.18, the block diagram of a MLP-ANN with two hidden layers and a linear output layer is shown. The overall model complexity is determined by n_1 and n_2 , in addition to n_a and n_b. For the MLP-ANN model, the number of parameters to be estimated is given by:

$$N_{par} = (n_a + n_b + 2)n_1 + (n_1 + 1)n_2 + n_2 + 1. \tag{3.34}$$

Examples of MLP-ANN models are shown in the case study in Sections 6.3.2 and 6.4. Advantages of the MPL-ANN model are the comprehensive nonlinear dynamical input/output relationship and its highly flexible and modular structure.

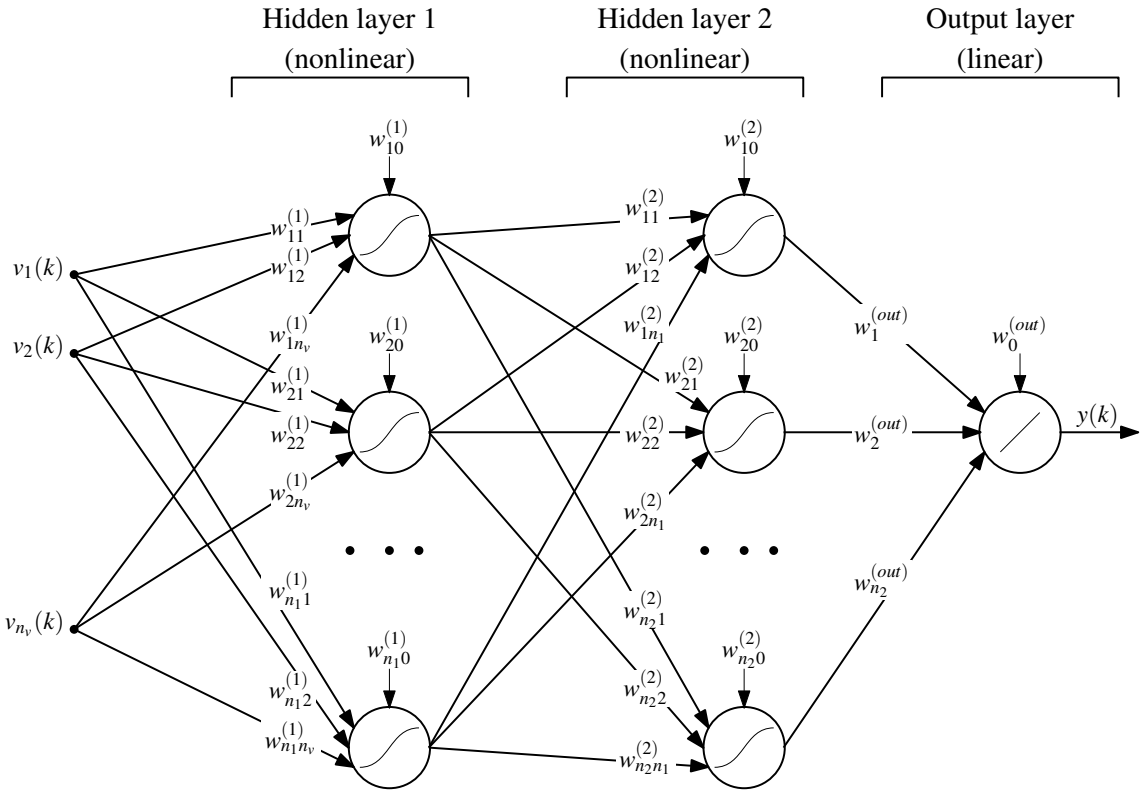

Figure 3.18: MLP-ANN with two nonlinear hidden layers and one linear output layer.

3.2.4 Discrete-time dynamical order and delay time estimation

As explained in Sections 3.1.1.2 and 3.1.1.4, by increasing the model order, the model complexity and flexibility increase, and the model becomes capable of a richer variety of dynamical behaviours but, at the same time, excessively high orders introduce an overfitting problem, which reduces the ability of the model in generalising on fresh data. In the case of DT NARX models, introduced in Section 3.2.3, an important part of the model structure selection is the choice of the delay n_d and the dynamical orders n_a and n_b. In the case of an ARX model structure, n_a, n_b and n_d are estimated by implementing a systematic trial and error process on several ARX models, with varying n_a, n_b and n_d, and selecting the values which give the best model performance, as measured by a LF, which represents a measure of the modelling error. For each ARX model estimation, independent training and validation data sets are utilised. At the end, the simplest ARX model, able to repeat the validation data with a sufficient accuracy, is selected (parsimonious model) [247]. The use of a systematic incremental evaluation process on several ARX models with varying n_a, n_b and n_d, in order to calculate the dynamical order and the time delay of a linear system, is a well established procedure, and is generally computationally fast; for example, see [248], where an ARX model for a heating system is identified from measured data; in [249], an ARX structure is identified in order to model a reactor-exchanger; in [210] [211], ARX models are identified in order to implement the FSE forecasting inside the chamber of the Pico OWC plant in the Azores; in [250] ARX models are identified to perform the weekly electricity consumption forecasting for a power board.

In the case of nonlinear models, there are not straightforward methodologies to calculate n_a, n_b and n_d, and the problem of the order determination is still not satisfactorily solved. This is

mainly due to the significant interaction between the optimal nonlinear structure and the optimal dynamical order. A widely applied approach, for linear and nonlinear systems, is to identify different models having increasing orders and to select the best compromise between complexity and accuracy, represented by the fact the LF value does not reduce significantly, by increasing the order of the system, larger then a specific value [141] [205]. Therefore, in this thesis, first n_a, n_b and n_d are estimated by implementing a systematic trial and error process on several ARX models, and then the same values are utilised for the nonlinear models (e.g. Hammerstein model, KGP model, ANN models, etc.) [9] [8] [10] [12]. The performance of a model, in fitting the experimental data, depends simultaneously on the selected structure and on the dynamical order and delay time of the model. Maintaining the same dynamical order and delay time for the linear and nonlinear structures provides the possibility to show how the different nonlinear model structures influences the performance in fitting the experimental data, with a focus on nonlinear modelling capability.

3.3 Hydrodynamic WEC parameter estimation

Given a parametric model structure and the measured input/output data from an investigated process, the objective of SI is to find the value for the model parameters, $\boldsymbol{\theta}$, in order to obtain the 'best' model to describe the process. Therefore, it is necessary to select a quantifiable criteria to evaluate the performance of a model. The essence of a model is the prediction aspect; therefore, the performance of a model should be evaluated depending on the prediction ability, as outlined by Ljung in [204]. In other words, the objective is to reduce the difference between the process output, $y_u(k)$, and the model output prediction, $\hat{y}(k,\boldsymbol{\theta})$. Usually, the process output, $y_u(k)$ is not known; only the measured version, $y(k)$, is available, which is corrupted with an additive noise, $\xi_n(k)$ (see Fig. 3.19). It is important to underline that, in a NWT, signals can be measured without requiring physical sensor devices, which are typical sources of random and systematic errors in the measurements. Therefore, in NWT data, negligible 'noise', barring some small numerical error, is present; therefore, there is no necessity to provide a coloured noise structure in the mathematical model [9] [8] [10] [12].

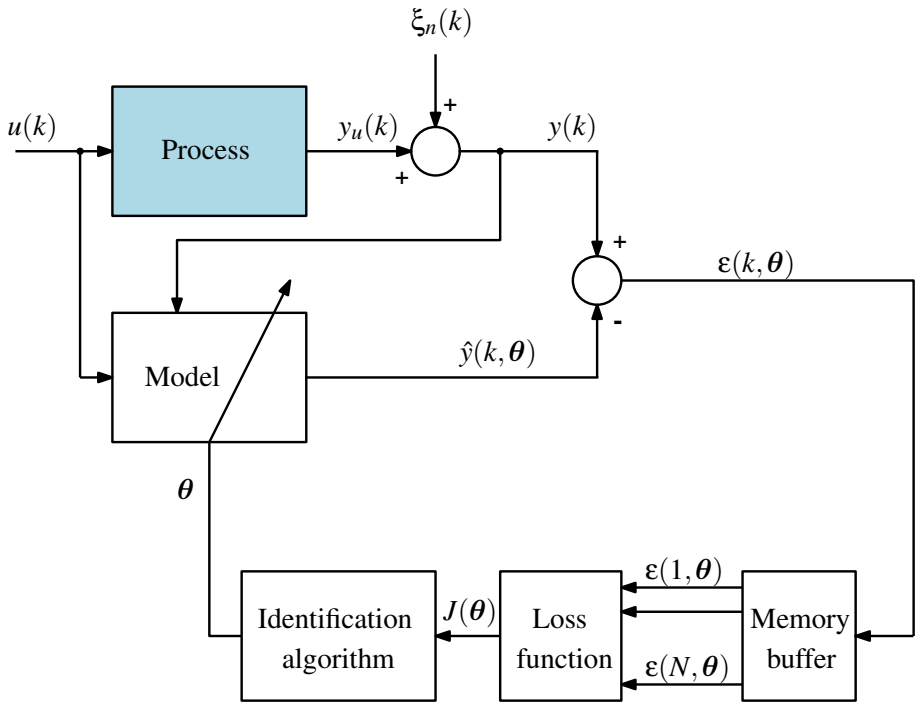

Figure 3.19: System identification block diagram.

Define the prediction error (or residual) as the difference between the one-step-ahead output model prediction, $\hat{y}(k,\boldsymbol{\theta})$, and the measured output from the process, $y(k)$ [205] [247]:

$$\varepsilon(k,\boldsymbol{\theta}) = y(k) - \hat{y}(k,\boldsymbol{\theta}) \tag{3.35}$$

In (3.35), the notation $\hat{y}(k,\boldsymbol{\theta})$ and $\varepsilon(k,\boldsymbol{\theta})$ indicate that the model prediction and the residual error depend on model parameters $\boldsymbol{\theta}$. Define the LF as [205]:

$$J(\boldsymbol{\theta}) = \sum_{k=1}^{N} l\Big(\varepsilon(k,\boldsymbol{\theta})\Big) \tag{3.36}$$

where l is a scalar function of the prediction error, and N is the number of data samples. The estimated model parameters, $\hat{\boldsymbol{\theta}}$, are obtained minimising the LF:

$$\hat{\boldsymbol{\theta}} = \underset{\boldsymbol{\theta}}{argmin}\Big(J(\boldsymbol{\theta})\Big) \tag{3.37}$$

It is possible to obtain alternative parameter estimation approaches, depending on the choice of l in (3.36). A very common choice, convenient for analysis and computation, is the LS method, where [204]:

$$l\Big(\varepsilon(k,\boldsymbol{\theta})\Big) = \frac{1}{2}\varepsilon^2(k,\boldsymbol{\theta}), \tag{3.38}$$

which leads to the MSE:

$$J(\boldsymbol{\theta}) = \frac{1}{2}\sum_{k=1}^{N}\varepsilon^2(k,\boldsymbol{\theta}) = \frac{1}{2}\parallel \boldsymbol{\varepsilon}(\boldsymbol{\theta}) \parallel_2^2 = \frac{1}{2}\boldsymbol{\varepsilon}(\boldsymbol{\theta})^T\boldsymbol{\varepsilon}(\boldsymbol{\theta}) \tag{3.39}$$

where:

$$\boldsymbol{\varepsilon}(\boldsymbol{\theta}) = \begin{bmatrix}\varepsilon(1,\boldsymbol{\theta}) & \varepsilon(2,\boldsymbol{\theta}) & \ldots & \varepsilon(N,\boldsymbol{\theta})\end{bmatrix}^T. \tag{3.40}$$

In equations (3.38) and (3.39), the constant $\frac{1}{2}$ appears, but it is also common to utilise alternative constants, such as $\frac{1}{N}$ or $\frac{1}{2N}$ [205]. The optimization problem of equation (3.37) may be linear or nonlinear, depending on the relationship between J and the parameters $\boldsymbol{\theta}$, as explained in Sections 3.3.1 and 3.3.2. For compactness, in this thesis, $\hat{y}(k,\boldsymbol{\theta})$, $\varepsilon(k,\boldsymbol{\theta})$ and $\boldsymbol{\varepsilon}(\boldsymbol{\theta})$ are sometimes replaced with $\hat{y}(k)$, $\varepsilon(k)$ and $\boldsymbol{\varepsilon}$, respectively.

3.3.1 Least squares parameter estimation

As introduced in Section 3.2.3, a model with an output, $\hat{y}$, is linear in the unknown parameter vector, $\boldsymbol{\theta}$, if the model output is given by:

$$\hat{y}(k) = \theta_1\varphi_1(k) + \cdots + \theta_q\varphi_q(k) = \boldsymbol{\varphi}(k)^T\boldsymbol{\theta} \tag{3.41}$$

where

$$\boldsymbol{\varphi}(k) = \begin{bmatrix}\varphi_1(k) & \varphi_2(k) & \cdots & \varphi_q(k)\end{bmatrix}^T \tag{3.42}$$

is the variable vector (also termed regressor vector), and

$$\boldsymbol{\theta} = \begin{bmatrix}\theta_1 & \theta_2 & \ldots & \theta_q\end{bmatrix}^T. \tag{3.43}$$

Assuming that N data samples of $y(k)$, $\varphi_1(k)$, $\varphi_2(k)$,..., $\varphi_q(k)$ have been measured ($k = 1,...,N$), the difference between the measured data and the model prediction at each sample is:

$$\varepsilon(k) = y(k) - \hat{y}(k) = y(k) - \begin{bmatrix}\varphi_1(k) & \varphi_2(k) & \cdots & \varphi_q(k)\end{bmatrix}\boldsymbol{\theta} \tag{3.44}$$

for $k = 1,...,N$. In matrix form:

$$\boldsymbol{\varepsilon} = \mathbf{y} - \hat{\mathbf{y}} = \mathbf{y} - \boldsymbol{\Phi}\boldsymbol{\theta} \tag{3.45}$$

where:

$$\varepsilon = \begin{bmatrix} \varepsilon(1) & \varepsilon(2) & ... & \varepsilon(N) \end{bmatrix}^T, \tag{3.46}$$

$$\mathbf{y} = \begin{bmatrix} y(1) & y(2) & ... & y(N) \end{bmatrix}^T, \tag{3.47}$$

$$\hat{\mathbf{y}} = \begin{bmatrix} \hat{y}(1) & \hat{y}(2) & ... & \hat{y}(N) \end{bmatrix}^T \tag{3.48}$$

and

$$\mathbf{\Phi} = \begin{bmatrix} \varphi_1(1) & \varphi_2(1) & ... & \varphi_q(1) \\ \varphi_1(2) & \varphi_2(2) & ... & \varphi_q(2) \\ \vdots & \vdots & \ddots & \vdots \\ \varphi_1(N) & \varphi_2(N) & ... & \varphi_q(N) \end{bmatrix}. \tag{3.49}$$

$\mathbf{\Phi} \in \Re^{N \times q}$ is termed the data matrix [251] or the regression matrix [205] and $\mathbf{y} \in \Re^{N \times 1}$ is termed the observation vector [251]. The LF (3.39), constructed with the LS method, can be rearranged as:

$$\begin{aligned} J(\boldsymbol{\theta}) &= \frac{1}{2}\sum_{k=1}^{N} \varepsilon^2(k,\boldsymbol{\theta}) = \frac{1}{2}\varepsilon(\boldsymbol{\theta})^T\varepsilon(\boldsymbol{\theta}) = \frac{1}{2}(\mathbf{y}-\hat{\mathbf{y}}(\boldsymbol{\theta}))^{\mathbf{T}}(\mathbf{y}-\hat{\mathbf{y}}(\boldsymbol{\theta})) \\ &= \frac{1}{2}(\mathbf{y}-\mathbf{\Phi}\boldsymbol{\theta})^T(\mathbf{y}-\mathbf{\Phi}\boldsymbol{\theta}) = \frac{1}{2}(\mathbf{y}^T-\boldsymbol{\theta}^T\mathbf{\Phi}^T)(\mathbf{y}-\mathbf{\Phi}\boldsymbol{\theta}) \\ &= \frac{1}{2}\mathbf{y}^T\mathbf{y} - \frac{1}{2}\mathbf{y}^T\mathbf{\Phi}\boldsymbol{\theta} - \frac{1}{2}\boldsymbol{\theta}^T\mathbf{\Phi}^T\mathbf{y} + \frac{1}{2}\boldsymbol{\theta}^T\mathbf{\Phi}^T\mathbf{\Phi}\boldsymbol{\theta} \\ &= \frac{1}{2}\boldsymbol{\theta}^T\mathbf{H}\boldsymbol{\theta} + \mathbf{h}^T\boldsymbol{\theta} + h_0 \end{aligned} \tag{3.50}$$

where $\mathbf{H} = \mathbf{\Phi}^T\mathbf{\Phi}$, $\mathbf{h} = -\mathbf{\Phi}^T\mathbf{y}$ and $h_0 = \frac{1}{2}\mathbf{y}^T\mathbf{y}$. Equation (3.50) follows due to the fact that $\boldsymbol{\theta}^T\mathbf{\Phi}^T\mathbf{y}$ is a scalar, so that $\boldsymbol{\theta}^T\mathbf{\Phi}^T\mathbf{y} = (\boldsymbol{\theta}^T\mathbf{\Phi}^T\mathbf{y})^T = \mathbf{y}^T\mathbf{\Phi}\boldsymbol{\theta}$ [252] [253]. The objective is to find the parameter vector, $\hat{\boldsymbol{\theta}}$, which minimizes the LF (3.50):

$$\hat{\boldsymbol{\theta}} = \underset{\boldsymbol{\theta}}{argmin}\Big(J(\boldsymbol{\theta})\Big) \tag{3.51}$$

Equation (3.50) is the expression of a quadratic form [254]; therefore, when the model output is linear in the parameters and the sum of squares is chosen as the LF, a LS problem arises [141] [255], which is characterised by a quadratic LF (do not confuse with linear programming, which is characterised by a multidimensional linear LF). If $\mathbf{H}$ is positive definite, $J(\boldsymbol{\theta})$ is an elliptic paraboloid (see Fig. 3.20 in the case of $\boldsymbol{\theta} \in \Re^2$) and it has a unique minimum given [214] [253] by:

$$\hat{\boldsymbol{\theta}} = (\mathbf{\Phi}^{\mathrm{T}}\mathbf{\Phi})^{-1}\mathbf{\Phi}^{\mathrm{T}}\mathbf{y}. \tag{3.52}$$

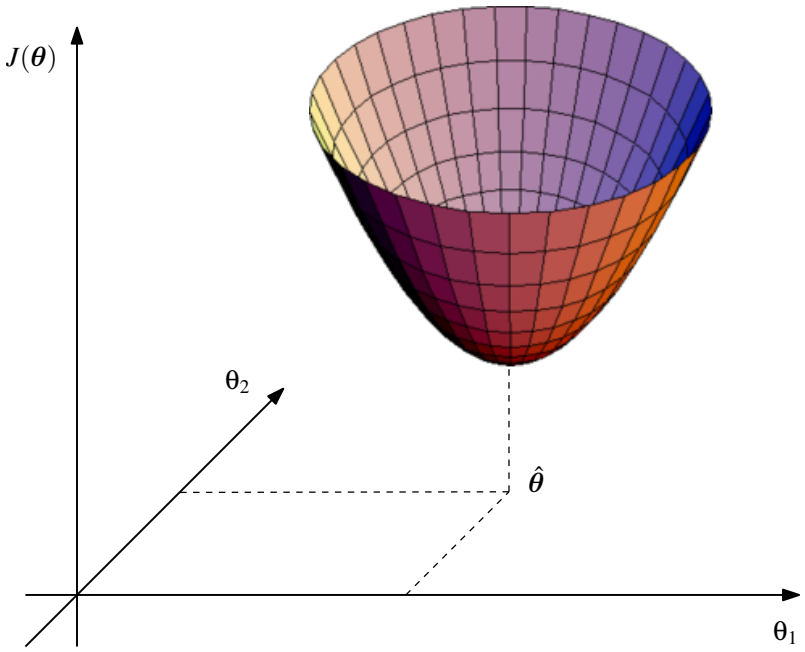

Figure 3.20: If $\mathbf{\Phi}^T\mathbf{\Phi}$ is positive definite, $J(\boldsymbol{\theta})$ is an elliptic paraboloid (in this figure, $\boldsymbol{\theta} \in \Re^2$) .

Since the coefficients $\mathbf{H}$, $\mathbf{h}$ and h_0 of the paraboloid (3.50) depend on the measured data $\mathbf{\Phi}$ and $\mathbf{y}$, different experiments lead to different associated paraboloids, possibly having the minimum for a different $\hat{\boldsymbol{\theta}}$. Therefore, it is clear that the identified model, characterised by $\hat{\boldsymbol{\theta}}$, is strongly related to the experiment utilised, and that the model may not be representative in the case of a different experiment. The property of having a unique optimum solution, which can be calculated analytically with (3.52), makes LS estimation very attractive [205].

3.3.1.1 LS resolution method: QR factorization

The minimization of the LF (3.50) is not computed directly utilising equation (3.52), because the use of $\mathbf{\Phi}^{\mathrm{T}}\mathbf{\Phi}$ increases the possibility of obtaining an ill-conditioned problem [204] [256] [257]. Instead, a QR factorization method is implemented, which computes the LS solution directly from $\mathbf{\Phi}$, without forming $\mathbf{\Phi}^{\mathrm{T}}\mathbf{\Phi}$ [251] [257]. Given the known regression matrix $\mathbf{\Phi} \in \Re^{N\times q}$ and the observation vector $\mathbf{y} \in \Re^{N\times 1}$, the unknown solution is represented by the vector $\hat{\boldsymbol{\theta}} \in \Re^{q\times 1}$. The QR factorization method is based on the following main steps [251] [257] :
1) Calculate an orthogonal matrix $\mathbf{Q} \in \Re^{N\times N}$ and an upper triangular matrix $\mathbf{R} \in \Re^{N\times q}$, so that $\mathbf{\Phi} = \mathbf{QR}$. See Fig. 3.21(a). There are different methods to compute the QR factorization, such as the GramSchmidt orthogonalization or the more efficient and stable Householder reflection method [257] [258] (for this work, the QR factorization is computed by using the Matlab *qr* command, based on the Householder reflection method).
2) Calculate $\hat{\mathbf{R}}$, taking the upper square $q \times q$ part of $\mathbf{R}$ (therefore, $\hat{\mathbf{R}} \in \Re^{q\times q}$), as shown in Fig. 3.21(a). It is important to underline that $\hat{\mathbf{R}}$ is an upper triangular matrix.
3) Calculate the vector $\mathbf{d} = \mathbf{Q}^T\mathbf{y}$, where $\mathbf{d} \in \Re^{N\times 1}$. See Fig. 3.21(b).
4) Calculate $\hat{\mathbf{d}}$, taking the first q elements of $\mathbf{d}$ (therefore, $\hat{\mathbf{d}} \in \Re^{q\times 1}$), as shown in Fig. 3.21(b).
5) The solution is obtained by resolving the system $\hat{\mathbf{R}}\hat{\boldsymbol{\theta}} = \hat{\mathbf{d}}$ (see Fig. 3.21(c)). Since $\hat{\mathbf{R}}$ is an upper triangular matrix, the system $\hat{\mathbf{R}}\hat{\boldsymbol{\theta}} = \hat{\mathbf{d}}$ is resolved easily by using back-substitution.

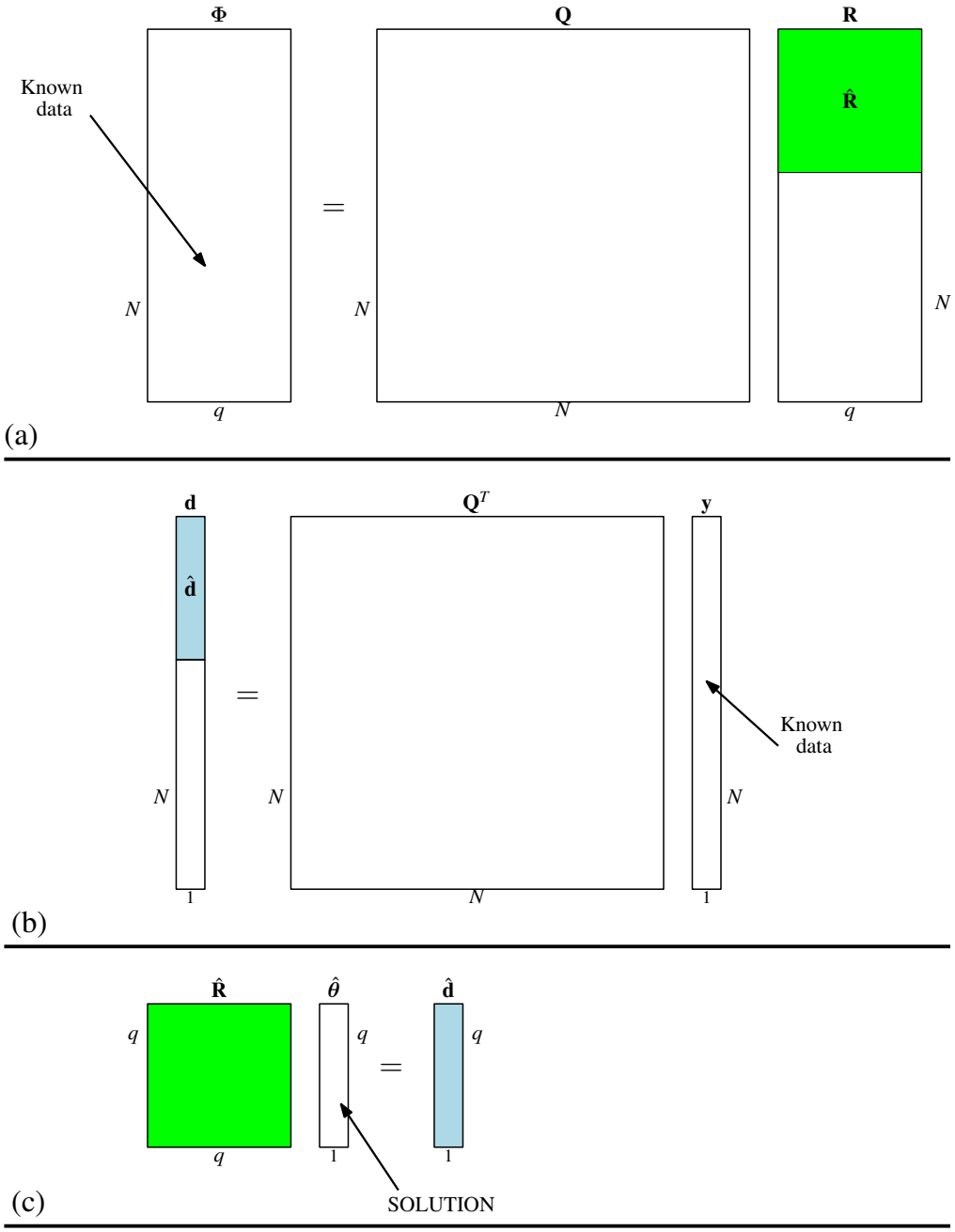

Figure 3.21: QR factorization method to resolve LS problems.

3.3.1.2 Constrained linear optimization

Given a linear model (3.41), a LF defined by (3.50), and supposing that the parameters also have to satisfy the linear equality constraint:

$$\mathbf{A}\boldsymbol{\theta} = \mathbf{e}, \tag{3.53}$$

the value of the parameter vector $\hat{\boldsymbol{\theta}}$, which simultaneously minimizes the LF and satisfies the constraint, is given by [141] [205]:

$$\hat{\boldsymbol{\theta}} = \hat{\boldsymbol{\theta}}^{(uc)} - (\boldsymbol{\Phi}^T\boldsymbol{\Phi})^{-1}\mathbf{A}^T(\mathbf{A}(\boldsymbol{\Phi}^T\boldsymbol{\Phi})^{-1}\mathbf{A}^T)^{-1}(\mathbf{A}\hat{\boldsymbol{\theta}}^{(uc)} - \mathbf{e}), \tag{3.54}$$

where $\hat{\boldsymbol{\theta}}^{(uc)}$ is calculated by utilising QR factorization (see Section 3.3.1.1). In Fig. 3.22, the geometric interpretation of constrained linear optimization is shown.

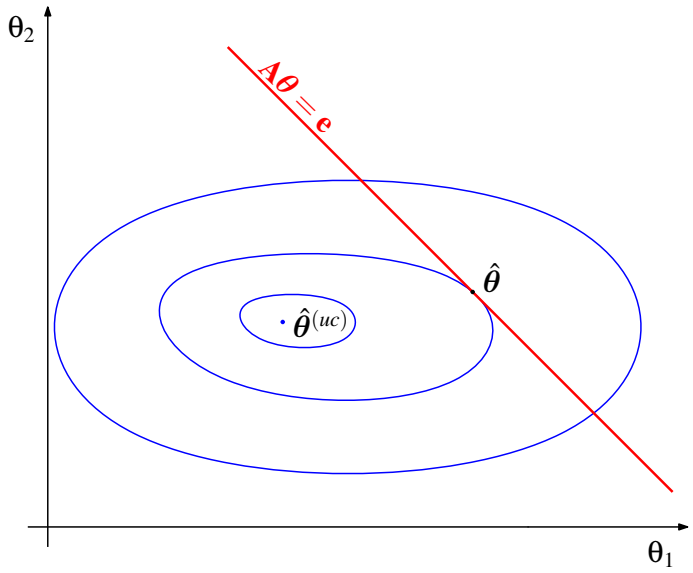

Figure 3.22: Constrained linear optimization, in the case of $\boldsymbol{\theta} \in \Re^2$. The closed lines represent the contour lines of the LF; whereas, the straight line represents the linear constraint $\mathbf{A}\boldsymbol{\theta} = \mathbf{e}$. In the figure, the unconstrained solution, $\hat{\boldsymbol{\theta}}^{(uc)}$, and the constrained solution, $\hat{\boldsymbol{\theta}}$, are shown.

3.3.1.3 ARX model identification

Suppose that, by performing some experiments on a process under study, the signals $\{u(k)\}$ and $\{y(k)\}$ (for $k = 1,...,N$) are generated and utilised as input and output identification data, respectively. Suppose that an ARX model is selected in order to describe the behaviour of the process (see Section 3.2.3.1):

$$\hat{y}(k) = \sum_{i=1}^{n_a} a_i y(k-i) + \sum_{i=0}^{n_b} b_i u(k-n_d-i) \tag{3.55}$$

where $\hat{y}$ indicates the model prediction and y the measured data. Equations (3.41) (3.42) (3.43) become, respectively:

$$\hat{y}(k) = \boldsymbol{\varphi}_{arx}(k)^T\boldsymbol{\theta}_{arx}, \tag{3.56}$$

$$\boldsymbol{\varphi}_{arx}(k) = \begin{bmatrix} y(k-1) & y(k-2) & \dots & y(k-n_a) & u(k-n_d) & u(k-n_d-1) & \dots & u(k-n_d-n_b) \end{bmatrix}^T \tag{3.57}$$

and

$$\boldsymbol{\theta}_{arx} = \begin{bmatrix} a_1 & a_2 & \dots & a_{n_a} & b_0 & b_1 & \dots & b_{n_b} \end{bmatrix}^T. \tag{3.58}$$

Equation (3.56) shows that the ARX model is linear in the parameter vector $\boldsymbol{\theta}_{arx}$. By defining:

$$\tau = max\{n_a, (n_b + n_d)\}, \tag{3.59}$$

the first τ values of the data are utilised as initial conditions; therefore, the first possible predicted model output is for $k = \tau + 1$. By defining:

$$\widetilde{N} = \begin{cases} N & \text{if } n_d \geq 0 \\ N + n_d & \text{if } n_d < 0 \end{cases} \tag{3.60}$$

the last possible predicted model output is for $k = \widetilde{N}$. Therefore, equations (3.47) and (3.49) become [248] [221]:

$$\mathbf{y} = \begin{bmatrix} y(\tau+1) & y(\tau+2) & \dots & y(\widetilde{N}) \end{bmatrix}^T \tag{3.61}$$

and

$$\mathbf{\Phi} = \begin{bmatrix} y(\tau) & \dots & y(\tau+1-n_a) & u(\tau+1-n_d) & \dots & u(\tau+1-n_d-n_b) \\ y(\tau+1) & \dots & y(\tau+2-n_a) & u(\tau+2-n_d) & \dots & u(\tau+2-n_d-n_b) \\ \vdots & \ddots & \vdots & \vdots & \ddots & \vdots \\ y(\widetilde{N}-1) & \dots & y(\widetilde{N}-n_a) & u(N) & \dots & u(N-n_b) \end{bmatrix}. \tag{3.62}$$

As explained in Section 3.3.1.1, the estimated parameters $\hat{\boldsymbol{\theta}}_{arx}$ are determined by employing a QR factorization.

3.3.1.4 Hammerstein model identification

Suppose that some experiments are carried out on a process under study, and that the signals $\{u(k)\}$ and $\{y(k)\}$ (for $k = 1, ..., N$) are generated and utilised as input and output identification data, respectively. Suppose that a Hammerstein model is selected in order to describe the behaviour of the process. As explained in Section 3.2.3.3, the Hammerstein model is composed of two different sub-blocks, a NLS block and an ARX block. The relationship between the input and the output of the Hammerstein model is given by:

$$\hat{y}(k) = \sum_{i=1}^{n_a} a_i y(k-i) + \sum_{i=0}^{n_b} b_i r\Big(u(k-n_d-i)\Big), \tag{3.63}$$

where $\hat{y}$ indicates the model prediction and y the measured data. The nonlinear static function, r, of the Hammerstein model can be approximated with a linear combination of basis functions; in this way it is possible to apply linear regression for the identification. For simplicity, monomials can be selected as basis functions $\{u^0, u^1, u^2, ..., u^{n_c}\}$; therefore, the relationship between the input and the output of the NLS block is:

$$s(k) = c_1 u(k) + c_2 u^2(k) + ... + c_{n_c} u^{n_c}(k) \tag{3.64}$$

where, $c_0 = 0$ (it is imposed that applying a null input the output has to be zero).

In the case where measurements of $u(k)$ and $y(k)$ are available, but not of $s(k)$, the identification of the NLS and ARX blocks can be achieved in different ways [259]:
1) By simultaneously estimating the parameters a_i, b_i and c_i, by solving a nonlinear optimization problem (the LF is not a quadratic function of the parameters), which requires the employment of iterative numerical methods, as explained in Section 3.3.2.
2) By employing the Narendra-Gallman algorithm [259] [260], where the identification is carried out by alternately adjusting the coefficients of the nonlinear and the linear sub-blocks. In this way, the problem is resolved with an iteration of linear optimization sub-problems.
The main disadvantage, of both 1) and 2), is that the identified model does not necessarily converge to the model which minimizes the MSE between measured output and model predictions [260]. On the other hand, when measurements of $u(k)$, $y(k)$ and $s(k)$ are available, the NLS and ARX sub-blocks of the Hammerstein model can be identified separately, with a two-step algorithm,

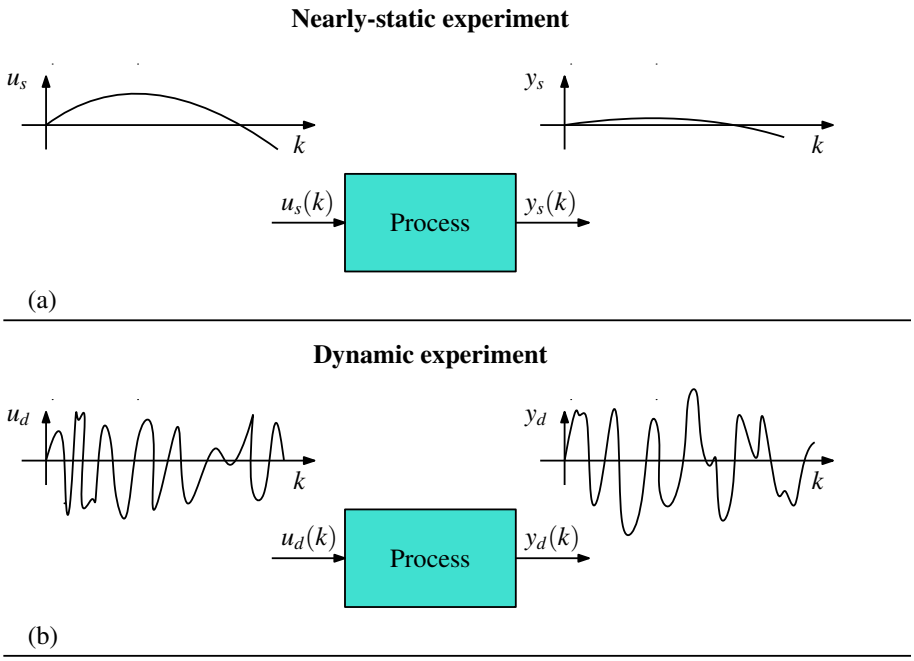

Figure 3.23: Experiments utilised for the identification of Hammerstein and FBO models. (a) Nearly-static experiment: the signals $u_s(k)$ and $y_s(k)$ change very slowly, in order to capture the static relationship between input and output. (b) Dynamic experiment: the signals $u_d(k)$ and $y_d(k)$ have a good coverage of the frequencies where the system has a significant non-zero frequency response (dynamically rich signals).

by employing linear regression and with the guarantee that each identified sub-block minimizes the MSE between measured output and model predictions, for each sub-block [240] [241]. The identification data gathering for the Hammerstein model is accomplished utilising two different experiments: the nearly-static experiment and the dynamic experiment.

• In the *nearly-static experiment*, the input signal, $u(k)$, changes very slowly through its full amplitude range, in order to capture the static relationship between the input signal and the output signal, $y(k)$. The measured input and output data, produced by the nearly-static experiment, are denoted $u_s(k)$ and $y_s(k)$, respectively, where the subscript 's' indicates 'static' (see Fig. 3.23(a)). The output signal, $y_s(k)$, is independent of the dynamic characteristics of the ARX block (the input signal is slow enough to make the ARX dynamical effects negligible and only the static nonlinear block transforms the input signal into the output signal). The measured signals $\{u_s(k)\}$ and $\{y_s(k)\}$ (with $k = 1,...,N$) are utilised in order to identify the static block. Since the signals are changing very slowly and, for the ARX block, the $K_{dc} = 1$ (see Section 3.2.3.3), it follows that $s(k) \simeq y_s(k)$. Therefore, the input/output signals of the static block are known and it is possible to identify the coefficient c_i, as shown in Fig. 3.24(a). Equations (3.41) (3.42) (3.43) (3.47) and (3.49) become, respectively:

$$\hat{s}(k) = \varphi_{H_c}(k)^T \boldsymbol{\theta}_{H_c}, \tag{3.65}$$

$$\varphi_{H_c}(k) = \left[[u_s(k)]^1 \;\; [u_s(k)]^2 \;\; ... \;\; [u_s(k)]^{n_c} \right]^T, \tag{3.66}$$

$$\boldsymbol{\theta}_{H_c} = \left[c_1 \;\; c_2 \;\; ... \;\; c_{n_c} \right]^T, \tag{3.67}$$

$$\mathbf{y} = \left[y_s(1) \;\; y_s(2) \;\; ... \;\; y_s(N) \right]^T \tag{3.68}$$

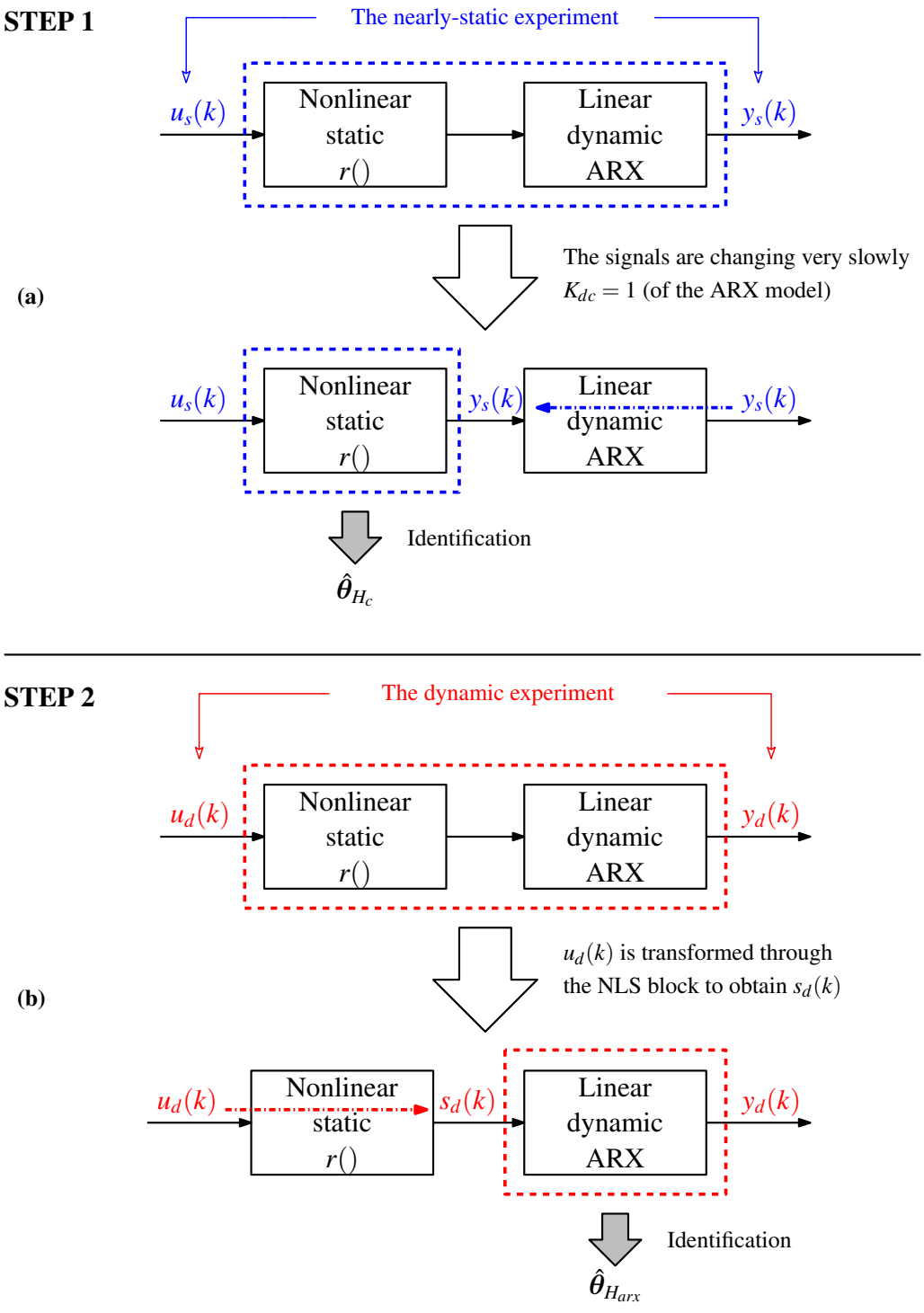

Figure 3.24: The two-step algorithm for the identification of the Hammerstein model. (a) STEP 1: The data collected by the nearly-static experiment are utilised for the identification of the NLS block. (b) STEP 2: The data collected by the dynamic experiment are utilised for the identification of the ARX block.

and

$$\mathbf{\Phi} = \begin{bmatrix} [u_s(1)]^1 & [u_s(1)]^2 & ... & [u_s(1)]^{n_c} \\ [u_s(2)]^1 & [u_s(2)]^2 & ... & [u_s(2)]^{n_c} \\ \vdots & \vdots & \ddots & \vdots \\ [u_s(N)]^1 & [u_s(N)]^2 & ... & [u_s(N)]^{n_c} \end{bmatrix}. \tag{3.69}$$

The estimated parameters $\hat{\boldsymbol{\theta}}_{H_c}$ are determined by utilising a QR factorization algorithm (see Section 3.3.1.1).

• In the *dynamic experiment*, the measured input and output data, denoted $\{u_d(k)\}$ and $\{y_d(k)\}$, respectively, (with $k = 1,...,N$), have a good coverage of the frequencies where the system has a significant non-zero frequency response (dynamically rich signals), as shown in Fig. 3.23(b); the subscript '*d*' indicating 'dynamic'. $\{u_d(k)\}$ and $\{y_d(k)\}$ are employed to identify the ARX parameter vector (see Section 3.3.1.3):

$$\boldsymbol{\theta}_{H_{arx}} = \begin{bmatrix} a_1 & a_2 & ... & a_{n_a} & b_0 & b_1 & ... & b_{n_b} \end{bmatrix}^T. \tag{3.70}$$

Initially, the input, $u_d(k)$, is transformed by the nonlinear static block to obtain $s_d(k)$, by using equation (3.64) (the parameters c_i are now known). Next, $\{s_d(k)\}$ and $\{y_d(k)\}$ are used as an input/output pair, in order to identify the ARX parameters, $\hat{\boldsymbol{\theta}}_{H_{arx}}$, under the constraint $\mathbf{A}\boldsymbol{\theta}_{H_{arx}} = e$, where $\mathbf{A} = [1,1,...,1] \in \Re^{1\times(n_a+n_b+1)}$ and $e = 1$ (see Section 3.2.3.3), as shown in Fig. 3.24(b). As explained in Section 3.3.1.3, the first possible predicted model output is for $k = \tau+1$ (the first τ values of the data are utilised as initial conditions for the model), where $\tau = max\{n_a,(n_b+n_d)\}$; the last possible predicted model output is for $k = \widetilde{N}$, where:

$$\widetilde{N} = \begin{cases} N & \text{if } n_d \geq 0, \\ N+n_d & \text{if } n_d < 0. \end{cases} \tag{3.71}$$

Equations (3.47) and (3.49) become:

$$\mathbf{y} = \begin{bmatrix} y_d(\tau+1) & y_d(\tau+2) & ... & y_d(\widetilde{N}) \end{bmatrix}^T \tag{3.72}$$

and

$$\mathbf{\Phi} = \begin{bmatrix} y_d(\tau) & ... & y_d(\tau+1-n_a) & s_d(\tau+1-n_d) & ... & s_d(\tau+1-n_d-n_b) \\ y_d(\tau+1) & ... & y_d(\tau+2-n_a) & s_d(\tau+2-n_d) & ... & s_d(\tau+2-n_d-n_b) \\ \vdots & \ddots & \vdots & \vdots & \ddots & \vdots \\ y_d(\widetilde{N}-1) & ... & y_d(\widetilde{N}-n_a) & s_d(N) & ... & s_d(N-n_b) \end{bmatrix}, \tag{3.73}$$

respectively. The estimated parameters are determined, by using equation (3.54), as:

$$\hat{\boldsymbol{\theta}}_{H_{arx}} = \hat{\boldsymbol{\theta}}^{(uc)}_{H_{arx}} - (\mathbf{\Phi}^T\mathbf{\Phi})^{-1}\mathbf{A}^T(\mathbf{A}(\mathbf{\Phi}^T\mathbf{\Phi})^{-1}\mathbf{A}^T)^{-1}(\mathbf{A}\hat{\boldsymbol{\theta}}^{(uc)}_{H_{arx}} - \mathbf{d}), \tag{3.74}$$

where the unconstrained parameter vector $\hat{\boldsymbol{\theta}}^{(uc)}_{H_{arx}}$ is calculated by utilising QR factorization (see Section 3.3.1.1). The Hammerstein model is a good example to show the utility of identifying the single sub-blocks by utilising data from different experiments, intentionally designed for the specific sub-block.

3.3.1.5 FBO model identification

The identification of the FBO model, introduced in Section 3.2.3.4, is based on two different identification experiments (nearly-static and dynamic experiments, shown in Fig. 3.23), and a two-step algorithm, similar to the approach utilised for the Hammerstein model identification (see Section 3.3.1.4). The nonlinear static function, *g*, of the FBO model can be approximated with a

polynomial; therefore, the relationship between the input and the output of the NLS block is given by:

$$-f_{re}(k) = c_1 y(k) + c_2 y^2(k) + ... + c_{n_c} y^{n_c}(k) \tag{3.75}$$

where, $c_0 = 0$ (by imposing the condition $f_{re} = 0$ when $y = 0$).

• In the *nearly-static experiment*, the system is very slowly excited (eliminating any dynamical effect), in order to capture the static relationship between the input and output signals of the NLS block, through the full output amplitude range. By carrying out the nearly-static experiment, the data $\{u_s(k)\}$ and $\{y_s(k)\}$ (with k = 1,...,N) are gathered. In the context of wave energy systems, as explained in Sections 3.2.2 and 3.2.3.4, the FBO model structure has been suggested by Cummins' equation; in particular, $u(k)$ is the PTO force applied to the WEC (for the case where the excitation force, f_e, and the mooring force, f_m, are zero), $y(k)$ is the body displacement from the equilibrium position, and $f_{re}(k)$ is the restoring force applied to the WEC by gravity and buoyancy forces. Since, under static conditions, the applied f_{pto} is balanced by an equal and opposite f_{re}, during the nearly-static experiment $u_s(k) \simeq -f_{re.s}(k)$ ($f_{re.s}$ represents the restoring force during the static experiment), the measurement of $u_s(k)$ provides knowledge of $f_{re.s}(k)$. The data $\{-f_{re.s}(k)\}$ and $\{y_s(k)\}$ are utilised to identify the static block, as shown in Fig. 3.25(a). Equations (3.43), (3.47) and (3.49) become, respectively:

$$\boldsymbol{\theta}_{F_c} = \begin{bmatrix} c_1 & c_2 & ... & c_{n_c} \end{bmatrix}^T, \tag{3.76}$$

$$\mathbf{y} = \begin{bmatrix} -f_{re.s}(1) & -f_{re.s}(2) & ... & -f_{re.s}(N) \end{bmatrix}^T \tag{3.77}$$

and

$$\boldsymbol{\Phi} = \begin{bmatrix} [y_s(1)]^1 & [y_s(1)]^2 & ... & [y_s(1)]^{n_c} \\ [y_s(2)]^1 & [y_s(2)]^2 & ... & [y_s(2)]^{n_c} \\ \vdots & \vdots & \ddots & \vdots \\ [y_s(N)]^1 & [y_s(N)]^2 & ... & [y_s(N)]^{n_c} \end{bmatrix}. \tag{3.78}$$

The estimated parameters, $\hat{\boldsymbol{\theta}}_{F_c}$, are calculated by utilising QR factorization (see Section 3.3.1.1).

• In the *dynamic experiment*, the measured input and output data, denoted $\{u_d(k)\}$ and $\{y_d(k)\}$, respectively, where $k = 1, ..., N$, are dynamically rich signals (see Fig. 3.23(b)). The subscript 'd' indicates 'dynamic'. The data $\{u_d(k)\}$ and $\{y_d(k)\}$ are employed to identify the ARX parameter vector (see Section 3.3.1.3), represented by:

$$\boldsymbol{\theta}_{F_{arx}} = \begin{bmatrix} a_1 & a_2 & ... & a_{n_a} & b_0 & b_1 & ... & b_{n_b} \end{bmatrix}^T. \tag{3.79}$$

Initially, the output $y_d(k)$ is transformed by the NLS block to obtain $-f_{re.d}(k)$, by utilising equation (3.75) (since the parameters c_i are now known). Then, the input of the ARX block is calculated with the equation $e_d(k) = u_d(k) - \Big(-f_{re.d}(k)\Big)$. As a consequence, both input and output signals of the ARX block are known (respectively $\{e_d(k)\}$ and $\{y_d(k)\}$) and it is possible to identify the ARX parameters, $\hat{\boldsymbol{\theta}}_{F_{arx}}$ (See Fig. 3.25(b)). As explained in Section 3.3.1.3, the first possible predicted ARX output is for $k = \tau + 1$ (the first τ values of the data are utilised as initial conditions), where $\tau = max\{n_a, (n_b + n_d)\}$. The last possible predicted ARX output is for $k = \widetilde{N}$, where:

$$\widetilde{N} = \begin{cases} N & \text{if } n_d \geq 0, \\ N + n_d & \text{if } n_d < 0. \end{cases} \tag{3.80}$$

Equations (3.47) and (3.49) become:

$$\mathbf{y} = \begin{bmatrix} y_d(\tau+1) & y_d(\tau+2) & ... & y_d(\widetilde{N}) \end{bmatrix}^T \tag{3.81}$$

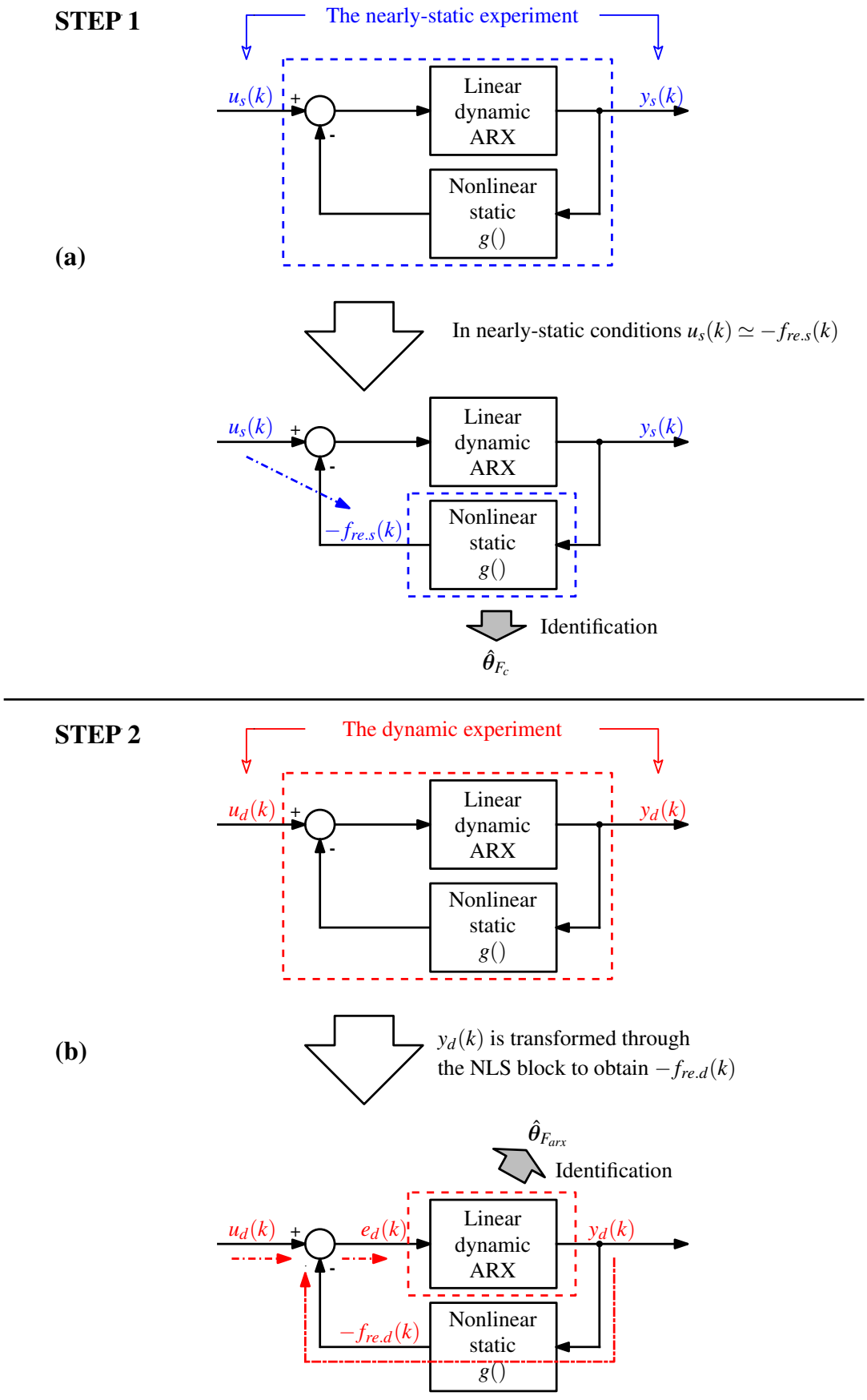

Figure 3.25: The two-step algorithm for the identification of the FBO model. (a) STEP 1: The data collected by the nearly-static experiment are utilised for the identification of the NLS block. (b) STEP 2: The data collected by the dynamic experiment are utilised for the identification of the ARX block.

and

$$\mathbf{\Phi} = \begin{bmatrix} y_d(\tau) & \dots & y_d(\tau+1-n_a) & e_d(\tau+1-n_d) & \dots & e_d(\tau+1-n_d-n_b) \\ y_d(\tau+1) & \dots & y_d(\tau+2-n_a) & e_d(\tau+2-n_d) & \dots & e_d(\tau+2-n_d-n_b) \\ \vdots & \ddots & \vdots & \vdots & \ddots & \vdots \\ y_d(\widetilde{N}-1) & \dots & y_d(\widetilde{N}-n_a) & e_d(N) & \dots & e_d(N-n_b) \end{bmatrix}, \quad (3.82)$$

respectively. The estimated parameters $\hat{\boldsymbol{\theta}}_{F_{arx}}$ are calculated by utilising QR factorization (see Section 3.3.1.1). The FBO model is a good example to show the utility of identifying the single sub-blocks by utilising data from different experiments, intentionally designed for the specific sub-block.

3.3.1.6 KGP model identification

Suppose that, by performing some experiments on a process under study, the signals $\{u(k)\}$ and $\{y(k)\}$ (for $k = 1,...,N$) are generated and utilised as input and output identification data, respectively. Suppose that a KGP model is selected in order to describe the behaviour of the process. As explained in Section 3.2.3.5, the output of the KGP model, in the case where the cross-product terms are removed, is given by:

$$\hat{y}(k) = \sum_{j=1}^{n_p} \Big[\sum_{i=1}^{n_a} a_{ij} y^j(k-i) + \sum_{i=0}^{n_b} b_{ij} u^j(k-n_d-i) \Big],$$

where $\hat{y}$ indicates the model prediction and y the measured data. Equations (3.41), (3.42) and (3.43) become, respectively:

$$\hat{y}(k) = \boldsymbol{\varphi}_{kgp}(k)^T \boldsymbol{\theta}_{kgp}, \quad (3.83)$$

$$\begin{aligned} \boldsymbol{\varphi}_{kgp}(k) \quad = \quad & \Big[y(k-1) \ \dots \ y(k-n_a) \ \ u(k-n_d) \ \dots \ u(k-n_d-n_b) \\ & \ y^2(k-1) \ \dots \ y^2(k-n_a) \ \ u^2(k-n_d) \ \dots \ u^2(k-n_d-n_b) \ \dots \\ & \ y^{n_p}(k-1) \ \dots \ y^{n_p}(k-n_a) \ \ u^{n_p}(k-n_d) \ \dots \ u^{n_p}(k-n_d-n_b) \Big]^T \end{aligned} \quad (3.84)$$

and

$$\boldsymbol{\theta}_{kgp} = \big[a_{11} \ \dots \ a_{n_a 1} \ \ b_{01} \ \dots \ b_{n_b 1} \ \ a_{12} \ \dots \ a_{n_a 2} \ \ b_{02} \ \dots \ b_{n_b 2} \ \dots \ a_{1 n_p} \ \dots \ a_{n_a n_p} \ \ b_{0 n_p} \ \dots \ b_{n_b n_p} \big]^T. \quad (3.85)$$

Equation (3.83) shows that the KGP model is linear in the parameter vector $\boldsymbol{\theta}_{kgp}$. Equation (3.47) becomes:

$$\mathbf{y} = \big[y(\tau+1) \quad y(\tau+2) \quad \dots \quad y(\widetilde{N}) \big]^T, \quad (3.86)$$

where τ and $\widetilde{N}$ are defined in Section 3.3.1.3. For the KGP model, each of the $(\widetilde{N}-\tau)$ rows of the data matrix $\mathbf{\Phi}$, defined by (3.49), has the form:

$$\begin{aligned} & \Big[y(k-1) \ \dots \ y(k-n_a) \ \ u(k-n_d) \ \dots \ u(k-n_d-n_b) \\ & \ y^2(k-1) \ \dots \ y^2(k-n_a) \ \ u^2(k-n_d) \ \dots \ u^2(k-n_d-n_b) \ \dots \\ & \ y^{n_p}(k-1) \ \dots \ y^{n_p}(k-n_a) \ \ u^{n_p}(k-n_d) \ \dots \ u^{n_p}(k-n_d-n_b) \Big], \end{aligned} \quad (3.87)$$

where $k = (\tau+1),...,\widetilde{N}$. The estimated parameters $\hat{\boldsymbol{\theta}}_{kgp}$ are determined by utilising a QR factorization algorithm (see Section 3.3.1.1).

3.3.2 Nonlinear optimization

For models that are nonlinear in the parameters, $\boldsymbol{\theta}$, the linear regression techniques, presented in Section 3.3.1, can not be used for model parameter identification. The main idea of optimization is to minimise some LF, $J(\boldsymbol{\theta})$, which is a measure of error between the model prediction and the recorded data. Given a model nonlinear in the parameters, $J(\boldsymbol{\theta})$ will have a global minimum and may have many local minima (see Fig. 3.26) and no analytical solution exists; therefore, the use of an iterative optimization algorithm is required. Good references, in order to find nonlinear optimization details, include [141] [205] [261] [262] [263].

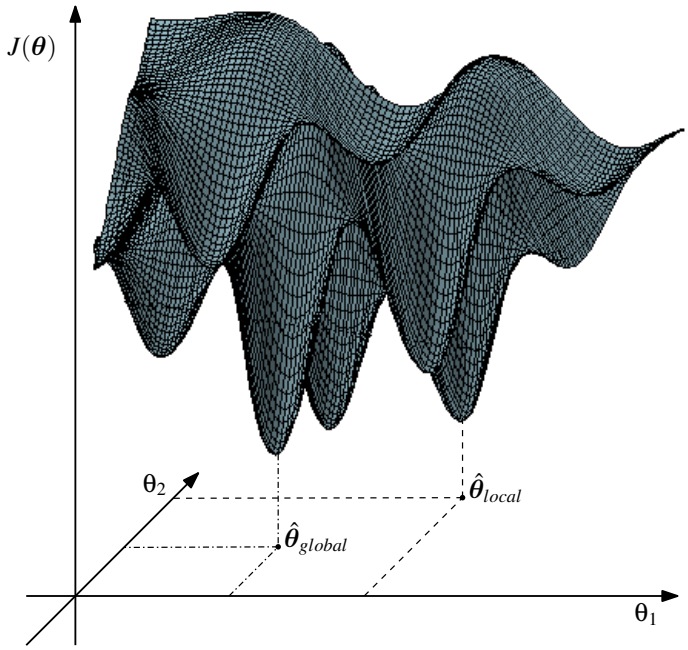

Figure 3.26: In the case of a model nonlinear in the parameters, the LF, $J(\boldsymbol{\theta})$, may have a global minimum and many local minima.

3.3.2.1 Nonlinear optimization method classification

In the literature, there are many optimization algorithms, and no single algorithm is suitable for all problems [264]. Different criteria exist, in order to classify the optimization method, depending on the properties that are compared:

- Criterion 1: algorithms can be classified as line search or trust-region methods [265]:
  - ◇ A *line search method* is an iterative algorithm in the form (see Fig 3.27):

$$\boldsymbol{\theta}_k = \boldsymbol{\theta}_{k-1} + \delta_{k-1}\boldsymbol{\nu}^{\nabla}_{k-1} \tag{3.88}$$

where the new parameter vector, $\boldsymbol{\theta}_k$, is calculated from the previous $\boldsymbol{\theta}_{k-1}$, by moving in a direction $\boldsymbol{\nu}^{\nabla}_{k-1}$, with a step size (also denoted learning rate [266]) δ_{k-1}. Therefore, at each iteration, the algorithm determines, according to a fixed rule, a direction of movement, and searches for a (relative) minimum of the LF on that line. Once the new point is found, a new direction is determined and the process is repeated. Therefore, a line search method first decides the search direction, $\boldsymbol{\nu}^{\nabla}_{k-1}$, and then chooses an appropriate step length, δ_{k-1} [263].

◇ In a *trust-region method*, at the step $k-1$, the LF $J(\boldsymbol{\theta})$ is approximated, in a trust-region around the current point $\boldsymbol{\theta}_{k-1}$, with a parametric version (such as a quadratic approximation), $J^{(a)}_{k-1}(\boldsymbol{\theta})$ [267]. Then, inside the trust-region, the minimizing algorithm applies the same strategy of a line search method on $J^{(a)}_{k-1}(\boldsymbol{\theta})$ (instead of on $J(\boldsymbol{\theta})$). The size of the trust-region may change at

each step and the selected size is important to the effectiveness of each step [265] [268]. A trust-region method first chooses a maximum searching distance (the trust-region size), then calculates a direction $\boldsymbol{\nu}_{k-1}^{\nabla}$, and finally a step size δ_{k-1}, in order to obtain the best improvement inside the trust-region. It is very common to utilise a quadratic function for $J_{k-1}^{(a)}(\boldsymbol{\theta})$.

• Criterion 2: algorithms can be classified as deterministic or stochastic methods [264]:

◇ A *deterministic algorithm* works in a mechanically deterministic way, without the introduction of any random decision; therefore, given the same initial point, the algorithm will reach the same final solution.

◇ In a *stochastic algorithm*, the presence of some randomness in the algorithm, will probably lead to a different solution every time the algorithm is run, even if the problem to solve is the same [205] [264].

• Criterion 3: algorithms can be classified as trajectory-based or population-based methods:

◇ A *trajectory-based algorithm*, at each step, calculates a single solution point, which will trace out a piecewise zig-zag path, as the optimization process continues (see Fig. 3.27).

◇ A *population-based algorithm* calculates, at each iteration, multiple solutions, which will interact with each other to generate a new set of solutions [264]. Examples of population-based algorithms are genetic algorithms (GA) and particle swarm algorithms [261].

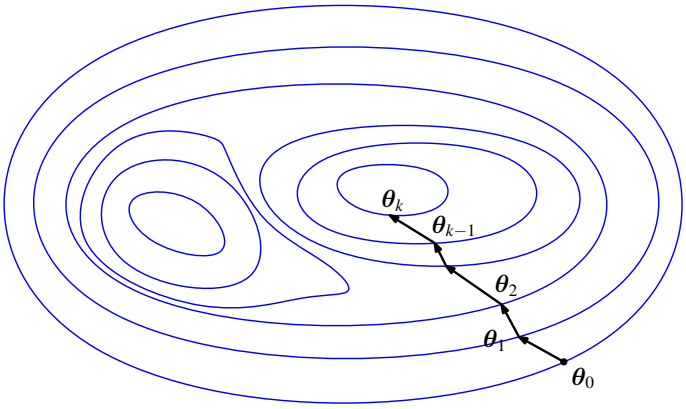

Figure 3.27: Trajectory drown by an iterative line search method, in the case of $\boldsymbol{\theta} \in \Re^2$ and of a LF with two minima. The algorithm starts from the initial point $\boldsymbol{\theta}_0$. The closed lines represent the contour lines of the LF.

3.3.2.2 Common nonlinear optimization algorithms

The iterative algorithm of equation (3.88), utilised for line search methods, provides a common foundation for a large number of optimization algorithms. Indeed, the search direction, $\boldsymbol{\nu}_{k-1}^{\nabla}$, can be written as the LF gradient, $\nabla J(\boldsymbol{\theta}_{k-1})$ (in general, $\nabla J(\boldsymbol{\theta})$ always indicates the direction of the steepest ascent in $\boldsymbol{\theta}$, and $-\nabla J(\boldsymbol{\theta})$ the direction of the steepest descent [266]), rotated and scaled by some direction matrix, $\mathbf{R}_{k-1}$ [205]:

$$\boldsymbol{\nu}_{k-1}^{\nabla} = -\mathbf{R}_{k-1} \nabla J(\boldsymbol{\theta}_{k-1}) \tag{3.89}$$

Different choices of $\mathbf{R}_{k-1}$ lead to different optimization methods, as explained below:

• *Newton's method*. In this case, $\mathbf{R}_{k-1}$ is chosen as the inverse of the Hessian matrix of the LF, calculated at the point $\boldsymbol{\theta}_{k-1}$ [141] [205]:

$$\mathbf{R}_{k-1} = \left(\nabla^2 J(\boldsymbol{\theta}_{k-1}) \right)^{-1} \tag{3.90}$$

Compared to the steepest descent method [205], Newton's method has a faster convergence but, at the same time, has the requirement for second order derivatives that, if not available analytically, have to be computed utilising finite difference techniques. Therefore, if the Hessian matrix is not known analytically, Newton's method becomes computationally expensive, even for medium sized problems. Another important drawback is the required inversion of the Hessian matrix, which strongly limits the size of the studied problem [205].

• *Quasi-Newton method*. The calculation of the Hessian matrix and its inversion, necessary in Newton's method, can be replaced by an appropriate approximation, involving first order derivatives alone, obtaining in this way the family of quasi-Newton methods [141] [205]. The most common algorithms, in order to calculate the approximation of the inverse of the Hessian for the quasi-Newton method, are the DFP (Davidon, Fletcher, Powell) and the BFGS (Broyden, Fletcher, Goldfarb, Shanno) algorithms. For more details, see [141] [205] [265].

• *Conjugate gradient method*. In all quasi-Newton methods, the memory requirement and the computational complexity increase quadratically with the number of parameters. Therefore, for large problems, the approximation of the Hessian matrix is not convenient. As an alternative, given a q-dimensional parameter vector, $\boldsymbol{\theta}$, conjugate gradient methods utilise q different search directions $\boldsymbol{\nu}_i^{\nabla}$, each one conjugate with the others ($\boldsymbol{\nu}_i^{\nabla}$ and $\boldsymbol{\nu}_j^{\nabla}$ are conjugate, with respect to the symmetric positive definite matrix $\mathbf{A}_c$, if $(\boldsymbol{\nu}_i^{\nabla})^T \mathbf{A}_c \boldsymbol{\nu}_j^{\nabla} = 0$ [265]), without a direct approximation of the Hessian matrix. In conjugate gradient methods, the memory requirement and the computational complexity increase linearly with the number of parameters q [205]. A drawback is the larger required number of iterations for convergence, compared to quasi-Newton methods. The conjugacy of the search directions tends to deteriorate during the running of the algorithm; therefore, a typical solution is to restart the algorithm after every q steps, by imposing the search vector equal to the negative gradient direction [205]. For more details see [265] [269] [262] [263].

• *Genetic algorithms*. Genetic algorithms are stochastic, population-based optimization techniques, based on Darwin's theory of natural selection. The great success of natural evolution in the development of new species, which are able to adapt to changing environmental conditions, suggests an innovative approach to mathematical optimization problems [270]. Each possible solution to the optimization problem, in GAs, is represented by an individual (one point in the parameter space) belonging to a population (a set of possible solutions). During each successive generation, a GA selects a sub-population, by implementing a fitness-based process, where fitter solutions (as measured by a LF) are typically more likely to be selected. The selected sub-population is combined to originate a new generation, such that the average 'quality' of the new population is improved. Each solution is coded in a string (the chromosome), by utilising an encoding technique (e.g. binary and floating point coding [271]), which represents the genetic information of the individual. By operating on the strings of the selected 'parent' solutions, a new individual is generated. Three main genetic operations are utilised to create the new generation: crossover, mutation and elitism [205] [261] [272] [273].

3.3.2.3 ANN model identification

The identification of a MLP-ANN, introduced in Section 3.2.3.6, involves tuning the value of weights and biases of the network, in order to optimize the network performance on the available input/output training data. By utilising the MSE as measure of the error, defined in (3.39), from equations (3.33) and (3.35) it is possible to write:

$$\begin{aligned} J(\boldsymbol{\theta}_{ann}) &= \frac{1}{2}\sum_{k=1}^{N}\Big[y(k)-\hat{y}(k,\boldsymbol{\theta}_{ann})\Big]^2 \\ &= \frac{1}{2}\sum_{k=1}^{N}\Big[y(k)-\sum_{i=0}^{n_2} w_i^{(out)}\Psi_i\Big(\sum_{j=0}^{n_1} w_{ij}^{(2)}\Psi_j\big(\sum_{l=0}^{n_v} w_{jl}^{(1)} v_l(k)\big)\Big)\Big]^2, \end{aligned} \tag{3.91}$$

where a MLP-ANN with two nonlinear hidden layers and one linear output layer is utilised. The unknown parameter vector is given by:

$$\boldsymbol{\theta}_{ann} = \Big[w_{11}^{(1)} \quad \ldots \quad w_{n_1 n_v}^{(1)} \quad w_{11}^{(2)} \quad \ldots \quad w_{n_2 n_1}^{(2)} \quad w_1^{(out)} \quad \ldots \quad w_{n_2}^{(out)}\Big]^T. \tag{3.92}$$

Equation (3.91) shows that $J(\boldsymbol{\theta}_{ann})$ is not a quadratic function of $\boldsymbol{\theta}_{ann}$; therefore, it is not possible to utilise the linear optimization methods introduced in Section 3.3.1. Historically, a common way to train a MLP-ANN is the use of the back-propagation algorithm [238] [245] [266]. It is possible to show that the methodology applied by the back-propagation algorithm is just an equivalent way to calculate the search direction and the learning rate, utilised by the recursive derivative-based techniques (3.88) [205] [266]. In the context of a MLP-ANN training, usually, each single iterative line search step is denoted an epoch. Any of the recursive trajectory-based algorithm for nonlinear optimization, presented in Section (3.88) can be used for a MLP-ANN training [244] [274] [275]. In particular, when the number of neurons increases, a good choice is the conjugate gradient algorithm, which is computational efficient and shown to have good performance for ANN models [244] [245] [274] [276]. A MLP-ANN can be retrained on the same data over successive epochs (batch training mode); in this way, all the data training set is applied to the network before weights and biases are updated. An alternative approach is the calculation of new parameter values at each time step (incremental training mode); therefore, the utilised data are different at each epoch. For most problems, a batch training has a faster convergence then an incremental training [244]. In addition, population-based algorithms, such as GAs, can be utilised for a MLP-ANN identification [277].

Section 3.1.1.2 has already introduced that, when the model complexity increases, the identified model becomes more flexible and able to show more sophisticated dynamical behaviour but, at the same time, unnecessarily high complexity can render the model less capable of generalising on new data. In Section 3.2.4, it has been explained that n_a, n_b and n_d of a DT nonlinear model can be estimated by implementing a systematic trial and error process on several ARX models. In the case of MLP-ANN models, the model complexity, in addition to n_a, n_b and n_d, is given also by n_1 and n_2, which are the number of neurons in the two hidden layers (in the case where the two hidden layer ANN structure, described by (3.33), is utilised). It is not straightforward to calculate the optimal values for n_1 and n_2, but it is known that the model performance is poor, if the network is not complex enough and, on the other hand, there is the risk of overfitting, if the network is too complex [244].

3.4 Hydrodynamic WEC model validation

As explained in Section 3.1.1.4, model validation is an important step in SI. The first model assessment is computed on the training data and, if the results are not satisfactory with the training data, the model cannot be accepted. In this case, the problem may be an incorrect selected model, which is not able to describe the complexity of the process [205], or the identification algorithm

may provide a parameter vector too far from the optimal solution. In a case where the performance achieved on the training data is acceptable, the real validation assessment comes when the model is tested on new data, that is, when the model has to predict the outcome of an experiment which was not used for the model parameter identification [278]. In order to deliver the training and validation steps, the available data is divided into separate training and validation data sets [205] [221]. It is important to remember that a model, which fits the training data well, is not necessary a good model on different experimental data (i.e. overfitting problem). Common methods utilised for model validation are the 1-step (ahead) prediction test and the multi-step (ahead) prediction test [221]:

• *1-step (ahead) prediction test*. The model output prediction, $\hat{y}$, is calculate by utilising only the process measurements u and y (no predicted past values of the output, $\hat{y}$, are used), as shown in Fig. 3.28(a). At each time step, the prediction error $e(k) = y(k) - \hat{y}(k)$ is computed. 1-step prediction tests are often not sufficient to show model inadequacy and even models with low accuracy may generate almost perfect 1-step predictions [221].

• *Multi-step (ahead) prediction test*. The mathematical model is initialised by a few known measured output values and, successively, the model output is calculated by the previous model predicted output, $\hat{y}$, and by the given measured input, u, as shown in Fig. 3.28(b). Therefore, at each time step the output error $e(k)$ quickly accumulates.

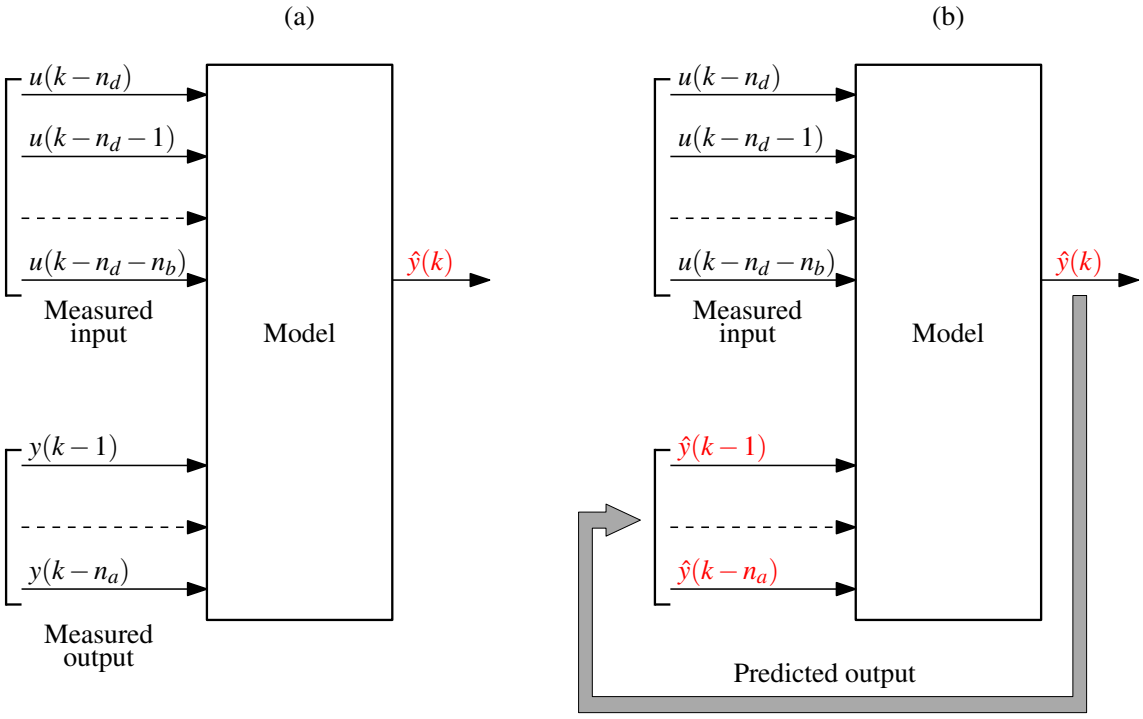

Figure 3.28: (a) 1-step prediction (b) Multi-step prediction.

Different error metrics can be utilised to compare the model prediction, $\hat{y}(k)$, with the measured signal, $y(k)$ (either for 1-step or multi-step predictions):

• The *mean squared error* [279]. As explained in Section 3.3, the MSE is defined as:

$$MSE = \frac{1}{N}\sum_{k=1}^{N} |y(k) - \hat{y}(k)|^2, \tag{3.93}$$

where the constant $\frac{1}{N}$ is commonly replaced by $\frac{1}{2}$ or $\frac{1}{2N}$ [205]. In this section, the constant $\frac{1}{N}$ is utilised to maximise the compatibility with the other error metrics introduced. The main disadvantage is that the MSE is not normalised with respect to the magnitude of $y(k)$; therefore, it is difficult to compare different fitting results.

• The *mean absolute percentage error (MAPE)*. In order to obtain a metric normalised with respect to the magnitude of $y(k)$, the MAPE is defined [279] as:

$$MAPE = \frac{100}{N}\sum_{k=1}^{N}\frac{|y(k)-\hat{y}(k)|}{|y(k)|} \tag{3.94}$$

However, a drawback of the MAPE is that it can give a distorted picture of the error, in the case where there are zero (or nearly-zero) values in the measured signal, $y(k)$. Since, in the context of wave energy, it is common that $y(k)$ oscillates around the zero value, there is a good possibility of obtaining a distorted picture of the error. For example, Fig. 3.29 shows the presence of spikes of the quantity $|y(k)-\hat{y}(k)|/|y(k)|$, when the measured displacement, $y(k)$, crosses the zero value.
• The *normalised root mean-squared error (NRMSE)*, defined [8] [12] as:

$$NRMSE = \frac{\| y(k)-\hat{y}(k) \|_2}{\| y(k) \|_2} = \frac{\sqrt{\frac{1}{N}\sum_{k=1}^{N}|y(k)-\hat{y}(k)|^2}}{\sqrt{\frac{1}{N}\sum_{k=1}^{N}|y(k)|^2}}, \tag{3.95}$$

has the advantage of being normalised with respect to the magnitude of $y(k)$ and, at the same time, the presence of nearly-zero values in the measured signal $y(k)$ does not alter the picture of the error.

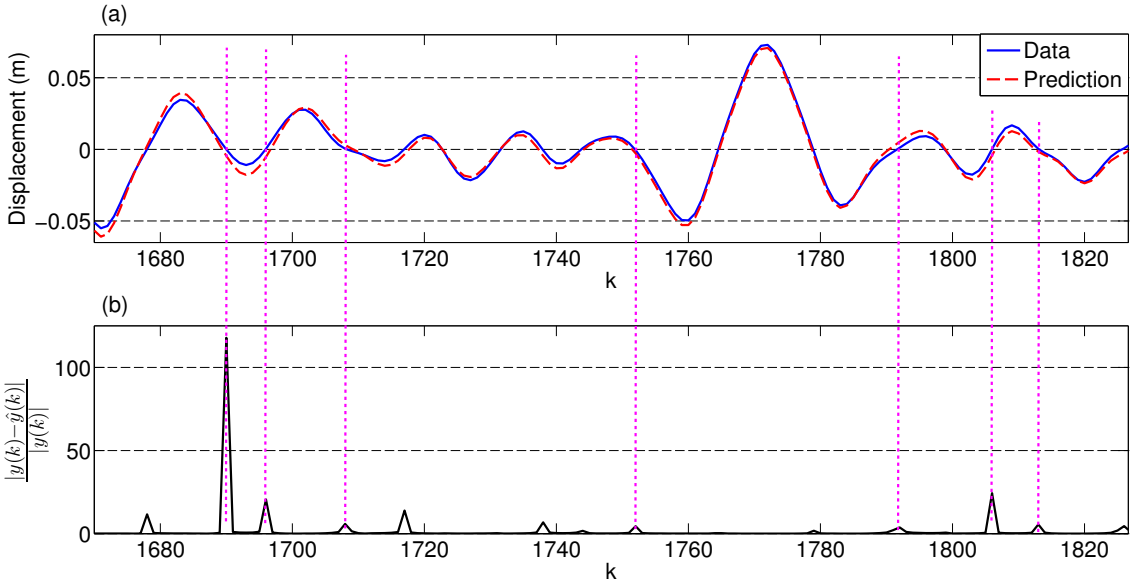

Figure 3.29: (a) Time evolution of the body displacement provided by the experimental data and predicted by the model. (b) Time evolution of the quantity $|y(k)-\hat{y}(k)|/|y(k)|$.

3.5 Summary and discussion

This chapter has introduced the fundamental aspects of SI, a discipline well known in a variety of engineering subjects; in this thesis, SI is applied for WECs modelling. Section 3.1 shows that SI is based on an iterative sequence of four steps (experiment design and data gathering, model order and structure selection, fitting criterion and identification algorithm selection, and model validation). At the end of the SI procedure, an identified model is provided. It is crucial to stress that a model is identified on some training data, but the quality of the model has to be evaluated on some fresh data (validation data); indeed, a model not able to generalize on new data is a relatively worthless model, but just provides an imperfect copy of the original training data, with no useful

interpolation value. Usually, the use of SI to resolve an engineering problem does not lead to an ideal unique answer, but provides a variety of possible solutions, depending on decisions taken during the SI procedure, which could be all correct and reasonable. Furthermore, the definition of a 'best' model may change from application to application; the best model usually meaning the best compromise for the specific application. The ideal compromise sought in this thesis is that between a high model prediction accuracy (increased with the introduction of nonlinearity) and a low computational requirement. In Section 3.2, by starting from Cummins' equation, different CT model structures have been obtained, and utilised as a guideline for the construction of DT model structures, obtaining grey-box models such as FBO and Hammerstein model structures. Furthermore, DT black-box model structures are proposed, such as ARX, KGP and ANN models. In Section 3.3, the use of linear and nonlinear optimization for the identification of the parameters of WEC model structures is explained, underlining the crucial difference between a model with a nonlinear input/output relationship and a model nonlinear in the parameters. Indeed, it is possible to have models with a nonlinear input/output relationship but being linear in the parameters (such as Hammerstein and KGP models), which have the relevant advantage of requiring only linear optimization for parameter identification. On the other hand, ANNs are nonlinear both in the input/output relationship and in the parameters, with the drawback of requiring a nonlinear optimization. In Section 3.4, the model validation concept is introduced, and the importance of the model testing on new data is stressed. The important SI step, regarding experiment design and data gathering, is introduced in Section 3.1.1.1 and will be comprehensively illustrated in Chapter 4, in the specific case of wave tank experiment design for WEC model identification.

Chapter 4

Wave tank experiment design for WEC model identification

4.1 Introduction

In Section 3.1.1.1, the importance of utilising informative data for system identification, especially in the presence of nonlinear systems, was introduced. This chapter focuses on an experiment design in wave tanks (for both NWT and RWT), in order to generate data for WEC model identification. In recent years, a significant variety of different WECs have been studied in RWTs, in order to analyse their hydrodynamic characteristics. Often, the experiments are based on a WEC subject to incoming waves, which can be regular monochromatic waves or irregular waves with a specific wave spectrum (wave spectra are usually characterised by a significant wave height and a peak period). The data generated by these kinds of experiments can be utilised for WEC model identification, but the possibility of designing an experiment, specifically for WEC model identification, can render the generated data more informative and effective, in order to obtain an accurate identified model. It is important to stress that, by extending the duration of an experiment, the amount of information contained in the data usually increases but, at the same time, there are increasing disadvantages, for both NWT and RWT cases. Indeed, in the case of a CFD-NWT, the amount of computation time can become unsustainable (the computation time could be up to 1000 times the simulation time, as suggested in Section 2.3) whereas, in the case of a RWT, a set of long tank experiments corresponds to an increase of the facility renting costs. In the wave energy community, it is usual to use monochromatic waves in order to study the WEC hydrodynamic behaviour at a specific wave frequency and amplitude; therefore, in order to cover the whole input range in both frequency and amplitude (in this case the input is the FSE), the number of experiments quickly becomes significantly large, leading to a considerable experimental time to collect all the required information. An interesting alternative is the use of 'time-shrunk' input signals, characterised by a high concentration of information. These particular signals contain the whole variety of frequencies and amplitudes, necessary to excite the system over the whole range of operation, in a more compacted time frame. In the case where the mathematical model structure, utilised to model the process, is available before the experiment realization, the experiment design can be even more optimised. Indeed, it is usual to describe a complex system as the interconnection of smaller sub-systems, each one having a specific input and output. Therefore, the design of a set of experiments, each one designed to excite a different sub-block, leads to the direct simulation/measure of the input and output of each sub-system, providing the data for the identification of each sub-block.

This chapter is laid out as follows: Section 4.2 describes the design of excitation signals for data generation, with Section 4.2.1 explaining the main excitation signal characteristics (spectral content, amplitude range and amplitude distribution) and Section 4.2.2 illustrating a variety of pos-

sible input excitation signals. In Section 4.3, different typologies of WT experiments are shown, with Section 4.3.2 describing the WT identification experiments (free decay, input wave, input force and prescribed motion experiments) and Section 4.3.1 explaining the WT preliminary experiments (free decay and input force preliminary experiments). In Section 4.4, a methodology to compare 2D NWT data with 3D BEM (in this case WAMIT) data is presented. Finally, a summary and discussion are presented in Section 4.5.

4.2 Design of excitation signals for data generation

4.2.1 Excitation signal characteristics

In this section, the main characteristics, utilised to evaluate the quality of an excitation signal for WEC model identification, are presented. In section 4.2.1.1, the description of the signal spectral content is introduced. Section 4.2.1.2 explains the important aspect of having a good coverage of the full input and output amplitude signal ranges. Section 4.2.1.3 illustrates the aspect that a good excitation signal should have an equal amplitude distribution, in order to excite the system uniformly.

4.2.1.1 Signal spectral content

The essence of the frequency description of a signal, represented by a spectrum (there are several variations of spectrum definition, such as energy spectrum or power spectrum) is to decompose the waveform into a summation of sinusoids of different frequencies [222] [280]. The amplitude spectrum of the input signal determines the frequencies at which the power is introduced into the system. It is important to underline that the quality of the identified system is higher at the frequencies which are strongly excited by the input signal; for example, in the case where the input signal is a single sine wave of frequency ω_1, the identified model is a good representation of the process only for frequency ω_1 [205]. Therefore, during the identification experiment design, it is important to guarantee that the input excitation signal has a good coverage of the frequencies where the system has a significant non-zero frequency response.

The fundamental tool to describe the frequency content of a CT signal is the Fourier transform, which represents a signal, $u(t)$, as an infinite sum of sinusoids of infinite different frequencies. Mathematically, the Fourier transform is defined [222] [281] as:

$$U(f) = \int_{-\infty}^{\infty} u(t) e^{-i2\pi ft} dt. \tag{4.1}$$

The Fourier transform, $U(f)$, is a complex function and can be expressed as:

$$U(f) = |U(f)| e^{iArg\left(U(f)\right)}, \tag{4.2}$$

where the modulus, $|U(f)|$, provides an indication of the amount of harmonic content of the signal $u(t)$ at a frequency f, and where $Arg\left(U(f)\right)$ is the phase of $U(f)$. The different spectral definitions, available in the literature (e.g. energy spectrum or power spectrum), depend on the characteristic of the signal $u(t)$ (e.g. continuous/discrete-time or with finite/infinite energy), but the different spectra are very closely related to the square of the absolute value of the signal Fourier transform [280].

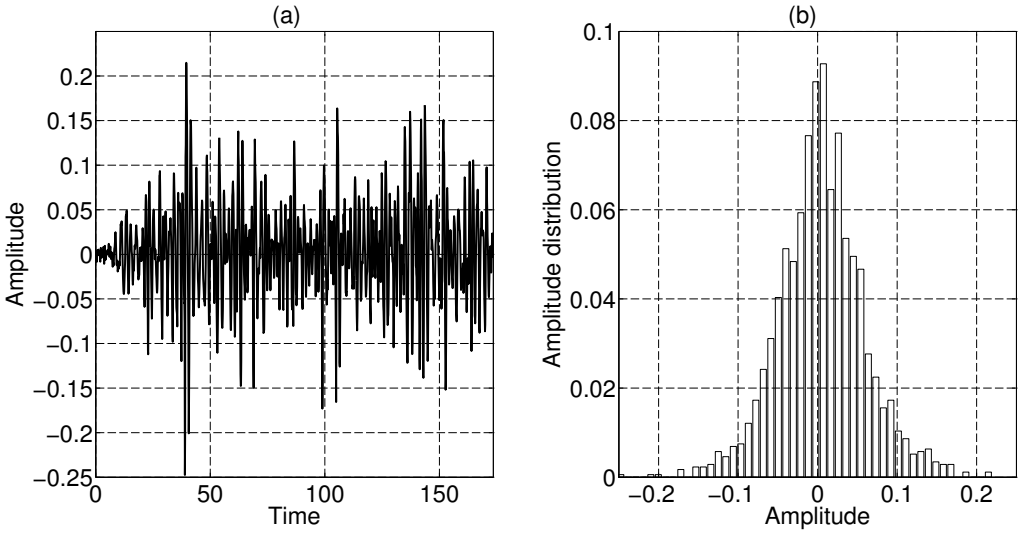

Figure 4.1: (a) Signal time evolution. (b) Signal amplitude distribution.

4.2.1.2 Input and output signal amplitude ranges

For any real physical system, the input and output signal ranges are bounded between a maximum and minimum level, because physical survivability issues of the system (e.g. the applied electric signal at the input of an amplifier or the PTO force applied to a floating WEC), or because the system is intentionally designed to work in a specific range, in order to exhibit some desired properties (e.g. linearity or the absence of harmonic distortion). In the identification experiment design, it is important to restrict the input and output amplitude to the ranges at which the system is supposed to normally operate, in order to provide, to the SI procedure, the essentially different behaviours that the mathematical model has to be able to repeat and exhibit. Indeed, it is not advantageous to introduce unnecessary complexity in the model structure, just in order to describe the system behaviour, in conditions which are not of interest, from a practical point of view. For example, in the case of WEC modelling for power production, the objective is to obtain a model able to describe the WEC dynamic in power production mode, and not in extreme sea conditions, when the WEC switches to survival mode. If the presence of system nonlinearity is anticipated, it is important to properly excite the system in order to observe the system response over the full range of interest; indeed, model extrapolation is more inaccurate than model interpolation [205]. It is worthwhile stressing that designing an identification experiment, which covers the full range of the output, is not straightforward, because there is no direct imposition on the output by any actuator; indeed, the output is just how the system responds to the input. Therefore, in the case of unknown nonlinear systems, the ability to predict what the output range will be, as a consequence of the chosen input, may be very complex.

4.2.1.3 Signal amplitude distribution and data sparseness

In Section 4.2.1.2, it was explained that it is important to cover the input signal range to obtain an accurate identified model. It is relevant to understand that covering the input range well is necessary but is not sufficient; it is also important *how* the range is covered. Indeed, an important signal characteristic, which has to be taken into consideration during the experiment design, is the (instantaneous) amplitude distribution, which can be visualised by plotting the signal samples in a histogram [222] [282]. For example, Fig. 4.1(a) shows a sample signal time evolution and Fig. 4.1(b) the corresponding amplitude signal distribution. In order to excite the system uniformly and obtain the same amount of information of each signal level, the amplitude distribution of the input signal should, ideally, be uniformly distributed [205].

A better way to understand the importance of the signal amplitude distribution, is to consider the general DT model of Fig. 4.2, which represents the block diagram of a general NARX discrete-time model (see Section 3.2.3). The unknown function γ provides the system output, $y(k)$, as a response to the vector $\mathbf{V}(k) \in \Re^{(n_a+n_b+1)}$, which is defined as (see Section 3.2.3.6):

$$\mathbf{V}(k) = \Big[y(k-1) \;\; ... \;\; y(k-n_a) \;\; u(k-n_d) \;\; u(k-n_d-1) \;\; ... \;\; u(k-n_d-n_b) \Big] \tag{4.3}$$

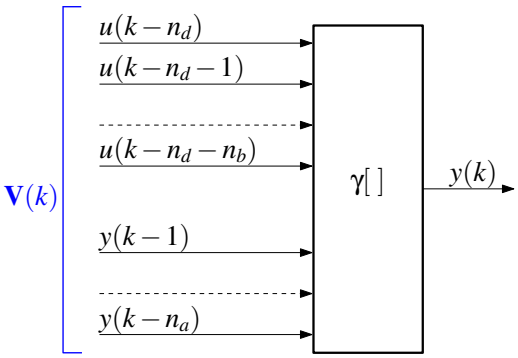

Figure 4.2: Block diagram for a general NARX discrete-time model, where $y(k) = \gamma\big[\mathbf{V}(k)\big]$.

Therefore, the identification of the system corresponds to the identification of the function γ. In order to correctly identify γ, it is important that the cloud of points $\{\mathbf{V}(k)\}$, available from the experimental data, is uniformly distributed in the domain space, inside an area bounded by the decided input and output ranges. As a simple explanatory example, consider the case of a system having $\mathbf{V}(k) \in \Re^2$ with $\mathbf{V}(k) = [u(k), u(k-1)]$, and excited by one of the following four different input signals:
*S*1) $u(k) = \sin(10k)$.
*S*2) $u(k) = \sin(10k) + \sin(1.3k)$.
*S*3) $u(k) = \sin(10k) + \xi_n(k)$, where $\xi_n(k)$ is white noise, uniformly distributed in the interval [-0.1 , 0.1].
*S*4) $u(k) = \xi_n(k)$, where $\xi_n(k)$ is white noise, uniformly distributed in the interval [-1 , 1].
Fig. 4.3 shows the cloud of points, $\{\mathbf{V}(k)\} \subset \Re^2$, in the case of the pure harmonic signal *S*1; it is possible to see that the covered space is just the border of an ellipse, a cloud of points with little spread (inside and outside the ellipse the space is not covered at all) [283], and composing a nonconvex space (a set *C* is convex if the line segment between any two points in *C* lies in *C* [255]). Fig. 4.4 shows the cloud of points, $\{\mathbf{V}(k)\} \subset \Re^2$, in the *S*2 case, in which a second harmonic, at a higher frequency, has been added to the input signal. The situation appears improved, the cloud of points is spread inside the ellipse, and is assuming the broad characteristics of a convex set (there are no significant 'holes' inside the ellipse). Fig. 4.5 shows the *S*3 case, in which random noise has been added to the single harmonic signal *S*1. In this case, the covered space is nonconvex and is not significantly spread. Finally, Fig. 4.6 shows the *S*4 case, in which the input signal is pure random noise, with equal distribution probability in the range [-1,1]. In this case, the cloud of points, $\{\mathbf{V}(k)\}$, is uniformly distributed and has the broad characteristics of a convex set (there are no significant holes). Therefore, it is clear how different signals cover in a very different way the $\{u(k), u(k-1)\}$ plane. In the simple examples, with input signals *S*1, *S*2, *S*3 and *S*4, the output of the system is assumed to be dependent only on the present and past values of the input, u. In the more general case of an autoregressive model, as shown in Fig. 4.2, $\mathbf{V}(k)$ also contains shifted values of the output, y. This aspect introduces a complication in the experiment design; indeed, if on one side there is the direct control on the amplitude distribution of the input signal (the signal is designed to have that specific amplitude distribution), on the other side, there is no direct control on the distribution of the output, y, which depends only on how the system responds to the input.

In the case of an unknown nonlinear system, the possibility of predicting the output distribution as a consequence of the chosen input is not straightforward, as already outlined in Section 4.2.1.2.

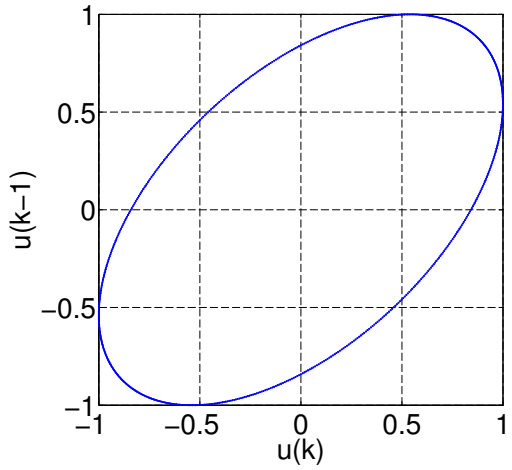

Figure 4.3: The signal cloud, $\{u(k), u(k-1)\} \subset \Re^2$, in the case of the signal $S1$.

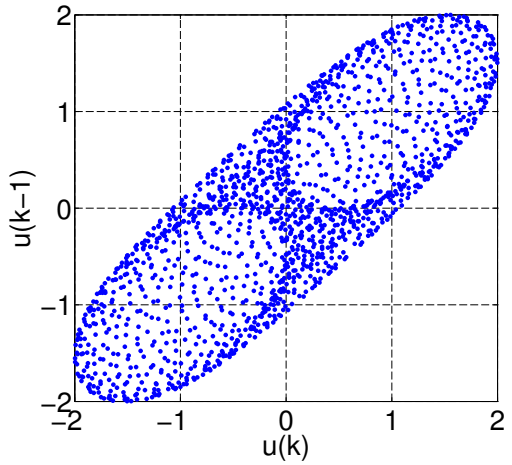

Figure 4.4: The signal cloud, $\{u(k), u(k-1)\} \subset \Re^2$, in the case of the signal $S2$.

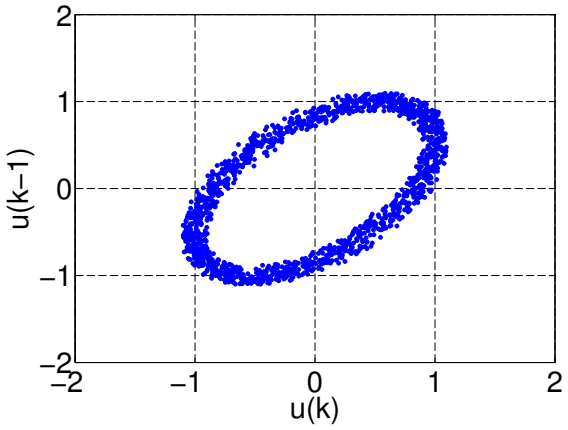

Figure 4.5: The signal cloud, $\{u(k), u(k-1)\} \subset \Re^2$, in the case of the signal $S3$.

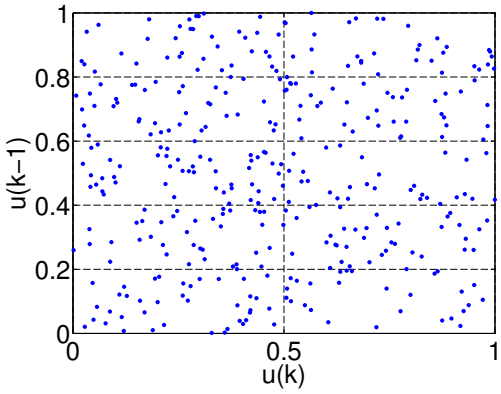

Figure 4.6: The signal cloud, $\{u(k), u(k-1)\} \subset \Re^2$, in the case of the signal $S4$.

Another way to describe the amplitude distribution of a signal, $u(t)$, is provided by the crest factor, $C_r(u)$, defined as the ratio of the signal peak value, u_{peak}, to its root mean square (RMS) value in the bandwidth of interest, which is also termed the 'effective' RMS value, u_{rmse}, [192] [204]:

$$C_r(u) = \frac{u_{peak}}{u_{rmse}}, \tag{4.4}$$

where

$$u_{peak} = \max_{t \in [0,T]} |u(t)|, \tag{4.5}$$

$$u_{rmse} = u_{rms} \sqrt{\frac{\text{signal power (energy) in the band of frequencies of interest}}{\text{total signal power (energy)}}}, \tag{4.6}$$

$$u_{rms} = \sqrt{\frac{1}{T} \int_0^T u^2(t) dt}, \tag{4.7}$$

where T is the measurement time, and $u_{rmse} \leq u_{rms}$. Signals having an impulsive shape have a large crest factor, and they introduce less power into the system, compared to signals having the same peak value, but a smaller crest factor [192].

4.2.2 Excitation signal typology

As outlined in Section 3.1.1.1, the signal, used to excite the system during the experiment, plays an important role in SI. Ideally, the objective is to excite the system as much as possible, in the shortest possible time, in order to obtain all the required identification information. Useful signals in SI are random and pseudorandom binary signals, random amplitude random period signals, chirp signals and multisine signals, which are introduced and explained in the following Sections 4.2.2.1, 4.2.2.2 4.2.2.4 and 4.2.2.3, respectively.

4.2.2.1 Random and pseudorandom binary signals

A random binary signal (RBS) is a random signal which can assume one of only two different values at any given sample time. If p is the probability of assuming one value, obviously, the probability of assuming the other value is $(1-p)$ [141] [204]. A pseudorandom binary signal (PRBS) is a periodic binary sequence (there are only two amplitude levels) that, despite the fact that it is a deterministic sequence, exhibits statistical characteristics similar to a RBS [214]. The switches between the two levels can occur only on a discrete-time grid, at multiples of the sampling period, T_s [192] [204]. See Fig. 4.7 for a RBS/PRBS signal time evolution example. It is interesting to underline that RBSs and PRBSs have a crest factor equal to one, the best possible crest factor and, for this reason, they represent a benchmark [192]. RBSs and PRBSs are widely used for linear

system identification; however, Leontaritis and Billings [284] show that a RBS/PRBS may not be ideal for the identification of nonlinear systems. Indeed, in the case of nonlinear systems, it is essential that all the interesting frequencies, amplitudes and all their combinations are present in the input signal. In a RBS/PRBS, obviously, only two values are present and all the other values in between are, essentially, missing. Fig. 4.8 depicts the signal cloud, $\{u(k), u(k-1)\} \subset \Re^2$, of a RBS/PRBS, having -1 and 1 as possible signal values. It is shown that the signal cloud covers only four isolated points in the $\Re^2$ space: (-1,-1), (-1,1), (1,-1) and (1,1), clearly indicating the inadequacy of this signal for nonlinear system identification (the covered space is almost empty and nonconvex). For this reason, other types of excitation signals are preferred for the identification of nonlinear systems, such as RARP, chirp and multisine signals.

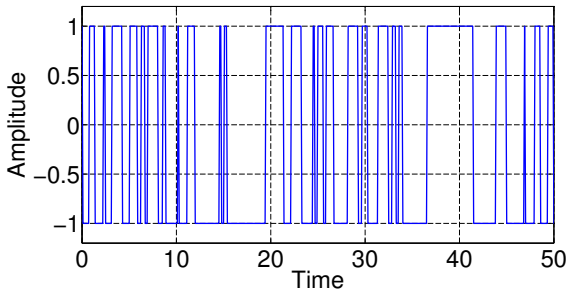

Figure 4.7: Sample RBS/PRBS signal time evolution for $t = kT_s$, in the case where the two allowed amplitude values are -1 and +1.

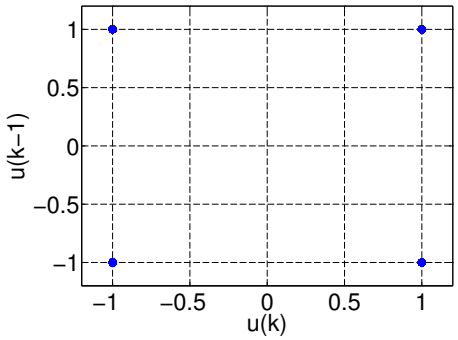

Figure 4.8: The signal cloud, $\{u(k), u(k-1)\} \in \Re^2$, for a RBS/PRBS, in the case of the two allowed amplitude values are -1 and +1.

4.2.2.2 Random amplitude random period signal

A crucial aspect of nonlinear systems is that they have dynamics that are amplitude dependent. The RBS/PRBS, seen in Section 4.2.2.1, does not assume all the possible values of the input system range (they can assume only two different values); therefore, RBS/PRBS signals are not typically used for the nonlinear system identification. Pseudorandom sequences with randomly varying amplitudes (or random amplitude random period (RARP) signals) overcome this limitation, by introducing also a random change in the signal amplitude. The switches between different levels can occur only on a discrete-time grid, at multiples of the sampling period, T_s. A RARP signal can be seen as a sequence of adjacent rectangular pulses with different width, T_r, and amplitude, A_r (see Figs. 4.9 and 4.10(a)). The construction of the RARP signal is achieved by specifying the statistical characteristics of the discrete random variable T_r, termed switching period, and the continuous random variable A_r, in order to decide the width and the amplitude of each rectangular

pulse, respectively [141]. Given a maximum and a minimum width of the single rectangular pulse, represented respectively by $T_r^{(max)}$ and $T_r^{(min)}$, T_r assumes all the values $T_r = nT_s$ (where n is an integer number) in the interval $[T_r^{(min)}, T_r^{(max)}]$, with probability mass function (PMF), f_{T_r}. Similarly, given a maximum and a minimum amplitude for the signal, represented respectively by $A_r^{(max)}$ and $A_r^{(min)}$, A_r assumes values in the interval $[A_r^{(min)}, A_r^{(max)}]$, with a probability density function (PDF), f_{A_r}. The RARP signals, used for this thesis, have constant f_{T_r} and f_{A_r}, as shown in Fig. 4.10. A RARP signal is obtained by sequentially constructing each pulse; at the beginning of each new pulse, specific values of T_r and A_r are selected, indicating the unique width and amplitude of the new pulse.

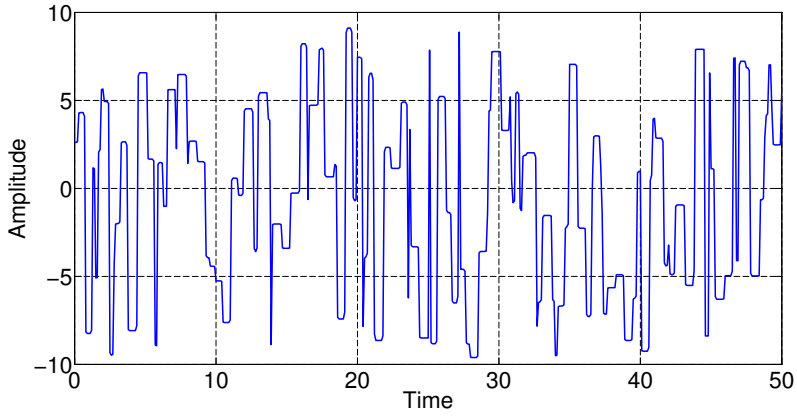

Figure 4.9: Sample RARP signal time evolution, for $t = kT_s$.

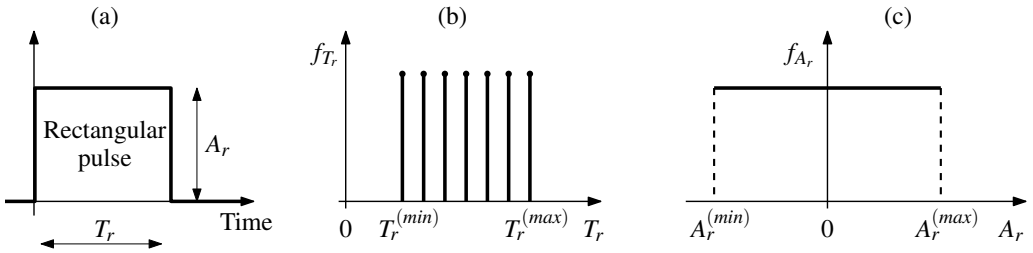

Figure 4.10: RARP signal: (a) Rectangular pulse time evolution. (b) The width of each rectangular pulse is described by a constant PMF, f_{T_r}. (c) The amplitude of each rectangular pulse is described by a constant PDF, f_{A_r}.

In a RARP signal, the presence of rectangular pulses with different widths is important for the frequency richness of the signal; indeed, short pulses introduce higher frequencies into the spectrum, whereas, longer pulses correspond to a low frequency content [205] [227]. The frequency content (shown in Fig. 4.11(c)) and the amplitude distribution (shown in Fig. 4.11(d)) of different realizations of the same RARP stochastic process may vary due to the inherent randomness of the signal. However, as the signal length increases, the amplitude distribution converges to a flat coverage of the desired range, shown in Fig. 4.10(c) and the frequency content converges to a spectral limit. Fig. 4.12 shows the signal cloud, $\{u(k), u(k-1)\} \subset \Re^2$, for a RARP signal. It is possible to see that the cloud of points is well distributed and has the broad characteristics of a convex set (there are no significant holes), indicating a good quality signal. It is interesting to note that the majority of points of the cloud are located on the diagonal line, which represents the points $u(k) = u(k-1)$. Indeed, the only points outside the diagonal are the points representing a switching of the RARP signal from one value to another one, as shown in Fig. 4.13.

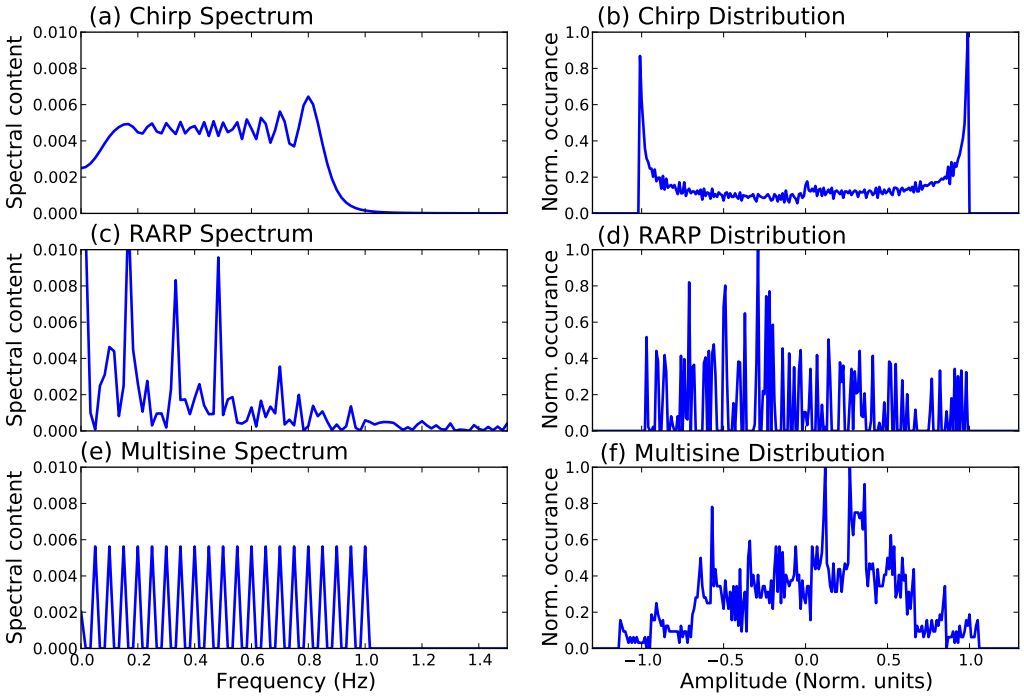

Figure 4.11: Spectrum and amplitude distribution for chirp, RARP and multisine signals.

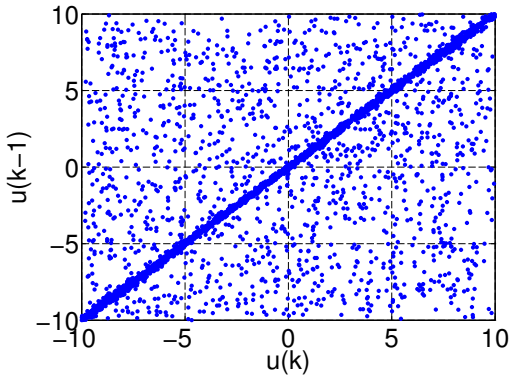

Figure 4.12: The signal cloud, $\{u(k), u(k-1)\} \subset \Re^2$, for a RARP signal.

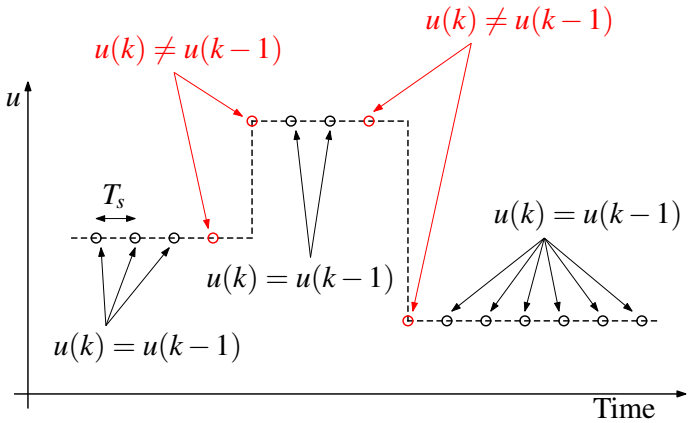

Figure 4.13: The plotted time evolution of a sample RARP signal shows the points representing a switching of the RARP signal from one value to another ($u(k) \neq u(k-1)$) and the points without a switching ($u(k) = u(k-1)$).

4.2.2.3 Multisine signal

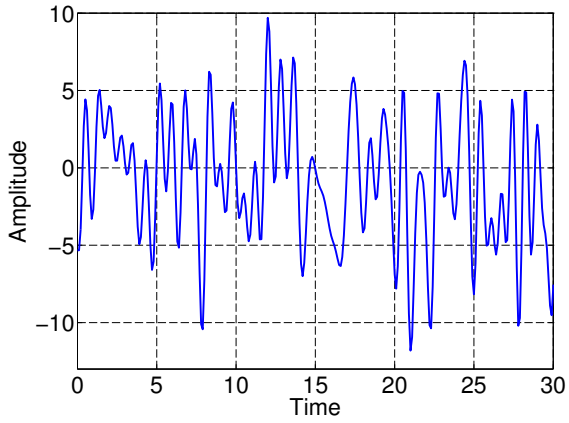

Figure 4.14: Sample multisine signal time evolution for $t = kT_s$.

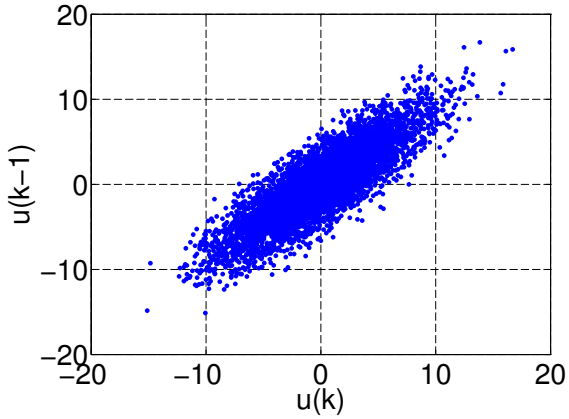

Figure 4.15: The signal cloud, $\{u(k), u(k-1)\} \subset \Re^2$, for a multisine signal.

A multisine signal, shown in Fig 4.14, is the superposition of N_s sine waves:

$$u(k) = \sum_{n=1}^{N_s} A_n \sin(2\pi f_n k T_s + \varphi_n) \tag{4.8}$$

where f_n is the frequency, φ_n the phase and A_n the maximum amplitude of the n-th sinusoid (in the literature, A_n is commonly termed amplitude of the sinusoid but, in this chapter, A_n is termed the maximum amplitude, to avoid any ambiguity with the (instantaneous) amplitude of the signal $u(t)$). If $f_n = nf_1$, where f_1 is the lowest frequency (also termed fundamental frequency), then the sinusoids are equidistant in frequency (see Fig. 4.11(e)) [192] [214] [242] [285]. The multisine signal allows strong control over the spectral content, with free choice for the maximum amplitude of each harmonic. For example, Fig. 4.11(e) shows a multisine signal having a fundamental frequency of 0.05 Hz and equal maximum amplitude for every harmonic up to 1 Hz. For a multisine signal there is flexibility in the amplitude distribution design (Fig. 4.11(f)); indeed, the amplitude distribution is determined by the phases of the harmonic components, which leads to control over the amplitude content in the multisine signals, through phase optimisation techniques (without changing the amplitude spectrum) [192] [218]. Typically, the crest factor for a multisine signal is 1.7 [192]. Fig. 4.15 shows the signal cloud $\{u(k), u(k-1)\} \subset \Re^2$, for a multisine signal. It is possible to see that the cloud of points is well distributed and has the broad characteristics of a convex set (there are no significant holes), indicating a good quality signal.

4.2.2.4 Chirp signal

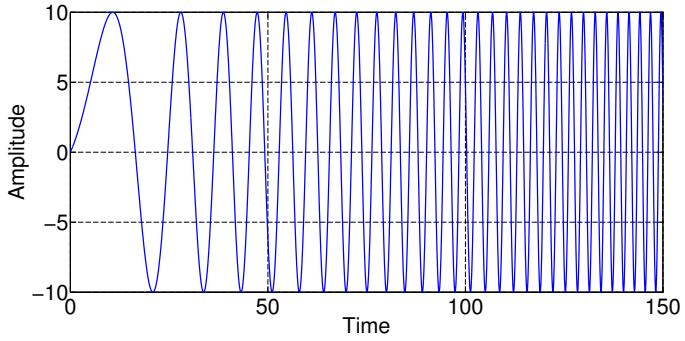

Figure 4.16: Sample chirp signal time evolution for $t = kT_s$.

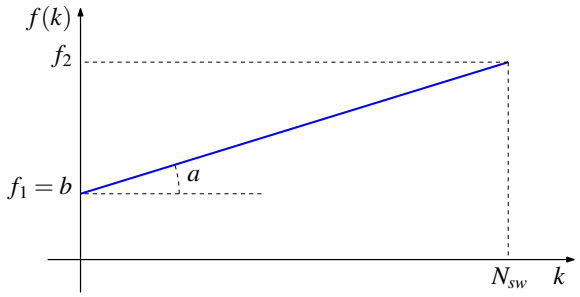

Figure 4.17: Time evolution of the instantaneous frequency $f(k)$ for a chirp signal.

A chirp signal (also termed swept sine), shown in Fig. 4.16, is a sine wave signal characterised by a variable instantaneous frequency, $f(k)$, which sweeps up and/or down, in the user-selected frequency-band $[f_1, f_2]$, in one sweep period $T_{sw} = N_{sw}T_s$, where T_s is the signal sampling period and $(N_{sw}+1)$ is the number of samples contained in one sweep period [192] [227] [286]:

$$u(k) = A_c \sin\left[2\pi f(k) k T_s + \varphi\right] \tag{4.9}$$

where A_c is the maximum amplitude and φ the initial phase. The instantaneous frequency, $f(k)$ is specified to change linearly with k (as shown in Fig. 4.17), so that:

$$f(k) = ak + b \tag{4.10}$$

Therefore, by imposing the limiting values of $f(k)$, given by:

$$\begin{cases} f_1 = a0 + b & \text{for } k = 0 \\ f_2 = aN_{sw} + b & \text{for } k = N_{sw} \end{cases} \tag{4.11}$$

it follows that:

$$b = f_1 \tag{4.12}$$

and

$$a = \frac{f_2 - f_1}{N_{sw}} = (f_2 - f_1)\frac{T_s}{T_{sw}} \tag{4.13}$$

Therefore, the instantaneous frequency becomes:

$$f(k) = f_1 + \frac{f_2 - f_1}{N_{sw}} k \tag{4.14}$$

By introducing (4.14) into (4.9), it follows that:

$$u(k) = A_c \sin\left[2\pi\left(f_1 k + \frac{f_2 - f_1}{N_{sw}} k^2\right) T_s + \varphi\right] \tag{4.15}$$

Equation (4.15) shows that a chirp signal, having an instantaneous frequency $f(k)$, which changes linearly with k, is a sinusoid with an argument that changes quadratically with k; for this reason, (4.15) is also termed a quadratic-phase sinusoid [285] [287].

The chirp signal's frequency sweeps a desired range linearly during the signal duration; therefore, its frequency content is distributed fairly evenly across that range (see Fig. 4.11(a)). Most of the power of the chirp signal is distributed in the user-selected frequency-band $[f_1, f_2]$ [192]. The (instantaneous) amplitude of the chirp signal is well bounded, with free choice in setting A_c. However, there is no choice over the amplitude distribution, which is well defined and has two peaks near the extremes where the signal slows, stops and changes direction at every oscillation (see Fig. 4.11(b)). A chirp signal has typically a crest factor equal to 1.45 [192]. Fig. 4.18 shows the signal cloud, $\{u(k), u(k-1)\} \subset \Re^2$, for a chirp signal. It is possible to see that the cloud of points forms a set, that we may call a 'chirp-leaf', which is well distributed inside its border and has the broad characteristics of a convex set (there are no significant holes), indicating a good quality signal. In Fig. 4.18, the areas with higher point density are the upper-right and lower-left corners, which correspond to the maximum and minimum limits of the signal in Fig. 4.16, when it slows, stops and changes direction.

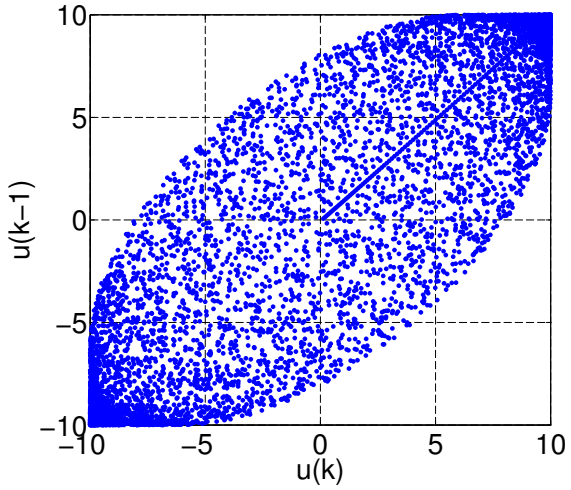

Figure 4.18: The signal cloud, $\{u(k), u(k-1)\} \subset \Re^2$, for a chirp signal (chirp-leaf).

4.3 Wave tank experiment typology

The experiments carried out in a WT (either NWT or RWT) can be divided in two main categories [7] [9] [10]:

• *Wave tank preliminary experiments*, which can be utilised to determine a rough measurement of the resonant frequency and bandwidth of the device and, therefore, help in the identification experiment design (see Section 4.3.1).

• *Wave tank identification experiments*, which are used to generate data to identify parametric models (see Section 4.3.2).

4.3.1 Wave tank preliminary experiments

Two simple preliminary experiments can be used to determine a rough measurement of the resonant frequency and the bandwidth of the WEC, thereby informing the identification experiments

(see Section 4.3.2), regarding where the input power spectrum should be allocated. Both preliminary experiments involve a very low total amount of kinetic and potential energy in the device and the fluid, which results in relatively fast CFD simulations, for NWT experiments. This allows the preliminary experiments to be quickly executed before the identification experiments are carried out. The WT preliminary experiments are [7] [9] [10]:

• *Free decay preliminary experiments* (presented in Section 4.3.1.1).

• *Input force preliminary experiments* (presented in Section 4.3.1.2).

4.3.1.1 Free decay preliminary experiments

In a free decay experiment, a body is initially displaced from its equilibrium position, by providing initial conditions, such as position, velocity and acceleration, and the resulting body motion, $y(t)$, recorded. For the heave, pitch and roll modes of motion, the mismatch between the gravitational and buoyancy forces acts as the restoring force. The surge, sway and yaw modes have no natural restoring forces; however, a spring force can be applied to the body, to allow free decay experiments to be performed for these modes of motion [11]. As an example, consider a free decay

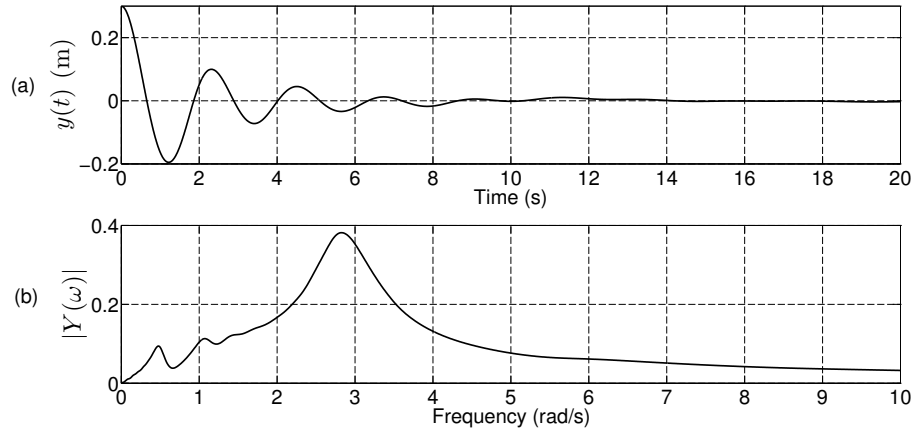

Figure 4.19: Free decay experiment of a sphere with a 1 m radius and 1 m draft, carried out in a 2D NWT. The initial body displacement is 0.3 m, the initial body velocity is zero. (a) Body displacement time evolution. (b) Body displacement spectral content.

experiment of a sphere with a 1 m radius and 1 m draft, implemented in a 2D NWT (the same body will be used, in Chapter 6, for the identification of $f_{in} \rightarrow y$, $\eta \rightarrow y$ and $\eta \rightarrow f_e$ models). The body is released from an initial displacement of 0.3 m and with a null initial velocity. The experimental data $y(t)$ is represented in Fig. 4.19(a), where it is possible to see that the oscillation period, T_{od}^{WT}, is constant and equal to 2.2 s; the superscript 'WT' indicates that the oscillation period has been obtained by utilising data generated in a real or numerical WT (in this section data generated from a BEM code are also used). The oscillation frequency (also termed the damped natural frequency) can be calculated by T_{od}^{WT} as:

$$\omega_{od}^{WT} = \frac{2\pi}{T_{od}^{WT}}, \tag{4.16}$$

which provides $\omega_{od}^{WT} = 2.86$ rad/s. Alternatively, the Fourier transform $Y(\omega) = \mathscr{F}\left[y(t)\right]$, which furnishes information regarding the spectral content of the free decay oscillation signal, can be used to extract information regarding both ω_{od}^{WT} and the bandwidth of $y(t)$.

Oscillation frequency variation of linear and nonlinear systems

Given a linear or a nonlinear system, it is important to underline that the oscillation frequency, observed in a free decay experiment is not necessarily constant, but could change in time during

the experiment, as shown in the following linear and nonlinear system cases.

• *Linear system case.* Given a general floating body in water, which can be described by the differential equation:

$$\sum_{q=0}^{n} a_q y^{(q)}(t) = \sum_{q=0}^{m} b_q u^{(q)}(t) \tag{4.17}$$

where $u(t)$ is the input system (such as a PTO force applied directly on the body) and $y(t)$ is the output body displacement. The Laplace transform of the free decay oscillation (the zero-input component of the output) is given, in the case of distinct poles (see equations (A.21) and (A.27)), by :

$$Y(s) = \frac{[\sum_{q=1}^{n}\sum_{j=1}^{q} a_q s^{q-j} y^{(j-1)}(0) - \sum_{q=1}^{m}\sum_{j=1}^{q} b_q s^{q-j} u^{(j-1)}(0)]}{\sum_{q=0}^{n} a_q s^q} = \sum_{j=1}^{n} \frac{k_j}{(s-p_j)}, \tag{4.18}$$

where $p_j = (\sigma_j + i\omega_j)$ are the poles of the system. As explained in Appendix A.5, each complex conjugate pair of poles $p = (\sigma + i\omega)$ and $p^* = (\sigma - i\omega)$) provides a contribution to the output equal to:

$$r(t) = \mathscr{L}^{-1}\Big[\frac{k}{s-p}\Big] + \mathscr{L}^{-1}\Big[\frac{k^*}{s-p^*}\Big] = 2|k|e^{\sigma t}\cos\Big(\omega t + Arg(k)\Big) \tag{4.19}$$

where k depends on the system initial conditions. As an example, consider a linear 4-th order system, having a transfer function given by:

$$H(s) = \frac{20(s-z_1)}{(s-p_1)(s-p_2)(s-p_3)(s-p_4)}, \tag{4.20}$$

where $z_1 = 1$ is the zero and $p_1 = (-0.1 + i5)$, $p_2 = (-0.1 - i5)$, $p_3 = (-0.3 + i19)$ and $p_4 = (-0.3 - i19)$ are the poles. In this case, the system is characterised by the absence of dominant poles, since it is not true that $|-0.1| \ll |-0.3|$. The pole locations are shown in Fig. 4.20. The system, represented by its transfer function (4.20), has a free decay oscillation that can be obtained by (4.18) and (4.19), given by:

$$y(t) = r_1(t) + r_2(t) \tag{4.21}$$

where

$$r_1(t) = 2|k_1|e^{-0.3t}\cos\Big[19t + Arg(k_1)\Big] \tag{4.22}$$

$$r_2(t) = 2|k_2|e^{-0.1t}\cos\Big[5t + Arg(k_2)\Big] \tag{4.23}$$

The initial conditions of the free decay experiment determine the k_1 and k_2 values and, consequently, the contribution from $r_1(t)$ and $r_2(t)$ to the solution in (4.21). For example, for initial conditions of $y(0) = 0$, $y^{(1)}(0) = 0.3$, $y^{(2)}(0) = 20$, and $y^{(3)}(0) = 0$, the resulting $r_1(t)$ and $r_2(t)$ are plotted in Fig. 4.21, where it is possible to see that $r_2(t)$ is the most persistent contribution, and that $r_1(t)$ is not significant after about 8 s. The resulting free decay output (4.21) is shown in Fig. 4.22, which shows that, especially in the first 4 s, the presence of the oscillation at 19 rad/s is important, and that after 8 s it is possible to only observe an oscillation at 5 rad/s.

Consider the same system transfer function structure of (4.20), with the same zero at $s = 1$ but, this time, with a dominant complex conjugate pair of poles: $p_1 = (-0.1 + i5)$, $p_2 = (-0.1 - i5)$, $p_3 = (-7 + i19)$ and $p_4 = (-7 - i19)$ (in this case $|-0.1| \ll |-7|$), as shown in Fig. 4.23. Given the same initial conditions $y(0) = 0$, $y^{(1)}(0) = 0.3$, $y^{(2)}(0) = 20$, and $y^{(3)}(0) = 0$, the resulting damped oscillations $r_1(t)$ and $r_2(t)$ are shown in Fig. 4.24, where it is possible to see that $r_2(t)$ is the most persistent contribution, and that $r_1(t)$ is not significant after about 0.3 s. The resulting free decay output (4.21) is plotted in Fig. 4.25, which shows that only the model frequency of 5 rad/s is relevant in the free decay oscillation.

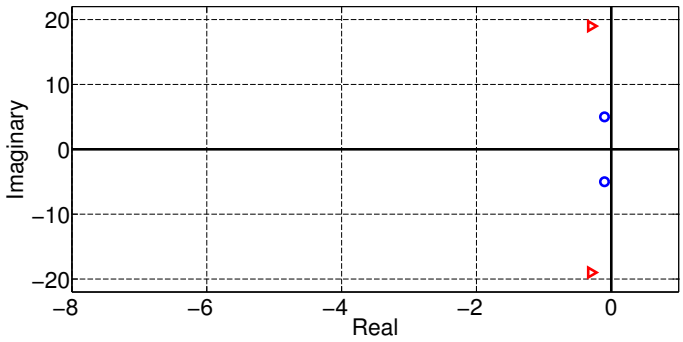

Figure 4.20: Pole locations on the complex plane, where $p_1 = (-0.1 + i5)$, $p_2 = (-0.1 - i5)$, $p_3 = (-0.3 + i19)$ and $p_4 = (-0.3 - i19)$ (no presence of dominant poles). The poles represented with the same symbol are a complex conjugate pair.

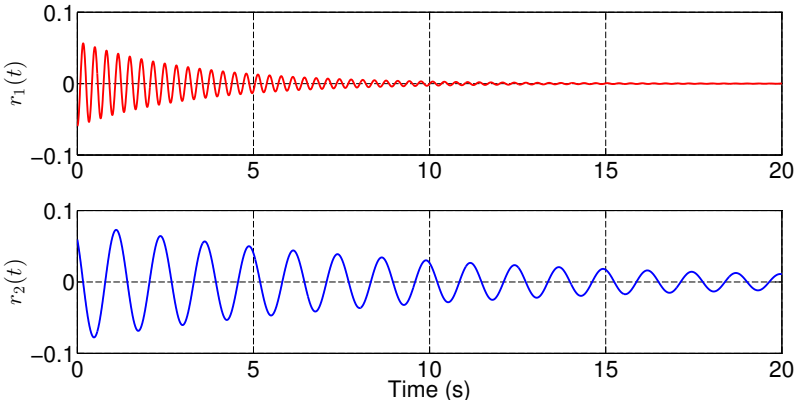

Figure 4.21: The transfer function (4.20), with $z_1 = 1$, $p_1 = (-0.1 + i5)$, $p_2 = (-0.1 - i5)$, $p_3 = (-0.3 + i19)$, and $p_4 = (-0.3 - i19)$, generates the damped oscillations $r_1(t) = 2|k_1|e^{-0.3t}\cos\left[19t + Arg(k_1)\right]$ and $r_2(t) = 2|k_2|e^{-0.1t}\cos\left[5t + Arg(k_2)\right]$, in the case of initial conditions equal to $y(0) = 0$, $y^{(1)}(0) = 0.3$, $y^{(2)}(0) = 20$, and $y^{(3)}(0) = 0$.

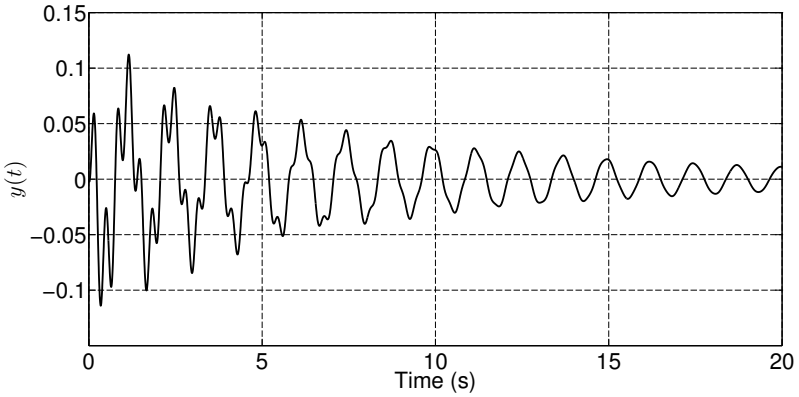

Figure 4.22: The free decay output of the system (4.20), with $z_1 = 1$, $p_1 = (-0.1 + i5)$, $p_2 = (-0.1 - i5)$, $p_3 = (-0.3 + i19)$, and $p_4 = (-0.3 - i19)$, in the case of initial conditions equal to $y(0) = 0$, $y^{(1)}(0) = 0.3$, $y^{(2)}(0) = 20$, and $y^{(3)}(0) = 0$.

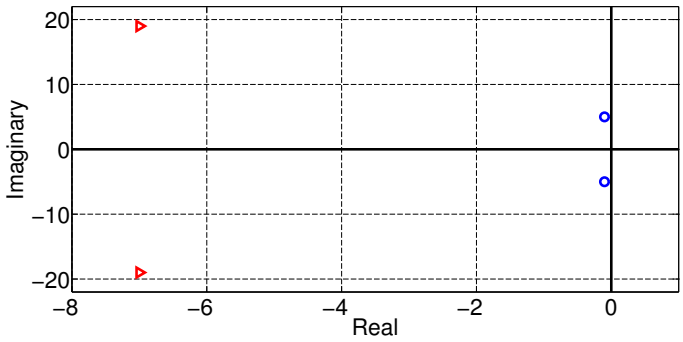

Figure 4.23: Pole locations on the complex plane, where $p_1 = (-0.1 + i5)$, $p_2 = (-0.1 - i5)$, $p_3 = (-7 + i19)$, and $p_4 = (-7 - i19)$ (presence of dominant poles). The poles represented with the same symbol are a complex conjugate pair.

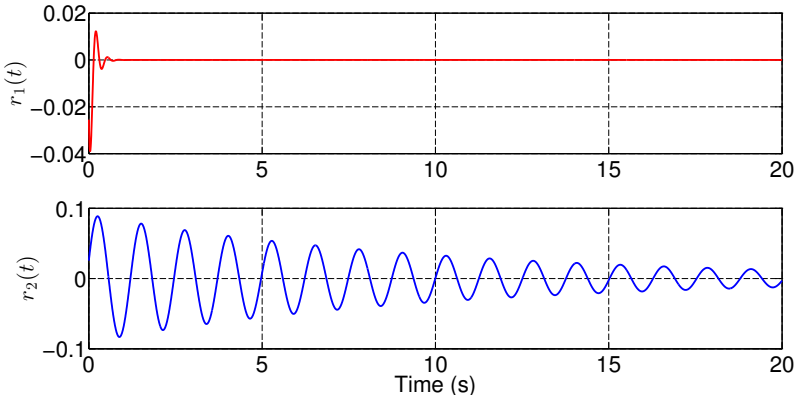

Figure 4.24: The transfer function (4.20), with $z_1 = 1$, $p_1 = (-0.1 + i5)$, $p_2 = (-0.1 - i5)$, $p_3 = (-7 + i19)$, and $p_4 = (-7 - i19)$, generates the damped oscillations $r_1(t) = 2|k_1|e^{-7t}\cos\left[19t + Arg(k_1)\right]$ and $r_2(t) = 2|k_2|e^{-0.1t}\cos\left[5t + Arg(k_2)\right]$, in the case of initial conditions equal to $y(0) = 0$, $y^{(1)}(0) = 0.3$, $y^{(2)}(0) = 20$, and $y^{(3)}(0) = 0$.

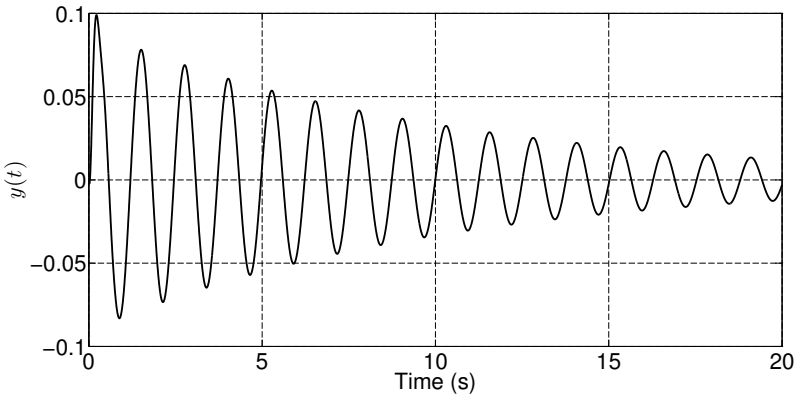

Figure 4.25: The free decay output of the system (4.20), with $z_1 = 1$, $p_1 = (-0.1 + i5)$, $p_2 = (-0.1 - i5)$, $p_3 = (-7 + i19)$, and $p_4 = (-7 - i19)$, in the case of initial conditions equal to $y(0) = 0$, $y^{(1)}(0) = 0.3$, $y^{(2)}(0) = 20$, and $y^{(3)}(0) = 0$.

• *Nonlinear system case.* In the case of a free decay experiment for a nonlinear system, the oscillation frequency variation is more complex than in the linear case, indeed, it depends on the variation of the oscillation amplitude. In the literature, there are numerous examples of nonlinear systems, which are characterised by a free decay oscillation with an oscillation frequency that changes in time during the experiment. For example consider a nonlinear undamped pendulum [288] [289] [290]:

$$\frac{d^2\theta(t)}{dt^2} + k\sin[\theta(t)] = 0, \tag{4.24}$$

a nonlinear damped pendulum [289] [290]:

$$\frac{d^2\theta(t)}{dt^2} + 2\gamma\frac{d\theta(t)}{dt} + k\sin[\theta(t)] = 0, \tag{4.25}$$

a nonlinear pendulum in presence of a viscous force [289]

$$\frac{d^2\theta(t)}{dt^2} + C_v\frac{d\theta(t)}{dt}\left|\frac{d\theta(t)}{dt}\right| + k\sin[\theta(t)] = 0 \tag{4.26}$$

and a spring-mass system characterised by a general nonlinear restoring term $R[.]$ [288]:

$$m\frac{d^2y(t)}{dt^2} + R[y(t)] = 0 \tag{4.27}$$

In [67], a free decay experiment, carried out in a NWT, for a semisubmerged sphere with radius and draft of 0.125 m and initial displacement of -0.1 m, shows an oscillation frequency increment with the oscillation amplitude reduction.

Free decay oscillation frequency measure

The main objective of a free decay preliminary experiment is measuring the free decay oscillation frequency, ω_{od}^{WT}, to be used as an approximation of the resonant frequency ω_m (the frequency at which the modulus of the frequency response has the maximum) of the $f_{in} \to y$ and $\eta \to y$ models, in order to design the input signal for the input wave and input force identification experiments. Furthermore, the bandwidth of $Y(\omega)$, which is the Fourier transform of the free decay displacement $y(t)$, may suggest the bandwidth that the excitation signal has to span. An important question is if it is correct to utilise ω_{od}^{WT} as an approximation of ω_m. The answer is not straightforward, indeed, the two frequency measures in general are different as well known for a 2nd-order system. For example, consider a mechanical oscillator described by a linear 2nd-order constant-coefficient ODE:

$$m\ddot{y}(t) + b\dot{y}(t) + ky(t) = f_{in}(t) \tag{4.28}$$

where f_{in} and y are the system input and output, respectively. Equation (4.28) can be written in the frequency domain as:

$$[-\omega^2 m + i\omega b + k]Y(\omega) = F_{in}(\omega) \tag{4.29}$$

where $Y(\omega)$ and $F_{in}(\omega)$ are the Fourier transforms of $y(t)$ and $f_{in}(t)$, respectively. Equation (4.28) can be rearranged [69] [291] as:

$$\ddot{y}(t) + \gamma\,\dot{y}(t) + \omega_o^2\,y(t) = \frac{1}{m}f_{in}(t) \tag{4.30}$$

where

$$\omega_o = \sqrt{\frac{k}{m}} \tag{4.31}$$

is the undamped natural frequency and

$$\gamma = \frac{b}{m} \tag{4.32}$$

is the damping coefficient. By setting $f_{in}(t) = 0$ in (4.30), the associated homogeneous equation is obtained:

$$\ddot{y}(t) + \gamma\,\dot{y}(t) + \omega_o^2\,y(t) = 0 \tag{4.33}$$

The free decay oscillation is the solution of equation (4.33) and in the case of $\gamma^2 \leq 4\omega_o^2$ (under-damped case) the solution is a damped oscillation given by [69] [290] [291]:

$$y(t) = Ae^{-\frac{\gamma}{2}t}\cos\left[\left(\sqrt{\omega_0^2 - \frac{\gamma^2}{4}}\right)t + \varphi\right] \tag{4.34}$$

where A and φ depend on the free decay initial conditions, and

$$\omega_{od} = \sqrt{\omega_o^2 - \frac{\gamma^2}{4}} = \sqrt{\frac{k}{m} - \frac{1}{4}\left(\frac{b}{m}\right)^2} \tag{4.35}$$

is the damped natural frequency. In Fig. 4.26(b), an example of a free decay damped oscillation is shown. By setting $\gamma = 0$, in equation (4.33), the solution is an undamped oscillation with frequency ω_o, given by equation (4.31); in Fig. 4.26(c), an example of an undamped free decay oscillation is shown.

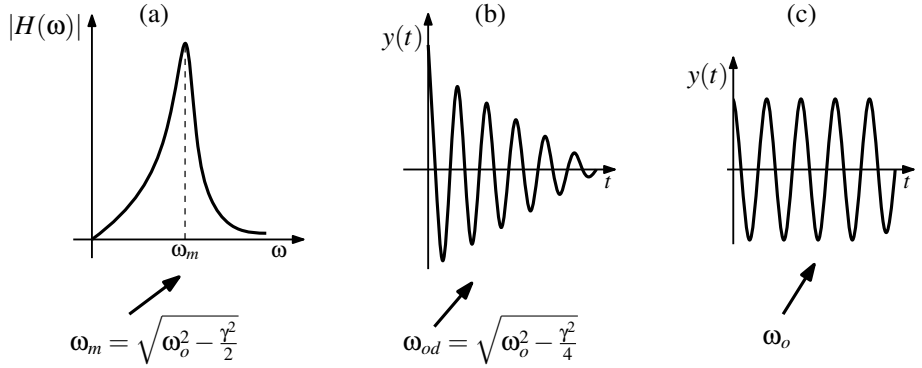

Figure 4.26: A system, described by a constant-coefficient 2nd-order ODE $\ddot{y}(t) + \gamma\,\dot{y}(t) + \omega_o^2\,y(t) = \frac{1}{m}f_{in}(t)$, is associated with: (a) a resonant frequency ω_m, (b) an oscillation frequency (also termed damped natural frequency) ω_{od} and (c) an undamped natural frequency ω_o.

In the case where an external harmonic force $f_{in}(t) = F_0\cos(\omega t)$ is present in equation (4.30), the steady-state solution of (4.30) is given by [290] [292]:

$$y(t) = F_0|H(\omega)|\cos\Big(\omega t + Arg\big(H(\omega)\big)\Big) \tag{4.36}$$

where $H(\omega)$ is obtained by equations (4.29), (4.31) and (4.32), and is given by:

$$H(\omega) = \frac{Y(\omega)}{F_{in}(\omega)} = \frac{1}{m(\omega_o^2 - \omega^2 + j\omega\gamma)} \tag{4.37}$$

It is possible to show that $|H(\omega)|$ has its maximum at the resonant frequency, which is given [141] [290] [291] by:

$$\omega_m = \sqrt{\omega_o^2 - \frac{\gamma^2}{2}} = \sqrt{\frac{k}{m} - \frac{1}{2}\left(\frac{b}{m}\right)^2}, \tag{4.38}$$

as shown in Fig. 4.26(a). Therefore, by comparing equations (4.35) and (4.38), it follows that $\omega_m \leq \omega_{od} \leq \omega_o$.

The well known analysis applied to the mechanical oscillator, described by equation (4.28), can be extended to a linear hydrodynamic oscillator, described by equation (2.89) [69]:

$$\{-\omega^2[M + m_a(\omega)] + i\omega N(\omega) + K\}Y(\omega) = F_{in}(\omega) \tag{4.39}$$

where the hydrodynamic coefficients $m_a(\omega)$, $N(\omega)$ and K can be calculated by a BEM software package. The comparison of equations (4.29) and (4.39) shows that a correspondence between the coefficients of the two equations exists:

$$m \iff [M + m_a(\omega)] \tag{4.40}$$

$$b \iff N(\omega) \tag{4.41}$$

$$k \iff K \tag{4.42}$$

A relevant difference is that equation (4.29) is characterised by constant coefficients, whereas equation (4.39) has frequency dependent coefficients. However, in the case where $y(t)$, which is the inverse Fourier transform of $Y(\omega)$, oscillates as a pure sinusoid with a single frequency, the coefficients of equation (4.39) assume a specific value, by substituting the actual frequency. Therefore, equations (4.31), (4.35) and (4.38), in the case of a hydrodynamic oscillator, become, respectively [1] [22] [69] [293]:

$$\omega_o^{BEM} = \sqrt{\frac{K}{M + m_a(\omega_o^{BEM})}}, \tag{4.43}$$

$$\omega_{od}^{BEM} = \sqrt{\frac{K}{M + m_a(\omega_{od}^{BEM})} - \frac{1}{4}\left(\frac{N(\omega_{od}^{BEM})}{M + m_a(\omega_{od}^{BEM})}\right)^2} \tag{4.44}$$

and

$$\omega_m^{BEM} = \sqrt{\frac{K}{M + m_a(\omega_m^{BEM})} - \frac{1}{2}\left(\frac{N(\omega_m^{BEM})}{M + m_a(\omega_m^{BEM})}\right)^2} \tag{4.45}$$

where the superscript 'BEM' indicates that the solutions are obtained by utilising information generated in a BEM software package (in this case WAMIT). It is important to note that, in the case of a free decay experiment, the time evolution of the body displacement is not a pure monochromatic harmonic at a single frequency but a damped oscillation, which has a proper frequency spread, as shown in Fig. 4.19(b); therefore, equations (4.43), (4.44) and (4.45) provide approximations of ω_o, ω_{od} and ω_m, respectively [22].

The transfer function of the linear $f_{in} \rightarrow y$ WEC model, described by equation (4.39), is given by:

$$H_{f_{in}\rightarrow y}^{BEM}(\omega) = \frac{1}{-\omega^2[M + m_a(\omega)] + i\omega N(\omega) + K} \tag{4.46}$$

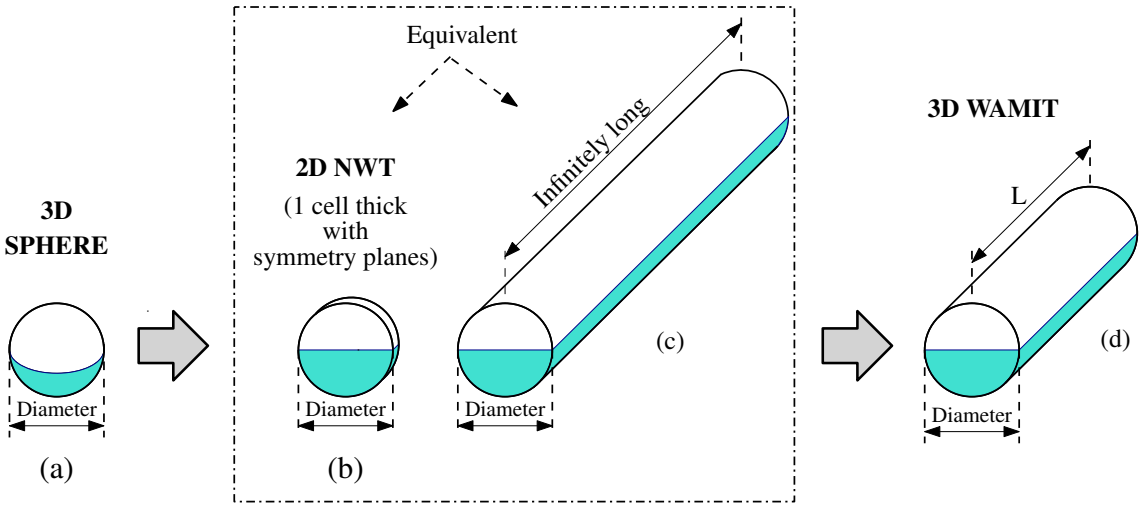

Figure 4.27: (a) 3D sphere. (b) In a 2D NWT, the sphere becomes a one cell thick circle, with symmetry planes on the front and back faces of the domain. (c) Infinitely long horizontal cylinder (equivalent to the one cell thick circle). (d) The infinitely long horizontal cylinder can be approximated well in WAMIT by a horizontal cylinder with a finite length L.

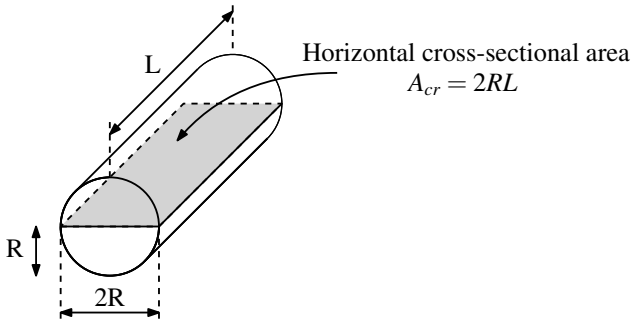

Figure 4.28: Horizontal cross-sectional area of an horizontal cylinder with a 50% draft.

As an example, consider a spherical WEC moving in heave, with a 1 m radius and 1 m draft (see Fig. 4.27(a)). In a 2D NWT, the sphere becomes a circle with a 1 m radius, 1 m draft and one cell thick (see Fig. 4.27(b)), which is equivalent to an infinitely long horizontal cylinder (see Fig. 4.27(c)), as explained in Section 4.4. The infinitely long horizontal cylinder can be approximated well in WAMIT by a horizontal cylinder with a 1 m radius, 1 m draft and 25 m length (as explained in the details of Section 4.4), which has the body mass given by:

$$M = \frac{\rho}{2} R^2 \pi L, \tag{4.47}$$

(where ρ is the water density, $\rho/2$ is the body density, R is the cylinder radius and L is the cylinder length), a restoring coefficient (see Section 2.2.7) given by:

$$K = \rho g A_{cr} \tag{4.48}$$

(where $A_{cr} = 2RL$ is the horizontal cross-sectional area, as shown in Fig. 4.28, and g is the gravitational acceleration) and WAMIT curves $m_a(\omega)$, $N(\omega)$ and $|H_e(\omega)|$ shown in Figs. 4.29, 4.30 and 4.31, respectively. The transfer function $H^{BEM}_{f_{in}\to y}(\omega)$ of the horizontal cylinder with a 1 m radius, 1 m draft and 25 m length, calculated with equation (4.46), is shown in Fig. 4.32, which illustrates that $H^{BEM}_{f_{in}\to y}(\omega)$ has a peak at a frequency $\omega^{BEM}_m = 2.8$ rad/s and that $Y(\omega)$ have a peak at a frequency $\omega^{WT}_{od} = 2.86$ rad/s. Therefore, ω^{WT}_{od} and ω^{BEM}_m, of the $f_{in} \to y$ linear model, are very similar. Furthermore, Fig. 4.32 shows that the bandwidth of $Y(\omega)$ and $H^{BEM}_{f_{in}\to y}(\omega)$ are different but significantly similar. Therefore, the conclusion is that the oscillation frequency ω^{WT}_{od} and the bandwidth, obtained by the free decay preliminary experiment in the WT (either NWT or RWT), can be used to design the excitation signal spectrum for input force experiments (see Section 4.3.2.3), as shown in Fig. 4.33.

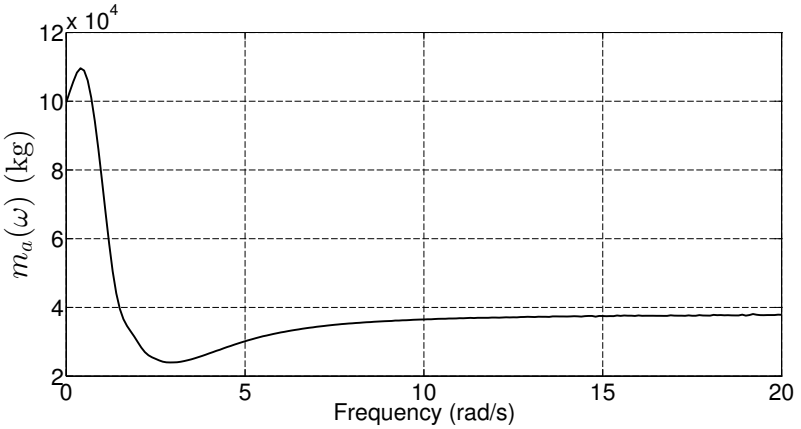

Figure 4.29: Added mass curve, calculated by WAMIT, of a horizontal cylinder moving in heave, with 25 m length, 1 m radius and 1 m draft (used to approximated an infinitely long horizontal cylinder).

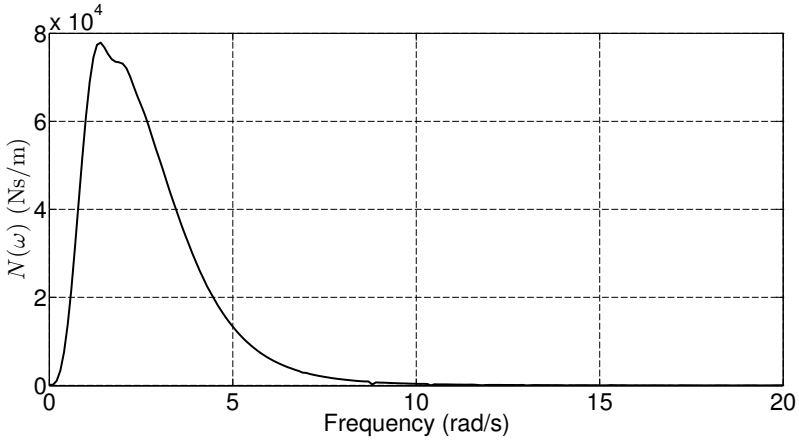

Figure 4.30: Radiation resistance curve, calculated by WAMIT, of a horizontal cylinder moving in heave, with 25 m length, 1 m radius and 1 m draft (used to approximated an infinitely long horizontal cylinder).

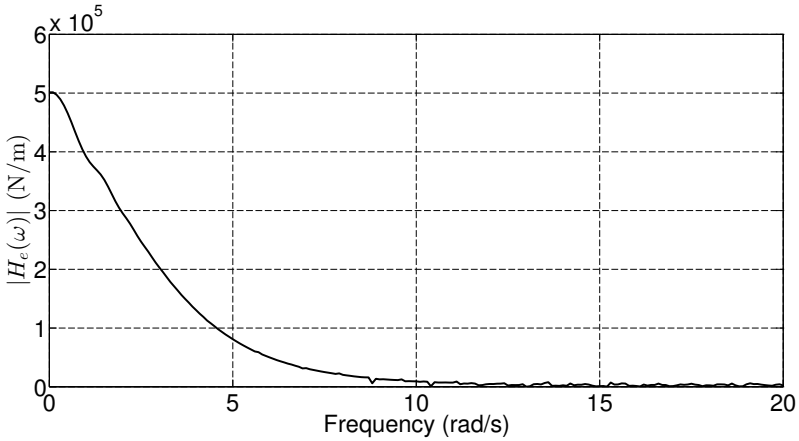

Figure 4.31: Excitation force curve, calculated by WAMIT, of a horizontal cylinder moving in heave, with 25 m length, 1 m radius and 1 m draft (used to approximate an infinitely long horizontal cylinder).

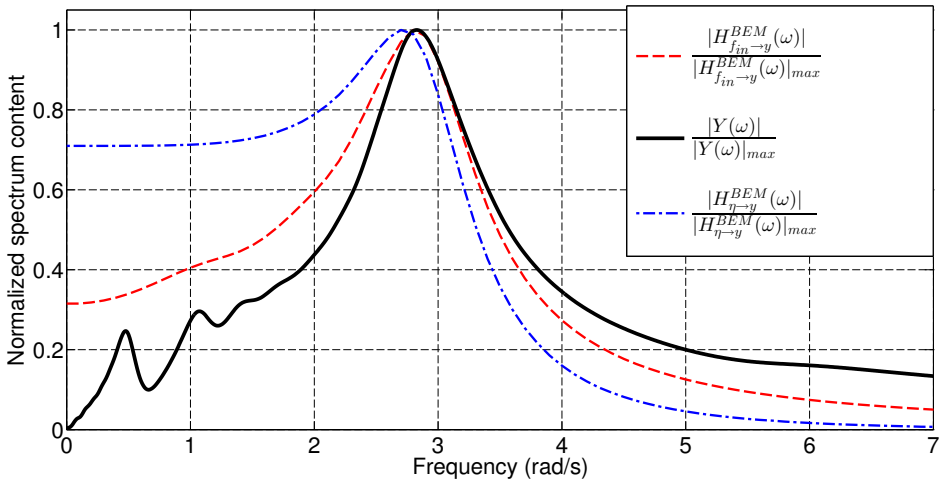

Figure 4.32: Normalized spectrum content comparison. $|H^{BEM}_{f_{in}\to y}(\omega)|$, $|Y(\omega)|$ and $|H^{BEM}_{\eta\to y}(\omega)|$ have a peak at frequencies 2.8 rad/s, 2.86 rad/s and 2.7 rad/s, respectively.

The difference between the bandwidth of $Y(\omega)$ and $H^{BEM}_{f_{in}\to y}(\omega)$ can be explained by observing the Laplace transforms $Y(s)$ and $H^{BEM}_{f_{in}\to y}(s)$, given by equations (4.49) and (4.50), respectively. Indeed,

$$Y(s) = \mathscr{L}\left[y(t)\right] = \frac{P(s)}{\sum_{i=0}^{n} a_i s^i} \tag{4.49}$$

where $P(s)$ is a polynomial in s, the coefficients of which depend on the initial conditions of the free decay experiment, and the denominator of (4.49) is the characteristic polynomial of the WEC model, which depends on model poles (see Appendix Section A.6). Given $h^{BEM}_{f_{in}\to y}(t) = \mathscr{F}^{-1}\left[H^{BEM}_{f_{in}\to y}(\omega)\right]$, it is possible to write (see equation (A.22)):

$$H^{BEM}_{f_{in}\to y}(s) = \mathscr{L}\left[h^{BEM}_{f_{in}\to y}(t)\right] = \frac{\sum_{i=0}^{m} b_i s^i}{\sum_{i=0}^{n} a_i s^i} \tag{4.50}$$

where the numerator and denominator depend on model zeros and poles, respectively. Therefore, (4.49) and (4.50) have the same denominator but a different numerator, resulting in a different bandwidth.

The excitation signal design, for an input wave experiment (see Section 4.3.2.2), requires the knowledge of the transfer function of the linear $\eta \to y$ model, which is the product of $H_e(\omega)$ and $H^{BEM}_{f_{in}\to y}(\omega)$ (see block diagram in Fig. 3.4). Therefore, by using equation (4.46), it follows that:

$$H^{BEM}_{\eta\to y}(\omega) = \frac{Y(\omega)}{\overline{\eta}(\omega)} = H_e(\omega) H^{BEM}_{f_{in}\to y}(\omega) = \frac{H_e(\omega)}{-\omega^2[M + m_a(\omega)] + i\omega N(\omega) + K} \tag{4.51}$$

where $Y(\omega)$ and $\overline{\eta}(\omega)$ are the Fourier transforms of $y(t)$ and $\eta(t)$, respectively. Fig. 4.32 shows that the resonant frequency ω^{BEM}_m of $H^{BEM}_{\eta\to y}(\omega)$ is very similar to ω^{WT}_{od}, and that $H^{BEM}_{\eta\to y}(\omega)$ has a significant response from zero to a maximum frequency, which can be roughly indicated by the upper frequency of the bandwidth of $Y(\omega)$ (about 7 rad/s). Therefore, the spectral information of the free decay preliminary experiment in the WT (either a NWT or a RWT), can be used to design the excitation signal spectrum for input wave experiments (see Section 4.3.2.2), as shown in Fig. 4.33.

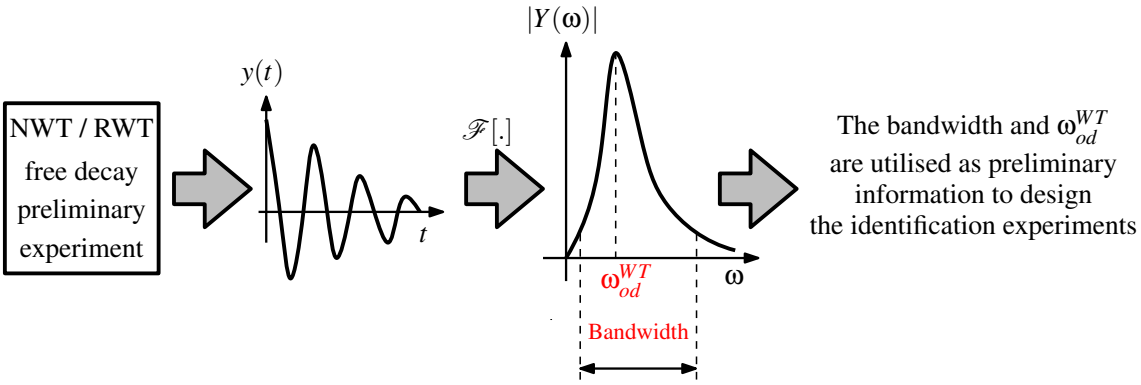

Figure 4.33: A free decay preliminary experiment can be used to determine a rough measurement of the resonant frequency and the bandwidth of the WEC, informing the input force and input wave identification experiments, where their input power spectrum should be allocated.

Comparison of WT free decay preliminary experiment data with BEM (WAMIT) data

In the case of a relatively small body displacement and velocity, WEC dynamics are usually well approximated by a linear model; therefore, the damped natural frequency ω^{WT}_{od}, calculated by WT data, would be reasonably similar to ω^{BEM}_{od}, computed by BEM data. The calculation of ω^{WT}_{od} and

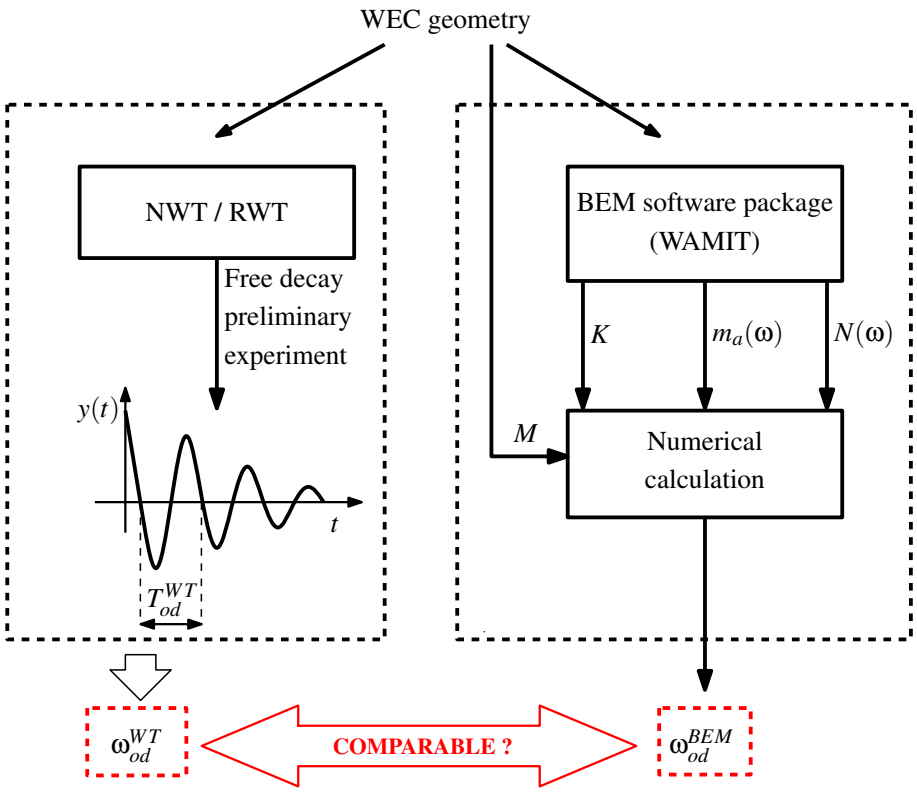

Figure 4.34: Block diagram for the comparison of a free decay preliminary experiment with WAMIT data, by using equations (4.16) and (4.44), respectively.

ω_{od}^{BEM} can be carried out by using equations (4.16) and (4.44), respectively. Consider the case of a sphere moving in heave, with a 1 m radius and 1 m draft (see Fig. 4.27(a)), and implemented in a 2D NWT (see Fig. 4.27(b)), which corresponds, in WAMIT, to a horizontal cylinder moving in heave, with 25 m length, 1 m radius and 1 m draft (see Fig. 4.27(d)), as explained in Section 4.4. For this body geometry, it follows that $\omega_{od}^{WT} = 2.86$ rad/s and $\omega_{od}^{BEM} = 2.76$ rad/s, which show good agreement between WT and WAMIT data. Fig. 4.34 shows the block diagram for the comparison of a free decay preliminary experiment with WAMIT data.

4.3.1.2 Input force preliminary experiments

In an input force experiment, a PTO force, f_{pto}, is directly applied to the body as an input, assuming null excitation and mooring forces ($f_{in} = f_{pto} + f_e + f_m = f_{pto}$), and the resulting body displacement measured as output. Fig. 4.35 shows that the block $f_{in} \rightarrow y$ takes as input the summation of the three forces f_e, f_{pto} and f_m. The data generated in an input force experiment are $\{f_{in}(k)\}$ and $\{y_{in}(k)\}$, (with $k =, 1..., N$), as shown in Table 4.1. In order to avoid any ambiguity, in the case where different WT experiment typologies are utilised to identify different sub-blocks of the same WEC model (see for example Section 6.3.1), in the symbolism y_{in}, the subscript '*in*' confirms that the input of the model is an input force. The objective of the input force preliminary experiment is to obtain a first indication regarding the resonant frequency and the bandwidth of the $f_{in} \rightarrow y$ model, which is highlighted with a dotted line in Fig. 4.35, in order to design the excitation signal for the input wave and input force identification experiments, which are explained in Sections 4.3.2.2 and 4.3.2.3, respectively. In the case where the body oscillations are small, a WEC is often well described by a linear $f_{in} \rightarrow y$ model, with Fourier transfer function $H_{f_{in} \rightarrow y}(\omega)$. The calculation of $H_{f_{in} \rightarrow y}(\omega)$ can be carried out by applying a small amplitude chirp signal (see Section 4.2.2.4), as a direct force on the device. Unlike the chirp signal used for the identification experiments (see Section 4.3.2.3), which must cover a desired amplitude range, the chirp signal,

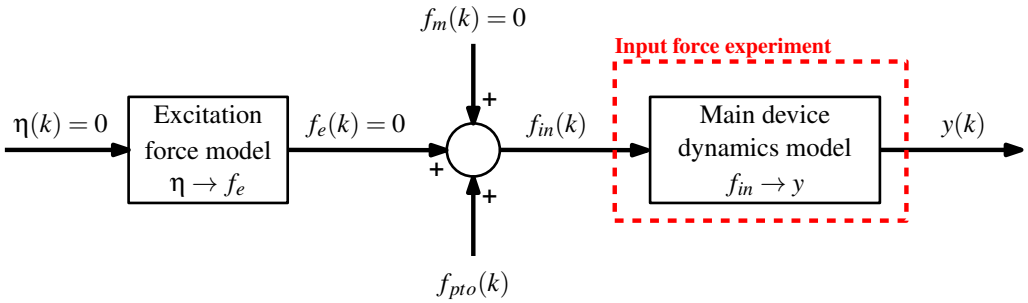

Figure 4.35: Block diagram of a WEC hydrodynamic model. The data $\{f_{in}(k)\}$ and $\{y_{in}(k)\}$, generated in a WT input force preliminary experiment, are utilised to obtain a first indication regarding the resonant frequency and the bandwidth of the $f_{in} \rightarrow y$ model (highlighted by the dashed line). In the case of a WT input force identification experiment, the data $\{f_{in}(k)\}$ and $\{y_{in}(k)\}$ are utilised to identify the $f_{in} \rightarrow y$ model.

in this preliminary experiment, can be of very low amplitude (but it should not be lower than the amplitude of the additive noise, present in RWT measurements), allowing fast computation times, in the case where a CFD-NWT is being used. Consider a spherical WEC with a 1 m radius, 1 m draft, moving in heave and implemented in a 2D NWT (the same body utilised in Section 4.3.1.1). The utilised exciting signal, $f_{in}(t)$, is a chirp signal, which linearly sweeps the frequency range 0-12.6 rad/s in 600 s, where the superscript 'WT' indicates that WT data are utilised (in this section data generated by a BEM package are also utilised). Fig. 4.36(a) shows the first 200 s of $f_{in}(t)$. The consequent body displacement, $y(t)$, obtained in the 2D CFD-NWT, is represented in Fig. 4.36(b). The Fourier transfer function of the linear $f_{in} \rightarrow y$ model can be calculated as:

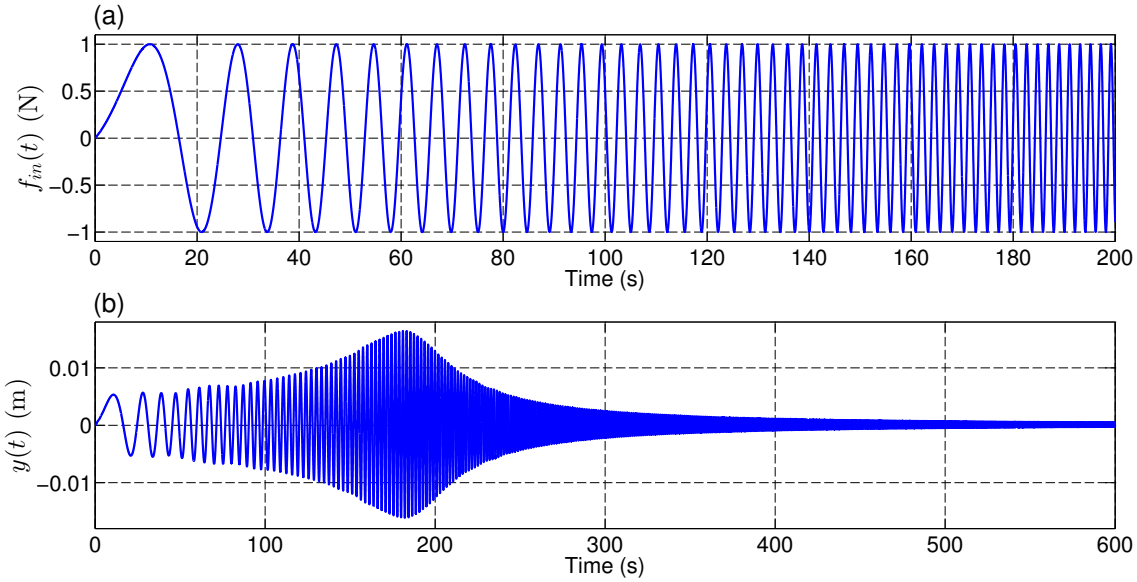

Figure 4.36: Input force preliminary experiment utilising a small chirp signal. (a) Excitation force applied to the body. (b) Consequent body displacement.

$$H^{WT}_{f_{in} \rightarrow y}(\omega) = \frac{Y(\omega)}{F_{in}(\omega)} \tag{4.52}$$

where $Y(\omega)$ and $F_{in}(\omega)$ are the Fourier transforms of the measured $y(t)$ and $f_{in}(t)$, respectively. In the case where significant additive noise is present in the measurements of $f_{in}(t)$ and $y(t)$, equation (4.52) may provide poor accuracy in the calculation of $H^{WT}_{f_{in} \rightarrow y}(\omega)$; in this case, the transfer function

can be computed [141] [222] [294] as:

$$H^{WT}_{f_{in}\to y}(\omega) = \frac{S^{WT}_{fy}(\omega)}{S^{WT}_{ff}(\omega)} \tag{4.53}$$

where $S^{WT}_{fy}(\omega)$ is the cross-spectrum of the signals $f_{in}(t)$ and $y(t)$, and $S^{WT}_{ff}(\omega)$ the spectrum of $f_{in}(t)$. Fig. 4.37 shows the transfer function $H^{WT}_{f_{in}\to y}(\omega)$ (calculated by using equation (4.52) and the signals shown in Fig. 4.36), with a resonant frequency of 2.83 rad/s, and suggests that the excitation signal of the identification experiments should be designed to span the region of 0-7 rad/s. Fig. 4.38 shows the main idea of the input force preliminary experiment.

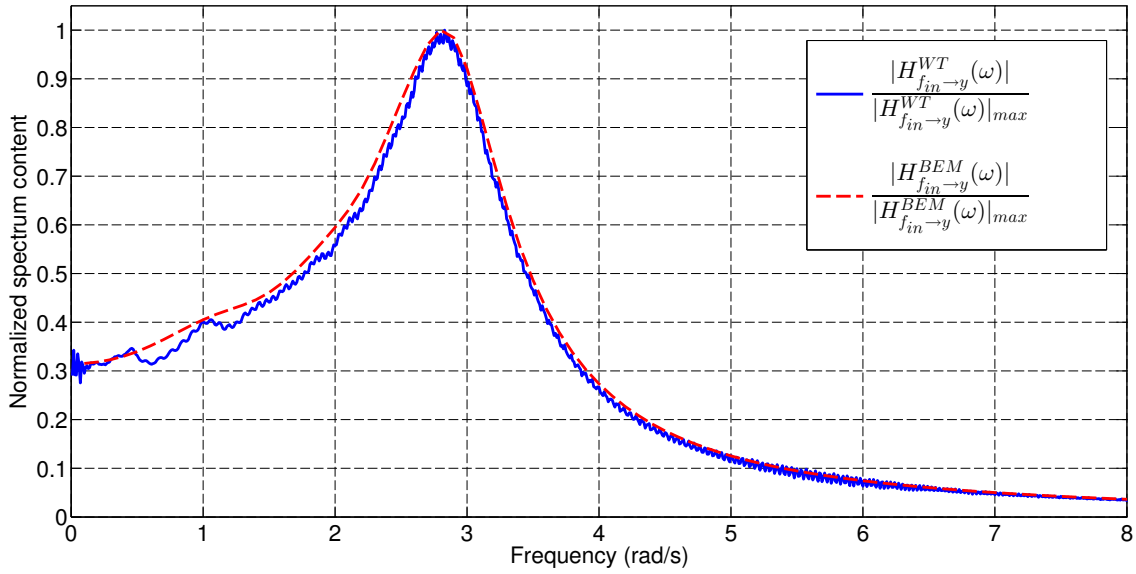

Figure 4.37: Comparison of input force preliminary experiment data, generated in a 2D NWT (in the case of a 2D circle with a 1 m radius and 1 m draft), with BEM (WAMIT) data.

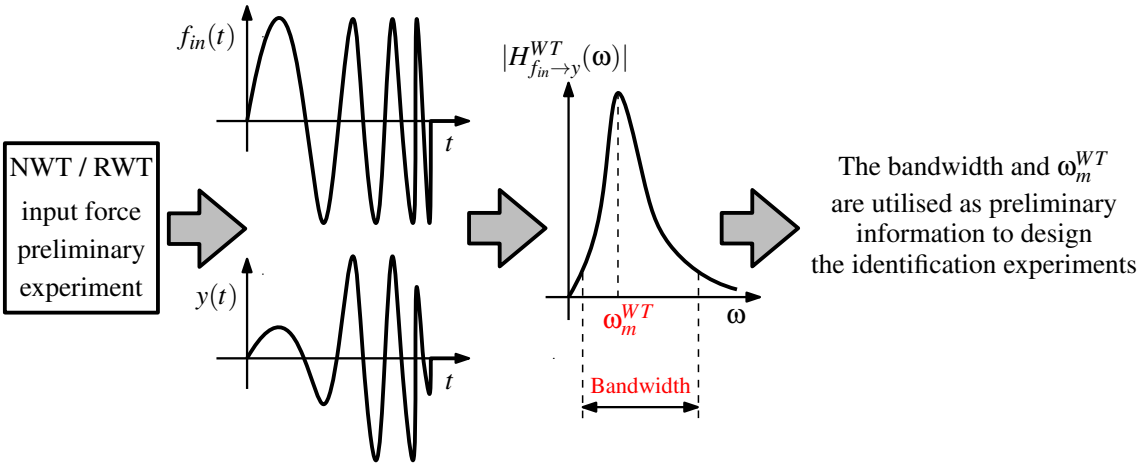

Figure 4.38: An input force preliminary experiment can be used to determine a rough measurement of the resonant frequency and the bandwidth of the WEC, informing the identification experiments where the input power spectrum should be allocated.

As explained in Section 4.3.1.1, when the body displacement and velocity are relatively small, the WEC dynamics are often well approximated by a linear model and results obtained by WT data

and BEM data should be similar. Therefore, the transfer function $H^{WT}_{f_{in}\to y}(\omega)$ (calculated by using the measured signals $y(t)$, $f_{in}(t)$ and either equation (4.52) or (4.53)) should have good agreement with $H^{BEM}_{f_{in}\to y}(\omega)$ (calculated by using equation (4.46) and the hydrodynamic coefficients provided by WAMIT). Fig. 4.39 shows the block diagram for the comparison of WT input force preliminary experiment data and WAMIT data. $H^{WT}_{f_{in}\to y}(\omega)$ and $H^{BEM}_{f_{in}\to y}(\omega)$ are plotted in Fig. 4.37, in the case of the 2D circle with a 1 m radius and 1 m draft, showing good agreement between WT and WAMIT data.

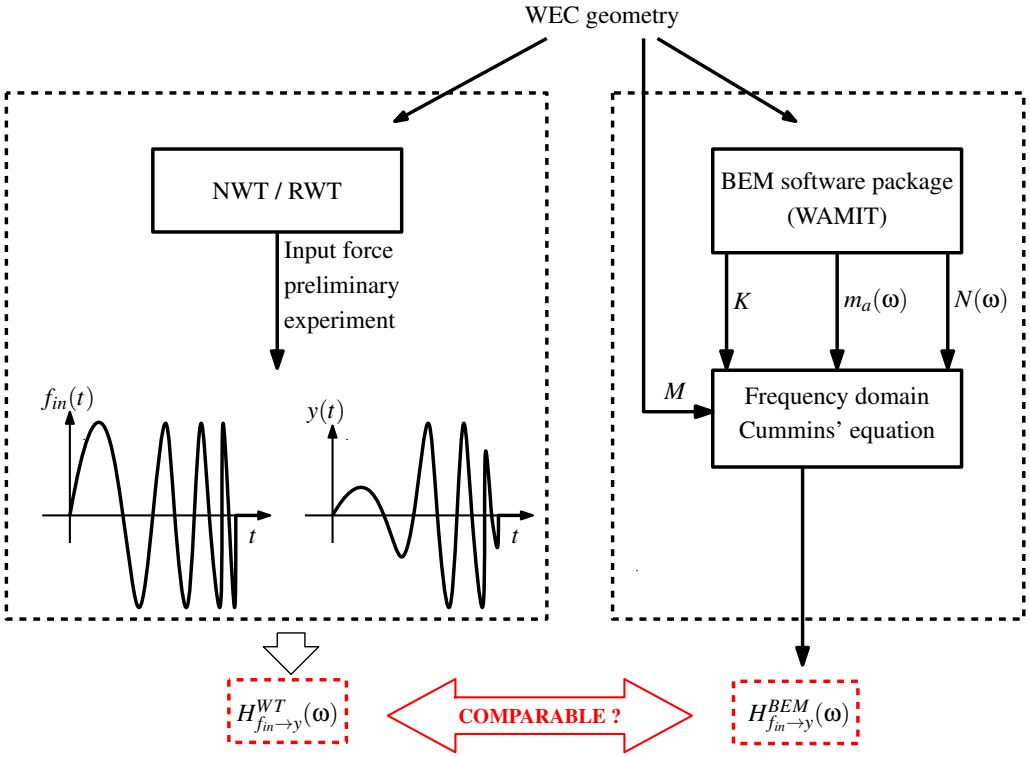

Figure 4.39: Block diagram for the comparison of WT input force preliminary experiment data with BEM (WAMIT) data.

4.3.2 Wave tank identification experiments

This section details a variety of WT experiments utilised to produce data to identify the parameters of a WEC model or model sub-blocks [7] [9] [10] [12] [13]:
- *Free decay experiments* (presented in Section 4.3.2.1).
- *Input wave experiments* (explained in Section 4.3.2.2).
- *Input force experiments* (illustrated in Section 4.3.2.3).
- *Prescribed motion experiments* (presented in Section 4.3.2.4).

4.3.2.1 Free decay identification experiments

As explained in Section 4.3.1.1, in a free decay experiment, a body is initially displaced from its equilibrium position, by providing initial conditions, such as position, velocity and acceleration, and the resulting body motion recorded. A free decay preliminary experiment is used to provide an indication of the system's resonant frequency and bandwidth; in the case of a free decay identification experiment, the collected data are used to identify the system dynamics (see the case study in Chapter 5). The data generated in a free decay experiment is the body displacement $\{y(k)\}$, with $k = 1...,N$, as shown in Table 4.1.

Experiment type	Input signal type {Input symbol}	Output signal type {Output symbol}
Free decay	- -	Body displacement $\{y(k)\}$
Input wave body motion	FSE $\{\eta(k)\}$	Body displacement $\{y_\eta(k)\}$
Input wave excitation force	FSE $\{\eta(k)\}$	Excitation force $\{f_e(k)\}$
Input force	PTO force $\{f_{in}(k)\}$	Body displacement $\{y_{in}(k)\}$
Prescribed motion	Body displacement $\{y_s(k)\}$	Restoring force $\{f_{b.s}(k)\}$

Table 4.1: Data generated in the different WT experiments.

4.3.2.2 Input wave identification experiments

In the case of input wave experiments, the waves are created in the WT and the FSE, η, is measured at a specific location, providing the data, $\{\eta(k)\}$ (with $k = ,1...,N$), which is used as the input signal for the WEC model identification. Often, the FSE is required to be known at the WEC's center of mass; in this case, it is not possible to directly measure this quantity, since the body occupies that space. A possible solution is the employment of techniques of spatial reconstruction of the wave field, using a group of sensors located in the proximity of the floating body. Alternatively, the experiment can be decomposed into two separate experiments where, firstly the input waves are generated and measured in the absence of the WEC (Fig. 4.40(a)), and then the experiment is repeated with the same input waves being generated with the WEC in place (Fig. 4.40(b)). It is important to underline that the frequency and amplitude ranges of the input signal, for the input wave experiments, are limited by the underlying fluid dynamics and limiting wave steepness. The choice of input signals should be guided by the sea states the WEC is expected to operate in. The experiments can be designed using either specific individual sea spectra, or by creating a generalised broad-banded spectrum spanning the entire set of expected spectra likely to be encountered at a location. Monochromatic waves are also a possibility, if desired.

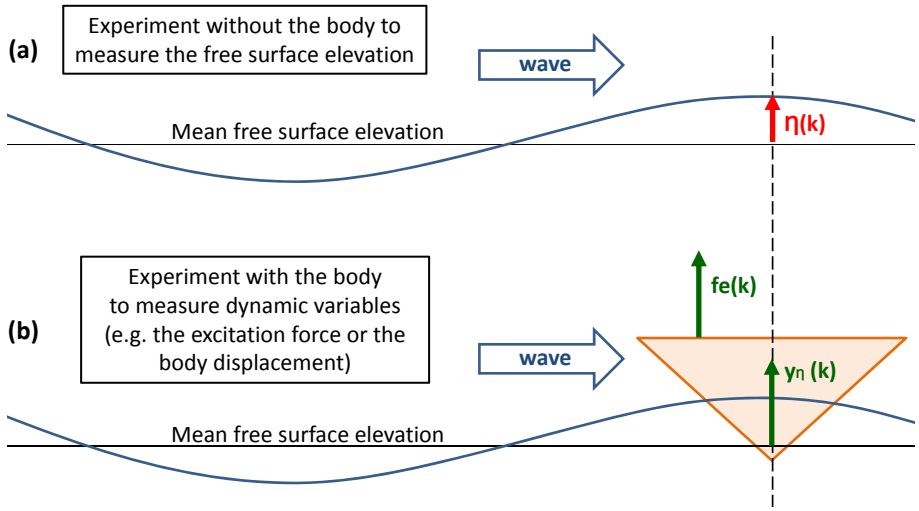

Figure 4.40: The input wave experiment is carried out in two steps (a) Step 1: the input waves are generated and the FSE at the desired position measured without the body. (b) Step 2: the experiment is repeated, with the same input waves being generated with the WEC in place, in order to measure dynamic variables (e.g. the excitation force or the body displacement).

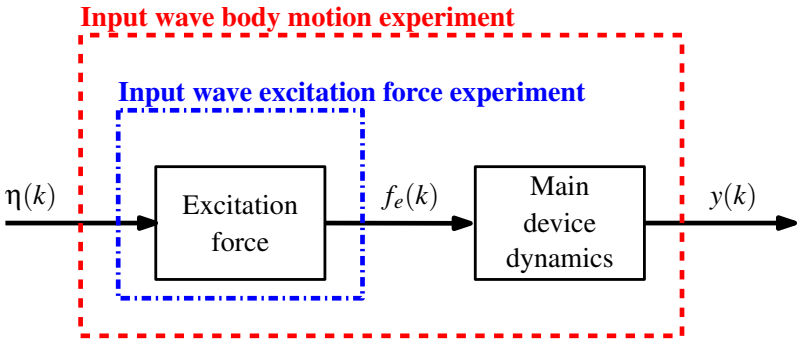

Figure 4.41: Block diagram of a WEC hydrodynamic model. The data $\{\eta(k)\}$ and $\{y_\eta(k)\}$, generated in an input wave body motion experiment, are utilised to identify the model highlighted by the dashed line. The data $\{\eta(k)\}$ and $\{f_e(k)\}$, generated in an input wave excitation force experiment, are utilised to identify the model highlighted by the dash-dotted line.

Depending on the physical quantity utilised as the model output, there are two different options for an input wave experiment: body motion and excitation force [7] [9] [12]:

• The *input wave body motion experiment*. In this case, the position and/or velocity is measured and used as the output signal for the model identification. The data generated in an input wave body motion experiment are $\{\eta(k)\}$ and $\{y_\eta(k)\}$ (with $k = ,1...,N$), as shown in Table 4.1. In order to avoid any ambiguity, in the case where different WT experiment typologies are utilised to identify different sub-blocks of the same WEC model (for example see Section 6.4), in the symbolism y_η, the subscript 'η' confirms that the input of the model is a FSE. The WEC can be constrained to different degrees of freedom, as required. Fig. 4.41 illustrates a WEC hydrodynamic block diagram (developed in Section 3.2.2), where it is shown that the data, generated by an input wave body motion experiment, can be utilised to identify the hydrodynamic model highlighted with the dashed line.

• The *input wave excitation force experiment*. The body is held fixed and the force, applied from the fluid on the body, is measured and used as the output signal for the identification of the excitation force model. The data generated in an input wave excitation force experiment are $\{\eta(k)\}$ and $\{f_e(k)\}$, with $k = ,1...,N$ (as shown in Table 4.1), which can be used to identify the hydrodynamic model block, highlighted with the dash-dotted line in Fig. 4.41. The use of input wave excitation force experiments for WEC model identification is explained in Section 6.2.

4.3.2.3 Input force identification experiments

As explained in Section 4.3.1.2, in an input force experiment, a PTO force, f_{pto}, is directly applied to the body as an input, assuming null excitation and mooring forces ($f_{in} = f_{pto} + f_e + f_m = f_{pto}$), and the resulting body displacement measured as output. The data generated in an input force experiment are $\{f_{in}(k)\}$ and $\{y_{in}(k)\}$, (with $k = ,1...,N$), as shown in Table 4.1. The input and output data generated can be used to identify the hydrodynamic model block, $f_{in} \rightarrow y$, highlighted with a dotted line in Fig. 4.35. Unlike the input wave experiment, where the choice of input signal is constrained by the laws of fluid dynamics, the input force experiment allows total freedom over the choice of input signal to be applied to the system by an actuator. As explained in Section 4.2.1.1, the input signal has to cover the WEC frequency range of interest. This could be ascertained from some rough measurement of the resonant frequency and bandwidth of the device, for example by using free decay and input force preliminary experiments (see Sections 4.3.1.1 and 4.3.1.2), and the range of sea frequencies in which the WEC is expected to operate. Usually the bandwidth of the device and of the sea waves are well connected; however, the device may also be subject to high frequency inputs from mooring snap loads, maximum stroke end-stop collisions, latching control etc. The nature of the input force experiment provides the possibility of exciting

the system in a broad band to also cover the high frequencies. The typical signals utilised in an input force experiment are chirp, RARP and multisine signals (see Section 4.2.2) [7] [8] [9] [10]. The use of input force experiments for WEC model identification is shown in Section 6.3.

4.3.2.4 Prescribed motion identification experiments

In a prescribed motion experiment, the body moves along a predefined trajectory (input signal), while the resulting fluid body interaction force (output signal) is recorded, assuming no wave excitation. In the case where the body moves very slowly, the total force applied from the fluid to the body corresponds to the (static) buoyancy force, f_b. By adding the gravitational force to f_b, the restoring force, f_{re}, is obtained (see Section 2.2.7). Therefore, as an example, the data generated with a prescribed motion experiment can be used to identify the static relationship between the body displacement and the hydrostatic restoring force. During the experiment, the body is displaced through its full range of motion and the resulting hydrostatic force on the body is measured. The data generated by the prescribed motion experiment are $\{y_s(k)\}$ (the body displacement) and $\{f_{b.s}(k)\}$ (the hydrostatic force), for $N = 1,...,N$, as shown in Table 4.1. In order to avoid any ambiguity, in the case where different WT experiment typologies are utilised to identify different sub-blocks of the same WEC model, in the symbolisms y_s and $f_{b.s}$, the subscript 's' confirms '(nearly) static'. For example, the data generated by a prescribed motion experiment can be used to identify the static block of a Hammerstein model, highlighted in Fig. 4.42(a) (see Sections 3.3.1.4, 6.2 and 6.3.1), or the static block of a FBO model, highlighted in Fig. 4.42(b) (see Sections 3.3.1.5 and 6.3.1).

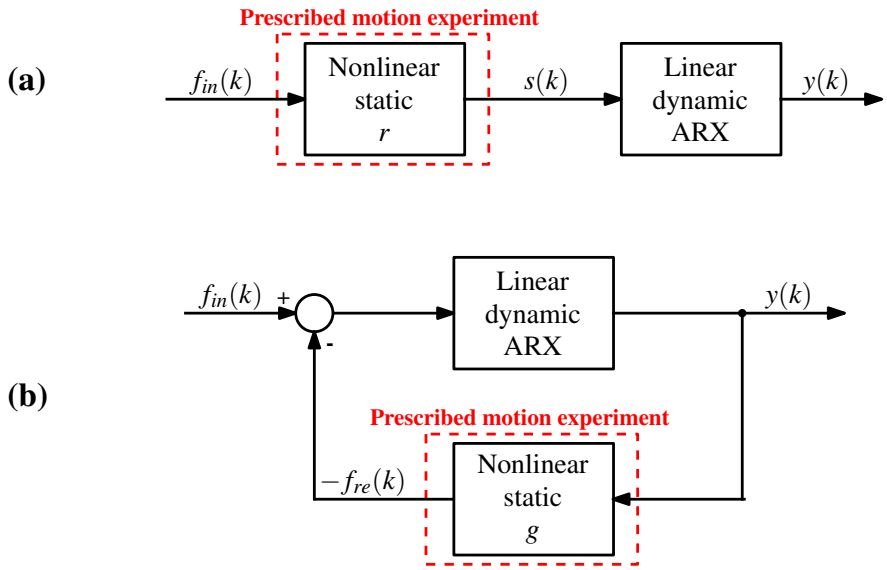

Figure 4.42: Block diagrams of WEC hydrodynamic models. The data $\{y_{re}(k)\}$ and $\{f_{re}(k)\}$, generated by a prescribed motion experiment, are utilised to identify: (a) The static block, highlighted by the dashed line, of a Hammerstein model. (b) The static block, highlighted by the dashed line, of a FBO model.

4.4 Comparison of 2D NWT data with 3D BEM (WAMIT) data

The comparison between data generated by a WT and a BEM software package (such as WAMIT) can be useful in order to verify the presence of nonlinearity in the WT experiments (see Chapter 5). The body geometry implemented in WAMIT is three-dimensional; therefore, in the case of a

RWT or a 3D NWT, the comparison between WT data and WAMIT data is straightforward, since the same geometry is utilised in the WT and in WAMIT (see Fig. 4.43).

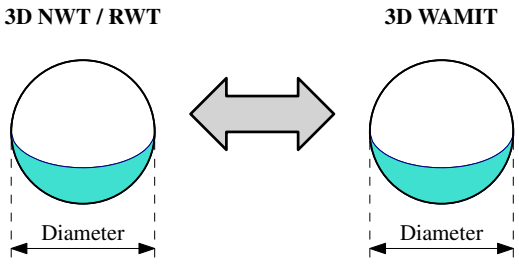

Figure 4.43: The comparison of 3D NWT/RWT data with 3D BEM (WAMIT) data is obtained by utilising the same geometry in the NWT/RWT and BEM code (in this case a sphere).

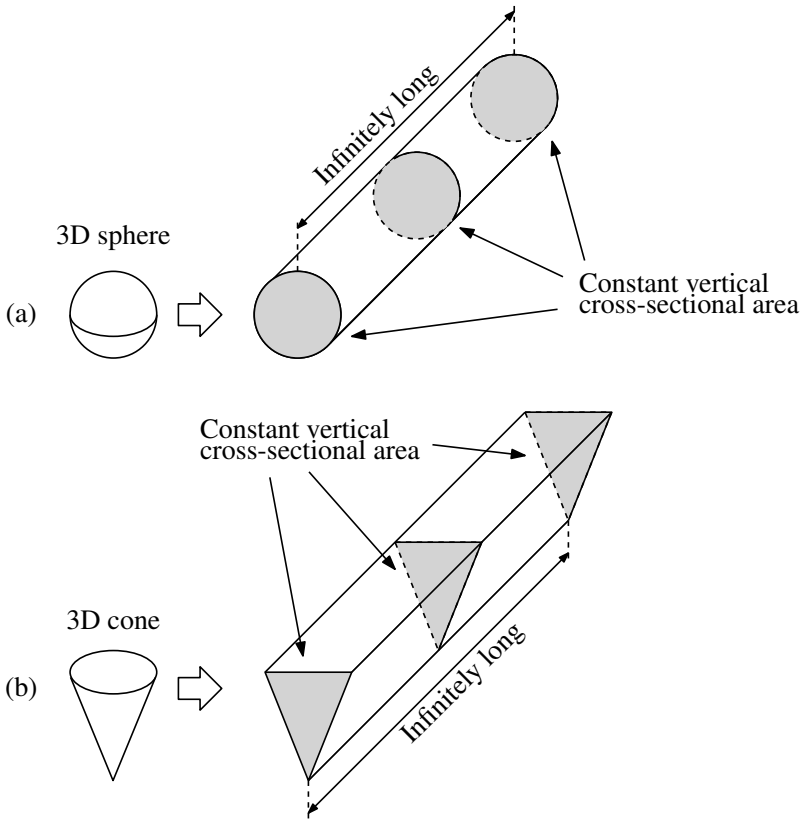

Figure 4.44: A 2D NWT is one cell thick and symmetry planes are imposed on the front and back faces of the domain; therefore, the body geometry is an infinitely long horizontal bar, having a constant vertical cross-sectional area. (a) A 3D sphere becomes an infinitely long horizontal bar, having a vertical cross-section of a circle. (b) A 3D cone becomes an infinitely long horizontal bar, having a vertical cross-section of a triangle.

In Section 2.3, it is explained that a CFD-NWT is very time consuming; therefore, 2D NWTs are often used to allow timely investigation of an optimal experiment design, before moving to the much more computationally complex 3D NWT. In the case of a 2D NWT, the comparison with 3D WAMIT data is not straightforward; a 2D NWT is one cell thick and symmetry planes are imposed on the front and back faces of the domain; therefore, the body geometry is an infinitely long horizontal bar, having a constant vertical cross-sectional area [7] [12] [14] [35]. As examples, a 3D sphere becomes an infinitely long horizontal bar, having a vertical cross-section of a circle (see Fig. 4.44(a)), and a 3D cone becomes an infinitely long horizontal bar, having a vertical

cross-section of a triangle (see Fig. 4.44(b)). Since the body represented in a 2D NWT has infinite length, in Newton's 2nd law

$$\sum_i f_i(t) = M\ddot{y}(t), \tag{4.54}$$

the body mass, M, and the forces acting on the body, $f_i(t)$, are infinitely large. Consequently, even $m_a(\omega)$, $N(\omega)$ and $H_e(\omega)$ are infinitely large, indeed, they are parts of the hydrodynamic forces, as equations (2.89) and (2.91) show. On the other hand, it is important to observe that each truncated piece of the infinitely long horizontal body, having a length L, is characterised by:

• A finite mass, $M^{(L)} = A_{vcr}L\rho_b$, where A_{vcr} is the vertical cross-sectional area and ρ_b the body density. Therefore, $M^{(L)}$ is linearly proportional to L.

• Finite forces, $f_i^{(L)}$, acting on the body. The force applied from the water to the body is calculated on the total wetted body surface, as shown by equation (2.11); therefore, since the total wetted body surface increases linearly with L, the added mass, $m_a^{(L)}(\omega)$, the radiation resistance, $N^{(L)}(\omega)$, and the excitation force, $H_e^{(L)}(\omega)$, of the truncated body are expected to increase linearly with L.

Since, in a 2D NWT, the body is an infinitely long horizontal bar, by implementing a long horizontal bar in WAMIT (long enough to approximate an infinitely long bar), results obtained by a 2D NWT and WAMIT can be compared. The ideal finite length of the WAMIT horizontal bar is not obvious and requires investigation. Consider a 3D spherical WEC with a 1 m radius and 1 m draft (see Fig. 4.27(a)); in a 2D NWT, the sphere becomes a circle with a 1 m radius, 1 m draft and one cell thick (see Fig. 4.27(b)), which is equivalent to an infinitely long horizontal cylinder (see Fig. 4.27(c)). In WAMIT, six different horizontal cylinders are considered, with a 1 m radius, 1 m draft and lengths of 1, 2, 5, 10, 25 and 50 m, as approximations of an infinitely long horizontal cylinder. In Fig. 4.45, the $m_a(\omega)$ curves of the six different cylinders are plotted,

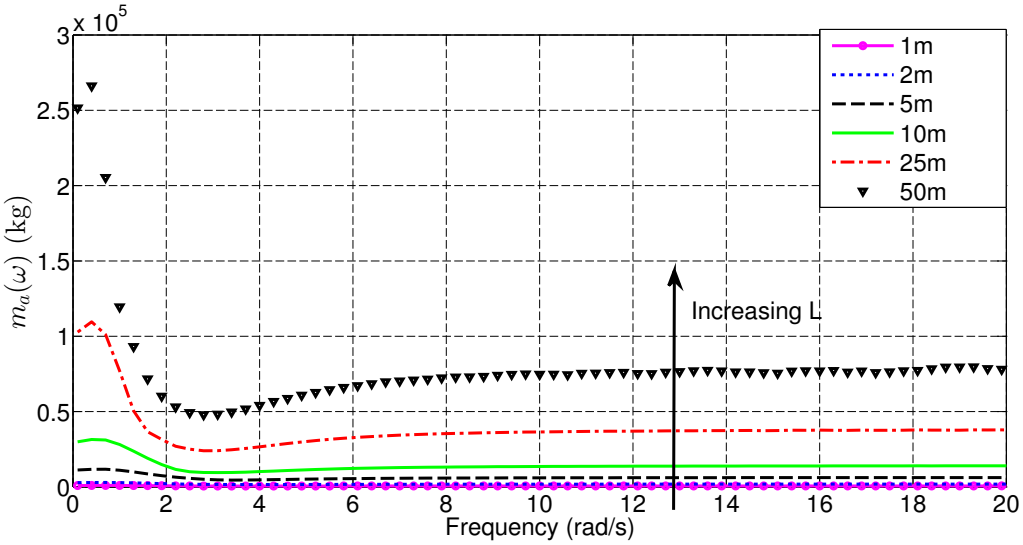

Figure 4.45: $m_a(\omega)$ curves, calculated by WAMIT, for six different 1 m radius horizontal cylinders, with lengths of 1, 2, 5, 10, 25 and 50 m. The curves increase unbounded with L.

showing that the curves increase with L. In Fig. 4.46, the value of $m_a(\omega)$ for $\omega = 3$ rad/s is plotted for each cylinder, showing that the added mass increases linearly with L, as expected. By defining the added mass per unit length as:

$$m_a^{(ul)}(\omega) = \frac{m_a(\omega)}{L} \tag{4.55}$$

and by plotting $m_a^{(ul)}(\omega)$ of the six different cylinders in Fig. 4.47, it is possible to see that the curves converge to a limit curve by increasing L, and that, for $L \geq 25$ m, the curve does not change significantly (apart from the very low frequencies). In particular, $m_a^{(ul)}(\omega)$, for $\omega = 3$ rad/s, is

plotted in Fig. 4.48, for each of the six different cylinder lengths. The same approach can be used by defining the radiation resistance per unit length as:

$$N^{(ul)}(\omega) = \frac{N(\omega)}{L} \tag{4.56}$$

and the excitation force per unit length as:

$$H_e^{(ul)}(\omega) = \frac{H_e(\omega)}{L} \tag{4.57}$$

Figs. 4.49, 4.50, 4.51 and 4.52 show the WAMIT results for the radiation resistance. In particular, Fig. 4.51 shows that, for $L \geq 25$ m, the $N^{(ul)}(\omega)$ curves do not change significantly. Figs. 4.53, 4.54, 4.55 and 4.56 show the WAMIT results for the excitation force. In particular, Fig. 4.55 shows that, for $L \geq 25$ m, the $H_e^{(ul)}(\omega)$ curves do not change significantly.

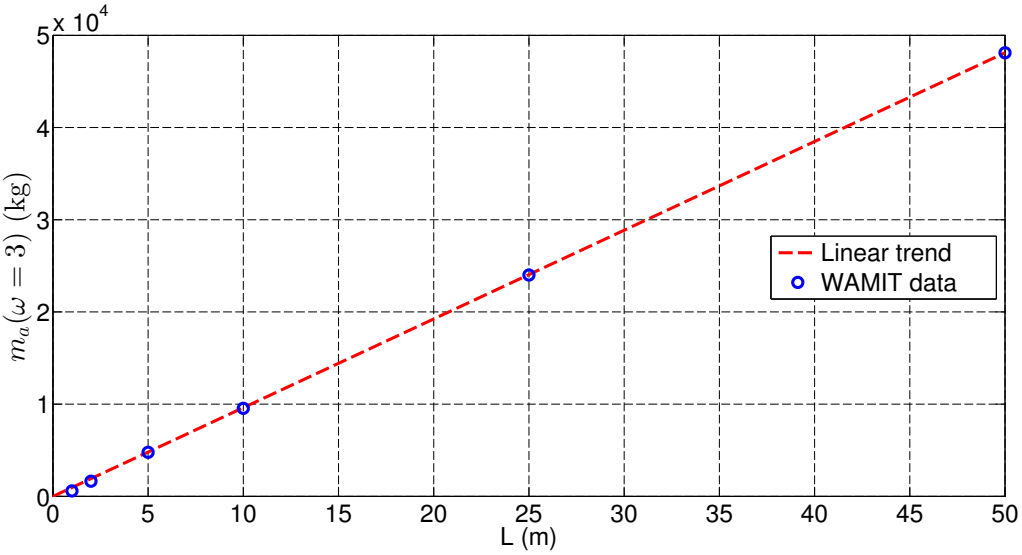

Figure 4.46: $m_a(\omega = 3)$ values, calculated by WAMIT, for six different 1 m radius horizontal cylinders, with lengths of 1, 2, 5, 10, 25 and 50 m. The values increase unbounded and linearly with L.

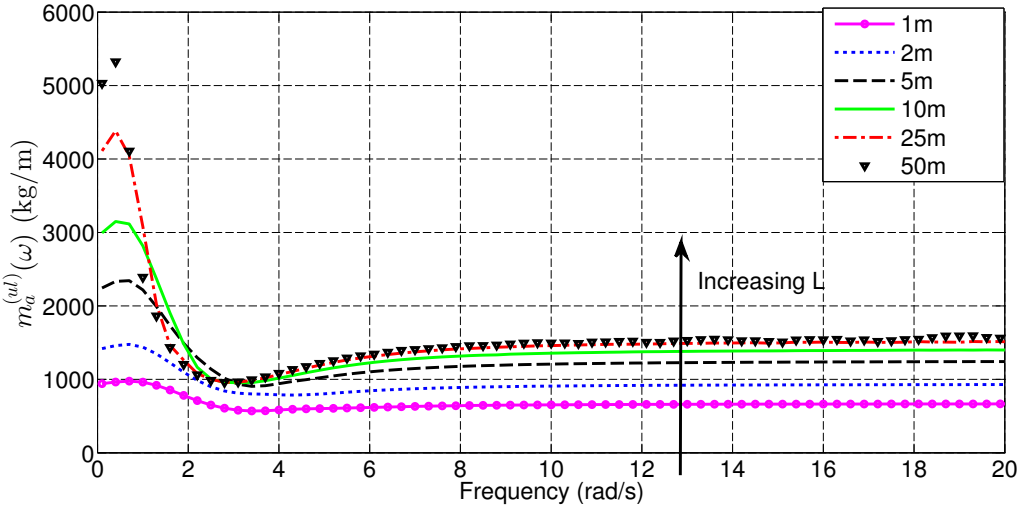

Figure 4.47: $m_a^{(ul)}(\omega)$ curves, calculated by using WAMIT data, for six different 1 m radius horizontal cylinders, with lengths of 1, 2, 5, 10, 25 and 50 m. The curves increase with L and converge to an upper limit curve. For $L \geq 25$ m the curve does not change significantly (apart from the very low frequencies).

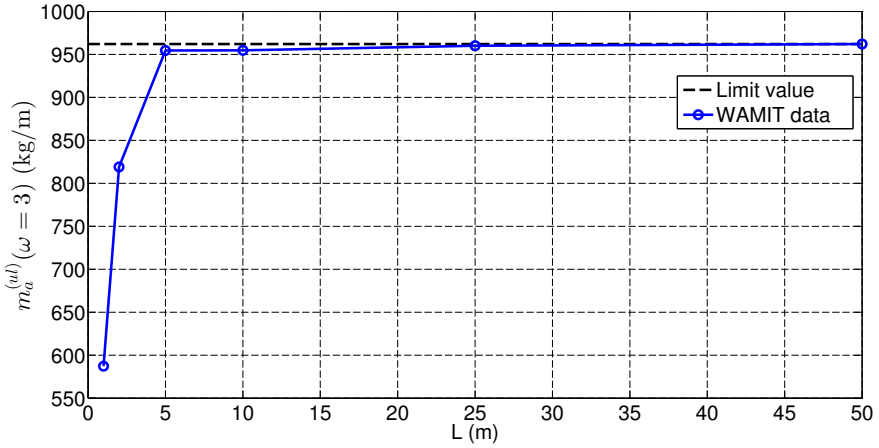

Figure 4.48: $m_a^{(ul)}(\omega = 3)$ values, calculated by using WAMIT data, for six different 1 m radius horizontal cylinders, with lengths of 1, 2, 5, 10, 25 and 50 m. The values increase with L and converge to an upper limit value.

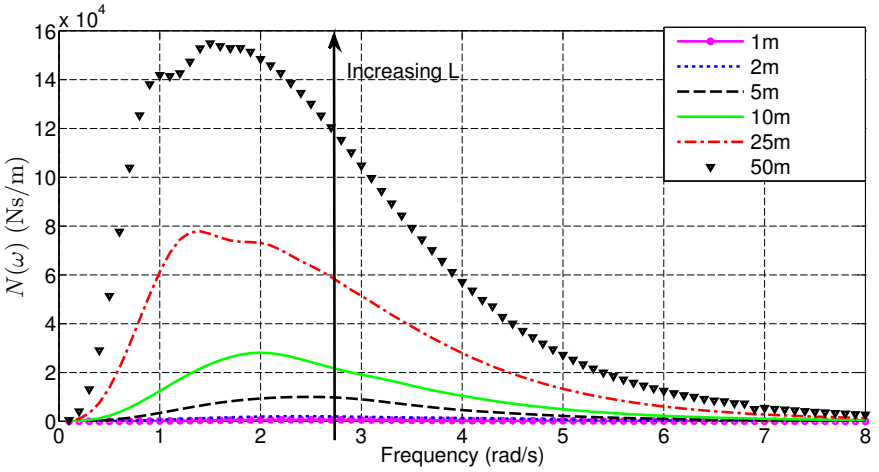

Figure 4.49: $N(\omega)$ curves, calculated by WAMIT, for six different 1 m radius horizontal cylinders, with lengths of 1, 2, 5, 10, 25 and 50 m. The curves increase unbounded with L.

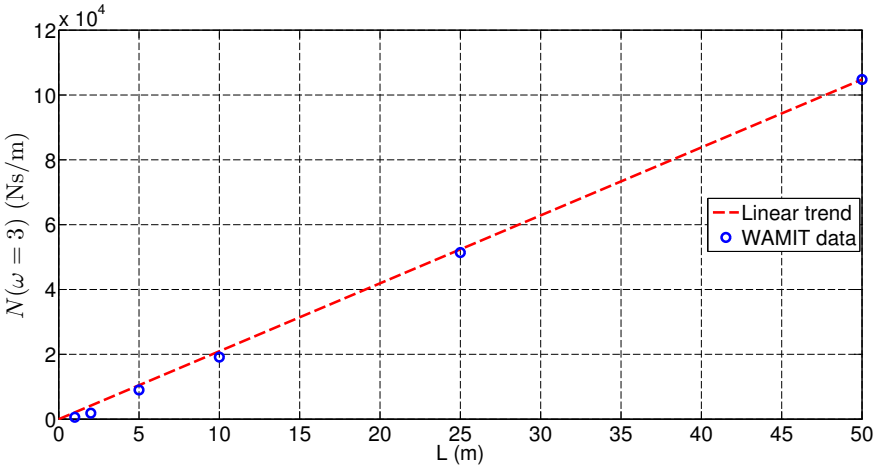

Figure 4.50: $N(\omega = 3)$ values, calculated by WAMIT, for six different 1 m radius horizontal cylinders, with lengths of 1, 2, 5, 10, 25 and 50 m. The values increase unbounded and linearly with L.

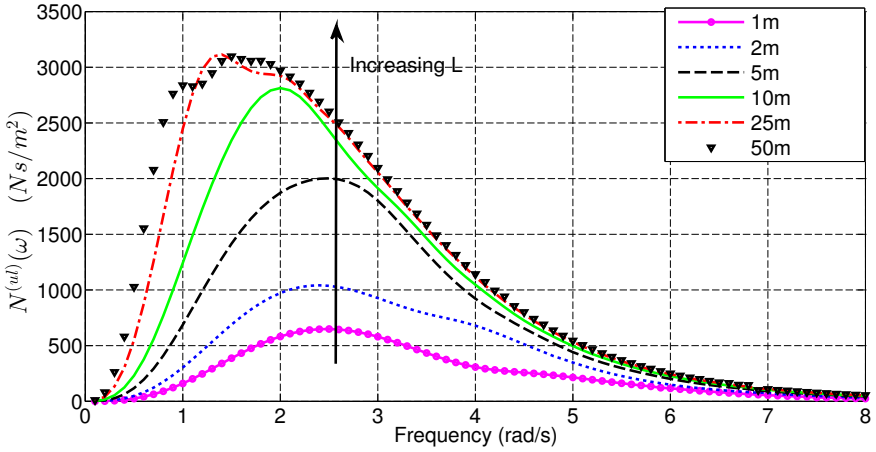

Figure 4.51: $N^{(ul)}(\omega)$ curves, calculated by using WAMIT data, for six different 1 m radius horizontal cylinders, with lengths of 1, 2, 5, 10, 25 and 50 m. The curves increase with L and converge to an upper limit curve. For $L \geq 25$ m the curve does not change significantly.

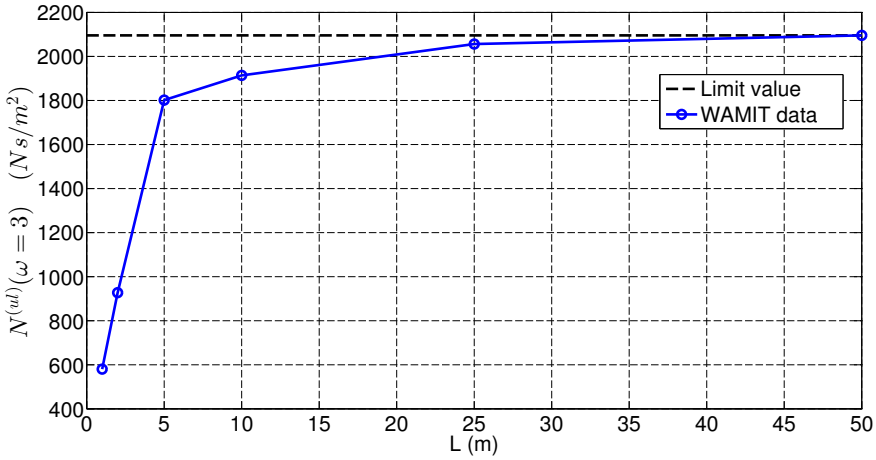

Figure 4.52: $N^{(ul)}(\omega = 3)$ values, calculated by using WAMIT data, for six different 1 m radius horizontal cylinders, with lengths of 1, 2, 5, 10, 25 and 50 m. The values increase with L and converge to an upper limit value.

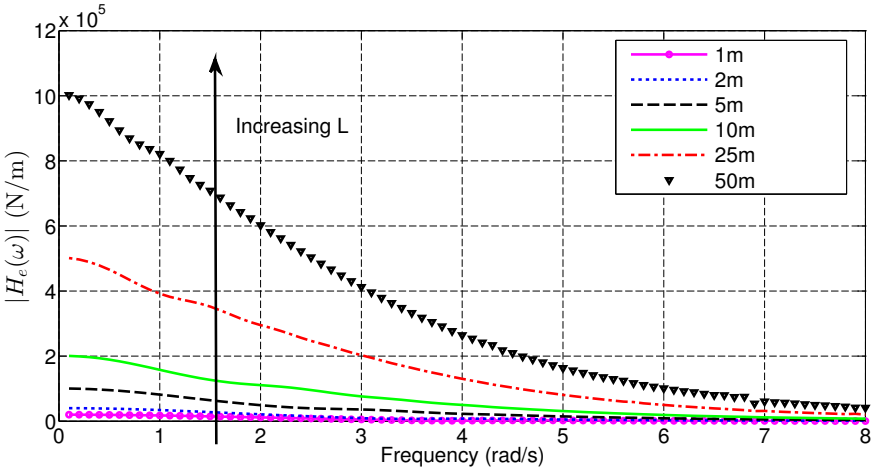

Figure 4.53: $|H_e(\omega)|$ curves, calculated by WAMIT, for six different 1 m radius horizontal cylinders, with lengths of 1, 2, 5, 10, 25 and 50 m. The curves increase unbounded with L.

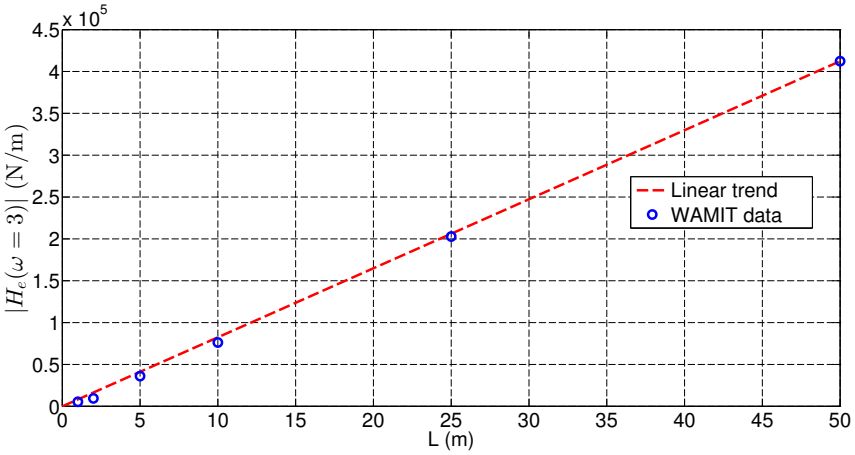

Figure 4.54: $|H_e(\omega = 3)|$ values, calculated by WAMIT, for six different 1 m radius horizontal cylinders, with lengths of 1, 2, 5, 10, 25 and 50 m. The values increase unbounded and linearly with L.

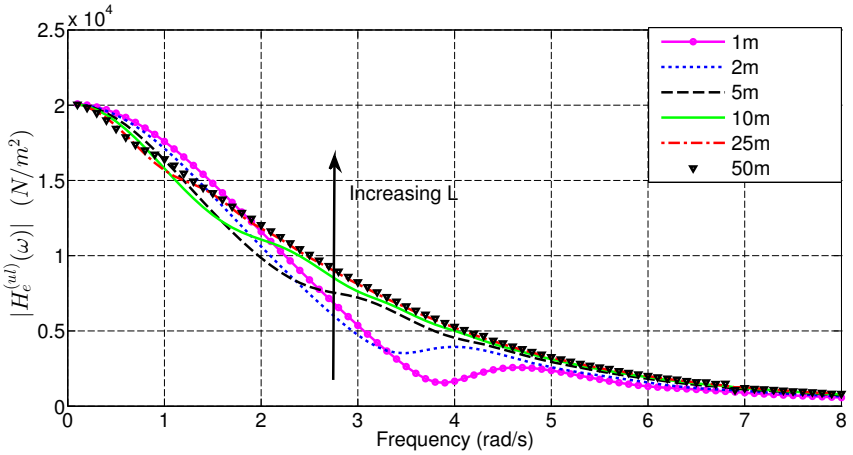

Figure 4.55: $|H_e^{(ul)}(\omega)|$ curves, calculated from WAMIT data, for six different 1 m radius horizontal cylinders, with lengths of 1, 2, 5, 10, 25 and 50 m. The curves increase with L and converge to an upper limit curve. For $L \geq 25$ m the curve does not change significantly.

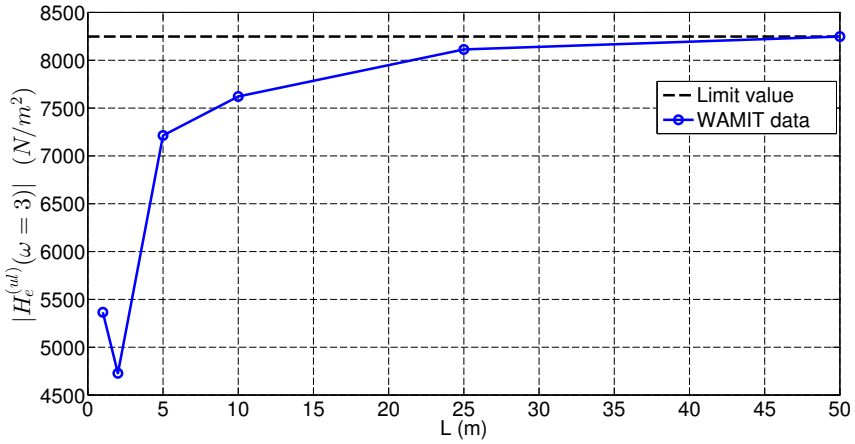

Figure 4.56: $|H_e^{(ul)}(\omega = 3)|$ values, calculated by using WAMIT data, for six different 1 m radius horizontal cylinders, with lengths of 1, 2, 5, 10, 25 and 50 m. The values increase with L and converge to an upper limit value.

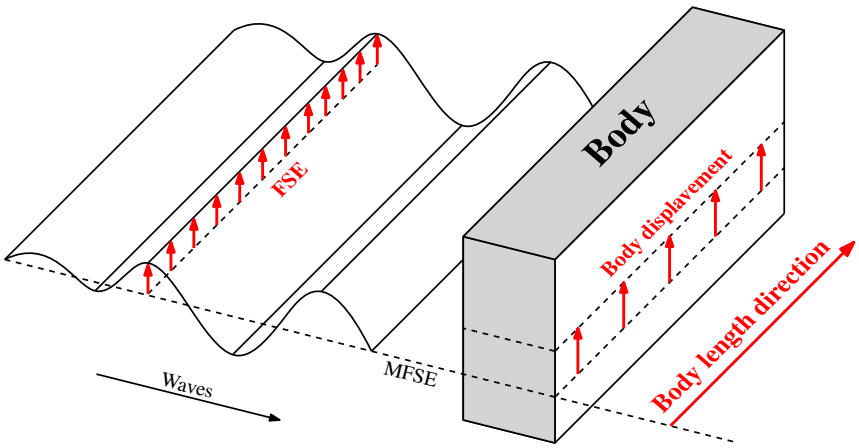

Figure 4.57: In a 2D NWT, the body displacement and the FSE are assumed to be constant along the body length direction.

The transfer function, of the linear $f_{in} \to y$ model, is obtained by the frequency domain Cummins' equation (4.39):

$$H_{f_{in}\to y}(\omega) = \frac{Y(\omega)}{F_{in}(\omega)} = \frac{1}{-\omega^2[M + m_a(\omega)] + i\omega N(\omega) + K} \tag{4.58}$$

where the numerator, $Y(\omega)$, is independent of L (in a 2D NWT, the body displacement is assumed to be constant along the body length direction, as shown in Fig. 4.57), and the denominator, $F_{in}(\omega)$, increases linearly with L. Therefore, $|H_{f_{in}\to y}(\omega)|$ is expected to decrease with a trend $\propto 1/L$. In Fig. 4.58, the curves representing $|H_{f_{in}\to y}(\omega)|$ of the six different cylinders are plotted, confirming that the curves decrease in height with L. In Fig. 4.59, the value of $|H_{f_{in}\to y}(\omega)|$ for $\omega = 3$ rad/s is plotted for each cylinder, showing the trend $\propto 1/L$, as expected. Therefore, in this case, the normalization of the curves per unit length is obtained by:

$$H^{(ul)}_{f_{in}\to y}(\omega) = H_{f_{in}\to y}(\omega) L \tag{4.59}$$

In Fig. 4.60, the curves $|H^{(ul)}_{f_{in}\to y}(\omega)|$ of the six cylinders are plotted, where it is possible to see that the curves converge to a limit curve by increasing L, and that, for $L \geq 25$ m, the curves do not change significantly. In Fig. 4.61, the values $|H^{(ul)}_{f_{in}\to y}(\omega)|$, for $\omega = 3$ rad/s, are plotted for the six cylinders.

The block diagram of Fig. 3.4 shows that the transfer function of the linear $\eta \to y$ model is given by:

$$H_{\eta\to y}(\omega) = \frac{Y(\omega)}{\overline{\eta}(\omega)} = H_e(\omega) H_{f_{in}\to y}(\omega) \tag{4.60}$$

where both the denominator $\overline{\eta}(\omega)$, which is the Fourier transform of $\eta(t)$, and the numerator $Y(\omega)$ are independent of L (in a 2D NWT, the body displacement and the FSE are assumed to be constant along the body length direction, as shown in Fig. 4.57). Therefore, $H_{\eta\to y}(\omega)$ is independent of L (if L is sufficiently large to approximate an infinitely long cylinder) and the normalization per unit length is not necessary. In Fig. 4.62, the $|H_{\eta\to y}(\omega)|$ curves of the six different cylinders are plotted, showing that, by increasing L, the curves converge to a limit curve and that, for $L \geq 10$ m, the curves do not change significantly. In Fig. 4.63, the value of $|H_{\eta\to y}(\omega)|$, for $\omega = 3$ rad/s, is plotted for each cylinder.

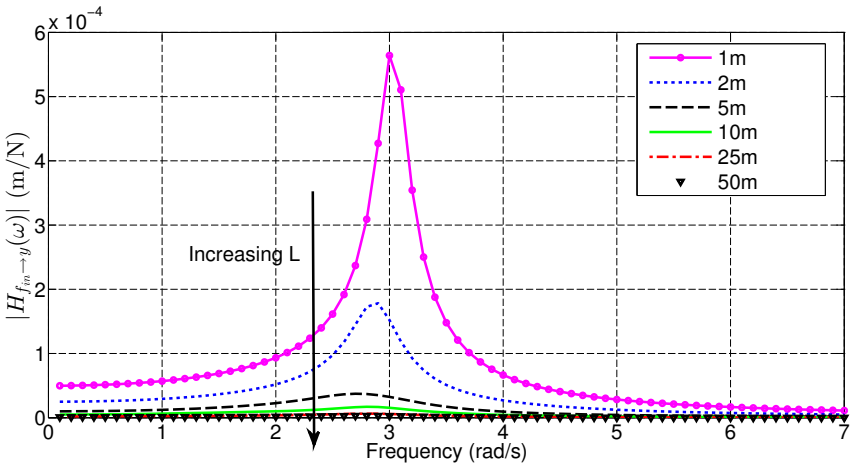

Figure 4.58: $|H_{f_{in}\to y}(\omega)|$ curves, calculated from WAMIT data, for six different 1 m radius horizontal cylinders, with lengths of 1, 2, 5, 10, 25 and 50 m. The curves decrease with L.

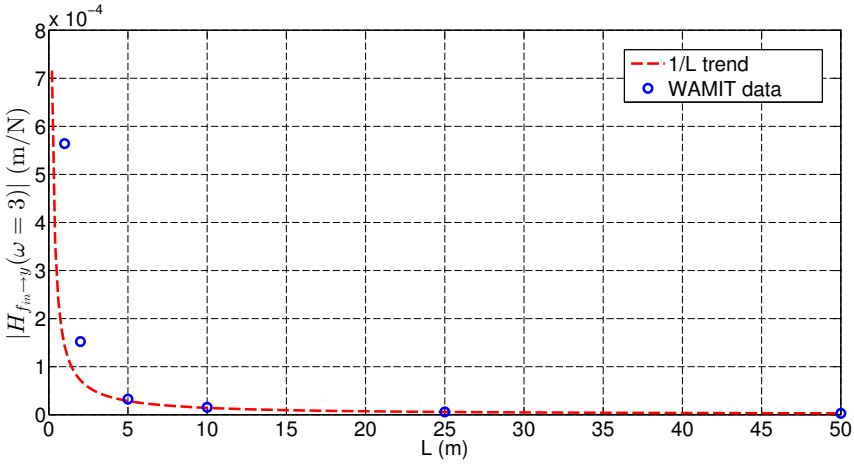

Figure 4.59: $|H_{f_{in}\to y}(\omega = 3)|$ values, calculated from WAMIT data, for six different 1 m radius horizontal cylinders, with lengths of 1, 2, 5, 10, 25 and 50 m. The values decrease with a $1/L$ trend.

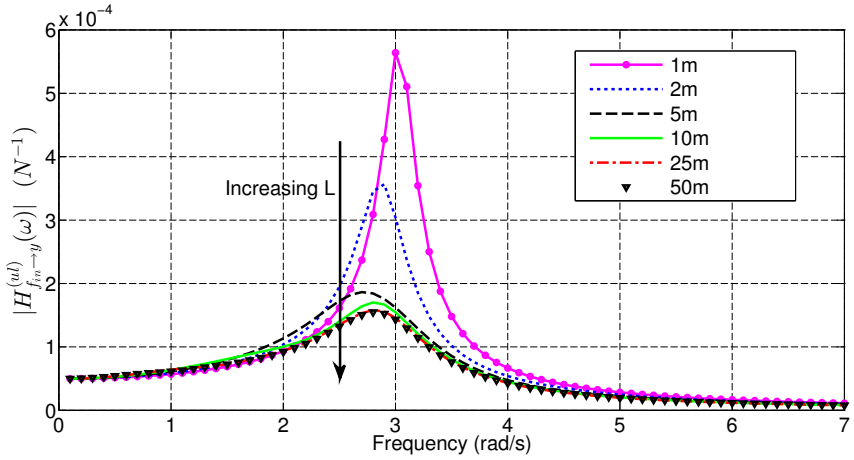

Figure 4.60: $|H^{(ul)}_{f_{in}\to y}(\omega)|$ curves, calculated by using WAMIT data, for six different 1 m radius horizontal cylinders, with lengths of 1, 2, 5, 10, 25 and 50 m. The curves decrease with L and converge to an lower limit curve. For $L \geq 25$ m the curve does not change significantly.

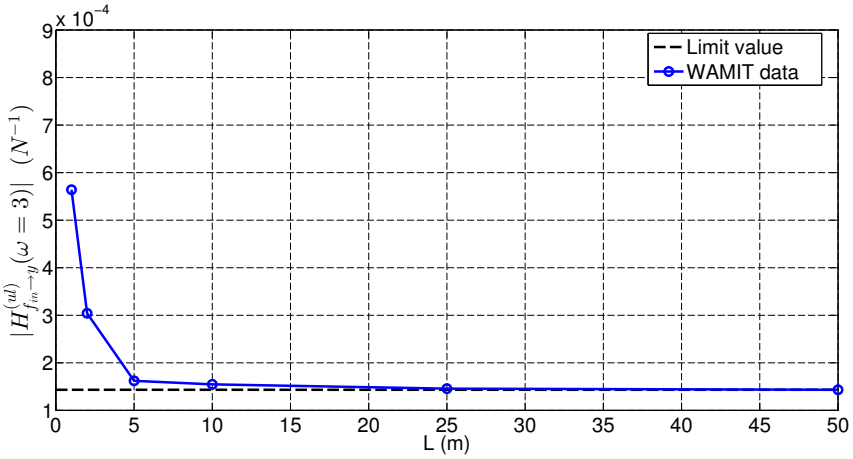

Figure 4.61: $|H^{(ul)}_{f_{in}\to y}(\omega = 3)|$ values, calculated by using WAMIT data, for six different 1 m radius horizontal cylinders, with lengths of 1, 2, 5, 10, 25 and 50 m. The values decrease with L and converge to an lower limit value.

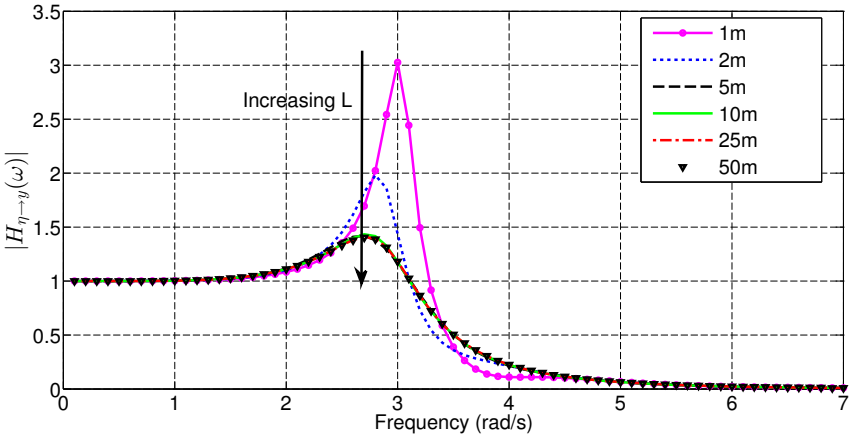

Figure 4.62: $|H_{\eta\to y}(\omega)|$ curves, calculated from WAMIT data, for six different 1 m radius horizontal cylinders, with lengths of 1, 2, 5, 10, 25 and 50 m. The curves decrease with L and converge to a limit curve. For $L \geq 5$ m the curve does not change significantly.

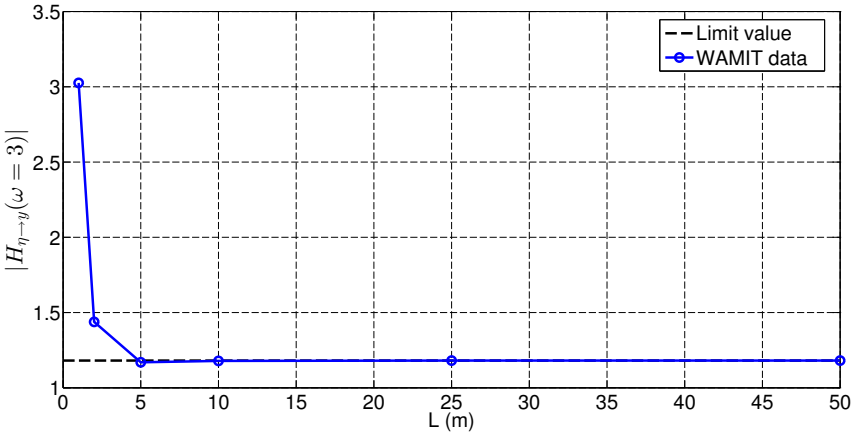

Figure 4.63: $|H_{\eta\to y}(\omega = 3)|$ values, calculated from WAMIT data, for six different 1 m radius horizontal cylinders, with lengths of 1, 2, 5, 10, 25 and 50 m. The values decrease with L and converge to a limit value.

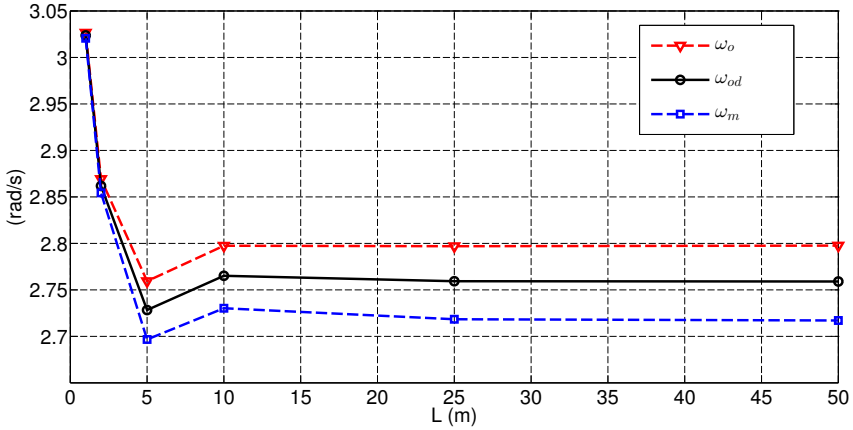

Figure 4.64: ω_o, ω_{od} and ω_m values, calculated from WAMIT data, for six different 1 m radius horizontal cylinders, with lengths of 1, 2, 5, 10, 25 and 50 m. The frequencies converge to limit values, by increasing L.

Fig. 4.64 shows the values of the frequencies ω_o, ω_{od} and ω_m, obtained by WAMIT data and equations (4.43) (4.44) (4.45), for the six different cylinders, where it is possible to see that, for $L \geq 25$ m, the values do not change significantly.

In WAMIT, the computation time is proportional to the number of panels utilised to approximate the body surface and, consequently, to the body length L. The increment of L, in order to better approximate an horizontal infinitely long body, has to be justified by a sufficient improvement in accuracy. The quantities $m_a^{(ul)}(\omega)$, $N^{(ul)}(\omega)$, $H_e^{(ul)}(\omega)$, $H_{f_{in}\to y}^{(ul)}(\omega)$, $H_{\eta\to y}(\omega)$, ω_o, ω_{od} and ω_m, calculated from WAMIT data for a 3D horizontal cylinder, moving in heave, with different lengths, a 1 m radius and 1 m draft, do not change significantly, for $L \geq 25$ m; therefore, in this study case, the conclusion is that a 25 m long cylinder is a sufficient approximation of a horizontal infinitely long body of a 2D tank.

4.5 Summary and discussion

This chapter explains the experiment design in WTs (for both NWT and RWT), in order to generate informative data for WEC model identification. Nonlinear dynamic systems are significantly more complex than linear ones, and if the gathered data are not informative enough, the identified model will not be sufficiently accurate. The objective of an experiment design is to obtain informative data, on the WEC under investigation, in the shortest possible time; indeed, by extending the duration of an experiment, in the case of a CFD-NWT, the amount of computation time could become unsustainable and, in the case of a RWT, the facility renting costs could be excessive. In WT experiments, the use of 'time-compacted' input signals, characterised by a high concentration of information, are crucial. Section 4.2.1 describes the excitation signal characteristics, such as spectral content, amplitude range and amplitude distribution, utilised in order to evaluate the quality of an excitation signal. The conclusion is that the designed excitation signal should cover the full input and output amplitude signal ranges and the bandwidth, where the system has a significant non-zero frequency response. Furthermore, the amplitude distribution of the input signal should be uniform, in order to excite the system uniformly. Section 4.2.2 introduces different input excitation signals, explaining that RBS/PRBS are not suitable for nonlinear system identification; instead, RARP, chirp and multisine signals have appropriate characteristic for their use in nonlinear SI. Section 4.3.2 introduces a variety of WT identification experiments, such as free decay, input wave, input force and prescribed motion experiments. Section 4.3.1 explains the use of WT preliminary experiments (which are characterised by a fast computation time, in case of a CFD-NWT), such as free decay and input force preliminary experiments, to obtain rough measurement of the resonant frequency and the bandwidth of the WEC, informing the successive identification

experiments where the input power spectrum should be allocated. Furthermore, since the body displacement is relatively small in the WT preliminary experiments, the WEC behaviour can be reasonably described by a linear model and the WT experimental data can be compared with fully linear BEM results. In the case of a 2D NWT, the comparison with 3D BEM data is not straightforward; indeed, in a 2D NWT, the body geometry is an infinitely long horizontal bar, having a constant vertical cross-sectional area. In Section 4.4, a methodology to compare 2D NWT data with 3D BEM data is presented.

Chapter 5

Identification of CT linear hydrodynamic models from free decay NWT experiments

5.1 Introduction

As explained in Section 2.6, a significant number of WEC models are based on a parametric state-space representation of Cummins' equation (2.86), whose parameters are identified from LPT-BEM data. LPT is based on strong hypotheses, which completely remove the hydrodynamic nonlinearity of the fluid-body interaction (see Section 2.4); therefore, the resulting WEC models have good accuracy only for small body displacement (in comparison to the body dimensions). A way to increase the model accuracy, in the case of larger body displacement, is by introducing some nonlinear terms in the model structure, such as nonlinear restoring, Froude-Krylov and viscous drag forces (see Section 2.6.2), with the consequent disadvantage of increasing both the model complexity and computation time, together with the loss of some desirable properties, such as superposition and frequency domain description. In this chapter, a different methodology is proposed, in order to obtain WEC models characterised by both a linear structure and increased accuracy (compared to LPT-BEM models), even in the case of a large body displacement. The basic idea is to select a parametric state-space model structure and identify the unknown parameters from free decay CFD-NWT data, instead of BEM data. CFD-NWTs generate data rich information, in contrast to the limited scope of data generated by LPT-BEM solvers and so it is possible to extract hydrodynamic nonlinearity information, which is 'injected' into the linear model. The identified model is purely linear, but its average behaviour is more representative of the actual nonlinear process (in the operating amplitude region the model is identified from), compared to the average behaviour of a linear model, identified from BEM data. Since the identified model depends heavily on the data it is identified from, in this chapter, four different free decay experiments are utilised, characterised by four different initial body displacements. In contrast to traditional system identification, where forcing input signals are used to excite the system dynamics, in this chapter, only free decay experiments are employed (no input signals). An important advantage of free decay experiments, over input wave, input force and prescribed motion experiments (see Sections 4.3.2.2, 4.3.2.3 and 4.3.2.4, respectively) is that free decay experiments are simple to realise, both in a NWT and a RWT, since no actuators to move the WEC, or strategies for wave generation and absorption, are required. In [165], independently of this work (which is published in [11] and [14]), Armesto develops a similar approach to identify an OWT state-space model, representing the Cummins' equation, from free decay CFD-NWT data. The main distinction, between the work of Armesto and the present work, is in the different identification strategy. In Armesto's approach, the radiation and restoring terms are identified together from the same data; in this work, instead, the identification of the restoring term precedes the identification of the radiation term, by using knowledge of the hydrostatic force versus body displacement, reducing the

dimension of the parameter space and simplifying the search for a global minimum. Furthermore, in Armesto's method, no constraints on the parameters are introduced, in order to obtain stable and passive linear models; in contrast, in this work, new *a priori* constraints on the parameters are introduced in the identification, in order to guarantee the stability and passivity of the model. As a case study, the methodology presented in this chapter is applied to a floating vertical cylinder, but the method can be utilised with a body having any shape or oscillating in an other DoF (i.e. pitching).

This chapter is laid out as follows: Section 5.2 describes the SI data generation, with Section 5.2.1 explaining the 3D CFD-NWT and floating body geometry, implemented in OpenFOAM, Section 5.2.2 illustrating the four NWT experimental data sets generated, and Section 5.2.3 describing the comparison of NWT free decay identification experiment data with BEM data. In Section 5.3, the selected linear model structure is presented. In Section 5.4, the identification methods are explained, with Section 5.4.1 describing the proposed identification method from NWT data, and Section 5.4.2 illustrating the traditional model identification from BEM data. In Section 5.5, the results of the identification methods are illustrated. Finally, a summary and discussion are presented in Section 5.6.

5.2 NWT implementation and generated NWT data description

5.2.1 NWT and floating body description

The data utilised in this chapter are generated in a 3D CFD-NWT, implemented in OpenFOAM (see Section 2.3.1). The tank has the geometry of a vertical cylinder, with a 5 m height, 50 m radius and is filled with 3 m of water (with a density of 997 kg/m^3) and the remaining 2 m is air, as shown in Fig. 5.1. The floating body under investigation is a vertical cylinder with a 391.5 kg mass, 0.5 m radius and 0.5 m draft, as shown in Fig. 5.2. The body is placed in the exact centre of the tank and has an equilibrium buoyancy position 50% submerged, so that its center of mass coincides with the still water level at the centre of the tank. Since the body is constrained to move in heave only, static stability is not an issue. Four free decay experiments (see Section 4.3.2.1) with varying initial vertical displacements of 5, 10, 20 and 45 cm, above the equilibrium position, (all the experiments have an initial null body velocity) were conducted in the NWT.

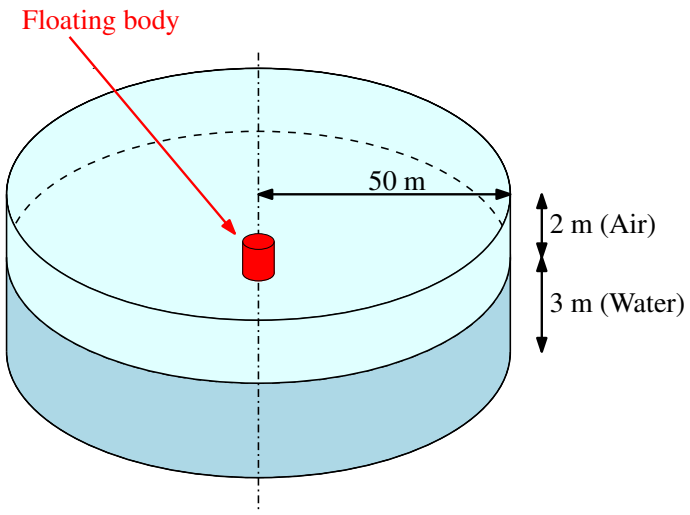

Figure 5.1: Cylindrical NWT, used for the free decay experiments.

As explained in Section 2.3, an important step in the CFD-NWT implementation is the mesh

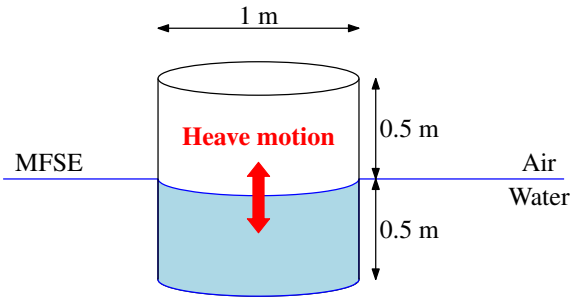

Figure 5.2: The 3D floating cylinder considered in the present case study.

specification, which determines the accuracy and computation time of the simulations. It is possible to take advantage of the symmetry of the NWT and body geometries, in order to simplify the meshing process and reduce the consequent computation time of the simulations. The utilised tank and body are axisymmetric (the condition of rotational symmetry is satisfied) and the body only moves in heave along the tank's central axis; therefore, only one slice of the full circle (see Figs. 5.3 and 5.4) needs to be modelled, if symmetric boundary conditions are applied, as implemented in OpenFOAM [50], by using the *wedge* command. The arc of the wedge spans one degree in angle and is only one cell thick, effectively transforming the 3D problem into a 2D problem, which significantly reduces the number of cells needed to mesh the domain, considerably speeding up run time. The vertical component of the surface force, applied from the fluid to the body (see Section 2.2.1), is given by:

$$f_{fl.y} = \int_S (\boldsymbol{\Sigma}\,\mathbf{n}) \cdot \mathbf{i_y}\, dS = 360 \int_{S_{we}} (\boldsymbol{\Sigma}\,\mathbf{n}) \cdot \mathbf{i_y}\, dS \tag{5.1}$$

where $\boldsymbol{\Sigma}$ is the total stress tensor (given by the summation of pressure and viscous stresses), $\mathbf{n}$ is the unit normal vector to the surface, $\mathbf{i_y}$ is the unit vertical vector, S is the wetted body surface and S_{we} is the wetted body surface of the one degree wedge (see Fig. 5.3). Therefore, the total force, applied from the fluid to the body, is 360 times the force calculated by the NWT, which utilises the one degree wedge. The tank is meshed with hexahedral cells, by using OpenFOAM's mesh generator *blockMesh* [50]. In the horizontal direction, there are 1000 cells with exponentially increasing length, so that the first cell, in the centre of the tank, has a 2.4 mm length and the last cell, next to the tank wall, has a 240 mm length (see Figs. 5.4 and 5.5). This allows a fine mesh resolution near the body, while reducing the total number of cells needed to cover the full width of the tank. In the vertical direction, 1000 cells with a uniform height of 5 mm are used.

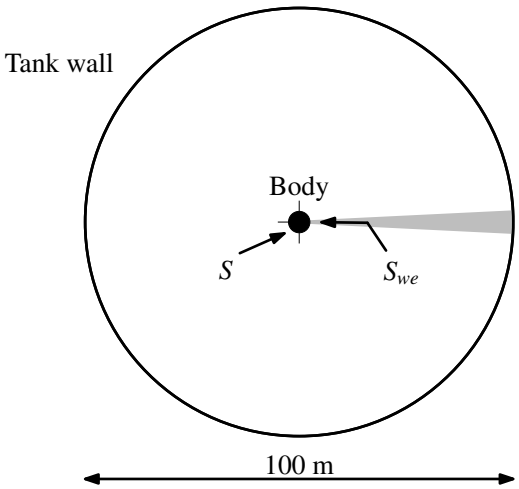

Figure 5.3: Top view of the NWT used for the free decay experiments, where axisymmetry has enabled the tank's circular cross-section to be represented by a narrow wedge in OpenFOAM.

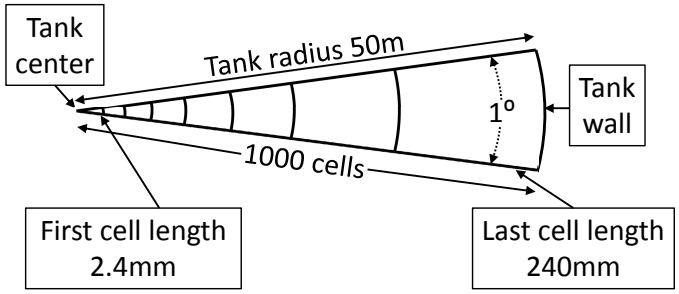

Figure 5.4: Schematic top view of the one cell thick wedge, implemented in OpenFOAM. In the horizontal direction there are 1000 cells with exponentially increasing length.

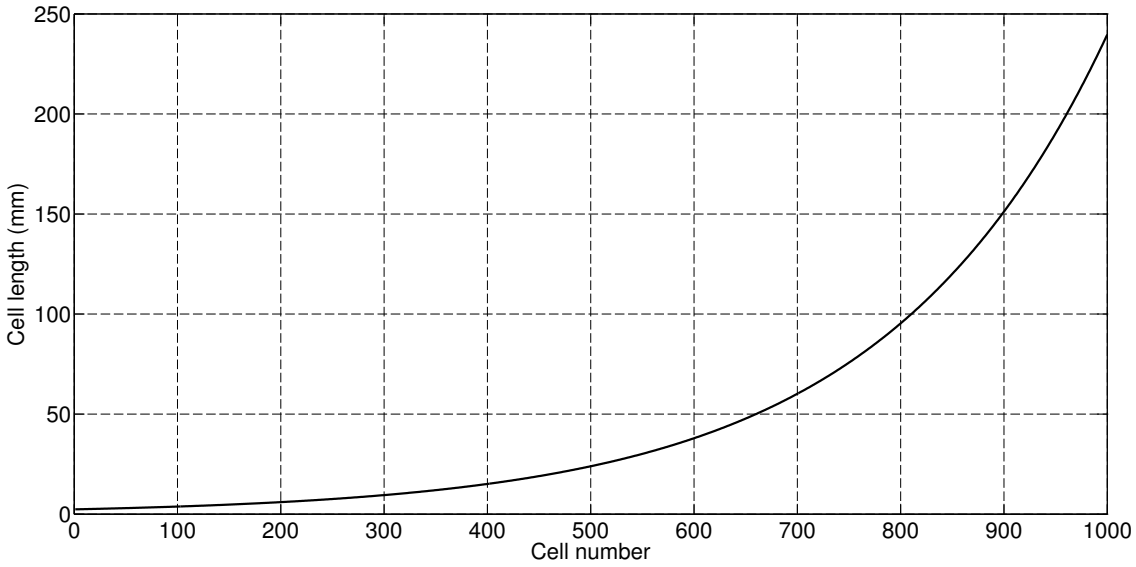

Figure 5.5: In the horizontal direction of the 2D NWT, there are 1000 cells with exponentially increasing length.

5.2.2 Generated NWT data description

The CFD-NWT free decay experiments are simulated for 12 s, and the large tank diameter is chosen to eliminate the effect of wave reflection from the side walls of the tank during the experiments. Indeed, the reflected waves, at the tank walls, may be a source of measurement error; Fig. 5.6 (which is a CFD post processing view of the dynamic pressure field in the water after 6 seconds of simulation) shows that the generated waves, propagating from the oscillating body, do not reach the tank walls by the half way mark of the simulation; therefore, the waves will not be reflected back to the body before the end of the 12 s simulation.

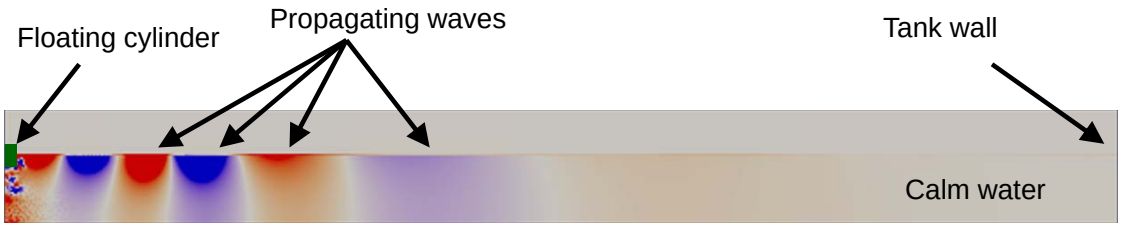

Figure 5.6: CFD-NWT post process of the dynamic pressure field in the tank, after 6 s of the 12 s simulation, for the 45 cm initial amplitude free decay experiment (the tank points with positive dynamic pressure are coloured in red, blue points represent negative pressure).

OpenFOAM calculates the total and dynamic pressures in the fluid at each time step and offers functions, which integrate these values over the wetted body surface, in order to provide the total and dynamic forces applied from the fluid to the body. The hydrostatic force, applied from the fluid to the body, can be calculated by subtracting the dynamic force from the total force. Therefore, each experiment provides the body displacement, $y(t_j)$, the dynamic, static and total heave forces, applied from the fluid to the body (360 times the forces calculated by the NWT), respectively denoted $f_{fl}^D(t_j)$, $f_{fl}^S(t_j)$ and $f_{fl}(t_j)$, where $j = 1,2,...,N$, with $N = 4800$ (the signal sampling time is $T_s = 0.0025$ s). Fig. 5.7 shows $y(t_j)$, $f_{fl}^D(t_j)$, $f_{fl}^S(t_j)$ and $f_{fl}(t_j)$ for the experiment with initial displacement 45 cm. Given $f_{fl}^S(t_j)$ and the body mass, M, it is possible to obtain the restoring force applied on the body (see Section 2.2.7):

$$f_{re}(t_j) = f_{fl}^S(t_j) - Mg \tag{5.2}$$

In Figs. 5.8, 5.9 and 5.10, the signals $y(t_j)$, $f_{fl}^S(t_j)$ and $f_{re}(t_j)$ are plotted, respectively, for the experiments with initial displacements of 5, 10, 20 and 45 cm. Note that, in Fig. 5.9, f_{fl}^S converges to the limit 3841 N, in each experiment; indeed, at equilibrium, the static force and the gravitational force, $Mg = 391.5 \times 9.81 = 3841$, have the same intensity and opposite directions (see Section 2.2.7). In order to illustrate the inherent nonlinear hydrodynamic effects, captured by the CFD-NWT simulations, the results in Figs. 5.8 and 5.10 are normalised against their initial value and plotted in Figs. 5.11 and 5.12, respectively. Linearity would require these free decay curves to overlay each other when normalised (if linear scaling applies). However, due to nonlinear effects, such as viscosity and vortex shedding (shown in Fig. 5.13), the normalised NWT responses vary for different initial amplitudes.

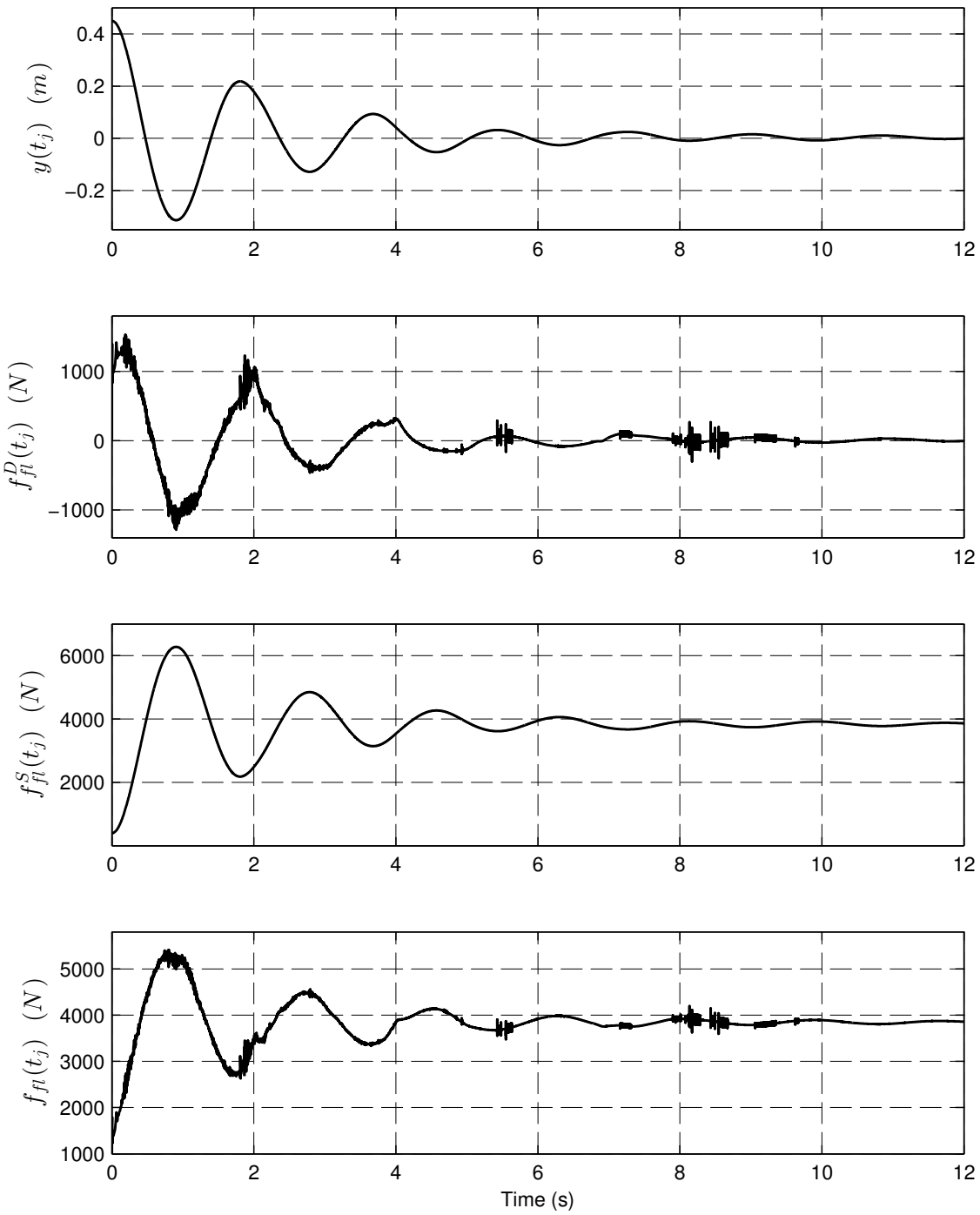

Figure 5.7: NWT experimental data for the free decay experiment with a 45 cm initial displacement. The experiment provides the body displacement, $y(t_j)$, the dynamic, static and total heave forces, applied from the fluid to the body (360 times the forces calculated by the NWT), respectively denoted $f_{fl}^D(t_j)$, $f_{fl}^S(t_j)$ and $f_{fl}(t_j)$.

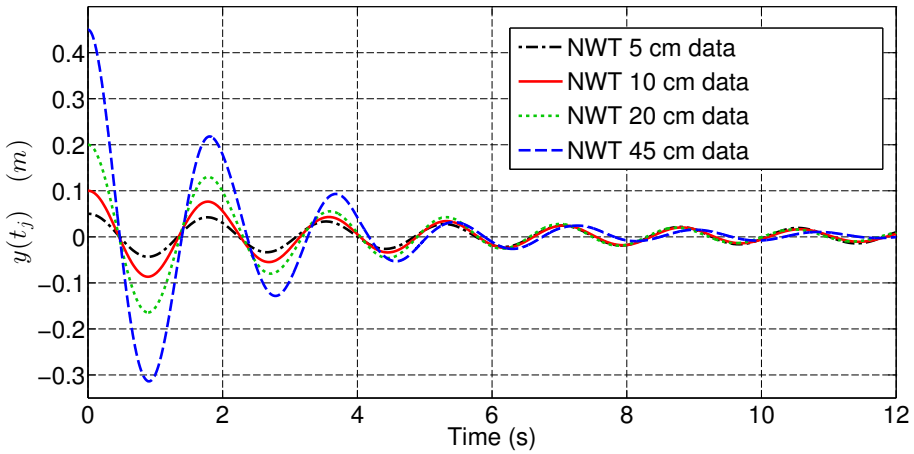

Figure 5.8: Body displacement in the NWT free decay experiments.

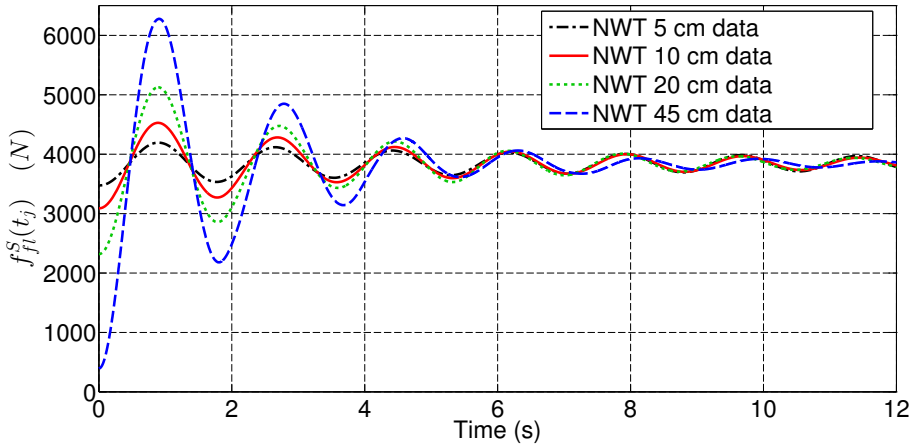

Figure 5.9: Static force applied from the fluid to the body in the NWT free decay experiments.

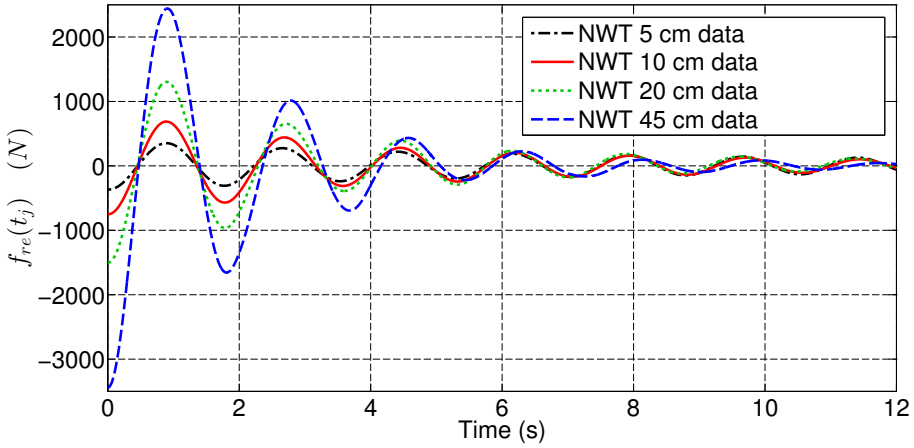

Figure 5.10: Restoring force applied to the body in the NWT free decay experiments.

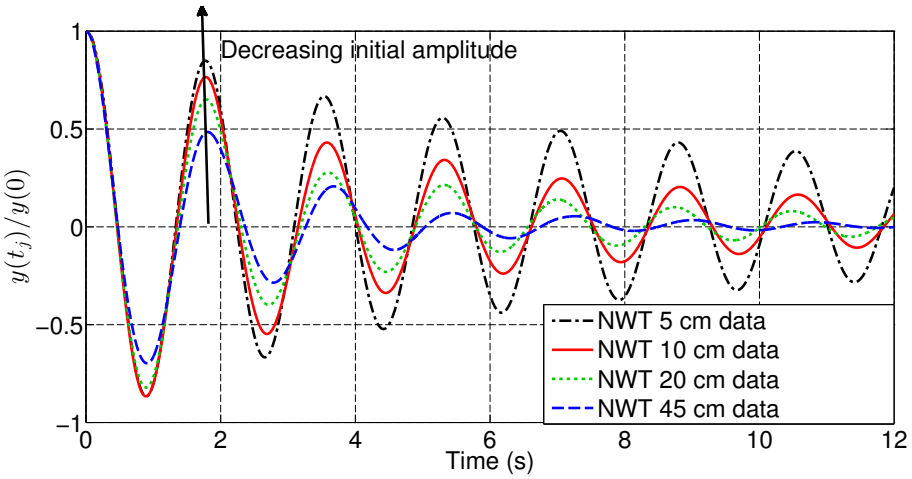

Figure 5.11: Simulated body displacement from NWT free decay experiments, normalised against their initial position.

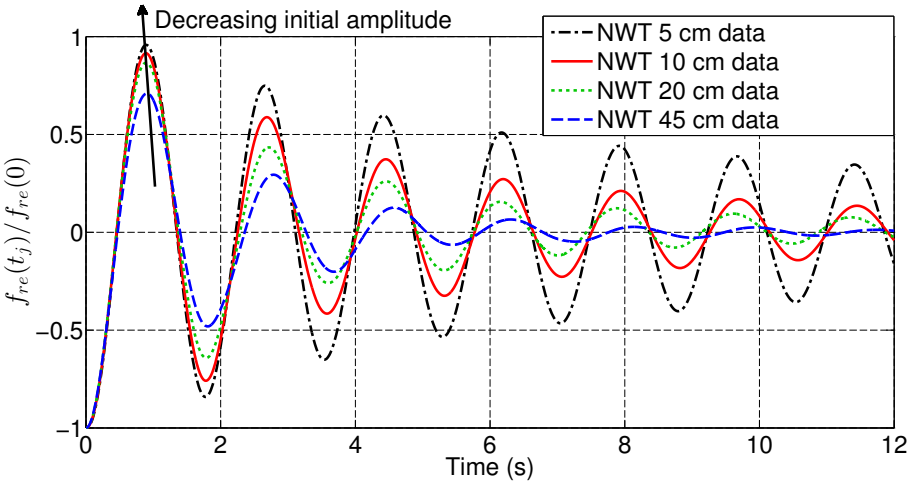

Figure 5.12: Simulated restoring force from NWT free decay experiments, normalised against their initial value.

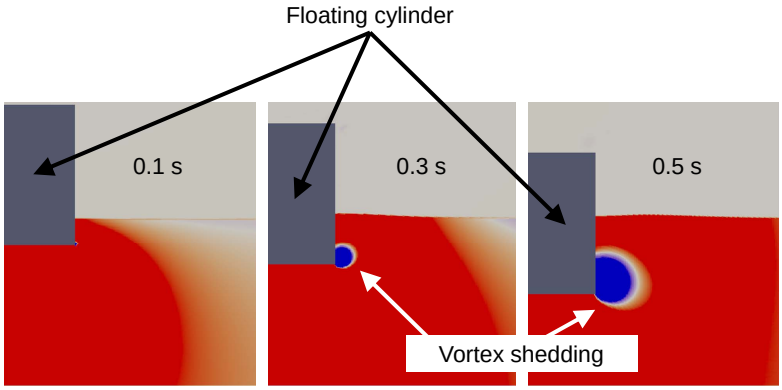

Figure 5.13: The dynamic pressure, calculated by the NWT, in the fluid around the floating cylinder at 0.1 s, 0.3 s and 0.5 s, showing the creation of a vortex structure by the sharp bottom corner of the cylinder. The tank points with positive dynamic pressure are coloured in red, blue points represent negative pressure.

5.2.3 Comparison of NWT free decay identification experiment data with BEM data

As explained in Section 4.3.1.1, in the case of a relatively small body displacement and velocity, WEC dynamics are usually well approximated by a linear model; therefore, the damped natural frequency ω_{od}^{NWT}, calculated from a NWT free decay experiment with a small initial condition (compared to the body dimensions), would be reasonably similar to ω_{od}^{BEM}, computed from BEM data (Fig. 4.34 shows the block diagram for ω_{od}^{NWT} and ω_{od}^{BEM} comparison). Figs. 5.14 and 5.15 show, respectively, $m_a(\omega)$ and $N(\omega)$ calculated by WAMIT, for the same cylinder utilised in the NWT experiments (a vertical cylinder, moving in heave, with a 0.5 m radius and 0.5 m draft). The comparison between the damped natural frequency $\omega_{od}^{NWT} = 3.6$ rad/s, calculated from NWT data with equation (4.16), and $\omega_{od}^{BEM} = 3.57$ rad/s, computed from BEM data with equation (4.44), shows very good agreement. Fig. 5.16 shows graphically the very good agreement between ω_{od}^{NWT} and ω_{od}^{BEM}, where the peak of $|Y(\omega)|$ occurs at ω_{od}^{NWT} and the peak of $|H_{f_{in}\to y}^{BEM}(\omega)|$ occurs at $\omega_m^{BEM} \simeq \omega_{od}^{BEM}$, as shown in Section 4.3.1.1.

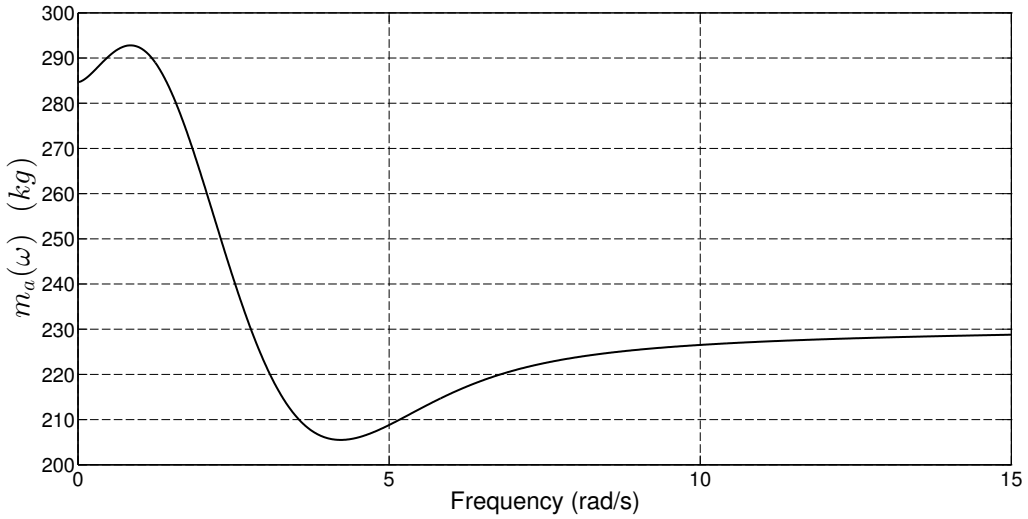

Figure 5.14: Added mass curve, calculated by WAMIT, of a vertical cylinder moving in heave, with a 0.5 m radius and 0.5 m draft.

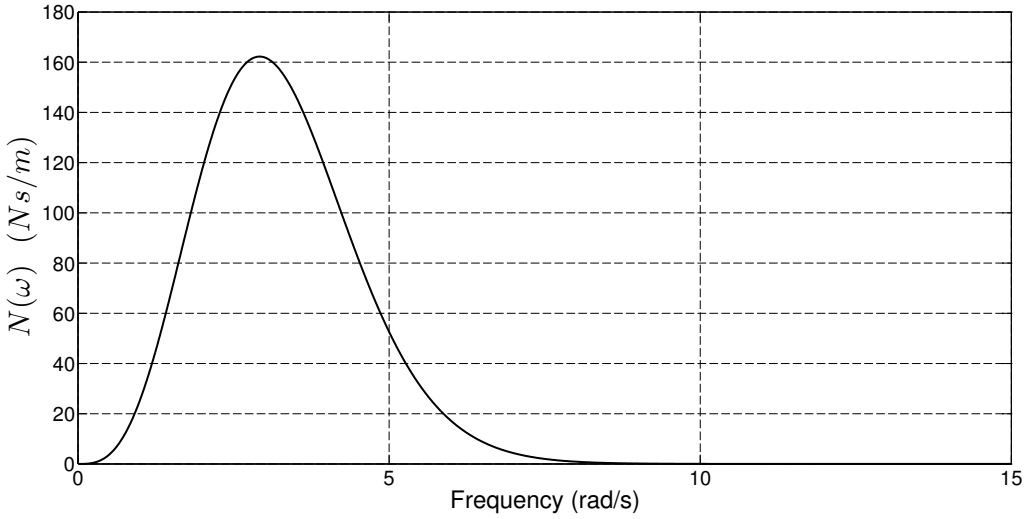

Figure 5.15: Radiation resistance curve, calculated by WAMIT, of a vertical cylinder moving in heave, with a 0.5 m radius and 0.5 m draft.

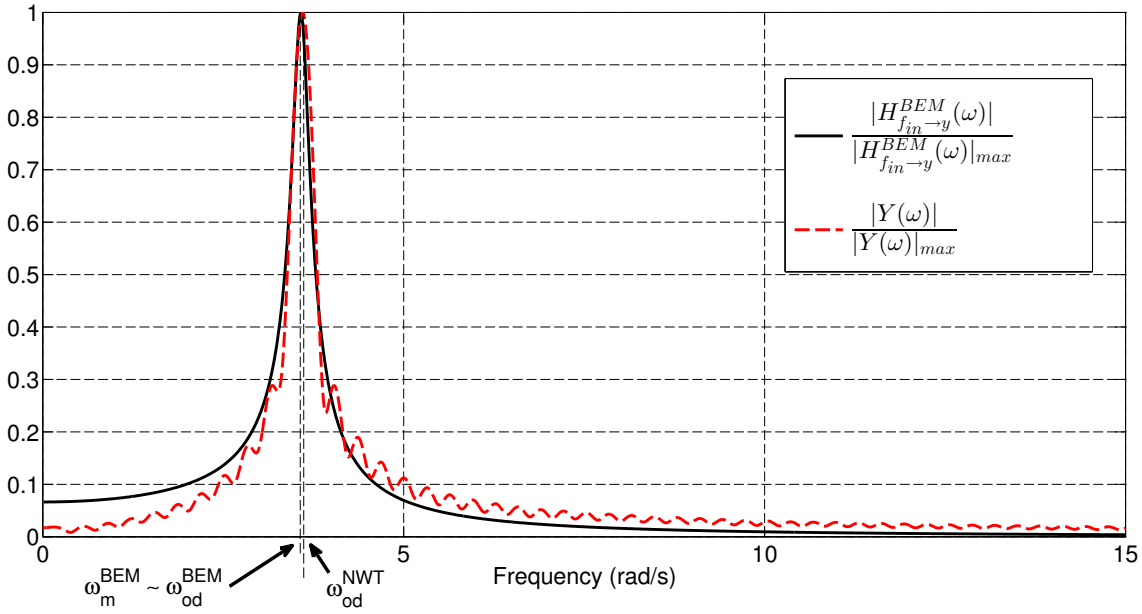

Figure 5.16: Graphical comparison of ω_{od}^{NWT} and ω_{od}^{BEM}. The peak of $|Y(\omega)|$ (for the free decay experiment with a 5 cm initial displacement) occurs at $\omega_{od}^{NWT} = 3.6$ rad/s, and the peak of $|H_{f_{in}\to y}^{BEM}(\omega)|$ occurs at $\omega_m^{BEM} \simeq \omega_{od}^{BEM} = 3.57$ rad/s.

5.3 Hydrodynamic WEC model description

As explained in Section 2.6.1, a large number of WEC models are based on the linear Cummins' equation, which can be implemented in different ways (e.g. constant-coefficient differential equation, transfer function, convolution integral and state-space model). The mathematical state-space description is very convenient for the analysis and design of control systems and is very common in the control engineering community. In this chapter, Cummins' equation is converted into a state-space model in two different steps. Initially, the radiation convolution sub-system is converted into a state-space model [74], which, subsequently, is introduced into a larger state-space model (here termed the Cummins' state-space model) [9] [11] [74] [75] [295]. As explained in Section

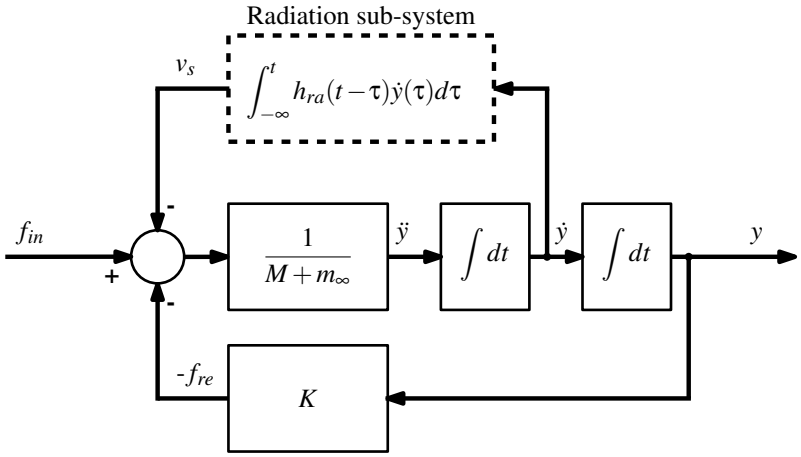

Figure 5.17: Cummins' equation block diagram; the dashed line highlights the radiation sub-system.

2.6.1, in Cummins' equation (2.86), the radiation sub-system is described by the LTI convolution

integral (see Fig. 5.17), given by:

$$v_s(t) = \int_{-\infty}^{t} h_{ra}(t-\tau)\dot{y}(\tau)d\tau, \tag{5.3}$$

and the reduced radiation impedance is given by equation (2.74):

$$H_{ra}(\omega) = \mathscr{F}\Big[h_{ra}(t)\Big] = N(\omega) + i\omega\big[m_a(\omega) - m_\infty\big]. \tag{5.4}$$

The radiation sub-system (5.3) can be represented by the state-space model given by:

$$\begin{aligned} \dot{\mathbf{x}}_\mathbf{s}(t) &= \mathbf{A_s}\mathbf{x_s}(t) + \mathbf{B_s}\dot{y}(t) \\ v_s(t) &= \mathbf{C_s}\mathbf{x_s}(t) \end{aligned} \tag{5.5}$$

where

$$\mathbf{x_s}(t) = \begin{bmatrix} x_{s.1}(t) & x_{s.2}(t) & \cdots & x_{s.n}(t) \end{bmatrix}^T \tag{5.6}$$

is the state vector, composed by n elements. Equation (2.99) becomes

$$g_{ra}(t) = \mathbf{C_s} e^{\mathbf{A_s}t}\mathbf{B_s} \tag{5.7}$$

and, from equations (2.100) and (2.94), it follows that:

$$G_{ra}(s) = \mathscr{L}\Big[g_{ra}(t)\Big] = \mathbf{C_s}(s\mathbf{I} - \mathbf{A_s})^{-1}\mathbf{B_s} = \frac{b_m s^m + ... + b_1 s + b_0}{s^n + a_{n-1}s^{n-1} + ... + a_1 s + a_0} \tag{5.8}$$

The Fourier transform of $g_{ra}(t)$ is given by:

$$G_{ra}(\omega) = \mathscr{F}\Big[g_{ra}(t)\Big] = G_{ra}(s)\Big|_{s=i\omega} = \frac{b_m(i\omega)^m + ... + b_1(i\omega) + b_0}{(i\omega)^n + a_{n-1}(i\omega)^{n-1} + ... + a_1(i\omega) + a_0} \tag{5.9}$$

The convolution integral (5.3) and the state-space model, of equation (5.5), are equivalent if $h_{ra}(t) = g_{ra}(t)$ (and consequently $H_{ra}(\omega) = G_{ra}(\omega)$, where $H_{ra}(\omega) = \mathscr{F}\Big[h_{ra}(t)\Big]$). This exact equivalence holds only for a state-space model of infinite order (i.e. $n = \infty$); however, an approximation is generally made to represent the convolution integral with a state-space model of finite order n, as:

$$Re\{G_{ra}(\omega)\} \simeq Re\{H_{ra}(\omega)\} = N(\omega) \tag{5.10}$$

and

$$Im\{G_{ra}(\omega)\} \simeq Im\{H_{ra}(\omega)\} = \omega\big[m_a(\omega) - m_\infty\big] \tag{5.11}$$

From equation (5.11), it follows that:

$$m_a(\omega) \simeq \frac{Im\{G_{ra}(\omega)\}}{\omega} + m_\infty \tag{5.12}$$

Furthermore, $G_{ra}(\omega)$ must also satisfy the properties of $H_{ra}(\omega)$, described by equations (2.75) - (2.80). A consequence of equations (2.75) and (5.9) is that:

$$\lim_{\omega\to 0} G_{ra}(\omega) = \frac{b_0}{a_0} = 0 \tag{5.13}$$

and, therefore, it follows [85] that:

$$b_0 = 0 \tag{5.14}$$

An implication of equations (2.76) and (5.9) is that:

$$\lim_{\omega\to\infty} G_{ra}(\omega) = \frac{b_m(i\omega)^m}{(i\omega)^n} = 0 \tag{5.15}$$

Therefore, since it it assumed that $b_m \neq 0$, it follows that $n > m$, which means that $G_{ra}(s)$ is strictly proper. A consequence of equations (A.8) and (2.79) is that:

$$\lim_{t \to 0^+} h_{ra}(t) = \lim_{s \to \infty} sY(s) = \lim_{s \to \infty} \frac{b_m s^{m+1}}{s^n} \neq 0 \tag{5.16}$$

and since $n > m$, it follows [85] that:

$$m = n - 1 \tag{5.17}$$

Therefore, by introducing equations (5.14) (5.17) in (5.8) and (5.9), it follows that:

$$G_{ra}(s) = \frac{b_{n-1}s^{n-1} + ... + b_1 s}{s^n + a_{n-1}s^{n-1} + ... + a_1 s + a_0} \tag{5.18}$$

$$G_{ra}(\omega) = \frac{b_{n-1}(i\omega)^{n-1} + ... + b_1(i\omega)}{(i\omega)^n + a_{n-1}(i\omega)^{n-1} + ... + a_1(i\omega) + a_0} \tag{5.19}$$

As explained in Section 2.6.1, there are many possible equivalent realisations of a state-space model. Here, for the state-space model described by equation (5.5), which is utilised for the radiation sub-system, the observable companion-form realisation is used, since it has the advantage of only requiring a small number of non-zero parameters, with $\mathbf{A_s}$, $\mathbf{B_s}$ and $\mathbf{C_s}$ given [74] [88] [144] [296] by:

$$\mathbf{A_s} = \begin{bmatrix} 0 & 0 & 0 & ... & 0 & -a_0 \\ 1 & 0 & 0 & ... & 0 & -a_1 \\ 0 & 1 & 0 & ... & 0 & -a_2 \\ \vdots & \vdots & \vdots & \ddots & \vdots & \vdots \\ 0 & 0 & 0 & ... & 0 & -a_{n-2} \\ 0 & 0 & 0 & ... & 1 & -a_{n-1} \end{bmatrix}, \tag{5.20}$$

$$\mathbf{B_s} = \begin{bmatrix} 0 & b_1 & b_2 & ... & b_{n-2} & b_{n-1} \end{bmatrix}^T \tag{5.21}$$

and

$$\mathbf{C_s} = \begin{bmatrix} 0 & 0 & 0 & ... & 0 & 1 \end{bmatrix}. \tag{5.22}$$

Cummins' equation (2.86) can be represented by an overall state-space model, which contains the state-space model (5.5) of the radiation sub-system [9] [11] [14]. The first step is to define new variables, as follows:

$$x_{n+1}(t) = y(t) \tag{5.23}$$

and

$$x_{n+2}(t) = \dot{x}_{n+1}(t) = \dot{y}(t) \tag{5.24}$$

and the new state vector as:

$$\mathbf{x}(t) = \Big[\underbrace{x_1(t) \ \ ... \ \ x_n(t)}_{\mathbf{x_s}(t)} \ \ x_{n+1}(t) \ \ x_{n+2}(t) \Big]^T \tag{5.25}$$

where $y(t)$ is the body displacement and $\mathbf{x_s}(t)$ is defined by equation (5.6). From equation (5.24), it follows that:

$$\dot{x}_{n+2}(t) = \ddot{y}(t) \tag{5.26}$$

By introducing equations (5.6), (5.22) and (5.24) into equation (5.5), it follows that:

$$\begin{aligned} \dot{\mathbf{x}}_\mathbf{s}(t) &= \mathbf{A_s}\mathbf{x_s}(t) + \mathbf{B_s}x_{n+2}(t) \\ v_s(t) &= \mathbf{C_s}\mathbf{x_s}(t) = x_n(t) \end{aligned} \tag{5.27}$$

By introducing equations (5.3), (5.23), (5.26) and (5.27) in equation (2.86), it follows that:

$$(M + m_\infty)\dot{x}_{n+2}(t) + x_n(t) + Kx_{n+1}(t) = f_{in}(t) \tag{5.28}$$

and, therefore, that:

$$\dot{x}_{n+2}(t) = -\frac{1}{M+m_\infty}x_n(t) - \frac{K}{M+m_\infty}x_{n+1}(t) + \frac{1}{M+m_\infty}f_{in}(t) \tag{5.29}$$

Equations (5.20), (5.21), (5.22), (5.25), (5.27) and (5.29) can be combined, in order to express Cummins' equation in the following state-space model [11] [14] [74] form:

$$\begin{aligned} \dot{\mathbf{x}}(t) &= \mathbf{A}\mathbf{x}(t) + \mathbf{B}f_{in}(t) \\ y(t) &= \mathbf{C}\mathbf{x}(t) \end{aligned} \tag{5.30}$$

where:

$$\mathbf{A} = \begin{bmatrix} 0 & 0 & 0 & \dots & 0 & -a_0 & 0 & 0 \\ 1 & 0 & 0 & \dots & 0 & -a_1 & 0 & b_1 \\ 0 & 1 & 0 & \dots & 0 & -a_2 & 0 & b_2 \\ \vdots & \vdots & \vdots & \ddots & \vdots & \vdots & \vdots & \vdots \\ 0 & 0 & 0 & \dots & 0 & -a_{n-2} & 0 & b_{n-2} \\ 0 & 0 & 0 & \dots & 1 & -a_{n-1} & 0 & b_{n-1} \\ 0 & 0 & 0 & \dots & 0 & 0 & 0 & 1 \\ 0 & 0 & 0 & \dots & 0 & -\frac{1}{M+m_\infty} & -\frac{K}{M+m_\infty} & 0 \end{bmatrix}, \tag{5.31}$$

$$\mathbf{B} = \begin{bmatrix} 0 & 0 & \dots & 0 & 0 & \frac{1}{M+m_\infty} \end{bmatrix}^{\mathbf{T}}, \tag{5.32}$$

$$\mathbf{C} = \begin{bmatrix} 0 & 0 & \dots & 0 & 1 & 0 \end{bmatrix}. \tag{5.33}$$

The linear hydrodynamic model, described by equations (5.25) and (5.30)-(5.33), is parametrised by $2n+2$ parameters (i.e. M, K, m_∞, a_0,...,a_{n-1}, b_1,...,b_{n-1}) and its output $y(t)$ is the superposition of the zero-input component and the zero-state component, evaluated as (see Section 2.6.1):

$$y(t) = \mathbf{C}e^{\mathbf{A}(t-t_0)}\mathbf{x}(t_0) + \int_{t_0}^{t} \mathbf{C}e^{\mathbf{A}(t-\tau)}\mathbf{B}f_{in}(\tau)d\tau \tag{5.34}$$

If $t_0 = 0$ and $f_{in}(t) = 0 \; \forall \, t$, then

$$y(t) = \mathbf{C}e^{\mathbf{A}t}\mathbf{x}(0). \tag{5.35}$$

Equation (5.35) describes the free decay oscillation of a floating body, where $x_{n+1}(0)$ represents the initial displacement of the body from its equilibrium position, and $x_{n+2}(0)$ the initial body velocity.

5.4 Hydrodynamic WEC model parameter identification

In Sections 5.2 and 5.3, the experimental data gathering and WEC model structure have, respectively, been explained. In this section, the fitting criterion and identification algorithm are illustrated in detail. In Section 5.4.1, the parameter vector is identified by using a proposed new strategy, based on NWT data. In Section 5.4.2, the parameter vector, of the same WEC model structure, is identified by using a traditional methodology, based on BEM data, which will be used as a benchmark for the new methodology. Both methodologies, presented in Sections 5.4.1 and 5.4.2, do not identify the body mass M; rather, they assume it as a known property of the WEC being investigated (M can be determined from a variety of numerical modelling tools, such as AutoCAD, or measured directly). Therefore, the model identification methodologies focus only on the $2n+1$ parameters, related to the restoring and radiation forces (i.e. K, m_∞, a_0,...,a_{n-1}, b_1,...,b_{n-1}).

5.4.1 Hydrodynamic WEC model parameter identification from free decay NWT data

The model parameter vector identification is carried out in two different steps, using NWT free decay data (as shown in the block diagram of Fig. 5.18):
• *The restoring term estimate.* From static fluid force and body displacement data sets, the restoring coefficient K is identified (best LS linear approximation of the linear/nonlinear restoring force), by utilising linear regression, as explained in Section 5.4.1.1.
• *The radiation and added mass terms estimate.* Once estimated K, the unknown parameters m_∞, a_0,..., a_{n-1}, b_1,..., b_{n-1} are identified, by fitting the free decay response of Cummins' state-space model with the data (nonlinear optimization), as explained in Section 5.4.1.2.

5.4.1.1 Restoring term estimate

As explained in Section 2.2.7, in the case where a body has a variable horizontal cross-sectional area, the restoring force is a nonlinear function of the body displacement, and is given by:

$$f_{re}(y) = \rho g \Delta V_b(y) \tag{5.36}$$

where $\Delta V_b(y)$ is the submerged body volume variation, obtained by moving the body from its static equilibrium. Equation (5.36) can be approximated with the linear equation given by:

$$f_{re}(y) = -Ky \tag{5.37}$$

where $K > 0$ is the restoring coefficient, which is identified with a LS fitting. Fig. 5.19 shows a general example of a nonlinear $f_{re}(y)$ curve and its linear approximation, which is graphically represented by a straight line with slope $-K$, passing through the origin. The NWT data $\{y(t_j)\}$ and $\{f_{re}(t_j)\}$ (for $j = 1,...,N$) can be utilised as input and output data, respectively, for the LS identification of the model, described by equation (5.37). Therefore, equations (3.41) (3.42) (3.43) (3.47) and (3.49) become, respectively:

$$\hat{f}_{re}(t_j) = \boldsymbol{\varphi}(t_j)^T \boldsymbol{\theta}_{re}, \tag{5.38}$$

$$\boldsymbol{\varphi}(t_j) = \Big[-y(t_j) \Big], \tag{5.39}$$

$$\boldsymbol{\theta}_{re} = \big[K \big], \tag{5.40}$$

$$\mathbf{y} = \big[f_{re}(t_1) \quad f_{re}(t_2) \quad ... \quad f_{re}(t_N) \big]^T, \tag{5.41}$$

and

$$\boldsymbol{\Phi} = \begin{bmatrix} -y(t_1) \\ -y(t_2) \\ \vdots \\ -y(t_N) \end{bmatrix}. \tag{5.42}$$

Equation (5.38) shows that the model is linear in the parameter vector $\boldsymbol{\theta}_{re}$ (in this case, the parameter vector is composed of one element). As explained in Section 3.3.1.1, the estimated parameter vector $\hat{\boldsymbol{\theta}}_{re}$ is determined by employing a QR factorization. It is important to note that the identified K can be considered an average restoring effect, which may change, depending on the identification data. In contrast, in the case of identification from BEM data (see Section 5.4.2) the identified restoring term depends only on the cross-sectional area of the body at equilibrium, since infinitesimally small deviations around the equilibrium position are assumed in LPT. Therefore, in the case where K is identified from BEM data, the identified linear restoring curve is always tangential to the nonlinear restoring curve at the origin, as shown in Fig. 5.19.

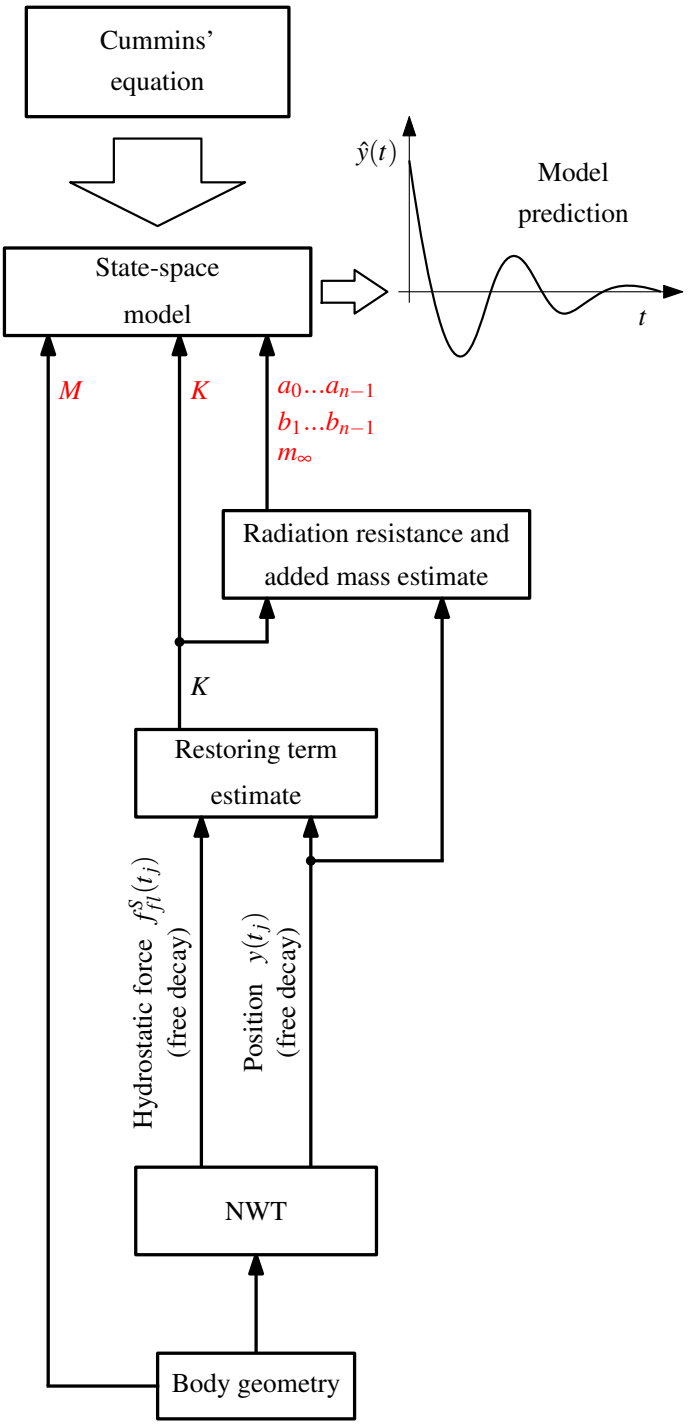

Figure 5.18: Block diagram of the sequence of steps to estimate the model parameter vector, from a NWT free decay experiment.

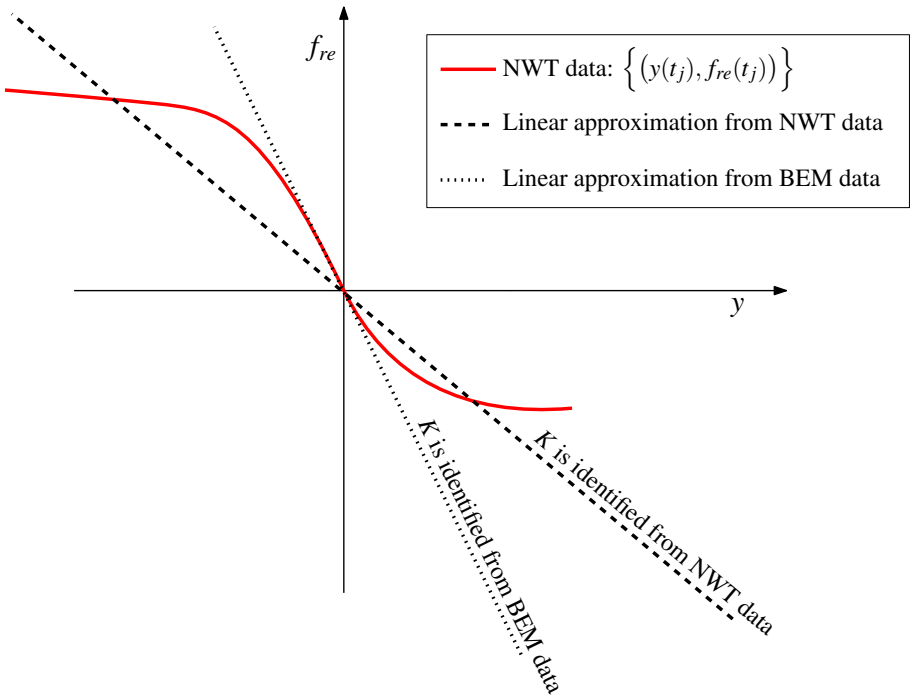

Figure 5.19: Graphical representation of the estimated linear restoring force from NWT and BEM data. The slope of the lines is equal to $-K$.

5.4.1.2 Radiation resistance and added mass estimate

Once K is identified, using the methodology explained in Section 5.4.1.1, the unknown parameter vector $\boldsymbol{\theta} = [m_\infty \; a_0 \ldots a_{n-1} \; b_1 \ldots b_{n-1}]$ of Cummins' state-space model, described by equations (5.25) and (5.30)-(5.33) is identified by fitting the model free decay prediction from NWT data. The model free decay prediction is given by equation (5.35), where all the elements of $\mathbf{x}(0)$ are null, excluding $x_{n+1}(0)$, which is set equal to the initial displacement of the NWT experiment utilised (note that $x_{n+1}(t) = \hat{y}(t)$). The free decay model prediction, $\hat{y}$, and the free decay NWT data, y, are fitted with a LS criteria, given by:

$$\hat{\boldsymbol{\theta}} = \underset{\boldsymbol{\theta}}{argmin}\, J(\boldsymbol{\theta}) \tag{5.43}$$

where

$$J(\boldsymbol{\theta}) = \sum_q \left| y(t_q) - \hat{y}(t_q, \boldsymbol{\theta}) \right|^2 \tag{5.44}$$

and $\hat{\boldsymbol{\theta}}$ is the parameter vector giving the best LS fit. The optimization problem, in equations (5.43)-(5.44), is nonlinear in the parameters, with a strong sensitivity to the initial seed $\boldsymbol{\theta}_0$, caused by a loss function with multiple local minima (see Section 3.3.2).

An important aspect of any identification problem is the use of prior available information regarding the process under study, which is, in this case, a body floating on water, characterised by the properties of stability and passivity [86] (passivity describes an intrinsic characteristic of systems that can store and dissipate energy but not create it, as outlined in Section 2.4.1.2); therefore, it is desirable that the identified model inherits these properties, in order to ensure compatibility with the process [86]. Consequently, given the linear hydrodynamic model, described by equations (5.25) and (5.30)-(5.33), it is necessary to find constraints on the parameters, in order to guarantee the properties of passivity and stability for both the radiation sub-system (5.5) and Cummins' state-space model (5.30). In the current work, new *a priori* constraints on the parameters $C_j^{in}(\boldsymbol{\theta}) \leq 0$, for $j = 1, ..., N_c$, are introduced into the optimization, in order to guarantee the stability and passivity of both the radiation state-space model (5.5) and the Cummins'state-space model (5.30). Therefore, the unconstrained optimization problem of equations (5.43)-(5.44) becomes the constrained

optimization problem:

$$\begin{cases} \hat{\boldsymbol{\theta}} = \underset{\boldsymbol{\theta}}{argmin}\, J(\boldsymbol{\theta}) \\ C_j^{in}(\boldsymbol{\theta}) \leq 0 \quad \text{for} \;\; j = 1,...,N_c \end{cases} \tag{5.45}$$

where $J(\boldsymbol{\theta})$ is given by equation (5.44). For linear-time-invariant systems, a necessary and sufficient condition for passivity is that the real part of the transfer function is positive for all frequencies (positive realness) [86] [157]. It is important to note that Cummins' equation (2.86) has the structure of a negative feedback interconnection, as shown in Fig. 5.20, where the blocks, highlighted by the dash-dotted line, represent the passive forward path [85] [157] and the radiation sub-system is the feedback path. Since a negative feedback interconnection of passive systems is passive [85] [157], the Cummins' state-space model, described by equation (5.30), is passive if and only if the radiation state-space model, described by equation (5.5) is passive (i.e. $Re[G_{ra}(\omega)] \geq 0 \;\; \forall\, \omega$).

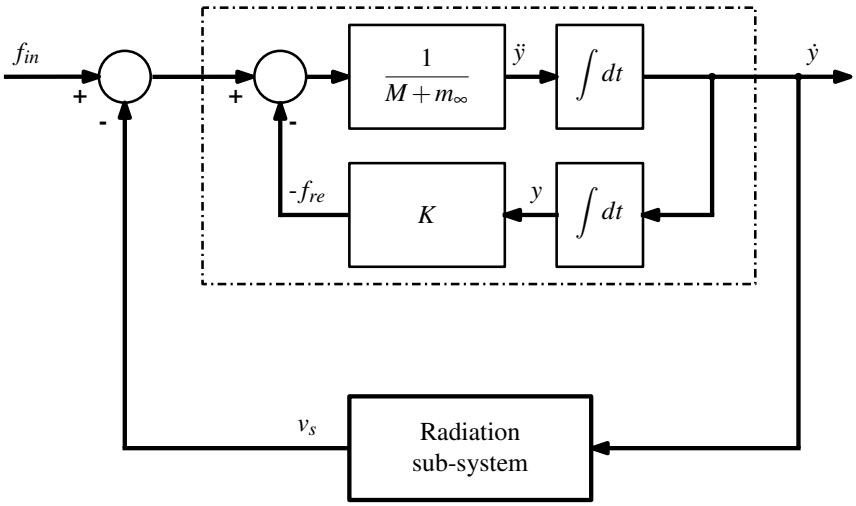

Figure 5.20: Negative feedback structure of Cummins' equation.

The stability of the radiation sub-system, expressed as a Laplace rational transfer function, can be tested by applying the Routh-Hurwitz stability criterion (see Appendix A.7) to the polynomial in the denominator of equation (5.18), in order to find analytical constraints on the parameters a_i, for $i = 0,...,(n-1)$. The poles p_1,...,p_{n+2} of Cummins' state-space model (5.30) correspond to the $n+2$ eigenvalues of the matrix $\mathbf{A}$, given by equation (5.31). The stability of Cummins' state-space model is guaranteed by introducing the nonlinear constraints $Re[p_i] \leq 0$, for $i = 1,...,(n+2)$, into the optimization constraints $\mathbf{C}^{in}(\boldsymbol{\theta}) = [C_1^{in}(\boldsymbol{\theta}) \;...\; C_{N_c}^{in}(\boldsymbol{\theta})]$. It is not straightforward to find an analytical expression in order to calculate the real part of the poles p_1,...,p_{n+2} with respect to the parameter vector $\boldsymbol{\theta}$, but it is possible to resolve the problem numerically. The nonlinear constrained problem, expressed by equations (5.45), is solved by converting it into a sequence of nonlinear unconstrained problems. The main idea is to iteratively call the unconstrained optimization algorithm, by using the solution of the previous iteration. For this reason, this methodology is also termed sequential unconstrained minimization technique (SUMT) [297] [298]. The new unconstrained optimization problem is obtained by combining the original loss function, $J(\boldsymbol{\theta})$, and the constraints, $C_j^{in}(\boldsymbol{\theta})$, where $j = 1,..,N_c$, in a new augmented Lagrangian function, J_{ALF}, (also termed the Lagrangian barrier function) [298][299][300], defined as:

$$J_{ALF}(\mathbf{q}, \boldsymbol{\lambda}, \boldsymbol{\theta}) = J(\boldsymbol{\theta}) - \sum_{j=1}^{Nc} \lambda_j \log\left(q_j - C_j^{in}(\boldsymbol{\theta})\right) \tag{5.46}$$

where $\lambda_j \geq 0$ are the Lagrange multipliers , $q_j \geq 0$ are the shifts, $\boldsymbol{\lambda} = [\lambda_1,...,\lambda_{N_c}]$ and $\mathbf{q} = [q_1,...,q_{N_c}]$. By controlling the change of the λ_j and q_j values, it is possible to generate a se-

quence of unconstrained problems, which have solutions converging to the solution of the original constrained problem, given by equation (5.45) [297]. Fig. 5.21 shows the block diagram for the solution of the original constrained problem, by utilising J_{ALF}. In equation (5.46), when $q_j = 0$,

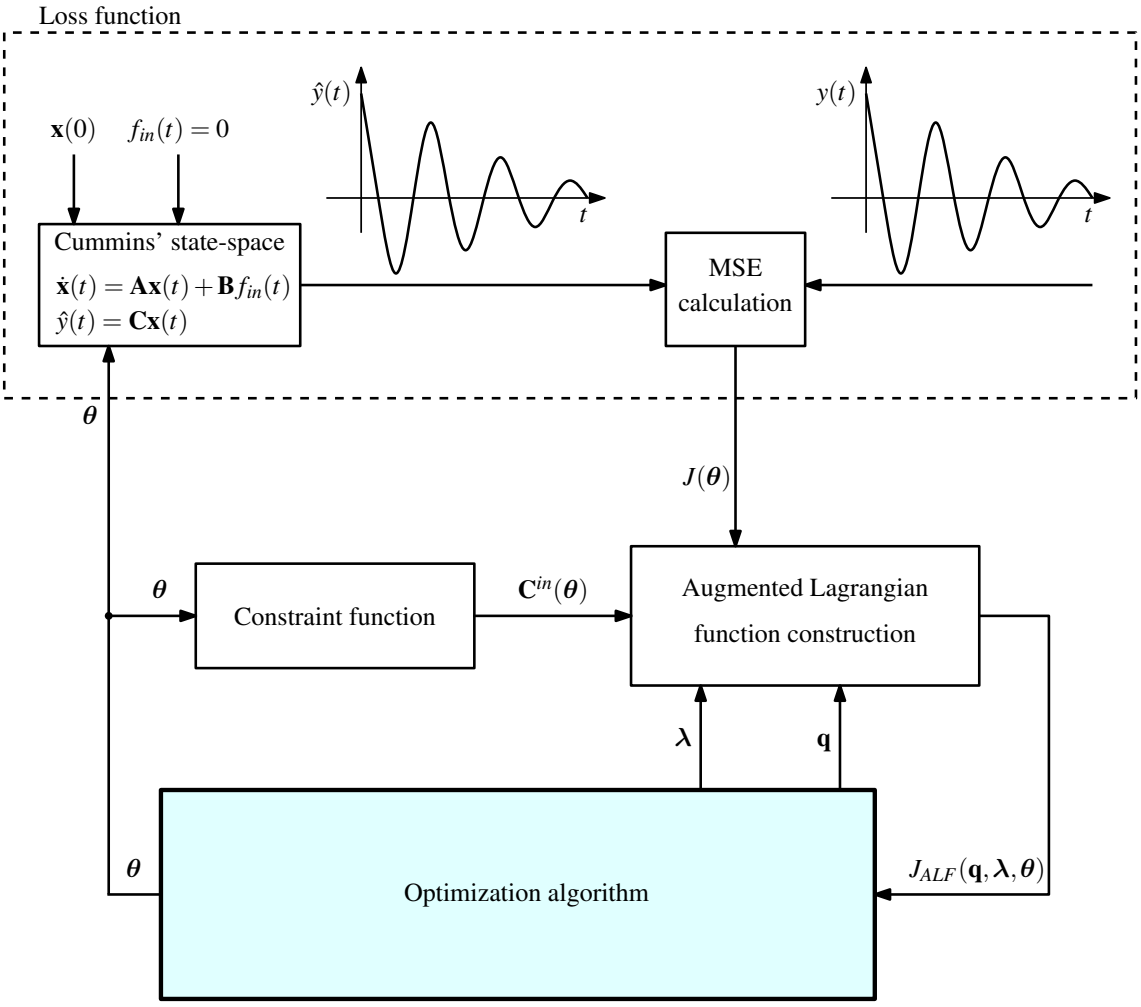

Figure 5.21: Block diagram of the optimization methodology to estimate the 2n parameters $\boldsymbol{\theta} = [m_\infty \; a_0 \ldots a_{n-1} \; b_1 \ldots b_{n-1}]$. Since only free decay experiments are considered, the external force f_{in} is set to zero.

and $\boldsymbol{\theta}$ moves from the feasible region (the region where constraints are satisfied, i.e. $C_j^{in}(\boldsymbol{\theta}) \leq 0$) toward the infeasible region (the region where constraints are violated, i.e. $C_j^{in}(\boldsymbol{\theta}) > 0$), approaching the feasible region border (see Fig. 5.22), it follows that $C_j^{in}(\boldsymbol{\theta}) \to 0^-$, $-\log(-C_j^{in}(\boldsymbol{\theta})) \to \infty$ (see Fig. 5.22(b)) and $J_{ALF}(\boldsymbol{\theta}) \to \infty$. Therefore, the border between the feasible and infeasible regions represents an infinite barrier for the optimization algorithm (the final effect is that the optimization is indirectly constrained) [299]. Each i-th sub-problem is characterised by different $\boldsymbol{\lambda}^{(i)}$ and $\mathbf{q}^{(i)}$ values, which are kept constant for the same sub-problem; therefore, each i-th sub-problem has a different shape of $J_{ALF}^{(i)}(\boldsymbol{\theta})$. In order to ensure that a good global solution of the i-th optimization sub-problem is achieved (and therefore a good global solution of the original constrained problem), a GA search method is employed (see Section 3.3.2.2), which maintains a number of candidate solutions spread across the search space, preventing the algorithm getting trapped in a local minimum. In particular, a Matlab implementation of a GA as a solver is utilised. The GA optimization has been set to have in each generation 300 individuals, 2 elite children that automatically survive to the next generation and about 50% of children generated with crossover and 50% with mutation (see Section 3.3.2.2). The algorithm stops when the value of the mean

1	a_0	0
a_1	0	0
c_1	c_2	0

Table 5.1: Table utilised for the Routh-Hurwitz stability criterion.

squared error is less than 10^{-15} or the number of generations reaches 100. By resolving each i-th optimization sub-problem, the sequences $\{\mathbf{q}^{(i)}\}$, $\{\boldsymbol{\lambda}^{(i)}\}$ and $\{J^{(i)}_{ALF}(\boldsymbol{\theta})\}$ are generated, which have the properties [267]:

$$\mathbf{q}^{(i)} \underset{i\to\infty}{\longrightarrow} \mathbf{0} \tag{5.47}$$

$$\boldsymbol{\lambda}^{(i)} \underset{i\to\infty}{\longrightarrow} \mathbf{0} \tag{5.48}$$

$$J^{(i)}_{ALF}(\boldsymbol{\theta}) \underset{i\to\infty}{\longrightarrow} J(\boldsymbol{\theta}) \tag{5.49}$$

The presence of the shift $\mathbf{q}^{(i)}$, in equation (5.46), avoids the inherent ill-conditioning, which is present in classical barrier-function methods [299]. Fig. 5.23 shows an example of $\{J^{(i)}_{ALF}(\boldsymbol{\theta})\}$ sequence generation, in order to resolve a constrained optimization problem.

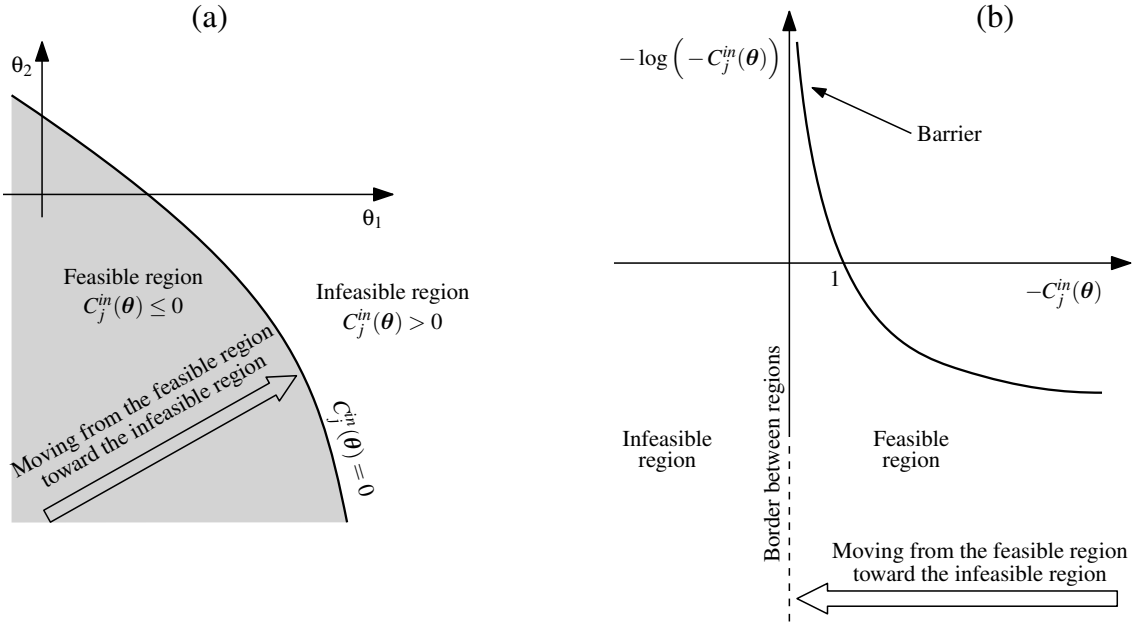

Figure 5.22: (a) Feasible and infeasible regions in the parameter plane (in this case, $\boldsymbol{\theta} = (\theta_1, \theta_2) \in \Re^2$). (b) The introduction of $-\log\left(-C^{in}_j(\boldsymbol{\theta})\right)$ terms, in an augmented Lagrangian function, creates a barrier between the feasible and infeasible regions.

The approximation of the radiation convolution integral (5.3) with a model having a transfer function (5.18) with $n = 2$, provides a good trade-off between accuracy and complexity [74]. Therefore, in the case of $n = 2$, the Cummins' state space (5.30) is of order 4, and the transfer function of the radiation sub-system, given by equation (5.18), becomes:

$$G_{ra}(s) = \frac{b_1 s}{s^2 + a_1 s + a_0} \tag{5.50}$$

By applying the Routh-Hurwitz stability criterion to the denominator of equation (5.50), Table

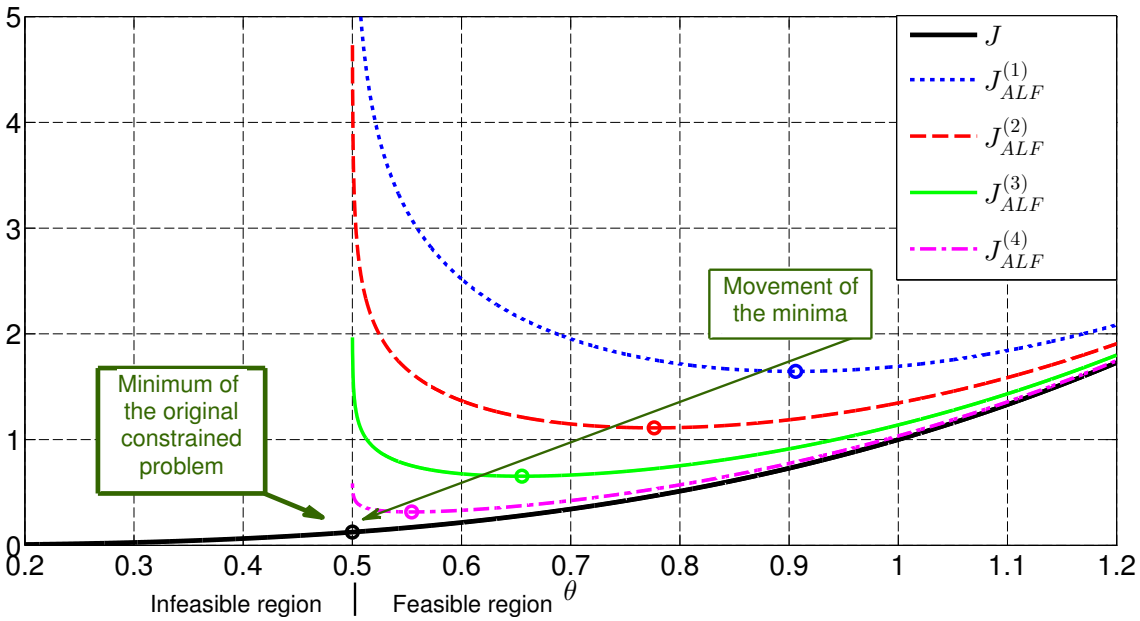

Figure 5.23: Example of $\left\{J^{(i)}_{ALF}(\boldsymbol{\theta})\right\}$ sequence generation, in the case of the minimization of $J(\theta) = \theta^3$, under the constraint $\theta \geq 0.5$, which leads to $C^{in} = 0.5 - \theta \leq 0$. In the case where q=0, it follows that $J^{(i)}_{ALF}(\lambda^{(i)}, \theta) = \theta^3 - \lambda^{(i)} \log(\theta - 0.5)$. The plotted curves are obtained for $\lambda^{(1)} = 1$, $\lambda^{(2)} = 0.5$, $\lambda^{(3)} = 0.2$ and $\lambda^{(4)} = 0.05$. The arrow shows that the minima of the $J^{(i)}_{ALF}(\lambda^{(i)}, \theta)$ converge to the minimum of the original constrained problem, represented by J.

A.1 of Appendix A.7, becomes Table 5.1, with $a_2 = 1$, and equation (A.29) becomes:

$$c_1 = \frac{-\det\begin{vmatrix} 1 & a_0 \\ a_1 & 0 \end{vmatrix}}{a_1} = \frac{a_1 a_0 - 1 \times 0}{a_1} = a_0 \tag{5.51}$$

The stability of the linear system (5.50) is guaranteed if there is no algebraic sign change in the elements of the first left column of Table 5.1, which is given by:

$$\begin{bmatrix} 1 & a_1 & a_0 \end{bmatrix}^T \tag{5.52}$$

and, therefore, if and only if:

$$a_1 > 0 \tag{5.53}$$

and

$$a_0 > 0 \tag{5.54}$$

Under the condition $n = 2$, equation (5.31) becomes:

$$\mathbf{A} = \begin{bmatrix} 0 & -a_0 & 0 & 0 \\ 1 & -a_1 & 0 & b_1 \\ 0 & 0 & 0 & 1 \\ 0 & -\frac{1}{M+m_\infty} & -\frac{K}{M+m_\infty} & 0 \end{bmatrix}, \tag{5.55}$$

and the stability of Cummins' state-space model, described by (5.30), is guaranteed if the four eigenvalues p_q of the matrix (5.55), which correspond to the poles of the system, satisfy the conditions:

$$Re\left[p_q\right] \leq 0 \quad \text{for } q = 1, \ldots, 4 \tag{5.56}$$

The study of the passivity of the radiation sub-system is carried out by calculating the Fourier transfer function of the system represented by the Laplace transfer function (5.50); therefore:

$$\begin{aligned} G_{ra}(\omega) &= G_{ra}(s)\Big|_{s=i\omega} = \frac{b_1 i\omega}{(i\omega)^2 + a_1 i\omega + a_0} = \frac{ib_1\omega}{[(a_0-\omega^2)+ia_1\omega]}\frac{[(a_0-\omega^2)-ia_1\omega]}{[(a_0-\omega^2)-ia_1\omega]} \\ &= \frac{a_1 b_1\omega^2 + ib_1\omega(a_0-\omega^2)}{(a_0-\omega^2)^2 + a_1^2\omega^2} \end{aligned} \tag{5.57}$$

From equations (5.10) and (5.57), it follows that:

$$N(\omega) \simeq Re\Big[G_{ra}(\omega)\Big] = \frac{a_1 b_1\omega^2}{(a_0-\omega^2)^2 + a_1^2\omega^2} \tag{5.58}$$

Therefore, $N(\omega) \geq 0 \ \ \forall\omega$, which represents the condition for the passivity of system (5.50), is true if and only if:

$$a_1 b_1 \geq 0 \tag{5.59}$$

From equations (5.53), (5.54), (5.56) and (5.59), it follows that, in the case of $n = 2$, the full set of optimization constraints are given by:

$$\begin{cases} C_1^{in}(\boldsymbol{\theta}) = -a_0 \leq 0 \\ C_2^{in}(\boldsymbol{\theta}) = -a_1 \leq 0 \\ C_3^{in}(\boldsymbol{\theta}) = -b_1 \leq 0 \\ C_4^{in}(\boldsymbol{\theta}) = Re[p_1] \leq 0 \\ C_5^{in}(\boldsymbol{\theta}) = Re[p_2] \leq 0 \\ C_6^{in}(\boldsymbol{\theta}) = Re[p_3] \leq 0 \\ C_7^{in}(\boldsymbol{\theta}) = Re[p_4] \leq 0 \end{cases} \tag{5.60}$$

Therefore, in the case of $n = 2$, equations (5.43), (5.44) and (5.60) represent the nonlinear constrained optimization problem, whose solution is shown in Section 5.5.

5.4.2 Hydrodynamic WEC model parameter identification from BEM data

A well established method to develop linear hydrodynamic models consists of using the frequency-dependent coefficients calculated by a BEM software package (see Section 2.4), in order to identify the parameter vector of Cummins' equation, which is approximated with a parametric model structure (see Section 2.6.1). This modelling approach has the advantage of obtaining models from limited information about the vessel, such as hull form and mass distribution, as shown in Fig. 5.24. Given the linear model structure, described by equations (5.25) and (5.30)-(5.33), it is necessary to find the $2n+1$ parameters K, m_∞, a_0,...,a_{n-1}, b_1...b_{n-1} (M is assumed to be known). The BEM software package (in this case WAMIT) provides the hydrodynamic coefficients K, m_∞ , $\{N(\omega_j)\}$ and $\{m_a(\omega_j)\}$ for $j = 1,2,...,N_\omega$, which can be used, together with equation (5.4), to calculate the reduced radiation impedance, given by:

$$H_{ra}(\omega_j) = N(\omega_j) + i\omega_j\big[m_a(\omega_j) - m_\infty\big], \tag{5.61}$$

as shown in the block diagram of Fig. 5.24. As explained in Section 5.3, the Fourier transfer function $G_{ra}(\omega_j,\boldsymbol{\theta})$ of the radiation-sub-system (5.5), is given by equation (5.19), which is a parametric approximation of the reduced radiation impedance (5.61). Therefore, it is possible to determine the unknown parameter vector $\boldsymbol{\theta}_{bem} = [a_0 \ ... \ a_{n-1} \ b_1 \ ... \ b_{n-1}]$ with a complex LS frequency response curve fitting method [85] [86] [88] [155], given by:

$$\hat{\boldsymbol{\theta}}_{bem} = \underset{\boldsymbol{\theta}_{bem}}{argmin} \sum_j \big|H_{ra}(\omega_j) - G_{ra}(\omega_j,\boldsymbol{\theta}_{bem})\big|^2 \tag{5.62}$$

which is a nonlinear optimization problem (see Section 3.3.2). In [165] and [74], stability and passivity properties are not considered during the model identification procedure, and no post

identification strategies are proposed, in order to obtain a stable and passive model. In [85] [86] [155] [157], stability is not enforced as a constraint and, consequently, the resulting radiation sub-system model, obtained by the LS minimization, may not necessarily be stable. Their proposed solution, after identification, is the reflection of the unstable poles from the right-hand side to the left-hand side of the complex plane, thus obtaining a suboptimal solution. In [85] [86] [155] [157] passivity is not introduced as a constraint and, therefore, the resulting radiation sub-system model, obtained by the LS minimization, may not necessarily be passive. Their proposed solution is to try different order approximations and choose the one that is passive. The restoring coefficient K, calculated by BEM software, is given by equation (2.37), which shows that K is proportional to the body horizontal cross-sectional area, A_{cr}, at the equilibrium position, as shown in Fig. 4.28. The hydrodynamic model identification method, explained in this section, is implemented in the well known MSS toolbox by Perez & Fossen [155], which uses a Gauss-Newton search algorithm (see Section 3.3.2.2) to resolve the nonlinear optimization problem (5.62). In Section 5.5, the linear hydrodynamic model, identified with the method explained in this section, is termed a boundary element method identified model (BEM-IM), as shown in Fig. 5.25.

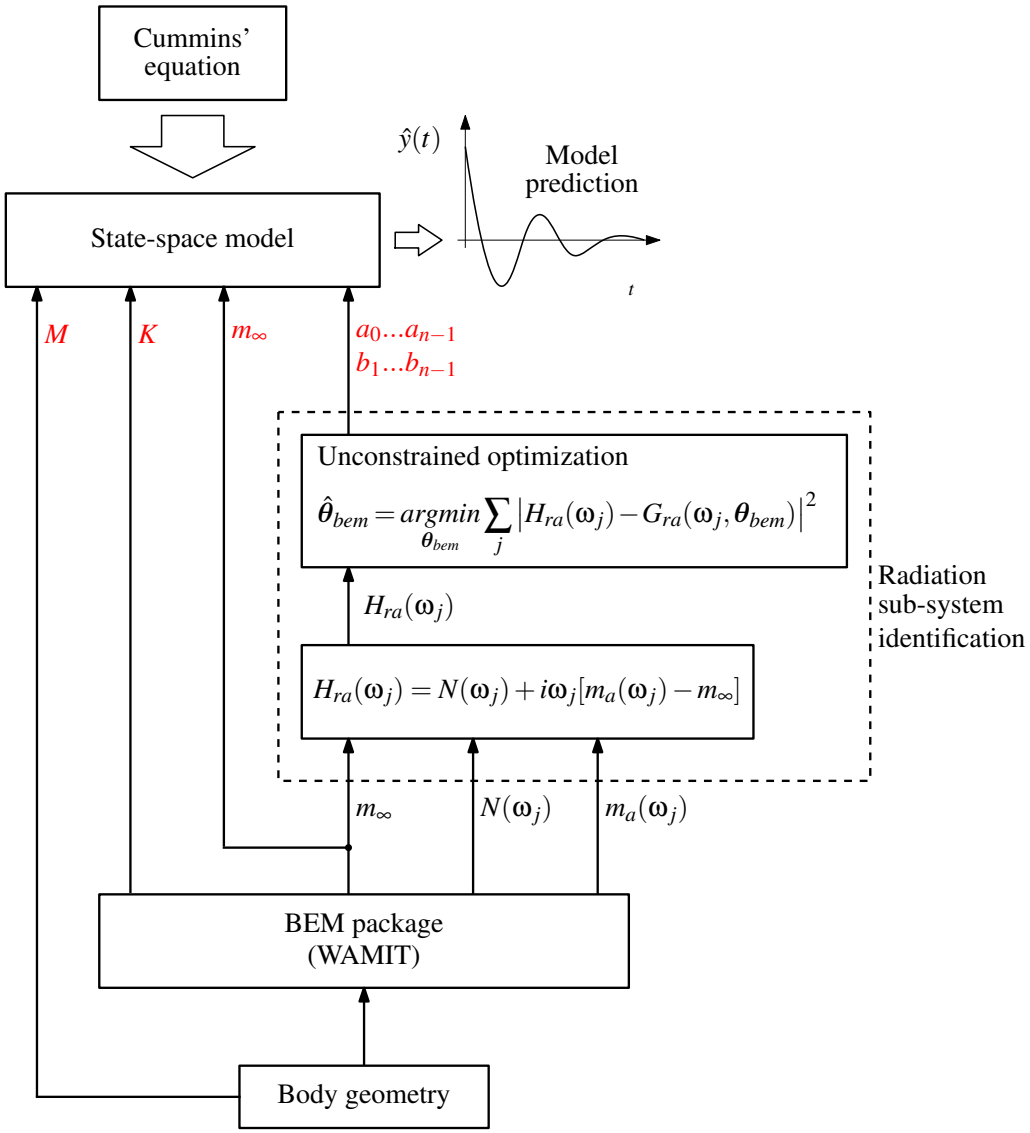

Figure 5.24: Block diagram of the sequence of steps to identify the BEM-IM model, from BEM data.

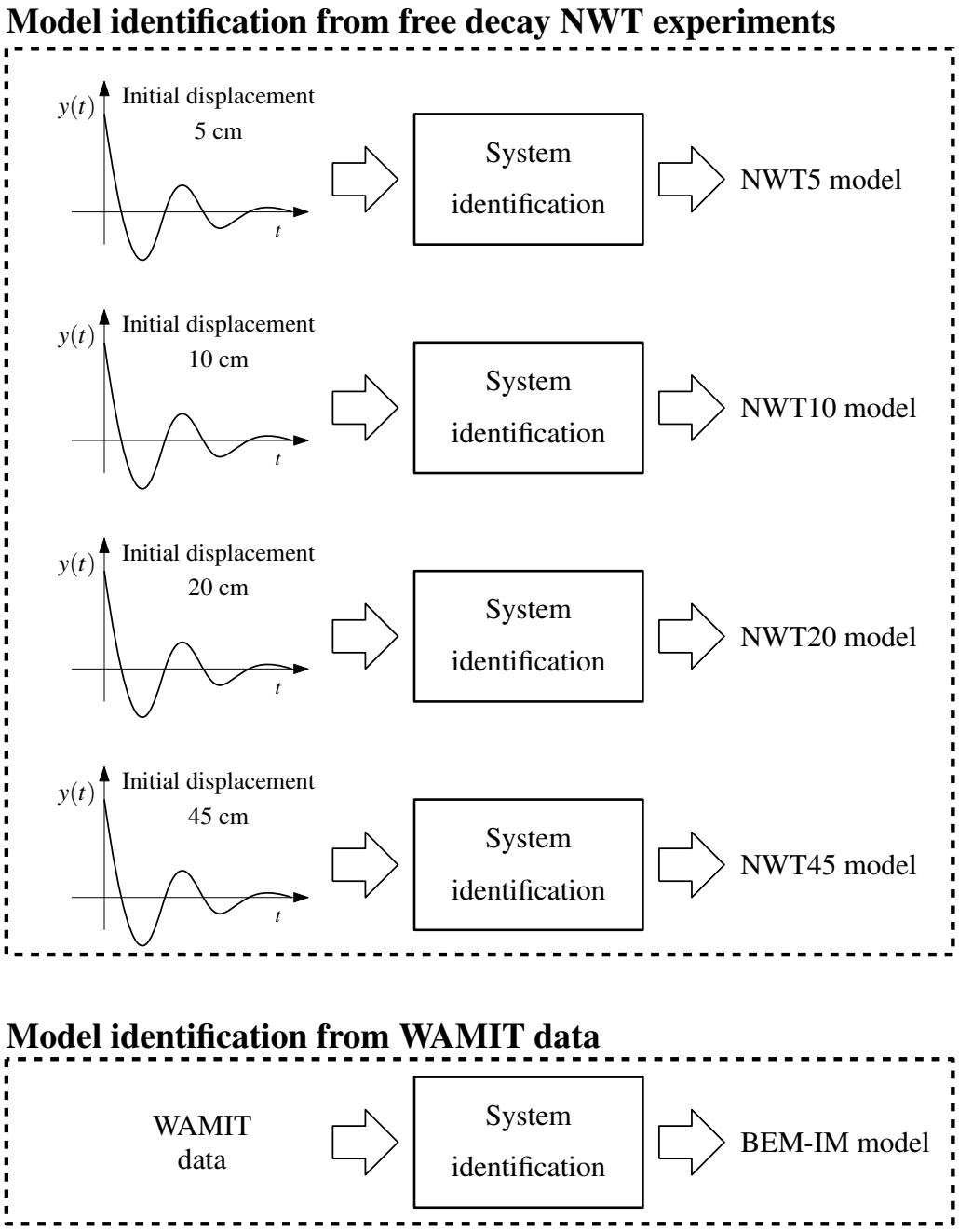

Figure 5.25: Four different free decay NWT experiments are available, characterised by initial body displacement equal to 5, 10, 20 and 45 cm. From each experiment a linear model is identified (denoted NWT5, NWT10, NWT20 and NWT45, respectively).The BEM-IM model's radiation parameter vector is identified using the toolbox by Perez&Fossen [155], taking as input the frequency domain hydrodynamic coefficients, calculated by using the BEM software WAMIT.

Model	$\hat{K}$ (N/m)	$\hat{a}_0$	$\hat{a}_1$	$\hat{b}_1$	$\hat{m}_\infty$ (kg)
NWT5	7704.8	6.1647	1.9037	468.35	245.31
NWT10	7704.7	8.1343	2.3840	760.35	254.77
NWT20	7704.8	8.5645	3.1069	1383.9	255.99
NWT45	7704.4	12.6962	9.7500	5398.7	244.44
BEM-IM	7681.6	7.6393	1.8582	315.82	230.20

Table 5.2: Estimated model parameters.

5.5 Results

As explained in Section 5.2, four different free decay NWT experiments are available, characterised by initial body displacement equal to 5, 10, 20 and 45 cm; from each experiment, a linear model is identified (see Section 5.4.1), denoted NWT5, NWT10, NWT20 and NWT45, respectively, as shown in Fig. 5.25 (the number in the name represents the initial amplitude of the free decay experiment from which the model is determined; i.e. NWT20 is the model whose parameters are determined from the free decay experiment, with 20 cm as initial amplitude). In this section, the performance of the models, identified by the new methodology based on NWT data, are compared to the performance of the traditional BEM-IM (see Section 5.4.2), which is used as a benchmark. The five identified models NWT5, NWT10, NWT20, NWT45 and BEM-IM have the same model structure, given by equations (5.25) and (5.30)-(5.33), where the radiation sub-system has order $n = 2$, as explained in Section 5.4.1.2; the only distinction between the five models is represented by the values of the parameters K, m_∞, a_0, a_1 and b_1, which are shown in Table 5.2. The cylindrical body, investigated in this case study, has a constant cross-sectional area; therefore, its hydrostatic restoring curve is a linear function of the displacement away from its equilibrium position. This is confirmed by the graph of Fig. 5.26 of the restoring force versus body position, for the 45 cm initial amplitude NWT experiment, which is shown in Fig. 5.27. The utilised cylindrical body is characterised by $K = \rho g A_{cr} = 997 \times 9.81 \times 0.5^2 \times \pi = 7681.6$ N/m. The results in Table 5.2 show excellent agreement for the restoring force parameter, K, across all five models. The value of the remaining four parameter m_∞, a_0, a_1 and b_1 vary between the different models, in an attempt to model the significant variation between the different sets of free response data. These response differences, evident in Fig. 5.11, show more significant damping for larger initial amplitudes (and subsequent oscillations).

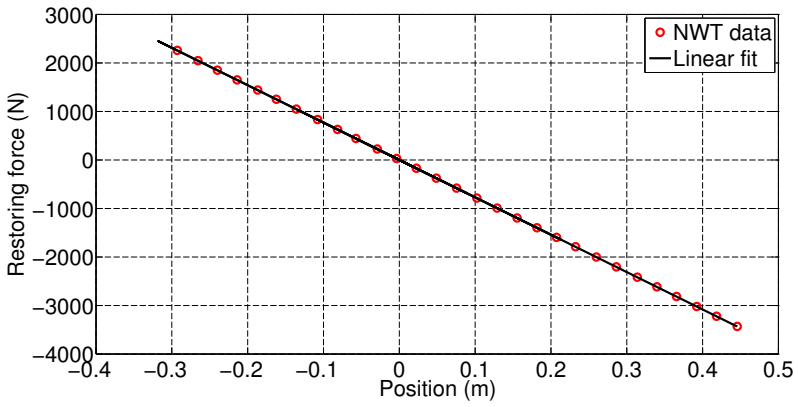

Figure 5.26: Restoring force vs. position for the free decay experiment with 45 cm initial displacement, and its calculated linear fit to obtain the parameter K.

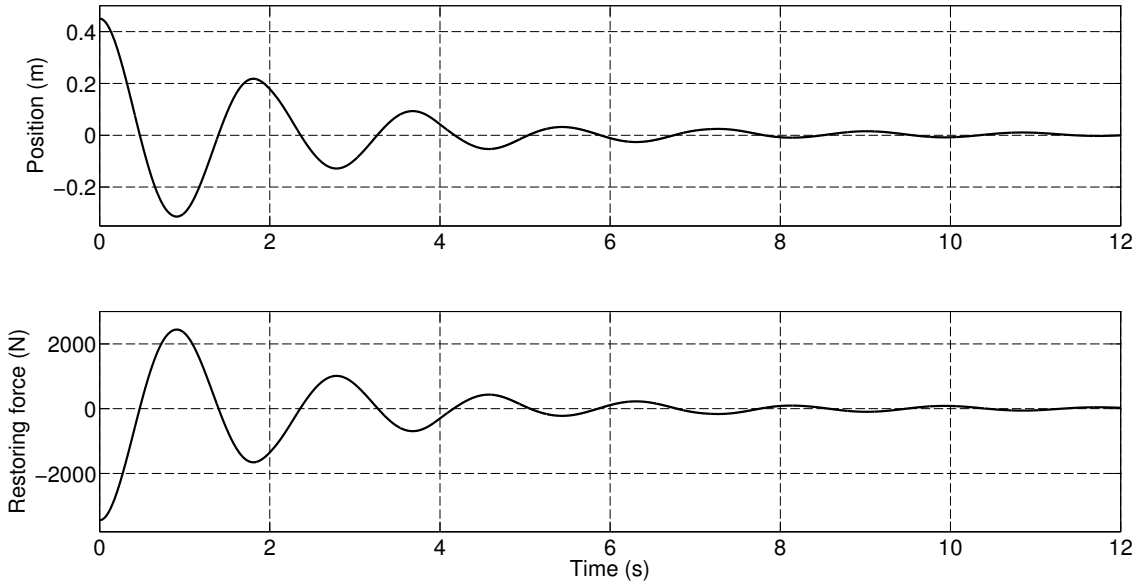

Figure 5.27: Time evolution of the body position and restoring force, for the free decay experiment with 45 cm initial displacement.

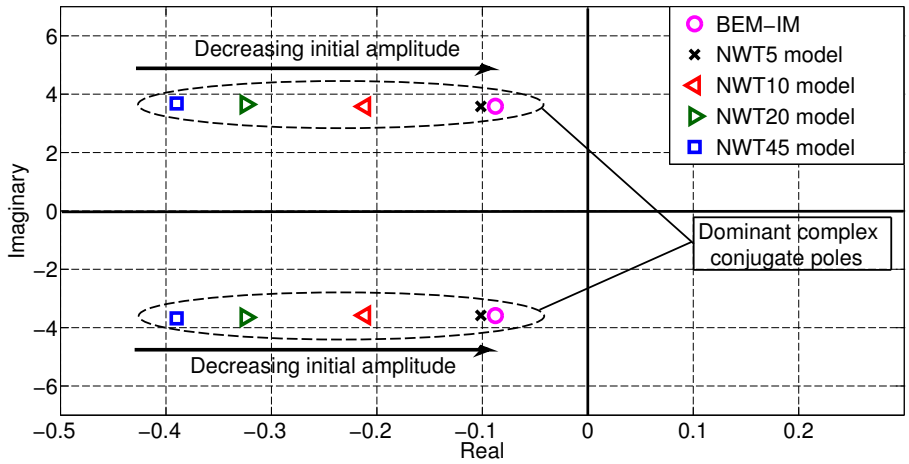

Figure 5.28: Location on the complex-plane of the dominant poles of Cummins' state-space model, described by equation (5.30).

The calculation of the model poles can provide a useful analysis tool. For a stable linear system, the dominant poles are those closest to the imaginary axis and represent slower modes i.e. lower damping effects (the oscillations decay more slowly). Fig. 5.28 shows that the models, whose parameters are determined from the larger initial amplitude conditions, do indeed have stronger damping than for models determined from the smaller amplitude conditions, mainly due to nonlinear viscous damping during the initial phase; the arrows in Fig. 5.28 show this trend. The only form of energy dissipation of the five identified models (i.e. BEM-IM, NWT5, NWT10, NWT20 and NWT45 models) is through the radiation term $N(\omega)$, given by equation (5.10). All the different dissipative effects, modelled by CFD (viscosity, vortex shedding and, as well as, wave radiation), are all therefore encapsulated into the radiation term of the linear models. Each identified model is characterised by a different radiation sub-system, represented by $N(\omega)$ and $m_a(\omega)$, which can be calculated with equations (5.10) and (5.12), respectively. Fig. 5.29 plots the radiation resistances for the different identified models and shows that the models, identified from NWT data with larger initial amplitude, have larger radiation resistances, as predicted by the information shown in Figs. 5.11 and 5.28. Fig. 5.29 also shows that the radiation resistances, of the

identified models, satisfy the properties $\lim_{\omega\to 0} N(\omega) = 0$, $\lim_{\omega\to\infty} N(\omega) = 0$ and $N(\omega) \geq 0 \; \forall \; \omega$, which are described by equations (2.75), (2.76) and (2.78), respectively. Fig. 5.30 shows that the added mass, given by equation (5.12), also varies between the different models. Figs. 5.28, 5.29 and 5.30 show that, the models identified from NWT data, by decreasing the initial body amplitude, converge to the model identified from BEM data, as expected.

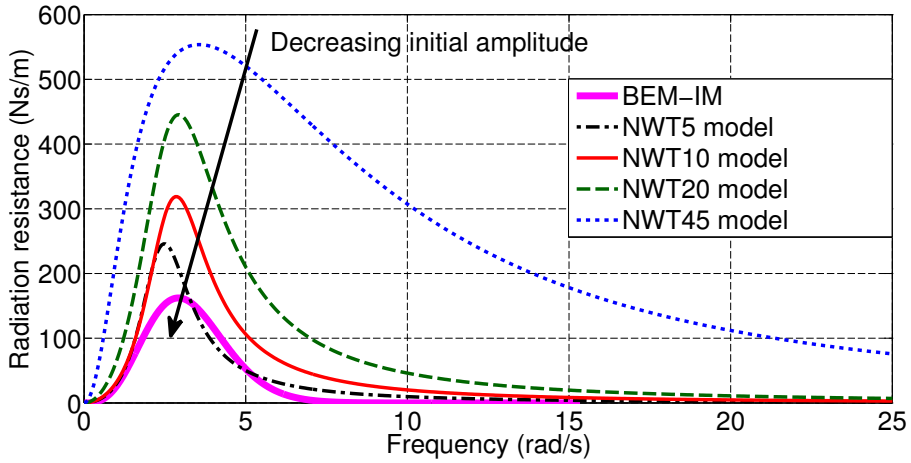

Figure 5.29: Radiation resistance of the linear systems identified from NWT experiments and WAMIT data.

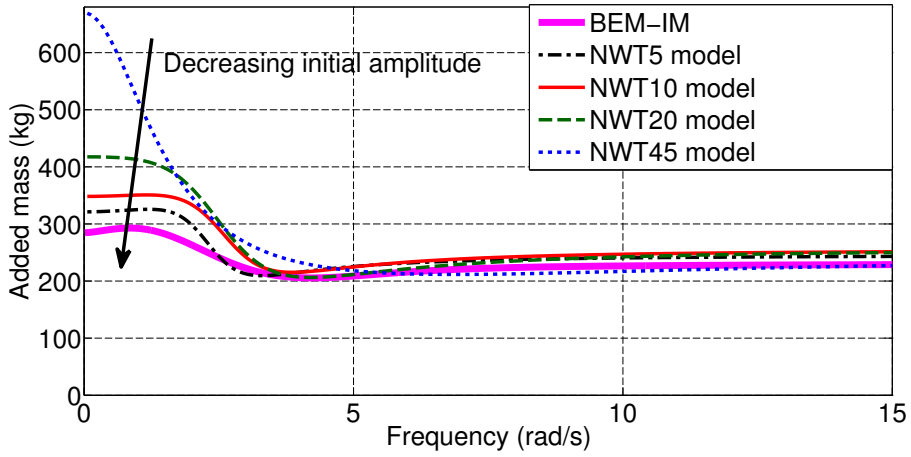

Figure 5.30: Added mass of the linear systems identified from NWT experiments and WAMIT data.

It is important to stress that the five identified models are representative in the NWT operating (amplitude) region they are identified from, which can be graphically represented by the free decay body position-velocity-planes, shown in Fig. 5.31. It is possible to see that the space bounded by the 5 cm free decay spiral, in Fig. 5.31(a), is significantly smaller than the space bounded by the 45 cm free decay spiral, in Fig. 5.31(d). The space bounded by the BEM data is just a point at the origin of the position-velocity-plane. Each model represents the 'best' linear model able to repeat the nonlinear NWT behaviour, inside the whole bounded region is identified from, which loses fidelity as it tries to predict system behaviour away from this region.

This is shown in Fig. 5.32, which plots the NWT data from the 45 cm free decay experiment, together with the free decay predictions of the different models, when given an initial amplitude of 45 cm. As expected, the NWT45 model predicts closest to the NWT experimental data, since it is the exact dataset the model was identified from. The other model predictions are progressively

worse, the further their initial amplitude is from the 45 cm point. The BEM-IM model has the worst fit, which is also expected, considering it is identified from WAMIT data, which represents the body hydrodynamics for an infinitesimally small deviation around the equilibrium position. In order to further illustrate the loss in fidelity of the linear models, as they try to predict the system behaviour for different amplitudes, Table 5.3 lists the NRMSE percentage between the different model predictions and the four different NWT experiment data sets. The NRMSE percentage is defined as:

$$NRMSE\% = 100\frac{\sqrt{\sum_q \left|y(t_q)-\hat{y}(t_q)\right|^2}}{\sqrt{\sum_q \left|y(t_q)\right|^2}} \tag{5.63}$$

where $\hat{y}$ is the model prediction and y the NWT free decay oscillation. Table 5.3 shows that each model predicts well in the response region it was identified from, and then predicts progressively worse, as the initial amplitude becomes larger or smaller than the initial amplitude of the data, which the model was identified from. It is important to underline that the identification regions, shown in Fig. 5.31, are of increasing sizes and contained one inside another, like Russian Matryoshka dolls; the model, identified from a larger region, has to average its behaviour on the whole identification region, losing accuracy if is validated exclusively in a smaller region. By comparing Figs. 5.31(d) and 5.33, it is possible to see that, in the case of an initial displacement of 45 cm, the trajectory converges faster to the equilibrium position in the body position-velocity-plane, than the trajectory starting from 5 cm, as expected from the presence of stronger dissipative nonlinearities, such as viscosity and vortex shedding, in the case of 45 cm initial displacement. As expected, the best performance of the BEM-IM model is for the experiment with a 5 cm initial displacement, which is the closest experiment to an infinitesimally small deviation around the equilibrium position. However, even for the small 5 cm experiment, the NWT5 model performs better than the BEM-IM model, indicating that nonlinearities are already present in the data.

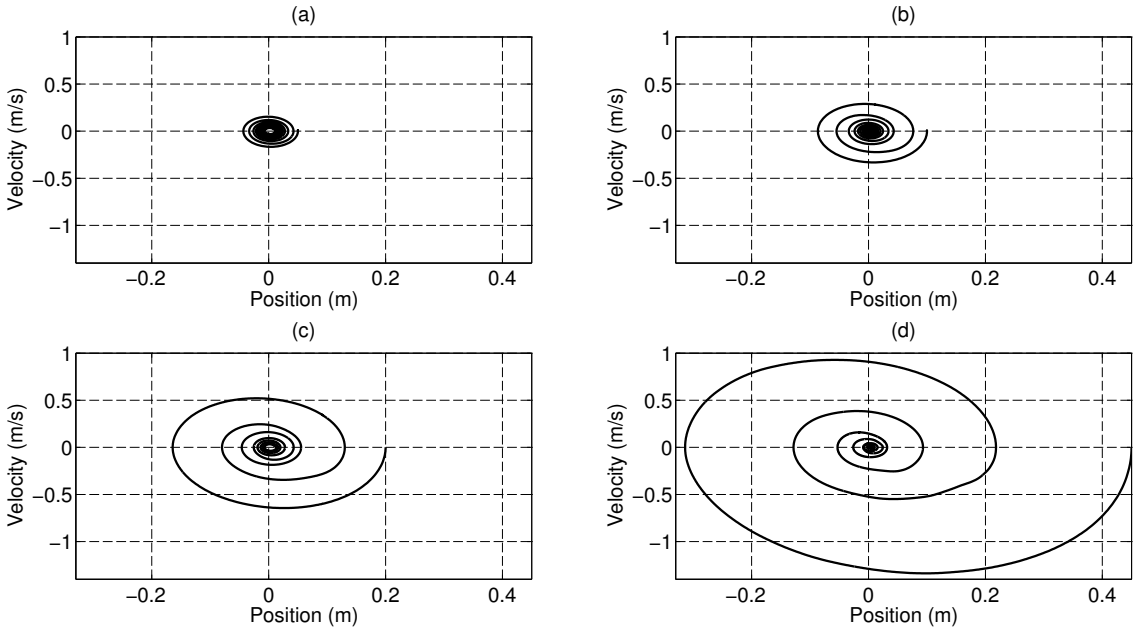

Figure 5.31: Body position-velocity-plane, for the four NWT free decay experiments, with different initial conditions: (a) 5 cm, (b) 10 cm, (c) 20 cm and (d) 45 cm.

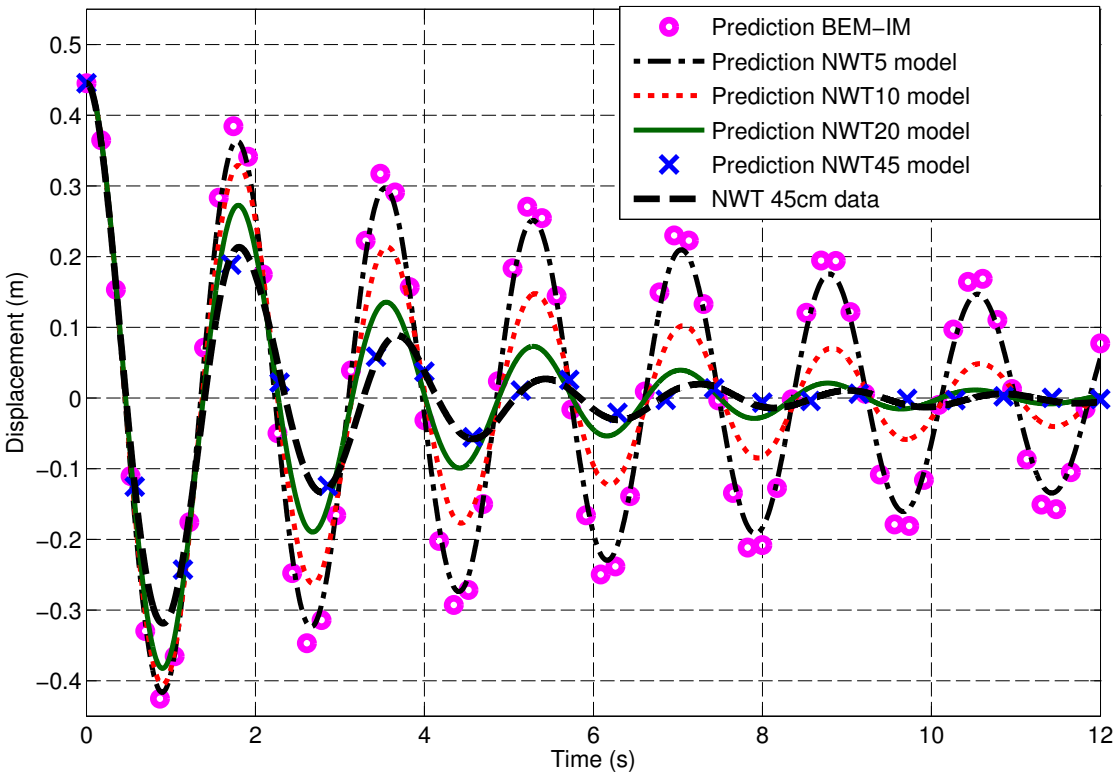

Figure 5.32: Free decay predictions by BEM-IM, NWT5, NWT10, NWT20 and NWT45 models, for the same initial displacement 45 cm. Also plotted the NWT simulation, with initial displacement of 45 cm.

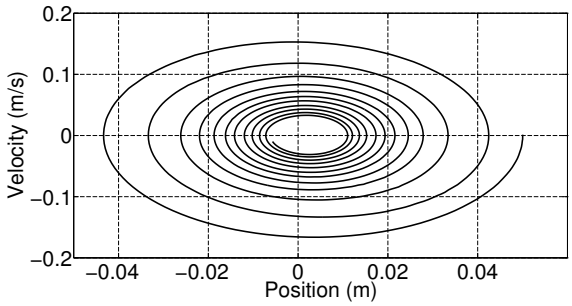

Figure 5.33: Body position-velocity-plane, for the NWT free decay experiments with initial displacement of 5 cm (zoom of Fig. 5.31(a)).

		Experiment initial amplitude			
		5 cm	10 cm	20 cm	45 cm
Model	NWT5	**4.35**%	34.0%	54.0%	67.6%
	NWT10	43.4%	**7.32**%	28.6%	46.5%
	NWT20	83.3%	34.1%	**7.54**%	26.4%
	NWT45	123%	65.9%	31.0%	**7.93**%
	BEM-IM	**10.8**%	55.7%	98.2%	140.6%

Table 5.3: NRMSE% between the predictions by the NWT5, NWT10, NWT20, NWT45 and BEM-IM, models and the NWT data with initial conditions 5, 10, 20 and 45 cm. The best result for each model is highlighted in bold.

It is interesting to underline that the identification method, utilised in this chapter with NWT data, can be utilised in the case of RWT data, by just introducing a small variation to the method. Indeed, the restoring term identification requires knowledge of the restoring force (which can be obtained by the static heave force, as shown in equation (5.2)) versus the body displacement (see Section 5.4.1.1), which can be obtained in a RWT by utilising a prescribed motion experiment (see Section 4.3.2.4), as shown in Fig. 5.34.

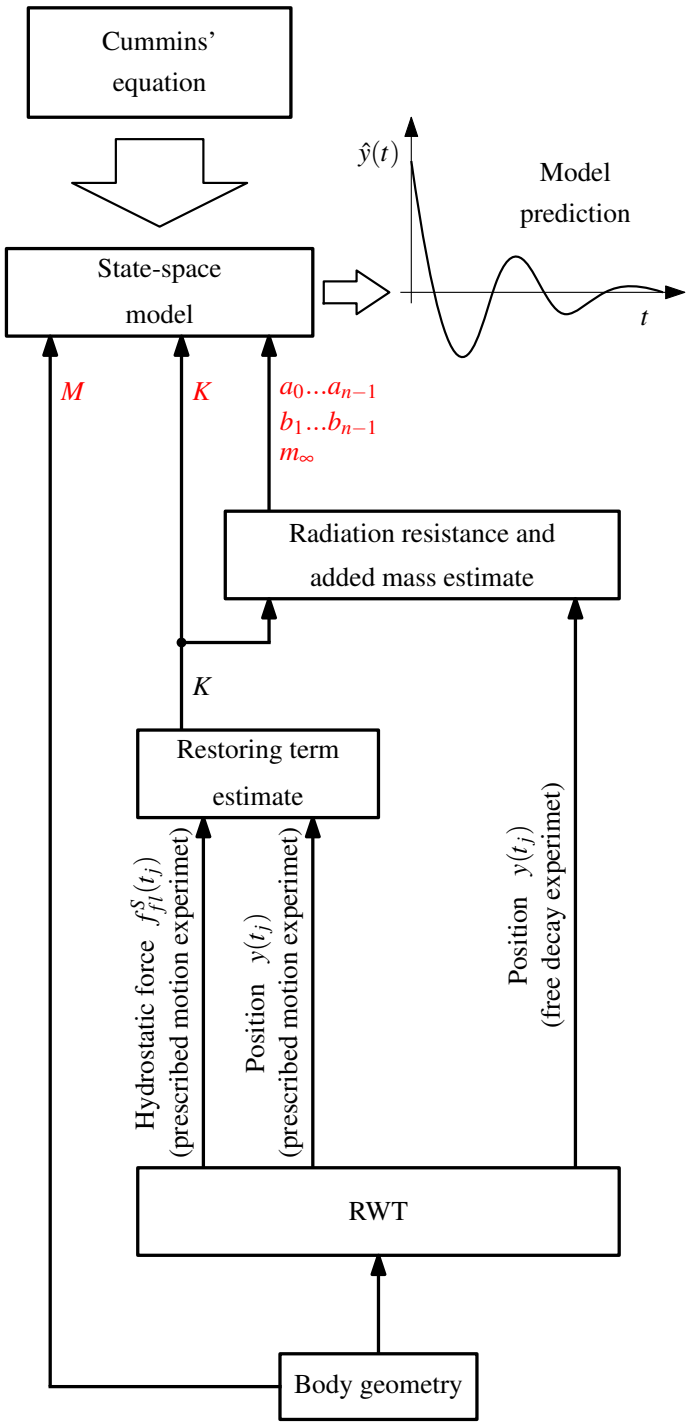

Figure 5.34: Block diagram of the sequence of steps to estimate the model parameter vector, from RWT data, by utilising free decay and prescribed motion experiments.

5.6 Summary and discussion

In this chapter, a new methodology for linear hydrodynamic parametric model identification is presented, which is based on the use of CFD-NWT data, instead of traditional LPT-BEM data. The major improvement is due to the fact that LPT is based on strong assumptions, which totally remove hydrodynamic nonlinear effects, such as viscosity, nonlinear restoring force and vortex shedding. Since SI techniques can introduce into the model only the information contained in the identification data, the models identified from LPT-BEM data are not able to describe nonlinear hydrodynamic effects. On the other hand, NWT data contain the full range of effects, described by the Navier-Stokes equations, obtained by paying the price of a high computation time. The main ingredients of SI, i.e. experimental data gathering, model structure selection and fitting criterion and identification algorithm selection (see Section 3.1.1), are presented in Sections 5.2, 5.3 and 5.4, respectively. Four different NWT free decay experiments, characterised by initial body displacement of 5, 10, 20 and 45 cm, are generated in the NWT, by utilising a floating vertical cylinder with a 391.5 kg mass, 0.5 m radius and 0.5 m draft. The normalization of the free decay body displacement, against their initial value, shows the presence of significant nonlinear damping effects in the data, such as viscosity and vortex shedding. Each experiment is utilised to identify a linear model. An additional model, BEM-IM, is identified from traditional BEM data, and utilised as a benchmark for the performance of the other models. The results of this chapter show that models, whose parameters are determined from the larger initial amplitude conditions, have larger damping effects than models determined from the smaller amplitude conditions. The comparison of model predictions shows that each model is representative of the region it is identified from. The results, obtained from the BEM-IM model, quickly lose fidelity, as the oscillation amplitudes become significant (which is a serious limitation of linear potential theory). Even in the experiment with the smaller initial condition of 5 cm, the NWT5 model performs better than the BEM-IM model, which shows that the BEM-IM model is not describing nonlinearities, already present in the experimental data. Furthermore, the linear models NWT5, NWT10, NWT20 and NWT45 are representative in the operating amplitude region they are identified from, and then lose fidelity as they try to predict WEC behaviour away from this region (as shown by the identification on a free decay experiment and the validation on the other three free decay experiments). The results of this chapter indicate that different linear models are required to represent different operating amplitudes (which can be associated with different sea states). Since NWT data can be simulated for different operating regions, this gives the present method an advantage over LPT-BEM, as LPT-BEM only gives parameters valid only for very small operating condition. The ability to develop different linear models locally representative of different operating regions opens the door for adaptive models (and possibly adaptive control) approaches, which switch between different representative linear models at different operating conditions. The convergence of the hydrodynamic models, derived through the proposed identification method, to those obtained by using BEM data, as the oscillation amplitude asymptotically approaches zero (i.e. dominant complex conjugate poles, radiation resistance and added mass), provides a confirmation of the quality of the proposed modelling approach. The presented methodology shows the power of model complexity reduction, based on SI and NWT-CFD data, by providing identified models, able to behave similarly to CFD models, but with the important advantage of a reduced computation time. The drawback of the new methodology, proposed in this chapter, is the use of CT model structures, which leads to nonlinear optimization, with a strong sensitivity to the initial seed, caused by a loss function with multiple local minima. In Chapters 6 and 7, nonlinear DT model structures, linear in the parameters, are proposed in order to obtain identification methods, based on linear optimization from NWT and RWT data, respectively,

Chapter 6

Identification of DT hydrodynamic parametric models from input/output NWT experiments

6.1 Introduction

In Section 3.2 Cummins' equation is used to provide the general hydrodynamic model structure, shown in Fig. 6.1, where:
• $\eta \rightarrow y$ denotes the family of all models (linear or nonlinear) having the FSE as input and the body displacement as output.
• $f_{in} \rightarrow y$ denotes the family of all models (linear or nonlinear) having $f_{in}(t) = f_e(t) + f_{pto}(t) + f_m(t)$ as input and the body displacement as output, where f_e, f_{pto} and f_m are the excitation, PTO and mooring forces, respectively.
• $\eta \rightarrow f_e$ denotes the family of all models (linear or nonlinear) having the FSE as input and the excitation force as output.

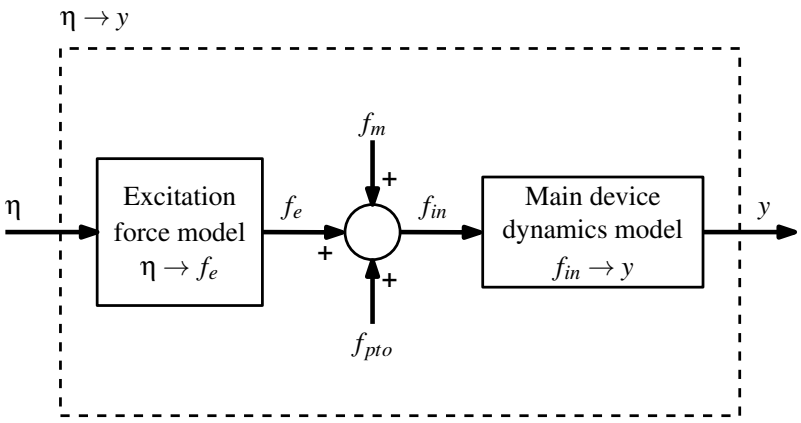

Figure 6.1: General block diagram of a WEC model, inspired by Cummins' equation. The blocks $\eta \rightarrow f_e$, $f_{in} \rightarrow y$ and $\eta \rightarrow y$ can be linear or nonlinear.

In Chapter 5, a case study for the identification of CT state-space models from NWT experiments is presented, underlining that CT model structures provide a good insight into system understanding since, usually, CT models are derived from physical principles and the model parameters are strongly related to the physical system properties. In Chapter 5, the main drawback of the use of CT model structures involves the consequent adoption of nonlinear optimization strate-

gies, which are necessary in order to identify the model parameter vector, since the loss function, associated with the CT model structure, is characterised by the presence of multiple local minima and, therefore, a strong sensitivity to the initial optimization seed. In this chapter, DT model structures are utilised, which have the disadvantage of losing the physical meaning of the parameters (see Section 3.2.3) but, on the other hand, DT model structures provide greater flexibility in the construction of nonlinear input/output model structures, which are linear in the parameters (see Section 3.1.1), with the consequent employment of convex optimization. Furthermore, as explained in Section 3.2.3, DT models have other important advantages over CT models (i.e. the nature of DT data is particularly compatible with digital computer calculations, the majority of SI techniques are based on discrete-time models and, from the point of view of control applications, DT model descriptions are more suitable). In this chapter, a variety of DT model structures (i.e. ARX, Hammerstein, FBO, ANN and KGP models), belonging to the model families $\eta \rightarrow y$, $f_{in} \rightarrow y$ and $\eta \rightarrow f_e$, are identified from CFD-NWTs, by carrying out input wave excitation force, prescribed motion, input force and input wave body motion experiments, (see Section 4.3).

This chapter is laid out as follows: Section 6.2 describes the identification of DT models, belonging to the $\eta \rightarrow f_e$ model family, from 2D CFD-NWT data, for the case study of three different infinitely long horizontal bars, having the vertical cross-sections of a triangle, a circle and a box; with Section 6.2.1 explaining the utilised NWT and floating body, Section 6.2.2 illustrating the generated NWT data, Section 6.2.3 describing the model structures employed and their identification, and Section 6.2.4 showing model performance and results.
Section 6.3.1 describes a first case study of DT model identification, belonging to the $f_{in} \rightarrow y$ model family, from 3D CFD-NWT data, for the case study of a conical floating body; with Section 6.3.1.1 explaining the NWT and floating body employed, Section 6.3.1.2 illustrating the generated NWT data, Section 6.3.1.3 describing the utilised model structures and their identification, and Section 6.3.1.4 showing model performance and results.
Section 6.3.2 describes a second case study of DT model identification, belonging to the $f_{in} \rightarrow y$ model family, from 2D CFD-NWT data, for the case study of an infinitely long horizontal cylinder; with Section 6.3.2.1 explaining the utilised NWT and floating body, Section 6.3.2.2 illustrating the generated NWT data, Section 6.3.2.3 describing the model structures employed and their identification, and Section 6.3.2.4 showing model performance and results.
Section 6.4 describes the identification of DT models, belonging to the $\eta \rightarrow y$ model family, from 2D CFD-NWT data, for the case study of an infinitely long horizontal cylinder; with Section 6.4.1 explaining the utilised NWT and floating body, Section 6.4.2 illustrating the generated NWT data, Section 6.4.3 describing the model structures employed and their identification, and Section 6.4.4 showing model performance and results. Finally, a summary and discussion are presented in Section 6.5.

6.2 Identification of $\eta \rightarrow f_e$ models (a case study)

The study of the dynamics of a WEC requires the knowledge of all the forces applied on the WEC, in particular, the force applied by the incident waves to the body (excitation force). When the body is in motion, the excitation force is not directly measurable; however, the excitation force is a vital variable required by energy maximising control systems [301] and, in the absence of a direct measurement, a suitable model is required in order to produce an excitation force estimate. In this section, the attention is focused on modelling the relationship between the undisturbed FSE, η, measured in a stationary position that corresponds to the center of mass of the body, and the excitation force, f_e, that is the force experienced by the body when it is held fixed in the presence of waves (see Section 2.4.1.1). In the context of linear models, based on the hypotheses of small waves, inviscid and incompressible fluid, the relationship between η and f_e can be described in the time domain via a convolution integral or, in frequency domain, with a transfer function (see Section 2.4.1.1). When the wave amplitude increases, becoming of the same order of magnitude of the dimensions of the body, some nonlinear effects may appear, and the use of nonlinear input/output model structures has to be considered. In this case study, three different NARX DT model structures (see Section 3.2.3), belonging to the $\eta \rightarrow f_e$ model family (see Fig. 6.2), are considered, i.e. ARX, Hammerstein and KGP model structures. The models are first trained with a NWT experimental data set and, successively, their performance validated with a second NWT experimental data set.

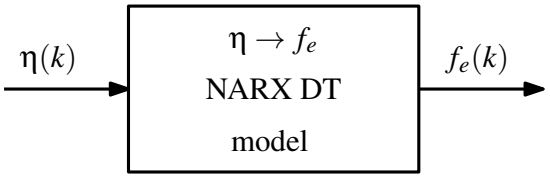

Figure 6.2: General NARX DT model to describe the relationship between FSE and excitation force.

6.2.1 NWT and floating body description

This case study considers a 2D NWT, implemented in OpenFOAM (see Section 2.3.1). The tank is 50 m deep, with walls 100 m from the device and with wave creation and absorption implemented via the *waves2FOAM* package [52], by utilising two 95 m long relaxation zones, situated 5 m either side of the device (see Fig. 6.3). Above the water, there is a volume of air with a 5 m height. The tank is one cell thick, corresponding to a thickness of 1 cm, and symmetry planes are defined at the front and back faces. In the NWT, there is a total of 72,000 cells. Three different bodies are utilised, having the geometries and dimensions shown in Fig. 6.4. Since the experiments are carried out in a 2D NWT, the body geometries of the test devices are infinitely long horizontal bars (see Section 4.4), having vertical cross-sections of a triangle, a circle and a box. The three bodies are fixed with a 1 m draft, which is 50% of the device height. In the context of 2D NWT simulations, the waves move along a direction perpendicular to the infinitely long horizontal body axis (see Fig. 4.57), therefore, no wave directionality effects on the body are investigated.

6.2.2 Generated NWT data description

Two different experiment types are performed in order to provide the model identification data, the input wave excitation force experiment and the prescribed motion experiment.

Input wave excitation force experiments
The input wave excitation force experiment (see Section 4.3.2.2) involves holding the body fixed,

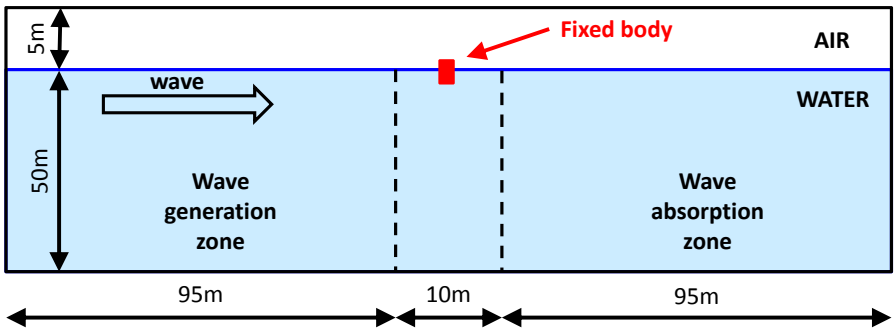

Figure 6.3: NWT side view.

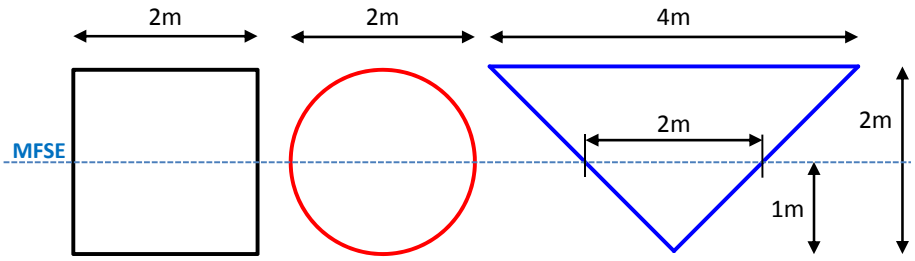

Figure 6.4: Test device geometries: box, circle and triangle. The dotted line represents the mean free surface elevation.

in the presence of input waves, and measuring the resulting hydrodynamic force applied from the fluid to the body. As explained in Section 2.4.1.1, the definitions of the Froude-Krylov and excitation forces are not unique, they can be calculated by considering only the dynamic pressure, due to the incident field, or by utilising the total pressure (static plus dynamic pressure). In the present work, the excitation force counts only the dynamic part of the pressure; and so, the excitation force is zero if there are no incident waves (otherwise, by considering static plus dynamic pressure, the excitation force would be equal to the buoyancy force, in the absence of incident waves). Therefore, the excitation force is given by removing the hydrostatic force f_{fl}^{o}, experienced by the device in the absence of waves, from the total measured force, $f_{fl}(k)$, applied from the fluid to the body, and is given by:

$$f_{e.d}(k) = f_{fl}(k) - f_{fl}^{o} \tag{6.1}$$

The input wave excitation force experiment produces two signals for model identification, one

Experiment type	Input signal type {Input symbol}	Output signal type {Output symbol}	Identified model
Input wave excitation force	FSE $\{\eta_d(k)\}$	Excitation force $\{f_{e.d}(k)\}$	ARX Hammerstein (ARX block) KGP
Prescribed motion	FSE $\{\eta_s(k)\}$	Excitation force $\{f_{e.s}(k)\}$	Hammerstein (static block)

Table 6.1: Generated data in the different experiment types.

containing the FSE, $\{\eta_d(k)\}$, and, the other, the resulting excitation force, $\{f_{e.d}(k)\}$ (with $k = ,1...,N$), as shown in Table 6.1 (both considered positive when they are upward). Since this experiment is used to identify the dynamics of the system under study, it is important that the input signal $\{\eta_d(k)\}$ has a good coverage of the frequencies and amplitude ranges, where the system has to operate (see Section 4.2.1). In the symbolisms $f_{e.d}$ and η_d, the subscript 'd' indicates 'dy-

namic'. As explained in Section 4.3.2.2, since the FSE is required to be known at the WEC's center of mass, it is not possible to directly measure the FSE, since the body occupies that space, and the input wave excitation force experiment is decomposed into two separate sub-experiments, as shown in Fig. 4.40.

The excitation force curve, $H_e(f)$, calculated by WAMIT, can be used as a first indication, in order to design the FSE excitation signal bandwidth. As explained in Section 4.4, by implementing a long horizontal bar in WAMIT (for the geometry employed, a length of 25 m has been shown sufficient), the infinitely long horizontal bar, in a 2D NWT, can be approximated by the horizontal finite length body in WAMIT. Fig. 6.5, shows the the excitation force curve, calculated by WAMIT, of the horizontal cylinder, of 25 m length, where it is possible to see that the larger $|H_e(f)|$ values occur in the bandwidth [0 , 0.2] Hz. For this case study, two different FSE realizations are generated (one for model identification and the other for model validation) from the sea state having a JONSWAP spectrum [73] [302], characterised by a $H_s = 1.5$ m significant wave height and a $T_p = 10$ s peak period. The spectral content of the FSE signal, used for model identification, is shown in Fig. 6.6. Each sea state realization has been obtained as a multisine signal, consisting of 50 equally spaced frequencies in the range 0.005-0.495 Hz ($\Delta f = 0.01$ Hz), by selecting a random phase for each harmonic. The first sea state realization is used with each body geometry, in order to generate the training experiments $T1$, $C1$ and $B1$, for the triangle, circle and box, respectively (see Figs. 6.7 and 6.8). All the training experiments have a duration of 600 s and a sampling period $T_s = 0.1$ s (therefore, the number of generated samples is N=6000). Similarly, the second sea state realization is used with each body geometry, in order to generate the validation experiments $T2$, $C2$ and $B2$ (see Fig. 6.9). All validation experiments have a duration of 400 s and $T_s = 0.1$ s (therefore, the number of generated samples is N=4000). In Figs. 6.8(a) and 6.9(a), it is possible to see that the training and validation FSE realizations have been intentionally constructed in a way so that the device is never overtopped or dried out (i.e. $-1 < \eta(k) < 1$ for any k).

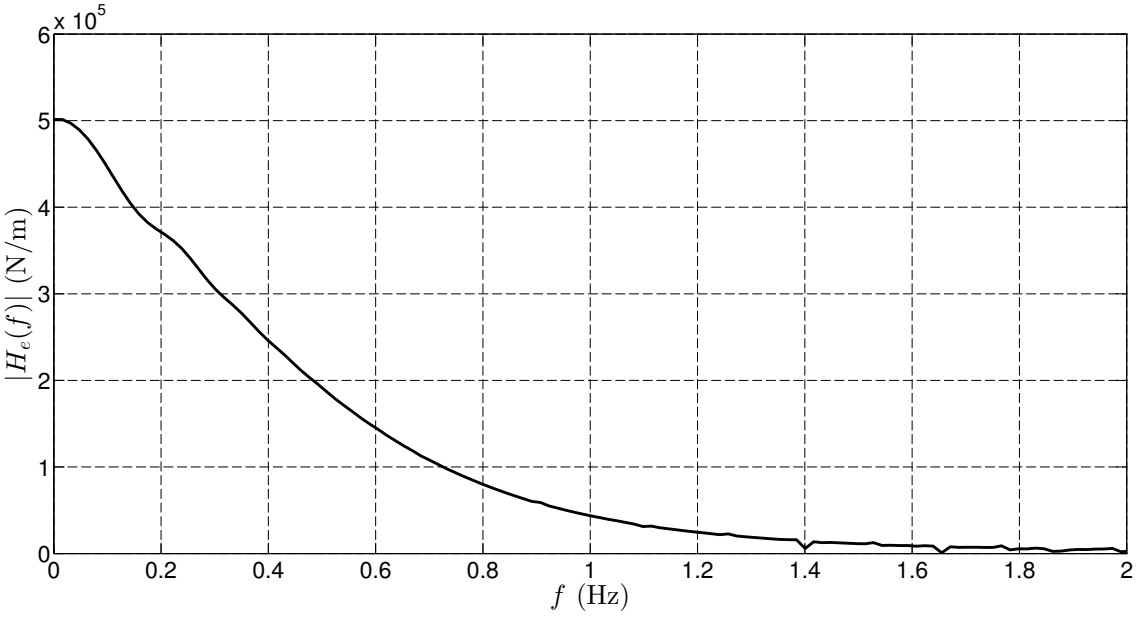

Figure 6.5: Excitation force curve, calculated by WAMIT, of the horizontal cylinder with 25 m length, 1 m radius and 1 m draft (used to approximate an infinitely long horizontal cylinder).

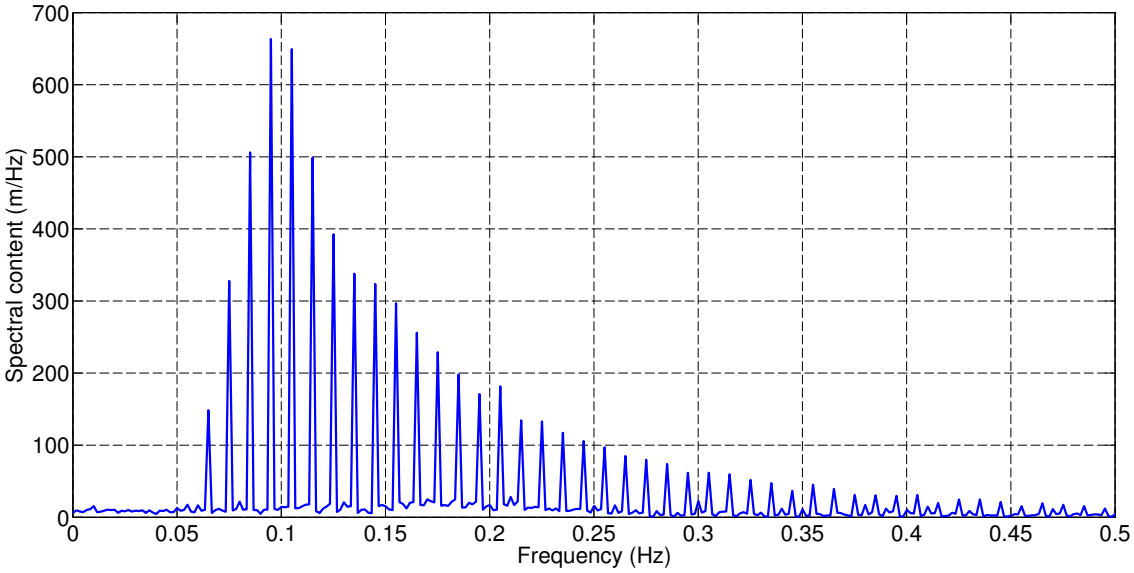

Figure 6.6: Fourier transform of the FSE signal of the input wave excitation force experiment, used for training. The FSE realization is generated from the sea state having a JONSWAP spectrum characterised by $H_s = 1.5$ m and $T_p = 10$ s. The FSE signal has been obtained as a multisine signal, consisting of 50 equally spaced frequencies in the range 0.005-0.495 Hz ($\Delta f = 0.01$ Hz), by selecting a random phase for each harmonic.

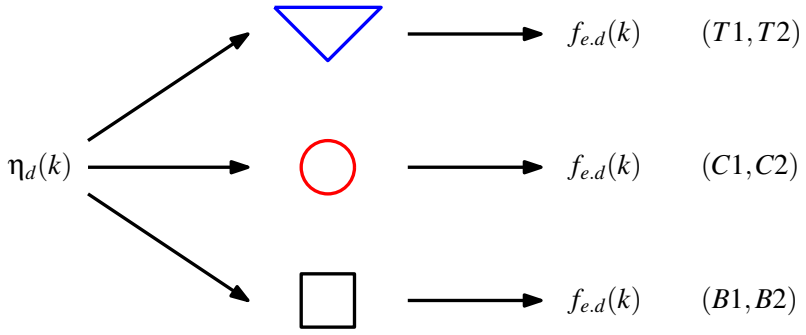

Figure 6.7: From each FSE signal, utilised in the input wave excitation force experiments, three different excitation force signals are obtained, one for each geometry.

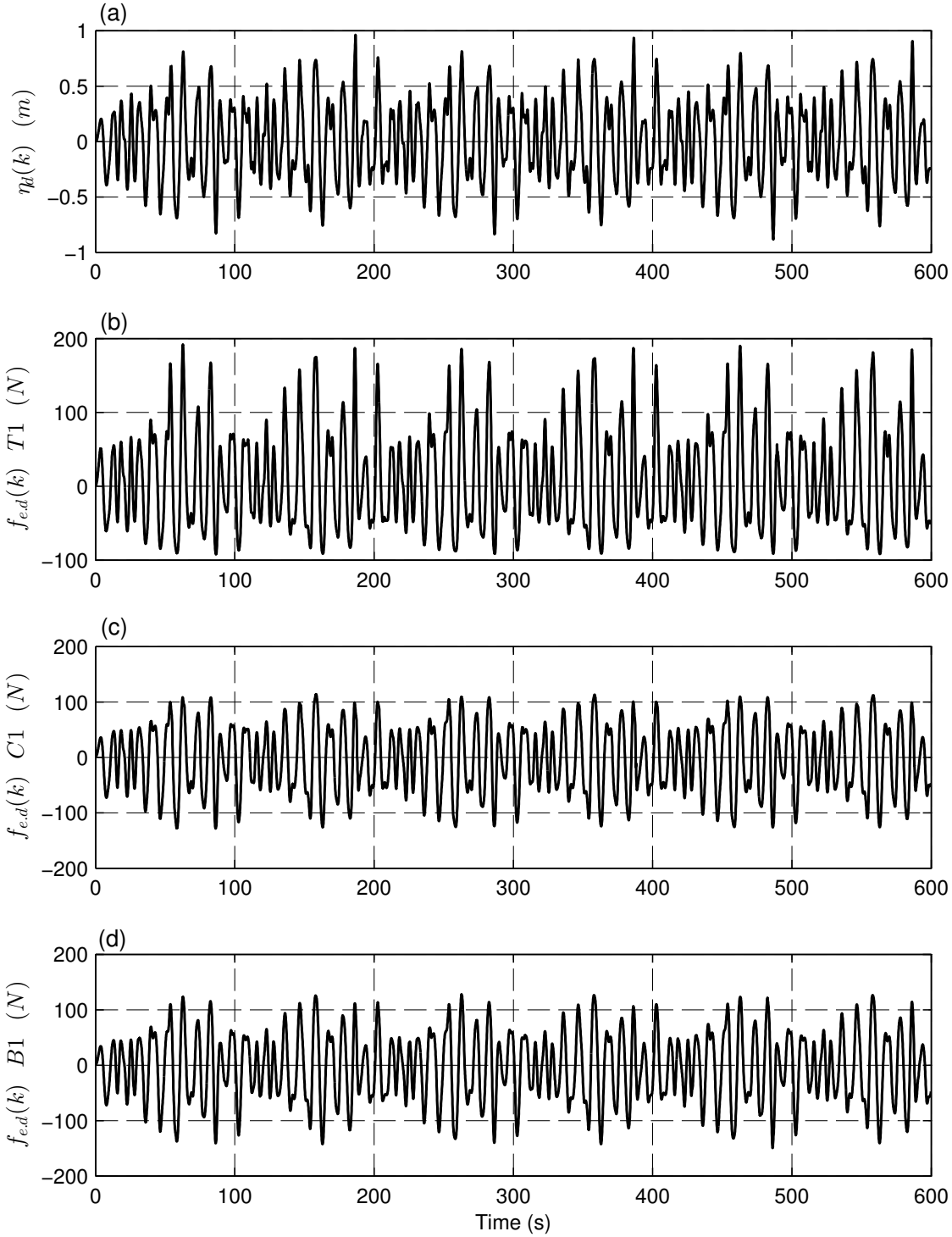

Figure 6.8: Training data, generated with the input wave excitation force experiments. (a) FSE signal. (b) Excitation force signal, in the case of the triangular body (experiment $T1$). (c) Excitation force signal, in the case of the circular body (experiment $C1$). (d) Excitation force signal, in the case of the rectangular body (experiment $B1$).

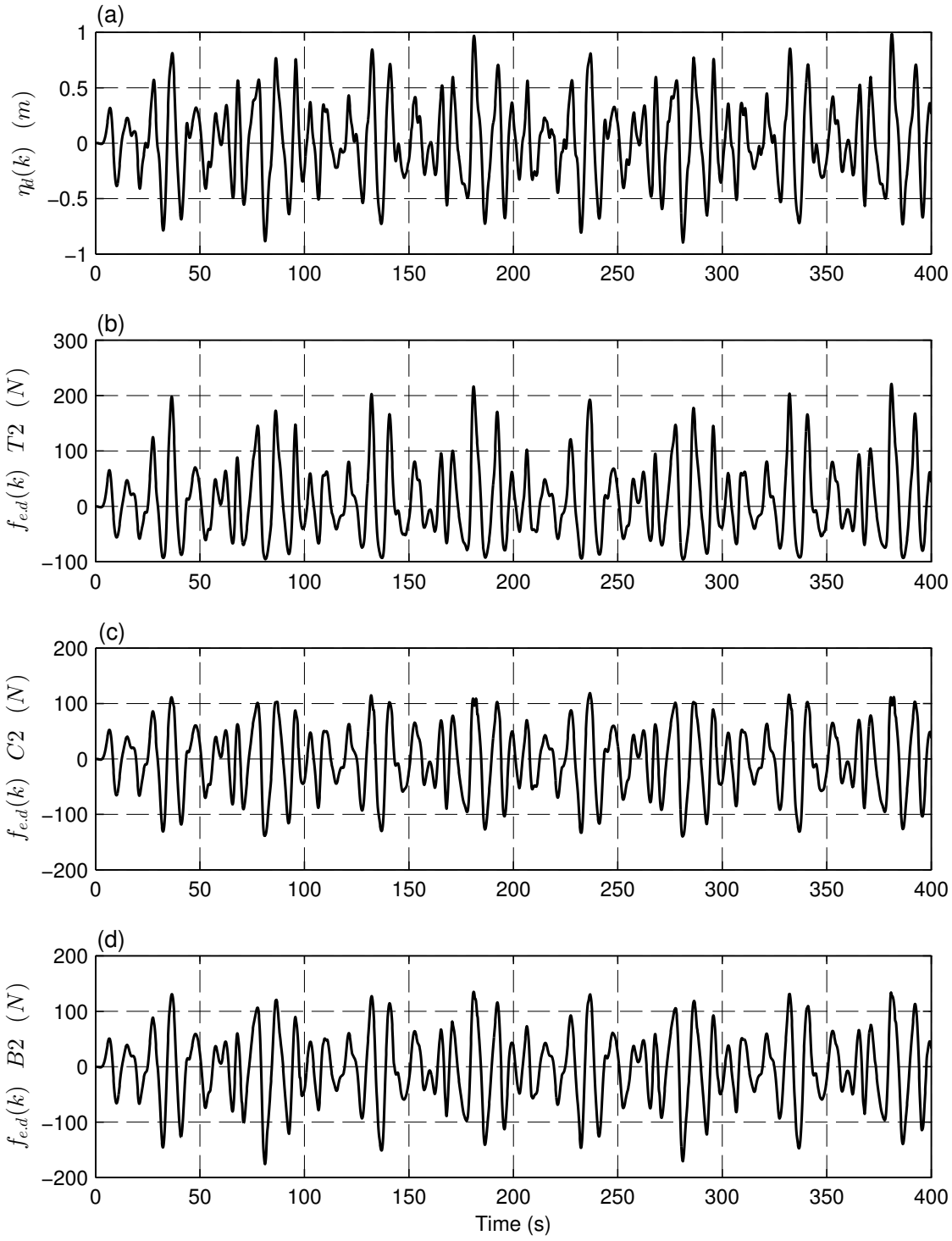

Figure 6.9: Validation data, generated with the input wave excitation force experiments. (a) FSE signal. (b) Excitation force signal, in the case of the triangular body (experiment $T2$). (c) Excitation force signal, in the case of the circular body (experiment $C2$). (d) Excitation force signal, in the case of the rectangular body (experiment $B2$).

Prescribed motion experiments

This experiment is used to identify the static curve of the Hammerstein model (see Section 3.3.1.4). Ideally, in order to obtain the static relationship between the FSE and the excitation force, the body is held fixed and the FSE is very slowly increased (in order to make the dynamic effects negligible) from the bottom to the top of the body (producing the FSE signal, $\{\eta_s(k)\}$), and the resulting force, applied from the fluid to the body, $\{f_{fl.s}(k)\}$, is measured, as explained in Section 4.3.2.4 (see Fig. 6.10(a)). Since the dynamic effects are negligible, $f_{fl.s}(k)$ corresponds to the hydrostatic force. The subscript 's' indicates '(almost) static'. However, in terms of implementing the experiment in the NWT, it is easier to keep the water level constant and slowly submerge the body (producing the body displacement signal, $\{y_s(k)\}$, to obtain the measurement of the same hydrostatic force signal $\{f_{fl.s}(k)\}$ (see Fig. 6.10(b)). From the measurements $\{y_s(k)\}$ and $\{f_{fl.s}(k)\}$, it is possible to obtain the FSE signal, given by:

$$\eta_s(k) = -y_s(k) \tag{6.2}$$

and the excitation force, given by:

$$f_{e.s}(k) = f_{fl.s}(k) - f^o_{fl.s} \tag{6.3}$$

where $f^o_{fl.s}$ is the fluid hydrostatic force, when the body draft is 1 m. Therefore, two signals are produced by the prescribed motion experiment for model identification, the input $\{\eta_s(k)\}$, given by equation (6.2), representing the FSE, and the output $\{f_{e.s}(k)\}$, given by equation (6.3), representing the excitation force, for $k = 1, ..., N$ (see Table 6.1). The results from the prescribed motion experiment, in the case of the triangle, are shown in Fig. 6.11. Fig. 6.11(a) shows the FSE, starting from the bottom of the device and slowly rising, until the device is completely submerged. Fig. 6.11(b) shows the excitation force on the body during this FSE change. Fig. 6.11(c) plots the excitation force as a function of the FSE, showing the nonlinear nature of the relationship for the triangular geometry. Fig. 6.12 and 6.13 show the results, from the prescribed motion experiment, for the circle and the box, respectively. The restoring curves, resulting from NWT data, are compared with the analytical restoring curves (resulting by geometrical volume calculations [303]) in Figs. 6.14(a), 6.14(b) and 6.14(c) for the triangle, circle and box, respectively, where it is possible to see the excellent agreement.

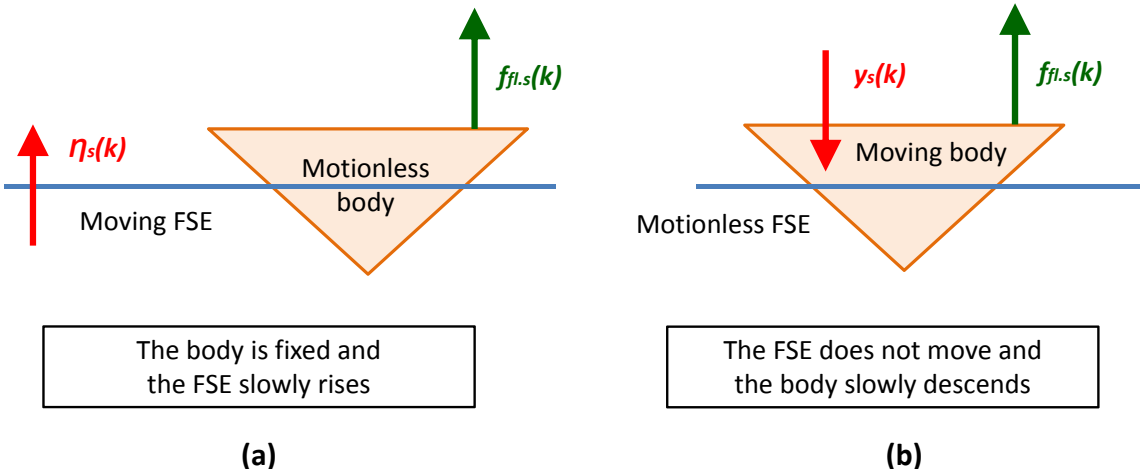

Figure 6.10: (a) The body is held fixed and the FSE is very slowly increased from the bottom to the top of the body and the resulting force, applied from the fluid to the body, is measured. (b) Prescribed motion experiment: the water level is kept constant and the body is slowly submerged to obtain the measurement of the body displacement and the force applied by the fluid to the body.

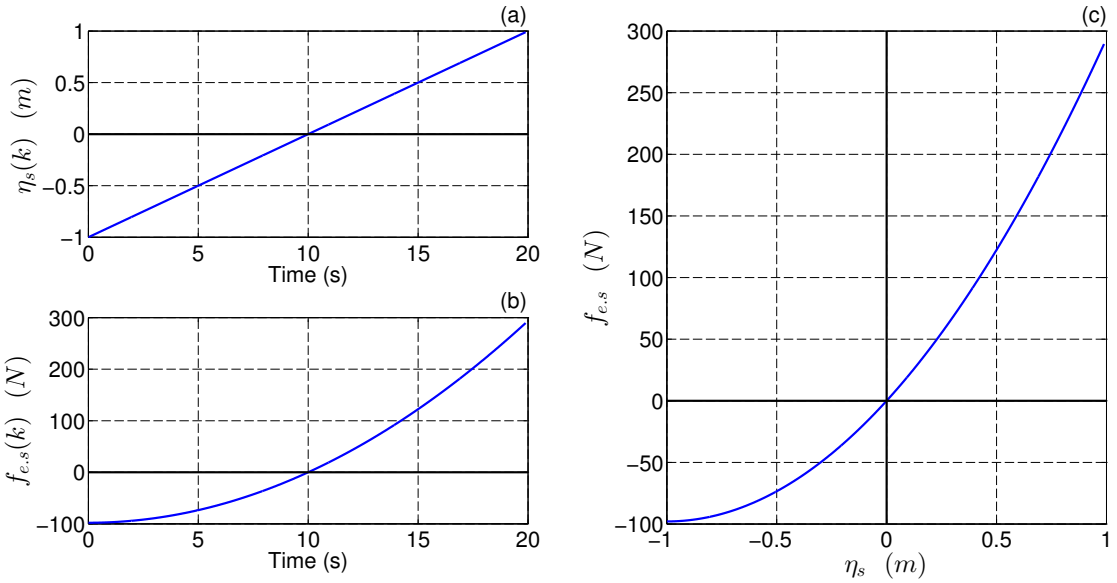

Figure 6.11: Prescribed motion experiment in the case of the triangle: (a) FSE signal. (b) Excitation force signal. (c) Excitation force as a function of the FSE.

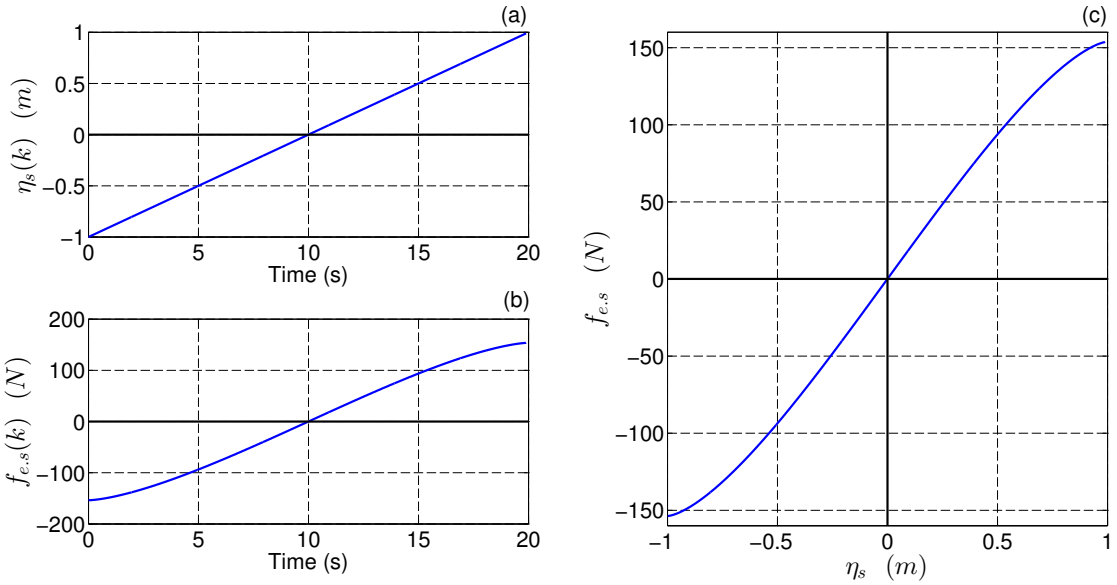

Figure 6.12: Prescribed motion experiment in the case of the circle: (a) FSE signal. (b) Excitation force signal. (c) Excitation force as a function of the FSE.

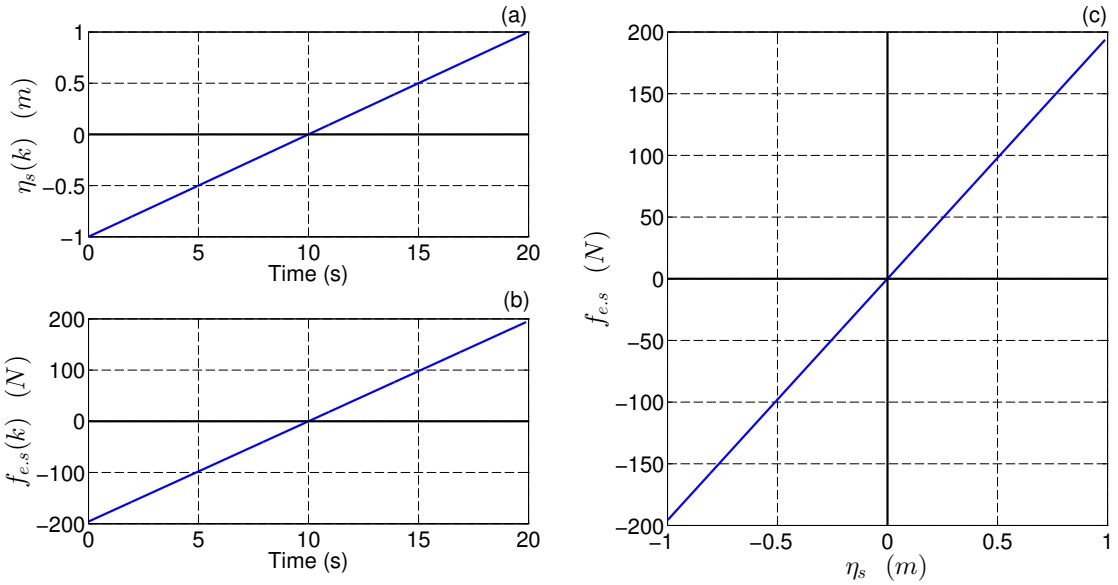

Figure 6.13: Prescribed motion experiment in the case of the box: (a) FSE signal. (b) Excitation force signal. (c) Excitation force as a function of the FSE.

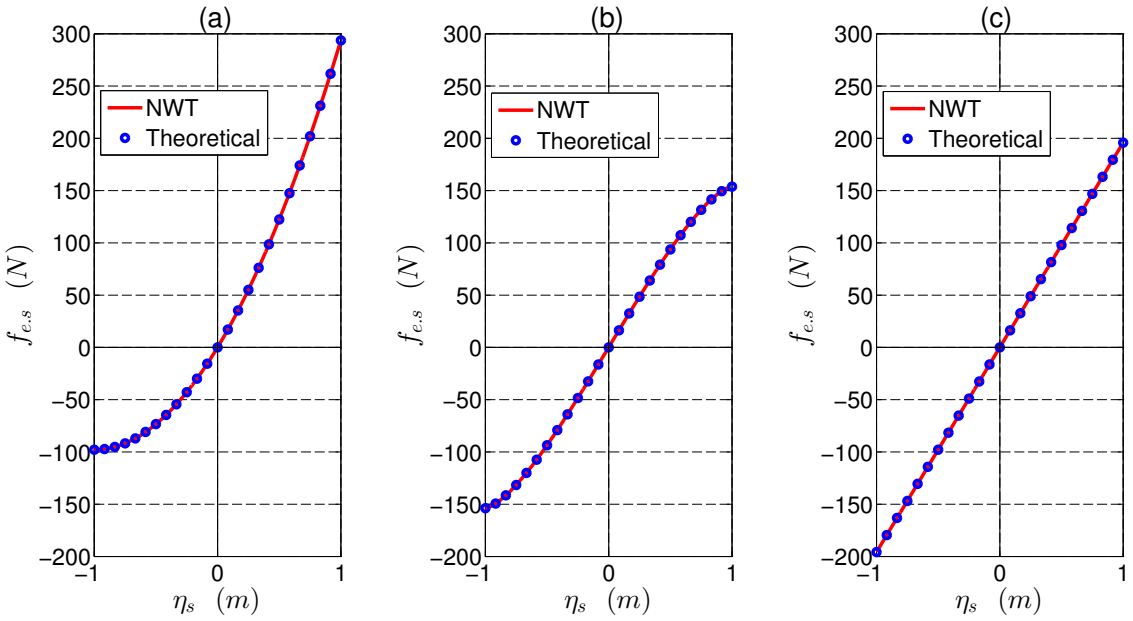

Figure 6.14: Comparison of the NWT data, resulting from the prescribed motion experiment, with the theoretical curves. (a) Triangle. (b) Circle. (c) Box.

6.2.3 Model description and identification

ARX model

In the case of the $\eta \rightarrow f_e$ model family, the ARX model structure is given by (see Section 3.2.3.1):

$$f_e(k) = \sum_{i=1}^{n_a} a_i y(k-i) + \sum_{i=0}^{n_b} b_i \eta(k-n_d-i) \tag{6.4}$$

By performing the input wave excitation force experiment, the signals $\{\eta_d(k)\}$ and $\{f_{e.d}(k)\}$, for $k = 1...N$, are generated (see Section 6.2.2), which can be utilised as the input and output signals, respectively, for the identification of the ARX model. The first possible predicted model output is for $k = \tau + 1$ (see Section 3.3.1.3), where:

$$\tau = max\{n_a, (n_b + n_d)\} \tag{6.5}$$

The last possible predicted model output is for $k = \widetilde{N}$ (see Section 3.3.1.3), where:

$$\widetilde{N} = \begin{cases} N & \text{if } n_d \geq 0, \\ N + n_d & \text{if } n_d < 0. \end{cases} \tag{6.6}$$

In the case of ARM model identification, equations (3.61) and (3.62) become:

$$\mathbf{y} = \begin{bmatrix} f_{e.d}(\tau+1) & f_{e.d}(\tau+2) & ... & f_{e.d}(\widetilde{N}) \end{bmatrix}^T \tag{6.7}$$

and

$$\mathbf{\Phi} = \begin{bmatrix} f_{e.d}(\tau) & ... & f_{e.d}(\tau+1-n_a) & \eta_d(\tau+1-n_d) & ... & \eta_d(\tau+1-n_d-n_b) \\ f_{e.d}(\tau+1) & ... & f_{e.d}(\tau+2-n_a) & \eta_d(\tau+2-n_d) & ... & \eta_d(\tau+2-n_d-n_b) \\ \vdots & \ddots & \vdots & \vdots & \ddots & \vdots \\ f_{e.d}(\widetilde{N}-1) & ... & f_{e.d}(\widetilde{N}-n_a) & \eta_d(N) & ... & \eta_d(N-n_b) \end{bmatrix}, \tag{6.8}$$

respectively. The estimated parameter vector $\hat{\boldsymbol{\theta}}_{arx} = [a_1 \ \ ... \ \ a_{n_a} \ \ b_0 \ \ ... \ \ b_{n_b}]^T$ is determined by utilising $\mathbf{y}$, $\mathbf{\Phi}$ and QR factorization (see Section 3.3.1.1) to resolve the LS problem.

Hammerstein model

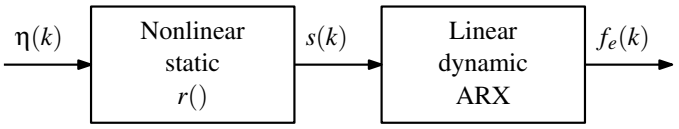

Figure 6.15: Block diagram of the Hammerstein model for a $\eta \rightarrow f_e$ hydrodynamic structure.

The Hammerstein model block diagram, shown in Fig. 6.15, is described by an input/output relationship (see Section 3.2.3.3) given by:

$$f_e(k) = \sum_{i=1}^{n_a} a_i f_e(k-i) + \sum_{i=0}^{n_b} b_i r\Big(\eta(k-n_d-i)\Big) \tag{6.9}$$

The nonlinear static function $r()$ is parametrized with a polynomial; therefore, the relationship between the input and the output of the nonlinear static block is given by:

$$s(k) = c_1\eta(k) + c_2\eta^2(k) + ... + c_{n_c}\eta^{n_c}(k) \tag{6.10}$$

where $c_0 = 0$ is imposed (in the absence of waves, the excitation force has to be zero, as explained in Sections 2.4.1.1 and 6.2.2). The Hammerstein model is identified by following the two steps

explained in Section 3.3.1.4. In the first step, the data generated by the prescribed motion experiment $\{\eta_s(k)\}$ and $\{f_{e.s}(k)\}$ (see Section 6.2.2) are employed. As explained in Section 3.3.1.4, in (almost) static conditions:

$$\{s_s(k)\} = \{f_{e.s}(k)\} \tag{6.11}$$

Therefore, $\{\eta_s(k)\}$ and $\{f_{e.s}(k)\}$ are the input and output data, respectively, which can be utilised in order to identify the Hammerstein static block $r()$, *separately* from the linear dynamic block. It is important to underline that the $f_{e.s}(\eta_s)$ curve is just the buoyancy force $f_b(\eta_s)$ curve vertically shifted, as shown in Fig. 6.16 (note that the $f_{e.s}(\eta_s)$ curve passes throughout the origin). In this way, the Hammerstein model black-box structure is given a lighter shade of 'grey', by considering the physical meaning of the nonlinear static function.

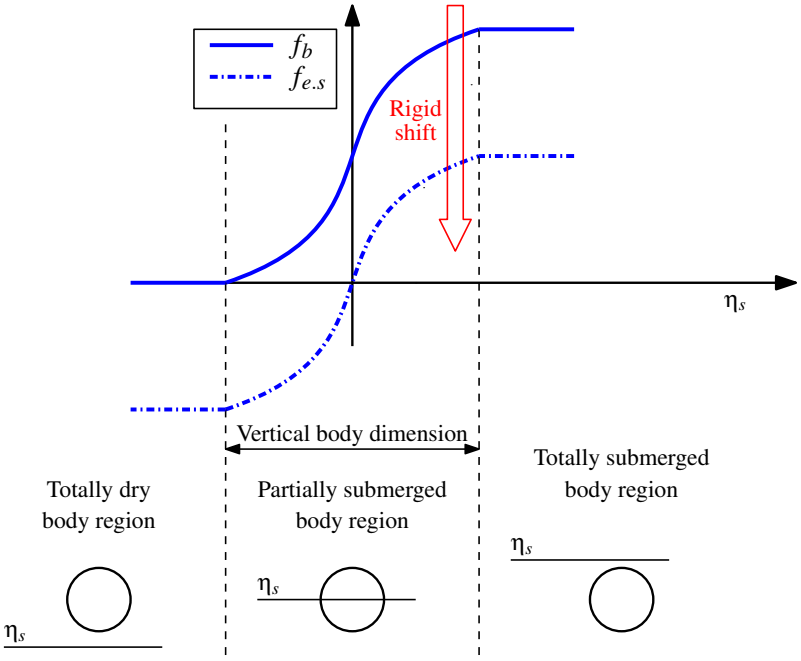

Figure 6.16: The $f_{e.s}(\eta_s)$ curve is the buoyancy force $f_b(\eta_s)$ curve, vertically shifted.

In this case, equations (3.68) and (3.69) become:

$$\mathbf{y} = \begin{bmatrix} f_{e.s}(1) & f_{e.s}(2) & \dots & f_{e.s}(N) \end{bmatrix}^T \tag{6.12}$$

and

$$\mathbf{\Phi} = \begin{bmatrix} [\eta_s(1)]^1 & [\eta_s(1)]^2 & \dots & [\eta_s(1)]^{n_c} \\ [\eta_s(2)]^1 & [\eta_s(2)]^2 & \dots & [\eta_s(2)]^{n_c} \\ \vdots & \vdots & \ddots & \vdots \\ [\eta_s(N)]^1 & [\eta_s(N)]^2 & \dots & [\eta_s(N)]^{n_c} \end{bmatrix}, \tag{6.13}$$

respectively. The estimated parameter vector $\hat{\boldsymbol{\theta}}_{H_c} = [c_1 \quad \dots \quad c_{n_c}]^T$ is determined by utilising $\mathbf{y}$, $\mathbf{\Phi}$ and QR factorization to resolve the LS problem. The parameter vector $\hat{\boldsymbol{\theta}}_{H_c}$ is calculated for different values of n_c, together with the associated static curve fitting error, given by equations (3.95) and (6.10):

$$NRMSE(n_c) = \frac{\| f_{e.s}(k) - \sum_{j=1}^{n_c} c_j \eta_s^j(k) \|_2}{\| f_{e.s}(k) \|_2} = \frac{\sqrt{\sum_{k=1}^{N} |f_{e.s}(k) - \sum_{j=1}^{n_c} c_j \eta_s^j(k)|^2}}{\sqrt{\sum_{k=1}^{N} |f_{e.s}(k)|^2}} \tag{6.14}$$

The smallest n_c, which leads to a fitting error of less than 3%, is selected (as a good compromise between parsimony and accuracy). Fig. 6.17 shows the fitting error of the Hammerstein static

curve as a function of n_c, and the identified values of n_c for the different geometries (n_c equal to 1, 2 and 3 for box, triangle and circle respectively, as shown in Table 6.2). Fig. 6.18 shows, for the three different geometries, the polynomial fitting of the data from the prescribed motion experiments (polynomial fitting of the static curve of the Hammerstein model).

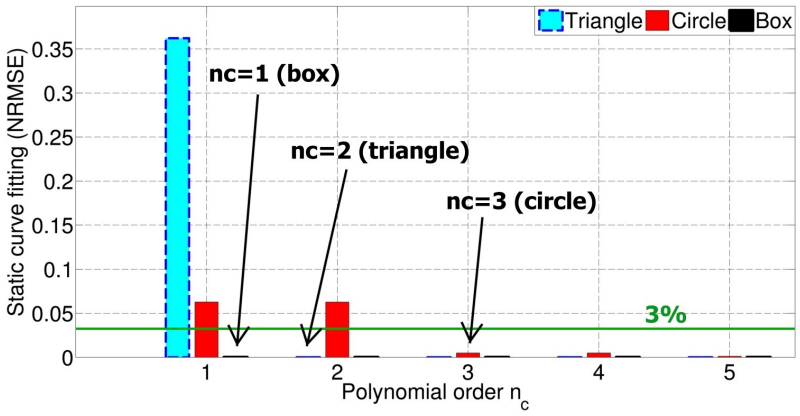

Figure 6.17: The fitting error of the static curve of the Hammerstein model for different polynomial order n_c. The smallest n_c, which guarantees a fitting error of less than 3%, is chosen. In the case of the box, the static curve is a straight line; therefore, the fitting error is already zero for $n_c = 1$.

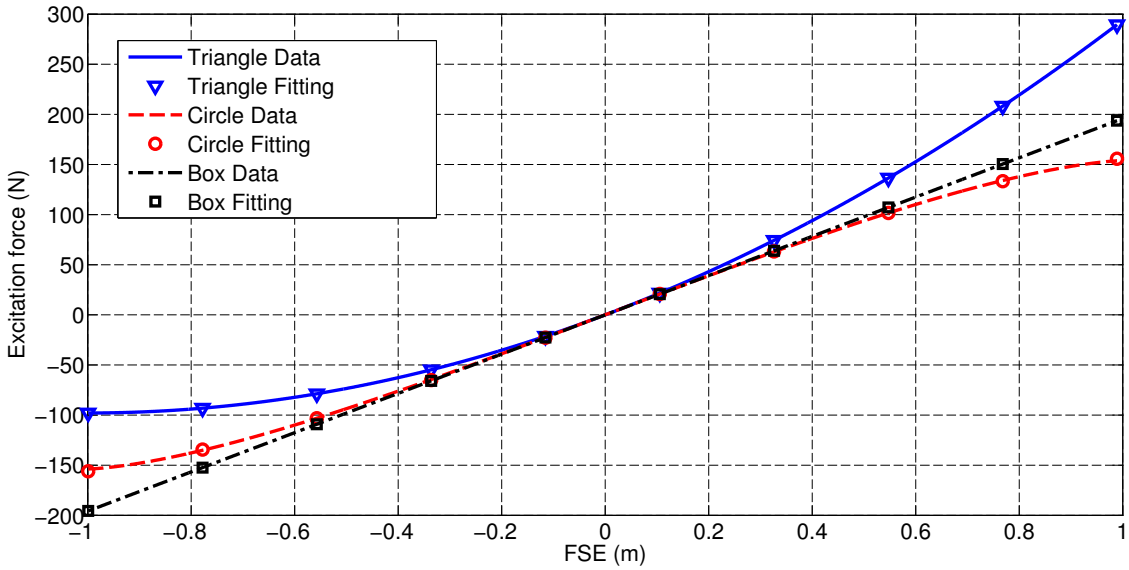

Figure 6.18: Results from the prescribed motion experiments and polynomial fitting of the Hammerstein static curves, in the case of the triangular ($n_c = 2$), circular ($n_c = 3$) and rectangular ($n_c = 1$) geometries.

In the second step, the ARX block is identified by utilising the signals $\{\eta_d(k)\}$ and $\{f_{e.d}(k)\}$, generated in the input wave excitation force experiment (see Section 6.2.2). Now that the parameter vector $\hat{\theta}_{H_c}$ is known, the input $\{\eta_d(k)\}$ is transformed through the nonlinear static block, in order to obtain $\{s_d(k)\}$, by using equation (6.10). Next, $\{s_d(k)\}$ and $\{\eta_d(k)\}$ are used as the input and output data, in order to identify the ARX parameter vector, $\hat{\theta}_{H_{arx}}$, under the constraint that the DC gain of the ARX model is unity equal to one (see Section 3.3.1.4). In this case, equations (3.72) and (3.73) become:

$$\mathbf{y} = \left[f_{e.d}(\tau+1) \quad f_{e.d}(\tau+2) \quad \ldots \quad f_{e.d}(\widetilde{N}) \right]^T \tag{6.15}$$

and

$$\mathbf{\Phi} = \begin{bmatrix} f_{e.d}(\tau) & \dots & f_{e.d}(\tau+1-n_a) & s_d(\tau+1-n_d) & \dots & s_d(\tau+1-n_d-n_b) \\ f_{e.d}(\tau+1) & \dots & f_{e.d}(\tau+2-n_a) & s_d(\tau+2-n_d) & \dots & s_d(\tau+2-n_d-n_b) \\ \vdots & \ddots & \vdots & \vdots & \ddots & \vdots \\ f_{e.d}(\widetilde{N}-1) & \dots & f_{e.d}(\widetilde{N}-n_a) & s_d(N) & \dots & s_d(N-n_b) \end{bmatrix}, \quad (6.16)$$

respectively, where τ and $\widetilde{N}$ are given by equations (6.5) and (6.6), respectively. The estimated parameter vector $\hat{\boldsymbol{\theta}}_{H_{arx}} = [a_1 \ \dots \ a_{n_a} \ b_0 \ \dots \ b_{n_b}]^T$ is given by:

$$\hat{\boldsymbol{\theta}}_{H_{arx}} = \hat{\boldsymbol{\theta}}^{(uc)}_{H_{arx}} - (\mathbf{\Phi}^T\mathbf{\Phi})^{-1}\mathbf{A}^T(\mathbf{A}(\mathbf{\Phi}^T\mathbf{\Phi})^{-1}\mathbf{A}^T)^{-1}(\mathbf{A}\hat{\boldsymbol{\theta}}^{(uc)}_{H_{arx}} - \mathbf{d}), \quad (6.17)$$

where $\mathbf{A} = [1,1,...,1] \in \Re^{1\times(n_a+n_b+1)}$ and $\mathbf{d} = 1$ (see Section 3.3.1.4), and the unconstrained parameter vector, $\hat{\boldsymbol{\theta}}^{(uc)}_{H_{arx}}$, is calculated by utilising QR factorization to resolve the LS problem.

KGP model

In the case of the $\eta \rightarrow f_e$ model family, the KGP model structure, where the cross-product terms are removed in order to reduce the possibility of stability problems (see Section 3.2.3.5), is described by the input/output relationship given by:

$$f_e(k) = \sum_{j=1}^{n_p}\Big[\sum_{i=1}^{n_a} a_{ij} f_e^j(k-i) + \sum_{i=0}^{n_b} b_{ij}\eta^j(k-n_d-i)\Big] \quad (6.18)$$

In this case, equation (3.72) becomes:

$$\mathbf{y} = \begin{bmatrix} f_{e.d}(\tau+1) & f_{e.d}(\tau+2) & \dots & f_{e.d}(\widetilde{N}) \end{bmatrix}^T, \quad (6.19)$$

where τ and $\widetilde{N}$ are given by equations (6.5) and (6.6), respectively, and each of the $(\widetilde{N}-\tau)$ rows of the data matrix $\mathbf{\Phi}$, defined by (3.49), has the form:

$$\begin{bmatrix} f_{e.d}(k-1) \ \dots \ f_{e.d}(k-n_a) \ \ \eta_d(k-n_d) \ \dots \ \eta_d(k-n_d-n_b) \\ f^2_{e.d}(k-1) \ \dots \ f^2_{e.d}(k-n_a) \ \ \eta^2_d(k-n_d) \ \dots \ \eta^2_d(k-n_d-n_b) \ \dots \\ f^{n_p}_{e.d}(k-1) \ \dots \ f^{n_p}_{e.d}(k-n_a) \ \ \eta^{n_p}_d(k-n_d) \ \dots \ \eta^{n_p}_d(k-n_d-n_b) \end{bmatrix}, \quad (6.20)$$

where $k = (\tau+1),...,\widetilde{N}$. The estimated parameter vector, $\hat{\boldsymbol{\theta}}_{kgp}$, is determined by utilising $\mathbf{y}$, $\mathbf{\Phi}$ and QR factorization to resolve the LS problem.

6.2.4 Results

By utilising the methodology illustrated in Section 3.2.4, the dynamical orders n_a and n_b, and the input delay time n_d can be identified for the NARX models, utilised for the three geometries (each geometry is associated with specific n_a, n_b and n_d values). For each geometry, the first step is to obtain an indication regarding possible values of n_a, n_b and n_d, by identifying 3100 different ARX structures, by utilising all the possible combinations of the integers $1 \leq n_a \leq 10$, $0 \leq n_b \leq 9$ and $-20 \leq n_d \leq +10$ (it is possible to efficiently realize this calculation with the use of the Matlab command *arxstruc*). Since n_a provides the number of poles of the system, it is the most important parameter and it is the first to be estimated. In Fig. 6.19, the loss function $LF = LF(n_a,n_b,n_d)$, in the case of the triangular geometry for the training experiment $T1$, is plotted versus n_a, where each vertical line shows the range of LF for a specific value of n_a and for $0 \leq n_b \leq 9$ and $-20 \leq n_d \leq +10$. The objective is to obtain small values of LF, and it is possible

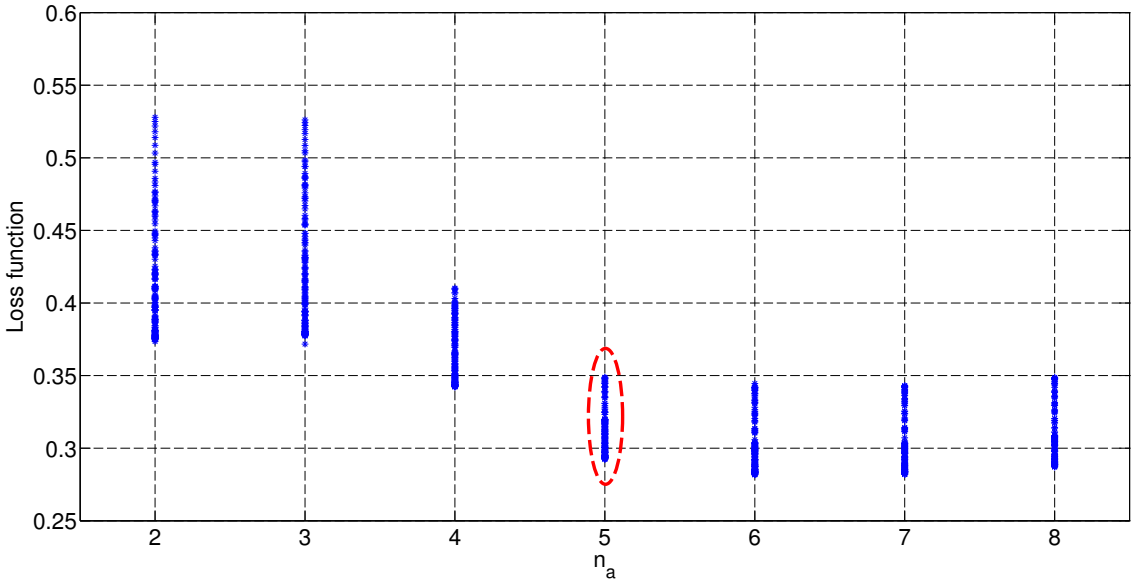

Figure 6.19: $LF = LF(n_a, n_b, n_d)$, in the case of the triangular geometry for the training experiment $T1$, is plotted versus n_a, where each vertical line shows the range of LF for a specific value of n_a and for $0 \leq n_b \leq 9$ and $-20 \leq n_d \leq +10$. There is no significant reduction of LF for $n_a > 5$; therefore, $n_a = 5$ is the correct value to obtain a parsimonious model structure.

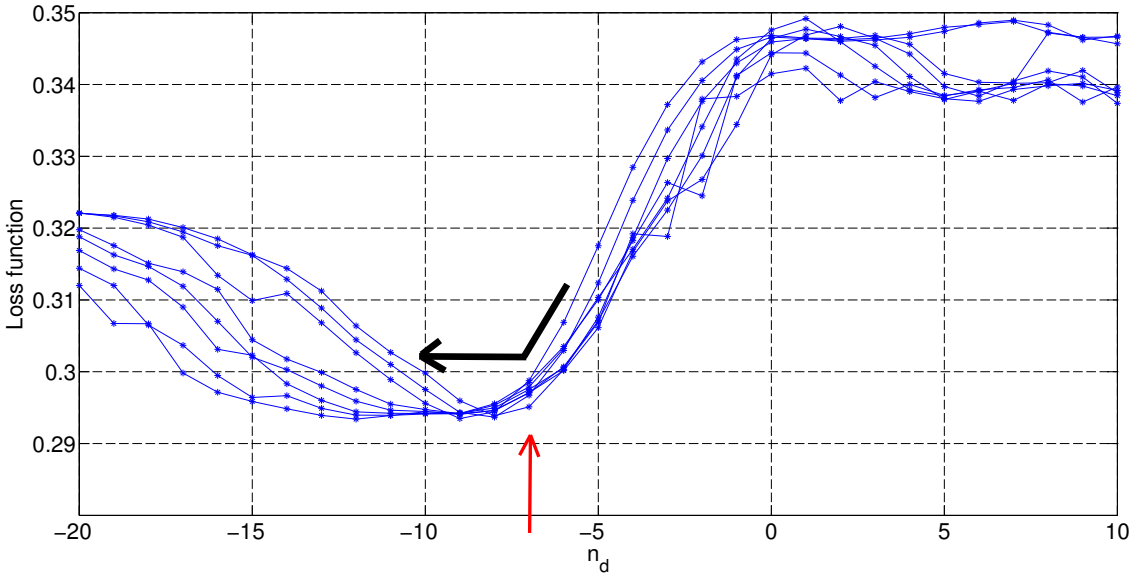

Figure 6.20: LF curves for the experiment $T1$, for $n_a = 5$ and $0 \leq n_b \leq 9$. By increasing n_b the LF does not reduce anymore, this occurs when $n_d = -7$.

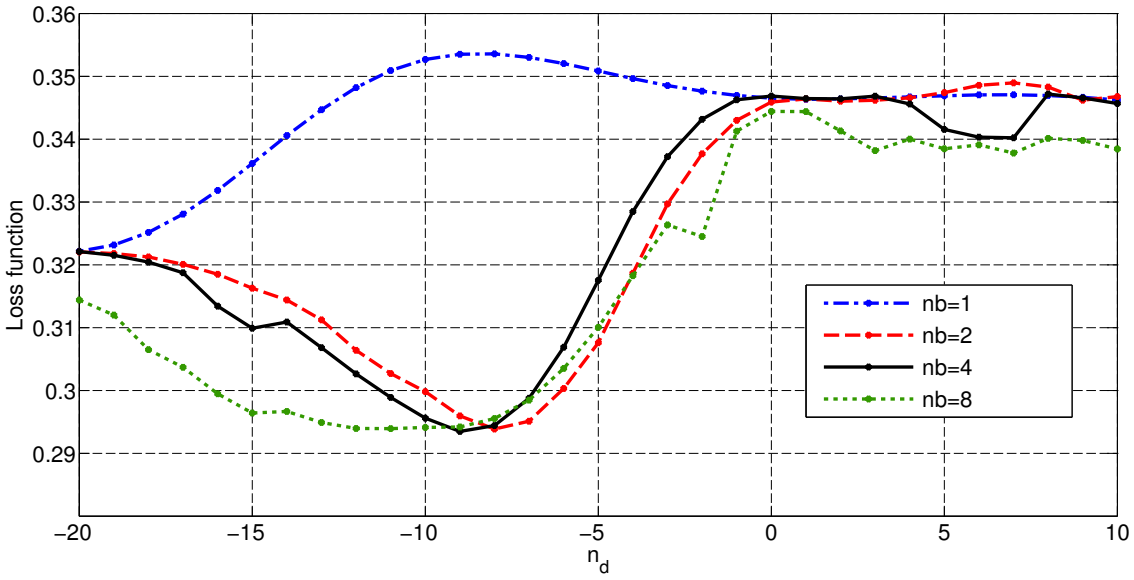

Figure 6.21: LF curves for experiment $T1$ in the case of $n_a = 5$ and $n_b = 1$, 2, 4 and 8. LF has minima at $n_d = -8$ (if $n_b = 2$), at $n_d = -9$ (if $n_b = 4$) and at $n_d = -10$ (if $n_b = 8$).

to see that there is no significant reduction of LF for $n_a > 5$, showing that $n_a = 5$ is the correct value to obtain a parsimonious model structure. Once n_a is selected, the next step is the estimation of n_b and n_d.

By plotting a different LF curve versus n_d, for each value of n_b, shows that the minimum of the LF occurs at different n_d, dependently on the value of n_b. Fig. 6.20 shows the LF curves for experiment $T1$, for the case of $n_a = 5$ and $0 \leq n_b \leq 9$; it is possible to see that the minima of the curves stop decreasing for about n_d equal to -7 (as indicated by the two arrows in the picture). In particular, Fig. 6.21 shows the LF curves for experiment $T1$, for the case of $n_a = 5$ and $n_b =$ 1, 2, 4 and 8; it is possible to see that LF has a minimum at $n_d = -8$ (if $n_b = 2$), at $n_d = -9$ (if $n_b = 4$) and at $n_d = -10$ (if $n_b = 8$). The objective is to obtain small values of LF, and it is possible to see that there is no significant difference for $n_b = 2$, 4 or 8, showing that $n_b = 2$ is the correct value to obtain a parsimonious model structure. Fig. 6.22 shows the loss function versus n_d, in the case of $n_a = 5$ and $n_b = 2$, where it is possible to see that the minimum value occurs for $n_d = -8$. The same strategy is utilised for the identificatin of n_a, n_b and n_d for circle and box geometries, by utilising experiment $C1$ and $B1$, respectively; the results are summarized in Table 6.2. As expected, the n_d identified for the three different geometries are negative, compatibly with the fact that the relationship between η and f_e is noncausal (see Section 2.4.1.1). The estimated values of n_d show that the triangle is the most noncausal body, followed by the box and circle. This degree of noncausality can be geometrically explained by remembering that η is measured in a point placed in the centre of the body and that the body experiences a force before the wave crest arrives to the body centre. In Fig. 6.23, the three geometries are plotted overlapped, in order to show that the wave crest interacts first with the triangle, than with the box and the circle.

Geometry	n_a	n_b	n_d	n_c	n_p
Triangle	5	2	-8	2	2
Circle	3	2	-6	3	2
Box	3	2	-7	1	2

Table 6.2: Identified n_a, n_b, n_d, n_c and n_p for the triangular, circular and rectangular geometries.

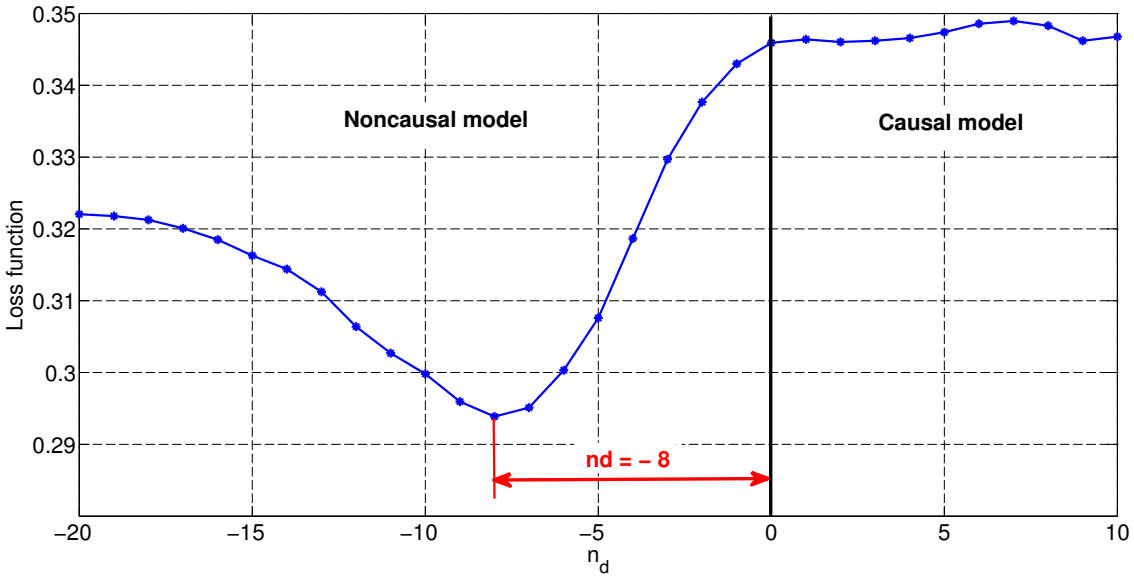

Figure 6.22: LF curves for experiment $T1$. Determination of $n_d = -8$, for the triangular geometry, in the case of $n_a = 5$ and $n_b = 2$.

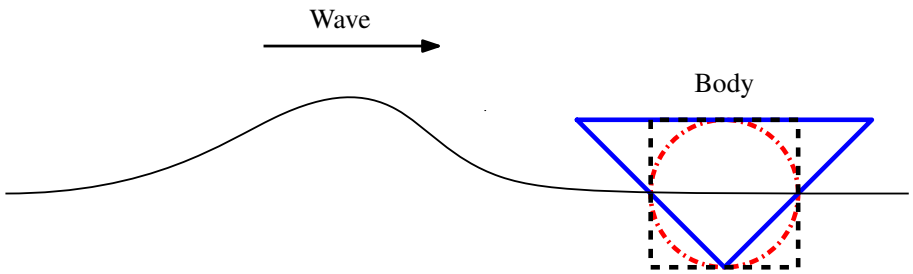

Figure 6.23: The three geometrical body are plotted overlapped, in order to show that the wave crest interacts first with the triangle, than with the box and the circle.

By utilising the n_a, n_b and n_d values of Table 6.2, and the methodology described in Section 6.2.3, three different ARX models are identified with the training experiments $T1$, $C1$ and $B1$, for the triangle, circle and box, respectively. Since the models utilised are linear in the parameters, the use of a 1-step prediction criterion, for the identification of the models, leads to a convex optimization problem (the advantageous convex optimization would be lost by using a multi-step prediction criterion for the training). Therefore, each model is trained with a 1-step prediction criterion and, once identified, the model is used to make a multi-step prediction (see Section 3.4) on the same training data; Table 6.3 shows the NRMSE multi-step prediction performance for each ARX model. Since a model, which fits well the training data, is not necessary a good model on a different experiment (potential overfitting problem), the three identified ARX models are utilised to make multi-step predictions on the data provided by the validation experiments $T2$, $C2$ and $B2$, for the triangle, circle and box, respectively. Table 6.4 shows the NRMSE multi-step prediction performance, on validation data. Similarly, three Hammerstein and KGP models are trained with experiments $T1$, $C1$ and $B1$, and multi-step predictions are made on experiments $T1$, $C1$, $B1$, $T2$, $C2$ and $B2$; the fitting results are shown in Tables 6.3 and 6.4. In the case of the KGP model, the polynomial order $n_p = 2$ has been identified, observing that larger values of n_p improve the training fitting but degrade the quality of the validation fitting (i.e. overfitting). In Tables 6.3 and 6.4, it is possible to observe that, for all 6 experiments, the KGP model is shown to be the best (marked in green and with the number (1)) , followed by the Hammerstein model (marked in orange and with the number (2)) and finally the ARX model (marked in red and with the number (3)). Therefore,

it is possible to conclude that the problem under investigation includes nonlinearities, and that the nonlinear identified models are able to describe them.

Geometry	ARX	Hammerstein	KGP
Triangle	0.2316 (3)	0.1060 (2)	0.0792 (1)
Circle	0.1233 (3)	0.1135 (2)	0.0922 (1)
Box	0.1311 (3)	0.1270 (2)	0.0961 (1)

Table 6.3: NRMSE multi-step performance model on training data. The best model performance is marked in green and with the number (1), the second model performance is marked in orange and with the number (2), and the worst model performance is marked in red and with the number (3).

Geometry	ARX	Hammerstein	KGP
Triangle	0.2486 (3)	0.1125 (2)	0.0876 (1)
Circle	0.1295 (3)	0.1163 (2)	0.1016 (1)
Box	0.1350 (3)	0.1309 (2)	0.1014 (1)

Table 6.4: NRMSE multi-step performance model on validation data. The best model performance is marked in green and with the number (1), the second model performance is marked in orange and with the number (2), and the worst model performance is marked in red and with the number (3).

By analysing the results for the different geometries in Tables 6.3 and 6.4, it is possible to see that the linear ARX model structure finds the triangular geometry the most difficult to simulate, followed by the rectangular and the circular one. This suggests that the degree of nonlinearity in the data is greater in the triangular geometry, followed by the rectangular and then the circular one. From a fluid dynamics point of view, the amount of nonlinearity can be correlated to the body shapes, by observing that the triangle has the most nonlinear hydrostatic characteristics (see Fig. 6.18). On the other hand, the box has a linear restoring curve, but a very flat bottom with sharp corners, which can be the source of important nonlinear effects, based on viscosity and vortex shedding. Finally the circle has a moderate nonlinearity in the hydrostatic curve and a very smooth shape, which may create moderate viscosity and vorticity effects. Figs. 6.24 and 6.25 show, for experiments $T1$ and $T2$, respectively, the multi-step predictions of the identified ARX, Hammerstein and KGP models. It is possible to see that none of the identified models is perfect, but the linear model has particular difficulty in following peaks in the excitation force. In Fig. 6.26, the models, trained with experiment $T1$, are utilised to simulate multi-step predictions on the validation experiment, characterised by a sinusoidal FSE with an amplitude of 0.72 m and a frequency of 0.1 Hz; it can be seen that the fully nonlinear NWT simulation exhibits an asymmetric output, with respect to the MFSE, in response to the symmetrical sinusoidal η (a typical example of nonlinear behaviour), owing to the fact that the triangle's geometry is asymmetric with respect to the MFSE. The linear ARX model is not able to replicate this nonlinear behaviour and is outperformed by the nonlinear models, which approximate the asymmetric output well.

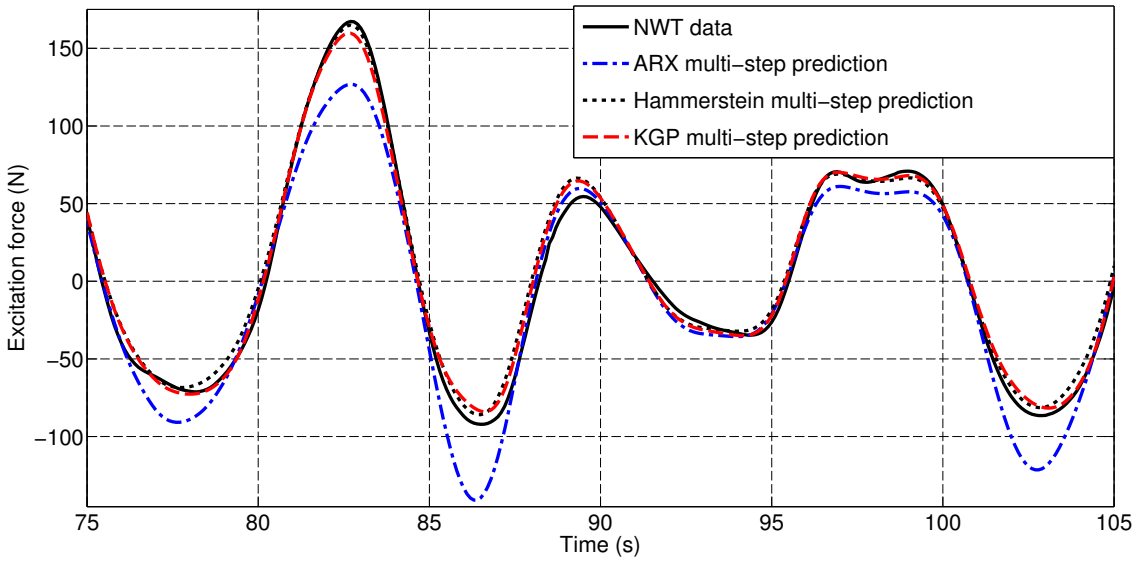

Figure 6.24: Multi-step predictions, of the identified models, on the training experiment $T1$ (only a portion of the data is plotted).

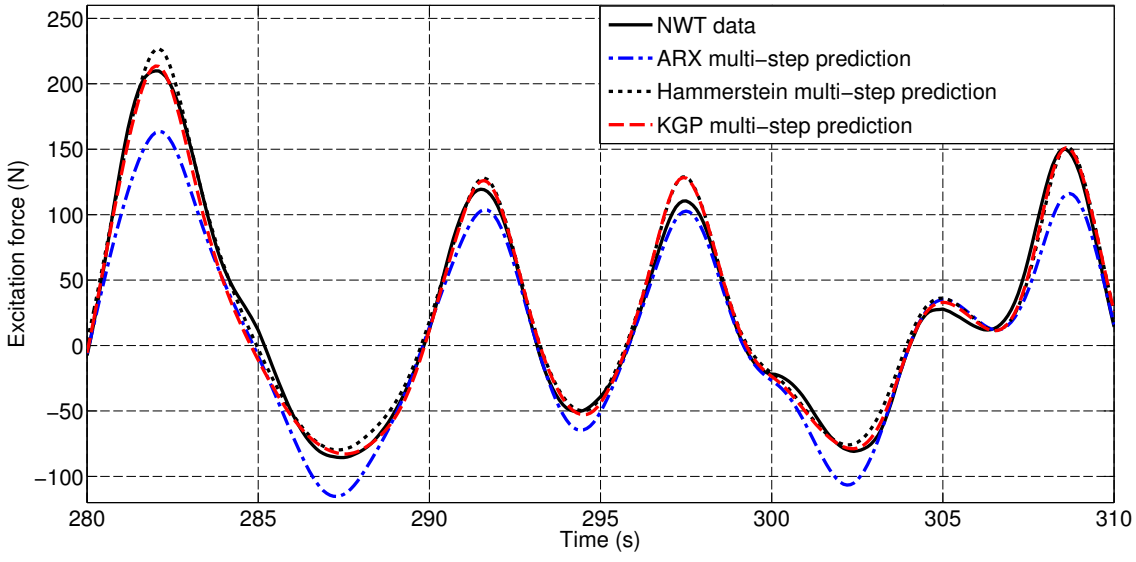

Figure 6.25: Multi-step predictions of the models (identified with $T1$), in the case of the validation experiment $T2$ (only a portion of the data is plotted).

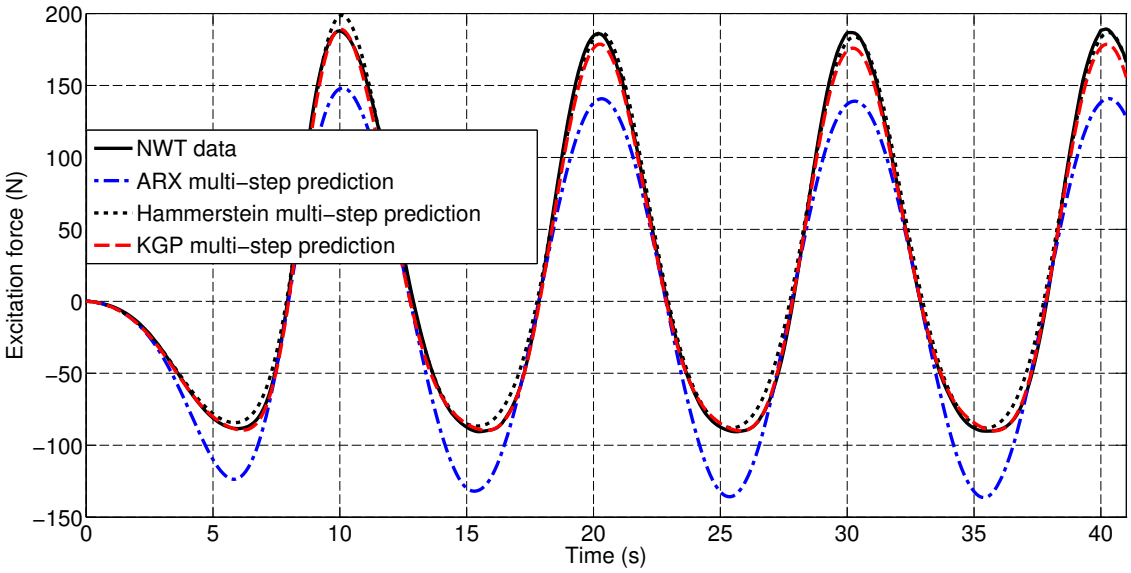

Figure 6.26: The models, trained with experiment $T1$, are utilised to simulate multi-step predictions on the validation experiment, characterised by a sinusoidal FSE with an amplitude of 0.72 m and a frequency of 0.1 Hz.

In general, the fitting error of an identified model is usually larger in validation than in training. By comparing the NRMSE of a model over training and validation (see Tables 6.3 and 6.4, respectively), it is possible to observe the degradation of performance of a model from training to validation. Therefore, in this thesis, a new metric is proposed, termed the normalised validation training degradation (NVTD) parameter, defined as:

$$NVTD = \frac{\text{NRMSE(validation) - NRMSE(training)}}{\text{NRMSE(training)}} \tag{6.21}$$

• In the case where NVTD < 0, the identified model performs better on the validation data than on the training data (the identified model shows good ability in generalizing on new data)
• In the case where NVTD $\simeq 0$, the identified model performs similarly on the validation and training data (the identified model shows good ability in generalizing on new data).
• In the case where NVTD $\gg 0$, the identified model performance degrades on the validation data (the identified model shows difficulties in generalizing on new data).
In this thesis, a NVTD = 0.25 is chosen as an upper threshold for a model having a good ability in generalizing. Table 6.5, shows the NVTD parameter, resulting from Tables 6.3 and 6.4, where it is possible to see that NVTD$<$ 0.25 always, indicating a parsimonious structure for the models and a good estimate for the parameter vectors.

Geometry	ARX	Hammerstein	KGP
Triangle	0.0734	0.0613	0.1061
Circle	0.0503	0.0247	0.1020
Box	0.0297	0.0307	0.0552

Table 6.5: NVTD parameter values, resulting from Tables 6.3 and 6.4.

6.3 Identification of $f_{in} \rightarrow y$ models (two case studies)

In this section, different NARX DT model structures (see Section 3.2.3), belonging to the $f_{in} \rightarrow y$ model family, are identified, in order to describe the heave motion of a floating body, in response to an input PTO force, under the hypotheses of no incident waves and no mooring forces. As shown in Fig. 6.27, the block $f_{in} \rightarrow y$ takes, as input, the summation of f_e, f_{pto} and f_m; therefore, the block is not able to differentiate between these three forces. This equivalence, within the assumption of separation of the fluid-body force in excitation, radiation and buoyancy forces (see Section 2.4.1), can be utilised for the identification of $f_{in} \rightarrow y$ models, by applying a dynamically rich PTO force. Indeed, as outlined in Section 4.2, the signal, used to excite the system during the experiment, plays an important role in SI. Ideally, in order to obtain all the required identification information, the input signal should be able to excite the system as much as possible, in the shortest possible time. The direct application of a PTO force allows total freedom over the choice of input signal to be applied to the system (unlike the input wave experiments, where the choice of input signal is constrained by the laws of fluid dynamics). Two different case studies of $f_{in} \rightarrow y$ model identification are considered, in the first case (see Sections 6.3.1), sinusoidal PTO force signals are intentionally chosen with a low frequency content to emphasize the static nonlinearity of the restoring force, whereas, in the second case (see Section 6.3.2), different dynamically rich PTO force signals are utilised (i.e. RARP, multisine and chirp signals).

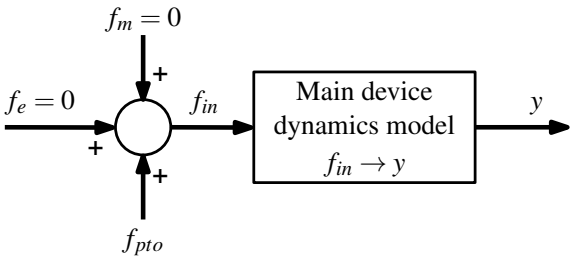

Figure 6.27: General block diagram of a WEC model, inspired by the CT Cummins' equation, to describe the relationship between f_{in} and y, in the case of no incident waves and no mooring forces.

6.3.1 Conical body case ($f_{in} \rightarrow y$ models)

In this case study, three different NARX DT model structures, belonging to the $f_{in} \rightarrow y$ model family, are identified (i.e. ARX, Hammerstein and FBO model structures), in order to describe the heave motion of a floating conical body, in response to an input PTO force, under the hypotheses of no incident waves and no mooring forces. The data, utilised for model identification, are generated in a 3D CFD-NWT. Initially, a simple linear ARX model is considered and, then, the addition of a nonlinear static block is demonstrated to enable the model to capture nonlinear hydrodynamic effects. The PTO force signal is intentionally chosen with a low frequency content (a pure sinusoid of 0.125 Hz) to emphasize the static nonlinearity of the restoring force, by reducing other possible velocity-dependent nonlinearities. For comparison with the linear ARX model, a traditional linear CT model (in this chapter termed the Cummins-BEM model), based on a parametric form of Cummins' equation, is also evaluated, by using frequency domain hydrodynamic coefficients, calculated by the BEM software WAMIT.

6.3.1.1 NWT and floating body description

The data utilised in this case study are generated in a 3D CFD-NWT, implemented in OpenFOAM (see Section 2.3.1). The tank has a geometry of a parallelepiped, with a 3 m height, 21 m width and 21 m thickness; above the water, there is a volume of air with a 1.5 m height, as shown in Fig. 6.28. The test device is placed in the exact centre of the tank. The geometry of the device is a vertical cone, which has strong known nonlinearities in its restoring force, and is thus chosen to illustrate the different model capabilities of handling this effect. The cone has a mass of 130.5 kg, a diameter and height of 1 m and is orientated with its axis aligned vertically, with the base above the tip. The cone's mass density is 50% of the water density, resulting in a submerged draft of about 0.8 m (see Fig. 6.29). The body only moves in heave along the tank's central axis and, by utilising the symmetry of the NWT and body geometries, it is possible to simplify the meshing process and reduce the spatial computation domain, by modelling only a quarter of the NWT and body (as shown in Fig. 6.30), with the consequent reduction of the computation time of the simulations (the symmetric boundary conditions are implemented in OpenFOAM, by using the *wedge* command [50]). The quarter NWT contains a total of 142,000 cells. It is important to underline that the vertical force, applied from the fluid to the body, is 4 times the vertical force calculated by the NWT.

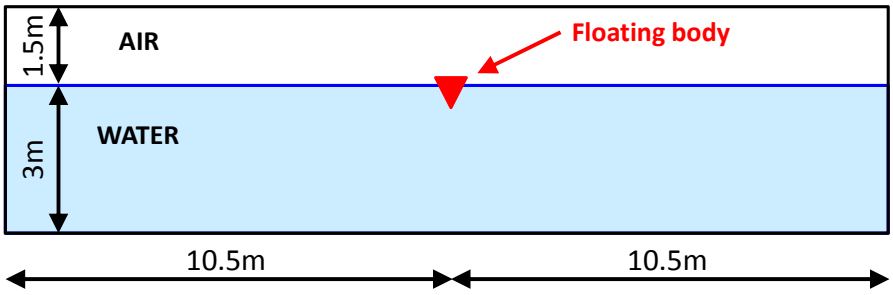

Figure 6.28: NWT side view.

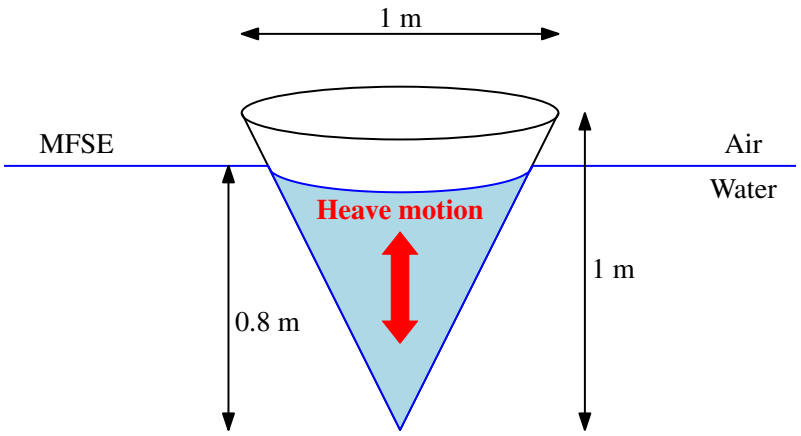

Figure 6.29: Body geometry.

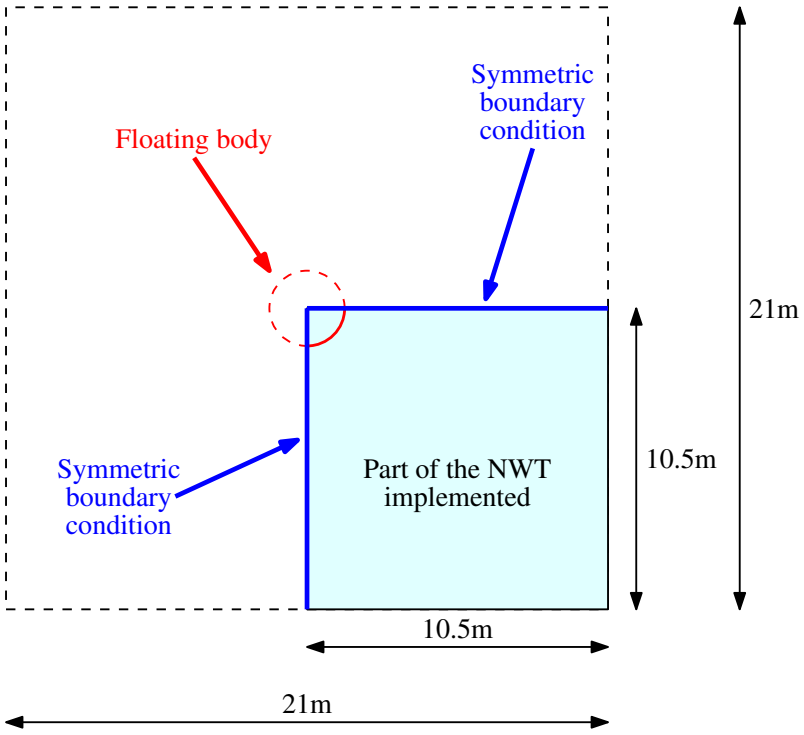

Figure 6.30: NWT top view. The spatial computation domain is reduced by modelling only a quarter of the NWT and the body, by using symmetric boundary conditions, with the consequent reduction of the computation time of the simulations.

6.3.1.2 Generated NWT data description

The utilised nonlinear model structures (i.e. Hammerstein and FBO models) contain two different types of blocks: the linear dynamic block and the nonlinear static block. This section details the two different NWT experiments, used to identify these two different types of blocks. The input force experiment is used to identify the linear dynamic block and the nonlinear static block is identified with the prescribed motion experiment.

Input force experiments

The input force experiment (see Section 4.3.2.3) excites the body with a PTO input force, $\{f_{in.d}(k)\}$, and measures the resulting body motion, $\{y_{in.d}(k)\}$, both considered positive when they are upward (see Table 6.6). The subscript 'd' indicates 'dynamic'. The input force experiments have a duration of 60 s and a sampling period $T_s = 0.1$ s. In this case study, the input force experiment is utilised for the identification of the dynamic block of the Hammerstein, FBO and ARX models, as shown in Table 6.6. The signal $\{f_{in.d}(k)\}$ represents the force applied to the complete cone (the force is four times the force simulated by the quarter NWT, shown in Fig. 6.30). Two different input force experiments are carried out:

• *Input force experiment 1:* The body is subject to a sinusoidal input PTO force, having a relatively low frequency of 0.125 Hz and a relatively small amplitude of 240 N. The frequency of this experiment was intentionally chosen low, to emphasize the static nonlinearity of the restoring force, by reducing other possible velocity-dependent nonlinearities. The body is also initially displaced 30 cm above its equilibrium position, allowing its free decay oscillation to be superimposed on the response to the PTO force, as shown in Fig. 6.31.

• *Input force experiment 2:* The only difference of this experiment, with input force experiment 1, is in the amplitude of the sinusoidal input PTO force, in this it case has a larger amplitude of 960 N, as shown in Fig. 6.32.

Experiment type	Input signal type {Input symbol}	Output signal type {Output symbol}	Identified model
Input force	PTO force $\{f_{in.d}(k)\}$	Body displacement $\{y_{in.d}(k)\}$	ARX Hammerstein (ARX block) FBO (ARX block)
Prescribed motion	Body displacement $\{y_s(k)\}$	Buoyancy force $\{f_{b.s}(k)\}$	Hammerstein (static block) FBO (static block)

Table 6.6: Generated data in the different NWT experiments.

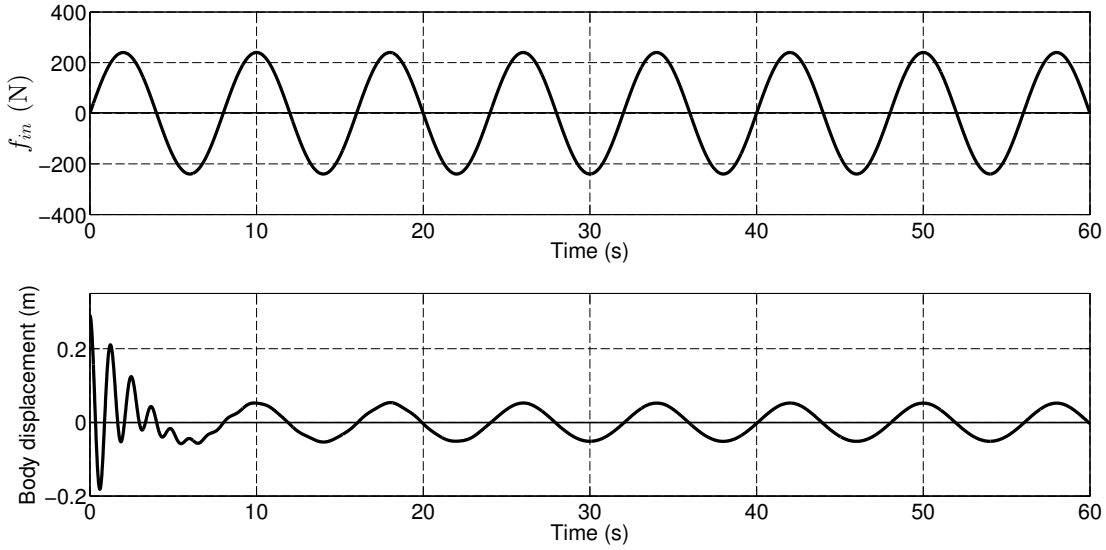

Figure 6.31: NWT data from input force experiment 1, for the complete cone (the force is four times the force simulated by the quarter NWT, shown in Fig. 6.30). The body is subject to a sinusoidal input PTO force, and is also initially displaced 30 cm above its equilibrium position, allowing its free decay oscillation to be superimposed on the response to the PTO force.

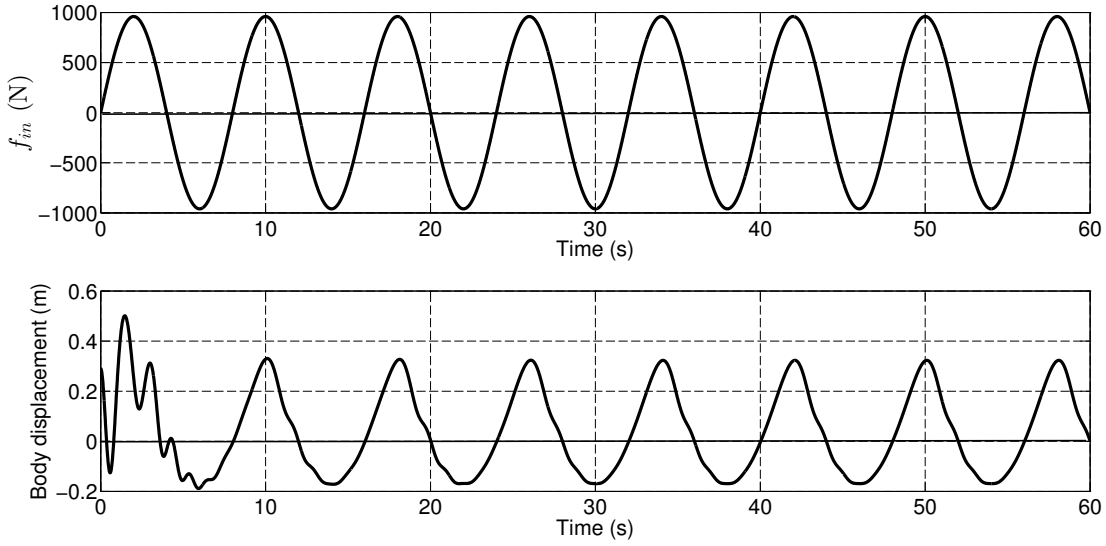

Figure 6.32: NWT data from input force experiment 2, for the complete cone (the force is four times the force simulated by the quarter NWT, shown in Fig. 6.30). The body is subject to a sinusoidal input PTO force, and is also initially displaced 30 cm above its equilibrium position, allowing its free decay oscillation to be superimposed on the response to the PTO force.

Prescribed motion experiments

The prescribed motion experiment (see Section 4.3.2.4) can be used to identify the static relationship between the body displacement and the hydrostatic force. The body is displaced through its full range of motion and the resulting force, applied from the fluid to the body, is measured, which corresponds to the buoyancy force (since the body moves very slowly, all the hydrodynamic effects are negligible). Two vectors, containing the body displacement, $\{y_s(k)\}$, and the hydrostatic (buoyancy) force, $\{f_{b.s}(k)\}$, are produced by this experiment, as shown in Table 6.6. The subscript 's' indicates '(almost) static'. The results from the prescribed motion experiment are shown in Fig. 6.33, with Fig. 6.33(a) showing the motion of the body, starting from the fully submerged position and slowly moving out of the water, and Fig. 6.33(b) showing the hydrostatic force on the body, during this motion. At the beginning of the simulation, which corresponds to the totally submerged cone, the hydrostatic force is equal to 2560 N, which is analytically confirmed by $f_b = \rho g V_b$ = 2560 N, where $\rho = 997$ kg/m^3 is the water density, g the gravitational acceleration and $V_b = \pi R^2 h/3$ the totally submerged volume, where $R = 0.5$ m and $h = 1$ m, are the cone radius and height, respectively. The information provided by this experiment can be manipulated,

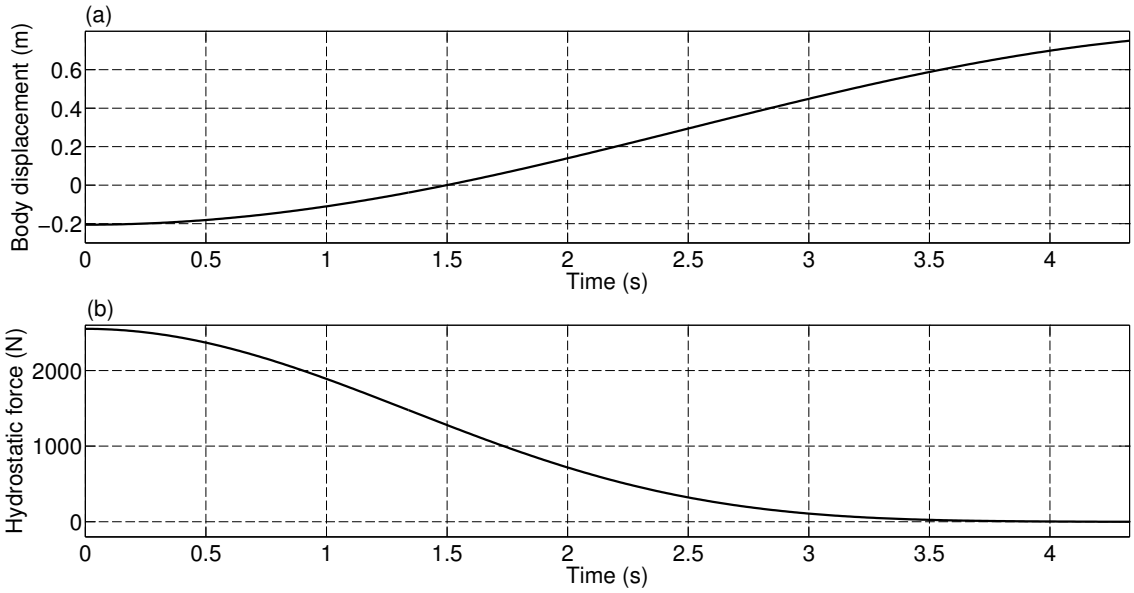

Figure 6.33: NWT data from the prescribed motion experiment for the complete cone (the force is four times the force simulated by the quarter NWT, shown in Fig. 6.30). (a) Motion of the body, starting from the fully submerged position and slowly moving out of the water. (b) Hydrostatic force on the body, during the motion.

in order to identify the static curves of the Hammerstein and FBO models. In Fig. 6.34(a), the hydrostatic force is plotted as a function of the position, which shows the nonlinear nature of this relationship. The restoring force on the body is given by $f_{re} = f_b - Mg$ (see Section 2.2.7); therefore, the restoring curve, shown in Fig. 6.34(b), is just the curve of Fig. 6.34(a), vertically shifted. The static curve $g()$, of the FBO model, shown in Fig. 6.34(c), has the body displacement and $-f_{re}$ as input and output variables, respectively (see Section 6.3.1.3). Therefore, $g()$ is obtained by mirroring the curve shown in Fig. 6.34(b), with respect to the horizontal axis. In static conditions, the body does not move as a consequence of the fact that the force applied by the PTO is balanced by the restoring force; therefore, in static conditions $f_{in} = -f_{re}$. The Hammerstein static curve, $r()$, shown in Fig. 6.34(d), has f_{in} and the body displacement as input and output variables, respectively (see Section 6.3.1.3 for details). As a consequence, Fig. 6.34(d) can be obtained by swapping horizontal and vertical axes of Fig. 6.34(c). In this way, by considering the physical

meaning of the nonlinear static function, the Hammerstein and FBO model structures are given a lighter shade of 'grey. Fig. 6.35 shows the comparison of the NWT data, resulting from the prescribed motion experiment, with the theoretical cone restoring curve, resulting from analytical volume calculations [303]; it is possible to see the excellent agreement.

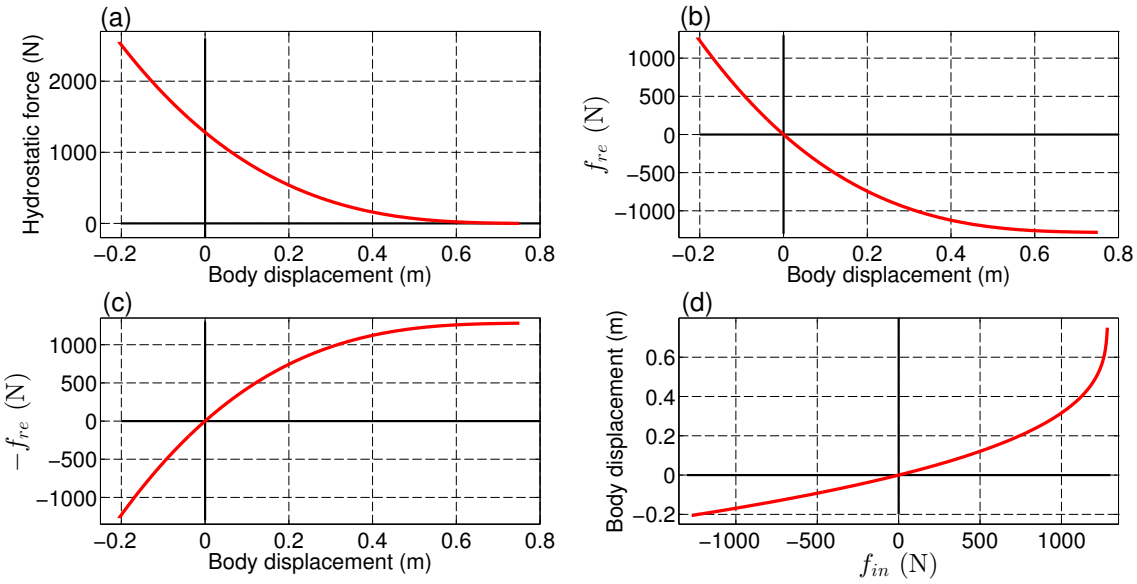

Figure 6.34: (a) Hydrostatic force as a function of the body position (results from the prescribed motion experiment). (b) Restoring force as a function of the body position. (c) FBO static curve $g()$. (d) Hammerstein static curve $r()$.

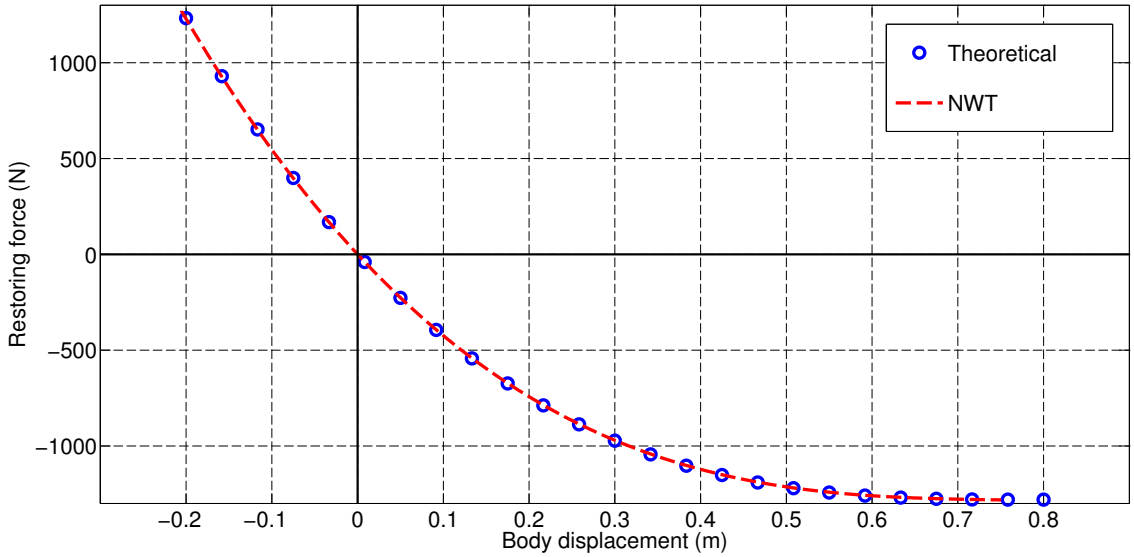

Figure 6.35: Comparison of the NWT data, resulting from the prescribed motion experiment, with the theoretical restoring curve of the cone.

6.3.1.3 Model description and identification

ARX model

In the case of the $f_{in} \rightarrow y$ model family, the input/output relationship of the ARX model structure

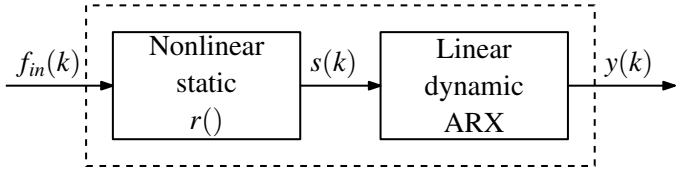

Figure 6.36: Block diagram of the Hammerstein model for a $f_{in} \rightarrow y$ hydrodynamic structure.

is given (see Section 3.2.3.1) by:

$$y(k) = \sum_{i=1}^{n_a} a_i y(k-i) + \sum_{i=0}^{n_b} b_i f_{in}(k-n_d-i) \tag{6.22}$$

By performing the input force experiment, the signals $\{f_{in.d}(k)\}$ and $\{y_{in.d}(k)\}$, for $k = 1...N$, are generated (see Section 6.3.1.2), which can be utilised as input and output data, respectively, for the identification of the ARX model. The first possible predicted model output is for $k = \tau + 1$, where τ is given by equation (6.5). The last possible predicted model output is for $k = \widetilde{N}$, where $\widetilde{N}$ is given by equation (6.6). In this case, equations (3.61) and (3.62) become:

$$\mathbf{y} = \begin{bmatrix} y_{in.d}(\tau+1) & y_{in.d}(\tau+2) & \dots & y_{in.d}(\widetilde{N}) \end{bmatrix}^T \tag{6.23}$$

and

$$\mathbf{\Phi} = \begin{bmatrix} y_{in.d}(\tau) & \dots & y_{in.d}(\tau+1-n_a) & f_{in.d}(\tau+1-n_d) & \dots & f_{in.d}(\tau+1-n_d-n_b) \\ y_{in.d}(\tau+1) & \dots & y_{in.d}(\tau+2-n_a) & f_{in.d}(\tau+2-n_d) & \dots & f_{in.d}(\tau+2-n_d-n_b) \\ \vdots & \ddots & \vdots & \vdots & \ddots & \vdots \\ y_{in.d}(\widetilde{N}-1) & \dots & y_{in.d}(\widetilde{N}-n_a) & f_{in.d}(N) & \dots & f_{in.d}(N-n_b) \end{bmatrix}, \tag{6.24}$$

respectively. The estimated parameter vector, $\hat{\boldsymbol{\theta}}_{arx} = [a_1 \ \dots \ a_{n_a} \ \ b_0 \ \dots \ b_{n_b}]^T$, is determined by utilising $\mathbf{y}$, $\mathbf{\Phi}$ and QR factorization to resolve the LS problem (see Section 3.3.1.1).

Hammerstein model

The Hammerstein model block diagram, shown in Fig. 6.36, is described by the input/output relationship (see Section 3.2.3.3) given by:

$$y(k) = \sum_{i=1}^{n_a} a_i y(k-i) + \sum_{i=0}^{n_b} b_i r\Big(f_{in}(k-n_d-i)\Big) \tag{6.25}$$

The nonlinear static function $r()$ is approximated with a polynomial; therefore, the relationship between the input and the output of the nonlinear static block is given by:

$$s(k) = c_1 f_{in}(k) + c_2 f_{in}^2(k) + \dots + c_{n_c} f_{in}^{n_c}(k) \tag{6.26}$$

where $c_0 = 0$; indeed, in the case of (almost) static conditions, no incident waves generated and in the absence of an applied PTO force, the body displacement has to be zero. The Hammerstein model is identified following the two steps explained in Section 3.3.1.4. In the first step, the data generated by the prescribed motion experiment $\{f_{b.s}(k)\}$ and $\{y_s(k)\}$ (see Section 6.3.1.2) are utilised to identify the nonlinear static function $r()$. As explained in Section 3.3.1.4, in (almost) static conditions:

$$\{s_s(k)\} = \{y_s(k)\} \tag{6.27}$$

and input PTO and restoring forces have same intensity and opposite direction (see Section 6.3.1.2), and so:

$$\{f_{in.s}(k)\} = -\big(\{f_{b.s}(k)\} - Mg\big). \tag{6.28}$$

Equations (6.27) and (6.28) provide output and input data, respectively, in order to identify the Hammerstein static block $r()$, *separately* from the linear dynamic block. In this case, equations (3.68) and (3.69) become:

$$\mathbf{y} = \begin{bmatrix} y_s(1) & y_s(2) & \dots & y_s(N) \end{bmatrix}^T \tag{6.29}$$

and

$$\mathbf{\Phi} = \begin{bmatrix} [f_{in.s}(1)]^1 & [f_{in.s}(1)]^2 & \dots & [f_{in.s}(1)]^{n_c} \\ [f_{in.s}(2)]^1 & [f_{in.s}(2)]^2 & \dots & [f_{in.s}(2)]^{n_c} \\ \vdots & \vdots & \ddots & \vdots \\ [f_{in.s}(N)]^1 & [f_{in.s}(N)]^2 & \dots & [f_{in.s}(N)]^{n_c} \end{bmatrix}, \tag{6.30}$$

respectively. The estimated parameter vector $\hat{\boldsymbol{\theta}}_{H_c} = [c_1 \ \dots \ c_{n_c}]^T$ is determined by utilising $\mathbf{y}$, $\mathbf{\Phi}$ and QR factorization to resolve the LS problem. In order to determine a parsimonious value of n_c, the parameter vector $\hat{\boldsymbol{\theta}}_{H_c}$ is calculated for different values of n_c, together with the associated static curve fitting error, given by equations (3.95) and (6.26):

$$NRMSE(n_c) = \frac{\| \, y_s(k) - \sum_{j=1}^{n_c} c_j f_{in.s}^j(k) \, \|_2}{\| \, y_s(k) \, \|_2} = \frac{\sqrt{\sum_{k=1}^{N} |y_s(k) - \sum_{j=1}^{n_c} c_j f_{in.s}^j(k)|^2}}{\sqrt{\sum_{k=1}^{N} |y_s(k)|^2}} \tag{6.31}$$

The smallest n_c, which leads to a fitting error of less than 3%, is selected (as a good compromise between parsimony and accuracy). Fig. 6.37 shows the NRMSE of the static curves of the Hammerstein model, as a function of n_c, where it is possible to see that $n_c = 10$ is the smallest polynomial order, which guarantees a fitting error of less than 3% (see Table 6.7). Fig. 6.38 shows the fitting of the static curve of the Hammerstein model, in the case of $n_c = 10$.

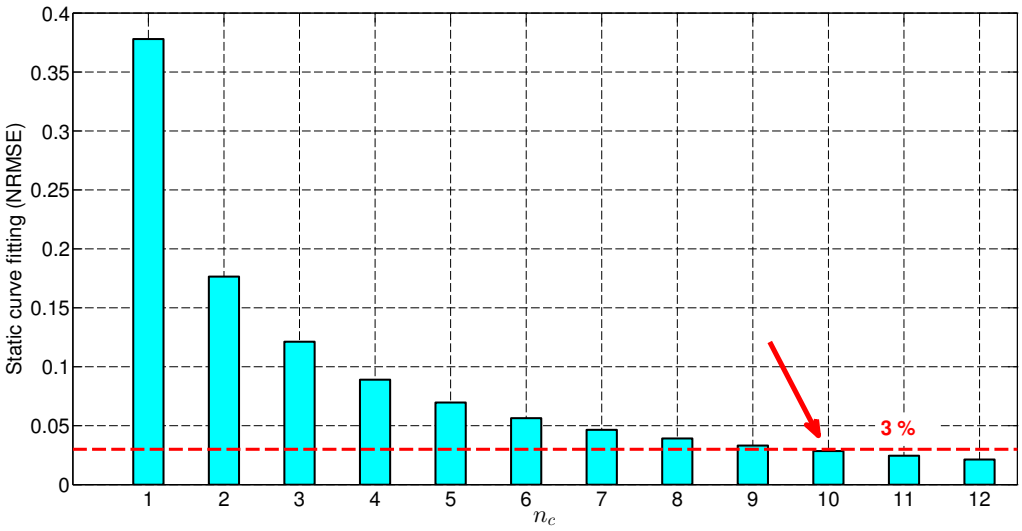

Figure 6.37: Fitting error of the static curve of the Hammerstein model, for different polynomial order n_c. A fitting error of less than 3% is given by $n_c = 10$.

n_a	n_b	n_d	n_c Hammerstein	n_c FBO
5	4	0	10	3

Table 6.7: n_a, n_b, n_d and n_c utilised for the different DT model structures.

In the second step, the ARX block is identified by utilising the signals $\{f_{in.d}(k)\}$ and $\{y_{in.d}(k)\}$, generated by the input force experiments (see Section 6.3.1.2). Now that the parameter vector $\hat{\boldsymbol{\theta}}_{H_c}$

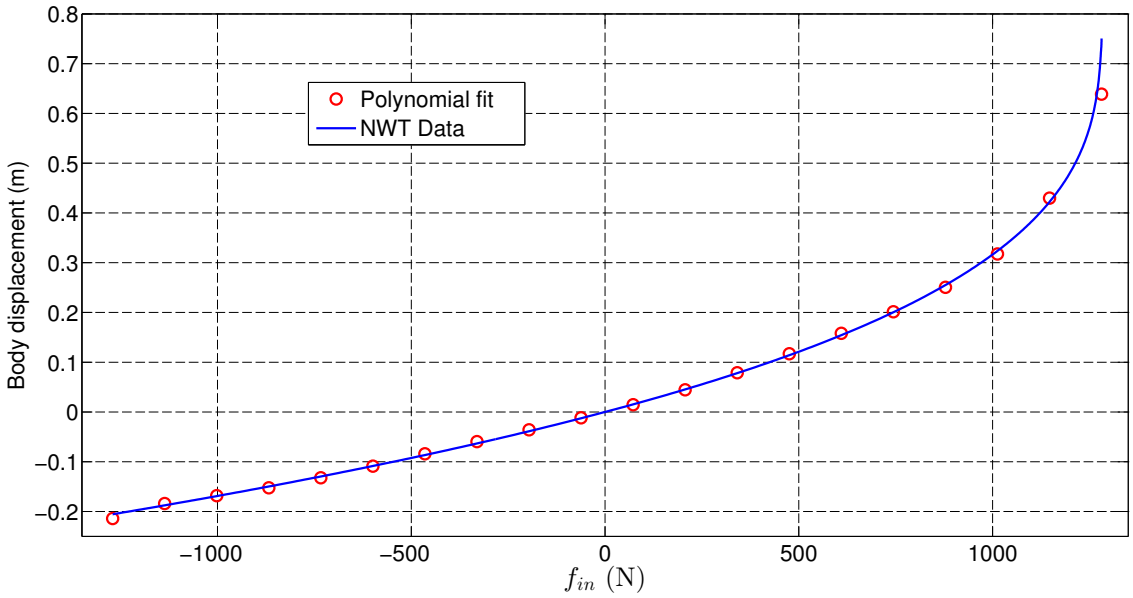

Figure 6.38: Hammerstein nonlinear static function $r()$ fitting, with $n_c = 10$.

is known, the input $\{f_{in.d}(k)\}$ is transformed through the nonlinear static block, in order to obtain $\{s_d(k)\}$, by using equation (6.26). Next, $\{s_d(k)\}$ and $\{y_{in.d}(k)\}$ are used as the input and output data to identify the ARX parameter vector, $\hat{\boldsymbol{\theta}}_{H_{arx}}$, under the constraint that the DC gain of the ARX model is unity (see Section 3.3.1.4). In this case, equations (3.72) and (3.73) become:

$$\mathbf{y} = \begin{bmatrix} y_{in.d}(\tau+1) & y_{in.d}(\tau+2) & \dots & y_{in.d}(\widetilde{N}) \end{bmatrix}^T \tag{6.32}$$

and

$$\boldsymbol{\Phi} = \begin{bmatrix} y_{in.d}(\tau) & \dots & y_{in.d}(\tau+1-n_a) & s_d(\tau+1-n_d) & \dots & s_d(\tau+1-n_d-n_b) \\ y_{in.d}(\tau+1) & \dots & y_{in.d}(\tau+2-n_a) & s_d(\tau+2-n_d) & \dots & s_d(\tau+2-n_d-n_b) \\ \vdots & \ddots & \vdots & \vdots & \ddots & \vdots \\ y_{in.d}(\widetilde{N}-1) & \dots & y_{in.d}(\widetilde{N}-n_a) & s_d(N) & \dots & s_d(N-n_b) \end{bmatrix}, \tag{6.33}$$

respectively, where τ and $\widetilde{N}$ are given by equations (6.5) and (6.6), respectively. The estimated parameter vector, $\hat{\boldsymbol{\theta}}_{H_{arx}} = [a_1 \ \dots \ a_{n_a} \ b_0 \ \dots \ b_{n_b}]^T$, is given by:

$$\hat{\boldsymbol{\theta}}_{H_{arx}} = \hat{\boldsymbol{\theta}}^{(uc)}_{H_{arx}} - (\boldsymbol{\Phi}^T\boldsymbol{\Phi})^{-1}\mathbf{A}^T(\mathbf{A}(\boldsymbol{\Phi}^T\boldsymbol{\Phi})^{-1}\mathbf{A}^T)^{-1}(\mathbf{A}\hat{\boldsymbol{\theta}}^{(uc)}_{H_{arx}} - \mathbf{d}), \tag{6.34}$$

where $\mathbf{A} = [1,1,...,1] \in \Re^{1\times(n_a+n_b+1)}$ and $\mathbf{d} = 1$ (see Section 3.3.1.4), and the unconstrained parameter vector, $\hat{\boldsymbol{\theta}}^{(uc)}_{H_{arx}}$, is calculated by utilising QR factorization to resolve the LS problem.

FBO model

As explained in Section 3.2.2, Cummins' equation can be expressed in the form of a FBO model, which has the block diagram shown in Fig. 6.39. In this negative feedback configuration, the nonlinear static block, $g()$, relates the body position to the negative of the restoring force $(-f_{re}(k))$; therefore, $g()$ can be identified *separately* from the linear dynamic block, from the knowledge of the restoring force as a function of the body position. The nonlinear static function $g()$ is approximated with a polynomial; therefore, the relationship between the input and the output of the nonlinear static block is given by:

$$-f_{re}(k) = c_1 y(k) + c_2 y^2(k) + ... + c_{n_c} y^{n_c}(k) \tag{6.35}$$

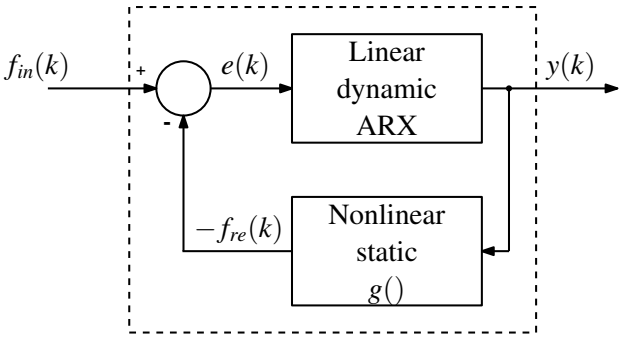

Figure 6.39: Block diagram of the FBO model, in the case of a $f_{in} \rightarrow y$ hydrodynamic structure.

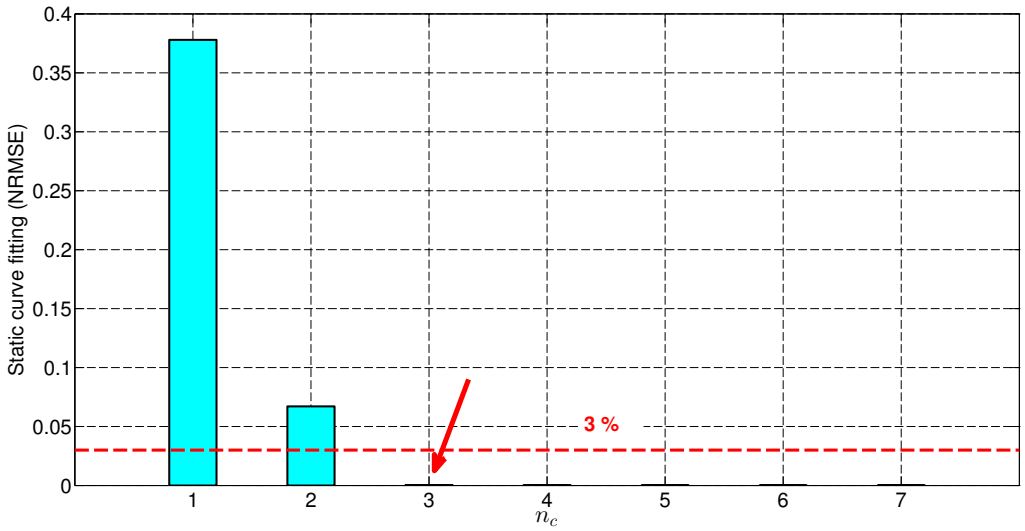

Figure 6.40: Fitting error of the static curve of the FBO model, for different polynomial order n_c. A fitting error of less than 3% is given by $n_c = 3$.

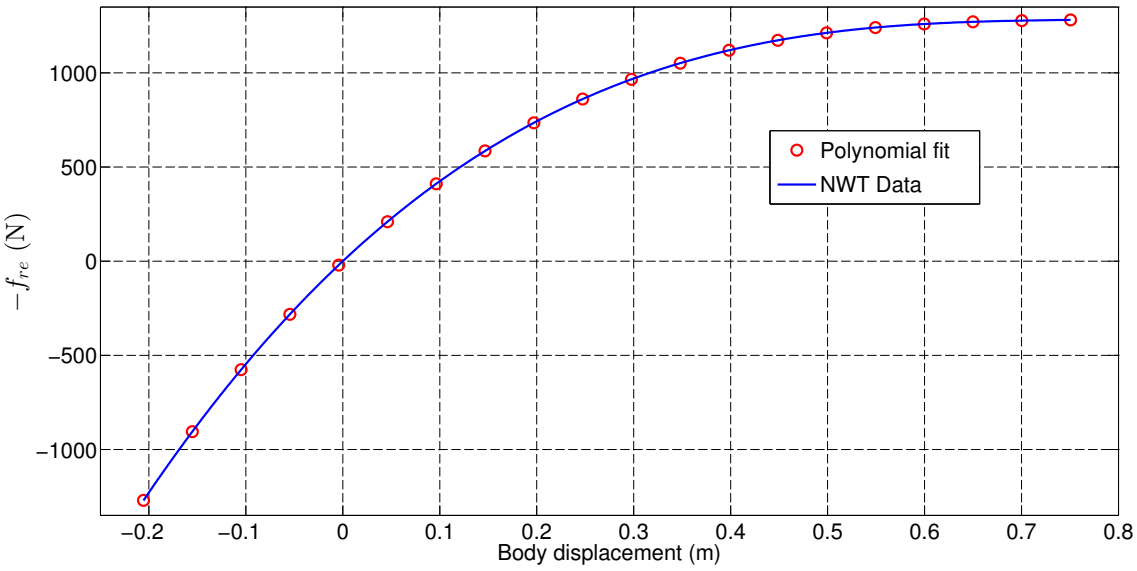

Figure 6.41: FBO nonlinear static function $r()$ fitting, with $n_c = 3$.

where $c_0 = 0$ is set (in the case of a null displacement from the equilibrium position, the restoring force has to be zero). The FBO model is identified following the two steps explained in Section 3.3.1.5.

In the first step, the data generated by the prescribed motion experiment $\{f_{b.s}(k)\}$ and $\{y_s(k)\}$ (see Section 6.3.1.2) can be utilised to identify the nonlinear static function $g()$. From $\{f_{b.s}(k)\}$ and from the definition of restoring force (see Section 2.2.7), it follows that:

$$\{-f_{re.s}(k)\} = -(\{f_{b.s}(k)\} - Mg) \tag{6.36}$$

Consequently, output and input identification data for the static block, respectively $\{-f_{re.s}(k)\}$ and $\{y_s(k)\}$, are available and the curve $g()$ can be identified, *separately*, from the linear dynamic block. In this case, equations (3.68) and (3.69) become:

$$\mathbf{y} = \begin{bmatrix} -f_{re.s}(1) & -f_{re.s}(2) & \dots & -f_{re.s}(N) \end{bmatrix}^T \tag{6.37}$$

and

$$\mathbf{\Phi} = \begin{bmatrix} [y_s(1)]^1 & [y_s(1)]^2 & \dots & [y_s(1)]^{n_c} \\ [y_s(2)]^1 & [y_s(2)]^2 & \dots & [y_s(2)]^{n_c} \\ \vdots & \vdots & \ddots & \vdots \\ [y_s(N)]^1 & [y_s(N)]^2 & \dots & [y_s(N)]^{n_c} \end{bmatrix}, \tag{6.38}$$

respectively. The estimated parameter vector, $\hat{\boldsymbol{\theta}}_{F_c} = [c_1 \ \dots \ c_{n_c}]^T$, is determined by utilising $\mathbf{y}$, $\mathbf{\Phi}$ and QR factorization to resolve the LS problem. Similarly to the Hammerstein model identification, in order to determine a parsimonious value of n_c, the parameter vector $\hat{\boldsymbol{\theta}}_{F_c}$ is calculated for different values of n_c, together with the associated static curve fitting error, given by equations (3.95) and (6.35):

$$NRMSE(n_c) = \frac{\| -f_{re.s}(k) - \sum_{j=1}^{n_c} c_j y_s^j(k) \|_2}{\| -f_{re.s}(k) \|_2} = \frac{\sqrt{\sum_{k=1}^{N} | -f_{re.s}(k) - \sum_{j=1}^{n_c} c_j y_s^j(k)|^2}}{\sqrt{\sum_{k=1}^{N} | -f_{re.s}(k)|^2}} \tag{6.39}$$

The smallest n_c, that leads to a fitting error of less than 3%, is selected (as a good compromise between parsimony and accuracy). Fig. 6.40 shows the NRMSE of the static curve of the FBO model, as a function of n_c, where it is possible to see that $n_c = 3$ is the smallest polynomial order, which guarantees a fitting error of less than 3% (see Table 6.7). Fig. 6.41 shows the fitting of the static curve of the FBO model for $n_c = 3$.

In the second step, the ARX block is identified by utilising the signals $\{f_{in.d}(k)\}$ and $\{y_{in.d}(k)\}$, generated by the input force experiment (see Section 6.3.1.2). Now that the parameter vector $\hat{\boldsymbol{\theta}}_{F_c}$ is known, the signal $\{y_{in.d}(k)\}$ is transformed through the nonlinear static block, in order to obtain $\{e_d(k)\}$, by using equation (6.35):

$$e_d(k) = f_{in.d}(k) - \Big(\sum_{j=1}^{n_c} c_j y_{in.d}^j(k) \Big) \tag{6.40}$$

As a consequence, both input and output signals of the ARX block are known ($\{e_d(k)\}$ and $\{y_{in.d}(k)\}$, respectively) and it is possible to identify the ARX parameters, $\hat{\boldsymbol{\theta}}_{F_{arx}}$ (See Section 3.3.1.5). In this case, equations (3.81) and (3.82) become:

$$\mathbf{y} = \begin{bmatrix} y_{in.d}(\tau+1) & y_{in.d}(\tau+2) & \dots & y_{in.d}(\widetilde{N}) \end{bmatrix}^T \tag{6.41}$$

and

$$\mathbf{\Phi} = \begin{bmatrix} y_{in.d}(\tau) & \dots & y_{in.d}(\tau+1-n_a) & e_d(\tau+1-n_d) & \dots & e_d(\tau+1-n_d-n_b) \\ y_{in.d}(\tau+1) & \dots & y_{in.d}(\tau+2-n_a) & e_d(\tau+2-n_d) & \dots & e_d(\tau+2-n_d-n_b) \\ \vdots & \ddots & \vdots & \vdots & \ddots & \vdots \\ y_{in.d}(\widetilde{N}-1) & \dots & y_{in.d}(\widetilde{N}-n_a) & e_d(N) & \dots & e_d(N-n_b) \end{bmatrix} \tag{6.42}$$

respectively, where τ and $\widetilde{N}$ are given by equations (6.5) and (6.6), respectively. The estimated parameter vector $\hat{\boldsymbol{\theta}}_{F_{arx}} = [a_1 \ \ldots \ a_{n_a} \ b_0 \ \ldots \ b_{n_b}]^T$ is determined by utilising $\mathbf{y}$, $\boldsymbol{\Phi}$ and QR factorization to resolve the LS problem.

Cummins-BEM model

A well established method to develop linear hydrodynamic models consists of using the frequency-dependent coefficients calculated by a BEM software package (see Section 2.4), in order to identify the parameter vector of Cummins' equation, which is approximated with the parametric model structure shown in Fig. 6.42 and, in this chapter, termed the Cummins-BEM model. The Fourier transfer function, $G_{ra}(\omega)$, of the radiation-sub-system, is a parametric rational function approximation of the reduced radiation impedance, given by equation (2.74). The radiation sub-system parameter values are identified by employing the toolbox in [155], which utilises the radiation resistance and the added mass (calculated by the BEM software WAMIT) and LS fitting in the frequency domain (see Section 2.6.1), in order to identify the hydrodynamic parametric model. The restoring coefficient, K, and the high-frequency asymptote of the added mass, m_∞, are also calculated by WAMIT.

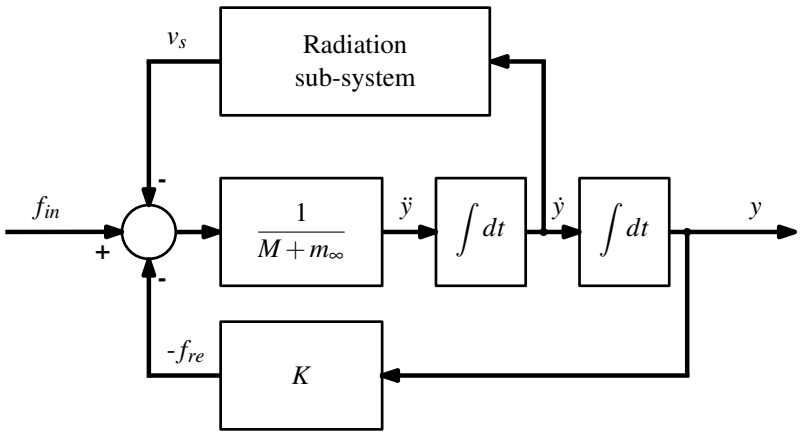

Figure 6.42: Block diagram of the Cummins-BEM model.

6.3.1.4 Results

By utilising the strategy illustrated in Section 3.2.4, the dynamical orders $n_a = 5$ and $n_b = 4$, and the input delay time $n_d = 0$ are identified for the NARX models, as shown in Table 6.7. In the case of input force experiments (both NWT and RWT), the PTO actuator applies a force directly on the body, removing any delay effect between the force applied and the body displacement; therefore, as expected, the identified delay time is null ($n_d = 0$). Fig. 6.43 shows the NWT simulation and the multi-step predictions of the linear ARX and Cummins-BEM models, in the case of input force experiment 1 (see Section 6.3.1.2), characterised by a sinusoidal input PTO force with a relatively small amplitude (240 N). The output contains two parts, the transient due to the initial displacement, and the steady-state response to the harmonic input. It can be seen that, for these small amplitude conditions, the linear models are shown here to work well, for both the transient and the steady-state parts. The NRMSE for the ARX and Cummins-BEM models are, respectively, 0.0862 and 0.0987.

A second set of model predictions are simulated in the case of input force experiment 2 (see Section 6.3.1.2), characterised by a sinusoidal input PTO force with a larger amplitude (960 N). The results are shown in Fig. 6.44, where it is possible to see that the resulting body motions are much larger and that the linear model predictions diverge from the NWT data. Table 6.8 shows the NRMSE multi-step prediction performance. The fully nonlinear NWT simulation exhibits

an asymmetric output, with respect to the equilibrium position, in response to the symmetrical sinusoidal input, owing to the fact that the cone's geometry makes it harder to push into the water than out. It is not possible for the linear models to replicate this nonlinear behaviour.

Finally, the predictions of the nonlinear models, in the case of input force experiment 2 (characterised by the larger input force amplitude of 960 N), are compared to the NWT simulation in Fig. 6.45. Here it can be seen that the nonlinear models outperform their linear counterparts' performance for the same case, shown in Fig. 6.44. The nonlinear models are able to replicate the asymmetric steady-state response, and better able to reproduce the transient oscillations, particularly the FBO model, which performs very well (see Table 6.8 for the NRMSE multi-step prediction performance).

Model	NRMSE
ARX	0.3190
Cummins-BEM	0.3348
Hammerstein	0.1343
FBO	0.0729

Table 6.8: NRMSE multi-step prediction performance of the identified models, in the case of input force experiment 2.

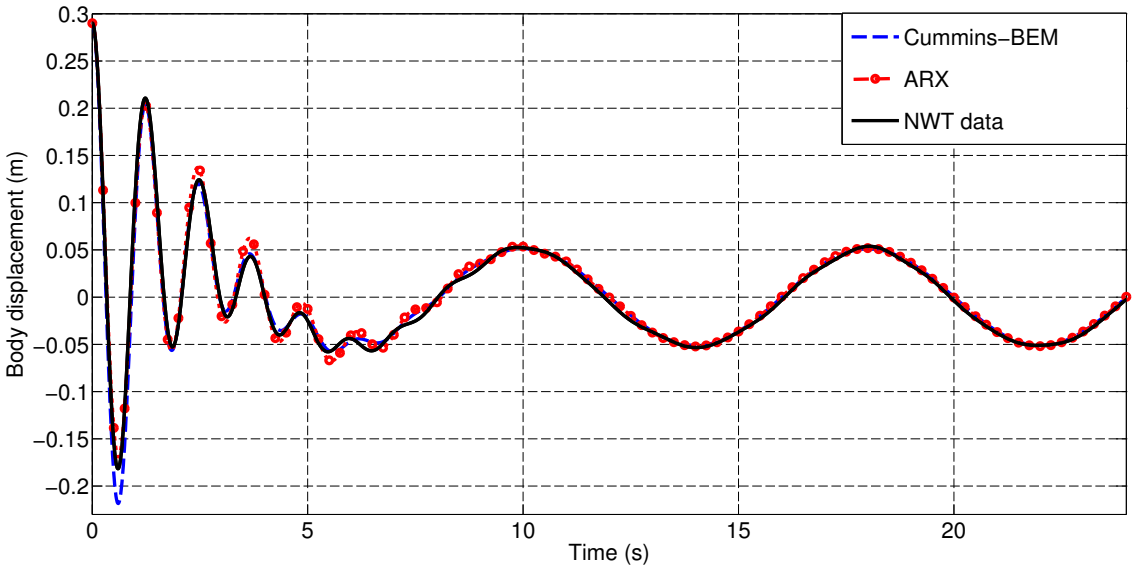

Figure 6.43: First 24 s of the multi-step predictions of the identified linear models (i.e. Cummins-BEM and ARX models), in the case of training input force experiment 1 (the input PTO force is a sinusoid of amplitude 240 N and frequency 0.125 Hz).

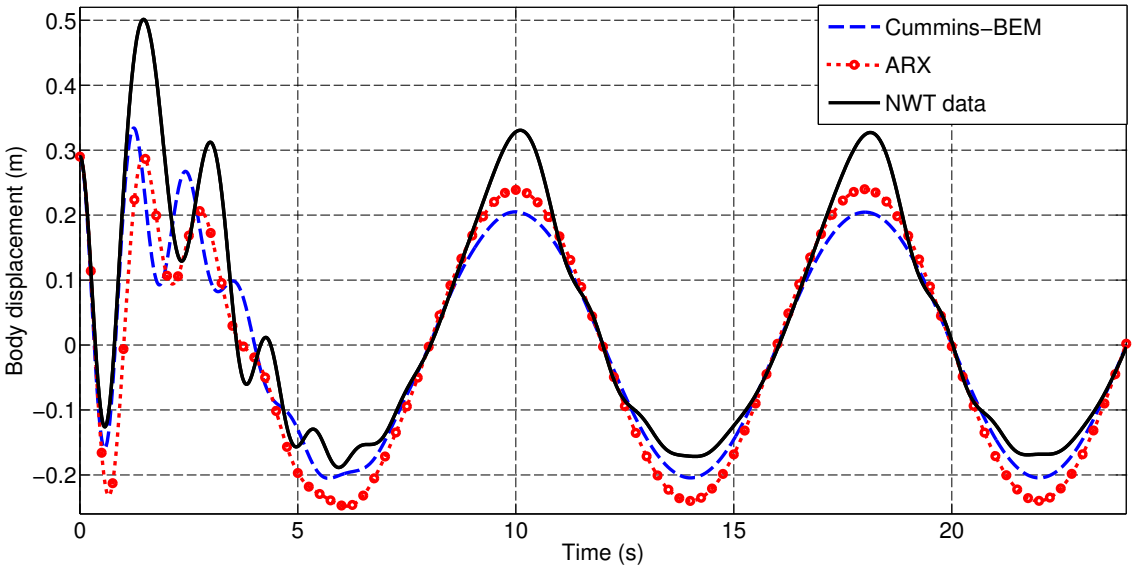

Figure 6.44: First 24 s of the multi-step predictions of the identified linear models (i.e. Cummins-BEM and ARX models), in the case of training input force experiment 2 (the input PTO force is a sinusoid of amplitude 960 N and frequency 0.125 Hz).

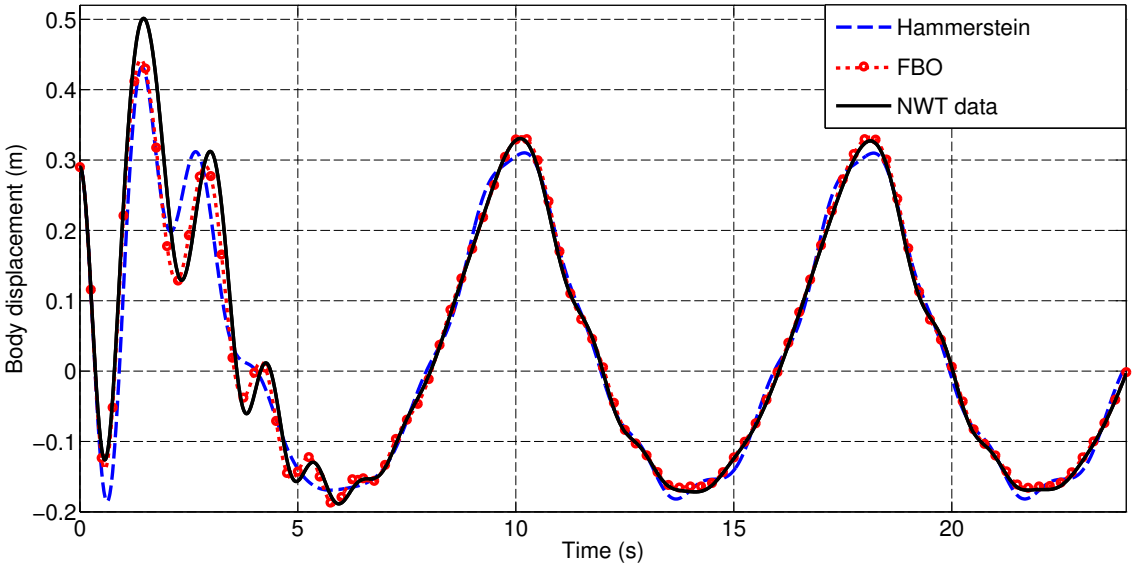

Figure 6.45: First 24 s of the multi-step predictions of the identified nonlinear models (i.e. Hammerstein and FBO models), in the case of training input force experiment 2 (the input PTO force is a sinusoid of amplitude 960 N and frequency 0.125 Hz).

6.3.2 Circular body case ($f_{in} \rightarrow y$ models)

In this case study, three different NARX DT model structures, belonging to the $f_{in} \rightarrow y$ model family, are identified (i.e. ARX, KGP and ANN model structures), in order to describe the heave motion of a floating 2D circular body, in response to an input PTO force, under the hypotheses of no incident waves and no mooring forces (see Fig. 6.27). The data, utilised for model identification, are generated in a 2D CFD-NWT. In the case of small body displacements, the relationship between f_{in} and y can be described by a linear model but, when the body displacement amplitude increases, becoming of the same order of magnitude of the dimension of the body, some nonlinear effects may appear, and the use of nonlinear input/output model structures has to be considered. In contrast to the case study of Section 6.3.1, where the input PTO force is a sinusoidal signal with a low frequency (chosen in order to emphasize the static nonlinearity of the restoring force, by reducing other possible velocity-dependent nonlinearities), in this case study, different dynamically rich PTO force signals (i.e. RARP, multisine and chirp signals) are utilised in order to obtain all the required identification information. The models are first trained with a NWT experimental data set and, subsequently, their performance validated with a second NWT experimental data set.

6.3.2.1 NWT and floating body description

This case study utilises the 2D NWT shown in Fig. 6.46, which is implemented by using OpenFOAM (see Section 2.3.1). The NWT has a 50 m depth and walls located 100 m from the centre of the tank, with wave absorption implemented via the *waves2FOAM* package [52], by utilising two 90 m long relaxation zones, situated 10 m either side of the device (located at the centre of the tank). Above the water, there is a volume of air with a 2.5 m height. The tank is one cell thick, with a thickness of 1 cm, and symmetry planes are defined at the front and back faces. A 2D circular device geometry is simulated, which relates to the cross-section of a horizontally aligned cylinder of infinite length (see Section 4.4). The cylinder has a radius of 1 m, a density of half the density of the water, so that it rests 50% submerged (see Fig. 6.47). Fig. 6.48 shows a view of the NWT mesh around the body, where it is possible to see that the cell dimensions exponentially increase, by moving from the centre of the tank to the tank walls; this provides a fine mesh resolution near the body, while reducing the total number of cells needed to cover the full NWT domain, for a total of 43,000 cells. The cylinder motion is constrained to heave in all the experiments. The variable cross-sectional area of the device geometry makes its hydrodynamic description challenging.

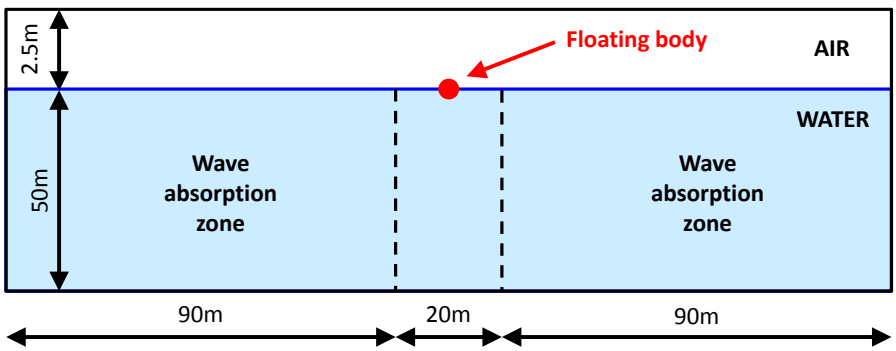

Figure 6.46: NWT side view.

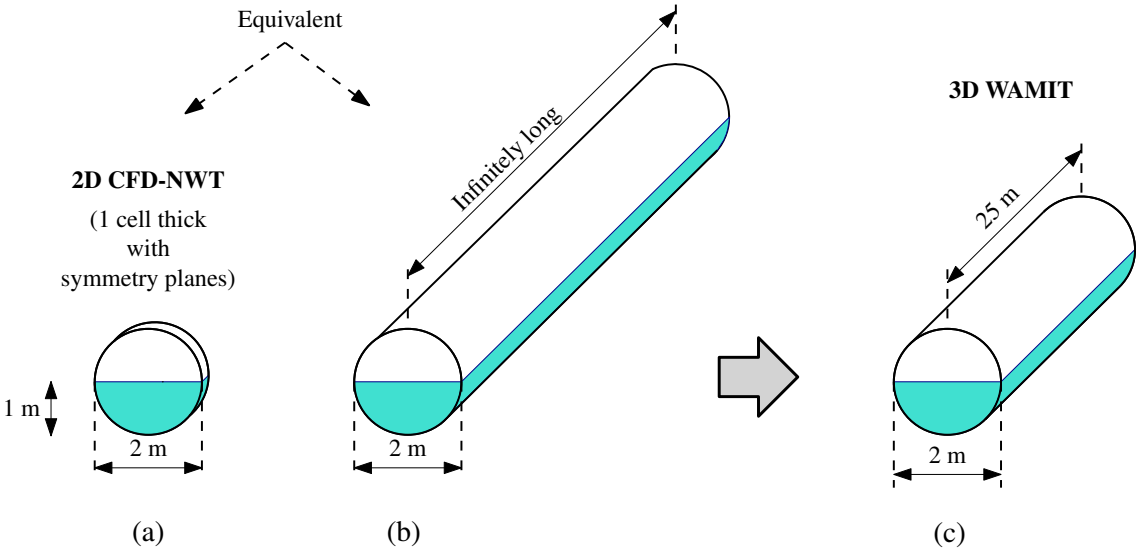

Figure 6.47: (a) 2D circular device with a 1 m radius and 1 m draft (implemented in a NWT with one cell thickness and symmetry planes on the front and back faces of the domain). (b) Infinitely long horizontal cylinder (equivalent to the one cell thick circle). (c) The infinitely long horizontal cylinder can be approximated well, in WAMIT, by a horizontal cylinder with a 25 m length.

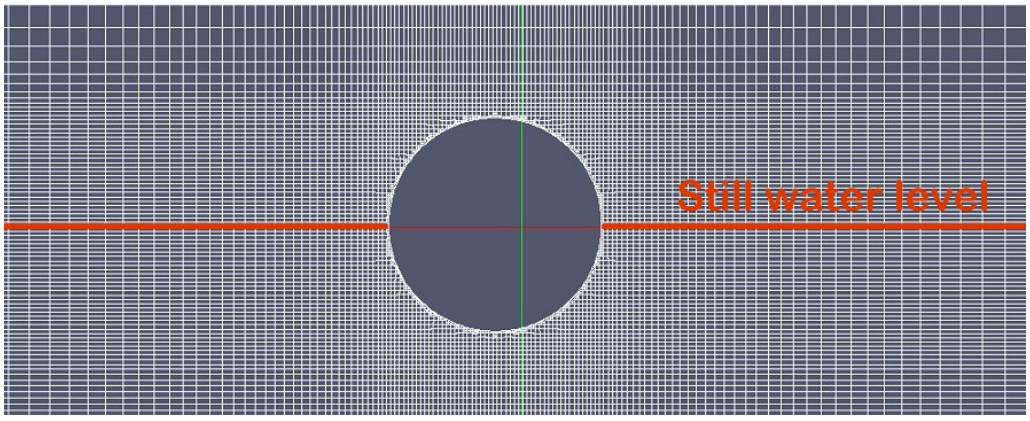

Figure 6.48: Mesh utilised, in the 2D CFD-NWT, around the circular body. The cell dimensions exponentially increasing moving from the centre of the tank to the tank walls, providing a fine mesh resolution near the body.

Experiment type	Input signal type {Input symbol}	Output signal type {Output symbol}	Identified model
Input force	PTO force $\{f_{in.d}(k)\}$	Body displacement $\{y_{in.d}(k)\}$	ARX KGP ANN

Table 6.9: Data generated, in the NWT, with the input force experiments.

6.3.2.2 Generated NWT data description

As explained in Section 4.3.2.3, an input force experiment is used to identify a hydrodynamic model between an input PTO force and the device motion (both considered positive when they are upward); two time series vectors are produced by these experiments for the model identification, one containing the input PTO force, $\{f_{in.d}(k)\}$, and the other the body displacement, $\{y_{in.d}(k)\}$, as shown in Table 6.9. The subscript 'd' indicates 'dynamic'. All the experiments, utilised in this case study, have a duration of 600 s and a sampling period $T_s = 0.1$ s. Since the thickness of the NWT is 1 cm, all the forces, calculated by the NWT and denoted $f_i^{(1cm)}$, are for a horizontal cylinder with a 1 cm thickness; therefore, a force applied on a body, having a general body thickness L_b, is given by:

$$f_i^{(L_b)} = \frac{f_i^{(1cm)}}{0.01} L_b, \tag{6.43}$$

All the forces considered in this case study are normalised for $L_b = 1$ m. As outlined in Section 4.2, the signal, used to excite the system during the experiment, plays an important role in SI. Ideally, in order to obtain all the required identification information, the input signal should be able to excite the system as much as possible, in the shortest possible time. It is important to ensure that the input excitation signal has a good coverage of the frequencies where the system has a significant non-zero frequency response. A circular body, in a 2D NWT, is equivalent to a horizontal infinitely long cylinder, which, under the hypotheses of small waves and body displacement, can be approximated by a 25 m long horizontal cylinder in WAMIT (see Section 4.4), as shown in Fig. 6.47. Fig. 6.49 shows the normalized transfer function $|H^{BEM}_{f_{in}\to y}(f)|/|H^{BEM}_{f_{in}\to y}(f)|_{max}$, resulting from WAMIT data, for the 25 m long horizontal cylinder; it is possible to see that the system has a significant non-zero frequency response in the bandwidth [0 , 1.5] Hz. In this case

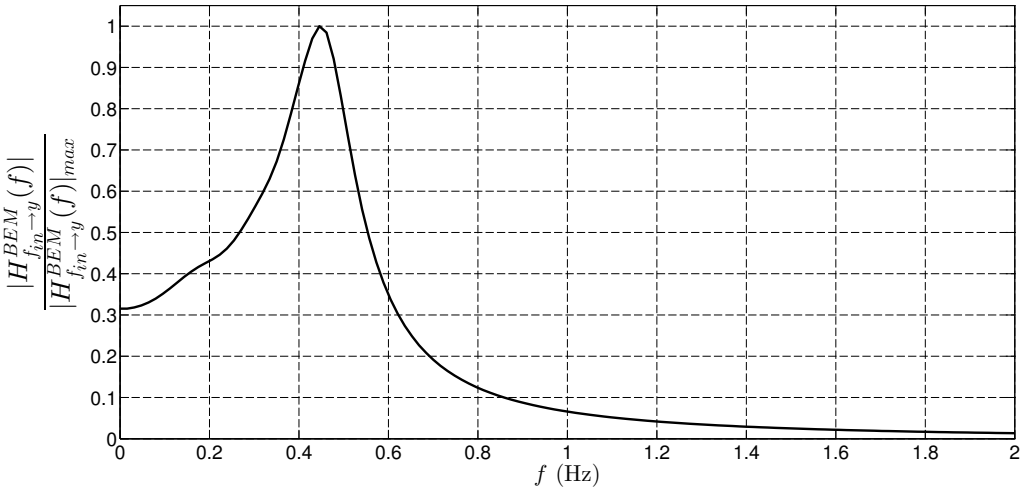

Figure 6.49: Normalized transfer function for a linear hydrodynamic $f_{in} \to y$ model, calculated from WAMIT data, for the 25 m long horizontal cylinder. The model has a significant non-zero frequency response in the bandwidth [0 , 1.5] Hz.

study, three different signal types are investigated for the input force experiments, a RARP signal type (see Section 4.2.2.2), a multisine signal type (see Section 4.2.2.3) and a chirp signal type (see Section 4.2.2.4). The signals are designed to span the force amplitude range of [-1 , 1] kN, and the frequency range of [0 , 1.5] Hz. Two versions of each signal are generated: one to be used for model training (see Figs. 6.51(a), 6.52(a) and 6.53(a)) and the second one for model validation (see Figs. 6.54(a), 6.55(a) and 6.56(a)).

RARP signal

The RARP signal is designed to have a random switching period with a constant probability density function (see Section 4.2.2.2) in the interval $[0.01, 0.67]$ s, as shown in Fig. 6.50(b), and a random force amplitude with a constant probability density function in the range $[-1, 1]$ kN, as shown in Fig. 6.50(c). The signal is randomly generated twice under these constraints, with one signal being used for model training and the second for model validation. Fig. 6.51 shows the first 100 s of the RARP training experiment (denoted $R1$) with Fig. 6.51(a) showing the input RARP force, and Fig. 6.51(b) the resulting body motion. Fig. 6.54 shows the first 100 s of the RARP validation experiment (denoted $R2$).

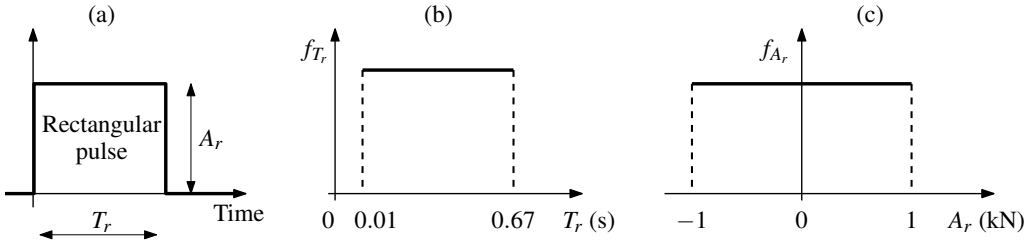

Figure 6.50: Characteristics of the RARP input PTO force signal, utilised in the CFD-NWT, in the case of the 2D circular device of Fig. 6.47(a), for the identification of DT $f_{in} \rightarrow y$ models. (a) Rectangular pulse time evolution. (b) The width of each rectangular pulse is described by a constant PDF, f_{T_r}. (c) The amplitude of each rectangular pulse is described by a constant PDF, f_{A_r}.

Multisine signal

The multisine signal is designed with a flat frequency spectrum with a fundamental frequency of 1/600 Hz and all harmonics up to 1.5 Hz (a total of 900 sinusoids). All frequency components have equal amplitudes, in order to create a flat spectrum, and are assigned random phases. The amplitude of the frequency components is manually tuned (uniformly across all frequencies) until the time series distribution spans the range [-1 , 1] kN. The signal is generated twice, by using the same frequency spectrum but with different random phases, with one signal for model training and the second for model validation. Figs. 6.52 and 6.55 show the first 100 s of the training experiment (denoted $M1$) and the validation experiment (denoted $M2$), respectively.

Chirp signal

The chirp signal is designed to linearly sweep from 0 to 1.5 Hz in 600 s, and to span the range [-1 , 1] kN. Fig. 6.53 shows the chirp training experiment (denoted $C1$) with Fig. 6.53(a) showing the first 200 s of the input PTO force, and Fig. 6.53(b) the complete 600 s body displacement signal. In order to generate a second signal for model validation, the chirp signal is reversed, linearly sweeping from 1.5 to 0 Hz. Fig. 6.56 shows the chirp validation experiment (denoted $C2$) with Fig. 6.56(a) showing the last 200 s of the input PTO force, and Fig. 6.56(b) the complete 600 s body displacement signal.

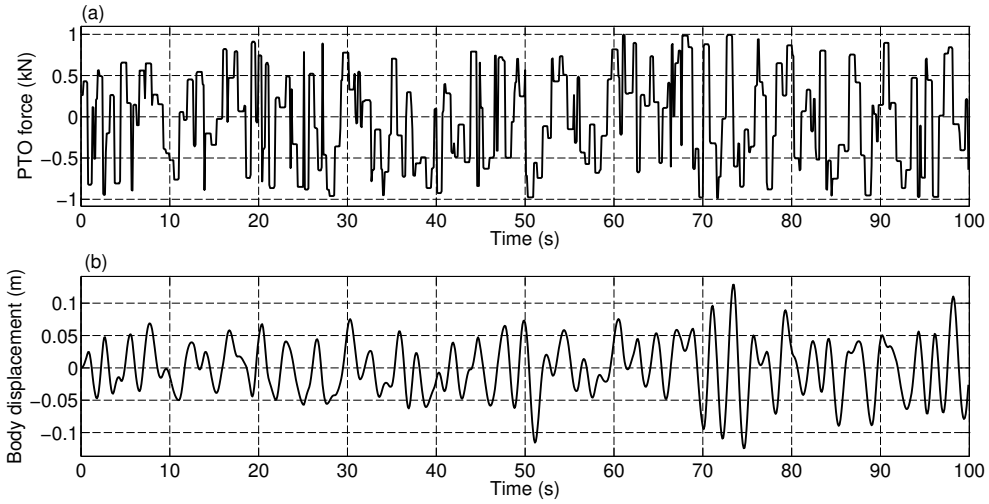

Figure 6.51: First 100 s of the training experimental data R1.

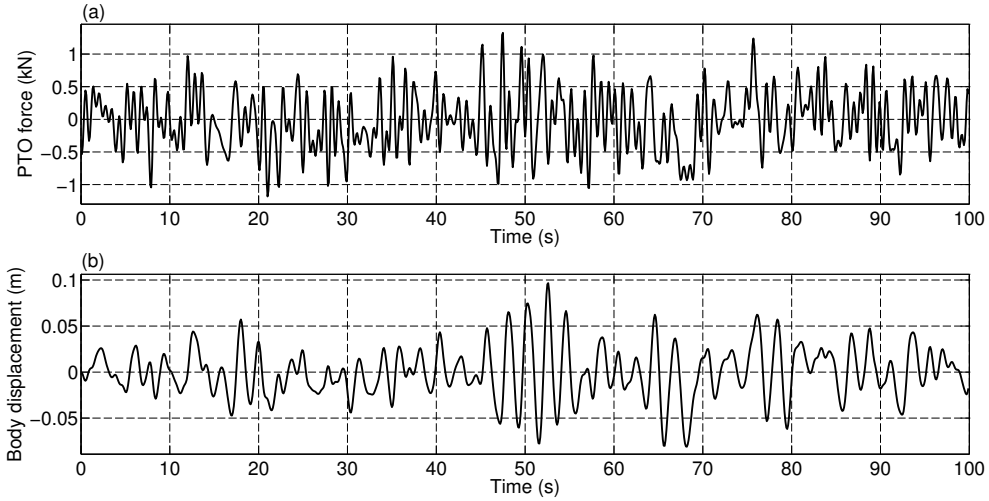

Figure 6.52: First 100 s of the training experimental data M1.

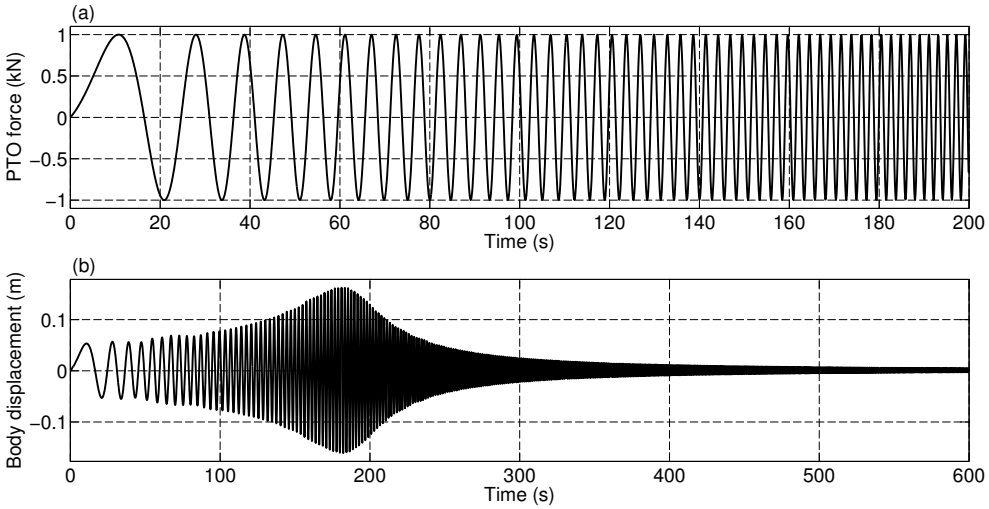

Figure 6.53: Training experimental data C1. (a) First 200 s of the input PTO force signal. (b) 600 s of the body displacement signal.

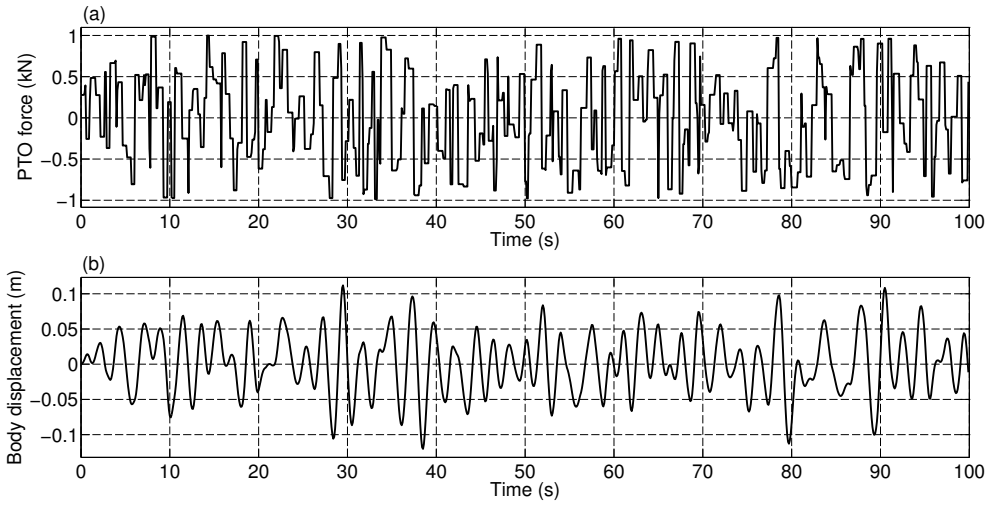

Figure 6.54: First 100 s of the validation experimental data R2.

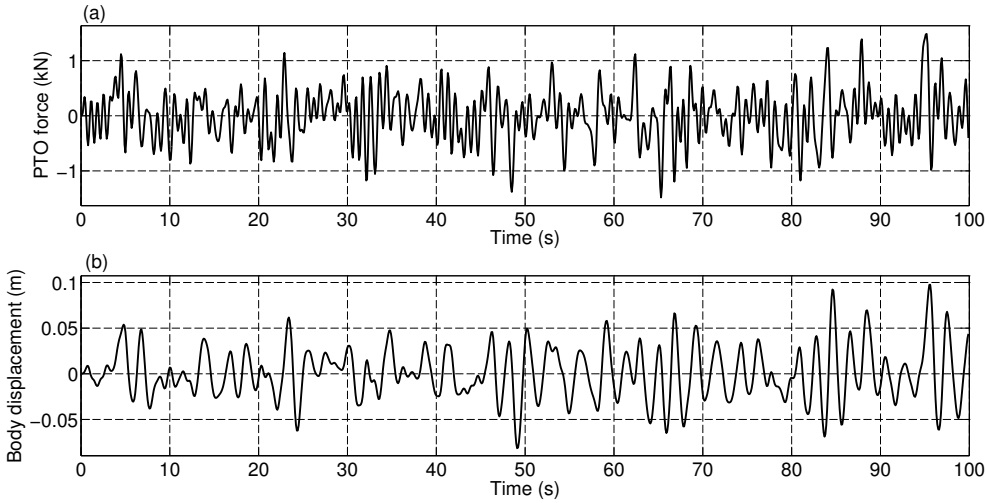

Figure 6.55: First 100 s of the validation experimental data M2.

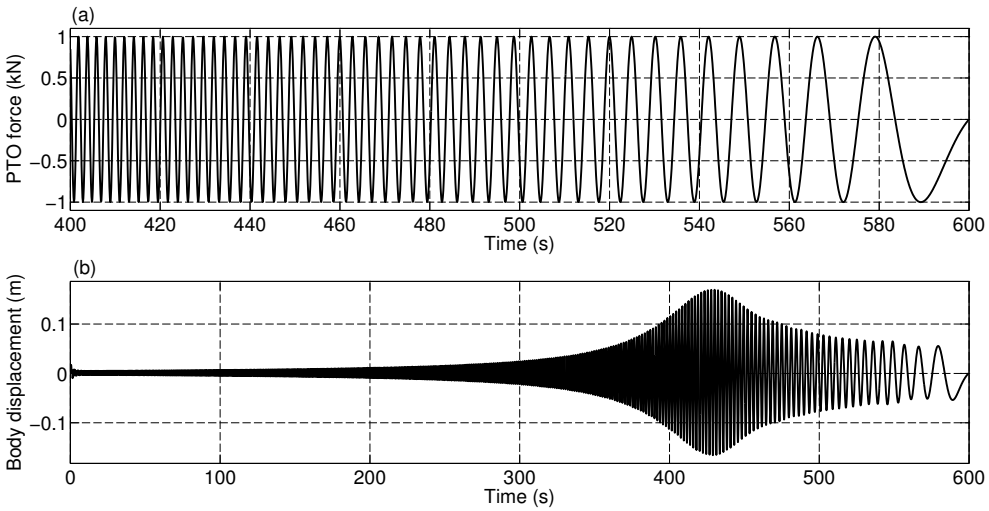

Figure 6.56: Validation experimental data C2. (a) Last 200 s of the input PTO force signal. (b) 600 s of the body displacement signal.

6.3.2.3 Model description and identification

ARX model

By performing the input force experiment, the signals $\{f_{in.d}(k)\}$ and $\{y_{in.d}(k)\}$ are generated (see Section 6.3.2.1), which can be utilised as input and output data, respectively, for the identification of the ARX model (see Section 6.3.1.3).

KGP model

In the case of the $f_{in} \rightarrow y$ model family, the KGP model structure, where the cross-product terms are removed in order to reduce the possibility of stability problems (see Section 3.2.3.5), is described by the input/output relationship given by:

$$y(k) = \sum_{j=1}^{n_p} \Big[\sum_{i=1}^{n_a} a_{ij} y^j(k-i) + \sum_{i=0}^{n_b} b_{ij} f_{in}^j(k-n_d-i) \Big] \tag{6.44}$$

In this case, equation (3.72) becomes:

$$\mathbf{y} = \begin{bmatrix} y_{in.d}(\tau+1) & y_{in.d}(\tau+2) & \dots & y_{in.d}(\widetilde{N}) \end{bmatrix}^T, \tag{6.45}$$

where τ and $\widetilde{N}$ are given by equations (6.5) and (6.6), respectively, and each of the $(\widetilde{N}-\tau)$ rows of the data matrix $\mathbf{\Phi}$, defined by (3.49), has the form:

$$\begin{bmatrix} y_{in.d}(k-1) & \dots & y_{in.d}(k-n_a) & f_{in.d}(k-n_d) & \dots & f_{in.d}(k-n_d-n_b) \\ y_{in.d}^2(k-1) & \dots & y_{in.d}^2(k-n_a) & f_{in.d}^2(k-n_d) & \dots & f_{in.d}^2(k-n_d-n_b) & \dots \\ y_{in.d}^{n_p}(k-1) & \dots & y_{in.d}^{n_p}(k-n_a) & f_{in.d}^{n_p}(k-n_d) & \dots & f_{in.d}^{n_p}(k-n_d-n_b) \end{bmatrix}, \tag{6.46}$$

where $k = (\tau+1), ..., \widetilde{N}$. The estimated parameter vector, $\hat{\boldsymbol{\theta}}_{kgp}$, is determined by utilising $\mathbf{y}$, $\mathbf{\Phi}$ and QR factorization to resolve the LS problem.

ANN model

The ANN model, shown in Fig. 6.57, is described by the input/output relationship (see Section 3.2.3.6), given by:

$$y(k) = \sum_{i=0}^{n_2} w_i^{(out)} \Psi_i \Big(\sum_{j=0}^{n_1} w_{ij}^{(2)} \Psi_j \big(\sum_{l=0}^{n_v} w_{jl}^{(1)} v_l(k) \big) \Big) \tag{6.47}$$

where

$$\begin{bmatrix} v_1(k) & \dots & v_{n_v}(k) \end{bmatrix} = \begin{bmatrix} y(k-1) & \dots & y(k-n_a) & f_{in}(k-n_d) & f_{in}(k-n_d-1) & \dots & f_{in}(k-n_d-n_b) \end{bmatrix},$$

$v_0(k) = 1$, $n_v = n_a + n_b + 1$, n_1 and n_2 are the number of neurons in the hidden layers 1 and 2, respectively, and $w_{ij}^{(1)}$, $w_{ij}^{(2)}$ and $w_i^{(out)}$ are the unknown weights (and biases) of the i-th perceptron neuron of the hidden layer 1, 2 and output, respectively.

It is not straightforward to calculate the optimal values for n_1 and n_2; a good compromise between complexity and accuracy of the model has been found by utilising $n_1 = 3$ and $n_2 = 5$ (see Table 6.10). The identification of the model requires the employment of nonlinear optimization techniques; in particular, the unknown parameter vector, $\boldsymbol{\theta}_{ann} = [w_{11}^{(1)}, ..., w_{n_1 n_v}^{(1)}, w_{11}^{(2)}, ..., w_{n_2 n_1}^{(2)}, w_1^{(out)}, ..., w_{n_2}^{(out)}]$, is identified by utilising a conjugate gradient algorithm in batch training mode (the ANN model is retrained with the same data over successive epochs), which is computational efficient and shown to have good performance for ANN models (see Section 3.3.2). In order to counter the difficulty of local minima in the search surface, a variety of initial conditions (100 instances) is used.

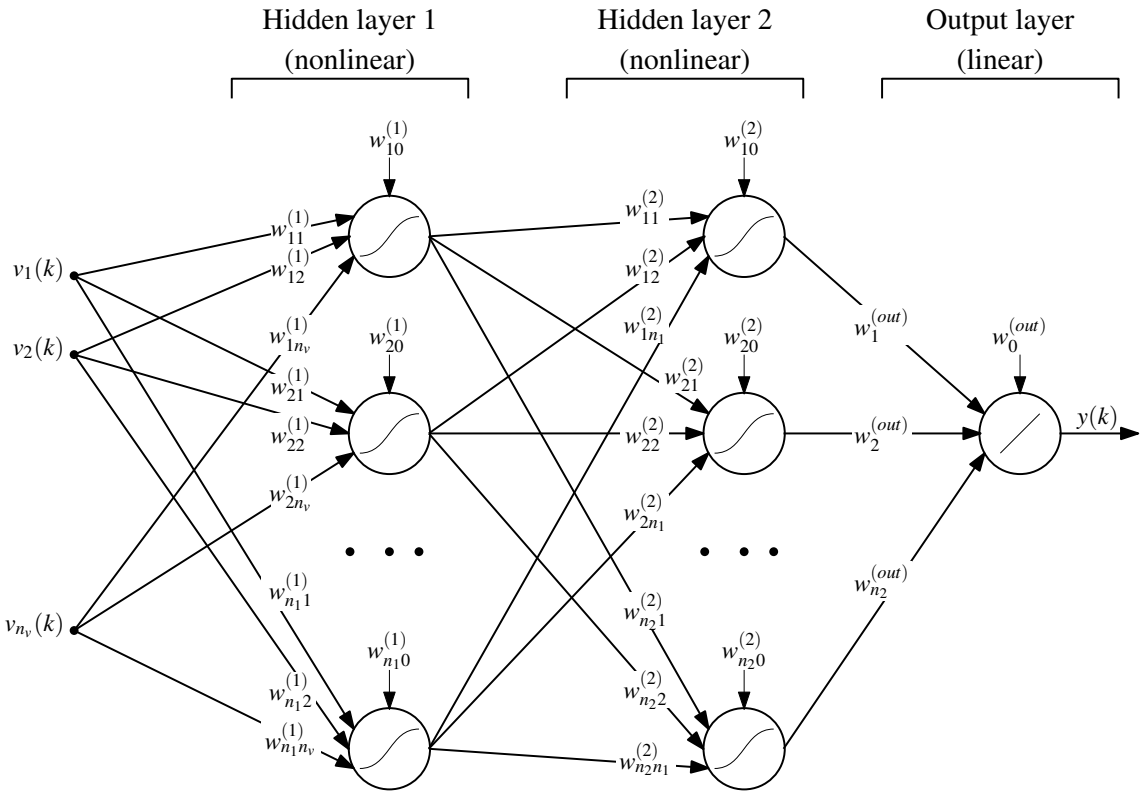

Figure 6.57: ANN model structure with two nonlinear hidden layers and one linear output layer.

6.3.2.4 Results

By utilising the strategy explained in Section 3.2.4, the dynamical orders $n_a = 4$ and $n_b = 2$, and the input delay time $n_d = 0$ are identified, as shown in Table 6.10. Indeed, Fig. 6.58 shows the loss function $LF = LF(n_a, n_b, n_d)$ versus n_a, for the training experiment $R1$, where each vertical line shows the range of LF for a specific value of n_a and for $1 \leq n_b \leq 8$ and $-8 \leq n_d \leq 4$. No significant reduction of LF for $n_a > 4$, showing that $n_a = 4$ is the correct value to obtain a parsimonious model structure. Fig. 6.59 shows the LF values in the case where $n_a = 4$, $n_b = 2$ and $-8 \leq n_d \leq 4$, where it is possible to see that the minimum occurs for $n_d = 0$. As explained in Section 6.3.1.4, since in the case of input force experiments the PTO actuator applies a force directly on the body, the expected identified delay time is null.

The polynomial order of the KGP model $n_p = 2$ is selected (see Table 6.10), by observing that larger values of n_p improve the training fitting but degrade the quality of the validation fitting (i.e. overfitting).

n_a	n_b	n_d	n_p	n_1	n_2
4	2	0	2	3	5

Table 6.10: n_a, n_b, n_d, n_p, n_1 and n_2 utilised for the different DT model structures.

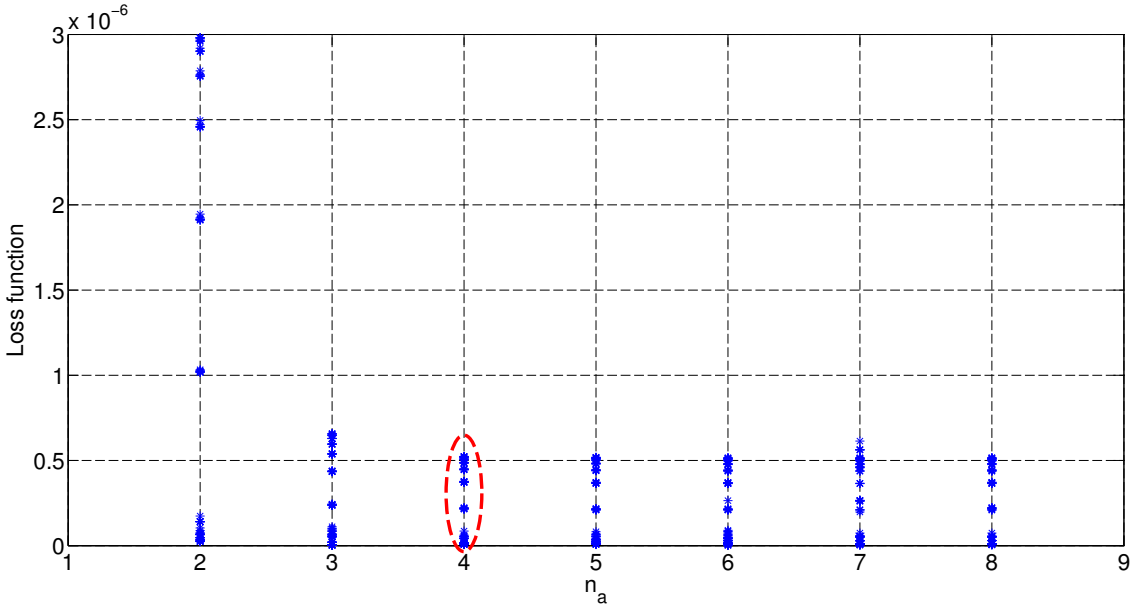

Figure 6.58: $LF = LF(n_a, n_b, n_d)$ is plotted versus n_a, in the case of the circular body of Fig. 6.47(a) and the training experiment $R1$, where each vertical line shows the range of LF for a specific value of n_a and for $1 \leq n_b \leq 8$ and $-8 \leq n_d \leq 4$. There is no significant reduction of LF for $n_a > 4$; therefore, $n_a = 4$ is the correct value to obtain a parsimonious model structure.

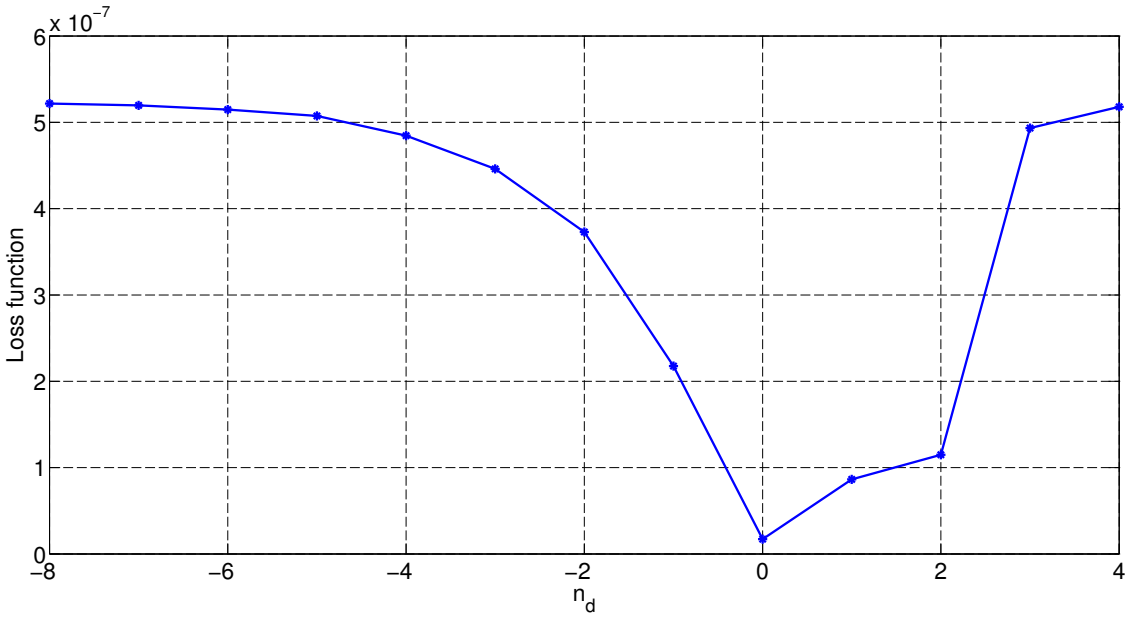

Figure 6.59: $LF = LF(n_a, n_b, n_d)$ is plotted versus n_d, for $n_a = 4$ and $n_b = 2$, in the case of the circular body of Fig. 6.47(a) and the training experiment $R1$. The minimum occurs for $n_d = 0$.

From each training experiments (i.e. $R1$, $M1$ and $C1$), three different models are identified (i.e. ARX, KGP and ANN models) with a 1-step prediction criterion (a total of 9 models). Once identified, each model is used to make a multi-step prediction (see Section 3.4) on the same training data, the model was identified from. Fig. 6.60 shows the multi-step predictions of the identified models, on the training experiment $M1$. Table 6.11 reports the NRMSE multi-step prediction performance for each identified model, showing that, for training data fitting, the ANN models always perform best (marked in green and with the number (1)), followed by the KGP models (marked in orange and with the number (2)). The ARX models have consistently the worst training performance (marked in red and with the number (3)), suggesting that the data contain nonlinearities, which the KGP models and the ANN models, in particular, are able to capture.

Since a model which fits the training data is not necessary a good model on a different experiment (i.e. the overfitting problem), each identified model with experiments $R1$, $M1$ and $C1$ is utilised to make multi-step predictions on the data provided from the validation experiments $R2$, $M2$ and $C2$. Fig. 6.61 shows the multi-step predictions of the models (identified with $M1$) in the case of the validation experiment $M2$. Table 6.12 shows the NRMSE multi-step prediction performance of the models, on the validation experiments $M2$, $R2$ and $C2$, where it is possible to see that the ANN model structure, which worked very well in training, has inconsistent performance and that the ARX models usually have poor performance. The KGP model structure shows qualities of both accuracy and consistency.

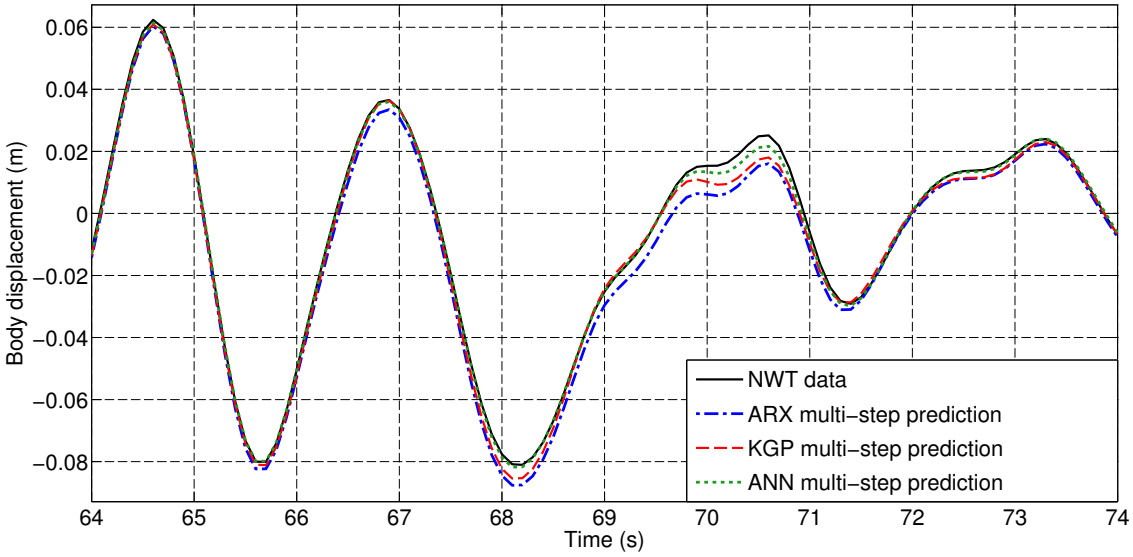

Figure 6.60: Multi-step predictions of the identified models, on the training experiment $M1$ (only a portion of the data is plotted).

	Model trained with		
	$M1$	$R1$	$C1$
ARX	0.1018 (3)	0.0820 (3)	0.0799 (3)
KGP	0.0810 (2)	0.0684 (2)	0.0536 (2)
ANN	0.0408 (1)	0.0536 (1)	0.0442 (1)

Table 6.11: NRMSE multi-step performance for training. The best model performance is marked in green and with the number (1), the second model performance is marked in orange and with the number (2), and the worst model performance is marked in red and with the number (3).

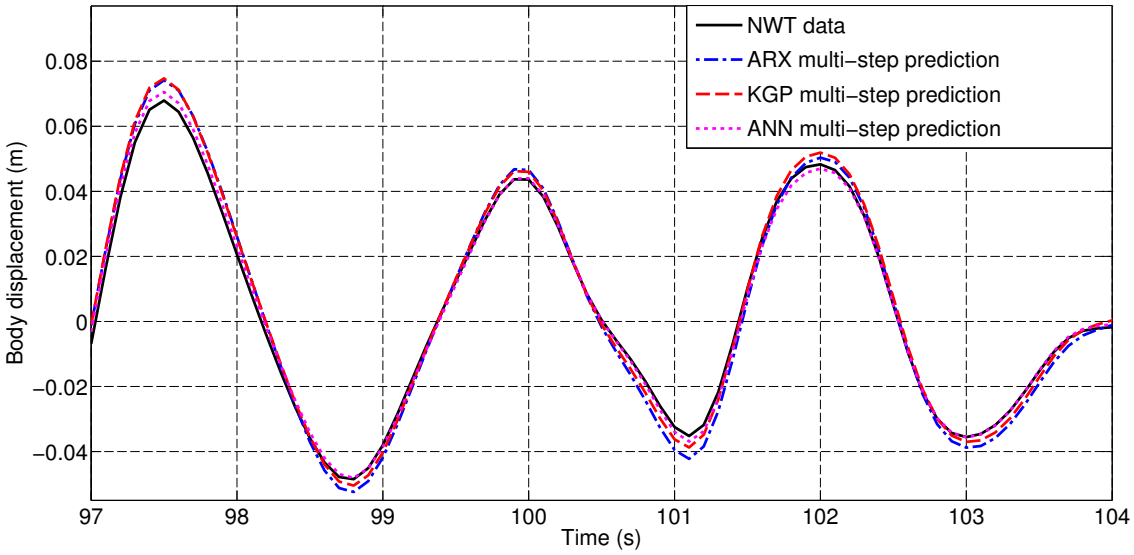

Figure 6.61: Multi-step predictions of the models (identified with $M1$) in the case of the validation experiment $M2$ (only a portion of the data is plotted).

			Model trained with		
			$M1$	$R1$	$C1$
Model validated with	$M2$	ARX	0.1005 (3)	0.0868 (3)	0.0988 (2)
		KGP	0.0807 (2)	0.0749 (2)	0.0748 (1)
		ANN	0.0414 (1)	0.0600 (1)	0.1162 (3)
	$R2$	ARX	0.1351 (3)	0.1240 (3)	0.1346 (2)
		KGP	0.1249 (1)	0.1192 (2)	0.1196 (1)
		ANN	0.1306 (2)	0.1099 (1)	0.1513 (3)
	$C2$	ARX	0.0828 (2)	0.0704 (2)	0.0757 (3)
		KGP	0.0654 (1)	0.0566 (1)	0.0513 (2)
		ANN	0.4572 (3)	0.1755 (3)	0.0497 (1)

Table 6.12: NRMSE multi-step performance model for validation. The best model performance is marked in green and with the number (1), the second model performance is marked in orange and with the number (2), and the worst model performance is marked in red and with the number (3).

As explained in Section 6.2.4, usually, the fitting error of an identified model is larger with validation data than with training data. The NRMSE multi-step prediction performance with training and validation data (see Tables 6.11 and 6.12, respectively) are used to calculate the NVTD parameter (see Table 6.13), defined by equation (6.21). A NVTD = 0.25 is chosen as an upper threshold for a model having a good ability to generalize and, in Table 6.13, each NVTD < 0.25 is written in bold, to indicate a good model performance. NVTD values, of the identified ARX and KGP models, show that the two model structures generalise quite well with experiments $M2$ and $C2$, indicating good quality of the utilised data and the identified parameter vector, but they show more difficulty on experiment $R2$. On the other hand, as already noted in Table 6.12, the identified ANN models are less consistent; indeed, they exhibit, in some cases, the ability to generalise well (training with $M1$ and validation with $M2$; training with $R1$ and validation with $M2$; training with $C1$ and validation with $C2$) and, in other cases, an inability to generalise (training with $C1$ and validation with $M2$; training with $M1$ and validation with $C2$; training with $R1$ and validation with $C2$; all validations with $R2$). The results show the supplemental difficulty for ANN identification, depending on the nonlinear optimization algorithm and larger number of parameters employed (see Table 6.14). It is interesting to note that all the identified models exhibit greater difficulty for

validation with experiment $R2$, possibly due to the fact that RARP signals have very sharp corners, corresponding to fast changes in the applied PTO force and resulting body acceleration, which can create nonlinear effects, which are not easily modelled.

			Model trained with		
			$M1$	$R1$	$C1$
Model validated with	$M2$	ARX	**-0.0128**	**0.0585**	**0.2365**
		KGP	**-0.0037**	**0.0950**	0.3955
		ANN	**0.0147**	**0.1194**	1.6290
	$R2$	ARX	0.3271	0.5122	0.6846
		KGP	0.5420	0.7427	1.2313
		ANN	2.2010	1.0504	2.4231
	$C2$	ARX	**-0.1866**	**-0.1415**	**-0.0526**
		KGP	**-0.1926**	**-0.1725**	**-0.0429**
		ANN	10.2059	2.2743	**0.1244**

Table 6.13: NVTD parameter values calculated from NRMSE multi-step prediction performance, by using the training and validation data of Tables 6.11 and 6.12, respectively. A NVTD = 0.25 is chosen as an upper threshold for a model having a good ability in generalizing, and each NVTD < 0.25 is written in bold.

ARX	KGP	ANN
7	14	50

Table 6.14: Number of identified parameters, for the different model structures, given by equations (3.9), (3.26) and (3.34).

The NRMSE multi-step performance for validation, shown in Table 6.12, can be utilised to analyse which signal typology produce more accurate models. For convenience, Table 6.12 is copied into Table 6.15, where extra information is added. Each row of Table 6.15 shows the performance of three models, having the same model structure but different parameter vector values, identified with three different experiments (i.e. $R1$, $M1$ and $C1$), and validated with the same experiment, which can be $R2$ or $M2$ or $C2$. The first row, for example, describes the performance of three different ARX models, identified with experiments $R1$, $M1$ and $C1$, and validated with experiment $M2$ (see Fig. 6.62(a)). The best model performance is marked in green and with the number (1), the second model performance is marked in orange and with the number (2), and the worst model performance is marked in red and with the number (3). Similarly, the last row describes the performance of three different ANN models, identified with experiments $R1$, $M1$ and $C1$, and validated with experiment $C2$ (see Fig. 6.62(b)). Therefore, first, second and third columns represent the performance of the models identified with experiments $R2$, $M2$ and $C2$, respectively. In each column, the number of cases the models performs best, medium or worst are counted; the results in percentage are shown in Fig. 6.63, where it is possible to see that the models, which perform best, are identified with $R1$, then $C1$ and finally $M1$, suggesting that the RARP signals perform better in identifying accurate models, followed by chirp signals.

			Model trained with		
			$M1$	$R1$	$C1$
Model validated with	$M2$	ARX	0.1005 (3)	0.0868 (1)	0.0988 (2)
		KGP	0.0807 (3)	0.0749 (2)	0.0748 (1)
		ANN	0.0414 (1)	0.0600 (2)	0.1162 (3)
	$R2$	ARX	0.1351 (3)	0.1240 (1)	0.1346 (2)
		KGP	0.1249 (3)	0.1192 (1)	0.1196 (2)
		ANN	0.1306 (2)	0.1099 (1)	0.1513 (3)
	$C2$	ARX	0.0828 (3)	0.0704 (1)	0.0757 (2)
		KGP	0.0654 (3)	0.0566 (2)	0.0513 (1)
		ANN	0.4572 (3)	0.1755 (2)	0.0497 (1)

Table 6.15: NRMSE multi-step performance model for validation. Each row represents the performance of three models, having the same model structure but different parameter vector values, identified with three different experiments (i.e. $R1$, $M1$ and $C1$), and validated with the same experiment, which can be $R2$ or $M2$ or $C2$. In each row, the best model performance is marked in green and with the number (1), the second model performance is marked in orange and with the number (2), and the worst model performance is marked in red and with the number (3).

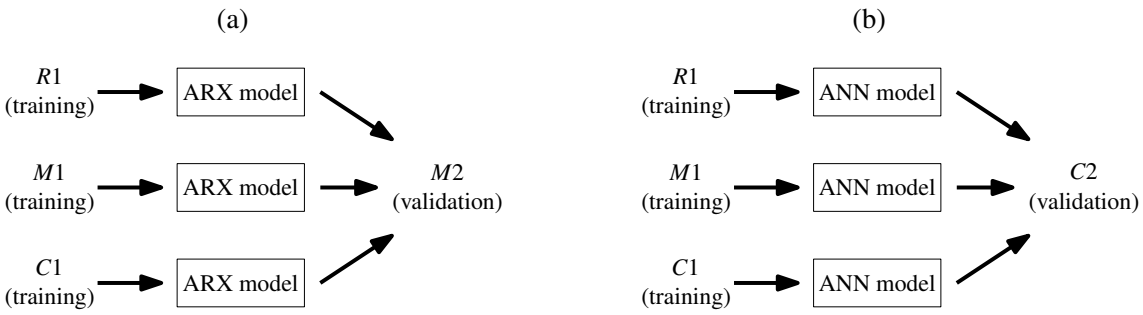

Figure 6.62: (a) Three different ARX models are identified with experiments $R1$, $M1$ and $C1$ and validated with the experiment $M2$. (b) Three different ANN models are identified with experiments $R1$, $M1$ and $C1$ and validated with the experiment $C2$.

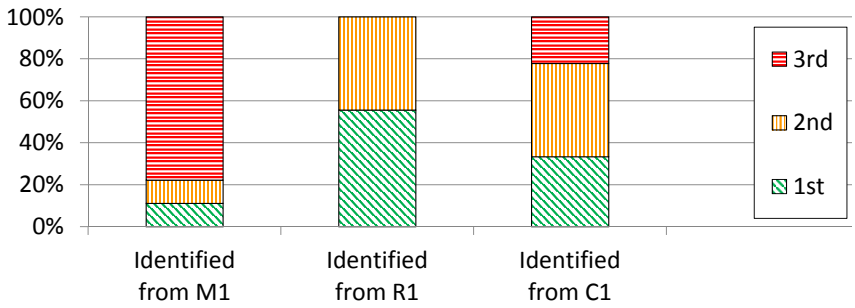

Figure 6.63: Number of cases in percentage when the models, identified with experiments $R1$, $M1$ and $C1$, performs best (1st), medium (2nd) or worst (3rd), with the validation data (i.e. $R2$, $M2$ and $C2$).

6.4 Identification of $\eta \rightarrow y$ models (a case study)

In this case study, three different NARX DT model structures, belonging to the $\eta \rightarrow y$ model family (see Fig. 6.64), are considered (i.e. ARX, KGP and ANN model structures), in order to describe the heave motion of a floating 2D circular body, in response to incident waves (the FSE is measured in a position that corresponds to the center of mass of the body), under the hypotheses of no PTO and no mooring forces. The data, utilised for model identification, are generated in a 2D CFD-NWT. In the case of small waves and body displacement, the relationship between η and y can be described by a linear model but, when the wave and body displacement amplitudes increase, becoming of the same order of magnitude of the dimensions of the body, some nonlinear effects may appear, and the use of nonlinear input/output model structures has to be considered. The models are first trained with a NWT experimental data set and, subsequently, their performance validated with a second NWT experimental data set.

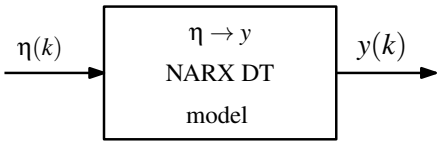

Figure 6.64: General NARX DT model to describe the relationship between FSE and body displacement.

6.4.1 NWT and floating body description

This case study utilises the 2D CFD-NWT depicted in Fig. 6.65 and implemented by utilising OpenFOAM (see Section 2.3.1). The NWT has a 50 m depth and walls located 100 m from the centre of the tank (where the floating body is located), with wave creation/absorption zones, implemented via the *waves2FOAM* package [52], by utilising two 90 m long relaxation zones, situated 10 m either side of the device. Above the water, there is a volume of air with a 2.5 m height. The tank is one cell thick, with a thickness of 1 cm, and symmetry planes are defined at the front and back faces. The cell dimensions exponentially increasing moving from the centre of the tank to the tank walls; this provides a fine mesh resolution near the body, while reducing the total number of cells needed to cover the full NWT domain, for a total of 43,000 cells. A 2D circular device geometry is simulated , which relates to the cross-section of a horizontally aligned cylinder of infinite length (see Section 4.4). The cylinder has a radius of 1 m and a density which is half that of the water, so that it rests 50% submerged, as shown in Fig. 6.66. The body motion is constrained in heave. In the context of 2D NWT simulations, the waves move along a direction perpendicular to the infinitely long horizontal body axis (see Fig. 4.57); therefore, no wave directionality effects on the body are investigated.

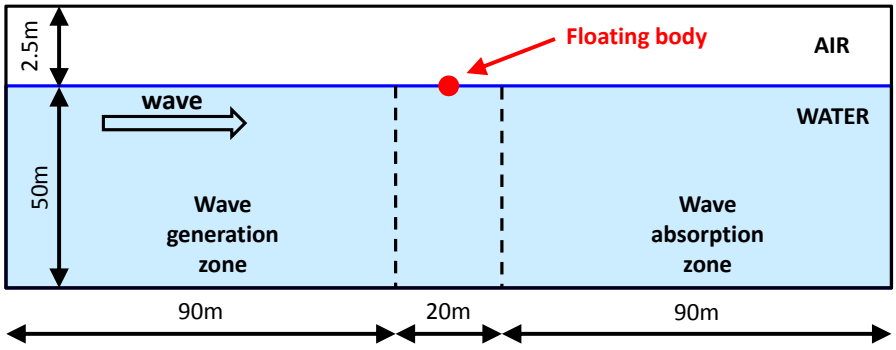

Figure 6.65: NWT side view.

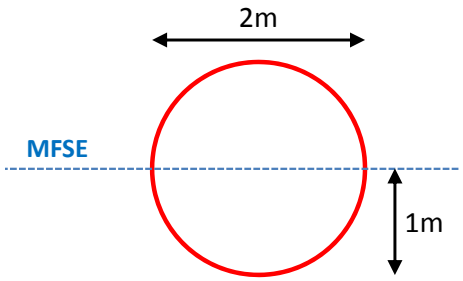

Figure 6.66: Side view of the 2D circular body. The dashed line represents the mean free surface elevation.

6.4.2 Generated NWT data description

In the input wave body motion experiment (see Section 4.3.2.2), the excitation on the body is provided exclusively by the incident waves generated in the NWT, no PTO force is applied, no mooring is present and the body displacement is measured. Two time series vectors are produced by this experiment for model identification, one containing the FSE, $\{\eta_d(k)\}$, and the other the body displacement, $\{y_d(k)\}$, both considered positive when they are upward (see Table 6.16). The subscript 'd' indicates 'dynamic'. All the experiments utilised in this section have a duration of 600 s and a sampling period $T_s = 0.1$ s. The free surface elevation at the body's vertical axis is considered as input to the model and must, therefore, be measured without the body in the tank. After the input wave series, $\{\eta_d(k)\}$, has been measured, the experiment is repeated with the body in place and the resulting body motion, $\{y_d(k)\}$, recorded.

Experiment type	Input signal type {Input symbol}	Output signal type {Output symbol}	Identified model
Input wave body motion	PTO force $\{\eta_d(k)\}$	Body displacement $\{y_d(k)\}$	ARX KGP ANN

Table 6.16: Generated data, in the NWT, with the input wave body motion experiments.

As explained in Section 4.2, in the experiment design, care must be taken to use excitation signals which provide an adequate distribution across the amplitude/frequency space. For the identification of models representative of a specific location, an excitation which covers the range of possibilities at the specific location should be chosen. However, the focus of the thesis is to show the new methodology, rather than provide a complete description of any particular location/device combination and, for simplicity, two different input wave experiments ($W1$ for training, and $W2$ for validation) are carried out, where the input wave signals are two different realizations of a commonly occurring sea state at the European Marine Energy Centre (EMEC) test site, with significant wave height $H_s = 0.6$ m and peak period $T_p = 8$ s. The input wave signals are multisine signals, consisting of 100 equally spaced frequencies, in the range [0.005 , 0.995] Hz (the frequency distance between two adjacent harmonics is given by $\Delta f = 0.01$ Hz), with amplitudes determined from a JONSWAP spectrum [73] [302] and randomly assigned phases. Both experiments $W1$ and $W2$ have a duration of 600 s and a sampling period $T_s = 0.1$ s. Figs. 6.67 and 6.68 show the data generated in experiments $W1$ and $W2$, respectively. Fig. 6.69 shows the spectral content of the FSE signal of the experiment $W1$.

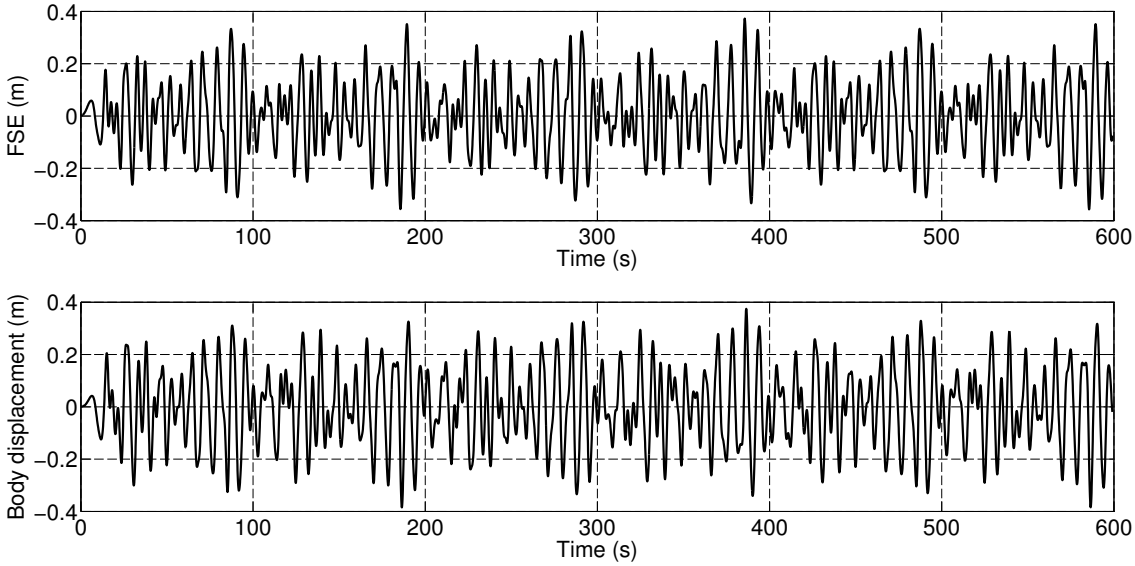

Figure 6.67: Training experimental data $W1$.

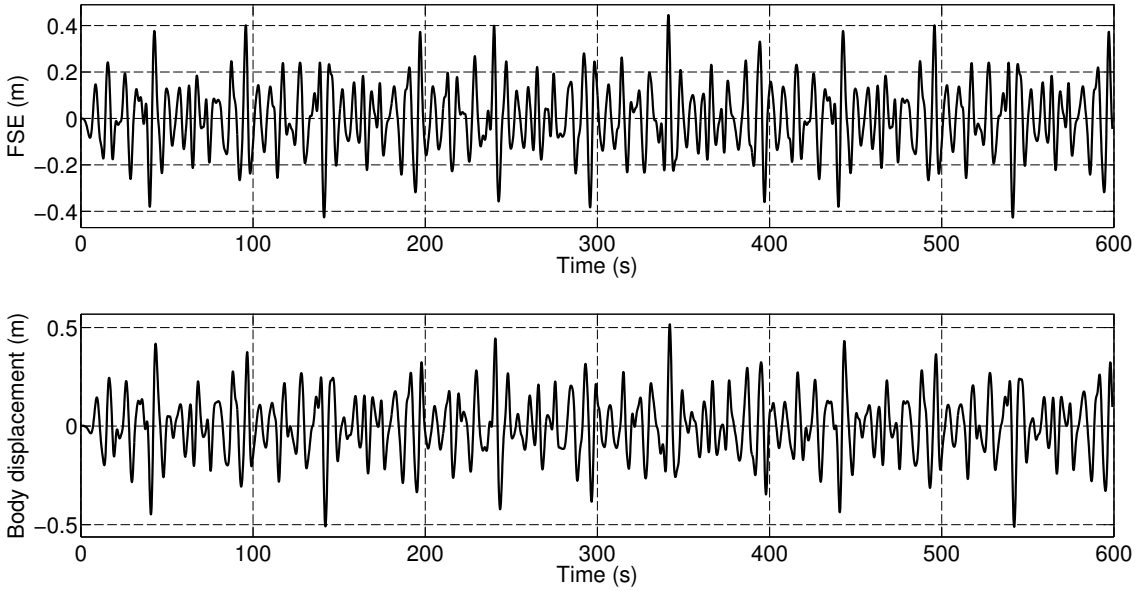

Figure 6.68: Validation experimental data $W2$.

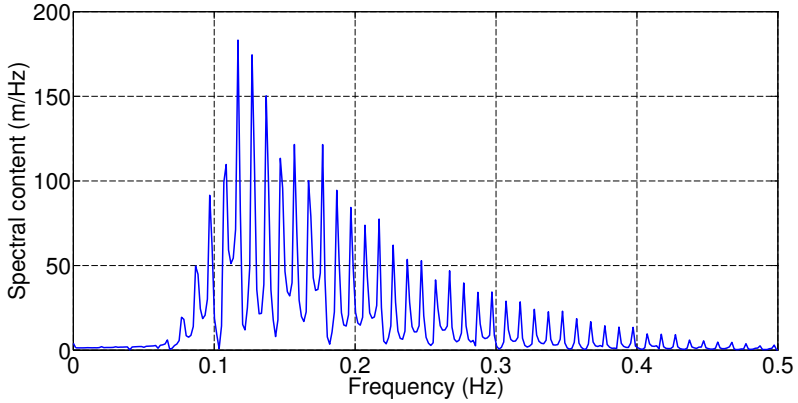

Figure 6.69: Spectral content of the FSE signal of the experiment $W1$.

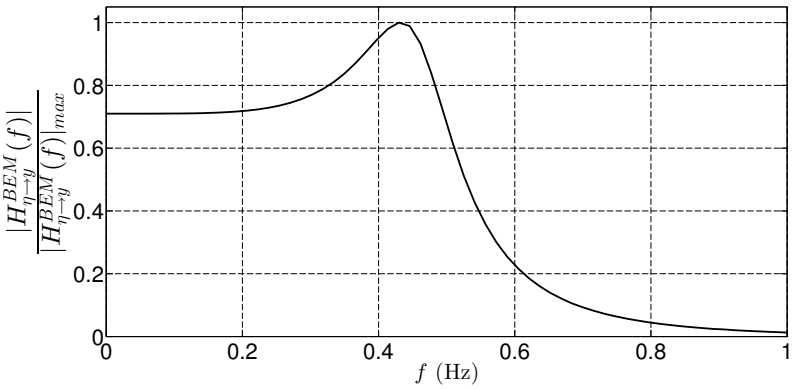

Figure 6.70: Normalized transfer function for a linear hydrodynamic $\eta \to y$ model, calculated from WAMIT data, for the 25 m long horizontal cylinder.

As explained in Section 6.3.2.1, the utilised 2D circular body is equivalent to an infinitely long horizontal cylinder, which can be approximated well, in WAMIT, by a horizontal cylinder with a 25 m length, as shown in Fig. 6.47. Fig. 6.70 shows the normalized transfer function $|H^{BEM}_{\eta\to y}(f)|/|H^{BEM}_{\eta\to y}(f)|_{max}$, resulting from WAMIT data, for the 25 m long horizontal cylinder. The nonlinear hydrodynamic effects (i.e. nonlinear Froude-Krylov, viscous and restoring forces) are strongly depending on the extent of the time-varying wetted body surface, which is the surface of interaction between the body and the water. Since the body displacement alone is not sufficient to provide an indication regarding the variation of the wetted body surface, it is more useful to take into consideration the relative float heave displacement, defined as $y_{RH}(k) = y(k) - \eta(k)$. Indeed, y_{RH} provides a more accurate measure of the amount of the body that is submerged in the water. In Fig. 6.71(a), the first 70 s of the body displacement and FSE are plotted together (generated with the experiment $W1$), in order to show the strong similarity of the two signals, suggesting that the body behaves like a wave follower [304]. In Fig. 6.71(b), y_{RH} is plotted for the whole experiment $W1$. In both experiments $W1$ and $W2$, $-0.1 \leq y_{RH} \leq 0.1$ m, as shown in Fig. 6.72(a); therefore, the wetted body surface does not change in a significant way during the experiments, suggesting that the involved hydrodynamic nonlinearities are modest (see Fig. 6.72(b)).

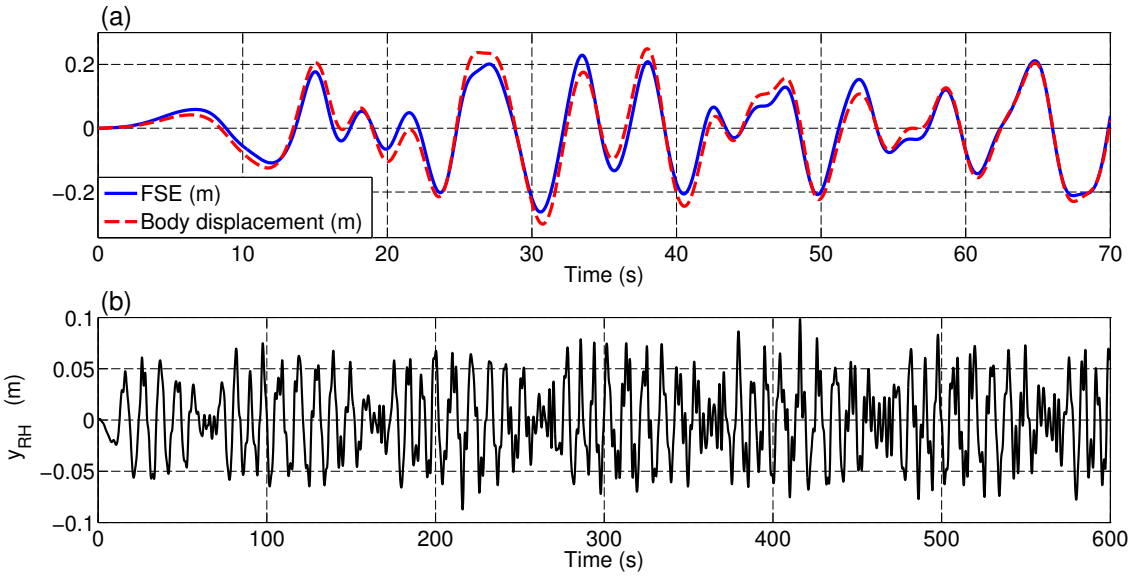

Figure 6.71: (a) First 70 s of the body displacement and FSE, generated with the experiment $W1$. (b) Relative float heave displacement for the whole experiment $W1$.

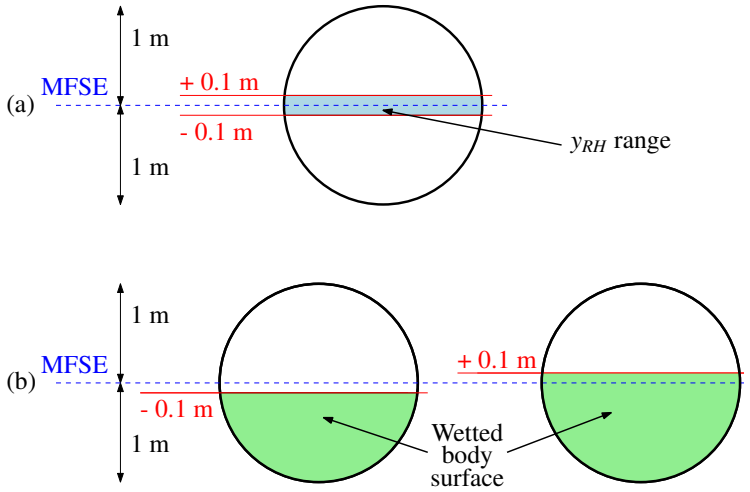

Figure 6.72: (a) In both experiments $W1$ and $W2$, $-0.1 \leq y_{RH} \leq 0.1$ m. (b) The wetted body surface does not change in a significant way during the experiments.

6.4.3 Model description and identification

ARX model

In the case of the $\eta \rightarrow y$ model family, the input/output relationship of the ARX model structure is given (see Section 3.2.3.1) by:

$$y(k) = \sum_{i=1}^{n_a} a_i y(k-i) + \sum_{i=0}^{n_b} b_i \eta(k-n_d-i) \tag{6.48}$$

By performing the input wave body motion experiment, the signals $\{\eta_d(k)\}$ and $\{y_d(k)\}$, for $k = 1...N$, are generated (see Section 6.4.2), which can be utilised as input and output for the ARX model identification. The first possible predicted model output is for $k = \tau + 1$, where τ is given by equation (6.5). The last possible predicted model output is for $k = \widetilde{N}$, where $\widetilde{N}$ is given by equation (6.6). In this case, equations (3.61) and (3.62) become:

$$\mathbf{y} = \begin{bmatrix} y_d(\tau+1) & y_d(\tau+2) & \dots & y_d(\widetilde{N}) \end{bmatrix}^T \tag{6.49}$$

and

$$\mathbf{\Phi} = \begin{bmatrix} y_d(\tau) & \dots & y_d(\tau+1-n_a) & \eta_d(\tau+1-n_d) & \dots & \eta_d(\tau+1-n_d-n_b) \\ y_d(\tau+1) & \dots & y_d(\tau+2-n_a) & \eta_d(\tau+2-n_d) & \dots & \eta_d(\tau+2-n_d-n_b) \\ \vdots & \ddots & \vdots & \vdots & \ddots & \vdots \\ y_d(\widetilde{N}-1) & \dots & y_d(\widetilde{N}-n_a) & \eta_d(N) & \dots & \eta_d(N-n_b) \end{bmatrix}, \tag{6.50}$$

respectively. The estimated parameter vector $\hat{\boldsymbol{\theta}}_{arx} = [a_1 \ \dots \ a_{n_a} \ b_0 \ \dots \ b_{n_b}]^T$ is determined by utilising $\mathbf{y}$, $\mathbf{\Phi}$ and QR factorization to resolve the LS problem.

KGP model

In the case of the $\eta \rightarrow y$ model family, the KGP model structure, where the cross-product terms are removed in order to reduce the possibility of stability problems (see Section 3.2.3.5), is described by the input/output relationship given by:

$$y(k) = \sum_{j=1}^{n_p} \left[\sum_{i=1}^{n_a} a_{ij} y^j(k-i) + \sum_{i=0}^{n_b} b_{ij} \eta^j(k-n_d-i) \right] \tag{6.51}$$

In this case, equation (3.72) becomes:

$$\mathbf{y} = \begin{bmatrix} y_d(\tau+1) & y_d(\tau+2) & \dots & y_d(\widetilde{N}) \end{bmatrix}^T, \tag{6.52}$$

where τ and $\widetilde{N}$ are given by equations (6.5) and (6.6), respectively, and each of the $(\widetilde{N}-\tau)$ rows of the data matrix $\mathbf{\Phi}$, defined by (3.49), has the form:

$$\begin{bmatrix} y_d(k-1) & \dots & y_d(k-n_a) & \eta_d(k-n_d) & \dots & \eta_d(k-n_d-n_b) \\ y_d^2(k-1) & \dots & y_d^2(k-n_a) & \eta_d^2(k-n_d) & \dots & \eta_d^2(k-n_d-n_b) & \dots \\ y_d^{n_p}(k-1) & \dots & y_d^{n_p}(k-n_a) & \eta_d^{n_p}(k-n_d) & \dots & \eta_d^{n_p}(k-n_d-n_b) \end{bmatrix}, \tag{6.53}$$

where $k=(\tau+1),\dots,\widetilde{N}$. The estimated parameter vector, $\hat{\boldsymbol{\theta}}_{kgp}$, is determined by utilising $\mathbf{y}$, $\mathbf{\Phi}$ and QR factorization to resolve the LS problem.

ANN model

The input/output relationship of the ANN model is given by equation (6.47), where, in the case of the $\eta \rightarrow y$ model family,

$$\begin{bmatrix} v_1(k) & \dots & v_{n_v}(k) \end{bmatrix} = \begin{bmatrix} y(k-1) & \dots & y(k-n_a) & \eta(k-n_d) & \eta(k-n_d-1) & \dots & \eta(k-n_d-n_b) \end{bmatrix},$$

A good compromise between complexity and accuracy of the model has been found by utilising $n_1=10$ and $n_2=10$ (see Table 6.17). The unknown parameter vector is identified by utilising a conjugate gradient algorithm in batch training mode (the ANN model is retrained with the same data over successive epochs), and a variety of initial conditions (100 instances) is used.

6.4.4 Results

By utilising the strategy explained in Section 3.2.4, the dynamical orders $n_a=8$ and $n_b=2$, and the input delay time $n_d=-7$ are identified (see Table 6.17). Fig. 6.73 shows the loss function $LF=LF(n_a,n_b,n_d)$ versus n_a, for training experiment $W1$, where each vertical line shows the range of LF for a specific value of n_a and for $1\leq n_b\leq 8$ and $-20\leq n_d\leq -3$. No significant reduction of LF for $n_a>8$, showing that $n_a=8$ is the correct value to obtain a parsimonious model structure. Fig. 6.74 shows the LF values in the case where $n_a=8$, $n_b=2$ and $-20\leq n_d\leq 10$; it is possible to see that the minimum value occurs for $n_d=-7$. As explained in Section 6.2.4, there is a noncausal relationship between the FSE and the excitation force, which leads the body to start moving before the wave crest reaches the centre of the body (where the FSE is measured). Therefore, also the relationship between η and y is noncausal (indeed, in this case study $n_d=-7$). The polynomial order of the KGP model $n_p=2$ is selected, observing that larger values of n_p improve the training fitting, but degrade the quality of the validation fitting (i.e. overfitting).

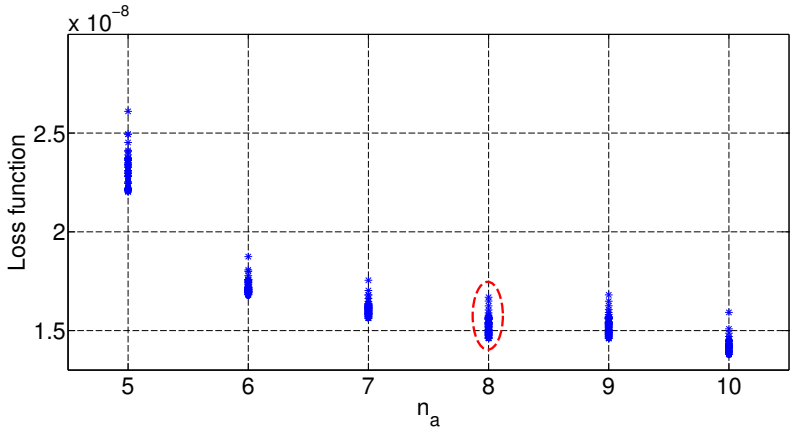

Figure 6.73: $LF=LF(n_a,n_b,n_d)$, in the case of the circular body of Fig. 6.66 and the training experiment $W1$, is plotted versus n_a, where each vertical line shows the range of LF for a specific value of n_a and for $1\leq n_b\leq 8$ and $-20\leq n_d\leq -3$. There is no significant reduction of LF for $n_a>8$; therefore, $n_a=8$ is the correct value to obtain a parsimonious model structure.

n_a	n_b	n_d	n_p	n_1	n_2
8	2	-7	2	10	10

Table 6.17: n_a, n_b, n_d, n_p, n_1 and n_2 utilised for the different DT model structures.

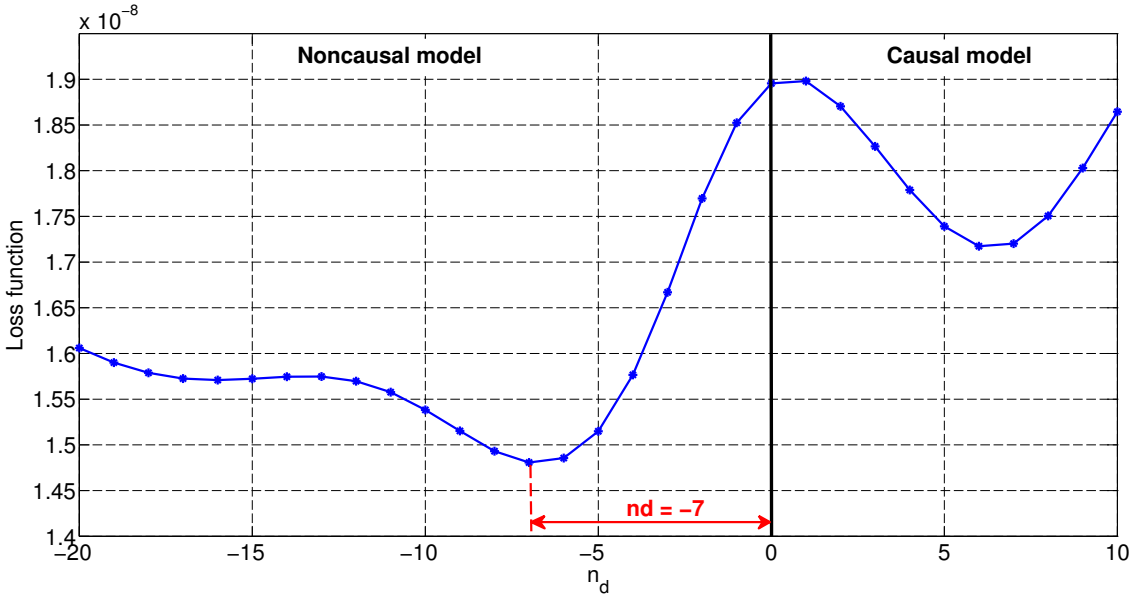

Figure 6.74: $LF = LF(n_a, n_b, n_d)$ is plotted versus n_d, for $n_a = 8$ and $n_b = 2$, in the case of the circular body of Fig. 6.66 and the training experiment $W1$. The minimum occurs for $n_d = -7$.

Fig. 6.75 shows, for training experiment $W1$, the multi-step predictions of ARX, KGP and ANN models. All the fitting results on training experiment $W1$ are summarised in Table 6.18, where it is possible to observe only small differences in the performance of the linear ARX model compared to the two nonlinear models, indicating that the floating body motion does not exhibit much nonlinear behaviour for the geometry and wave conditions chosen in this case study (as already predicted in Section 6.4.2, by observing the relative float heave displacement). However, even for more energetic sea states (and, in particular, longer wave periods), within power production ranges, the device response to wave excitation alone (for example in the absence of a PTO force) does not tend to become significantly nonlinear, as documented in [170]. The models trained with the $W1$ dataset are validated with the $W2$ dataset. Fig. 6.76 shows a comparison of the ARX, KGP and ANN model multi-step predictions against the validation data. The NRMSE performance for each of the different models against the validation data is summarised in Table 6.18, where it is possible to see that the ARX and KGP model are similar and that the ANN model loses prediction accuracy. In order to better understand the degradation of performance of each model from training to validation, the NVTD parameter , defined by equation (6.21), is calculated for each model (see Table 6.19). A NVTD = 0.25 is chosen as an upper threshold for a model having a good ability in generalizing and, in Table 6.19, each NVTD < 0.25 is written in bold, to indicate a good model performance. The NVTD results show the ARX and KGP models generalise quite well, indicating good quality of the utilised data and the identified parameter vector. On the other hand, the ANN model, which was the best in training, degrades considerably in validation, showing an inability to generalise, likely a consequence of the nonlinear optimization necessary to identify the ANN parameters, which does not guarantee the achievement of a global minimum. Furthermore, as shown in Table 6.20, the number of parameters for the ANN model is considerably larger than the number of parameters for the ARX and KGP models, increasing the difficulty of finding a global minimum.

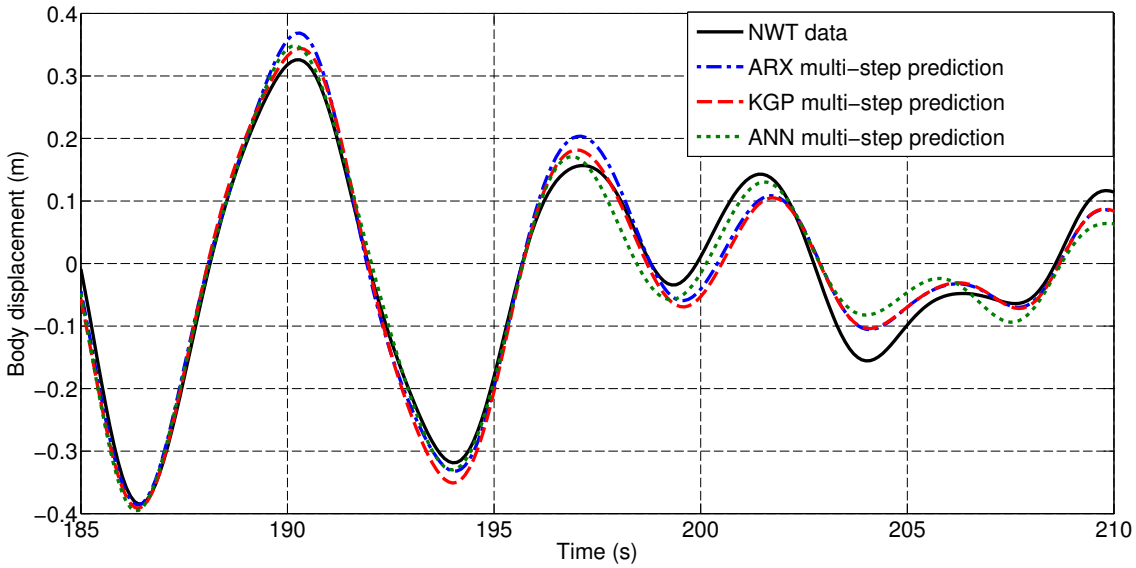

Figure 6.75: Multi-step predictions, of the identified models, on the training experiment $W1$.

	Model trained with $W1$	Model validated with $W2$
ARX	0.1721 (3)	0.1793 (2)
KGP	0.1713 (2)	0.1787 (1)
ANN	0.1671 (1)	0.2429 (3)

Table 6.18: NRMSE multi-step performance for training and validation. The best model performance is marked in green and with the number (1), the second model performance is marked in orange and with the number (2), and the worst model performance is marked in red and with the number (3).

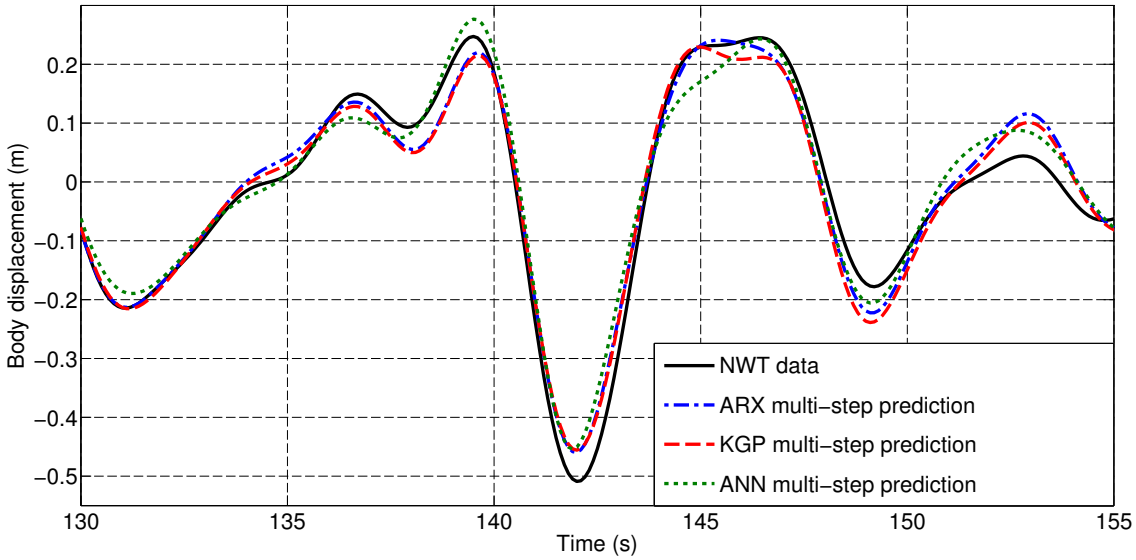

Figure 6.76: Multi-step predictions of the models (identified with $W1$), in the case of the validation experiment $W2$.

Model	NVTD
ARX	**0.0418**
KGP	**0.0432**
ANN	0.4536

Table 6.19: NVTD parameter values calculated from NRMSE multi-step prediction performance, by using the training and validation data of Table 6.18. A NVTD = 0.25 is chosen as an upper threshold for a model having a good ability in generalizing, and each NVTD < 0.25 is written in bold.

ARX	KGP	ANN
11	22	241

Table 6.20: Number of identified parameters, for the different model structures, given by equations (3.9), (3.26) and (3.34).

6.5 Summary and discussion

In this chapter, the framework for hydrodynamic model identification from recorded experimental data, developed in Chapters 3 and 4, is applied in four different case studies, by utilising data generated in 2D and 3D CFD-NWTs. In Chapter 5, the ID framework has been used for the identification of linear CT state-space models, underlining the advantage of a CT model structure in providing a good understanding of the system since, usually, CT models are derived from physical principles and the model parameters are strongly related to the physical system properties. On the other hand, the loss functions, associated with CT model structures, are usually characterised by the presence of multiple local minima, which requires the adoption of nonlinear optimization strategies, which are sensitive to the initial optimization seed. In this chapter, different linear and nonlinear DT model structures are utilised (i.e. ARX, Hammerstein, FBO, KGP and ANN model structures), which have the disadvantage of losing the physical meaning of the parameters but, on the other hand, give greater flexibility in the construction of nonlinear input/output model structures, which are linear in the parameters, with the consequent possibility of convex optimization. Under the hypotheses of small waves, inviscid fluid and small body displacement, linear model structures represent a convenient choice to describe the WEC dynamics. When the wave and body displacement amplitudes increase, becoming of the same order of magnitude of the dimensions of the body, some nonlinear hydrodynamic effects may appear, and the use of nonlinear input/output model structures can improve the model accuracy. Usually, the fitting error of an identified model is larger in validation than in training, for this reason, in this chapter, a new metric is proposed, termed NVTD parameter (see Section 6.2.4), in order to quantify the degradation of performance of a model, progressing from training to validation data sets.

Section 6.2 shows a case study where three different fixed 2D bodies are utilised, which have the vertical cross-sections of a triangle, a circle and a box. For each geometry, three different DT model structures (i.e. ARX, Hammerstein and KGP models), belonging to the $\eta \rightarrow f_e$ model family, are identified (for a total of 9 identified models). Since the experiments are carried out in a 2D CFD-NWT, the body geometries of the test devices are equivalent to infinitely long horizontal bars. In the NWT, two different kinds of experiments are carried out, the prescribed motion experiments, utilised to obtain data for the Hammerstein static curve identification (a different experiment for each geometry), and the input wave excitation force experiments, employed for the generation of data, utilised for the identification of the dynamic part of the model structures. Two different FSE realizations (one for model identification and the other for model validation) are utilised in the input wave excitation force experiments, which are realizations from the sea state having a JONSWAP spectrum with $H_s = 1.5$ m $T_p = 10$ s. The same FSE realizations are

utilised with all the geometries, for a total of 6 experiments. Each model is trained with a 1-step prediction criterion and, once identified, the model is used to make multi-step predictions on the same training data and on a different validation data set. For all 6 input wave excitation force experiments (both training and validation), the KGP model structure appears best, followed by the Hammerstein and finally the ARX model structure. None of the identified models is perfect, but the linear model has particular difficulty in following peaks in the excitation force. The data utilised in the case study show the presence of hydrodynamic nonlinearities, which the nonlinear identified models are able to describe. The analysis of the results for the different geometries, in training and validation, shows that the linear ARX model structure finds the triangular geometry to be the most difficult to simulate, followed by the rectangular and the circular geometries. This suggests that the degree of nonlinearity in the data is greater for the triangular geometry, followed by the rectangular and the circular geometries. From a fluid dynamics point of view, the degree of nonlinearity can be connected to the body shapes, by observing that the triangle has the most nonlinear hydrostatic curve. On the other hand, the box has a linear restoring curve, but a very flat bottom with sharp corners, which can be the source of important nonlinear effects, based on viscosity and vortex shedding. Finally the circle has a moderate nonlinearity in the hydrostatic curve and a very smooth shape, which may create a moderate viscosity and vorticity. The limitations of the linear ARX models, with respect to the nonlinear models, are shown in particular in the validation experiment for the triangular geometry, where the NWT data exhibit a symmetric (with respect to the MFSE) sinusoidal FSE at the input, and an asymmetric excitation force at the output, which is a typical example of nonlinear behaviour; indeed, the ARX model is not able to replicate the asymmetric behaviour. For all 9 identified models, a value of NVTD<0.25 was calculated, indicating a parsimonious structure for the models and a good estimate for the parameter vectors.

In Section 6.3.1, the heave motion of a 3D conical floating body, in response to an input PTO force (under the hypotheses of no incident waves and no mooring forces) is investigated. The conical body geometry is chosen because it is characterised by strong nonlinearities in its restoring force, which is appropriate to illustrate the different model capabilities of handling this effect. Three different DT model structures (i.e. ARX, Hammerstein and FBO models), belonging to the $f_{in} \rightarrow y$ model family, are identified. For comparison of the linear ARX model, a traditional linear CT model (in this chapter termed the Cummins-BEM model), based on a parametric form of Cummins' equation, is also evaluated, by using frequency domain hydrodynamic coefficients, calculated by the BEM software WAMIT. The identified ARX model structure is more accurate than the Cummins-BEM model. In the 3D CFD-NWT, two different kinds of experiments are carried out, the prescribed motion experiment, utilised to obtain data for the Hammerstein and FBO static curve identification, and the input force experiment, used for the generation of data, employed for the identification of the dynamic part of the model structure. Each model is trained with a 1-step prediction criterion and, once identified, the model is used to make a multi-step prediction on the same training data. Two different input force experiments are carried out in the NWT, both characterised by a sinusoidal PTO force signal with a low frequency, which emphasizes the static nonlinearity of the restoring force, by reducing other possible velocity-dependent nonlinearities. In both the input force experiments, the body is also initially displaced 30 cm above its equilibrium position, allowing its free decay oscillation to be superimposed on the response to the PTO force. The first input force experiment has a sinusoidal PTO force signal with a relatively small amplitude; in this case, the linear models show good performance in fitting the NWT body displacement, for both the transient and the steady-state motion. The second input force experiment has a sinusoidal PTO force signal with a larger amplitude; in this case, the fully nonlinear NWT simulation shows an asymmetric output, with respect to the equilibrium position, in response to the symmetrical sinusoidal input. It is not possible for the linear models to replicate this nonlinear behaviour. The linear models also show difficulty in the fitting of the transient part of the output. On the other hand, the nonlinear models are able to replicate the asymmetric steady-state response, and better able to reproduce the transient oscillations, particularly the FBO model, which performs very well.

In Section 6.3.2, the heave motion of a 2D circular floating body is investigated in response to an input PTO force, under the hypotheses of no incident waves and no mooring forces. Three different DT model structures (i.e. ARX, KGP and ANN model structures), belonging to the $f_{in} \rightarrow y$ model family, are identified. In contrast to the case study of Section 6.3.1, where the input PTO force is a sinusoidal signal with a low frequency, in this case study, three different dynamically rich PTO force signals (i.e. RARP, multisine and chirp signals) are utilised in order to obtain all the required identification information. Two versions of each signal type are generated, one to be used for model training and the other for model validation. By utilising a 1-step prediction criterion, from each training experiments (i.e. $R1$, $M1$ and $C1$), three different models are identified (i.e. ARX, KGP and ANN models), for a total of 9 models. Once identified, each model is used to make multi-step predictions on the same training data, and on a different validation data set. In the case of multi-step predictions on training data, the ANN models always perform best, followed by the KGP models, and finally the ARX models, suggesting that the data contain nonlinearities, which the KGP models and the ANN models, in particular, are able to capture. In the case of multi-step predictions on validation data, in general, the ANN model structure has inconsistent performance, the ARX model structure usually has poor performance, and the KGP model structure shows good accuracy and consistency. The results show the difficulty for ANN identification, depending on the nonlinear optimization algorithm and a larger number of parameters to be identified. An analysis regarding which signal type is more performing, in order to identify accurate models, shows that, in this case study, the RARP signal is more performing, in order to identify accurate models, followed by the chirp signal.

In Section 6.4, the heave motion of a 2D circular floating body is investigated, in response to incident waves, under the hypotheses of no PTO and no mooring forces. Three different DT model structures (i.e. ARX, KGP and ANN model structures), belonging to the $\eta \rightarrow y$ model family, are identified. Two different FSE signals (one for model identification and the other for model validation) are generated in the 2D CFD-NWT, which are realizations of the sea state, having a JONSWAP spectrum with $H_s = 0.6$ m $T_p = 8$ s. Each model is trained with a 1-step prediction criterion and, once identified, the model is used to make multi-step predictions on the same training data and on a different validation data set. The multi-step model predictions on training data, show only small differences in the performance of the linear ARX model compared to the two nonlinear models, indicating that the floating body motion does not exhibit much nonlinear behaviour for the geometry and wave conditions chosen in this case study. In the case of multi-step model predictions on the validation experiment, it is possible to see that the ARX and KGP model performance are similar and that the ANN model loses prediction accuracy. In particular, the calculated NVTD values show that the ARX and KGP models generalise quite well, indicating good quality of the utilised data and the identified parameter vector but, on the other hand, the ANN model, which is the best in training, degrades considerably in validation, showing an inability to generalise, likely a consequence of the nonlinear optimization and of the larger number of parameters to be identified.

Chapter 7

Identification of DT hydrodynamic parametric models from input/output RWT experiments

7.1 Introduction

In Chapters 3 and 4, a methodology for the identification of hydrodynamic models is introduced by utilising experimental data. In Chapters 5 and 6, the methodology is applied to data generated in a NWT, which are becoming more and more available thanks to increases in computing power [305]. However, in the wave energy field, RWTs are a popular tool to investigate the WEC characteristics, under controlled and repeatable conditions. Furthermore, a RWT furnishes an environment to repeatedly test, at small scale, rare sea conditions and verify the survivability characteristics of a WEC. Recently, the use of European RWTs has been promoted through the MARINET program [306], by offering free-of-charge access to companies and research groups to 45 different European marine renewable energy research infrastructures.

In this chapter, the framework for model identification, already applied to NWT data, is broadened to the context of data generated in a RWT, analysing the performance of identified linear and nonlinear models. The data utilised for this chapter were recorded at the Coastal Ocean And Sediment Transport (COAST) Laboratory of Plymouth University, UK, where hydrodynamic tests were carried out on a scaled Wavestar WEC point-absorber [307].

Section 7.2 describes the main advantages and disadvantages of a RWT compared to a NWT. Section 7.3, explains the main preprocessing operations necessary to apply to the data measured in a RWT, before using them for model identification and validation. Section 7.4 illustrates a particular case study, with Section 7.4.1 describing the characteristics of Plymouth facility, Section 7.4.2 illustrating the utilised scaled Wavestar WEC, Section 7.4.3 explaining the experiments used to collect the data and utilised in this chapter, Section 7.4.4 showing the utilised model structures and their identification and Section 7.4.5 illustrating the identified model performance. Finally, conclusions are drawn in Section 7.5.

7.2 RWT and NWT comparison

In the wave energy community, the two main sources of data, utilised to test and model WECs, are the experiments generated in a NWT (as utilised in Chapters 5 and 6), and the real experiments generated in a RWT. Both NWT and RWT have their own particular advantages and disadvantages, as explained in Sections 7.2.1 and 7.2.2.

7.2.1 RWT advantages compared to NWT

RWTs, compared to NWTs, have the following main advantages [7]:
• All NWTs are implemented by utilising mathematical models, which necessarily are an approximation of the real system under study (e.g. the approximations introduced from the turbulence model). Furthermore, the approximated equations utilised are resolved with numerical techniques, which introduce additional numerical errors. As a result, a NWT simulation does not completely correspond to the time-evolution of the real system. On the other hand, a RWT allows the observation and study of the real system, without the introduction of any modelling error.
• The NWTs implemented with CFD, and utilised for the data generation in Chapters 5 and 6, are characterised by a long computation time, which, typically, can be up to 1000 times the simulation time (e.g. 1 s of simulation time takes 1000 s to compute). It is important to underline that, based on the observation of the data for the last 40 years, the CPU power will double every 18 months in the next years; this will lead to a constant reduction of the computing costs [24].

7.2.2 RWT disadvantages compared to NWT

A RWT, compared to a NWT, has the following main disadvantages [10] [11]:
• In the majority of the cases, the device has to be scaled to perform a test in a RWT, introducing complications with scaling effects [308]. In a NWT, instead, the devices can be tested directly at any real scale.
• In a NWT, the device can be constrained to different modes of motion by utilising ideal numerical constraints; in a RWT, instead, it is necessary to utilise real mechanical restraints, which increase the cost of the tests and introduce friction, altering the device dynamics under investigation.
• In a RWT, there is the presence of random and systematic errors in the measurements. For example, in [212], the presence of the measurement error (introduced by the bending and torsion of the basin's bridge, which supports the WEC modal test) is outlined.
• In a RWT, it is not possible to directly measure the hydrodynamic force on the body.
• In a RWT, reflections from tank walls represents a considerable inconvenience, since they alter the wave field surrounding the WEC under investigation. The presence of beaches in a RWT reduces the problem but does not eliminate it. Another possibility to reduce the wave reflection is the use of active absorbing wavemakers, which are more effective than beaches, but more expensive [309]. In a NWT, the wave reflections can be effectively controlled by numerical absorption techniques.
• In a RWT, specialist equipment, including a prototype WEC device, is required, increasing the cost of the tests.
• In a RWT, motion capture requires the use of physical sensor devices, which can alter the device or fluid dynamics.

7.3 RWT data preprocessing

7.3.1 Calibration: zero error calculation and cancellation

As explained in Section 7.2.2, one of the disadvantages of a NWT is the presence of random and systematic errors in the measurements. Random errors are fundamentally due to physical noise (i.e. by natural fluctuations due to thermal particle motion) and, by their nature, they are unpredictable [310] [311]. On the other hand, systematic errors do not have a random nature and they can result from an erroneous calibration, leading to the presence of a constant bias uncertainty, called zero error (also known as offset error), on the measured quantity, as shown in Fig. 7.1 [312]. Examples of quantities, which can suffer of zero error in the RWT measurements, are the body

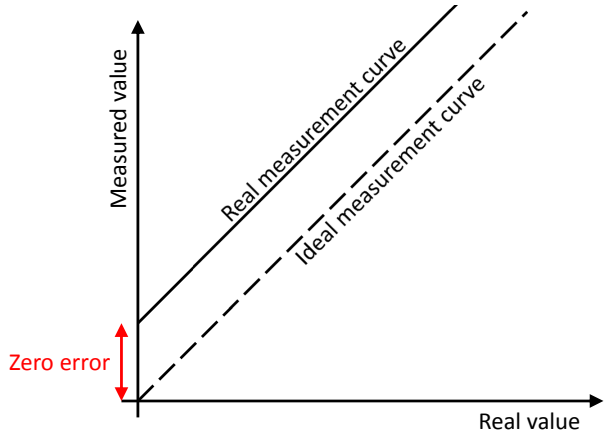

Figure 7.1: Relationships between the real value of a quantity and its measurement: the dashed line represents an ideal measurement curve (the measured value is equal to the real value), the continuous line represents a real measurement curve affected by a zero error.

displacement and the FSE [313] [314]. The objective of this chapter is to model the relationship between the FSE and body displacement. If the FSE is constantly zero at the input of the model (no waves), the body displacement, at the output of the model, has to be zero as well (without waves the body does not move from its equilibrium position). Therefore, the zero errors, present in the FSE and the body displacement measurements, have to be calculated and removed before the identification and validation of the models. The mean value of the FSE measured in a point of the tank should be zero, therefore, the cancellation of the zero error is straightforward; indeed, it is sufficient to calculate the mean value of the signal and remove it from the original signal:

$$\eta(k) = \eta_m(k) - \frac{1}{N_t}\sum_{k=1}^{N_t}\eta_m(k) \tag{7.1}$$

where η_m is the original measured FSE signal, η is the corrected FSE signal and N_t the total number of samples available for the FSE signal.

In contrast to the FSE, the body displacement can be a signal with non-zero mean value (for example in the case of a nonlinear asymmetric restoring force); therefore, it is not correct to remove the mean value from the original signal. Instead, a way to estimate the zero error of the body displacement is to start the experiment without any input excitement (no waves) for some seconds (for example 5 s) and to measure the corresponding and constant (apart from the random error on the measurement) body displacement. The initial sequence of nearly constant values of the measured body displacement can be averaged to reduce the influence of the random error on the estimation of the zero error. Once calculated, the zero error can be removed from the original signal:

$$y(k) = y_m(k) - \frac{1}{N_c}\sum_{k=1}^{N_c}y_m(k) \tag{7.2}$$

where y_m is the original measured body displacement signal, y is the corrected body displacement signal and N_c is the number of samples of the body displacement having an initial constant (apart from the random error on the measurement) signal value. Fig. 7.2 shows the measured FSE and body displacement before and after the zero error cancellation for experiment E_1.

7.3.2 Data interpolation

In general, in a RWT experiment, different physical quantities are measured using different sensors, each one characterised by its own sampling time. The experimental data set, utilised in this

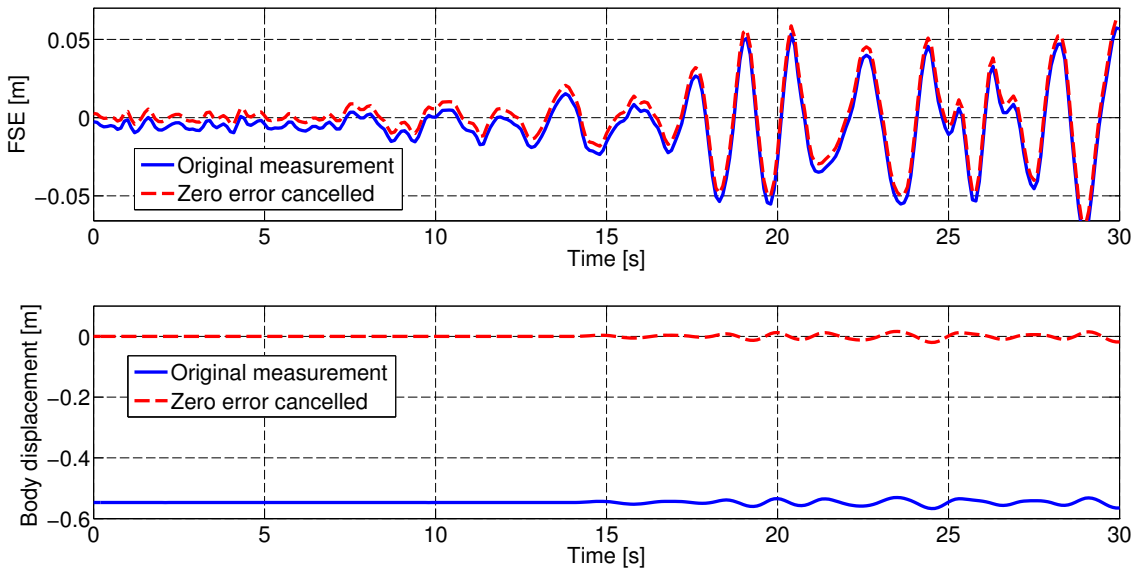

Figure 7.2: Measured FSE and body displacement before and after the zero error cancellation (in the case of experiment E_1).

chapter, consist of FSE measurements having a sampling time equal to 8 ms and body displacement measurements having a sampling time equal to 2 ms. Since it is necessary to have input and output variables with the same sampling time for the identification of the models, a preprocessing operation of interpolation is necessary before the use of the data. The data utilised in this chapter have been interpolated with a sampling time $T_s = 0.1$ s

7.4 Case study

7.4.1 Wave tank facility specifications (Plymouth)

The data utilised for this chapter have been collected during a period of four weeks in September 2013, through the MARINET access program at the COAST Laboratory of Plymouth University, UK [315]. The RWT is 35 m long by 15.5 m wide and with an adjustable floor, that can be set with a depth up to 3 m. (the data utilised in this chapter have been obtained with a 3 m depth floor). On the wave tank, 24 dry-backed flap wavemakers of 2.0 m hinge depth are installed, each of them individually controlled for wave generation. The presence of an absorbing beach significantly reduces the amplitude of reflected waves. Fig. 7.3 shows the COAST ocean wave basin.

7.4.2 Device specifications

The scaled Wavestar WEC studied is a point-absorber composed of a 1 m diameter hemispherical float, rigidly attached to a 2 m length arm (see Fig. 7.4) [316] [317]. The total weight of the float-arm system is 130 kg. The WEC is constrained to have a single DoF: the rigid float-arm structure rotates in pitch around a fixed hinge, located 1.69 m above the mean FSE. An hydraulic cylinder is attached to the support frame, roughly halfway down the arm, with the purpose of controlling the pitching motion of the device, by applying a PTO force. The WEC is attached to the bridge at the facility utilising a mounting frame. See Fig. 7.5 for the detailed mechanical drawing. The force applied from the hydraulic cylinder is described by $f_{cyl} = -K_{cyl}\Delta_{cyl} - D_{cyl}\dot{\Delta}_{cyl}$, where $K_{cyl} = 50$

Figure 7.3: RWT at the COAST Laboratory of Plymouth University. On the left, the dry-backed flap wavemakers are shown.

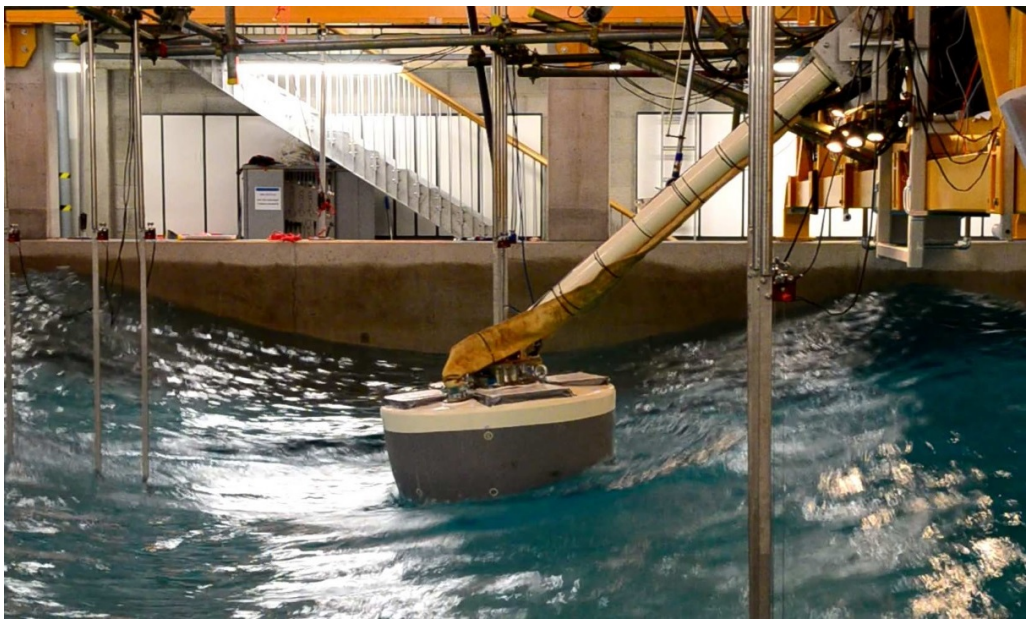

Figure 7.4: Scaled Wavestar WEC tested at Plymouth.

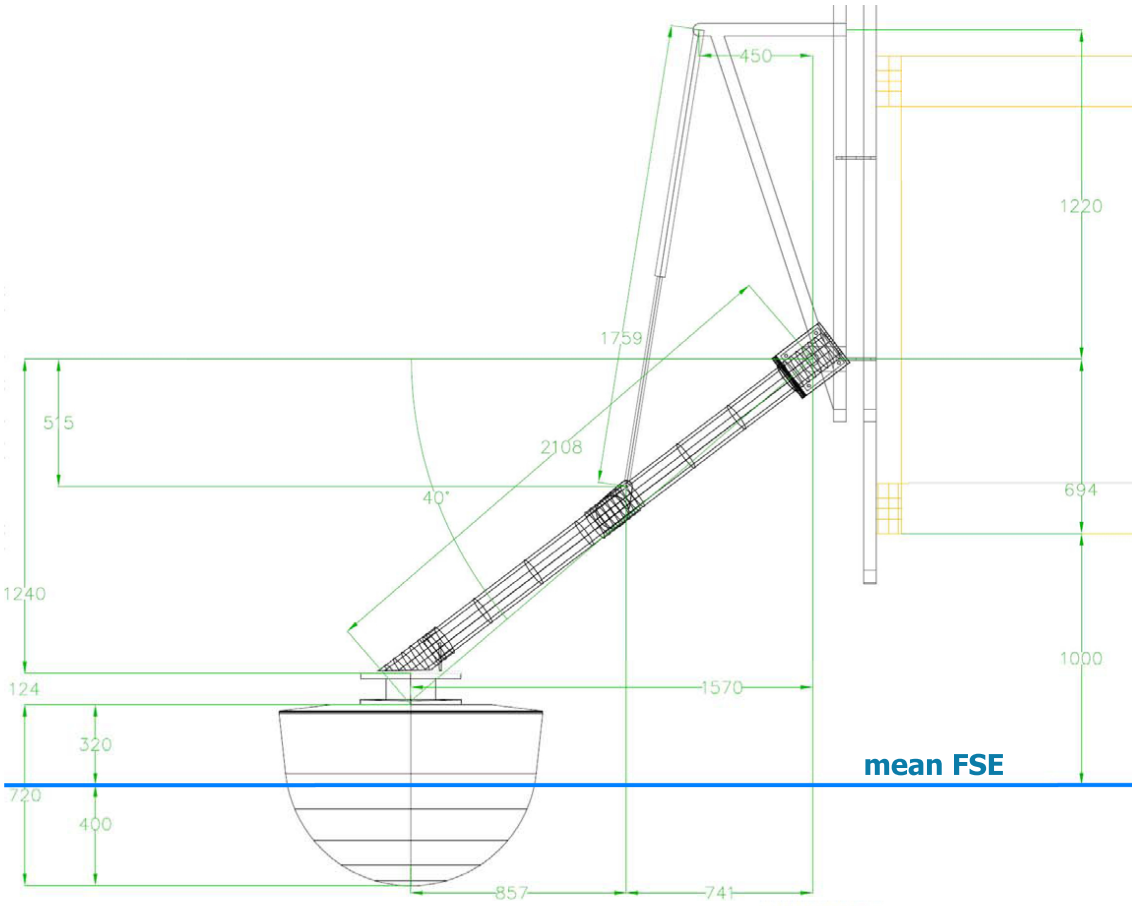

Figure 7.5: Mechanical dimensions in mm of the scaled Wavestar WEC. The WEC is depicted at its equilibrium position. In the picture, the mean FSE is also represented [316].

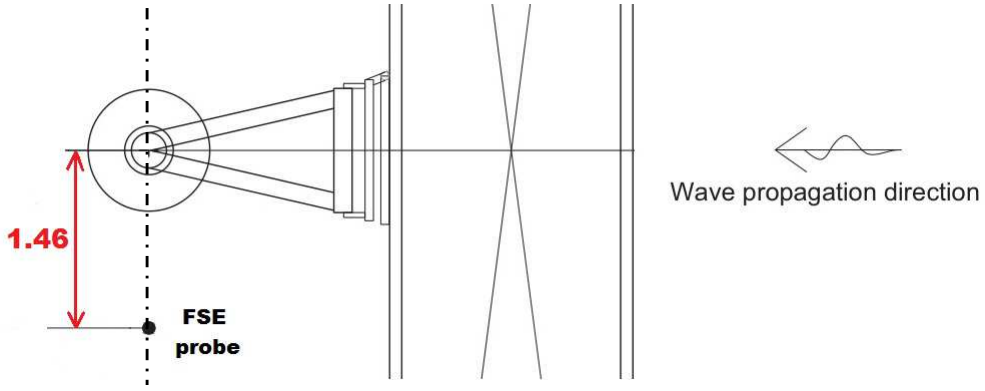

Figure 7.6: Relative position the WEC and the FSE probe (top view) [316].

Exp. name	H_s [m]	T_p [s]
E_1	0.124	2
E_2	0.184	2.5
E_3	0.245	3
E_4	0.369	2.5
E_5	0.490	3
E_6	0.720	4

Table 7.1: H_s and T_p of experiments E_1, E_2, E_3, E_4, E_5 and E_6

N/m, $D_{cyl} = 100$ Ns/m are the stiffness and damping coefficient, respectively, Δ_{cyl} is the hydraulic cylinder displacement and $\dot{\Delta}_{cyl}$ is the hydraulic cylinder velocity.

The input variable, utilised for the mathematical model, is the FSE available at the center of mass of the float, the measurement of which is problematic, since the body occupies that position. The problem is overcome by utilising a FSE probe that is at the side of the float, on a line parallel to the wavefront and passing through the center of mass of the float, as shown in Fig. 7.6. In this way, it is possible to obtain the FSE elevation at the center of mass of the float (plus the waves radiated by the body).

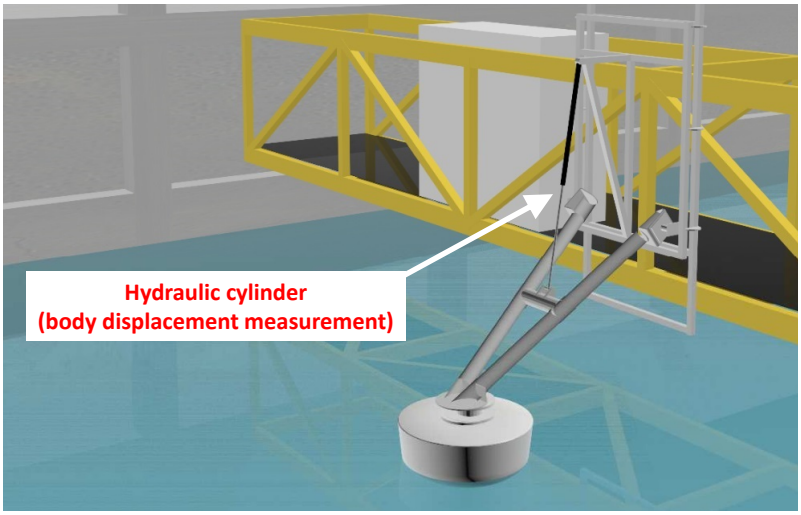

Figure 7.7: Scaled Wavestar WEC tested at Plymouth. The arrow shows the hydraulic cylinder used to measure the body displacement and to apply the PTO force [316].

7.4.3 Experimental data

In this chapter, 6 different RWT experiments are utilised for the WEC modelling. In each experiment, the waves are generated by the flap wavemakers and measured by the FSE probe, shown in Fig. 7.6; the waves create WEC motion, which is measured as an extension of the hydraulic cylinder, by a sensor (see Fig. 7.7) [316]. The cylinder displacement Δ_{cyl} (from the equilibrium position), measured by the sensor, is positive when the cylinder extends and, consequently, when the float enters into the water. It is desirable having a variable, representing the body displacement, which is positive when the float emerges from the water and negative when enters into the water; therefore, the body displacement is defined conventionally as $y = -\Delta_{cyl}$.

The FSE of each experiment is a realization of a different irregular sea state characterised by a JONSWAP spectrum. The significant wave height, H_s, and peak wave period, T_p, of the different experiments are shown in Table 7.1. In Figs. 7.8, 7.9, 7.10, 7.11, 7.12 and 7.13, it is possible to see the time evolution of the FSE and y for experiments E_1, E_2, E_3, E_4, E_5 and E_6 respectively.

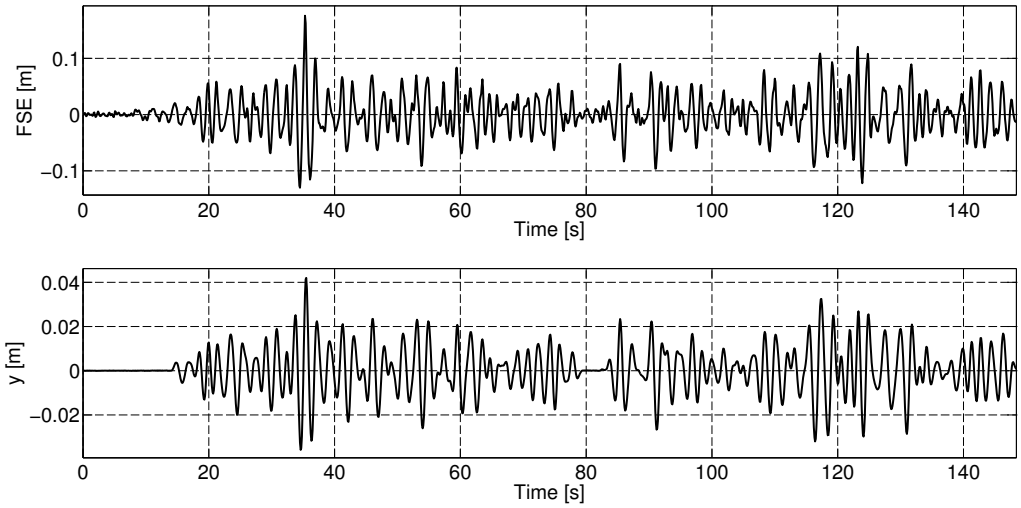

Figure 7.8: Signals time evolution for experiment E_1 ($H_s = 0.124$ m, $T_p = 2$ s).

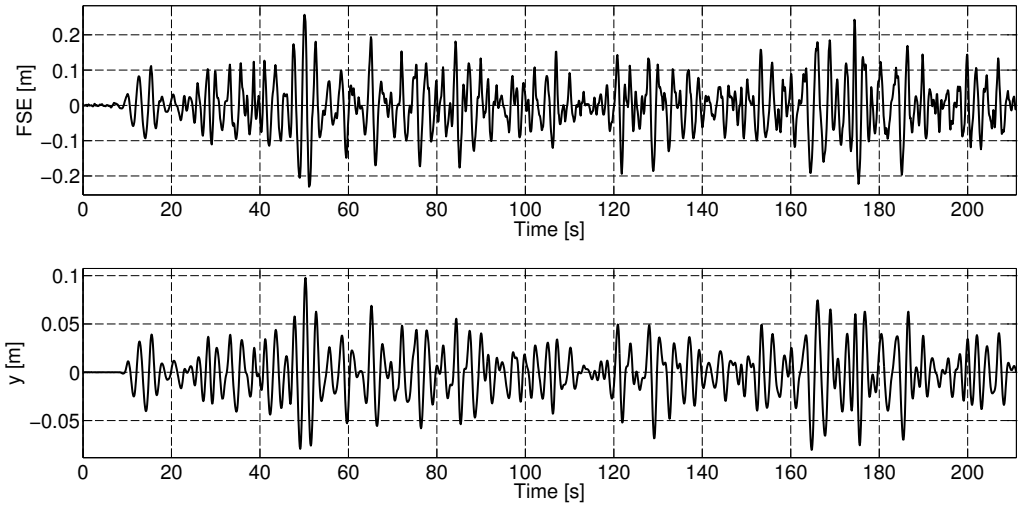

Figure 7.9: Signals time evolution for experiment E_2 ($H_s = 0.184$ m, $T_p = 2.5$ s).

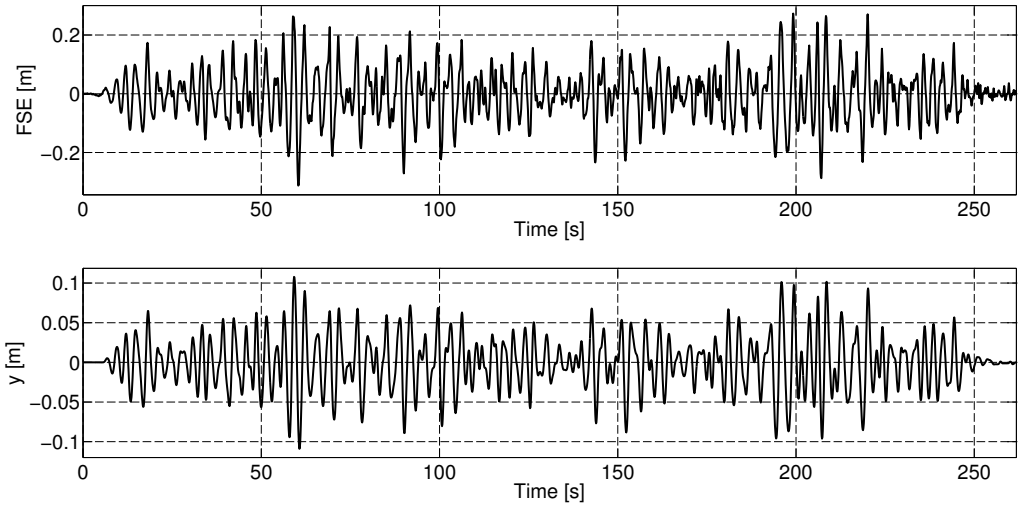

Figure 7.10: Signals time evolution for experiment E_3 ($H_s = 0.245$ m, $T_p = 3$ s).

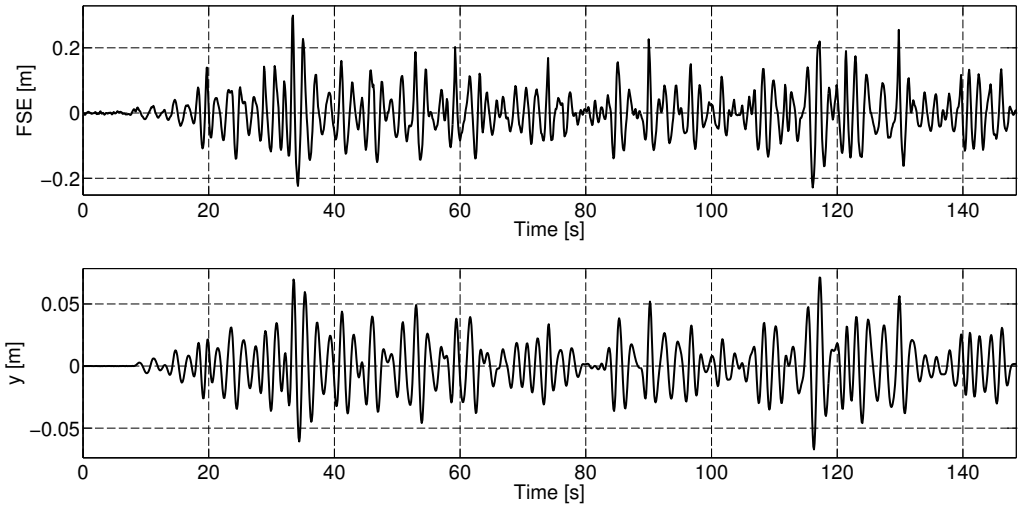

Figure 7.11: Signals time evolution for experiment E_4 ($H_s = 0.369$ m, $T_p = 2.5$ s).

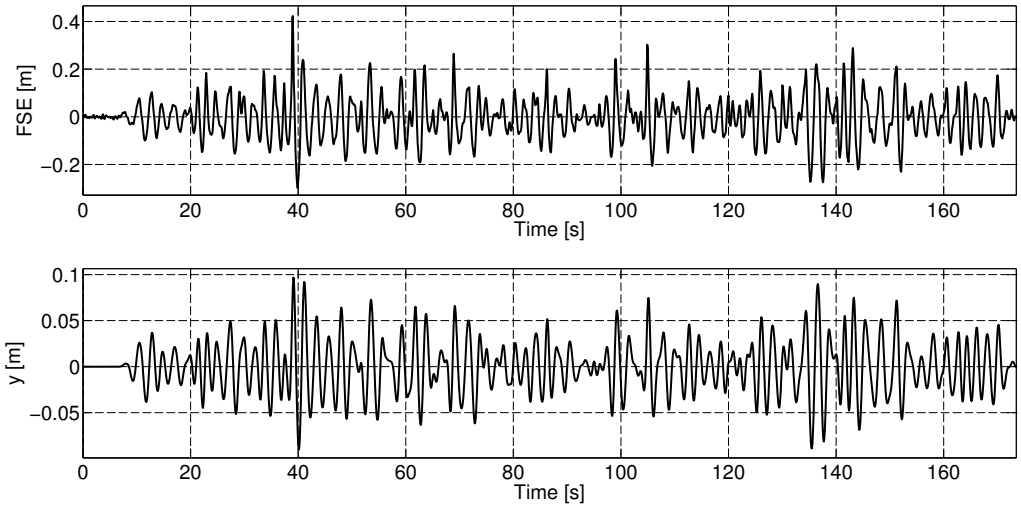

Figure 7.12: Signals time evolution for experiment E_5 ($H_s = 0.490$ m, $T_p = 3$ s).

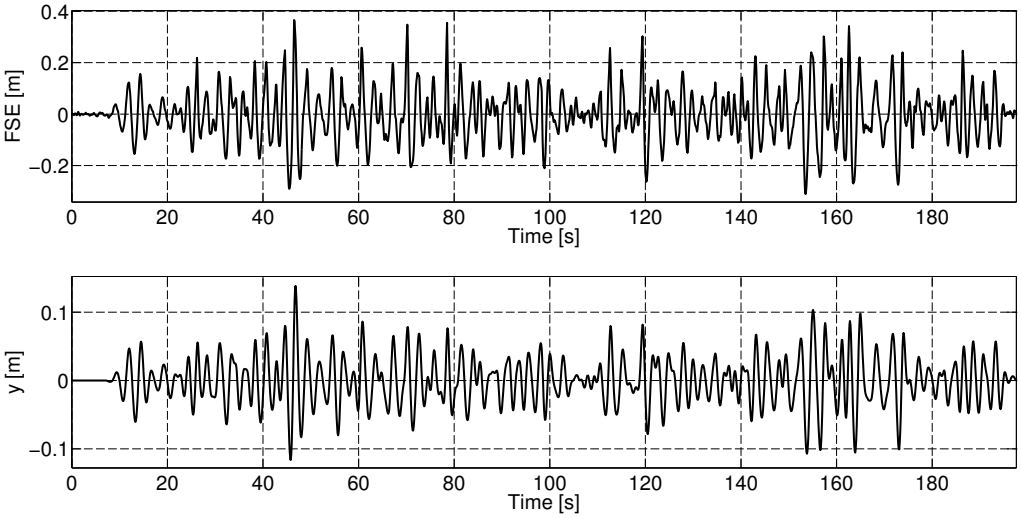

Figure 7.13: Signals time evolution for experiment E_6 ($H_s = 0.720$ m, $T_p = 4$ s).

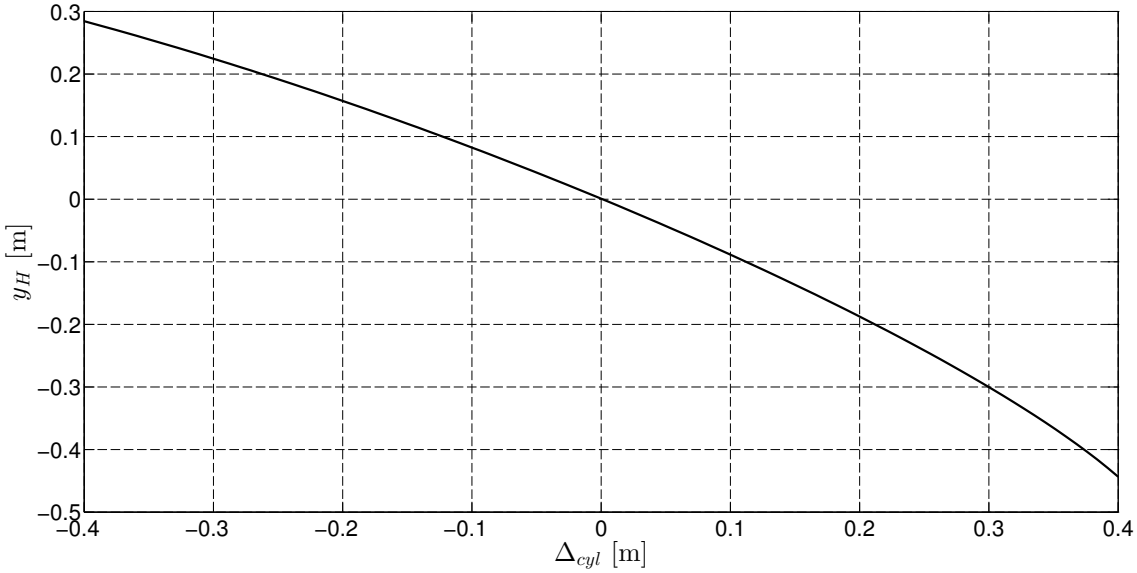

Figure 7.14: Transformation curve from the hydraulic cylinder displacement, Δ_{cyl}, into the float heave displacement, y_H.

7.4.4 Model selection

The Wavestar WEC is a well known device in the wave energy community, and it has been repeatedly studied in recent years. Different kinds of models have been utilised to describe its behaviour, some of them purely linear, based on the assumption of linear potential theory [318] and, more recently, nonlinear terms have been introduced into the models. In [75], a nonlinear hydrostatic restoring moment, described by a cubic polynomial function, is introduced into the model. In [75] and [182], a drag term is introduced by utilising Morison's equation. The accuracy of the nonlinear WEC models show some improvement, compared to the linear ones, especially for peak displacement but, at the same time, viscous drag moment can be negligible in the case of passively damping PTO [75]. In [170], the influence of the nonlinear Froude-Krylov force on the dynamics of a float is outlined (the float has the same geometry and dimensions of the scaled Wavestar WEC used in this chapter). All the previously mentioned nonlinear effects are strongly dependent on the extent of the time-varying wetted body surface, which is the surface of interaction between the body and the water. Since the body displacement alone is not sufficient to provide an indication of the variation of the wetted body surface, it is more useful to take into consideration the relative float heave displacement, y_{RH}, defined as $y_{RH}(k) = y_H(k) - \eta(k)$, where y_H is the float heave displacement. Indeed, y_{RH} provides a more accurate measure of the amount of the body that is submerged into the water. By using the mechanical information available in Fig. 7.5, it is possible to convert the hydraulic cylinder displacement, Δ_{cyl}, into the heave float displacement y_H. Fig. 7.14 shows the transformation curve from the hydraulic cylinder displacement into the float heave displacement. Fig. 7.15 represents the relative float heave displacement for experiment E_1. Fig. 7.15(a) shows the float heave displacement time evolution, Fig. 7.15(b) shows the float heave displacement probability distribution. Analogous plots for experiments E_2, E_3, E_4, E_5 and E_6 are shown in Appendix B, in Figs. B.1, B.2, B.3, B.4 and B.5. In the six experiments utilised in this chapter, the relative float heave displacement is, for the majority of the time, contained between -0.1 and +0.1 m. Fig. 7.16 shows that the float cross-sectional area does not change in a significant way for a relative float heave displacement between -0.1 and +0.1 m, suggesting that the involved hydrodynamic nonlinearities are modest.

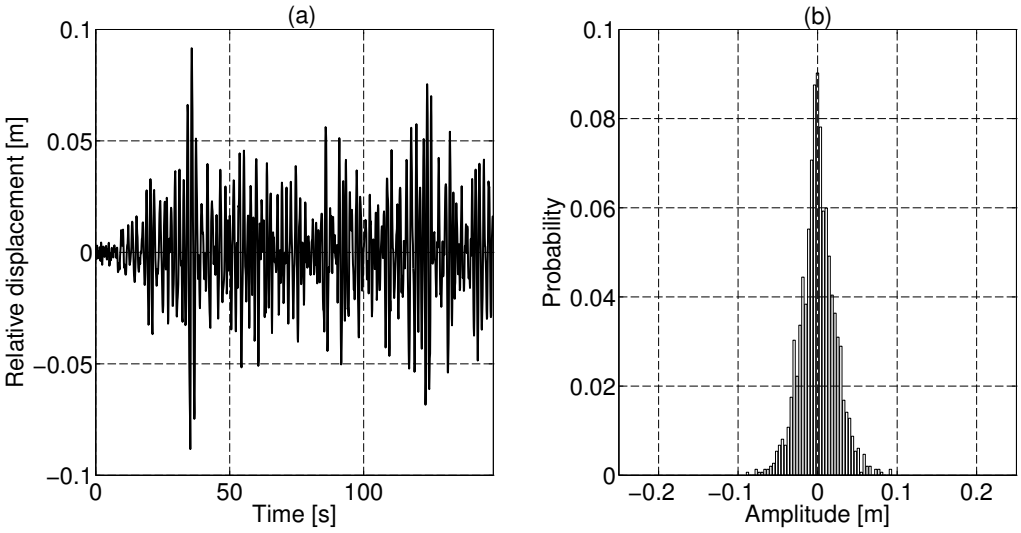

Figure 7.15: Relative float heave displacement for experiment E_1. (a) Time evolution (b) Probability distribution.

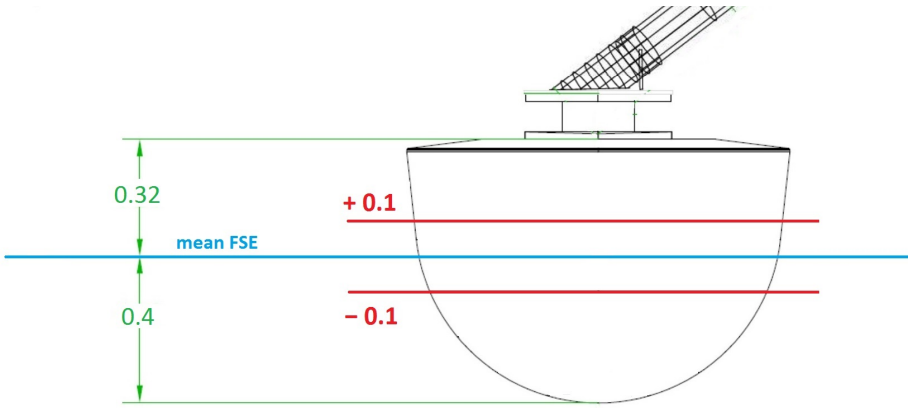

Figure 7.16: Mechanical dimensions of the float in meters. The body cross-sectional area does not change in a significant way for a relative float heave displacement between -0.1 and +0.1 m.

7.4.4.1 Model structures

From the considerations of Section 7.4.4, it is reasonable to suppose the presence of weak nonlinear effects; therefore, linear and nonlinear structures are investigated and their performances compared to verify the necessity of nonlinear models to describe experiments E_1,... E_6. The two utilised model structures, belonging to the $\eta \rightarrow y$ model family, are the linear ARX model (see Section 3.2.3.1):

$$y(k) = \sum_{i=1}^{n_a} a_i y(k-i) + \sum_{i=0}^{n_b} b_i \eta(k-n_d-i) \tag{7.3}$$

and the KGP model (see Section 3.2.3.5):

$$y(k) = \sum_{j=1}^{n_p} \left[\sum_{i=1}^{n_a} a_{ij} y^j(k-i) + \sum_{i=0}^{n_b} b_{ij} \eta^j(k-n_d-i) \right] \tag{7.4}$$

As explained in Section 3.2.3.5, the presence of the cross-product terms (between μ and y) in the KGP model structure can lead to potential, and unpredictable, stability problems. For this reason, the model described by (7.4) does not contain any cross-product terms. The ARX models provide a

reference linear model, with which nonlinear KGP models can be compared. As explained in Section 3.2.4, the estimated n_a, n_b and n_d for the ARX model, are also utilised with the KGP models since, maintaining the same dynamical order and delay time for the linear and nonlinear models, provides the possibility of isolating the comparative linear/nonlinear structure performances.

7.4.4.2 Dynamical orders and delay time identification

In this chapter, the same framework is utilised, as in Section 3.2.4 and Chapter 6 for the identification of the dynamical orders n_a, n_b and the delay time n_d of the DT linear and nonlinear models. A first indication, regarding possible values of n_a, n_b and n_d, is obtained by identifying 3100 different ARX structures, by utilising all the possible combinations of the integers $1 \leq n_a \leq 10$, $0 \leq n_b \leq 9$ and $-20 \leq n_d \leq +10$. In Fig. 7.17, the loss function $LF = LF(n_a, n_b, n_d)$, for the experiment E_1, is plotted versus n_a, where each vertical line shows the range of LF for a specific value of n_a and for $0 \leq n_b \leq 9$ and $-20 \leq n_d \leq +10$. The objective is to obtain small values of LF; therefore, the bottom of the vertical lines are the values to focus on. It is possible to see that there is no relevant reduction of LF for $n_a > 5$. Very similar results are obtained for experiments E_2, E_3, E_4, E_5 and E_6. In Appendix B, Figs. B.6, B.7, B.8, B.9 and B.10. show the associated plots. These results indicate that $n_a = 5$ is the correct value to obtain a parsimonious model structure.

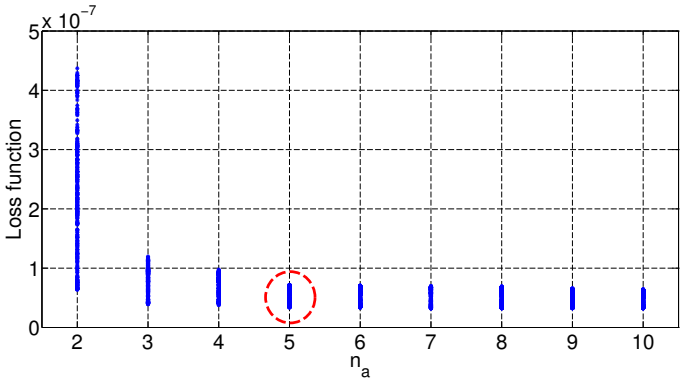

Figure 7.17: LF for experiment E_1. For $n_a > 5$ there is not any relevant reduction of the LF ($n_a = 5$ is the correct value to obtain a parsimonious model structure).

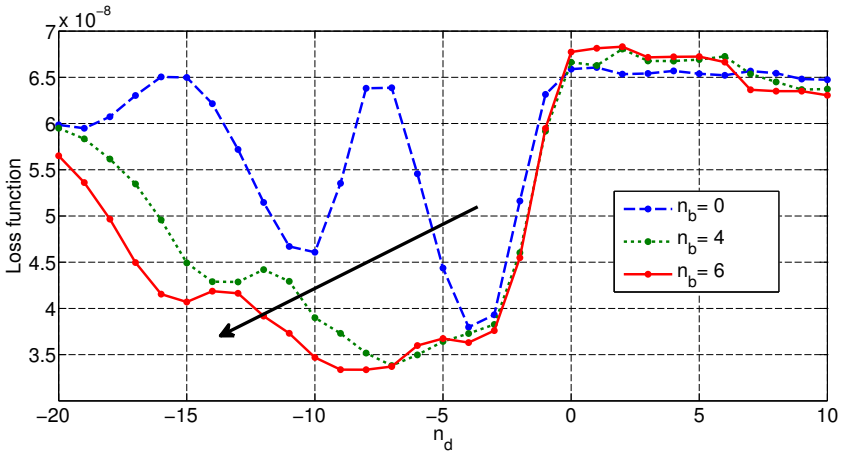

Figure 7.18: LF curves for experiment E_1 in the case of $n_a = 5$ and $n_b = 0$, 4 and 6. LF has a minimum at $n_d = -4$ (if $n_b = 0$), at $n_d = -7$ (if $n_b = 4$) and at $n_d = -8$ (if $n_b = 6$). The curves move down and left with n_b increasing from 0 to 4 to 6, as indicated by the black arrow.

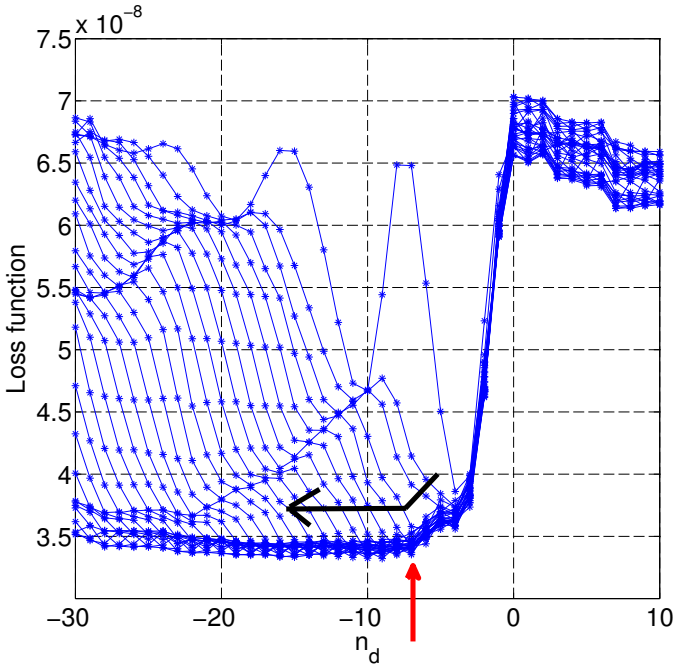

Figure 7.19: LF curves for experiment E_1. Increasing n_b the LF does not reduce anymore, this occurs when $n_d = -7$ ($n_a = 5$ has been already identified).

Once n_a is selected, the next step is the estimation of n_b and n_d. Plotting a different LF curve versus n_d, for each value of n_b, shows that the minimum of the LF occurs at different n_d, dependently on the value of n_b. Indeed, Fig. 7.18 shows the LF curves for experiment E_1 for the case of $n_a = 5$ and $n_b = 0$, 4 and 6; it is possible to see that LF has a minimum at $n_d = -4$ (if $n_b = 0$), at $n_d = -7$ (if $n_b = 4$) and at $n_d = -8$ (if $n_b = 6$). Fig. 7.18 also shows that the curves move down and left as n_b increases from 0 to 4 to 6, as indicated by the black arrow in the picture. By increasing n_b even more, the curves still move left but they stop moving down, as shown in Fig. 7.19 with $LF = LF(n_a = 5, 0 \leq n_b \leq 29, -30 \leq n_d \leq +10)$. The fact that the curves stop moving down is relevant, because it gives a clear indication that there is no advantage in introducing complexity into the model, for no gain in model fidelity (the minimum of LF stops decreasing). Plotting different LF curves versus n_d, on the same graph, for different value of n_b, is useful to obtain a first indication for the value of n_d. Indeed, Fig 7.19 shows that the minima of the curves stop decreasing for about n_d equal to -7. For experiments E_2, E_3, E_4, E_5 and E_6, the curves stop going down for $n_d = -8, -5, -8, -9$ and -11 respectively, suggesting a range of $-11 \leq n_d \leq -5$. In Appendix B, Figs. B.11, B.12, B.13, B.14 and B.15 show the associated plots. Now that a range for n_d is available, the next step is to find the associated range for n_b. Fig. 7.20 shows $LF = LF(n_a = 5, 0 \leq n_b \leq 20, -11 \leq n_d \leq -5)$ versus n_b, for the experiment E_1. Each vertical line shows the range of LF for a specific value of n_b, with $n_a = 5$ and n_d taking all the possible values between -11 and -5. In Fig. 7.20 it is possible to see that the bottom of the vertical lines of LF stops decreasing significantly for $n_b > 4$. By applying the same procedure for experiments E_2, E_3, E_4, E_5 and E_6, the LF ceases to reduce further for $n_b > 10, 7, 12, 7, 8$ respectively. In Appendix B, Figs. B.16, B.17, B.18, B.19 and B.20 show the associated plots. Therefore, the range $4 \leq n_b \leq 12$ associated with the range $-11 \leq n_d \leq -5$, is suggested. The use of an approximated model structure (ARX models) to describe the data, results in different suggested values of n_b and n_d from different experiments (however, the same $n_a = 5$ has been identified from all experiment). It is important to underline that the objective is the identification of the simplest model structure having the same n_a, n_b and n_d for all the different inputs (different FSE), able to provide multi-step predictions of the body displacement, as close as possible to the experimental data. Therefore, the multi-step predictions of the models are calculated starting from the smallest $n_b = 4$, and increasing in complexity until good average multi-step model performance

for experiments E_1, E_2, E_3, E_4, E_5 and E_6, is obtained. Good results are obtained for $n_b = 6$ (and the associated $n_d = -8$).

Table 7.2: Identified n_a, n_b, n_d and n_p for experiments E_1, E_2, E_3, E_4, E_5 and E_6

n_a	n_b	n_d	n_p
5	6	-8	2

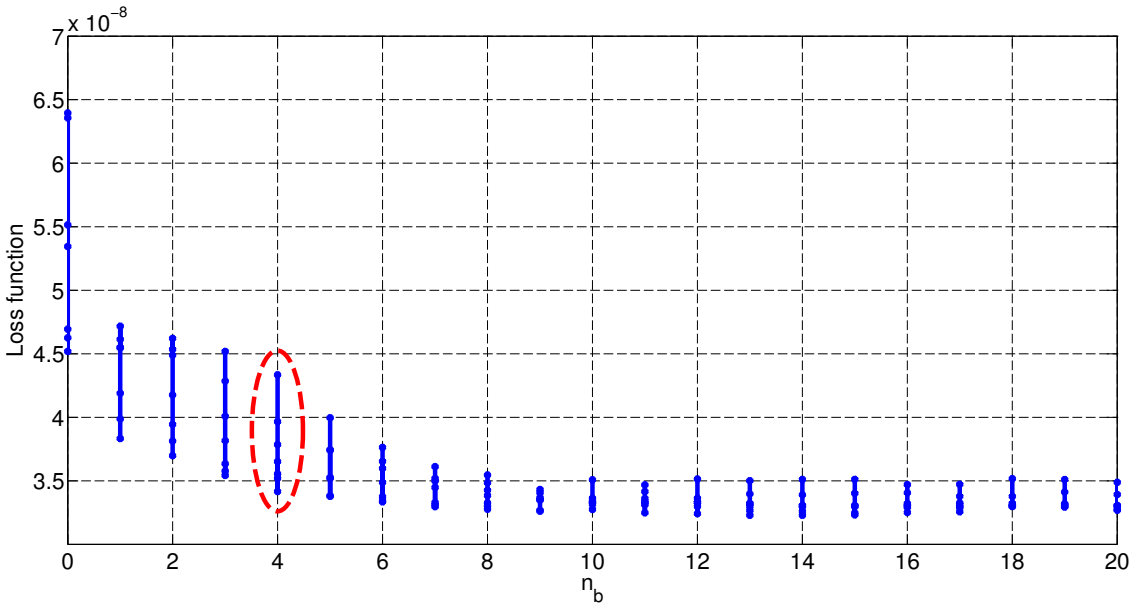

Figure 7.20: LF for experiment E_1 ($n_a = 5$, $-11 \leq n_d \leq -5$ and $0 \leq n_b \leq 20$). For this experiment, no relevant reduction of the LF for $n_b > 4$.

7.4.5 Model training and validation

In Section 7.4.4.2, the delay time and the dynamical orders of the model structures are estimated ($n_d = -8$, $n_a = 5$ and $n_b = 6$, as shown in Table 7.2) and now it is possible to proceed to the model training and validation, utilising the experimental data. The models have to describe the behaviour of the WEC in different sea states and there are different strategies to identify the model parameters.

A first possibility, referred here as single training, it is to identify a set of parameters for each available sea state (in this case six sea states) and for each model structure. Subsequently, the set of parameters, corresponding to the present sea state, is loaded into the model structure to predict the behaviour of the WEC. In this chapter, as explained in Section 7.4.3, each available experiment is a realization belonging to a different sea state (see Table 7.1). For the identification and validation of the model parameters, each experiment is divided in two parts: the first 70% time length part and the final 30% time length part. Each model is trained with a 1-step prediction on the first part and, once identified, the model is used to make a multi-step prediction on the same first 70% training part of the experiment, and a multi-step prediction on the final 30% validation part of the experiment (see Fig. 7.21).

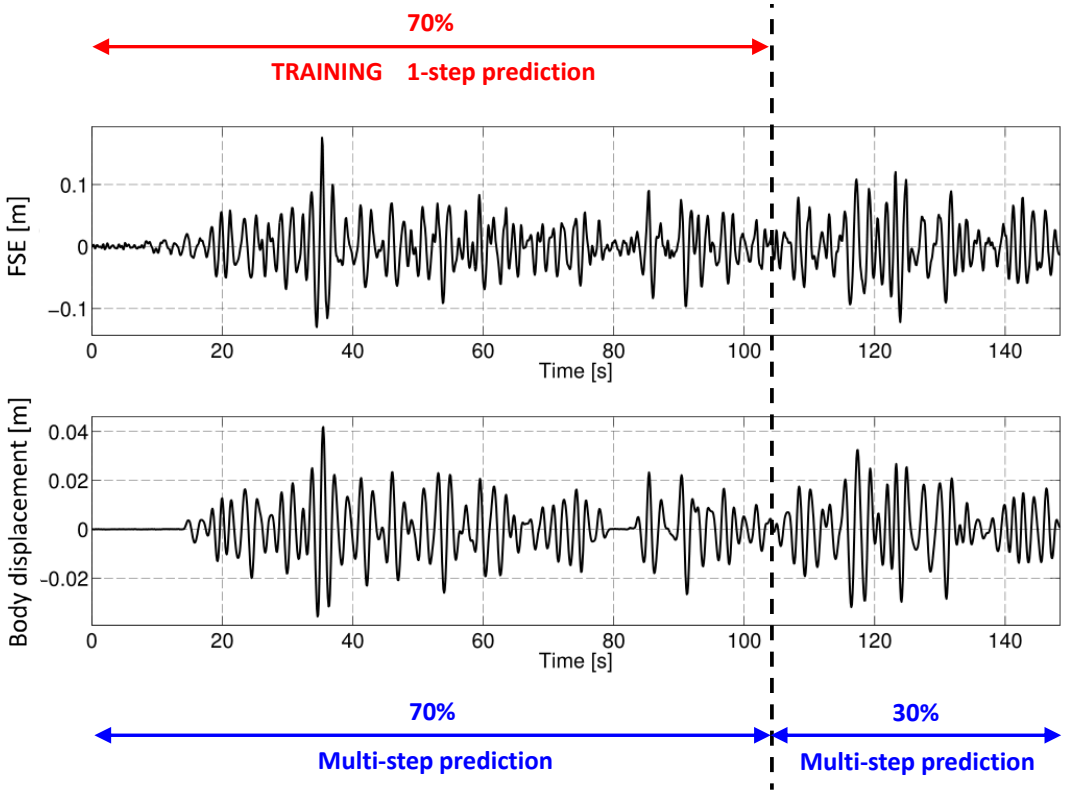

Figure 7.21: In the case of single training, each experiment is divided in two parts: the first 70% time length part and the final 30% time length part. Each model is trained with a 1-step prediction on the first part, and, once identified, it is used to make a multi-step prediction on the same first 70% training part of the experiment, and a multi-step prediction on the final 30% validation part of the experiment.

Exp part	Exp name	Tp [s]	Hs [m]	ARX fitt. error	KGP(2) fitt. error	KGP(3) fitt. error	KGP(4) fitt. error	KGP(5) fitt. error
First 70%	E_1	2	0.124	0.1484	0.1461	0.1442	0.1449	0.1402
Final 30%	E_1	2	0.124	0.1324	0.1273	0.1276	0.1358	0.1618
First 70%	E_2	2.5	0.184	0.1124	0.1119	0.1064	0.1028	0.0989
Final 30%	E_2	2.5	0.184	0.1170	0.1184	0.1190	0.1217	0.1237
First 70%	E_3	3	0.245	0.1009	0.0950	0.0923	0.0897	0.0889
Final 30%	E_3	3	0.245	0.1107	0.1097	0.1105	0.1079	0.1141
First 70%	E_4	2.5	0.369	0.1428	0.1330	0.1244	0.1223	0.1206
Final 30%	E_4	2.5	0.369	0.1377	0.1307	0.1435	0.1376	0.1621
First 70%	E_5	3	0.490	0.1433	0.1361	0.1335	0.1332	0.1314
Final 30%	E_5	3	0.490	0.1375	0.1263	0.1395	0.1404	0.1467
First 70%	E_6	4	0.720	0.1472	0.1401	0.1397	0.1354	0.1306
Final 30%	E_6	4	0.720	0.1387	0.1382	0.1407	0.1508	0.1682

Table 7.3: NRMSE models multi-step prediction performance with $n_a = 5$, $n_b = 6$ and $n_d = -8$. Each model is trained with a 1-step prediction on the first 70% part, and once identified, it is used to make a multi-step prediction on the same 70% training part of the experiment (reported in the table), and a multi-step prediction on the final 30% validation part of the experiment (reported in the table). The nonlinear KGP models are compared to the linear ARX models; in white when the nonlinear model performs better than the linear one, in red when the nonlinear model performs worse. The performance of the linear ARX models are in yellow.

Table 7.3 shows the NRMSE multi-step prediction performance for each model. Furthermore, the nonlinear KGP models are compared to the linear ARX model, in white when the nonlinear model performs better than the linear one, in red when the nonlinear model performs worse. The performance of the linear ARX models is shown in yellow. In each experiment (apart the final 30% of experiment E_2), the multi-step predictions of the KGP models, with $n_p = 2$, are better than the multi-step predictions of the ARX models, in both the initial 70% and final 30% validation parts, but the level of improvement is not significant. Furthermore, by increasing n_p to 3, the KGP multi-step predictions show a degradation in validation, compared to the KGP model with $n_p = 2$, indicating that $n_p = 3$ introduces too much complexity into the model, suggesting the presence of overfitting. Similar conclusions apply for n_p equal to 4 and 5. Therefore, the results clearly indicate that the floating body motion does not exhibit much nonlinear behaviour, as already predicted in Section 7.4.4, by observing the relative float heave displacement. Usually, the fitting error of an identified model is larger with validation data than with training data. The NRMSE multi-step prediction performance with training and validation data (see Table 7.3) are used to calculate the NVTD parameter (see Table 7.4), defined by equation (6.21). A NVTD = 0.25 is chosen as an upper threshold for a model having a good ability to generalize; therefore, Table 7.4 shows that all the identified ARX and KGP(2) models generalise quite well, indicating good quality of the utilised data and the identified parameter vector.

Experiment	ARX	KGP(2)
E_1	-0.1078	-0.1287
E_2	0.0409	0.0581
E_3	0.0971	0.1547
E_4	-0.0357	-0.0173
E_5	-0.0405	-0.0720
E_6	-0.0577	-0.0136

Table 7.4: NVTD parameter values calculated from NRMSE multi-step prediction performance, by using the data of Table 7.3.

A second possibility for the model identification, referred here as mixed training, is to obtain a unique set of parameters for each model structure, able to describe the behaviour of the WEC in any sea condition. Therefore, only one ARX model and one KGP model having $n_p = 2$ are identified. As in the case for single training, each experiment is divided in two parts: the first 70% time length part and the final 30% time length part. The first 70% of each dataset E_1, E_2, E_3, E_4, E_5 and E_6 are utilised together to train the models with a 1-step prediction criterion. Once the models are identified, they are validated with a multi-step prediction criterion on the final 30% part of each experiment (each model is validated in six different sea states). The NRMSE multi-step prediction performance for the models is shown in Table 7.5, where the nonlinear KGP models are compared to the linear ARX models; in white when the nonlinear model performs better than the linear one, in red when the nonlinear model performs worse. The performance of the linear ARX models is in yellow. The validation of the models shows that, in each experiment (apart from E_2 and E_3), the multi-step predictions of the KGP models, with $n_p = 2$, are better than the multi-step predictions of the ARX models but, once again, the level of improvement is not significant, confirming the linear nature of the data.

At this point, the following question is posed: to obtain a good prediction on a sea state, is it better to train the models only on the same sea state (to specialise the models only for the specific sea condition), or it is always better to train the models using all the information available, even if the extra information are from different sea states? In order to answer this question, the performance of the models identified with single training, shown in Table 7.3, and with mixed training, shown in Table 7.5, are compared in Table 7.6, where the boxes in white indicate that the model identified with single training performs better than the model identified with mixed training

trained, and in red when it performs worse. The results show that there is not a clear answer regarding if it is better identify the models using a single sea state or utilising simultaneously all the data from the different sea states.

Exp part	Exp name	Tp [s]	Hs [m]	ARX fitt. error	KGP(2) fitt. error
Final 30%	E_1	2	0.124	0.1482	0.1413
Final 30%	E_2	2.5	0.184	0.1160	0.1187
Final 30%	E_3	3	0.245	0.1355	0.1362
Final 30%	E_4	2.5	0.369	0.1388	0.1294
Final 30%	E_5	3	0.490	0.1364	0.1251
Final 30%	E_6	4	0.720	0.1363	0.1337

Table 7.5: Validation NRMSE models multi-step prediction performance with $n_a = 5$, $n_b = 6$ and $n_d = -8$ in the case where the models are trained with a 1-step prediction using simultaneously the first 70% part of all the experiments (mixed training). The models, once identified, are used to make a multi-step prediction on the final 30% validation part of each experiment (reported in the table). The nonlinear KGP model with $n_p = 2$ is compared to the linear ARX model; in white when the nonlinear model performs better than the linear one, in red when the nonlinear model performs worse. The performances of the linear ARX models are in yellow.

				Single training		Mixed training	
Exp part	Exp name	Tp [s]	Hs [m]	ARX fitt. error	KGP(2) fitt. error	ARX fitt. error	KGP(2) fitt. error
Final 30%	E_1	2	0.124	0.1324	0.1273	0.1482	0.1413
Final 30%	E_2	2.5	0.184	0.1170	0.1184	0.1160	0.1187
Final 30%	E_3	3	0.245	0.1107	0.1097	0.1355	0.1362
Final 30%	E_4	2.5	0.369	0.1377	0.1307	0.1388	0.1294
Final 30%	E_5	3	0.490	0.1375	0.1263	0.1364	0.1251
Final 30%	E_6	4	0.720	0.1387	0.1382	0.1363	0.1337

Table 7.6: Comparison of validation NRMSE models multi-step prediction performances in the cases of single and mixed training for $n_a = 5$, $n_b = 6$ and $n_d = -8$. Each model, once identified, is used to make a multi-step prediction on the final 30% validation part of each experiment (reported in the table). The boxes in white indicate that the model identified using single training performs better than the model identified using mixed training and in red when it performs worse.

The space of sea states (for example described in terms of H_s and T_p) can be discretized. The level of discretization is a compromise between the total number of sea states and the accuracy of each sea state description. A larger number of sea states requires more experiments and, consequently, a larger number of model parameters sets to interpolate between. Therefore, the number of utilised sea states should be limited, and the models should be able to describe any sea condition, by interpolating/extrapolating the information provided from the known sea states. In the case of the Wavestar WEC, six different experiments are available from six different sea states. The models are trained with a 1-step prediction, by simultaneously using 100% of five experiments and, once identified, they are used to make a multi-step prediction on 100% of the sixth missing experiment. In this way, the ability of the identified models to interpolate/extrapolate the information, provided from the known sea states to predict an unknown sea condition, is tested. In total, the procedure has been repeated six times, each time by changing the sixth missing experiment. In Table 7.7, the NRMSE multi-step prediction model performance, on validation data, is shown.

In a similar way, Tables 7.8, 7.9, 7.10, 7.11 and 7.12 show the NRMSE multi-step prediction model performance, on the validation experiments E_2, E_3, E_4, E_5 and E_6, respectively. Tables 7.7, 7.8, 7.9, 7.10, 7.11 and 7.12 show that the NRMSE multi-step prediction model performance are larger (but still comparable) than the NRMSE multi-step prediction model performance in Table 7.5, where the models are trained using the first 70% of all six experiments. The results indicate a good ability of the models to interpolate/extrapolate the information provided from the known sea states to predict an unknown sea condition. Also, in this case, in each experiment (apart from experiment E_2), the multi-step predictions of the KGP models with $n_p = 2$ are better than the multi-step predictions of the ARX models.

Exp name	Tp [s]	Hs [m]	ARX fitt. error	KGP(2) fitt. error
E_1	2	0.124	0.1674	0.1607

Table 7.7: Validation NRMSE models multi-step prediction performances, in case the models are trained with a 1-step prediction using simultaneously 100% of experiments E_2, E_3, E_4, E_5 and E_6. The models, once identified, are used to make a validation multi-step prediction on 100% of the experiment E_1 (reported in the table). The nonlinear KGP model with $n_p = 2$ is compared to the linear ARX model; in white when the nonlinear model performs better than the linear one, in red when the nonlinear model performs worse. The performance of the linear ARX model is in yellow.

Exp name	Tp [s]	Hs [m]	ARX fitt. error	KGP(2) fitt. error
E_2	2.5	0.184	0.1172	0.1186

Table 7.8: Validation NRMSE models multi-step prediction performances, in case the models are trained with a 1-step prediction using simultaneously 100% of experiments E_1, E_3, E_4, E_5 and E_6. The models, once identified, are used to make a validation multi-step prediction on 100% of the experiment E_2 (reported in the table). The KGP model with $n_p = 2$ is compared to the ARX model; in white when the nonlinear model performs better than the linear one, in red when the nonlinear model performs worse. The performance of the ARX model is in yellow.

Exp name	Tp [s]	Hs [m]	ARX fitt. error	KGP(2) fitt. error
E_3	3	0.245	0.1528	0.1526

Table 7.9: Validation NRMSE models multi-step prediction performances, in case the models are trained with a 1-step prediction using simultaneously 100% of experiments E_1, E_2, E_4, E_5 and E_6. The models, once identified, are used to make a validation multi-step prediction on 100% of the experiment E_3 (reported in the table). The KGP model with $n_p = 2$ is compared to the ARX model; in white when the nonlinear model performs better than the linear one, in red when the nonlinear model performs worse. The performance of the ARX model is in yellow.

Exp name	Tp [s]	Hs [m]	ARX fitt. error	KGP(2) fitt. error
E_4	2.5	0.369	0.1463	0.1366

Table 7.10: Validation NRMSE models multi-step prediction performances, in case the models are trained with a 1-step prediction using simultaneously 100% of experiments E_1, E_2, E_3, E_5 and E_6. The models, once identified, are used to make a validation multi-step prediction on 100% of the experiment E_4 (reported in the table). The KGP model with $n_p = 2$ is compared to the ARX model; in white when the nonlinear model performs better than the linear one, in red when the nonlinear model performs worse. The performance of the ARX model is in yellow.

Exp name	Tp [s]	Hs [m]	ARX fitt. error	KGP(2) fitt. error
E_5	3	0.490	0.1418	0.1374

Table 7.11: Validation NRMSE models multi-step prediction performances, in case the models are trained with a 1-step prediction using simultaneously 100% of experiments E_1, E_2, E_3, E_4 and E_6. The models, once identified, are used to make a validation multi-step prediction on 100% of the experiment E_5 (reported in the table). The KGP model with $n_p = 2$ is compared to the ARX model; in white when the nonlinear model performs better than the linear one, in red when the nonlinear model performs worse. The performance of the ARX model is in yellow.

Exp name	Tp [s]	Hs [m]	ARX fitt. error	KGP(2) fitt. error
E_6	4	0.720	0.1411	0.1340

Table 7.12: Validation NRMSE models multi-step prediction performances, in case the models are trained with a 1-step prediction using simultaneously 100% of experiments E_1, E_2, E_3, E_4 and E_5. The models, once identified, are used to make a validation multi-step prediction on 100% of the experiment E_6 (reported in the table). The KGP model with $n_p = 2$ is compared to the ARX model; in white when the nonlinear model performs better than the linear one, in red when the nonlinear model performs worse. The performance of the ARX model is in yellow.

7.5 Summary and discussion

In this chapter, the framework for model identification, developed in Chapters 3 and 4, and utilised in Chapters 5 and 6 with NWT data, is applied on real experimental data, obtained by studying a scaled Wavestar WEC, at the RWT of Plymouth University. Six different experiments are utilised, each one characterised by an irregular FSE belonging to a different sea state. For each experiment, the measurements of the FSE and of the body displacement are provided. For the identification of the models, having FSE and body displacement as input and output respectively, two different model structures are utilised: the ARX and KGP models. Both models are linear in the parameters, leading to the advantage of a linear optimization for their identification. Furthermore, the ARX model provides a reference input-output linear model for the input-output nonlinear KGP model. The common dynamical orders n_a, n_b and delay time n_d, which the ARX and KGP models share

($n_a = 5$, $n_b = 6$ and $n_d = -8$), are identified by utilising the same framework used in Chapters 3 and 6 with NWT data.

For the identification of the models, two different strategies are applied: single training and mixed training. With single training, for each model structure, a different parameter vector is identified for each available sea state; with mixed training, for each model structure, a unique parameter vector is identified, able to describe the behaviour of the WEC in any sea condition. In both strategies, in nearly all experiments, the validation of the models show that the multi-step predictions of the KGP models (with $n_p = 2$) are better than the multi-step predictions of the ARX models, but the level of improvement is not significant, showing that the hydrodynamic nonlinear effects, acting on the Wavestar WEC in the utilised experiments, are not significant, due to the reduced relative body displacement. The results also show that there is not a clear answer regarding the advantage of identifying the models by using a single sea state or utilising, simultaneously, all the experiments from the different sea states. An interesting potential future work is the study of the application of a PTO excitation force on the same Wavestar device, providing the possibility of creating a more significant relative body displacement and introducing, in this way, more nonlinear hydrodynamic effects into the system.

Chapter 8

Conclusions

Contemporary society is characterised by an increase of energy demand, in order to supply all the different humans activities. Wave energy represents an important resource of renewable energy, which can provide a significant support to the development of more sustainable energy solutions. The energy transported by the waves can be partially extracted by the PTO system, connected to the WEC. The amount of extracted energy can be increased by optimizing the WEC shape and the WEC-PTO control strategy, which both require mathematical hydrodynamic models, able to correctly describe the WEC-fluid interaction. The hydrodynamic laws are the foundations for a complete description of the WEC-fluid interaction, but their solution represents a very complex and challenging problem. Different approaches to hydrodynamic WEC-fluid interaction modelling, such as CFD and LPT (as reviewed in Chapter 2), lead to different mathematical models, each one characterised by different accuracy and computational speed. The main objective of this thesis is to obtain models which are between the CFD and LPT extremes, a good compromise able to describe the most important nonlinearities of the physical system, without requiring excessively computational time. A pragmatic framework is proposed in this thesis for hydrodynamic model construction, based on system identification, where models are determined from recorded experimental data. One of the major improvements proposed by this thesis is the use of CFD-NWT or RWT data, instead of traditional LPT-BEM data, for hydrodynamic model identification, since NWT and RWT data can contain the full range of nonlinear hydrodynamic effects (where the experiment is correctly designed).

In Chapter 3, CT hydrodynamic model structures are proposed, outlining the fact that they provide a good insight into system understanding since, usually, CT models are derived from physical laws and the model parameters are strongly related to the physical system properties. Chapter 5 shows that one of the main drawbacks of the use of CT model structures is the requirement of nonconvex optimization strategies, which are necessary in order to identify the model parameter vector, since the loss function, associated with the CT model structure, is characterised by the presence of multiple local minima and, therefore, a strong sensitivity to the initial optimization seed. Therefore, in this thesis, the use of DT model structures is proposed, which have the disadvantage of losing the physical meaning of the parameters but, on the other hand, DT model structures provide greater flexibility in the construction of nonlinear input/output model structures, which are linear in the parameters, with the consequent employment of convex optimization strategies.

This thesis proposes, in Chapter 4, the use of two typologies of WT experiments, the preliminary and identification experiments. The preliminary experiments (which are characterised by a fast computation time, in case of a CFD-NWT) are utilised to obtain a rough measurement of the resonant frequency and the bandwidth of the WEC, informing the successive identification experiments where the input power spectrum should be allocated. On the other hand, the identification experiments are utilised to produce data to identify the parameters of a WEC model or model sub-blocks. The hydrodynamic model identification framework, proposed in Chapters 3 and 4, is utilised for six different case studies, where the utilised CFD-NWT data are provided by Josh

Davidson from Maynooth University and the RWT data are provided by Morten Jakobsen from Aalborg University.

Chapters 5 and 6 show that the relevance of nonlinear hydrodynamic forces acting on a WEC, such as viscous drag, nonlinear restoring and Froude-Krylov forces, changes depending on the wave and oscillation amplitudes; indeed, large body amplitudes increase the nonlinear dissipative effects. The ideal WEC modelling solution is a nonlinear parametric model, characterised by a good compromise between accuracy and computation time, able to describe the whole operating amplitude-frequency region. Theoretically, if the model structure described exactly the physics of the WEC-fluid interaction, and if an infinity of experimental data were available, the SI framework would provide an accurate model, adapted for any operating region. Unfortunately, any real case is far from this ideal situation; indeed, the model structure is only a reasonable approximation of the process, and the amount of experimental data are limited, which leads to an accurate identified model only for a specific operating region. Chapter 5 shows the identification of a set of different models, where each identified model is representative in the operating amplitude region it is identified from, and then loses fidelity as it tries to predict the WEC dynamics away from this region. Therefore, the WEC behaviour could be described by switching between different representative models, at different operating conditions. The identification of such a model set requires the availability of a group of different experimental data, able to cover the whole WEC operational range of interest. Linear models, identified from LPT-BEM data, describe accurately only very small operating conditions, whereas linear models, identified from CFD-NWT data (i.e. ARX and state-space models), show in Chapters 5 and 6 average behaviour more representative of the actual nonlinear process (in the operating amplitude region the model is identified from), compared to linear models identified from LPT-BEM data. In Chapter 5, the results show that, as the average WEC displacement amplitude approaches zero in the NWT experimental data, the models identified converge to to those obtained by using LPT-BEM data (i.e. dominant complex conjugate poles, radiation resistance and added mass curves). Furthermore, in Chapter 5, new a-priori constraints on the parameters are utilised in the identification, in order to guarantee the stability and passivity of the models.

Chapters 6 shows that, when wave and body displacement amplitudes increase, the identified linear ARX models lose accuracy and, in general, nonlinear structures, identified from WT data too, are more accurate on the training data. This suggests that the data contain nonlinearities, which the nonlinear models are able to capture; in particular, linear models are not able to replicate asymmetric restoring force and asymmetric body displacement, in response to a symmetrical sinusoidal input, whereas nonlinear models approximate the asymmetric output well.

The fitting of model predictions with the training data can be improved by increasing the model complexity, but an unnecessarily large model complexity can reduce the ability of the model in generalising on new data (i.e. overfitting problem), making the model worthless. Therefore, it is very important to verify the performance of the identified model on fresh validation data. In Chapter 6, the results illustrate that the ANN models, which are always the best in training, have inconsistent performance in validation, showing the difficulty for ANN model identification, which depends on a larger number of parameters to be identified and on the use of nonlinear optimization algorithms, characterised by a sensitivity to the initial seed, caused by a loss function with multiple local minima. On the other hand, the KGP model structures, which are identified with convex optimization methods, have good accuracy and consistency on the validation data, as shown by the results in Chapter 6.

The results in Section 6.2 show that the degree of nonlinearity in the WEC-fluid interaction is strongly dependent on the body shape, which is responsible for the generation of viscous and vortex shedding effects and a nonlinear hydrostatic force. In particular, for the considered case study, the linear ARX model structure finds the triangular geometry the most difficult to simulate (and therefore suggesting that the triangular geometry generates the larger degree of nonlinear effects), followed by the rectangular and the circular geometry.

In Chapter 7, the framework for model identification, already applied to NWT data, is success-

fully broadened to the context of data generated in a RWT, where hydrodynamic tests were carried out on a scaled Wavestar WEC point-absorber. Single training and mixed training strategies are compared, in order to obtain accurate models able to generalize on fresh validation data. The performance of identified linear and nonlinear models shown to be very similar due to the very limited presence of nonlinear hydrodynamic effects in the utilised data. The results also show that there is not a clear answer regarding the advantage of identifying the models by using a single sea state or utilising, simultaneously, all the experiments from the different sea states.

The comparison between data generated by a WT (in the case of small wave and body displacements) and a LPT-BEM software package, such as WAMIT, can be useful in order to verify the presence of nonlinearity in the WT experiments. In the case of a 2D NWT, the comparison with 3D BEM data is not straightforward; indeed, in a 2D NWT, the body geometry is an infinitely long horizontal bar, having a constant vertical cross-sectional area. In Chapter 4, a methodology to compare 2D NWT data with 3D BEM data is proposed, based on the transformation of the original 3D body geometry into a new 3D horizontal bar, having an appropriate length L. In particular, the introduced per unit length quantities $m_a^{(ul)}(\omega)$, $N^{(ul)}(\omega)$, $F_e^{(ul)}(\omega)$, $H_{f_{in}\to y}^{(ul)}(\omega)$ and $H_{\eta\to y}^{(ul)}(\omega)$, calculated with WAMIT, are shown to converge to a limit curve obtained by 2D NWT data (see in particular Fig. 4.37, in the case of a 2D circular body), confirming the correctness of the proposed method. It is shown that an unbounded increment of L (which leads to an increment of the WAMIT computation time), in order to better approximate an horizontal infinitely long body, is not justified by a corresponding improvement in accuracy (i.e. for the considered horizontal cylinder, the appropriate body length is shown to be $L = 25$ m).

The identification of an accurate model requires the use of informative data, which are strongly dependent on the excitation signal utilised to influence the process during the experiment. Nonlinear dynamic systems are significantly more complex than linear ones; consequently, the choice of an excitation signal becomes even more crucial. The analysis carried out in Section 6.3.2, regarding which signal type performs better in identifying accurate models, shows that, in the case of heaving floating bodies, RARP signals (characterised by a very flat amplitude distribution) and chirp signals (characterised by a flat amplitude distribution, apart two peaks near the extremes of the amplitude range) are good candidates. Furthermore, Chapters 6 and 7 show that the data generated from input force experiments (where the PTO applies an external force on a WEC) contains, in general, a greater degree of nonlinearity compared to the data generated from input wave experiments. Indeed, the direct application of a PTO force, on the WEC, significantly enlarges the variation in the wetted body surface area during the experiment, enhancing the nonlinear Froude-Krylov hydrodynamic effects.

8.1 Future work

The SI framework presented in this thesis highlights several possible directions for further research, that can be addressed in order to advance the construction of models for WEC motion simulation, control and power production assessment.

• The case studies shown in this thesis, for simplicity and clarity, describe WEC dynamics in the case of a single DoF. It would be interesting to analyse single and multi-body WECs with multi DoF (or even WEC arrays), by developing new specific WT experiments and multi DoF hydrodynamic parametric models.

• The SI framework, presented in this thesis, is utilised for the construction of WEC hydrodynamic models; a possible area of research is the application of the presented work for the identification of models to also describe PTO and mooring systems, which are fundamental parts of the WEC design.

• In this thesis, the models are identified to describe the dynamics of heaving floating structures; a possible future work is the use of the developed SI framework, in order to model wave surge converters, overtopping devices and OWCs.

• The study in Chapter 7, carried out with the COAST Laboratory RWT data, does not provide a

clear answer as to whether it is better to train the models with single or mixed training. Possible future work is the analysis of new cases in order to better understand this aspect.

• In Chapters 6 and 7, the data, utilised for the identification of models belonging to the $\eta \rightarrow y$ model family, do not contain a high degree of nonlinearity; therefore, it would be interesting to use the SI framework, in the case of new data (containing a larger degree of nonlinearity), obtained from new body geometries and sea state conditions.

• This thesis develops a general SI framework and proposes a variety of parametric grey and black-box model structures, which show interesting solutions for the WEC-fluid interaction modelling problem. At the same time, the development of linear and nonlinear parametric hydrodynamic structures is not certainly considered complete with this thesis, and it is still an active and fascinating research topic for future work.

Appendix A

Laplace transform

A.1 Definition

Given a function $y(t)$, defined for all real numbers $t \geq 0$, its Laplace transform, $Y : A \subset \mathbb{C} \rightarrow \mathbb{C}$, where A is the region of convergence (ROC), is defined by [319] [320] [321] [322]:

$$Y(S) = \mathscr{L}\Big[y(t)\Big] = \int_0^{\infty} y(t)e^{-st}dt \tag{A.1}$$

where $s = \sigma + i\omega$ is a complex number, termed frequency variable (σ and ω are real numbers and i is the imaginary unit). The ROC of the Laplace transform is a right sided half plane, defined as $A = \{s \in \mathbb{C} \text{ with } Re[s] > \sigma_0 \in \Re\}$, where σ_0 is a real part of the rightmost pole of $Y(s)$.

The inverse Laplace transform recovers the original function $y(t)$ for $t \geq 0$, and gives zero for $t < 0$:

$$y(t) = \mathscr{L}^{-1}\Big[Y(s)\Big] = \frac{1}{2\pi i}\int_{\sigma-\infty}^{\sigma+\infty} y(t)e^{st}dS = \begin{cases} y(t) & t \geq 0 \\ 0 & t < 0 \end{cases} \tag{A.2}$$

where $\sigma > \sigma_0$. Therefore, in equation (A.2), the contour of integration is a straight line parallel to the imaginary axis contained in the ROC. As an example, given the complex function $Y(s) = 1/(s-p)$, with the pole $p = \sigma + i\omega$, the inverse Laplace transform is given by:

$$\mathscr{L}^{-1}\Big[\frac{1}{s-p}\Big] = e^{pt} = e^{\sigma t}\Big[\cos(\omega t) + i\sin(\omega t)\Big] \tag{A.3}$$

A.2 Properties

A.2.1 Linearity

Given the functions $y_1(t)$ and $y_2(t)$ and the constants c_1 and c_2, it is possible to write:

$$\mathscr{L}\Big[c_1y_1(t) + c_2y_2(t)\Big] = c_1\mathscr{L}\Big[y_1(t)\Big] + c_2\mathscr{L}\Big[y_2(t)\Big] \tag{A.4}$$

A.2.2 Laplace transform of derivatives

Given a function $y(t)$ with derivatives $y^{(i)}(t)$ for $i \geq 1$, it is possible to write [322] [323]:

$$\begin{aligned} \mathscr{L}\Big[y^{(i)}(t)\Big] &= s^iY(s) - s^{i-1}y(0) - s^{i-2}y^{(1)}(0) - s^{i-3}y^{(2)}(0) - ... - y^{(i-1)}(0) \\ &= s^iY(s) - \sum_{j=1}^{i} s^{i-j}y^{(j-1)}(0) \end{aligned} \tag{A.5}$$

In the case of $i = 0$, equation (A.5) has to be replaced with:

$$\mathscr{L}[y^{(0)}(t)] = \mathscr{L}\Big[y(t)\Big] = Y(s) \tag{A.6}$$

A.2.3 Laplace transform of a convolution function

Given two functions $x(t)$ and $y(t)$, null for $t < 0$ and with Laplace transform $X(s)$ and $Y(s)$, respectively, it follows that [320]:

$$\mathscr{L}\Big[\int_{-\infty}^{\infty} x(\tau)y(t-\tau)d\tau\Big] = X(s)Y(s) \tag{A.7}$$

A.2.4 Initial-value theorem

Given the functions $y(t)$ with Laplace transform $Y(s)$, it is possible to write [319] [320]:

$$\lim_{t\to 0^+} y(t) = \lim_{s\to\infty} sY(s) \tag{A.8}$$

A.3 Roots of a complex polynomial

•*Fundamental theorem of algebra*. Every complex polynomial $P : \mathbb{C} \to \mathbb{C}$, of order n, has exactly n roots [324] [325].
• In general, a complex polynomial can have real or complex roots. If the polynomial coefficients are real, the complex roots must occur in complex conjugate pairs $a \pm ib$ [292].

A.4 Partial fraction expansion

A rational function, given by

$$Y(s) = \frac{N(s)}{D(s)} = \frac{\sum_{j=0}^{m} b_j s^j}{\sum_{j=0}^{n} a_j s^j} \tag{A.9}$$

where $n > m$. In the case of $D(s)$ has no repeated roots, equation (A.9) can be written as:

$$Y(s) = \sum_{j=1}^{n} \frac{k_j}{s-p_j} \tag{A.10}$$

where:

$$k_j = \Big[Y(s)(s-p_j)\Big]_{s=p_j} \tag{A.11}$$

is termed residue of the p_j pole. It is important to underline that, if $p_j = p_q^*$, then $k_j = k_q^*$ (conjugate poles have conjugate residues).

A.5 Complex conjugate pairs of poles

Given the complex function:

$$Y(s) = \frac{k_1}{(s-p_1)} + \frac{k_1^*}{(s-p_1^*)} \tag{A.12}$$

where $p_1 = (\sigma_1 + i\omega_1)$, by utilising equations (A.3), (A.4) and (A.12), it follows that:

$$\begin{aligned} y(t) &= \mathscr{L}^{-1}\Big[Y(s)\Big] = k_1\mathscr{L}^{-1}\Big[\frac{1}{(s-p_1)}\Big] + k_1^*\mathscr{L}^{-1}\Big[\frac{1}{(s-p_1^*)}\Big] \\ &= k_1 e^{p_1 t} + k_1^* e^{p_1^* t} = 2Re\Big[k_1 e^{p_1 t}\Big] \\ &= 2|k_1|e^{\sigma_1 t}\cos\Big[\omega_1 t + Arg(k_1)\Big] \end{aligned} \tag{A.13}$$

A.6 Zero-input and zero-state components of the output of a linear model

Given a system described by the linear differential equation:

$$\sum_{k=0}^{n} a_k y^{(k)}(t) = \sum_{k=0}^{m} b_k u^{(k)}(t) \tag{A.14}$$

where $u(t)$ and $y(t)$ are input and output, respectively. By applying the Laplace transform (and its linearity) in (A.14), it follows that:

$$\sum_{k=0}^{n} a_k \mathscr{L}\Big[y^{(k)}(t)\Big] = \sum_{k=0}^{m} b_k \mathscr{L}\Big[u^{(k)}(t)\Big] \tag{A.15}$$

By applying (A.5) and (A.6) in (A.15), it follows that:

$$a_0 Y(s) + \sum_{k=1}^{n} a_k \Big(s^k Y(s) - \sum_{j=1}^{k} s^{k-j} y^{(j-1)}(0)\Big) = b_0 U(s) + \sum_{k=1}^{m} b_k \Big(s^k U(s) - \sum_{j=1}^{k} s^{k-j} u^{(j-1)}(0)\Big) \tag{A.16}$$

$$a_0 Y(s) + \sum_{k=1}^{n} a_k s^k Y(s) - \sum_{k=1}^{n}\sum_{j=1}^{k} a_k s^{k-j} y^{(j-1)}(0) = b_0 U(s) + \sum_{k=1}^{m} b_k s^k U(s) - \sum_{k=1}^{m}\sum_{j=1}^{k} b_k s^{k-j} u^{(j-1)}(0) \tag{A.17}$$

$$Y(s)\Big(\sum_{k=0}^{n} a_k s^k\Big) - \sum_{k=1}^{n}\sum_{j=1}^{k} a_k s^{k-j} y^{(j-1)}(0) = U(s)\Big(\sum_{k=0}^{m} b_k s^k\Big) - \sum_{k=1}^{m}\sum_{j=1}^{k} b_k s^{k-j} u^{(j-1)}(0) \tag{A.18}$$

$$Y(s) = \frac{\sum_{k=0}^{m} b_k s^k}{\sum_{k=0}^{n} a_k s^k} U(s) + \frac{\left[\sum_{k=1}^{n}\sum_{j=1}^{k} a_k s^{k-j} y^{(j-1)}(0) - \sum_{k=1}^{m}\sum_{j=1}^{k} b_k s^{k-j} u^{(j-1)}(0)\right]}{\sum_{k=0}^{n} a_k s^k} \tag{A.19}$$

Define:

$$P(s) = \sum_{k=1}^{n}\sum_{j=1}^{k} a_k s^{k-j} y^{(j-1)}(0) - \sum_{k=1}^{m}\sum_{j=1}^{k} b_k s^{k-j} u^{(j-1)}(0) \tag{A.20}$$

which is a polynomial in s of order $(n-1)$,

$$Y_{zi}(s) = \frac{P(s)}{\sum_{k=0}^{n} a_k s^k} \tag{A.21}$$

and

$$H(s) = \frac{\sum_{k=0}^{m} b_k s^k}{\sum_{k=0}^{n} a_k s^k} \tag{A.22}$$

$H(s)$ is termed the transfer function. Note that $Y_{zi}(s)$ and $H(s)$ have the same denominator (therefore same poles) but different numerator (therefore different zeros). By introducing equations (A.21) and (A.22) in (A.19), it follows that:

$$Y(s) = H(s)U(s) + Y_{zi}(s) \tag{A.23}$$

The inverse Laplace transform, of equation (A.23), is given by:

$$y(t) = y_{zs}(t) + y_{zi}(t) \tag{A.24}$$

where

$$y(t) = \mathscr{L}^{-1}\Big[Y(s)\Big] \tag{A.25}$$

$$y_{zs}(t) = \mathscr{L}^{-1}\Big[H(s)U(s)\Big] = \int_{-\infty}^{\infty} h(\tau)u(t-\tau)d\tau \tag{A.26}$$

$$y_{zi}(t) = \mathscr{L}^{-1}\Big[Y_{zi}(s)\Big] \tag{A.27}$$

$y_{zs}(t)$ and $y_{zi}(t)$ are termed the zero-state component and the zero-input component, respectively.

a_n	a_{n-2}	a_{n-4}	...
a_{n-1}	a_{n-3}	a_{n-5}	...
c_1	c_2	c_3	...
d_1	d_2	d_3	...
e_1	e_2	e_3	...
...	...	...	...

Table A.1: Routh-Hurwitz stability criterion table.

A.7 Routh-Hurwitz stability criterion

Given a complex polynomial, expressed as:

$$P(s) = \sum_{j=0}^{n} a_j s^j \tag{A.28}$$

with $s \in \mathbb{C}$ and $a_i \in \Re$, the Routh-Hurwitz stability criterion determines the number of roots of (A.28), which are located in the right half-plane [143] [326]. The criterion is based on the construction of Table A.1, which has $n+1$ rows, where the first two rows contain the polynomial coefficients. The subsequent c_k row is formed as follows:

$$c_1 = \frac{-\det\begin{vmatrix} a_n & a_{n-2} \\ a_{n-1} & a_{n-3} \end{vmatrix}}{a_{n-1}} = \frac{a_{n-1}a_{n-2} - a_n a_{n-3}}{a_{n-1}}, \tag{A.29}$$

$$c_2 = \frac{-\det\begin{vmatrix} a_n & a_{n-4} \\ a_{n-1} & a_{n-5} \end{vmatrix}}{a_{n-1}} = \frac{a_{n-1}a_{n-4} - a_n a_{n-5}}{a_{n-1}} \tag{A.30}$$

and in general

$$c_k = \frac{-\det\begin{vmatrix} a_n & a_{n-2k} \\ a_{n-1} & a_{n-2k-1} \end{vmatrix}}{a_{n-1}} = \frac{a_{n-1}a_{n-2k} - a_n a_{n-2k-1}}{a_{n-1}}, \tag{A.31}$$

where the integer index k assumes values from 1 to the integer part of $(n+1)/2$. The subsequent d_k row is formed as follows:

$$d_1 = \frac{-\det\begin{vmatrix} a_{n-1} & a_{n-3} \\ c_1 & c_2 \end{vmatrix}}{c_1} = \frac{c_1 a_{n-3} - a_{n-1}c_2}{c_1}, \tag{A.32}$$

$$d_2 = \frac{-\det\begin{vmatrix} a_{n-1} & a_{n-5} \\ c_1 & b_3 \end{vmatrix}}{c_1} = \frac{c_1 a_{n-5} - a_{n-1}c_3}{c_1} \tag{A.33}$$

and in general

$$d_k = \frac{-\det\begin{vmatrix} a_{n-1} & a_{n-2k-1} \\ c_1 & c_{k+1} \end{vmatrix}}{c_1} = \frac{c_1 a_{n-2k-1} - a_{n-1}c_{k+1}}{c_1}. \tag{A.34}$$

The procedure is the same for the subsequent rows (if present). The polynomial, expressed by equation (A.28), has a number of roots, located on the right half-plane, given by number of algebraic sign changes in the elements of the first left column of Table (A.1) [143].

Appendix B

Hydrodynamic model identification from RWT experiments

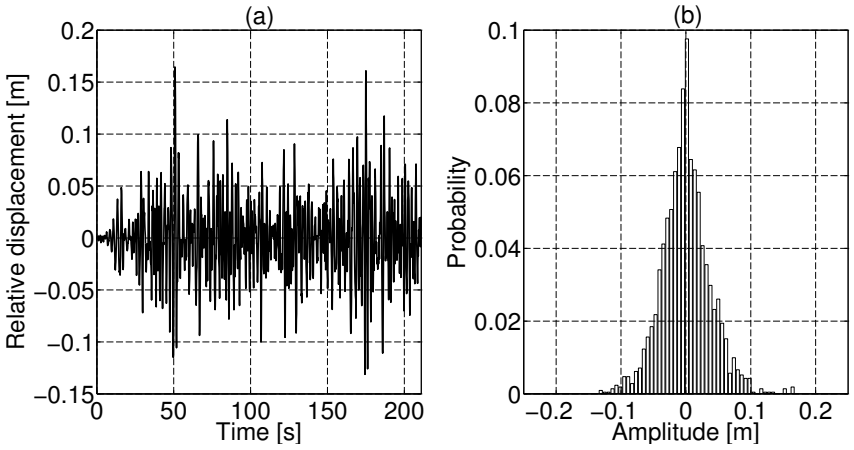

Figure B.1: Relative float heave displacement for experiment E_2. (a) Time evolution (b) Probability distribution.

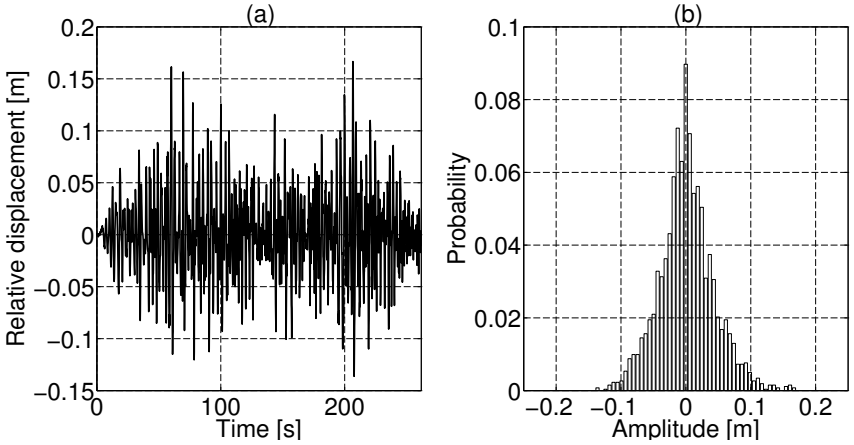

Figure B.2: Relative float heave displacement for experiment E_3. (a) Time evolution (b) Probability distribution.

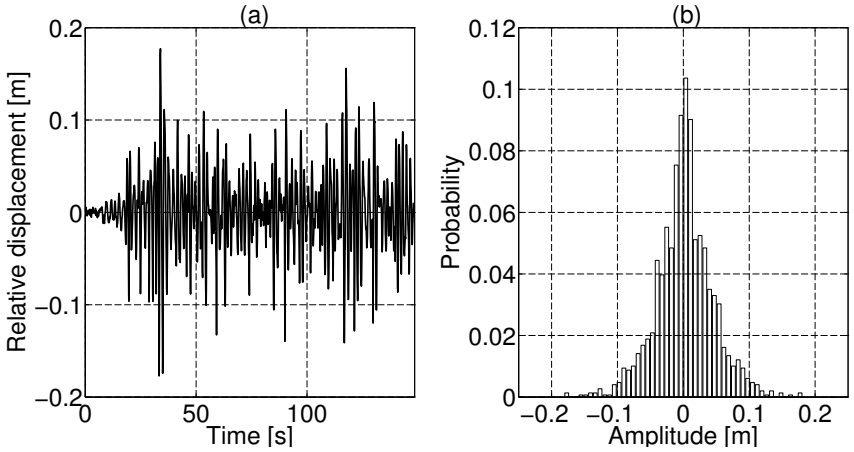

Figure B.3: Relative float heave displacement for experiment E_4. (a) Time evolution (b) Probability distribution.

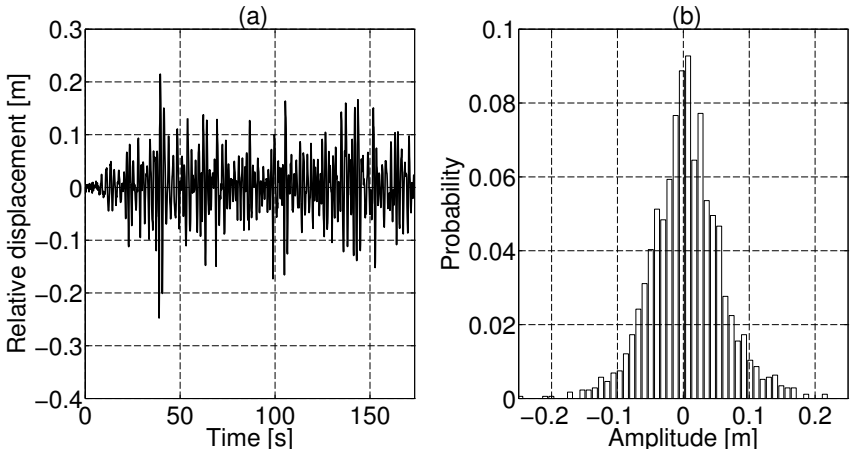

Figure B.4: Relative float heave displacement for experiment E_5. (a) Time evolution (b) Probability distribution.

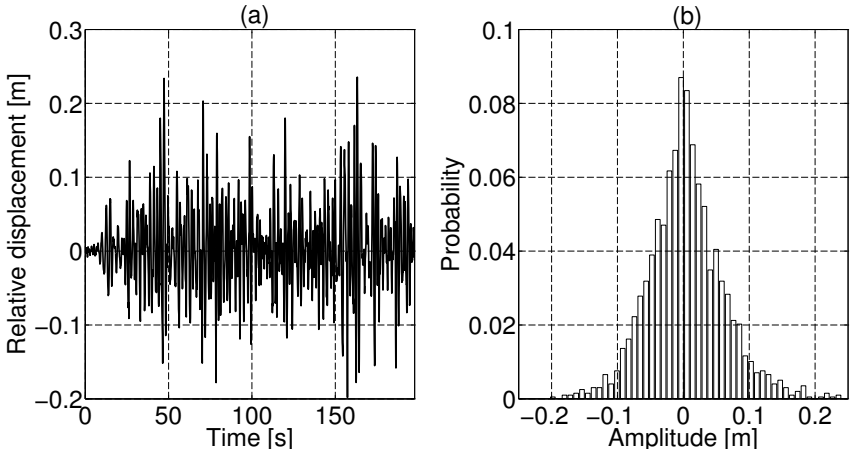

Figure B.5: Relative float heave displacement for experiment E_6. (a) Time evolution (b) Probability distribution.

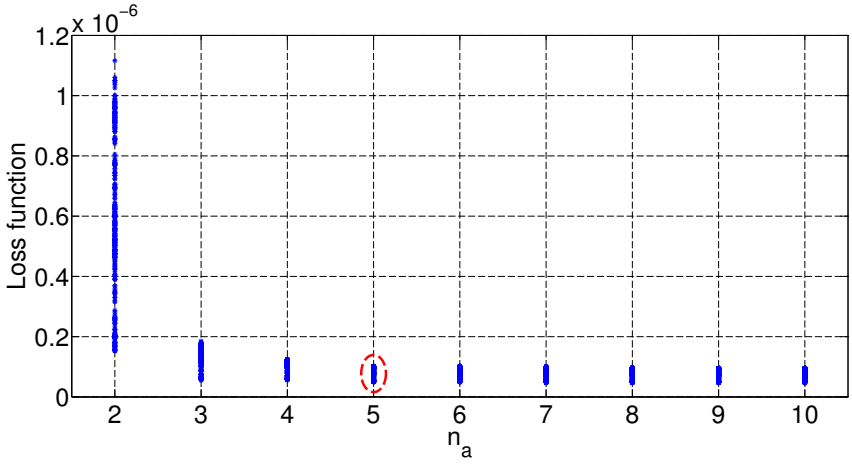

Figure B.6: LF for experiment E_2. For $n_a > 5$ there is no relevant reduction of the LF ($n_a = 5$ is the correct value to obtain a parsimonious model structure).

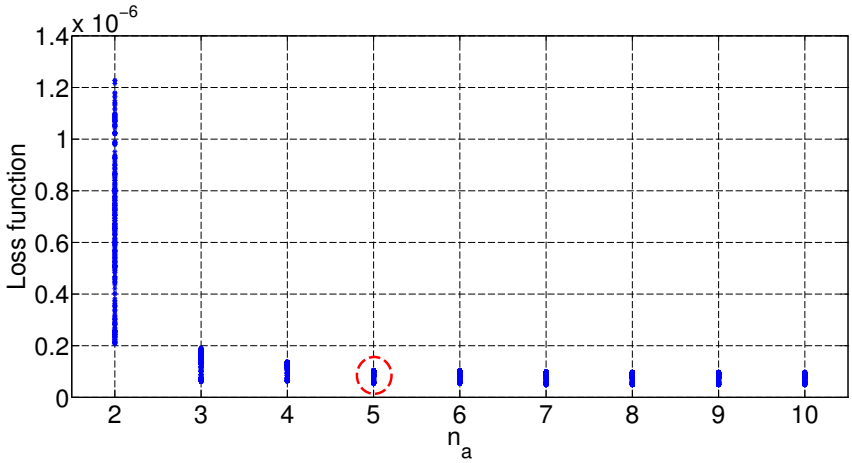

Figure B.7: LF for experiment E_3. For $n_a > 5$ there is no relevant reduction of the LF ($n_a = 5$ is the correct value to obtain a parsimonious model structure).

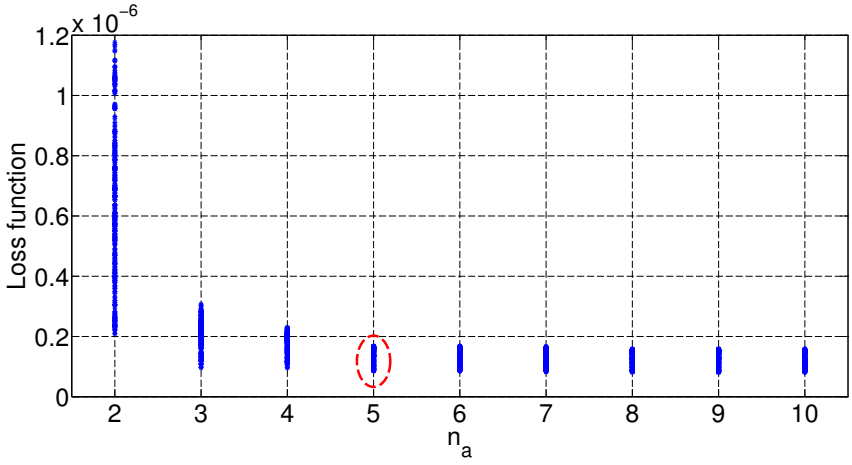

Figure B.8: LF for experiment E_4. For $n_a > 5$ there is no relevant reduction of the LF ($n_a = 5$ is the correct value to obtain a parsimonious model structure).

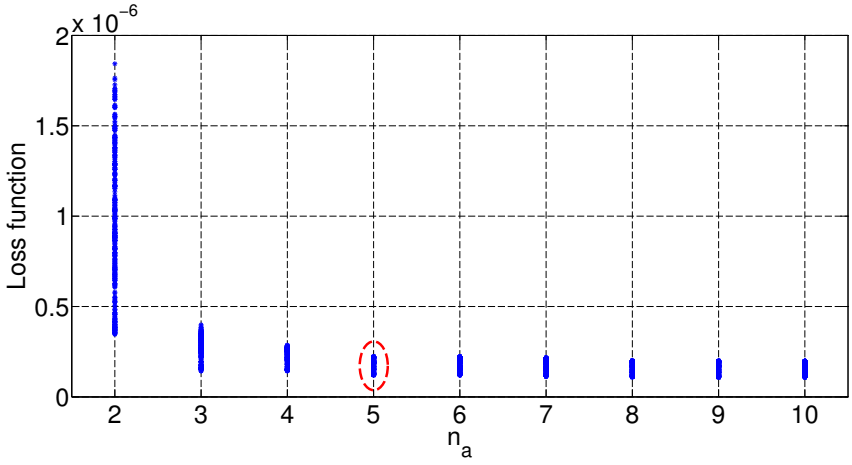

Figure B.9: LF for experiment E_5. For $n_a > 5$ there is no relevant reduction of the LF ($n_a = 5$ is the correct value to obtain a parsimonious model structure).

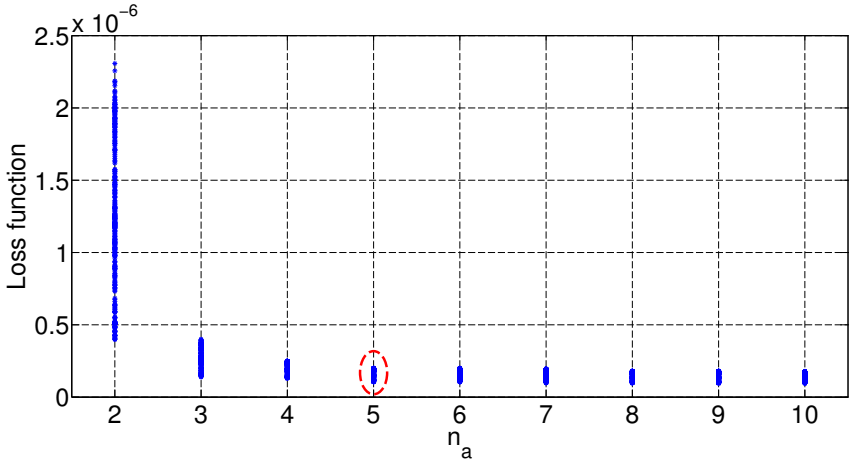

Figure B.10: LF for experiment E_6. For $n_a > 5$ there is no relevant reduction of the LF ($n_a = 5$ is the correct value to obtain a parsimonious model structure).

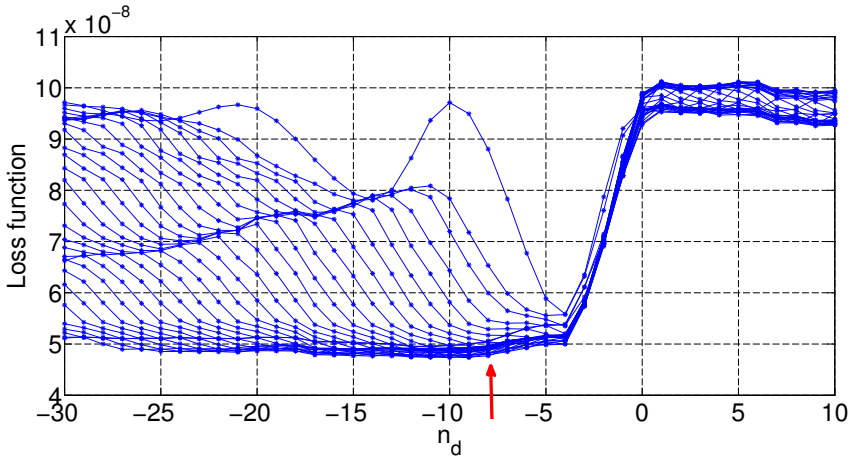

Figure B.11: LF curves for experiment E_2. Increasing n_b the LF does not reduce anymore, this happens when $n_d = -8$ ($n_a = 5$ has been already identified).

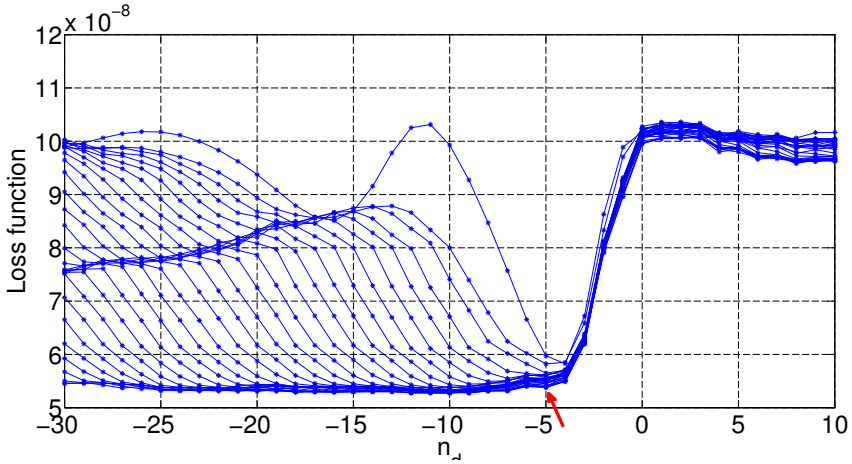

Figure B.12: LF curves for experiment E_3. Increasing n_b the LF does not reduce anymore, this happens when $n_d = -5$ ($n_a = 5$ has been already identified).

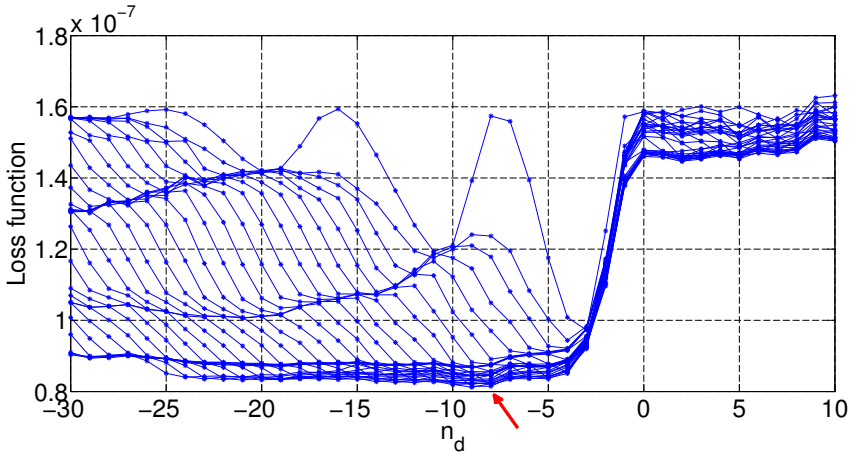

Figure B.13: LF curves for experiment E_4. Increasing n_b the LF does not reduce anymore, this happens when $n_d = -8$ ($n_a = 5$ has been already identified).

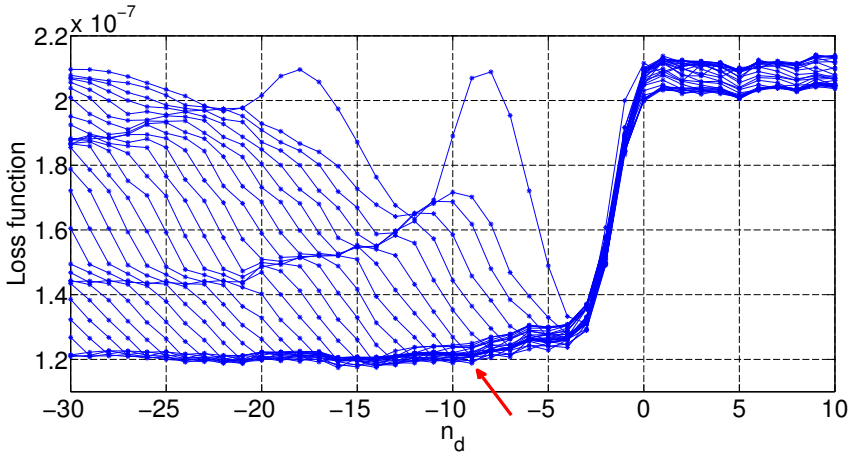

Figure B.14: LF curves for experiment E_5. Increasing n_b the LF does not reduce anymore, this happens when $n_d = -9$ ($n_a = 5$ has been already identified).

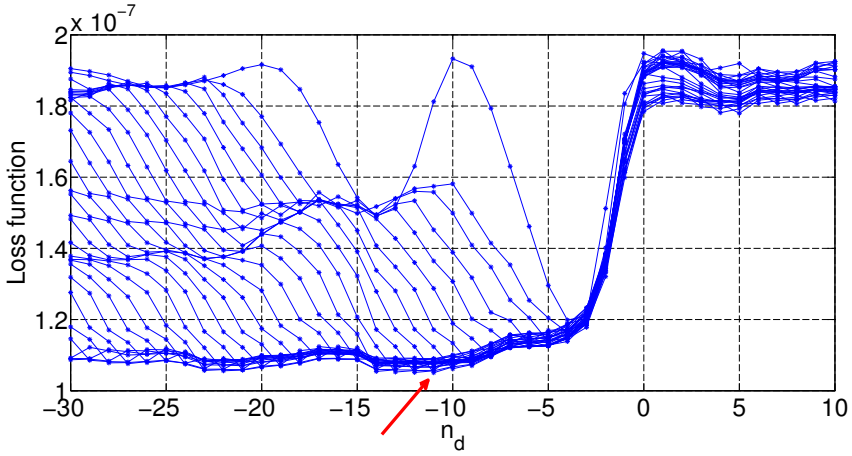

Figure B.15: LF curves for experiment E_6. Increasing n_b the LF does not reduce anymore, this happens when $n_d = -11$ ($n_a = 5$ has been already identified).

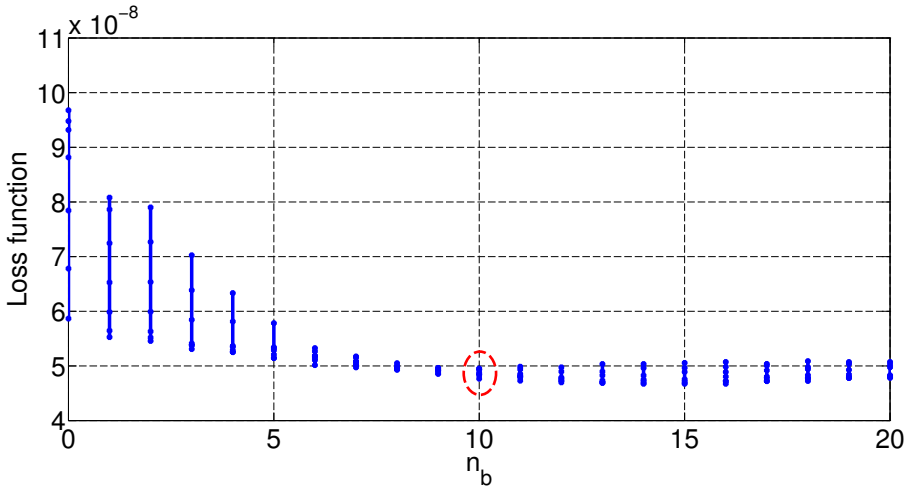

Figure B.16: LF for experiment E_2 ($n_a = 5$, $-11 \leq n_d \leq -5$ and $0 \leq n_b \leq 20$). For this experiment, no relevant reduction of the LF for $n_b > 10$.

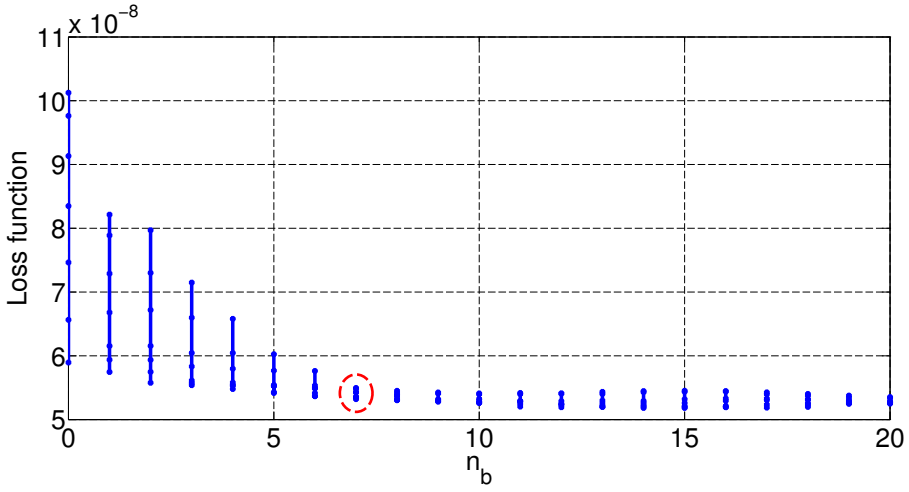

Figure B.17: LF for experiment E_3 ($n_a = 5$, $-11 \leq n_d \leq -5$ and $0 \leq n_b \leq 20$). For this experiment, no relevant reduction of the LF for $n_b > 7$.

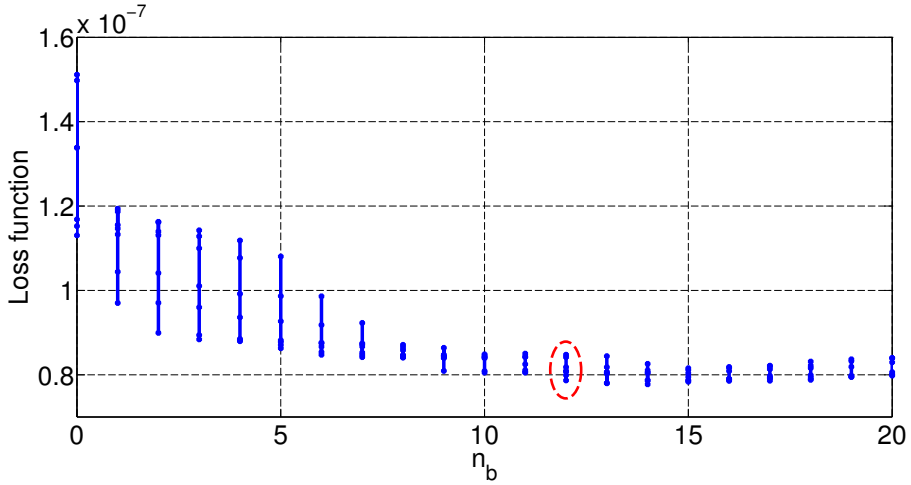

Figure B.18: LF for experiment E_4 ($n_a = 5$, $-11 \leq n_d \leq -5$ and $0 \leq n_b \leq 20$). For this experiment, no relevant reduction of the LF for $n_b > 12$.

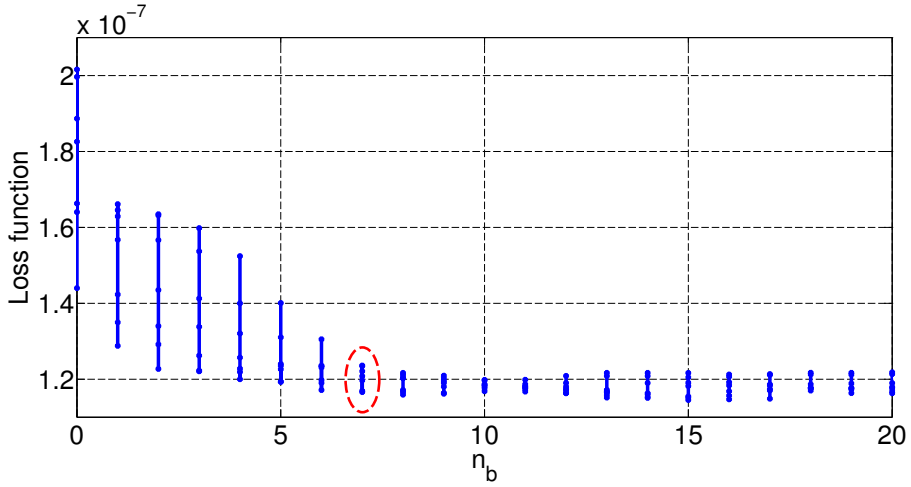

Figure B.19: LF for experiment E_5 ($n_a = 5$, $-11 \leq n_d \leq -5$ and $0 \leq n_b \leq 20$). For this experiment, no relevant reduction of the LF for $n_b > 7$.

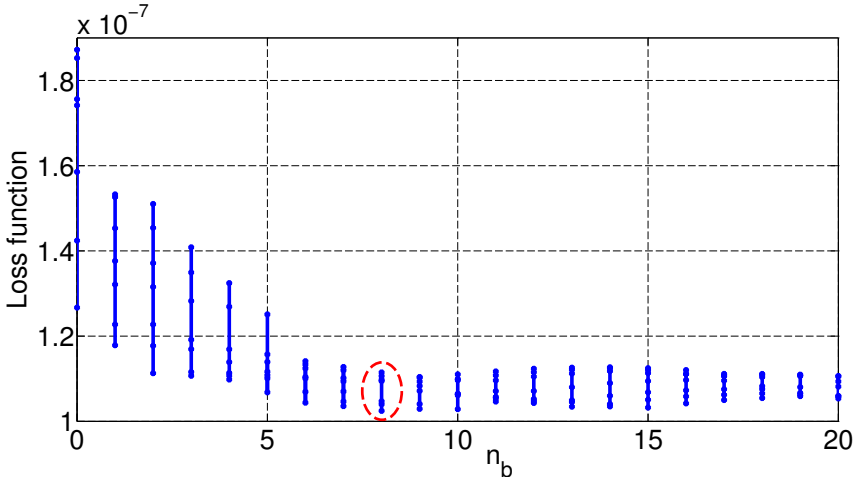

Figure B.20: LF for experiment E_6 ($n_a = 5$, $-11 \leq n_d \leq -5$ and $0 \leq n_b \leq 20$). For this experiment, no relevant reduction of the LF for $n_b > 8$.

Bibliography

[1] A. Pecher and J. Kofoed, *Handbook of Ocean Wave Energy*. Ocean Engineering & Oceanography, Springer International Publishing, 2016.

[2] M. R. Pachauri, R. K.and Allen, V. R. Barros, and J. Broome, "Climate change 2014, synthesis report," tech. rep., IPCC, 2014.

[3] "Energy roadmap 2050, impact assessment and scenario analysis," tech. rep., European Commission, 2011.

[4] I. López, J. Andreu, S. Ceballos, I. M. de Alegría, and I. Kortabarria, "Review of wave energy technologies and the necessary power-equipment," *Renewable and Sustainable Energy Reviews*, vol. 27, pp. 413–434, 2013.

[5] R. Pelc and R. M. Fujita, "Renewable energy from the ocean," *Marine Policy*, vol. 26, no. 6, pp. 471–479, 2002.

[6] J. Cruz, *Ocean Wave Energy: Current Status and Future Prespectives*. Green Energy and Technology, Springer Berlin Heidelberg, 2007.

[7] J. Davidson, S. Giorgi, and J. V. Ringwood, "Identification of wave energy device models from numerical wave tank data - Part 1: Numerical wave tank identification tests," *IEEE Transactions on Sustainable Energy*, vol. 7, no. 3, pp. 1012–1019, 2016.

[8] S. Giorgi, J. Davidson, and J. V. Ringwood, "Identification of wave energy device models from numerical wave tank data - Part 2: Data-based model determination," *IEEE Transactions on Sustainable Energy*, vol. 7, no. 3, pp. 1020–1027, 2016.

[9] M. Folley, ed., *Numerical Modelling of Wave Energy Converters: State-of-the-Art Techniques for Single Devices and Arrays*. Elsevier Science & Technology Books, London, UK, 2016.

[10] J. V. Ringwood, J. Davidson, and S. Giorgi, "Optimising numerical wave tank tests for the parametric identification of wave energy device models," in *Proceedings of the 34th International Conference on Ocean, Offshore and Arctic Engineering*, pp. 1–10, American Society of Mechanical Engineers, 2015.

[11] J. Davidson, S. Giorgi, and J. V. Ringwood, "Linear parametric hydrodynamic models for ocean wave energy converters identified from numerical wave tank experiments," *Ocean Engineering*, vol. 103, pp. 31–39, 2015.

[12] S. Giorgi, J. Davidson, and J. V. Ringwood, "Identification of nonlinear excitation force kernels using numerical wave tank experiments," in *Proceedings of the 9th European Wave and Tidal Energy Conference*, 2015.

[13] J. Davidson, S. Giorgi, and J. V. Ringwood, "Numerical wave tank identification of nonlinear discrete time hydrodynamic models," in *Proceedings of the 1st International Conference on Renewable Energies Offshore*, 2014.

[14] J. Davidson, S. Giorgi, and J. Ringwood, "Linear parametric hydrodynamic models based on numerical wave tank experiments," in *Proceedings of the 10th European Wave and Tidal Energy Conference*, 2013.

[15] H. Hahn, *Rigid Body Dynamics of Mechanisms: 1 Theoretical Basis*. Engineering online library, Springer, Berlin Heidelberg, 2002.

[16] A. Shabana, *Dynamics of Multibody Systems*. Cambridge University Press, 2005.

[17] O. Bauchau, *Flexible Multibody Dynamics*. Solid Mechanics and Its Applications, Springer, Netherlands, 2010.

[18] T. Fossen, *Handbook of Marine Craft Hydrodynamics and Motion Control*. Wiley, West Sussex, UK, 2011.

[19] J. Ferziger and M. Peric, *Computational Methods for Fluid Dynamics*. Springer, Berlin Heidelberg, 2012.

[20] I. Currie, *Fundamental Mechanics of Fluids (4th Edition)*. Civil and mechanical engineering, Marcel Dakker Inc., New York, US, 2003.

[21] I. A. Svendsen, *Introduction To Nearshore Hydrodynamics*. Advanced series on ocean engineering, World Scientific, Hackensack, NJ, US, 2006.

[22] J. Newman, *Marine Hydrodynamics*. Wei Cheng Cultural Enteroprise Company, London, UK, 1977.

[23] Wendt, *Computational Fluid Dynamics, An Introduction*. Springer, Berlin Heidelberg, Germany, 2009.

[24] P. K. Kundu and I. M. Cohen, *Fluid Mechanics (4th Edition)*. Academic Press, Burlington, US, 2008.

[25] J. F. Sini, *Mecanique des fluides, Thermofluides 2 THERF*. Departement Mecanique des fluideset Energetique, Ecole Centrale de Nantes, 2012.

[26] J. Journe and W. Massie, *Offshore Hydromechanics*. Delft University of Technology, Nederlands, 2001.

[27] G. D. Backer, *Hydrodynamic Design Optimization of WECs Consisting of Heaving Point Absorbers*. PhD thesis, Ghent University, 2009.

[28] H. A. Wolgamot and C. J. Fitzgerald, "Nonlinear hydrodynamic and real fluid effects on wave energy converters," *in Proceedings of the Institution of Mechanical Engineers, Part A: Journal of Power and Energy*, pp. 1–23, 2015.

[29] R. Genest and J. V. Ringwood, "A critical comparison of model-predictive and pseudospectral control for wave energy devices," *Journal of Ocean Engineering and Marine Energy*, pp. 1–15, 2016.

[30] E. J. Ransley, *Survivability of Wave Energy Converter and Mooring Coupled System using CFD*. PhD thesis, University of Plymouth, 2015.

[31] S. Yip, *Handbook of Materials Modeling*. Handbook of Materials Modeling, Springer Netherlands, 2007.

[32] D. Causon and C. Mingham, *Introductory finite difference methods for PDEs*. Bookboon, 2010.

[33] D. Causon, C. Mingham, and L. Qian, *Introductory finite volume methods for pdes*. Bookboon, 2011.

[34] M. J. Turner, "Stiffness and deflection analysis of complex structures," *Journal of the Aeronautical Sciences*, vol. 23, no. 9, pp. 805–853, 2012.

[35] E. Madenci and I. Guven, *The finite element method and applications in engineering using ANSYS®*. Springer, New York, US, 2015.

[36] J. Donea and A. Huerta, *Finite Element Methods for Flow Problems*. Finite Element Methods for Flow Problems, John Wiley & Sons, West Sussex, UK, 2003.

[37] C. W. Hirt and B. D. Nichols, "Volume of fluid (VOF) method for the dynamics of free boundaries," *Journal of computational physics*, vol. 39, no. 1, pp. 201–225, 1981.

[38] N. O. Moraga, L. A. Lemus, M. A. Saavedra, and R. A. Lemus-Mondaca, "VOF/FVM prediction and experimental validation for shear-thinning fluid column collapse," *Computers & Mathematics with Applications*, vol. 69, no. 2, pp. 89–100, 2015.

[39] J. F. McKibben and C. K. Aidun, "A volume-of-fluid computational technique for free surface flow problems," *Institute of Paper Science and Technology*, 1993.

[40] *Fluent Theory Guide (Version 15.0)*, ansys, inc. ed., 2015.

[41] A. E. Maguire, *Hydrodynamics, control and numerical modelling of absorbing wavemakers*. PhD thesis, University of Edinburgh, 2011.

[42] G. Lloyd and A. Espanoles, "Best practice guidelines for marine applications of computational fluid dynamics," *WS Atkins Consultants and Members of the NSC, MARNET-CFD Thernatic Network: London, UK*, p. 84, 2002.

[43] A. Iturrioz, R. Guanche, J. Lara, C. Vidal, and I. Losada, "Validation of openfoam® for oscillating water column three-dimensional modeling," *Ocean Engineering*, vol. 107, pp. 222–236, 2015.

[44] I. Simonetti, L. Cappietti, H. El Safti, and H. Oumeraci, "Numerical modelling of fixed oscillating water column wave energy conversion devices: Toward geometry hydraulic optimization," in *Proceedings of the 34th International Conference on Ocean, Offshore and Arctic Engineering*, pp. V009T09A031–V009T09A031, American Society of Mechanical Engineers, 2015.

[45] E. Mendoza, X. Chávez, J. C. Alcérreca-Huerta, and R. Silva, "Hydrodynamic behavior of a new wave energy convertor: The blow-jet," *Ocean Engineering*, vol. 106, pp. 252–260, 2015.

[46] L. Chen, *Modelling of Marine Renewable Energy*. PhD thesis, University of Bath, 2015.

[47] Y. Wei, A. Rafiee, A. Henry, and F. Dias, "Wave interaction with an oscillating wave surge converter, part I: Viscous effects," *Ocean Engineering*, vol. 104, pp. 185–203, 2015.

[48] P. Schmitt and B. Elsaesser, "On the use of openfoam to model oscillating wave surge converters," *Ocean Engineering*, vol. 108, pp. 98–104, 2015.

[49] V. Mishra, S. Beatty, B. Buckham, P. Oshkai, and C. Crawford, "Application of an arbitrary mesh interface for CFD simulation of an oscillating wave energy converter," in *Proceedings of the 11th European Wave and Tidal Energy Conference*, 2015.

[50] *OpenFOAM User Guide (Version 4.0)*, OpenFOAM Foundation ed., 2016.

[51] J. Davidson, M. Cathelain, L. Guillemet, T. Le Huec, and J. Ringwood, "Implementation of an openfoam numerical wave tank for wave energy experiments," in *Proceedings of the 11th European Wave and Tidal Energy Conference*, 2015.

[52] N. G. Jacobsen, D. R. Fuhrman, and J. Fredsøe, "A wave generation toolbox for the open-source CFD library: OpenFOAM," *International Journal for Numerical Methods in Fluids*, vol. 70, no. 9, pp. 1073–1088, 2012.

[53] J. Palm, C. Eskilsson, G. Moura Paredes, and L. Bergdahl, "CFD simulation of a moored floating wave energy converter," in *Proceedings of the 10th European Wave and Tidal Energy Conference*, 2013.

[54] G. C. J. Morgan, J. Zang, D. Greaves, A. Heath, C. Whitlow, and J. Young, "Using the rasinterfoam CFD model for wave transformation and coastal modelling," *Coastal Engineering Proceedings*, vol. 1, no. 32, p. 23, 2011.

[55] B. Chenari, S. Saadatia, and A. D. Ferreira, "Numerical modelling of regular waves propagation and breaking using waves2foam," *Journal of Clean Energy Technologies*, vol. 3, no. 4, pp. 276–281, 2015.

[56] Y. Li and M. Lin, "Wave-body interactions for a surface-piercing body in water of finite depth," *Journal of Hydrodynamics, Ser. B*, vol. 22, no. 6, pp. 745–752, 2010.

[57] Y. Li and M. Lin, "Regular and irregular wave impacts on floating body," *Ocean Engineering*, vol. 42, pp. 93–101, 2012.

[58] L. Chen, J. Zang, A. Hillis, G. Morgan, and A. Plummer, "Numerical investigation of wave–structure interaction using openfoam," *Ocean Engineering*, vol. 88, pp. 91–109, 2014.

[59] A. Iturrioz, R. Guanche, J. A. Armesto, C. Vidal, and I. J. Losada, "Experimental and numerical development of a floating multi-chamber OWC device," in *Proceedings of the 10th European Wave and Tidal Energy Conference*, 2013.

[60] J. A. Souza, E. D. d. Santos, and L. A. Isoldi, "Numerical simulation of an OWC devise," 2013.

[61] P. Schmitt, S. Bourdier, T. Whittaker, D. Sarkar, E. Renzi, F. Dias, K. Doherty, and J. van't Hoff, "Hydrodynamic loading on a bottom hinged oscillating wave surge converter," in *Proceedings of the 22nd International Offshore and Polar Engineering Conference*, International Society of Offshore and Polar Engineers, 2012.

[62] A. Henry, P. Schmitt, T. Whittaker, A. Rafiee, and F. Dias, "The characteristics of wave impacts on an oscillating wave surge converter," in *Proceedings of the 23rd International Offshore and Polar Engineering Conference*, International Society of Offshore and Polar Engineers, 2013.

[63] H. Akimoto, Y. Kim, and K. Tanaka, "Performance prediction of the rotational wave energy converter using single-bucket drag type turbine," in *Proceedings of the 33rd International Conference on Ocean, Offshore and Arctic Engineering*, pp. 1–8, American Society of Mechanical Engineers, 2014.

[64] J. Thaker and J. Banerjee, "Numerical simulation of periodic motion of two phases in a two-dimensional channel: application to wave energy converter," in *Proceedings of the 39th National Conference on Fluid Mechanics and Fluid Power*, 2012.

[65] A. King, "Numerical modelling of the bomborawave energy conversion device," in *Proceedings of the19th Australasian Fluid Mechanics Conference*, 2014.

[66] C. Eskilsson, J. Palm, J. P. Kofoed, and E. Friis-Madsen, "CFD study of the overtopping discharge of the wave dragon wave energy converter," in *Proceedings of the 1st International Conference on Renewable Energies Offshore*, pp. 287–294, 2015.

[67] G. Giorgi and J. V. Ringwood, "Implementation of latching control in a numerical wave tank with regular waves," *Journal of Ocean Engineering and Marine Energy*, vol. 2, no. 2, pp. 211–226, 2016.

[68] P. Schmitt, K. Doherty, D. Clabby, and T. Whittaker, "The opportunities and limitations of using CFD in the development of wave energy converters," in *Proceedings of the Marine and Offshore Energy Conference*, 2012.

[69] Falnes, *Ocean Waves and Oscillating Systems, Linear Interactions Including Wave-Energy Extraction*. Cambridge University Press, 2002.

[70] M. Folley, A. Babarit, B. Child, D. Forehand, L. OBoyle, K. Silverthorne, J. Spinneken, V. Stratigaki, and P. Troch, "A review of numerical modelling of wave energy converter arrays," in *Proceedings of the 31st International Conference on Ocean, Offshore and Arctic Engineering*, pp. 535–545, American Society of Mechanical Engineers, 2012.

[71] Q. Ma, *Advances in Numerical Simulation of Nonlinear Water Waves*. Advances in coastal and ocean engineering, World Scientific, 2010.

[72] C. Linton and P. McIver, *Handbook of Mathematical Techniques for Wave/Structure Interactions*. CRC Press, 2001.

[73] Faltinsen, *Sea Loads on Ships and Offshore Structures*. Cambridge University Press, 1990.

[74] Z. Yu and J. Falnes, "State-space modelling of a vertical cylinder in heave," *Applied Ocean Research*, vol. 17, no. 5, pp. 265–275, 1995.

[75] A. S. Zurkinden, F. Ferri, S. Beatty, J. P. Kofoed, and M. Kramer, "Non-linear numerical modeling and experimental testing of a point absorber wave energy converter," *Ocean Engineering*, vol. 78, pp. 11–21, 2014.

[76] M. Guérinel, M. Alves, and A. Sarmento, "Nonlinear modelling of the dynamics of a free floating body," in *Proceedings of the 9th European Wave and Tidal Energy Conference*, 2011.

[77] J.-C. Gilloteaux, G. Bacelli, and J. Ringwood, "A non-linear potential model to predict large-amplitudes-motions: application to a multi-body wave energy converter.," in *Proceedings of the World Renewable Energy Congress*, 2008.

[78] A. Babarit, H. Mouslim, A. Clément, and P. Laporte-Weywada, "On the numerical modelling of the non linear behaviour of a wave energy converter," in *Proceedings of the 28th International Conference on Ocean, Offshore and Arctic Engineering*, pp. 1045–1053, American Society of Mechanical Engineers, 2009.

[79] A. Merigaud, J.-C. Gilloteaux, and J. V. Ringwood, "A nonlinear extension for linear boundary element methods in wave energy device modelling," in *Proceedings of the 31st International Conference on Ocean, Offshore and Arctic Engineering*, pp. 615–621, American Society of Mechanical Engineers, 2012.

[80] B. King and R. Beck, "Time-domain analysis of wave exciting forces.," in *Proceedings of the International Workshop on Water Waves and Floating Bodies*, pp. 65–68, 1987.

[81] F. Korsmeyer, "The time domain diffraction problem," in *Proceedings of the 6th International Workshop on Water Waves and Floating Bodies*, 1991.

[82] J. Falnes, "On non-causal impulse response functions related to propagating water waves," *Applied Ocean Research*, vol. 17, no. 6, pp. 379–389, 1995.

[83] F. Fusco and J. V. Ringwood, "A study of the prediction requirements in real-time control of wave energy converters," *IEEE Transactions on Sustainable Energy*, vol. 3, no. 1, pp. 176–184, 2012.

[84] J. Tedd, P. Frigaard, *et al.*, "Short term wave forecasting, using digital filters, for improved control of wave energy converters," in *Proceedings of the 17th International Offshore and Polar Engineering Conference*, International Society of Offshore and Polar Engineers, 2007.

[85] T. Pérez and T. I. Fossen, "Practical aspects of frequency domain identification of dynamic models of marine structures from hydrodynamic data," *Ocean Engineering*, vol. 38, no. 2, pp. 426–435, 2011.

[86] T. Pérez and T. I. Fossen, "Time-vs. frequency-domain identification of parametric radiation force models for marine structures at zero speed," *Modeling, Identification and Control*, vol. 29, no. 1, pp. 1–19, 2008.

[87] B. Brogliato, *Dissipative Systems Analysis and Control: Theory and Applications*. Communications and Control Engineering, Springer, London, UK, 2007.

[88] R. Taghipour, T. Perez, and T. Moan, "Hybrid frequency–time domain models for dynamic response analysis of marine structures," *Ocean Engineering*, vol. 35, no. 7, pp. 685–705, 2008.

[89] A. H.-D. Cheng and D. T. Cheng, "Heritage and early history of the boundary element method," *Engineering Analysis with Boundary Elements*, vol. 29, no. 3, pp. 268–302, 2005.

[90] S. Kirkup, J. Yazdani, N. Mastorakis, M. Poulos, V. Mladenov, Z. Bojkovic, D. Simian, S. Kartalopoulos, A. Varonides, and C. Udriste, "A gentle introduction to the boundary element method in matlab/freemat," in *Proceedings of the WSEAS International Conference. Proceedings. Mathematics and Computers in Science and Engineering*, no. 10, WSEAS, 2008.

[91] C. Lee and J. Newman, "Computation of wave effects using the panel method," *Numerical Models in Fluid Structure Interaction*, vol. 42, pp. 211–251, 2005.

[92] C.-H. Lee, *Numerical methods for boundary integral equations in wave body interactions*. PhD thesis, Massachusetts Institute of Technology, 1988.

[93] F. Korsmeyer, C. Lee, J. Newman, and P. Sclavounos, "The analysis of wave effects on tension-leg platforms," in *Proceedings of the 7th International Conference on Offshore Mechanics and Arctic Engineering*, pp. 1–14, 1988.

[94] Y. Li and Y.-H. Yu, "A synthesis of numerical methods for modeling wave energy converter-point absorbers," *Renewable and Sustainable Energy Reviews*, vol. 16, no. 6, pp. 4352–4364, 2012.

[95] WAMIT Inc, *WAMIT User Manual (Version 7.0)*, 2013.

[96] ANSYS Inc., "Aqwa." `http://easc.ansys.com/Products/Other+Products/ANSYS+AQWA`.

[97] ANSYS Inc., *Aqwa Theory Manual (Version 15.0)*, 2013.

[98] A. Babarit and G. Delhommeau, "Theoretical and numerical aspects of the open source BEM solver NEMOH," in *Proceedings of the 11th European Wave and Tidal Energy Conference*, 2015.

[99] A. Babarit, *ACHIL3D User Manual (Version 2.011)*. Laboratoire de Mecanique des Fluides, Ecole Centrale de Nantes, 2010.

[100] A. Clément, "Using differential properties of the green function in seakeeping computational codes," in *Proceedings of the 7th Int. Conf. Numerical Ship Hydrodynamics*, pp. 6.5.1 – 6.5.15, 1999.

[101] M. Standing, "Use of potential flow theory in evaluating wave forces on offshore structures. power from sea waves," in *Proceedings of the Conf Inst Math Appl. Academic Press*, pp. 175–212, 1980.

[102] D. Pizer, "The numerical prediction of the performance of a solo duck.," in *Proceedings of the European Wave Energy Symposium*, 1993.

[103] R. Yemm, D. Pizer, and C. Retzler, "The wpt-375–a near-shore wave energy converter submitted to scottish renewables obligation 3," in *Proceedings of the 3rd Eur Wave Energy Conf*, vol. 2, pp. 243–249, 2000.

[104] D. Pizer, C. Retzler, and R. Yemm, "The opd pelamis: experimental and numerical results from the hydrodynamic work program," in *Proceedings of 4th European wave energy conference*, pp. 227–33, 2000.

[105] M. Folley, T. Whittaker, and A. Henry, "The effect of water depth on the performance of a small surging wave energy converter," *Ocean Engineering*, vol. 34, no. 8, pp. 1265–1274, 2007.

[106] A. Brito-Melo, A. Sarmento, A. Clément, and G. Delhommeau, "Hydrodynamic analysis of geometrical design parameters of oscillating water column devices," in *Proceedings of the 3rd European Wave Energy Conference*, 1998.

[107] G. Delhommeau, P. Ferrant, and M. Guilbaud, "Calculation and measurement of forces on a high speed vehicle in forced pitch and heave," *Applied ocean research*, vol. 14, no. 2, pp. 119–126, 1992.

[108] A. Babarit, A. H. Clément, and J.-C. Gilloteaux, "Optimization and time-domain simulation of the SEAREV wave energy converter," in *Proceedings of the 24th International Conference on Offshore Mechanics and Arctic Engineering*, pp. 703–712, American Society of Mechanical Engineers, 2005.

[109] M. Ruellan, H. BenAhmed, B. Multon, C. Josset, A. Babarit, and A. Clement, "Design methodology for a SEAREV wave energy converter," *IEEE Transactions on Energy Conversion*, vol. 25, no. 3, pp. 760–767, 2010.

[110] E. Renzi and F. Dias, "Resonant behaviour of an oscillating wave energy converter in a channel," *Journal of Fluid Mechanics*, vol. 701, pp. 482–510, 2012.

[111] F. Farley, R. Rainey, and J. Chaplin, "Rubber tubes in the sea," *Phil. Trans. R. Soc. A*, vol. 370, no. 1959, pp. 381–402, 2012.

[112] D. V. Evans and F. d. O. Antonio, *Hydrodynamics of Ocean Wave-Energy Utilization: IUTAM Symposium Lisbon/Portugal 1985*. Springer Science & Business Media, 2012.

[113] D. Pizer, "Numerical prediction of the performance of a solo duck," *Report of the Edinburgh Wave Power Project, Edinburgh, UK*, 1992.

[114] G. S. Payne, J. R. Taylor, T. Bruce, and P. Parkin, "Assessment of boundary-element method for modelling a free-floating sloped wave energy device. part 2: Experimental validation," *Ocean Engineering*, vol. 35, no. 3, pp. 342–357, 2008.

[115] M. Durand, A. Babarit, B. Pettinotti, O. Quillard, J. Toularastel, and A. Clément, "Experimental validation of the performances of the SEAREV wave energy converter with real time latching control," in *Proceedings of the 7th European Wave and Tidal Energy Conference*, vol. 1113, 2007.

[116] W. Koo and M.-H. Kim, "Freely floating-body simulation by a 2D fully nonlinear numerical wave tank," *Ocean Engineering*, vol. 31, no. 16, pp. 2011–2046, 2004.

[117] E. Guerber, M. Benoit, S. Grilli, and C. Buvat, "Numerical modeling of fully nonlinear interactions of ocean waves with a submerged moving body," in *Proceedings of the 3rd International Conference on Ocean Energy*, 2010.

[118] S. Grilli, "Fully nonlinear potential flow models used for long wave runup prediction," *Chapter in Long-Wave Runup Models,(eds. H. Yeh, P. Liu, and C. Synolakis)*, pp. 116–180, 1997.

[119] M. S. Longuet-Higgins and E. Cokelet, "The deformation of steep surface waves on water. i. a numerical method of computation," in *Proceedings of the Royal Society of London A: Mathematical, Physical and Engineering Sciences*, vol. 350, pp. 1–26, The Royal Society, 1976.

[120] J. E. Romate, *The numerical simulation of nonlinear gravity waves in three dimensions using a higher order panel method*. PhD thesis, Universiteit Twente, 1989.

[121] J. Broeze, *Numerical modelling of nonlinear free surface waves with a 3D panel method*. PhD thesis, Universiteit Twente, 1993.

[122] P. Ferrant, "Radiation and diffraction of nonlinear waves in three dimensions," in *Proceedings of the 7th Intl Conf on the Behaviour of Offshore Structures*, 1994.

[123] E. Guerber, M. Benoit, S. T. Grilli, and C. Buvat, "A fully nonlinear implicit model for wave interactions with submerged structures in forced or free motion," *Engineering Analysis with Boundary Elements*, vol. 36, no. 7, pp. 1151–1163, 2012.

[124] S. T. Grilli, J. Skourup, and I. A. Svendsen, "An efficient boundary element method for nonlinear water waves," *Engineering Analysis with Boundary Elements*, vol. 6, no. 2, pp. 97–107, 1989.

[125] S. T. Grilli and R. Subramanya, "Numerical modeling of wave breaking induced by fixed or moving boundaries," *Computational Mechanics*, vol. 17, no. 6, pp. 374–391, 1996.

[126] L. Letournel, P. Ferrant, A. Babarit, G. Ducrozet, J. C. Harris, M. Benoit, and E. Dombre, "Comparison of fully nonlinear and weakly nonlinear potential flow solvers for the study of wave energy converters undergoing large amplitude motions," in *Proceedings of the 33rd International Conference on Ocean, Offshore and Arctic Engineering*, pp. V09BT09A002–V09BT09A002, American Society of Mechanical Engineers, 2014.

[127] W. Bai and R. E. Taylor, "Higher-order boundary element simulation of fully nonlinear wave radiation by oscillating vertical cylinders," *Applied Ocean Research*, vol. 28, no. 4, pp. 247–265, 2006.

[128] A. Clement *et al.*, "Dynamic nonlinear response of OWC wave energy devices," *International Journal of Offshore and Polar Engineering*, vol. 7, no. 2, 1997.

[129] W. Koo and M.-H. Kim, "Nonlinear time-domain simulation of a land-based oscillating water column," *Journal of waterway, port, coastal, and ocean engineering*, vol. 136, no. 5, pp. 276–285, 2010.

[130] W. Koo and S. Kim, "Nonlinear time-domain simulation of backward bent duct buoy (bbdb) floating wave energy converter," in *Proceedings of the 10th European Wave and Tidal Energy Conference*, 2013.

[131] W. Koo, K.-R. Lee, *et al.*, "Numerical and experimental analysis of backward bent duct buoy (BBDB) wave energy converter," in *Proceedings of the 21st International Offshore and Polar Engineering Conference*, International Society of Offshore and Polar Engineers, 2011.

[132] W. Bai and R. E. Taylor, "Numerical simulation of fully nonlinear regular and focused wave diffraction around a vertical cylinder using domain decomposition," *Applied Ocean Research*, vol. 29, no. 1, pp. 55–71, 2007.

[133] W. Bai and R. E. Taylor, "Fully nonlinear simulation of wave interaction with fixed and floating flared structures," *Ocean Engineering*, vol. 36, pp. 223–236, 2009.

[134] P. D. Siddorn, *Efficient numerical modelling of wave-structure interaction*. PhD thesis, University of Oxford, 2012.

[135] M. Kashiwagi, "Non-linear simulations of wave-induced motions of a floating body by means of the mixed eulerian-lagrangian method," *Proceedings of the Institution of Mechanical Engineers, Part C: Journal of Mechanical Engineering Science*, vol. 214, no. 6, pp. 841–855, 2000.

[136] W. Cummins, "The impulse response function and ship motions," tech. rep., DTIC Document, 1962.

[137] T. F. Ogilvie, "Recent progress toward the understanding and prediction of ship motions," in *Proceedings of the 5th Symposium on naval hydrodynamics*, vol. 1, pp. 2–5, Bergen, Norway, 1964.

[138] Furuta, Sano, and Atherton, *State Variables Methods in Automatic Control*. John Wiley & Sons, New York, USA, 1988.

[139] K. Ogata, *Modern Control Engineering*. Instrumentation and controls series, Prentice Hall, 2010.

[140] K. Ogata, *System Dynamics*. Pearson Education, 2004.

[141] R. Isermann and M. Mnchhof, *Identification of Dynamic Systems, An Introduction with Applications*. Springer-Verlag Berlin Heidelberg, 2011.

[142] T. Ogunfunmi, *Adaptive Nonlinear System Identification: The Volterra and Wiener Model Approaches*. Signals and Communication Technology, Springer US, 2007.

[143] R. Stefani, *Design of Feedback Control Systems*. Oxford series in electrical and computer engineering, Oxford University Press, 2002.

[144] T. Kailath, *Linear Systems*. Prentice Hall, Inc, Englewood Cliffs, N.J., USA, 1980.

[145] K. Aström and R. Murray, *Feedback Systems: An Introduction for Scientists and Engineers*. Princeton University Press, 2010.

[146] A. Roessling and J. Ringwood, "Finite order approximations to radiation forces for wave energy applications," in *Proceedings of the 1st International Conference on Renewable Energies Offshore*, 2014.

[147] F. Hildebrand, *Introduction to Numerical Analysis*. Dover books on advanced mathematics, Dover Publications, 1987.

[148] S. Singh, *Application of prony analysis to characterize pulsed corona reactor measurements*. PhD thesis, The University of Wyoming, 2003.

[149] T. Verbrugghe, A. Nicolini, A. Kortenhaus, and L. Cappietti, "New results on hydrodynamic response of generic point-absorber wave energy converters," in *Proceedings of the 11th European Wave and Tidal Energy Conference*, 2015.

[150] C. Josset, A. Babarit, and A. Clément, "A wave-to-wire model of the SEAREV wave energy converter," *Proceedings of the institution of mechanical engineers, Part M: Journal of Engineering for the Maritime Environment*, vol. 221, no. 2, pp. 81–93, 2007.

[151] A. Babarit, A. Clement, J. Ruer, and C. Tartivel, "SEAREV: A fully integrated wave energy converter," in *Proceedings of the OWEMES*, vol. 9, 2006.

[152] S. Sutulo and C. G. Soares, "An implementation of the method of auxiliary state variables for solving seakeeping problems," *International shipbuilding progress*, vol. 52, no. 4, pp. 357–384, 2005.

[153] C. J. Damaren, "Time-domain floating body dynamics by rational approximation of the radiation impedance and diffraction mapping," *Ocean Engineering*, vol. 27, no. 6, pp. 687–705, 2000.

[154] K. E. Kaasen and K. Mo, "Efficient time-domain model for frequency-dependent added mass and damping," in *Proceedings of the 23rd International Conference on Offshore Mechanics and Arctic Engineering*, pp. 885–891, American Society of Mechanical Engineers, 2004.

[155] T. Perez and T. I. Fossen, "A matlab toolbox for parametric identification of radiation-force models of ships and offshore structures," *Modeling, Identification and Control*, vol. 30, no. 1, pp. 1–15, 2009.

[156] "MSS: Marine systems simulator." `http://www.marinecontrol.org/`.

[157] T. Perez and T. I. Fossen, "Identification of dynamic models of marine structures from frequency-domain data enforcing model structure and parameter constraints," *ARC Centre of Excellence for Complex Dynamic Systems and Control*, pp. 1–28, 2009.

[158] E. Kristiansen and O. Egeland, "Frequency-dependent added mass in models for controller design for wave motion damping," *Proc. 6th MCMC*, 2003.

[159] E. Kristiansen, Å. Hjulstad, and O. Egeland, "State-space representation of radiation forces in time-domain vessel models," *Ocean Engineering*, vol. 32, no. 17, pp. 2195–2216, 2005.

[160] M. Schmiechen, "On state space models and their application to hydrodynamic systems," tech. rep., NAUT Report 5002, Department of Naval Architecture, University of Tokyo, 1973.

[161] T. Booth, "Identifying the marine vehicle from the pulse response," *NASA STI/Recon Technical Report N*, vol. 80, p. 17347, 1975.

[162] Ø. Y. Rogne, *Numerical and Experimental Investigation of a Hinged 5-Body Wave Energy Converter*. PhD thesis, University of Science and Technology, 2014.

[163] Yu and Falnes, "State space modelling of dynamic systems in ocean engineering," *Journal of Hydrodynamic*, vol. 1, pp. 1–17, 1998.

[164] C. Signorelli, C. Villegas, and J. Ringwood, "Hardware-in-the-loop simulation of a heaving wave energy converter," in *Proceedings of the 9th European Wave and Tidal Energy Conference*, 2011.

[165] J. A. Armesto, R. Guanche, A. Iturrioz, C. Vidal, and I. J. Losada, "Identification of state-space coefficients for oscillating water columns using temporal series," *Ocean Engineering*, vol. 79, pp. 43–49, 2014.

[166] M. Lopes, J. Hals, R. Gomes, T. Moan, L. Gato, and A. d. O. Falcão, "Experimental and numerical investigation of non-predictive phase-control strategies for a point-absorbing wave energy converter," *Ocean Engineering*, vol. 36, no. 5, pp. 386–402, 2009.

[167] Ø. Y. Rogne, T. Moan, and S. Ersdal, "Identification of passive state-space models of strongly frequency dependent wave radiation forces," *Ocean Engineering*, vol. 92, pp. 114–128, 2014.

[168] M. Retes and J. V. Ringwood, "A review of wave-to-wire models for wave energy converters," *Energies*, vol. 9, no. 506, pp. 1–45, 2016.

[169] P. M. Retes, G. Giorgi, and J. Ringwood, "A review of non-linear approaches for wave energy converter modelling," in *Proceedings of the 11th European Wave and Tidal Energy Conference*, 2015.

[170] G. Giorgi and J. V. Ringwood, "Computationally efficient nonlinear Froude–Krylov force calculations for heaving axisymmetric wave energy point absorbers," *Journal of Ocean Engineering and Marine Energy*, vol. 1, no. 3, pp. 21–33, 2016.

[171] O. Dalane, F. F. Knutsen, and S. Loset, "Nonlinear coupled hydrostatics of floating conical platforms," in *Proceedings of the 28th International Conference on Ocean, Offshore and Arctic Engineering*, pp. 793–802, American Society of Mechanical Engineers, 2009.

[172] Y. Cao, G. Tahchiev, F. Zhang, J. V. Aarsnes, and E. B. Glomnes, "Effects of hydrostatic nonlinearity on motions of floating structures," in *Proceedings of the 29th International Conference on Ocean, Offshore and Arctic Engineering*, pp. 257–267, American Society of Mechanical Engineers, 2010.

[173] M. Lawson, Y.-H. Yu, A. Nelessen, K. Ruehl, and C. Michelen, "Implementing nonlinear buoyancy and excitation forces in the WEC-Sim wave energy converter modeling tool," in *Proceedings of the 33rd International Conference on Ocean, Offshore and Arctic Engineering*, pp. V09BT09A043–V09BT09A043, American Society of Mechanical Engineers, 2014.

[174] J.-C. Gilloteaux, *Mouvements de grande amplitude d'un corps flottant en fluide parfait. Application à la récupération de l'énergie des vagues.* PhD thesis, Ecole Centrale de Nantes, 2007.

[175] M. P. Retes, A. Mérigaud, J.-C. Gilloteaux, and J. V. Ringwood, "Nonlinear froude-krylov force modelling for two heaving wave energy point absorbers," in *Proceedings of the 9th European Wave and Tidal Energy Conference*, 2015.

[176] G. Giorgi, M. P. Retes, and J. V. Ringwood, "Nonlinear hydrodynamic models for heaving buoy wave energy converters," in *Proceedings of the 3rd Asian Wave and Tidal Energy Conference*, 2016.

[177] G. Giorgi and V. J. Ringwood, "Consistency of viscous drag identification tests for wave energy applications," in *Proceedings of the 12th European Wave and Tidal Energy Conference*, 2017.

[178] K. Horikawa and H. Maruo, *Nonlinear Water Waves: IUTAM Symposium, Tokyo/Japan, August 25–28, 1987*. IUTAM Symposia, Springer Berlin Heidelberg, 2012.

[179] A. Babarit, J. Hals, M. Muliawan, A. Kurniawan, T. Moan, and J. Krokstad, "Numerical benchmarking study of a selection of wave energy converters," *Renewable Energy*, vol. 41, pp. 44–63, 2012.

[180] J. Morison, J. Johnson, S. Schaaf, *et al.*, "The force exerted by surface waves on piles," *Journal of Petroleum Technology*, vol. 2, no. 5, pp. 149–154, 1950.

[181] T. Sarpkaya, *Wave Forces on Offshore Structures*. Wave Forces on Offshore Structures, Cambridge University Press, 2010.

[182] M. M. Jakobsen, S. Beatty, G. Iglesias, and M. M. Kramer, "Characterization of loads on a hemispherical point absorber wave energy converter," *International Journal of Marine Energy*, vol. 13, pp. 1–15, 2016.

[183] M. Folley, T. Whittaker, and J. Vant Hoff, "The design of small seabed-mounted bottom-hinged wave energy converters," in *Proceedings of the 7th European Wave and Tidal Energy Conference*, 2007.

[184] A. F. Davis, J. Thomson, T. R. Mundon, and B. C. Fabien, "Modeling and analysis of a multi degree of freedom point absorber wave energy converter," in *Proceedings of the 33rd International Conference on Ocean, Offshore and Arctic Engineering*, pp. V08AT06A046–V08AT06A046, American Society of Mechanical Engineers, 2014.

[185] S. Jin, B. Guo, R. Patton, J. Gilbert, and M. Abdelrahman, "Non-linear analysis of a point absorber wave energy converter," 2016.

[186] J. H. Bettencourt and F. Dias, "Analysis of vorticity dynamics in oscillating flows at low keulegan-carpenter numbers," *Proceedings of the 11th European Wave and Tidal Energy Conference*, 2015.

[187] M. A. Bhinder, *3D Non-linear Numerical Hydrodynamic Modelling of Floating Wave Energy Converters*. PhD thesis, Ecole Centrale de Nantes, 2013.

[188] M. A. Bhinder, A. Babarit, L. Gentaz, and P. Ferrant, "Effect of viscous forces on the performance of a surging wave energy converter," *Proceedings of ISOPE2012*, pp. 545–549, 2012.

[189] M. A. Bhinder, A. Babarit, L. Gentaz, and P. Ferrant, "Assessment of viscous damping via 3D-CFD modelling of a floating wave energy device," in *Proceedings of the 9th European Wave and Tidal Energy Conference*, 2011.

[190] S. Atluri, A. Magee, and K. Lambrakos, "CFD as a design tool for hydrodynamic loading on offshore structures," in *Proceedings of the 28th International Conference on Ocean, Offshore and Arctic Engineering*, pp. 499–507, American Society of Mechanical Engineers, 2009.

[191] R. Pintelon, P. Guillaume, Y. Rolain, J. Schoukens, and H. Van Hamme, "Parametric identification of transfer functions in the frequency domain-a survey," *IEEE Transactions on Automatic Control*, vol. 39, no. 11, pp. 2245–2260, 1994.

[192] R. Pintelon and J. Schoukens, *System Identification: A Frequency Domain Approach*. Wiley, 2012.

[193] Q. Meng, Y. Guan, and A. Xie, "A review of CFD-based system identification," in *Proceedings of the Chinese Control and Decision Conference*, 2011.

[194] A. Chicatelli, T. T. Hartley, G. Cole, and K. Melcher, "Interdisciplinary modeling using computational fluid dynamics and control theory," in *Proceedings of the American Control Conference*, vol. 3, pp. 3438–3443, IEEE, 1994.

[195] T. Z. Desta, K. Janssens, A. Van Brecht, J. Meyers, M. Baelmans, and D. Berckmans, "CFD for model-based controller development," *Building and Environment*, vol. 39, no. 6, pp. 621–633, 2004.

[196] T. Z. Desta, A. Van Brecht, J. Meyers, M. Baelmans, and D. Berckmans, "Combining CFD and data-based mechanistic (dbm) modelling approaches," *Energy and Buildings*, vol. 36, no. 6, pp. 535–542, 2004.

[197] T. Z. Desta, A. Van Brecht, J. Meyers, M. Baelmans, and D. Berckmans, "Numerical simulation and controller development for energy transfer in imperfectly mixed fluids," *Indoor and Built Environment*, vol. 14, no. 5, pp. 371–380, 2005.

[198] Y. Yang, M. A. Reuter, and D. T. Hartman, "CFD modelling for control of hazardous waste incinerator," *Control Engineering Practice*, vol. 11, no. 1, pp. 93–101, 2003.

[199] A. Gerber, R. Dubay, and A. Healy, "CFD-based predictive control of melt temperature in plastic injection molding," *Applied mathematical modelling*, vol. 30, no. 9, pp. 884–903, 2006.

[200] M. A. Rizzo, M. A. Santillo, A. K. Padthe, J. B. Hoagg, S. Akhtar, K. Powell, and D. S. Bernstein, "CFD-based adaptive flow control using armarkov disturbance rejection," in *Proceedings of the American Control Conference*, pp. 6–pp, IEEE, 2006.

[201] Q. Meng, Y. Guan, and X. Yan, "CFD-based system identification method for controlled system involved of fluid flow and heat/mass transfer," in *Proceedings of the Chinese Control and Decision Conference*, pp. 3274–3279, IEEE, 2011.

[202] M. Araki, H. Sadat-Hosseini, Y. Sanada, K. Tanimoto, N. Umeda, and F. Stern, "Estimating maneuvering coefficients using system identification methods with experimental, system-based, and CFD free-running trial data," *Ocean Engineering*, vol. 51, pp. 63–84, 2012.

[203] T. J. Cowan, A. S. Arena, and K. K. Gupta, "Accelerating computational fluid dynamics based aeroelastic predictions using system identification," *Journal of Aircraft*, vol. 38, no. 1, pp. 81–87, 2001.

[204] L. Ljung, *System Identification: Theory for the User (2nd Edition)*. Prentice Hall PTR, Upper Saddle River, NJ, USA, 1999.

[205] O. Nelles, *Nonlinear System Identification: From Classical Approaches to Neural Networks and Fuzzy Models*. Springer, Berlin Heidelberg, Germany, 2001.

[206] Y. Nievergelt, "A tutorial history of least squares with applications to astronomy and geodesy," *Journal of Computational and Applied Mathematics*, vol. 121, no. 1, pp. 37–72, 2000.

[207] L. Ljung, "Perspectives on system identification," *Annual Reviews in Control*, vol. 34, no. 1, pp. 1–12, 2010.

[208] G. Gkikas and G. Athanassoulis, "Development of a novel nonlinear system identification scheme for the pressure fluctuation inside an oscillating water column-wave energy converter part i: Theoretical background and harmonic excitation case," *Ocean Engineering*, vol. 80, pp. 84–99, 2014.

[209] I. López and G. Iglesias, "Efficiency of OWC wave energy converters: A virtual laboratory," *Applied Ocean Research*, vol. 44, pp. 63–70, 2014.

[210] F. Paparella, K. Monk, V. Winands, M. Lopes, D. Conley, and J. V. Ringwood, "Up-wave and autoregressive methods for short-term wave forecasting for an oscillating water column," *IEEE Transactions on Sustainable Energy*, vol. 6, no. 1, pp. 171–178, 2015.

[211] F. Paparella, K. Monk, V. Winands, M. Lopes, D. Conley, and J. V. Ringwood, "Benefits of up-wave measurements in linear short-term wave forecasting for wave energy applications," in *Proceedings of the IEEE Conference on Control Applications*, pp. 2048–2053, IEEE, 2014.

[212] R. G. Coe, G. Bacelli, D. Patterson, and D. G. Wilson, "Sand2016-10094 - advanced WEC dynamics & controls fy16 testing report," tech. rep., Sandia National Laboratories, 2016.

[213] G. Bacelli, R. G. Coe, D. Patterson, and D. Wilson, "System identification of a heaving point absorber: Design of experiment and device modeling," *Energies*, vol. 10, no. 4, p. 472, 2017.

[214] T. Soderstrom and P. Stoica, *System Identification*. Prentice Hall, Upper Saddle River, NJ, USA, 1989.

[215] E. Ikonen and K. Najim, *Advanced Process Identification and Control*. Automation and Control Engineering, Taylor & Francis, 2001.

[216] I. Landau and G. Zito, *Digital Control Systems: Design, Identification and Implementation*. Communications and Control Engineering, Springer London, 2007.

[217] O. Nelles and R. Isermann, "Identification of nonlinear dynamic systems classical methods versus radial basis function networks," in *Proceedings of the American Control Conference*, vol. 5, pp. 3786–3790, IEEE, 1995.

[218] J. Schoukens and R. R. Pintelon, *Identification of Linear Systems, A Practical Guideline to Accurate Modeling*. Pergamon Press, 1991.

[219] G. Strang, *Introduction to Linear Algebra*. Wellesley-Cambridge Press, 2003.

[220] K. J. Åström and P. Eykhoff, "System identificationa survey," *Automatica*, vol. 7, no. 2, pp. 123–162, 1971.

[221] S. Billings, *Nonlinear System Identification: NARMAX Methods in the Time, Frequency, and Spatio-Temporal Domains*. Wiley, 2013.

[222] D. Manolakis, V. Ingle, and S. Kogon, *Statistical and Adaptive Signal Processing: Spectral Estimation, Signal Modeling, Adaptive Filtering, and Array Processing*. Artech House signal processing library, Artech House, 2005.

[223] A. Papoulis and S. Pillai, *Probability, Random Variables and Stochastic Processes with Errata Sheet*. McGraw-Hill Series in Electrical and Computer Engineering, McGraw-Hill, 2001.

[224] D. Westwick and R. Kearney, *Identification of Nonlinear Physiological Systems*. Biomedical Engineering, IEEE press, John Wiley & Sons, Inc., 2003.

[225] Box, Jenkins, and Reinsel, *Time series analysis, forecasting and control*. Prentice Hall, Upper Saddle River, NJ, USA, 1994.

[226] K. Burnham and D. Anderson, *Model Selection and Inference: A Practical Information-Theoretic Approach*. Springer New York, 2013.

[227] M. Jelali and A. Kroll, *Hydraulic servo-systems: modelling, identification and control*. Springer Science & Business Media, 2012.

[228] W. S. Levine, ed., *The Control Systems Handbook: Control System Advanced Methods (2nd Edition)*. CRC Press, Boca Raton, Florida, USA, 2010.

[229] H. Unbehauen and G. Rao, "A review of identification in continuous-time systems," *Annual reviews in Control*, vol. 22, pp. 145–171, 1998.

[230] G. Rao and H. Unbehauen, "Identification of continuous-time systems," *IEE Proceedings-Control Theory and Applications*, vol. 153, no. 2, pp. 185–220, 2006.

[231] H. Garnier and L. Wang, *Identification of Continuous-time Models from Sampled Data*. Advances in Industrial Control, Springer London, 2008.

[232] R. K. Pearson, "Nonlinear input/output modelling," *Journal of Process Control*, vol. 5, no. 4, pp. 197–211, 1995.

[233] J. Abonyi and B. Feil, *Cluster Analysis for Data Mining and System Identification*. Birkhäuser Basel, 2007.

[234] J. Paduart, L. Lauwers, J. Swevers, K. Smolders, J. Schoukens, and R. Pintelon, "Identification of nonlinear systems using polynomial nonlinear state space models," *Automatica*, vol. 46, no. 4, pp. 647–656, 2010.

[235] Y. Li and A. Kareem, "Parametric modelling of stochastic wave effects on offshore platforms," *Applied Ocean Research*, vol. 15, no. 2, pp. 63–83, 1993.

[236] F. Fusco and J. V. Ringwood, "Short-term wave forecasting for real-time control of wave energy converters," *IEEE Transactions on Sustainable Energy*, vol. 1, no. 2, pp. 99–106, 2010.

[237] J. A. Cretel, G. Lightbody, G. P. Thomas, and A. W. Lewis, "Maximisation of energy capture by a wave-energy point absorber using model predictive control," *IFAC Proceedings Volumes*, vol. 44, no. 1, pp. 3714–3721, 2011.

[238] T. Hastie, R. Tibshirani, and J. Friedman, *The Elements of Statistical Learning: Data Mining, Inference, and Prediction (2nd Edition)*. Springer Series in Statistics, Springer New York, 2009.

[239] F. Giri and E.-W. Bai, *Block-oriented Nonlinear System Identification*. Springer, Berlin Heidelberg, Germany, 2010.

[240] R. K. Pearson and M. Pottmann, "Gray-box identification of block-oriented nonlinear models," *Journal of Process Control*, vol. 10, pp. 301–315, 2000.

[241] E.-W. Bai, "Decoupling the linear and nonlinear parts in Hammerstein model identification," *Automatica*, vol. 40, pp. 671–676, 2003.

[242] J. G. Proakis and D. G. Manolakis, *Digital Signal Processing, Principles Algorithms and Applications (4th Edition)*. Pearson Prentice Hall, Upper Saddle River, NJ, US, 2006.

[243] A. Janczak, *Identification of Nonlinear Systems Using Neural Networks and Polynomial Models: A Block-Oriented Approach*. Lecture Notes in Control and Information Sciences, Springer Berlin Heidelberg, 2009.

[244] H. Beale, Mark, T. Hagan, Martin, and B. Demuth, Howard, *MATLAB: Neural Network Toolbox, User's Guide*. MathWorks, Natick, Massachusetts, USA, 2014.

[245] M. T. Hagan, H. B. Demuth, and M. H. Beale, *Neural network design*. Pws Pub. Boston, 1996.

[246] K. Hornik, M. Stinchcombe, and H. White, "Multilayer feedforward networks are universal approximators," *Neural networks*, vol. 2, no. 5, pp. 359–366, 1989.

[247] L. Ljung, *MATLAB: System Identification Toolbox, User's Guide*. MathWorks, Natick, Massachusetts, USA, 2013.

[248] K. J. Keesman, *System Identification An Introduction*. Springer, 2011.

[249] Y. Chetouani, "Using ARX approach for modelling and prediction of the dynamics of a reactor-exchanger," in *Proceedings of the Institution of Chemical Engineers Symposium Series*, vol. 154, pp. 1–9, 2008.

[250] J. Ringwood, P. Austin, and W. Monteith, "Forecasting weekly electricity consumption: A case study," *Energy economics*, vol. 15, no. 4, pp. 285–296, 1993.

[251] G. Golub and C. Van Loan, *Matrix Computations (4th Edition)*. Matrix Computations, Johns Hopkins University Press, Baltimore, Maryland, USA, 2012.

[252] J. Feldman and R. Rojas, *Neural Networks: A Systematic Introduction*. Springer Berlin Heidelberg, 1996.

[253] N. Draper and H. Smith, *Applied regression analysis*. No. v. 1 in Wiley series in probability and statistics: Texts and references section, Wiley, 1998.

[254] J. R. Shewchuk, "An introduction to the conjugate gradient method without the agonizing pain," 1994.

[255] S. Boyd and L. Vandenberghe, *Convex optimization*. Cambridge University Press, 2004.

[256] J. Norton, *An Introduction to Identification*. Dover Books on Electrical Engineering Series, Dover Publications, 2009.

[257] T. Sauer, *Numerical Analysis*. Pearson Education, NY, USA, 2012.

[258] G. Stewart, *Matrix Algorithms: Volume 1: Basic Decompositions*. Society for Industrial and Applied Mathematics, 1998.

[259] E. Eskinat, S. H. Johnson, and W. L. Luyben, "Use of hammerstein models in identification of nonlinear systems," *AIChE Journal*, vol. 37, no. 2, pp. 255–268, 1991.

[260] K. Narendra and P. Gallman, "An iterative method for the identification of nonlinear systems using a hammerstein model," *IEEE Transactions on Automatic Control*, vol. 11, no. 3, pp. 546–550, 1966.

[261] J. Arora, *Introduction to Optimum Design*. Elsevier Science & Technology Books, 2016.

[262] D. Luenberger and Y. Ye, *Linear and Nonlinear Programming*. International Series in Operations Research & Management Science, Springer US, 2008.

[263] R. Fletcher, *Practical Methods of Optimization*. Wiley, 2013.

[264] S. Koziel and X. Yang, *Computational Optimization, Methods and Algorithms*. Studies in Computational Intelligence, Springer Berlin Heidelberg, 2011.

[265] J. Nocedal and S. Wright, *Numerical Optimization*. Springer Series in Operations Research and Financial Engineering, Springer New York, 2006.

[266] T. Mitchell, *Machine Learning*. McGraw-Hill, 1997.

[267] A. Conn, N. Gould, and P. Toint, *Trust Region Methods*. MPS-SIAM Series on Optimization, Society for Industrial and Applied Mathematics, 2000.

[268] T. Steihaug, "The conjugate gradient method and trust regions in large scale optimization," *SIAM Journal on Numerical Analysis*, vol. 20, no. 3, pp. 626–637, 1983.

[269] W. Press, *Numerical Recipes: The Art of Scientific Computing (3rd Edition)*. Cambridge University Press, 2007.

[270] D. Goldberg, *Genetic Algorithms in Search, Optimization, and Machine Learning*. Artificial Intelligence, Addison-Wesley Publishing Company, 1989.

[271] Z. Michalewicz, *Genetic Algorithms + Data Structures = Evolution Programs*. Artificial Intelligence, Springer Berlin Heidelberg, 2013.

[272] *Genetic Algorithm and Direct Search Toolbox, For Use with MATLAB*. MathWorks, Natick, Massachusetts, USA, 2004.

[273] D. Coley, *An Introduction to Genetic Algorithms for Scientists and Engineers*. World Scientific, 1999.

[274] M. F. Møller, "A scaled conjugate gradient algorithm for fast supervised learning," *Neural networks*, vol. 6, no. 4, pp. 525–533, 1993.

[275] Ö. Kişi and E. Uncuoglu, "Comparison of three back-propagation training algorithms for two case studies," *Indian journal of engineering & materials sciences*, vol. 12, no. 5, pp. 434–442, 2005.

[276] C. Charalambous, "Conjugate gradient algorithm for efficient training of artificial neural networks," *IEE Proceedings G-Circuits, Devices and Systems*, vol. 139, no. 3, pp. 301–310, 1992.

[277] U. Seiffert and B. Michaelis, "On the gradient descent in backpropagation and its substitution by a genetic algorithm," in *Proceedings of the IASTED International Conference Applied Informatics*, pp. 821–826, Citeseer, 2000.

[278] L. Ljung, "Some aspects on nonlinear system identification," *IFAC Proceedings Volumes*, vol. 39, no. 1, pp. 110–121, 2006.

[279] S. Makridakis and M. Hibon, *Evaluating Accuracy (or Error) Measures*. INSEAD working paper, INSEAD, 1995.

[280] L. Ljung and T. Glad, *Modeling of Dynamic Systems*. Prentice-Hall information and system sciences series, PTR Prentice Hall, 1994.

[281] E. O. Brigham, *The Fast Fourier Transform and Its Applications*. Prentice Hall, Upper Saddle River, NJ, USA, 1988.

[282] V. Marmarelis, *Analysis of Physiological Systems: The White-Noise Approach*. Computers in Biology and Medicine, Springer US, 2012.

[283] M. A. Vázquez and O. Agamennoni, "Approximate models for nonlinear dynamical systems and their generalization properties," *Mathematical and computer modelling*, vol. 33, no. 8, pp. 965–986, 2001.

[284] I. Leontaritis and S. Billings, "Model selection and validation methods for non-linear systems," *International Journal of Control*, vol. 45, no. 1, pp. 311–341, 1987.

[285] A. Oppenheim and R. Schafer, *Discrete-time Signal Processing (2nd Edition)*. Prentice Hall, Upper Saddle River, NJ, USA, 1999.

[286] G. Franklin, J. Powell, and M. Workman, *Digital control of dynamic systems*. Addison-Wesley world student series, Addison Wesley Longman, 1998.

[287] R. Easton, *Fourier Methods in Imaging*. The Wiley-IS&T Series in Imaging Science and Technology, Wiley, 2010.

[288] A. Piersol and T. Paez, *Harris' Shock and Vibration Handbook*. McGraw-Hill handbooks, McGraw-Hill Education, 2009.

[289] J. Thompson and H. Stewart, *Nonlinear Dynamics and Chaos*. Wiley, 2002.

[290] G. Baker and J. Blackburn, *The Pendulum: A Case Study in Physics*. OUP Oxford, 2005.

[291] F. Fusco, *Real-time Forecasting and Control for Oscillating Wave Energy Devices*. PhD thesis, Maynooth University, 2012.

[292] J. Juang and M. Phan, *Identification and Control of Mechanical Systems*. Cambridge University Press, 2001.

[293] U. Korde and J. Ringwood, *Hydrodynamic Control of Wave Energy Devices*. Cambridge University Press, 2016.

[294] J. Bendat and A. Piersol, *Random Data: Analysis and Measurement Procedures*. Wiley Series in Probability and Statistics, Wiley, 2011.

[295] A. De Andres, R. Guanche, J. Armesto, F. Del Jesus, C. Vidal, and I. Losada, "Time domain model for a two-body heave converter: Model and applications," *Ocean Engineering*, vol. 72, pp. 116–123, 2013.

[296] W. S. Levine, ed., *The Control Handbook: Control System Fundamental (2nd Edition)*. CRC Press, 2011.

[297] A. Fiacco and G. McCormick, *Nonlinear Programming: Sequential Unconstrained Minimization Techniques*. Classics in Applied Mathematics, Society for Industrial and Applied Mathematics, Philadelphia, US, 1990.

[298] P. Venkataraman, *Applied Optimization with MATLAB Programming*. Wiley, 2009.

[299] A. Conn, N. Gould, and P. Toint, "A globally convergent lagrangian barrier algorithm for optimization with general inequality constraints and simple bounds," *Mathematics of Computation of the American Mathematical Society*, vol. 66, no. 217, pp. 261–288, 1997.

[300] *MATLAB: Global Optimization Toolbox, User's Guide*. MathWorks,, 2015.

[301] J. Ringwood, G. Bacelli, and F. Fusco, "Energy-maximizing control of wave-energy converters: The development of control system technology to optimize their operation," *IEEE Control Systems Magazine*, vol. 34, no. 5, pp. 30–55, 2014.

[302] K. Hasselmann, T. Barnett, E. Bouws, H. Carlson, D. Cartwright, K. Enke, J. Ewing, H. Gienapp, D. Hasselmann, P. Kruseman, *et al.*, "Measurements of wind-wave growth and swell decay during the joint north sea wave project (JONSWAP)," tech. rep., Deutches Hydrographisches Institut, 1973.

[303] D. Zwillinger, *CRC Standard Mathematical Tables and Formulae (32nd Edition)*. Advances in Applied Mathematics, CRC Press, 2011.

[304] G. Giorgi, M. Penalba, and J. Ringwood, "Nonlinear hydrodynamic force relevance for heaving point absorber and oscillating surge converters," in *Proceedings of the Asian Wave and Tidal Energy Conference*, 2016.

[305] J. W. Kim, H. Jang, A. Baquet, J. O'Sullivan, S. Lee, B. Kim, A. Read, and H. Jasak, "Technical and economic readiness review of CFD-based numerical wave basin for offshore floater design," in *Proceedings of the Offshore Technology Conference*, Offshore Technology Conference, 2016.

[306] "Marine renewables infrastructure network," tech. rep., Marinet, 2015.

[307] Wavestar. `http://wavestarenergy.com/`.

[308] G. Payne, "Guidance for the experimental tank testing of wave energy converters," tech. rep., University of Edinburgh, 2008.

[309] A. Maguire and D. Ingram, "Hydrodynamics and absorption efficiencies of wavemakers," in *Proceedings of the 8th European Wave and Tidal Energy Conference*, 2009.

[310] H. J. Berendsen, *A student's guide to data and error analysis*. Cambridge University Press, 2011.

[311] "Deliverable d3.4 best practice for tank testing of small marine energy device (deliverable d3.4)," tech. rep., Equimar, 2010.

[312] M. Cable, *Calibration: A Technician's Guide*. ISA technician series, ISA, 2005.

[313] "Tank test related instrumentation and best practice (deliverable 4.01ec)," tech. rep., Marinet, 2014.

[314] J. Lawrence, B. Holmes, I. Bryden, D. Magagna, Y. Torre-Enciso, J.-M. Rousset, and H. Smith, "D2.1 wave instrumentation database," tech. rep., Marinet, 2012.

[315] "Coastal ocean and sediment transport (COAST) laboratory." `https://www.plymouth.ac.uk/research/institutes/marine-institute/coast-laboratory`.

[316] M. Jakobsen, "Technical report on wave-structure interactions on point absorbe," tech. rep., Aalborg University, 2014.

[317] M. Jakobsen, *Wave-Structure Interactions on Point Absorbers - an experimental study*. PhD thesis, Aalborg University, 2015.

[318] R. H. Hansen and M. M. Kramer, "Modelling and control of the wavestar prototype," in *Proceedings of the 9th European Wave and Tidal Energy Conference*, 2011.

[319] W. LePage, *Complex Variables and the Laplace Transform for Engineers*. Dover Books on Electrical Engineering, Dover Publications Inc., New York, US, 1980.

[320] A. Grove, *An introduction to the Laplace transform and the Z-transform*. Prentice Hall International, Hemel Hempstead, UK, 1991.

[321] Z. Karu, *Signals and Systems*. ZiZi Press, Huntsville, Alabama, US, 2001.

[322] K. Stroud and D. Booth, *Advanced Engineering Mathematics (Fourth edition)*. Palgrave Macmillan, New York, US, 2003.

[323] A. Snider, *Partial Differential Equations: Sources and Solutions*. Advances in Interfacial Engineering, Prentice Hall, Upper Saddle River, US, 1999.

[324] J. Bak and D. Newman, *Complex Analysis*. Undergraduate Texts in Mathematics, Springer New York, 2010.

[325] L. Ahlfors, *Complex Analysis (2nd Edition)*. International Series in Pure & Applied Mathematics, McGraw-Hill, Inc. New York, 1966.

[326] H. M. Power and R. J. Simpson, *Introduction to dynamics and control*. McGraw-Hill, New York, USA, 1978.